Advances in
Quantum Chemistry

Volume 59

EDITORIAL BOARD

Guillermina Estiú (University Park, PA, USA)
Frank Jensen (Aarhus, Denmark)
Mel Levy (Greensboro, NC, USA)
Jan Linderberg (Aarhus, Denmark)
William H. Miller (Berkeley, CA, USA)
John W. Mintmire (Stillwater, OK, USA)
Manoj Mishra (Mumbai, India)
Jens Oddershede (Odense, Denmark)
Josef Paldus (Waterloo, Canada)
Pekka Pyykkö (Helsinki, Finland)
Mark Ratner (Evanston, IL, USA)
Dennis R. Salahub (Calgary, Canada)
Henry F. Schaefer III (Athens, GA, USA)
John Stanton (Austin, TX, USA)
Harel Weinstein (New York, NY, USA)

Advances in QUANTUM CHEMISTRY

COMBINING QUANTUM MECHANICS AND MOLECULAR MECHANICS. SOME RECENT PROGRESSES IN QM/MM METHODS

VOLUME 59

Editors

JOHN R. SABIN
Quantum Theory Project
University of Florida
Gainesville, Florida

ERKKI BRÄNDAS
Department of Quantum Chemistry
Uppsala University
Uppsala, Sweden

Special Editor

SYLVIO CANUTO
Instituto de Física
Universidade de São Paulo
Brazil

ELSEVIER

Amsterdam • Boston • Heidelberg • London • New York • Oxford
Paris • San Diego • San Francisco • Singapore • Sydney • Tokyo

Academic Press is an imprint of Elsevier

Academic Press is an imprint of Elsevier
Linacre House, Jordan Hill, Oxford OX2 8DP, UK
32 Jamestown Road, London NW1 7BY, UK
Radarweg 29, PO Box 211, 1000 AE Amsterdam, The Netherlands
30 Corporate Drive, Suite 400, Burlington, MA 01803, USA
525 B Street, Suite 1900, San Diego, CA 92101-4495, USA

First edition 2010

Copyright © 2010, Elsevier Inc. All rights reserved

No part of this publication may be reproduced, stored in a retrieval system or transmitted in any form or by any means electronic, mechanical, photocopying, recording or otherwise without the prior written permission of the publisher

Permissions may be sought directly from Elsevier's Science & Technology Rights Department in Oxford, UK: phone (+44) (0) 1865 843830; fax (+44) (0) 1865 853333; email: permissions@elsevier.com. Alternatively you can submit your request online by visiting the Elsevier web site at http://www.elsevier.com/locate/permissions, and selecting: *Obtaining permission to use Elsevier material*

Notice
No responsibility is assumed by the publisher for any injury and/or damage to persons or property as a matter of products liability, negligence or otherwise, or from any use or operation of any methods, products, instructions or ideas contained in the material herein

ISBN: 978-0-12-380898-1
ISSN: 0065-3276

For information on all Academic Press publications
visit our website at elsevierdirect.com

Printed and bound in USA
10 11 12 13   10 9 8 7 6 5 4 3 2 1

Working together to grow
libraries in developing countries

www.elsevier.com | www.bookaid.org | www.sabre.org

ELSEVIER   BOOK AID International   Sabre Foundation

PREFACE

The last decade has seen an enormous increase in the use of QM/MM methods and the trend for the coming years is certainly to have an even larger increase. QM/MM is now the general name given for methods that combine quantum mechanics and molecular mechanics. Originally devised for dealing with the complex problem of proteins and enzymes, it is now used in a wide variety of physicochemical problems. For the study of a chemical reaction in an active site of an enzyme, it is conceivable that the amino acids located far from the active site will have considerable less importance. But QM/MM methods are also very important in the study of the spectroscopy of liquid systems. QM is needed to study the quantization of the energy levels and MM can be used to generate the liquid structure at nonzero temperatures. QM/MM methods have seen an extraordinary development allowing quantum chemistry to enter real everyday activity in most laboratories in chemistry and biochemistry. The necessity for a QM treatment (needed in spectroscopy and reactions, for instance) together with the difficulties of treating the entire system by QM imposes some compromising. This compromising comes by adding classical mechanics in a partition of the system. It is used in biomolecular structure and reactivity and in studying solvent effects. It is also considered in excited state dynamics, where the fate of the excitation energy depends on the environment around the chromophore. The development of QM/MM methods is a very active research area with different nuances. This gave the idea of editing a special issue of the *Advances in Quantum Chemistry* dedicated to the subject. This issue focuses on some of the recent progresses in QM/MM methods. Some leading research groups around the world have joined this project to give a review of their contribution to the field, including applications. In total, this issue is composed of 10 different chapters. The first chapter, by Tu and Laaksonen, shows the partition of the system into QM and MM parts; discusses the boundary and the coupling of these two parts. Computational aspects are then considered. In Chapter 2, Barone, Biczysko, and Brancato extend the range of computational spectroscopy by using QM/MM approaches using both time-dependent and time-independent routes. Applications in this case consider electronic spectra and magnetic properties and vibrational dynamics beyond the harmonic approximation. An important computational strategy for dealing with the large number of explicit solvent molecules and a multitude of configurations is the use of a mean field approximation. This has been successfully conducted by Aguilar and coworkers who replaced the configuration average of a given property by an average solvent perturbation. This is the subject treated in Chapter 3 where special attention is devoted to a combination of the mean field approximation with molecular dynamics. One of the most important aspects of the solvent interaction with a reference solute molecule is the understanding of the role played by the hydrogen bonds formed between the solute and the solvent and among the solvent. This specific interaction is at the heart of the proper existence of liquid water in room conditions. Attention to this is devoted by Mata and Cabral in Chapter 4, where the combined and sequential use of MM and QM is used to unravel the electronic properties of hydrogen bonded liquid systems, including water and ammonia. Further, water is responsible for easing chemical reactions that are important in biochemical and environmental processes. Water is in very important in host–guest chemistry and as such there is an increasing need for understanding the properties of the inclusion compounds. In Chapter 5 Lima, Heine, and Duarte present, discuss, and explore the simulation of polypeptide and their inclusion compounds with β-cyclodextrin. The theoretical tool used in this endeavor is the recent and successful dispersion-corrected–self-consistent charge–density functional tight binding model. Of course, biomolecular processes and properties are natural candidates for the application of the QM/MM methodology. Thus in Chapter 6, Groenhof, Boggio-Pasqua, Schäfer, and Robb discuss the computer simulation of the effect of the protein environment on photobiological processes. The theoretical concepts of photochemical reactions together with a practical simulation scheme for photochemical reactions in biomolecular systems are reviewed. This provides not only experimentally accessible information but also quantities that are more difficult to measure. Applications include photoactive yellow protein and reversible switchable fluorescent proteins. Molecular dynamics based on first-principle methods would be the ideal choice if it were not computationally very demanding for liquid systems of chemical interest. QM/MM methods are alternatives to a full QM dynamics. But simplified and efficient ab initio dynamics can still be performed for systems of interest. In this direction an ab initio quantum mechanics charge field molecular dynamics has been developed by Rode and collaborators. In Chapter 7 Hofer, Pribil, Randolf, and Rode present this methodology that overcomes the necessity of solute–solvent potentials. Comparison with other molecular dynamics simulation approaches are made and applications are shown for difficult cases of anions and cations in solution. Chapter 8 by Pierdominici-Sottile, Alberti, and Palma is dedicated to one very important aspect of chemical reaction that is the nuclear quantum effects. They discuss and use mixed-quantum/classical trajectories to study the effects of the nuclear quantum effects in chemical reactions and vibrational relaxation processes. Hence they study proton transfer in gas and condensed phases and vibrational relaxation processes. In chemical reactions in solution the essential quantity is the variation of the free energy along the process. A recent theory has been developed by the Osaka and Kyoto groups, where they use an energy representation for the hybrid QM/MM method. In this, the distribution function of the solute–solvent interaction is a fundamental quantity to obtain the solvation free energy. This is described in Chapter 9 by Takahashi, Matubayasi, and Nakano where they review this QM/MM-ER and describe important applications making also comparison with more traditional procedures. Interesting, they also introduce a novel implementation for redox reactions in biological molecules. Chapter 10 closes this issue with a review by Zhang, Lev, Cuervo, Noskov, and Salahub, that is also some guide to QM/MM methods. Essential and basic concepts with the related techniques are introduced, applications are discussed, and some possible answers to the utilization of QM/MM techniques in different studies taking place in condensed phase are provided.

Altogether this issue involves some of the recent progresses including different and complementary aspects of the QM/MM methodology for different applications in biochemistry and in solution chemistry.

I take this opportunity to thank the editors of the *Advances in Quantum Chemistry* for support and for the invitation to carry on this project. I specially thank all contributors for accepting my invitation. It is my hope that this issue will be useful to both the beginners and the experienced scientists, and thus contribute and stimulate further developments in this exciting and fast expanding research topic.

Sylvio Canuto
São Paulo, Brazil

CONTRIBUTORS

Numbers in parentheses indicate the pages where the authors' contributions can be found.

Manuel A. Aguilar (59)
Área de Química Física, Universidad de Extremadura, Avda. de Elvas s/n, 06071 Badajoz, Spain

Sebastián Fernández Alberti (247)
Universidad Nacional de Quilmes, Sáenz Peña 352, Bernal, B1876BXD, Bs. As., Argentina

Vincenzo Barone (17)
Scuola Normale Superiore, piazza dei Cavalieri 7, 56126 Pisa, Italy, E-mail: vincenzo.barone@sns.it

Malgorzata Biczysko (17)
Dipartimento di Chimica, Università di Napoli "Federico II," Complesso Univ. Monte S. Angelo, via Cintia, 80126 Napoli, Italy

Martial Boggio-Pasqua (181)
Laboratoire de Chimie et Physique Quantiques, IRSAMC, CNRS et Université de Toulouse, 118 Route de Narbonne, 31062 Toulouse, France

Giuseppe Brancato (17)
Italian Institute of Technology, IIT@NEST Center for Nanotechnology Innovation, Piazza San Silvestro 12, 56125 Pisa, Italy

B.J. Costa Cabral (99)
Grupo de Física-Matemática da Universidade de Lisboa, Avenue Professor Gama Pinto 2, 1649-003 Lisboa, Portugal

Javier Eduardo Cuervo (353)
Department of Chemistry; Institute for BioComplexity and Informatics—University of Calgary, Calgary, Alberta, Canada

Ignacio Fdez. Galván (59)
Área de Química Física, Universidad de Extremadura, Avda. de Elvas s/n, 06071 Badajoz, Spain

Guilherme Ferreira de Lima (145)
Departamento de Química, ICEx, Universidade Federal de Minas Gerais, UFMG, 31270-901 Belo Horizonte, MG, Brazil

Hélio Anderson Duarte (145)
Departamento de Química, ICEx, Universidade Federal de Minas Gerais, UFMG, 31270-901 Belo Horizonte, MG, Brazil, E-mail: duarteh@ufmg.br

Gerrit Groenhof (181)
Computational Biomolecular Chemistry, Department of Computational and Theoretical Biophysics, Max-Planck-Institute for Biophysical Chemistry, Am Fassberg 11, D-37077, Göttingen, Germany

Thomas Heine (145)
School of Engineering and Science, Jacobs University, Bremen, 28759 Bremen, Germany

Thomas S. Hofer (213)
Theoretical Chemistry Division, Institute of General, Inorganic and Theoretical Chemistry, University of Innsbruck, Innrain 52a, A-6020 Innsbruck, Austria, E-mail: t.hofer@uibk.ac.at

Aatto Laaksonen (1)
Division of Physical Chemistry, Arrhenius Laboratory, Stockholm University, 106 91 Stockholm, Sweden. E-mail: aatto@mmk.su.se

Bogdan Lev (353)
Department of Biological Sciences; Institute for BioComplexity and Informatics—University of Calgary, Calgary, Alberta, Canada

M. Elena Martín (59)
Área de Química Física, Universidad de Extremadura, Avda. de Elvas s/n, 06071 Badajoz, Spain

Ricardo A. Mata (99)
Grupo de Física-Matemática da Universidade de Lisboa, Avenue Professor Gama Pinto 2, 1649-003 Lisboa, Portugal

Nobuyuki Matubayasi (283)
Institute for Chemical Research, Kyoto University, Uji, Kyoto 611-0011, Japan, E-mail: nobuyuki@scl.kyoto-u.ac.jp

Aurora Muñoz-Losa (59)
Área de Química Física, Universidad de Extremadura, Avda. de Elvas s/n, 06071 Badajoz, Spain

Masayoshi Nakano (283)
Department of Materials Engineering Science, Graduate School of Engineering Science, Osaka University, Toyonaka, Osaka 560-8531, Japan

Sergei Yu Noskov (353)
Department of Biological Sciences; Institute for BioComplexity and Informatics—University of Calgary, Calgary, Alberta, Canada, E-mail: snoskov@ucalgary.ca

Juliana Palma (247)
Universidad Nacional de Quilmes, Sáenz Peña 352, Bernal, B1876BXD, Bs. As., Argentina

Gustavo Pierdominici-Sottile (247)
Universidad Nacional de Quilmes, Sáenz Peña 352, Bernal, B1876BXD, Bs. As., Argentina

Andreas B. Pribil (213)
Theoretical Chemistry Division, Institute of General, Inorganic and Theoretical Chemistry, University of Innsbruck, Innrain 52a, A-6020 Innsbruck, Austria

Bernhard R. Randolf (213)
Theoretical Chemistry Division, Institute of General, Inorganic and Theoretical Chemistry, University of Innsbruck, Innrain 52a, A-6020 Innsbruck, Austria

Michael A. Robb (181)
Department of Chemistry, Imperial College London, London SW7 2AZ, UK

Bernd M. Rode (213)
Theoretical Chemistry Division, Institute of General, Inorganic and Theoretical Chemistry, University of Innsbruck, Innrain 52a, A-6020 Innsbruck, Austria

Dennis R. Salahub (353)
Department of Chemistry; Institute for BioComplexity and Informatics; Institute for Sustainable Energy, Environment and Economy—University of Calgary, Calgary, Alberta, Canada, E-mail: dennis.salahub@ucalgary.ca

M. Luz Sánchez (59)
Área de Química Física, Universidad de Extremadura, Avda. de Elvas s/n, 06071 Badajoz, Spain

Lars V. Schäfer (181)
Department of Biophysical Chemistry, University of Groningen, Nijenborg 4, 9747 AG Groningen, The Netherlands

Catalina Soriano-Correa (59)
Laboratorio de Química Computacional. FES-Zaragoza, Universidad Nacional Autónoma de México, 09230 Iztapalapa, México D.F., Mexico

Hideaki Takahashi (283)
Division of Chemical Engineering, Department of Materials Engineering Science, Graduate School of Engineering Science, Osaka University, Toyonaka, Osaka 560-8531, Japan, E-mail: takahasi@cheng.es.osaka-u.ac.jp

Yaoquan Tu (1)
Biophysical and Theoretical Chemistry, School of Science and Technology, Örebro University, 701 82 Örebro, Sweden. E-mail: yaoquan.tu@oru.se

Rui Zhang (353)
Department of Chemistry; Institute for BioComplexity and Informatics—University of Calgary, Calgary, Alberta, Canada

CHAPTER 1

Implementing Quantum Mechanics into Molecular Mechanics—Combined QM/MM Modeling Methods

Yaoquan Tu[a] and **Aatto Laaksonen**[b]

Contents

---

1. INTRODUCTION

Quantum chemistry is a very powerful tool to study the properties of molecules and their reactions. The recent years' development in quantum chemistry methods, especially that of density functional theory (DFT) methods [1], has made it possible for quantum chemistry calculations to reach accuracies comparable to those obtained in experiments for molecules of moderate sizes. The rapid

---

[a] Biophysical and Theoretical Chemistry, School of Science and Technology, Örebro University, 701 82 Örebro, Sweden

[b] Division of Physical Chemistry, Arrhenius Laboratory, Stockholm University, 106 91 Stockholm, Sweden

E-mail addresses: yaoquan.tu@oru.se (Y. Tu), aatto@mmk.su.se (A. Laaksonen)

Advances in Quantum Chemistry, Vol. 59
ISSN: 0065-3276, DOI: 10.1016/S0065-3276(10)59001-4

© 2010 Elsevier Inc.
All rights reserved

development of computer technologies has greatly encouraged chemists to use quantum chemistry to understand, model, and predict molecular properties and their reactions, properties of nanometer materials, and reactions and processes taking place in biological systems [2–4].

To develop quantum chemistry methods, capable of treating large or complicated systems, has been one of the important subjects in quantum chemistry. In the early days, quantum chemists developed mostly semiempirical molecular orbital methods for the study of large systems [5–7]. These methods often involve many empirical parameters that are optimized by reproducing the properties of some reference molecules. Usually, the parameters are accurate for the systems they are parameterized for. For many properties, such as the relative energies of different conformations of a large molecule, the bonding energy, and structure of a hydrogen-bonded system, the results from semiempirical calculations are not reliable. This limits their applications to large systems, especially those where hydrogen bonds are important. In recent years, many first-principles quantum chemistry methods aimed for large molecular systems have been introduced [8–11].

For large systems, pure ab initio calculations are still very expensive. In many practical applications, we are only interested in the properties of a few molecules of a system or part of a large molecule. Many calculations are therefore only limited to these molecules or part of a large molecule. These studies can provide us with very useful information, but there are often cases where the effects from the surrounding molecules or the remaining part of a large molecule cannot be neglected. Typical examples involve the properties of a solute molecule in a solvent. If we use quantum chemistry to calculate the properties of the solute molecule and neglect the effects from the solvent molecules, the properties obtained correspond only to those of the isolated solute molecule. Another example is the enzymatic reactions occurring in biological systems. Usually, the active center of an enzyme consists typically of about 100 atoms or more, which already reaches the computational limit of many high-level quantum chemistry methods. Using a smaller cluster to represent an active center and studying it carefully with high-level quantum chemistry methods is the standard way usually carried out. However, such an approach may not be adequate since the surrounding atoms could obviously affect the barriers obtained [12,13]. Usually, the surrounding atoms can often stabilize the reactants and products and lower the barrier of a reaction. Without the surrounding atoms, the barrier calculated according to a smaller cluster becomes often overestimated.

In conventional quantum chemistry calculations, the effects from the surrounding atoms of a molecule or cluster are often recovered by using the polarizable continuum model (PCM) [14] in which the surrounding atoms are represented by a dielectric continuum with dielectric constant ε. In PCM, the microscopic structure of the surrounding atoms of a molecule is not considered, thus it is not adequate in cases where the structure of the surrounding atoms is important.

Combined quantum mechanical and molecular mechanical (QM/MM) methods, pioneered by Warshel and Levitt [15], can be considered as a compromise between the full QM calculation of a system and the QM treatment of part of the system with the surroundings being modeled by the PCM. In combined QM/MM methods [15–17], the surroundings of a molecule or cluster are explicitly represented as atoms, but their effects are modeled by an MM force field. Because all the atoms are explicitly represented and the interactions between the atoms are considered, the results obtained from a combined QM/MM calculation could be more accurate than those from a QM calculation with the PCM. Compared with the full QM treatment of a system, a combined QM/MM calculation is much faster since only a small part of the system is treated quantum mechanically. Therefore, combined QM/MM methods have the potentials of studying the properties and processes happening at the electronic scale in very large systems.

In the last decade, much effort has been made in developing reliable and accurate combined QM/MM methods, especially in the treatment of the boundary and interactions between the QM and MM parts [18–33]. There are increasing publications each year in applying the QM/MM methods to larger and more complicated systems. The purpose of this chapter is to introduce the reader to the area of combined QM/MM methods. We will not, however, consider different applications, but rather consider methodological aspects in the area, with the focus on the progress made in the last decade in the treatment of the QM/MM boundary and the QM/MM coupling.

2. PARTITION OF A SYSTEM INTO QM AND MM PARTS

In a combined QM/MM method, the system to be studied is partitioned into two parts; a QM part and an MM part (see Figure 1.1) [17]. The QM part has small number of atoms. It may be a molecule (such as a solute molecule in a solution) or several molecules, a fragment (or part) of a large molecule or a molecular complex (such as the active center of an enzymatic catalyzed reaction). The QM part corresponds to what we need to study in detail. Atoms in this part are explicitly expressed as electrons and nuclei and are described quantum mechanically. When a combined QM/MM method is used to study a system involving charge transfer, electron excitations, or chemical reactions, the corresponding region is always treated quantum mechanically. That is, the region is always included in the QM part.

The MM part is the “environment” to the QM part. Usually, it has much larger number of atoms than the QM part. This part is most often “nonreactive” and is treated by using a classical MM force field.

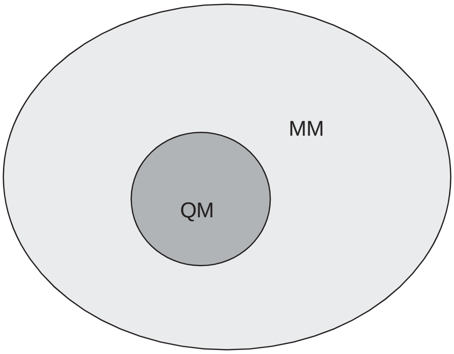

Figure 1.1 The combined QM/MM model.

"Nonreactive" also means that there is no charge transfer or other "chemical" exchange between the QM and MM parts.

For a large molecule, it becomes necessary to divide it into a QM part and an MM part. This division is often quite natural, especially for a large biomolecule where the main interest may be in the active site or a reaction center. In such a case, there are chemical bonds connecting the QM and the MM parts. Because the MM part is treated by a classical force field, the properties and electron densities of the QM atoms bonded to the MM atoms may change drastically. Therefore, the intermediate region between the two parts should be treated so that the effects from partitioning the QM and the MM parts across the bonds on the QM atoms are minimized. In practice, well-localized single bonds are terminated and the valences are satisfied on the QM atoms. The reason to choose well-localized single bonds is to make the theoretical treatment easier. Saturation of the valences on the QM atoms is done to keep the chemical properties of these atoms unchanged.

The choice of the QM/MM boundary can affect greatly the accuracy of a combined QM/MM calculation, such as the charge distribution of the QM part and the overall energy of the system, especially when the QM/MM boundary is within a molecule. It has been found that MM atoms with large magnitudes of charges close to the QM/MM boundary can lead to significant errors in energy [34]. Therefore, care must be taken when choosing a QM/MM boundary.

3. TREATMENT OF THE QM/MM BOUNDARY

There are several ways to treat the QM/MM boundary when a large molecule is divided into a QM part and an MM part [20–33]. Among the widely used ways are those using a hybrid orbital or a link atom to satisfy the valence of the QM atom on a QM/MM bond. In the early work of Warshel and Levitt [15], one single hybrid atomic orbital was placed on each MM atom, originally connected to a QM atom. These hybrid atomic orbitals are then involved in the calculation of the QM part to satisfy the valences. Rivail and coworkers [20,35–37] also used hybrid atomic orbitals in their localized self-consistent field (LSCF) method to treat the QM part. They assumed that the bond connecting a QM atom and an MM atom could be described by a “strictly localized bond orbital (SLBO),” considered to be one of the molecular orbitals of the QM part. However, the orbital is assumed to be “frozen” and therefore is not involved in the QM calculation. This is implemented by letting all the molecular orbitals (MOs), appearing in the QM calculation, to be orthogonal to the SLBO. The SLBOs are obtained by separate QM calculations of some small model molecules. They used the semiempirical neglect of the diatomic differential overlap (NDDO) QM method. Therefore, the orthogonalization can be easily implemented by using the hybrid atomic orbitals of the corresponding QM atom as a basis set and letting them to be orthogonal to the hybrid atomic orbital participating in the SLBO. The LSCF method has later been generalized to ab initio Hartree–Fock (HF), post HF, and DFT [36,37].

An approach similar to the LSCF method is the generalized hybrid orbital (GHO) method [21,38–40]. In this approach, a set of four atomic orbitals is assigned to each boundary MM atom (denoted by B), which was originally connected to a QM atom. The MM boundary atom B is usually chosen to be an SP^3 carbon. The hybrid orbitals on atom B are obtained by the local geometry of four atoms, the atom B and the other three MM atoms bonded to it. Among the four hybrid orbitals on the MM atom B, the orbital pointing to the boundary QM atom is called active orbital and is optimized through being involved in the self-consistent-field (SCF) procedure of the QM part. The other three orbitals do not participate in the SCF optimization procedure, but their effects are involved in the calculation of the effective Hamiltonian matrix. The GHO method was first incorporated into the QM calculations in the semiempirical NDDO method [21,38] and is later incorporated into those at the ab initio HF and DFT levels [39,40].

The hybrid orbital scheme can be improved by incorporating point charges distributed at the middle point of a QM/MM bond and at the QM and MM atoms on the bond. Through extensive optimization of the parameters used, such as the quantities of the point charges, accurate results, such as deprotonation energies and relative conformational energies, are obtained [41].

In the combined QM/MM calculations of large molecules, perhaps the most widely used approach is to use the so-called “link” or “dummy” atoms to satisfy the valences of the QM atoms binding to the MM atoms, as originally proposed in Refs. [16,17]. The most commonly used link atom is hydrogen, but in some other implementations, other types of atoms, such as halogen atoms are also used [42]. The use of halogen atoms as link atoms is in fact to mimic the methyl groups conventionally used in terminating the QM/MM bonds. The link atoms have the following characteristics: (i) A link atom is placed in the direction of the QM/MM bond and replaces the corresponding MM atom in the QM calculation. Link atoms are explicitly represented by electrons and nuclei. That is, they are exactly treated quantum mechanically. (ii) Link atoms are "invisible" to the MM atoms. In other words, there is no interaction between the link atoms and MM atoms. The interactions within the MM part are treated as if there were no link atoms. In ideal cases, link atoms and other MM atoms should simulate the effects of the fragments that are removed from the QM treatment.

The link atom scheme can be improved in several aspects. One of the improvements is to optimize the position of the link atom placed along a QM/MM bond. For example, through an appropriate choice of the position of the hydrogen link-atom along a specific QM/MM bond and using a Gaussian distributed charge, in instead of a point charge, to represent the corresponding MM atom in the QM calculation, results of comparable accuracy to other methods are obtained [28]. Using a one-free-valence atom with an effective core potential (ECP) can also improve the link atom scheme. For example, in the work of Zhang et al. [22], each boundary MM C atom is represented by a pseudo-atom F but with an optimized ECP. The pseudo-atom F can form a pseudo bond with the boundary QM C atom. The ECP is parameterized to mimic the normal C–C bond energetics. Compared with a normal C atom, the pseudo-atom F has three extra valence electrons which are used to satisfy the open valences. The ECP scheme has later been further extended. DiLabio et al. [26] used a one-electron effective potential for C to represent the boundary MM C atom used in the QM calculation. The boundary MM C atom has only one valence electron and the QM calculation time can be saved. Slavíček and Martínez [32] introduced multicentered valence electron effective potentials (MC-VEEPs) to represent the MM functional groups in a QM/MM boundary. The MC-VEEPs are parameterized by demanding that both occupied and virtual orbitals are described correctly, leading to the combined QM/MM calculations to be able to describe correctly the excitations in the QM regions.

The major effect from the treatment of a QM/MM boundary is on the electronic structure of the QM part. The aim of using hybrid orbitals or link atoms is to satisfy the valences on the QM atoms on the QM/MM bonds. From this point of view, hybrid orbitals would be physically more appropriate because a QM/MM bond was originally formed by hybrid orbitals. For example, a saturate C–C bond is known to be formed by two SP^3 hybrid orbitals, with one on each carbon atom. Indeed, through extensive optimization of the parameters involved in the hybrid orbital approaches, good results from the combined QM/MM calculations, as those from the purely QM calculations, are obtained. However, hybrid orbital approaches are not easy to implement in many practical applications, especially for many widely used quantum chemistry calculation packages, as some additional coding to the programs is required.

Using link atoms to satisfy the valences on the QM atoms at a QM/MM boundary is easier to implement in many practical calculations as link atoms are often normal hydrogen or halogen atoms so that coding a QM program is not required. It's difficult for link atoms to provide the same hybrid orbitals as those on the boundary MM atoms. Link atoms can also result in some additional undesirable energy that may affect the accurate description of a potential energy surface. However, the link atom scheme can be improved by various optimizations of parameters. The above-mentioned approaches, such as using pseudo-atom F with an optimized ECP and optimizing the position of the link atom along a QM/MM bond, are just two examples. The flexibility of the link atom scheme also makes it easy to use extended basis sets. After extensive optimization of the parameters involved, results of comparable good accuracy from both schemes can be obtained.

4. INTERACTIONS IN THE QM/MM COUPLING

In the combined QM/MM methods, the total energy of a system can be expressed as follows:

$$E_{\text{total}} = E_{\text{QM}} + E_{\text{MM}} + E_{\text{QM/MM}}, \tag{1}$$

where E_{QM} represents the QM energy of the QM part, E_{MM} is the energy of the MM part calculated by an MM force field, and $E_{\text{QM/MM}}$ is the interaction between the QM and MM parts. $E_{\text{QM/MM}}$ usually consists of three types of interactions: electrostatic interaction E_{ES}(QM/MM), van der Waals interaction E_{vdW}(QM/MM), and the MM-bonded interaction E_{bonded}(QM/MM). Therefore, we can express $E_{\text{QM/MM}}$ as follows:

$$E_{\text{QM/MM}} = E_{\text{ES}}(\text{QM/MM}) + E_{\text{vdW}}(\text{QM/MM}) + E_{\text{bonded}}(\text{QM/MM}), \tag{2}$$

where the term E_{bonded}(QM/MM) is calculated only when there are chemical bonds between the QM and MM parts. It involves the conventional bonded terms, such as bond stretching, angle bending, and rotational motion terms, with at least one atom from the QM part and at least one atom from the MM part. $E_{\text{bonded(QM/MM)}}$ is calculated with the same force field as for E_{MM}.

In combined QM/MM calculations, the QM calculations are often not carried out for the energy of the QM part, E_{QM}, but are performed for the sum of E_{QM} and E_{ES}(QM/MM), that is,

$$E_{\mathrm{QM}} + E_{\mathrm{ES}}(\mathrm{QM/MM}) = \langle \Psi | \hat{H}_{\mathrm{eff}} | \Psi \rangle. \tag{3}$$

The effective Hamiltonian $\hat{H}_{\mathrm{eff}}$ in the above equation can be expressed as

$$\hat{H}_{\mathrm{eff}} = \hat{H}_{\mathrm{QM}} + \hat{H}_{\mathrm{ES}}(\mathrm{QM/MM}), \tag{4}$$

where $\hat{H}_{\mathrm{QM}}$ is the Hamiltonian for the QM part and $\hat{H}_{\mathrm{ES}}$(QM/MM) is the Hamiltonian representing the interactions of electrons and nuclei in the QM part with the point charges of MM parts.

When there are chemical bonds between the QM and MM parts, the effective Hamiltonian $\hat{H}_{\mathrm{QM}}$ is different from that for the isolated QM part since the Hamiltonian should also involve those terms used for treating the QM/MM boundary, such as those using a hybrid orbital or a link atom to satisfy the valence of the QM atom on a QM/MM bond. This makes the QM energy different from that for the isolated system where the QM/MM boundary is not treated. The treatment of a QM/MM boundary will also affect the electrostatic interaction between the QM and MM parts because the hybrid orbitals or link atoms introduced to satisfy the valences of the QM atoms at the QM/MM boundary can interact with the charges in the MM part during the QM calculation. However, this undesirable effect of hybrid orbitals or link atoms on the QM/MM electrostatic interaction is usually rather small.

The QM/MM coupling can influence the properties from QM/MM calculations, especially the interaction energies between the QM and MM parts. The coupling is important when properties related to the energy, such as free energies, are studied. Thus care must be taken in considering the QM/MM coupling. In QM/MM calculations, there are two types of interactions between the QM and MM parts. One type is the van der Waals interaction that represents the dispersion interactions and the other is the short-range repulsive interactions between the QM and MM atoms. It is often expressed as the Lennard-Jones potential with

$$E_{\mathrm{vdW}}(\mathrm{QM/MM}) = \sum_{i \in \mathrm{QM}} \sum_{j \in \mathrm{MM}} 4\varepsilon_{ij} \left[\left(\frac{\sigma_{ij}}{R_{ij}} \right)^{12} - \left(\frac{\sigma_{ij}}{R_{ij}} \right)^{6} \right], \tag{5}$$

where R_{ij} is the distance between a QM atom i and an MM atom j . ε_{ij} and σ_{ij} are the standard Lennard-Jones parameters. Usually, the Lennard-Jones parameters are taken directly from a force field. When a QM/MM method is used to study a reaction in the QM region, the Lennard-Jones parameters used to represent the van der Waals interaction between the QM atoms and the MM atoms may change significantly and the Lennard-Jones parameters on the QM atoms are thus not clearly defined. It has also been found [43] that through the MD simulations of liquid water, where only one water molecule in the simulation box is treated quantum mechanically and the remaining water molecules are represented by the TIP3P force field model, the Lennard-Jones parameters can greatly affect the water structure and the potential energy. In principle, the effects of the Lennard-Jones parameters on the QM part can be diminished by just increasing the size of the QM part as the van der Waals interaction is of short range.

Another type of interaction in the QM/MM coupling is the electrostatic interaction, $\hat{H}_{\mathrm{ES}}(\mathrm{QM/MM})$, between the QM and MM atoms. This interaction originates from the interaction of the electrons and nuclei in the QM part with the point charges in the MM part and is involved in the SCF calculations of the QM part. Thus, MM charges can also affect directly the charge distribution in the QM part. In many QM/MM calculations, the MM charges are taken directly from an MM force field. Such charges are used in a force field to model the nonbonded Coulomb interaction between the MM atoms and are often optimized for simulations in condensed phases. Electrostatic interaction can affect greatly the QM/MM coupling. Whether such type of MM charges can be used directly in a combined QM/MM calculation is still not clear. It has been found that in combined QM/MM calculations of large molecules, the MM charges should be different from those from a force field as the MM charges from a force field also involve the polarization effects of the surroundings on the molecule [34]. In combined HF QM/MM simulations of water at ambient and supercritical conditions, it is also found that scaling down the MM charges can give reasonably good results [44]. This means that it may not be a good idea to use directly the MM charges from a force field in a combined QM/MM calculation. In fact, the QM/MM electrostatic interactions can also depend on the QM method used in the QM/MM calculations. For example, the HF/6-31G* calculations can often give larger dipole moments for small organic molecules. Thus, it can be expected that in a combined HF/6-31G* QM/MM calculation, the electrostatic interaction between the QM/MM coupling is overestimated.

A natural improvement on the QM/MM electrostatic coupling is to involve the polarization effects from the QM part to the MM part as well. A simple way can be found in the work by Singh and Kollman [16]. In their scheme, the coupling Hamiltonian between the QM part and the MM part remains the same as that used in the usual QM/MM calculations, whereas the polarization effects of the MM atoms by the QM atoms act only as a "compensation" to the total energy of the system and is obtained after the convergence of the QM calculation. This simple implementation improves the interaction energy between the two parts. However, because this energy is calculated classically, the electronic structure of the QM part has still not been improved. Some studies have shown that this type of "environmental polarization" may have significant effects on the electronic spectra of the QM part [45].

The effects of the MM polarization to the QM part were already included in the work by Warshel and Levitt [15]. Later, Luzhkov and Warshel [46,47] refined the model for both the ground and excited states. A detailed description of possible polarization schemes is given by Thompson et al. [48,49]. Since the charge distribution of the QM part can be polarized by the potential from the point charges and the induced dipole moments in the MM part and it can in turn polarize the MM part, the induced dipole moments in the MM part are calculated iteratively. Warshel and coworkers [15,47] introduced a simplified approach to calculate the induced dipole moments, where the iteration could be avoided.

Fluctuating charge (FC) model [50] provides an alternative way to treat the polarization problem. In the FC model, the central concept is the atomic charges. These charges can fluctuate with the environment to satisfy the principle of "electronegativity equalization." Therefore, the charge distribution also reflects the polarization of the environment to that atom and it is a natural concept to introduce the FC model into the combined QM/MM calculation.

5. COMPUTATIONAL ASPECTS

Recall that in the combined QM/MM methods, the QM calculations are performed according to the following Hamiltonian,

$$\hat{H}_{\text{eff}} = \hat{H}_{\text{QM}} + \hat{H}_{\text{ES}}(\text{QM/MM}). \tag{4}$$

Because $\hat{H}_{\text{eff}}$ involves the interactions of the electrons in the QM part with the point charges in the MM part, some additional integral calculations are needed. Usually, these integrals correspond to those of QM calculations of a molecular system in the presence of point charges. They are of the following form:

$$I_{\mu\nu} = \int \chi_\mu \left(-\frac{Q_m}{r_{im}} \right) \chi_\nu d\vec{r}_i, \tag{6}$$

where Q_m is the point charge on the MM atom m. $\vec{r}_i$ is the position of electron i in the QM region. χ_μ and χ_ν are basis functions. In ab initio calculations, the basis functions are Gaussian type of functions, whereas in semiempirical calculations (e.g., MNDO [5], AM1 [6], PM3 [7]), the basis functions are canonical valence atomic orbitals and are usually represented by Slater type of functions. The above type of integrals is added to the one-electron Hamiltonian matrixes during the SCF calculations of the QM part.

Under a given Gaussian basis set, the integrals given by Eq. (6) can be calculated accurately. There exist very efficient ways to calculate the integrals by using the recurrence relationship [51]. This is the case in many ab initio programs. Most ab initio programs (such as GAUSSIAN03 [52] and GAMESS [53]) involve the calculations of such type of integrals. Semiempirical MO methods (such as MNDO, AM1, and PM3) use the "frozen core" approximation and all the integrals (except for the overlap integrals) related to the valence electrons are calculated approximately. Therefore, the coupling Hamiltonian $\hat{H}_{\mathrm{ES}}(\mathrm{QM/MM})$ should be reformulated to conform to the "frozen core" approximation in the semiempirical QM calculations and the additional integrals [Eq. (6)] are also calculated approximately. For details, the reader may consult the papers [17,47,54].

To make practical use of the models discussed above may seem fairly complicated, requiring some knowledge in coding both quantum chemical software and MM software. Most molecular dynamics (MD) simulation programs use MM force fields to describe the interactions between the atoms, the easiest way to implement a combined QM/MM calculation is therefore to couple together an existing MD simulation code with a standard quantum chemistry program including the force calculation on the QM atoms and electric field calculation on the MM charge sites. The combined QM/MM calculations can be implemented by using a link program to combine a QM calculation program with an MD program with MM force field calculations. The link program is the interface between the QM calculation and the MM calculation. It takes care of the data transfer between the QM and the MM programs. The QM program calculates the properties related to the QM part. Sometimes, if a special treatment of a QM/MM boundary is required, most probably one has to modify the relevant quantum chemistry code. When a combined QM/MM calculation is required in an MD simulation, the MM program usually conducts the MD simulation as well.

As far as the QM programs are concerned, they can be divided into two types according to the level of approximation they use: there are ab initio packages, such as GAUSSIAN03 [52] and GAMESS [53]; DFT programs, such as deMon [55]; and at least about 20 other packages; there are also semiempirical calculation packages, such as AMPAC [56] and MOPAC [57].

There are several MM force fields available, such as OPLS [58], CHARMM [59], AMBER [60], GROMOS [61], MMFF [62], and CVFF [63], to mention a few. Most of them have been combined with the QM calculation programs and used in the combined QM/MM MD simulations. In our own work, we have combined either GAUSSIAN94 [52] or GAMESS [53] with our own simulation software which is the modified version of McMOLDYN package [64] to study solvation phenomena and radical systems [43,44,65,66].

There are also some special programs that are optimized for the QM/MM calculations [41,67]. In these programs, the QM/MM boundaries are usually treated more elegantly, with the parameters optimized according to small model molecules. Therefore, the QM/MM calculation results obtained from such programs are often more accurate. Also, these programs are often easy to use for the combined QM/MM calculations.

6. FUTURE PROSPECTS

In this chapter, we give a general outline of the combined QM/MM methods. Comparing with the full QM calculations of a system, combined QM/MM calculations are much faster because only limited number of atoms are treated quantum mechanically. Therefore, they can be used to study very large systems where limited QM calculations are required. This would greatly extend the application area of quantum chemistry. When combined with MD simulation techniques, combined QM/MM calculations can also be used to study the properties of condensed phases under certain temperatures and pressures. We believe that the methods will increasingly gain popularity in the future as feasible, good compromises to carry out QM calculations for systems where electron excitations, charge transfers, and chemical reactions take place. The applications may be found in the following fields:

(1) Solvent effects: This area covers the properties of solutes or chemical reactions in a solution and is particularly suitable to be studied using the combined QM/MM methods incorporated with MD simulation techniques.
(2) Reactions in biosystems: This area includes, for example, enzyme-catalyzed reactions and proton and electron transfer processes. The active center of such a reaction usually involves more than 100 atoms and the surroundings are important in determining the reaction barriers. Sometimes, even the free energies need to be calculated. In recent years, there are many combined QM/MM studies in this area. Combined QM/MM methods in combination with MD simulation techniques seem to be a very powerful tool.
(3) The properties and reactions related to clusters and nanomaterials: Theoretical study of these systems usually requires QM calculations, but the systems are often beyond the limit of full QM calculations. With combined QM/MM methods, many properties that need QM calculations can be studied.

As far as the combined QM/MM methods are concerned, the following aspects need to be considered:

(1) The QM/MM boundary: When a molecule is partitioned into a QM region and an MM region, the treatment of the QM/MM boundary is of

great importance. In principle, by increasing the size of the QM region, the effects from the QM/MM boundary can be reduced. However, this would greatly increase the computational time because most of the time in a combined QM/MM calculation is spend on the QM calculations. In the last decade, one has witnessed many ways to treat the QM/MM boundaries. But more accurate ways for the treatment of various QM/MM boundaries are still greatly desirable.

(2) The parameters used in the QM/MM couplings: Currently, the parameters used in a combined QM/MM calculation are taken directly from the MM force field used in it. Whether these parameters are appropriate for use in the combined QM/MM calculations needs to be investigated. The parameters could influence greatly the interactions between a QM molecule and MM molecules when a combined QM/MM calculation is used to study the interactions between the molecules. Therefore, more accurate ways to treat the QM/MM coupling or better parameterization are required in order to improve the interactions between the QM and MM parts.

REFERENCES

[1] R.G. Parr, W. Yang, Density-Functional Theory of Atoms and Molecules, Oxford University Press, New York, 1989.
[2] W. Koch, M.C. Holthausen, A Chemist's Guide to Density Functional Theory, Wiley VCH, New York, 2000.
[3] R. Nieminen, J. Phys. Cond. Matter 14 (2002) 2859.
[4] L. Noodleman, T. Lovell, W. Han, J. Li, F. Himo, Chem. Rev. 104 (2004) 459.
[5] M.J.S. Dewar, W. Thiel, J. Am. Chem. Soc. 99 (1997) 4899.
[6] M.J.S. Dewar, E.G. Zoebisch, E.F. Healy, J.J.P. Stewart, J. Am. Chem. Soc. 107 (1985) 3902.
[7] J.J.P. Stewart, J. Comput. Chem. 10 (1989) 209.
[8] B. Delley, J. Chem. Phys. 508 (1990) 92.
[9] http://www.turbomole.com/
[10] http://www.kjemi.uio.no/software/dalton/dalton.html
[11] http://www.icmab.es/siesta/index.php
[12] M.J. Field, J. Comput. Chem. 23 (2002) 48.
[13] A. Warshel, Annu. Rev. Biophys. Biomol. Struct. 32 (2003) 425.
[14] J. Tomasi, M. Persico, Chem. Rev. 94 (1994) 2027.
[15] A. Warshel, M. Levitt, J. Mol. Biol. 103 (1976) 227.
[16] U.C. Singh, P.A. Kollman, J. Comput. Chem. 7 (1986) 718.
[17] M.J. Field, P.A. Bash, M. Karplus, J. Comput. Chem. 11 (1990) 700
[18] A. Laaksonen, Y. Tu, Methods of incorporating quantum mechanical calculations into molecular dynamics simulations, in: P.B. Balbuena, J.M. Seminario (Eds.), Molecular Dynamics: From Classical to Quantum Methods, Elsevier Science, Amsterdam, 1999 (Chapter 1), pp. 1–29.
[19] H. Lin, D.G. Truhlar, Theor. Chem. Acc. 117 (2007) 185.
[20] V. Thery, D. Rinaldi, J. Rivail, B. Maigret, G.G. Ferenczy, J. Comput. Chem. 15 (1994) 269.
[21] J. Gao, P. Amara, C. Alhambra, M.J. Field, J. Phys. Chem. A 102 (1998) 4714.
[22] Y. Zhang, T. Lee, W. Yang, J. Chem. Phys. 110 (1999) 46.
[23] D.M. Philipp, R.A. Friesner, J. Comput. Chem. 20 (1999) 1468.

[24] I. Antes, W. Thiel, J. Phys. Chem. A 103 (1999) 9290.
[25] V. Kairys, J.H. Jensen, J. Phys. Chem. A 104 (2000) 6656.
[26] G.A. DiLabio, M.M. Hurley, P.A. Christiansen, J. Chem. Phys. 116 (2002) 9578.
[27] D. Das, K.P. Eurenius, E.M. Billings, P. Sherwood, D.C. Chatfield, M. Hodošček, et al., J. Chem. Phys. 117 (2002) 10534.
[28] P. Amara, M.J. Field, Theor. Chem. Acc. 109 (2003) 43.
[29] F. Bessac, F. Alary, Y. Carissan, J. Heully, J. Daudey, R. Poteau, J. Mol. Struct. (THEOCHEM) 632 (2003) 43.
[30] K. Yasuda, D. Yamaki, J. Chem. Phys. 121 (2004) 3964.
[31] H. Lin, D.G. Truhlar, J. Phys. Chem. A 109 (2005) 3991.
[32] P. Slavíček, T.J. Martínez, J. Chem. Phys. 124 (2006) 084107.
[33] Y. Shao, J. Kong, J. Phys. Chem. A 111 (2007) 3661.
[34] N. Reuter, A. Dejaegere, B. Maigret, M. Karplus, J. Phys. Chem. A 104 (2000) 1720.
[35] G. Monard, M. Loos, V. Thery, K. Baka, J. Rivail, Int. J. Quantum Chem. 58 (1996) 153.
[36] X. Assfeld, J. Rivail, Chem. Phys. Lett. 263 (1996) 100.
[37] N. Ferré, X. Assfeld, J. Rivail, J. Comput. Chem. 23 (2002) 610.
[38] P. Amara, M.J. Field, C. Alhambra, J. Gao, Theor. Chem. Acc. 104 (2000) 336.
[39] J. Pu, J. Gao, D.G. Truhlar, J. Phys. Chem. A 108 (2004) 632.
[40] J. Pu, J. Gao, D.G. Truhlar, Chem. Phys. Chem. 6 (2005) 1853.
[41] R.B. Murphy, D.M. Philipp, R.A. Friesner, J. Comput. Chem. 21 (2000) 1442.
[42] Hyperchem Users Manual, Computational Chemistry, Hypercube, Inc., Ontario, Canada, 1994.
[43] Y. Tu, A. Laaksonen, J. Chem. Phys. 111 (1999) 7519.
[44] Y. Tu, A. Laaksonen, J. Chem. Phys. 113 (2000) 11264.
[45] J. gao, J. Am. Chem. Soc. 116 (1994) 9324.
[46] V. Luzhkov, A. Warshel, J. Am. Chem. Soc. 113 (1991) 4491.
[47] V. Luzhkov, A. Warshel, J. Comput. Chem. 13 (1992) 199.
[48] M.A. Thompson, G.K. Schenter, J. Phys. Chem. 99 (1995) 6374.
[49] M.A. Thompson, J. Phys. Chem. 100 (1996) 14492.
[50] S.W. Rick, S.J. Stuart, B.J. Berne, J. Chem. Phys. 101 (1994) 6141.
[51] P.M.W. Gill, Adv. Quantum Chem. 25 (1994) 143.
[52] M.J. Frisch, G.W. Trucks, H.B. Schlegel, G.E. Scuseria, M.A. Robb, J.R. Cheeseman, et al., Gaussian 03, Gaussian, Inc., Wallingford CT, 2004.
[53] M.W. Schmidt, K.K. Baldridge, J.A. Boatz, S.T. Elbert, M.S. Gordon, J.H. Jensen, et al., J. Comput. Chem. 14 (1993) 1347.
[54] H. Liu, F. Müller-Plathe, W.F. van Gunsteren, J. Chem. Phys. 102 (1995) 1722.
[55] D.R. Salahub, R. Fournier, P. Mlynarski, I. Papai, A. St-Amant, J. Ushio, Gaussian-based density functional methodology, software and applications, in: J. Labanowsky, J. Andzelm (Eds.), Proceedings of the Ohio Supercomputer Center Workshop on the Theory and Applications of Density Functional Theory to Chemistry, Columbus Ohio, May 7–9, 1990, Springer Verlag, New York, 1991.
[56] D.L. Liotard, E.F. Healy, J.M. Ruiz, M.J.S. Dewar, MOPAC, QCPE nr. 506, QCPE Bull. 9 (1989) 123.
[57] J.J.P. Stewart, MOPAC, QCPE nr. 455, QCPE Bull. 10 (1990) 86.
[58] W.L. Jorgensen, J. Tirado-Rives, J. Am. Chem. Soc. 110 (1988) 1657.
[59] B.R. Brooks, R.E. Bruccoleri, B.D. Olafson, D.J. States, J. Swaminathan, M. Karplus, J. Comput. Chem. 4 (1983) 187.
[60] S.J. Weiner, P.A. Kollman, D.T. Nguyen, D.A. Case, J. Comput. Chem. 7 (1986) 230.
[61] W.F. Van Gunsteren, H.J.C. Berendsen, Groningen Molecular Simulation (GROMOS) Library Manual, Biomos, Nijenborgh 16, 9747 Groningen, The Netherlands, 1987.
[62] T.A. Halgren, J. Comput. Chem. 17 (1996) 490.
[63] P. Dauber-Osguthorpe, V.A. Roberts, D.J. Osguthorpe, J. Wolff, M. Genest, A.T. Hagler, Proteins 6 (1986) 82.

[64] A. Laaksonen, Comput. Phys. Comm. 42 (1986) 271.
[65] J. Wang, R.J. Boyd, A. Laaksonen, J. Chem. Phys. 104 (1996) 7261.
[66] L.A. Eriksson, A. Laaksonen, J. Chem. Phys. 105 (1996) 8195.
[67] P. Sherwood, A.H. de Vries, M.F. Guest, G. Schreckenbach, C.R.A. Catlow, S.A. French, et al., J. Mol. Struct. (Theochem) 632 (2003) 1.

CHAPTER 2

Extending the Range of Computational Spectroscopy by QM/MM Approaches: Time-Dependent and Time-Independent Routes

Vincenzo Barone[a], **Malgorzata Biczysko**[b] and **Giuseppe Brancato**[c]

Contents

---

[a] Scuola Normale Superiore, piazza dei Cavalieri 7, 56126 Pisa, Italy
[b] Dipartimento di Chimica, Università di Napoli “Federico II,” Complesso Univ. Monte S. Angelo, via Cintia, 80126 Napoli, Italy
[c] Italian Institute of Technology, IIT@NEST Center for Nanotechnology Innovation, Piazza San Silvestro 12, 56125 Pisa, Italy
E-mail address: vincenzo.barone@sns.it (V. Barone)

Advances in Quantum Chemistry, Vol. 59
ISSN: 0065-3276, DOI: 10.1016/S0651-3276(10)59002-6

© 2010 Elsevier Inc.
All rights reserved

1. INTRODUCTION

Nowadays, the characterization of complex biological systems or nanomaterials of direct technological interest relies more and more on computational approaches, for example, for the evaluation and rationalization of structural, energetic, electronic, and dynamic features [1–4]. On the experimental side accurate information can be gained, in principle, by a number of spectroscopic techniques, vibrational, magnetic as well as optical. Nevertheless, up to very recently direct comparisons between experimental and computed spectroscopic data have been rather scarce. Integrated approaches, capable of accurately simulating spectra, but at the same time easily accessible to nonspecialists, are highly desirable. Such tools would allow for the exploitation of the recent and ongoing developments that are taking place in the field of computational spectroscopy [5–13] resulting in easy and, ideally, automatic vis-à-vis comparison between experimental and theoretical results. In the present chapter, we discuss computational approaches in line with such a demand. In general, the accuracy of a simulated spectrum depends on the quality and a proper choice of a computational model: a reliable description of equilibrium structures, vibrational properties, and electronic structure is necessary. In case of macromolecular systems this task is not trivial and in this respect, the quantum mechanics/molecular mechanics (QM/MM) schemes are particularly well suited for systems where the most important spectroscopic features have a local character. In this spirit, it is possible to combine various computational schemes to create user-defined and/or problem-tailored approaches. This is particularly straightforward for solute–solvent systems, and a theoretical approach that seems, at the same time, more reliable from a physical point of view and computationally very effective consists in using hybrid QM/MM methods with nonperiodic boundary conditions and localized basis sets. Additional extension of such schemes toward discrete/continuum models allows conveniently reduce the number of degrees of freedom, while keeping all the important interactions with the bulk, modeled as a continuum. Specific intermolecular interactions between the solute and the solvent (e.g., hydrogen bonds) can be also retained, especially if they play a crucial role in determining the solute structural, dynamic, or spectroscopic properties, by including solvent molecules in the explicit treatment. Further, such conditions avoid the appearance of possible correlation effects [14–22] and other problems with charged systems [23,24] that may affect molecular calculations and simulations using periodic boundary conditions (PBCs). Being the quantum region, generally a small portion of the whole system, it is a natural choice to describe the electronic density in terms of atomic basis functions. In recent years, our group has developed several computational strategies aiming at the spectroscopic studies of macrosystems as (1) a discrete/continuum approach that can be nicely integrated with the hybrid scheme offered by own N-layered integrated molecular orbital and molecular mechanics (ONIOM) to perform QM/MM molecular dynamics (MD) simulations of complex systems in solution and (2) effective schemes to include vibrational effects within the time-independent framework.

2. THE QM/MM FRAMEWORK FOR SPECTROSCOPIC STUDIES

Hybrid QM/MM methodologies allow to combine two or more computational methods to effectively treat a complex molecular system with a large number of atoms (>100). Among others, the ONIOM [25–27] scheme has shown a great flexibility, as well as numerical stability, with a variety of quantum mechanical, semiempirical, and molecular mechanics methods, providing an accurate and well-defined Hamiltonian, energy gradient, and Hessian matrix. Also, in this framework, a quite general partitioning scheme can be used, in which the so-called layers, corresponding to parts of the system treated at the same level of theory, do not have to be inclusive. Accordingly, various physical and chemical properties can be evaluated, including those related to the derivative of the energy with respect to the electric field vector, such as vibrational frequencies and infrared (IR) intensities. As an example, in a simple two-layer system, where the region of interest is treated at QM level and the remaining system at MM level, each energy evaluation requires three different calculations according to the following expression:

$$E^{\mathrm{QM/MM}} = E^{\mathrm{QM}}_{\mathrm{model}} + E^{\mathrm{MM}}_{\mathrm{real}} - E^{\mathrm{MM}}_{\mathrm{model}}, \tag{1}$$

where the *real* system is the entire molecular system under consideration and the *model* is the core region to be modeled at the highest level of theory (e.g., a solute or part of it) plus the point charges located at the same positions of the remaining explicit MM atoms (e.g., the set of the partial atomic charges of a nonpolarizable force field). Such a decomposition, not derived straightforwardly, provides a well-defined, single-valued, and differentiable potential well suited to perform QM/MM calculations.

The standard QM/MM scheme briefly sketched above can be directly applied to spectroscopic studies performed within the time-independent framework. Such an approach is suitable for large and semirigid molecules, when nonadiabatic couplings are negligible, harmonic approximation reliable, and spectroscopic properties can be evaluated considering only small conformational region close to the equilibrium. Apart from their effectiveness, time-independent methods have the remarkable advantage to operate directly in the frequency domain, naturally allowing the determination of stick bands and their assignments.

However, large-amplitude motions and solvent librations cannot be described by computations based on a harmonic approximation or even when the perturbative anharmonic corrections are included (vide infra). Moreover, eigenstate-free time-dependent methods are the main (when not the only) route to deal with systems affected by significant nonadiabatic interactions for which eigenstate calculations are unfeasible, as is the case of conical intersections [28], or for systems propagating on highly anharmonic potential energy surfaces (PESs) [29,30]. In the former case, quantum dynamics (QD) treatments are necessary to take into account nonadiabatic effects. However, when the Born–Oppenheimer approximation remains valid dynamic effects can be properly described by the classical MD approaches. Then, appropriately tailored QM/MM schemes can be effectively explored to perform MD simulations and sample the general features of the configurational space with one or more trajectories. In this respect, we have recently developed the general liquid optimized boundary (GLOB) model [31,32], which can be successfully applied to perform QM/MM MD simulations of complex molecular systems in solution. Then, spectroscopic observables may be computed on the fly or in a second step by averaging over the corresponding estimators and suitable number of snapshots. In the general case of solute–solvent system, it is customary to carry out the same steps also for the molecules in the gas phase, just to have a comparison term for quantifying solvent effects. The a posteriori calculation of spectroscopic properties, compared to other on-the-fly approaches, allows us to exploit different QM/MM schemes for the MD simulations and the calculation of physical–chemical properties. In this way, a more accurate treatment for the more demanding molecular parameters, of both first [e.g., hyperfine coupling constants (hcc's)] and second (e.g., electronic g-tensor shifts) order, could be achieved independently of structural sampling methods provided the accuracy in reproducing reliable structures and statistics is proven for the latter.

2.1. Time-dependent approaches for QM/MM study of complex systems in solution: the GLOB model

In the framework of formally monoelectronic QM methods (e.g., Hartree–Fock or Kohn–Sham models), if $E^{\mathrm{QM/MM}}(\mathbf{P}_0, \mathbf{x})$ is the QM/MM gas-phase energy of the explicit system expressed as a function of the nuclear coordinates, $\mathbf{x}$, and the unpolarized (no solvent effects) one-electron density matrix, $\mathbf{P}_0$, then the solvation free energy, $\Delta A_{\mathrm{sol}}(\mathbf{x})$, at a specific molecular configuration can be written in analogy to Ref. [33] as the sum of the internal energy plus the so-called "mean field" (or potential of mean force) contribution that accounts for the interactions with the environment (solvent) minus the gas-phase energy:

$$\Delta A_{\mathrm{sol}}(\mathbf{x}) = (E^{\mathrm{QM/MM}}(\mathbf{P},\mathbf{x}) + W(\mathbf{P},\mathbf{x})) - E^{\mathrm{QM/MM}}(\mathbf{P}_0,\mathbf{x}), \qquad (2)$$

where $\Delta A_{\mathrm{sol}}(\mathbf{x})$ is the free energy of the system at a given molecular configuration and $W(\mathbf{P},\mathbf{x})$ is the mean field term. Note that $\mathbf{P}$ is explicitly present in the first two terms on the r.h.s. to imply that they are mutually polarized, that is, the mean field response is always considered at equilibrium and the electronic charge distribution is determined by a self-consistent calculation. In particular, we have integrated the mean field contributions as a modification of the ONIOM [25–27] scheme for the isolated systems as described in Refs. [31,32]. The mean field, W, is the potential experienced by the explicitly treated molecules in a given configuration $\{\mathbf{x}\}$ due to the average interactions with the environment. A number of discrete/continuum models have been proposed in the literature that differ in the way W is approximated. Here, according to the Ben–Naim's definition of the solvation process [34], we can conveniently assume that the mean field potential is composed of conceptually simple terms: a long-range electrostatic contribution due to the linear response of the polarizable dielectric continuum, and a short-range dispersion–repulsion contribution, which accounts effectively for the interactions in proximity of the cavity boundary, $W = W_{\mathrm{elec}} + W_{\mathrm{disp-rep}}$. In the following, we describe the essential features of the GLOB model (see Figure 2.1), a sophisticated and integrated method that allows to study efficiently solvent effects

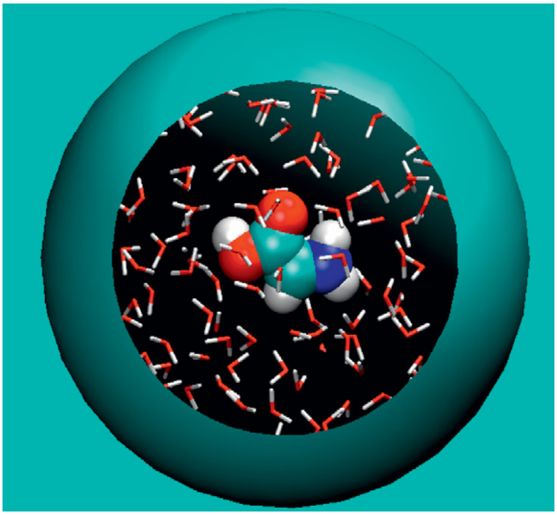

Figure 2.1 Graphical representation of a solute–solvent system simulated using the GLOB model: the explicit system is embedded into a spherical cavity of a dielectric continuum.

on generic solute molecules. According to the GLOB model, the explicit system is composed of the solute along with a few solvent molecules set up at different levels of theory, from computationally inexpensive, but less accurate, MM methods to more realistic hybrid QM/MM or full QM methods (see Refs. [31,33,35] for more details). Then, the explicit system (solute + solvent) is embedded into a suitable cavity of a dielectric continuum possibly with a regular and smooth shape, such as a sphere, an ellipsoid, or a spherocylinder. In combination with MD techniques, such a cavity could be kept fixed, corresponding to *NVT ensemble* conditions, or allowed to change volume, according to *NpT ensemble* simulations (vide infra).

2.1.1. Electrostatic contributions

The long-range electrostatic interactions between the system and the dielectric continuum are modeled by means of the conductor-like version [36–38] of the polarizable continuum model (PCM) [39], which is one of the most refined boundary element methods successfully used in many applications ranging from structure and thermodynamics to spectroscopy in both isotropic and anisotropic environments [39–41]. The continuum medium, which mimics the response of liquid bulk, is completely specified by a few parameters, for example, the dielectric permittivity (ϵ_r), and depends on the nature of the solvent and the physical conditions, such as density and temperature. To be specific, the reaction field, Φ_{RF}, that is, the electrostatic potential due to the induced polarization of the dielectric, is described in terms of apparent surface charges (q_{asc}) centered on small tiles, called *tesserae*, which are the results of a finely subdivision of the cavity surface into triangular area elements of about equal size, and computed by a self-consistent calculation with respect to the solute electronic density [42]. The computation of q_{asc} requires the solution of a system of N_{tes} linear equations, with N_{tes} the number of *tesserae*:

$$\mathbf{D} \cdot \mathbf{q}_{asc} = -\Phi_I, \tag{3}$$

where $\mathbf{q}_{asc}$ is the array of the “apparent surface charges,” Φ_I is the electrostatic potential evaluated at the center of each *tessera* due to only the charge distribution of the system, and $\mathbf{D}$ is a matrix that depends only on the surface topology and on the dielectric constant [37,38],

$$D_{ii} = \frac{\epsilon}{(\epsilon - 1)} 1.0694 \sqrt{\frac{4\pi}{a_i}}, \tag{4}$$

$$D_{ij} = \frac{\epsilon}{(\epsilon - 1)} \frac{1}{|\mathrm{s}_i - \mathrm{s}_j|}, \tag{5}$$

where s_i and a_i are, respectively, the position vector and the area of the ith *tessera* and ϵ is the continuum dielectric constant. Hence, for a given molecular configuration of the explicit system, $\mathbf{x}$, the q_{asc}'s are determined from Eq. (3) and the electrostatic potential, $\mathbf{\Phi}_{\mathrm{RF}}(\mathbf{r})$, and the corresponding free energy, W_{elec}, are given by

$$W_{\mathrm{elec}} = -\frac{1}{2}\mathbf{\Phi}^{+}\mathbf{D}^{-1}\mathbf{\Phi}. \tag{6}$$

Note that, when neglecting any cavity deformations as in the present model, the energy derivatives with respect to a generic coordinate assume a quite simple form with respect to the general case [37]. The cavity surface enclosing the molecular system has been partitioned using an improved GEPOL procedure [43,44], which is well suited for treating cavities of general shape, and Eq. (3) can be solved by matrix inversion, computing and storing $\mathbf{D}^{-1}$ only once at the beginning of the simulation.

2.1.2. Nonelectrostatic contributions

The dispersion–repulsion contribution, $W_{\mathrm{disp-rep}}$, which is related to short-range solvent (explicit)–solvent (implicit) interactions, has been introduced to remove any possible source of physical anisotropy in proximity to the cavity surface, that is, deviation from bulk behavior. According to several other methodologies [45–52] developed in the framework of QM continuum models, we have also treated $W_{\mathrm{disp-rep}}$ as a classical mean force potential not perturbing the system electronic density. In particular, $W_{\mathrm{disp-rep}}$ is obtained from an effective empirical procedure parametrized on structural and thermodynamic properties originally presented in Ref. [33] and further developed in Ref. [32] (see also Refs. [35 and 31] for applications in the context of MM and QM/MM MD simulations, respectively). Briefly, we have assumed that $W_{\mathrm{disp-rep}}$ can be represented by an effective potential acting on each explicit solvent molecule irrespective of the others, depending on only the molecule distance and, possibly, orientation with respect to the cavity surface. Further, $W_{\mathrm{disp-rep}}$ is expanded in a series of terms corresponding to increasing levels of approximation, as $W_{\mathrm{disp-rep}} = W^{0}_{\mathrm{disp-rep}} + W^{1}_{\mathrm{disp-rep}} + \cdots$. As an example, the first term, $W^{0}_{\mathrm{disp-rep}}$, which depends only on the distance of the center of mass of the solvent molecule from the cavity surface, does ensure an isotropic density distribution of the liquid at the interface with the continuum, so avoiding artifacts in the simulations due to the presence of a physical boundary as observed in other continuum-based methodologies [53–55]. Analogously, higher order terms are introduced, if needed, to prevent other possible physical deviations arising from liquid bulk, as the solvent polarization effect may appear by using discrete/continuum models. Hence, $W_{\mathrm{disp-rep}}$ can be expressed in a simple general form as

$$W_{\mathrm{disp-rep}} = \sum_{i}^{N}\lambda(\mathbf{r}_i), \tag{7}$$

where $\lambda(\mathbf{r}_i)$ is the potential acting on the *i*th molecule and the sum is extended over the total number of explicit solvent molecules. The basic idea that has been followed to derive the dispersion–repulsion free energy term consists in building up such a potential "on the fly" from a test simulation of a neat liquid by discretizing the distance from the cavity boundary with a set of equally spaced Gaussian functions, whose heights are adjusted after a certain time interval on the basis of the local density [33]. It is worth noting that the so obtained $W_{\mathrm{disp-rep}}$ term is parameterized for a given solvent at specific physical conditions (e.g., density and temperature), but we can reasonably assume that it is constant for any solution of the same solvent irrespective of the cavity size and shape, provided the boundary surface is smooth and the number of explicit solvent molecules are sufficiently large (see, e.g., Refs. [32 and 35]). As an example, in Figure 2.2 the profile of $W^0_{\mathrm{disp-resp}}(\mathbf{r})$ is shown for water and chloroform at normal conditions ($T = 300\,\mathrm{K}$; $\rho_{\mathrm{H_2O}} = 55.3\,\mathrm{mol/l}$, $\rho_{\mathrm{CHCl_3}} = 12.4\,\mathrm{mol/l}$) along with the corresponding density distribution evaluated locally at increasing distance from a spherical cavity surface: note that the average local density is always close to the overall density of the system.

2.1.3. Extension to the constant presssure/flexible volume (*NpT*) ensemble

In order to reproduce more closely usual experimental conditions, especially in the molecular simulations of complex and flexible systems in solution, we have recently extended the GLOB model to allow constant pressure simulation by defining an estimator of the instantaneous pressure on the basis of a microscopic partition function. At this point, it is noteworthy that while the statistical mechanics theory of macroscopic systems is well defined and widely accepted, there is not yet a similar consensus on a theory of microscopic systems. Here, we will consider specifically a microscopic system that is part of a more extended or, at limit, infinite system, for example, a small portion of a molecular liquid contained in a spherical region. For consistency with our previous definition of the GLOB model and starting from the assumption that a physical boundary does separate the microscopic and the remaining molecular systems, we prefer to derive a microscopic partition function according to the minimum energy principle of the Helmholtz free energy. The resulting expression of the instantaneous pressure to be used in *NpT ensemble* molecular simulations can be written as

$$p = \frac{NkT}{V} - \left(\frac{\partial U}{\partial V} + \frac{\partial W_{\mathrm{elec}}}{\partial V} + \frac{\partial W_{\mathrm{disp-rep}}}{\partial V}\right), \tag{8}$$

where N is the number of atoms, V the microscopic system volume, U the potential energy due to only the explicit inter- and intramolecular interactions, k the Boltzmann's constant, and T the absolute temperature. Note that

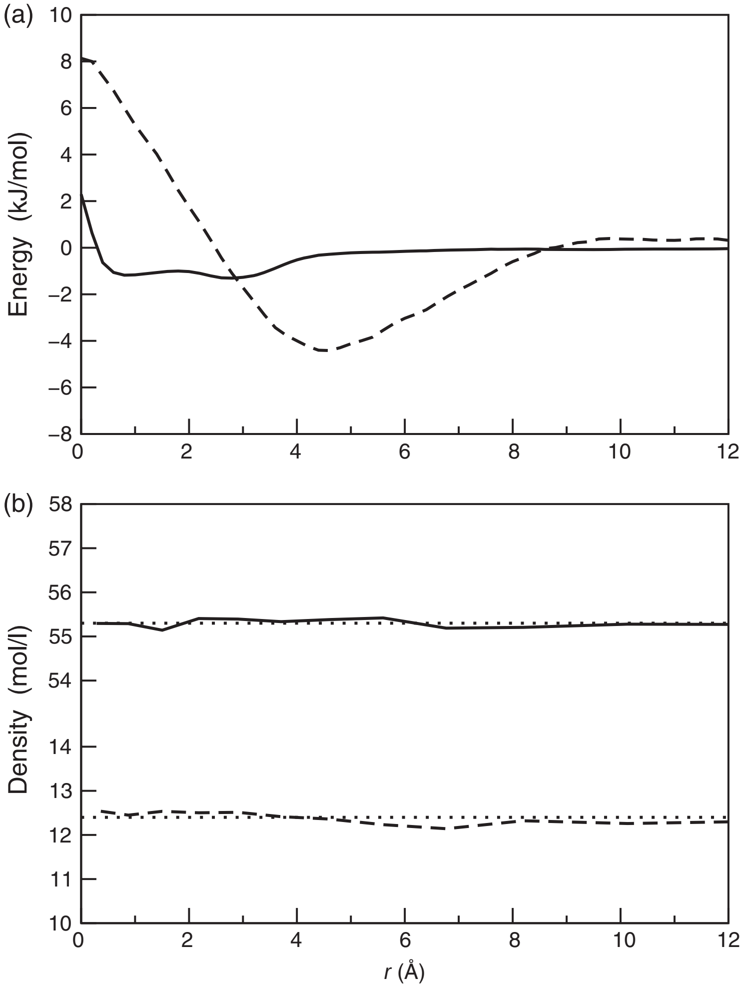

Figure 2.2 (a) $W^0_{\mathrm{disp-resp}}(\mathbf{r})$ (b) local density distribution for water (solid line) and chloroform (dashed line) at normal conditions ($T = 300$ K; $\rho_{\mathrm{H_2O}} = 55.3$ mol/l, $\rho_{\mathrm{CHCl_3}} = 12.4$ mol/l) evaluated at increasing distance from the cavity boundary along a radial direction (at the boundary surface, $r = 0$\AA). In (b), dotted lines represent average densities. Adapted from Ref. [32].

$(\partial U/\partial V)$ can be cast into the usual form of the virial equation $(-\Sigma_i^N \mathbf{r}_i \cdot \mathbf{f}_i/3V$, with $\mathbf{f}_i$ the force acting on the ith atom due to all other atoms). The derivatives of the mean field terms become quite simple in the case of a volume with a spherical symmetry and assuming that both the short-range potential and the external dielectric constant included in the $\mathbf{D}$ matrix do not change for small fluctuations of the microscopic system volume. Hence, we have

$$\frac{\partial W_{\text{disp}-\text{rep}}}{\partial V} = \sum_{i}^{N} \frac{\partial \lambda_i}{\partial \mathbf{r}_i} \frac{\mathbf{r}_i}{3V}, \tag{9}$$

$$\frac{\partial W_{\text{elec}}}{\partial V} = -\frac{1}{2}\frac{\partial \Phi^{\dagger}}{\partial V}\mathbf{D}^{-1}\Phi - \frac{1}{2}\Phi^{\dagger}\frac{\partial \mathbf{D}^{-1}}{\partial V}\Phi - \frac{1}{2}\Phi^{\dagger}\mathbf{D}^{-1}\frac{\partial \Phi}{\partial V}. \tag{10}$$

Note that the $\mathbf{D}^{-1}$ matrix can be computed by direct inversion at the beginning of the MD simulation and simply rescaled at each step, since the elements of the matrix are proportional to the cavity radius. Further, the pressure coupling can be efficiently introduced according to an extended phase-space scheme based on the Martyna–Tobias–Klein algorithm [56].

2.2. Time-independent approaches

2.2.1. Dynamic (Vibrational) effects beyond harmonic approximation

Within the time-independent framework nuclear dynamic effects can be included by computation of vibrationally averaged properties beyond harmonic approximation. In reality, the molecular structure is never fixed (in the space) and varies by small displacements, defined by molecular vibrations at the anharmonic zero point vibrational (ZPVE) energy level. To take into account these effects, which are able to tune molecular properties, it is necessary to perform vibrational computations beyond the harmonic approximation. However, full-dimensional anharmonic vibrational calculations still represent a complicated task, even for medium-size molecular systems. Although successful approaches for variational computations of vibrational energy levels within the vibrational self-consistent field methodology have been already reported [8,9,57–60] (including the treatment of molecules in electronic excited states [61,62] and the computation of Franck–Condon (FC) factors [63]), significant problems remain, especially in relation to the dimensionality of the PES. As the size of the molecular system increases, the number of calculations needed to describe the anharmonic PES becomes so large that accurate full-dimensional vibrational variational approaches will not be practical at least in the near future. On the other hand, in many cases the effect of anharmonicity can be accounted for by a second-order perturbative (PT2) inclusion of principal anharmonicities which provide much improved results at a reasonable cost [64–67].

In the framework of the Born–Oppenheimer approximation, we can speak of a PES and of a “property surface,” which, can be obtained from QM/MM computations at different nuclear configurations. In this scheme, expectation values of observables are obtained by averaging the different properties on the nuclear wave functions. In the perturbative model, the vibrational energy (in wave numbers) of asymmetric tops is given by

$$E_n = \xi_0 + \sum_i \omega_i \left(n_i + \frac{1}{2} \right) + \sum_i \sum_{j<i} \xi_{ij} \left(n_i + \frac{1}{2} \right) \left(n_j + \frac{1}{2} \right), \tag{11}$$

where the ω's are the harmonic wave numbers and the ξ's are simple functions of third (F_{ijk}) and semidiagonal fourth (F_{iijj}) energy derivatives with respect to normal modes $\mathbf{Q}$ [64]. Both F_{ijk} and F_{iijj} can be evaluated from numerical differentiation of analytical hessian matrices at geometries displaced by small increments, as described in Ref. [64]. In this context, availability of analytical second derivatives within the QM/MM scheme paves the route to the studies of vibrational properties beyond harmonic approximation for significantly larger molecular systems. We refer interested readers to Ref. [64] on the details of PT2 implementation. Here we only recall that, in the absence of resonances, fundamental vibrational frequencies (ν_i), first overtones [$2\nu_i$], combination bands [$\nu_i \nu_j$], and ZPVE (E_0) are given by

$$\nu_i = \omega_i + 2\xi_i + \frac{1}{2} \sum_{j \neq i} \xi_{ij}, \tag{12}$$

$$[2\nu_i] = 2\omega_i + 6\xi_{ii} + \sum_{j \neq i} \xi_{ij} = 2\nu_i + 2\xi_{ii}, \tag{13}$$

$$[\nu_i \nu_j] = \omega_i + \omega_j + 2\xi_{ii} + 2\xi_{jj} + 2\xi_{ij} + \frac{1}{2} \sum_{l \neq i,j} (\xi_{il} + \xi jl) = \nu_i + \nu_j + \xi_{ij}, \tag{14}$$

$$E_0 = \xi_0 + \frac{1}{2} \sum_i \left(\omega_i + \frac{1}{2} \xi_{ii} + \sum_{j>i} \frac{1}{2} \xi_{ij} \right), \tag{15}$$

To the first order, the vibrationally averaged value of a property Ω is expressed as

$$\langle \Omega \rangle_n = \Omega_e + \sum_i A_i \left(n_i + \frac{1}{2} \right), \tag{16}$$

where Ω_e is the value at the equilibrium geometry and

$$A_i = \frac{\beta_{ii}}{\omega_i} - \sum_j \frac{\alpha_j F_{iij}}{\omega_i \omega_j^2} \tag{17}$$

where α_i and β_{ii} are the first and second derivatives of the property with respect to the ith normal mode. The first term on the r.h.s. of Eq. (17) will be referred to in the following as harmonic and the second one as anharmonic.

It should be noted that PT2 computations for macromolecular systems with large number of normal modes are particularly sensitive to the proper treatment of Fermi resonances, which are known to plague the PT2 computations. It is therefore crucial to automatically neglect nearly singular contributions (deperturbed computations), effectively removing interactions in the second-order treatment, which are more properly treated in the first order. Our specific PT2 implementation uses criteria proposed by Boese and Martin [68] and such an automated scheme has been shown to provide accurate results at least for fundamental bands [69].

2.2.2. Vibrationally resolved electronic spectra

In the framework of the FC principle [70–72], time-independent ab initio approaches to simulate vibronic spectra are based on the computation of overlap integrals (known as FC integrals), between the vibrational wave functions of the electronic states involved in the transition. The computation of FC integrals requires a detailed knowledge of the multidimensional PESs of both electronic states or, within the harmonic approximation, at least computation of equilibrium geometry structures and vibrational properties. Till recently, computations of vibronic spectra have been limited to small systems or approximated approaches, but within QM/MM scheme simulations of spectra for significantly larger systems are possible. When treating such large systems, the inclusion of vibrational contributions becomes very challenging, since the number of vibrational states to be taken into account increases steeply with the dimension of the molecule and the spectral width. Nonetheless, most of the possible vibronic transitions do not contribute significantly to the spectrum. Therefore, the availability of effective selection criteria to individuate a priori the most relevant vibronic transitions within the dense bath of possible final states can make feasible the calculation of spectrum lineshapes also for macromolecular systems. In our approach an a priori method, called *FCclasses* [73,74], which provides very accurate vibrationally resolved spectra of medium and large molecular systems with limited computational resources has been applied. In this frame, the vibrationally resolved one-photon absorbtion (OPA), one-photon emission, and electronic circular dichroism (ECD) spectra can be simulated.

Let us start from a brief summary of the general mathematical frame for the spectra computations. The absorption spectrum, defined as the rate of energy absorption by a single molecule per unit radiant energy density, is given by the expression [6]

$$\sigma_{\mathrm{abs}}(\omega) = \frac{4\pi^2\omega}{3}\sum_f \left|\langle \Psi_i|\boldsymbol{\mu}|\Psi_f\rangle\right|^2 \delta(E_f - E_i + \hbar\omega). \tag{18}$$

On similar lines, the emission spectrum in photon counting experiments, defined as the rate of photon emission due to a single molecule is [6]

$$\sigma_{\mathrm{em}}(\omega) = \frac{4\omega^3}{3\hbar c^3} \sum_f \left| \langle \Psi_i | \boldsymbol{\mu} | \Psi_f \rangle \right|^2 \delta(E_f - E_i - \hbar\omega). \tag{19}$$

The stick spectra computed from Eqs. (18 and 19) are usually convoluted with a Lorentzian or a Gaussian function to simulate homogeneous or inhomogeneous broadening, respectively. In the following, we will discuss the simplest case of absorbtion or emission where the intensity of a spectrum line depends on the transition dipole moment integral $(\Psi_{\mathrm{i}} | \boldsymbol{\mu} | \Psi_{\mathrm{f}})$, where Ψ_i and Ψ_f are the molecular wave functions and $\boldsymbol{\mu}$ is the electric dipole moment. However, our approach is general and can be applied to any case of two interacting transition dipole moments as, for example, $\boldsymbol{m}$ and $\boldsymbol{\mu}$ in case of the ECD spectra. The ECD stick spectrum is obtained from the anisotropy of molar absorptivity $\varepsilon(\omega)$, which can be computed by the equation analogous to Eq. (18) where the square of the norm of the electric transition dipole moment integral is replaced by the imaginary part of the product of the electronic transition dipole moment with the magnetic transition dipole moment ($\boldsymbol{m}$)(see Ref. [75] for details).

Our approach is set up in the Born–Oppenheimer approximation; thus the wave function of each state can be expressed as a product of a nuclear ψ_{n} and an electronic ψ_{e} wave functions:

$$\langle \Psi_i | \boldsymbol{\mu} | \Psi_f \rangle = \langle \psi_{\mathrm{n}} \psi_{\mathrm{e}} | \, \boldsymbol{\mu} \, | \psi_e' \psi_n' \rangle. \tag{20}$$

The electric dipole moment can be separated into an electronic part $\boldsymbol{\mu}_{\mathrm{e}}$ and a nuclear part $\boldsymbol{\mu}_{\mathrm{n}}$. Replacing the electric dipole moment by these two components, the transition dipole moment integral can be divided into two terms:

$$\langle \Psi_i | \boldsymbol{\mu} | \Psi_f \rangle = \langle \psi_n \psi_e | \, \boldsymbol{\mu}_e \, | \psi_e' \psi_n' \rangle + \langle \psi_n \psi_e | \, \boldsymbol{\mu}_n \, | \psi_e' \psi_n' \rangle. \tag{21}$$

Because of the orthogonality of the electronic wavefunctions of different electronic states, the second term on the r.h.s. in Eq. (21) vanishes. As a consequence, the transition dipole moment integral depends on the nuclear wave functions and on the electronic transition moment $\boldsymbol{\mu}_{if} = \langle \psi_{\mathrm{e}} | \boldsymbol{\mu}_{\mathrm{e}} | \psi_e' \rangle$. Equation (21) can then be written as

$$\langle \Psi_i | \, \boldsymbol{\mu} \, | \Psi_f \rangle = \langle \psi_{\mathrm{n}} | \, \boldsymbol{\mu}_{if} \, | \psi_{\mathrm{n}}' \rangle. \tag{22}$$

Application of the Eckart conditions [76] allows to minimize the coupling between the rotational and vibrational motions of the nuclei in a molecule, and as much as possible separate the nuclear wave function into rotational and vibrational contributions. However, another problem remains since no general analytical expression exists for the electronic transition dipole moment: hence this integral must be approximated. This can be done by expanding the transition dipole moment in a Taylor series of the normal coordinates (either the set $\mathbf{Q}'$ of the final state or the set $\mathbf{Q}$ of the initial state). In our approach the expansion on $\mathbf{Q}'$ has been chosen

$$\mu_{if}(\mathbf{Q}') \simeq \mu_{if}(\mathbf{Q}'_0) + \sum_{k=1}^{N} \frac{\partial \mu_{if}}{\partial Q'_k} Q'_k + \frac{1}{2} \sum_{k=1}^{N} \sum_{l=1}^{N} \left(\frac{\partial^2 \boldsymbol{\mu}_{if}}{\partial Q'_k \partial Q'_l} \right)_0 Q'_k Q'_l + \cdots, \tag{23}$$

where Q'_0 refers to the equilibrium geometry of the final electronic state, while N is the number of normal modes.

Then, switching to the Dirac notation, replacing $\boldsymbol{\mu}_{if}$ by its Taylor expansion given in Eq. (23) and assuming that the harmonic approximation can be used to represent the vibrational wave function of the initial and final states as eigenstates of the N-dimensional harmonic oscillator, that is, by defining $|\chi_i\rangle = |\boldsymbol{\nu}\rangle$ and $|\chi_f\rangle = |\boldsymbol{\nu}'\rangle$, it is possible to write Eq. (22) as

$$\begin{aligned} \langle \Psi_i | \boldsymbol{\mu} | \Psi_f \rangle = \boldsymbol{\mu}_{if}(\mathbf{Q}'_0) \langle \boldsymbol{\nu} | \boldsymbol{\nu}' \rangle + \sum_{k=1}^{N} \left(\frac{\partial \boldsymbol{\mu}_{if}}{\partial Q'_k} \right)_0 \langle \boldsymbol{\nu} | Q'_k | \boldsymbol{\nu}' \rangle \\ + \frac{1}{2} \sum_{k=1}^{N} \sum_{l=1}^{N} \left(\frac{\partial^2 \boldsymbol{\mu}_{if}}{\partial Q'_k \partial Q'_l} \right)_0 \langle \boldsymbol{\nu} | Q'_k Q'_l | \boldsymbol{\nu}' \rangle. \end{aligned} \tag{24}$$

The current version of our approach allows to take into account the Taylor expansion up to diagonal second derivatives. The zero order, assuming that the transition dipole moment is unchanged during the transition is the FC [70–72] approximation, which is based on the assumption that molecular geometry does not change significantly during the transition, and therefore the electronic transition dipole moment can be treated as a constant. While this approximation is known to lead to very good results in many cases, it becomes not satisfactory for the dipole-forbidden [$\boldsymbol{\mu}_{if}(\mathbf{Q}'_0) = \mathbf{0}$] or weakly allowed transitions. In these cases, one needs to improve the model and to add the second term [Herzberg–Teller (HT) term]. Then, a limited change in the structure during the transition is taken into account. For many studied systems, the FC and HT approximations are sufficient to correctly describe both absorption and emission spectra, but for symmetry-forbidden transitions a correct reproduction of intensity of weak bands may require the inclusion of higher order terms [77].

Computation of the overlap integrals between initial and final vibrational states requires the use of a common coordinates set. Duschinsky proposed a solution to this problem by considering a linear transformation between the normal modes of the initial and the final states [78]:

$$\mathbf{Q}' = \mathbf{J}\mathbf{Q} + \mathbf{K}'. \tag{25}$$

The Duschinsky matrix $\mathbf{J}$ describes the projection of the normal coordinate basis vectors of the final state on those of the initial state and represents the rotation of the normal modes upon the transition. The displacement vector

$\mathbf{K}'$ represents the displacements of the normal modes between the initial and the final state structures.

Since $\mathbf{J}$ in principle is not diagonal, the calculation of the vibrational overlap integrals is not straightforward. In our case, both analytical [79,80] and recursive [81] approaches have been applied to compute terms on the r.h.s. of Eq. (24). Analytical methods can quickly and accurately compute the transition dipole moment integrals through ad hoc formulae, but the latter need to be generated beforehand. On the other side, recursive approaches provide methods to compute the overlap between given initial and final states through formulae that express it in terms of sums of integrals involving states with lower vibrational quantum numbers. Once the overlap between ground vibrational states has been calculated directly, that of any other transition can be obtained by recursively applying these formulae. More details on the recursion formulae applied in the presented approach can be found in Refs. [73,74,82].

The recursive approach can be in principle successfully applied to the computation of spectra of large molecular systems. However, in many cases the number of overlap integrals that must be taken into account can become extremely large, with a consequent increase in the required computational times and memory usage. Efficient computational strategies must be able to individuate in advance the relevant transitions among the infinite number of possible final states. Here, we use an *a priori* method called *FC classes* [73,74], which provides very accurate vibrationally resolved spectra of medium and large molecular systems with limited computational resources. According to this method, transitions are partitioned into *classes* C_n, depending on the number n of simultaneously excited normal modes of the final electronic state of the transition. The overlap integrals for single vibrations (class C_1) and combination of two normal modes (class C_2), are computed up to a chosen limit (it can be also very large, since computation is cheap; therefore, any loss of accuracy in this step can be avoided). The probabilities of all these transitions are then used in the computation of FC integrals for higher order classes, to obtain *a priori* estimates of the maximum quantum number that needs to be considered for each normal mode. To that end, for each class the allowed transitions are chosen iteratively, on the ground of a minimum threshold for C_1 and C_2 probabilities, so that the number of overlap integrals to be computed stays approximately below a user-defined limit ($N_{\mathrm{I}}^{\mathrm{max}}$), which rules the calculation accuracy (see Ref. [73] for further details).

However, when using an *a priori* method to selectively compute transitions, the convergence of the calculations and hence the reliability of their outcome needs to be evaluated. In the calculation of vibrationally resolved spectra, this can be easily done on the ground of analytical sum rules, by comparing the actual computed spectrum intensity $I_{\mathrm{tot}}^{\mathrm{n}}$ to the exact analytical limit $I_{\mathrm{tot}}^{\mathrm{a}}$. In the current approach spectrum convergence is always improved by increasing the limit for the number of integrals computed for each *class* of transitions: $N_{\mathrm{I}}^{\max}$. A higher number of allowed transitions obviously yields a better spectrum convergence but also directly increases the required computational time and memory usage.

Skipping prefactors and the dependence on the frequency, the intensity of a given transition is equal to $I(\boldsymbol{v},\boldsymbol{v}') = |\langle \boldsymbol{v}|\boldsymbol{\mu}_{if}(\mathbf{Q}')|\boldsymbol{v}'\rangle|^2$ and summing over all the possible final states one gets

$$I_{\mathrm{tot}}^{\mathrm{a}} = \sum_{\boldsymbol{v}'} |\langle\, \boldsymbol{v} \mid \boldsymbol{\mu}_{if}(\mathbf{Q}')\, |\boldsymbol{v}'\rangle|^2 = \sum_{\varrho=\xi,\theta,\zeta} \langle \boldsymbol{v}|\mu_{if_\varrho}^2(\mathbf{Q}') \mid \boldsymbol{v}\rangle, \tag{26}$$

where the superscript a indicates that the sum has been carried out analytically by exploiting the closure relation. In the limit of a complete inclusion of all the possible final states the numerical sum of the state-to-state intensities $I_{\mathrm{tot}}^{n} = \Sigma_{\boldsymbol{v}'} I(\boldsymbol{v},\boldsymbol{v}')$ must approach $I_{\mathrm{tot}}^{\mathrm{a}}$ and the ratio $C = I_{\mathrm{tot}}^{\mathrm{n}}/I_{\mathrm{tot}}^{\mathrm{a}}$ can be used to control the convergence, which is complete when $C = 1$ (see Refs. [74,82] for the more complex formulae required in case of HT computations). However, for large systems, a great number of transitions has to be considered to reach convergence of the spectrum intensity, and calculations although feasible can become computationally demanding. On the other side, usually the main scope is to correctly reproduce the spectrum lineshape and assign the most important vibronic transitions. It has been shown [73,74,83] that the spectrum lineshape usually converges much faster than C. The lineshape convergence can be easily checked by comparison of results calculated with two different thresholds for $N_{\mathrm{I}}^{\max}$.

It should be mentioned that while the presented approach is developed within harmonic approximation, it can be further extended to take into account anharmonic effects. As a first step in this direction a correction scheme to derive excited state's anharmonic frequencies from ground state data has been implemented [84]. Briefly, excited state mode-specific scaling factors can be derived from the ground state ones. These latter can be obtained theoretically, for example, from perturbative anharmonic frequency calculations [64], or from easily accessible ground state experimental data. Then, for each particular normal mode Q_k, the frequency scaling vector $\boldsymbol{\alpha}$ is computed first, using the formula $\alpha(k) = \nu(k)/\omega(k)$ where ν is the anharmonic frequency and ω is the harmonic frequency. To proceed further, we shall assume that, if there is a one-to-one relation between the normal modes Q_k and $Q_k^{'}$ of the initial and final states, the scaling factors α_k and $\alpha_k^{'}$ are equal. However, the normal modes are in general not coincident ($\mathbf{J} \neq \mathbf{I}$), and $\boldsymbol{\alpha}$ cannot be transferred directly to scale the frequencies of the final state. In other words, the scaling vector must be adapted to the excited state frequencies. In the case of small-amplitude vibrations, this can be obtained by expressing the normal modes of the excited state as linear combinations of the normal modes of the initial state, by means of the Duschinsky transformation. The $\mathbf{J}_{kl}$ coefficients can now be applied to derive the relation between the initial (k) and final (l) state mode-specific anharmonicity scaling factors:

$$\alpha_l^{'} = \sum_k^N \mathbf{J}_{lk}{}^2 \alpha_k \tag{27}$$

and then excited state anharmonic frequencies are simply computed as $\nu'(l) = \alpha'(l)\omega'(l)$.

2.3. Calculation of spectroscopic properties

2.3.1. Vibrational properties and infrared spectra

The theoretical solution of the vibrational problem for polyatomic molecules and the determination of the IR spectra are among the most important applications in computational chemistry. In practice, the most common way to evaluate molecular properties is still their computation at the "bottom of the well" corresponding to the global minimum. This approach assumes an ideal case of perfectly symmetric harmonic representation of the true shape of PES, as only then vibrationally averaged properties and those calculated at the "bottom of the well" are exactly coincident. But in reality the PES is always "anharmonic," leading to dissociation of molecules. The harmonic frequency calculations and computation of molecular properties at the "bottom of the well" do not take into account the anharmonic character of PES, but such approximations are still useful and allow determination of molecular properties in a simple manner. However, in many cases it is crucial to take into account the effects of nuclear motions beyond harmonic approximation. In particular, the electron spin resonance (ESR) parameters often show a strong dependence on the molecular geometry and it has been shown that the vibrational effects can change their values up to 25% [85]. It is important to recall that dynamic effects can be nonnegligible even at very low temperatures and for semirigid systems.

As sketched in Section 2.2.1 recently developed methods based on a quantum mechanical/stationary-state picture of the system, such as variational [86–88], self-consistent [9,57–60], and perturbative [64–67] treatments, provide accurate energy levels in terms of the ro-vibrational Hamiltonian by taking into account also anharmonic effects. In the challenging case of large systems in condensed phases, the use of effective QM/MM schemes combined with implicit solvent methods represents a viable choice to reduce the computational cost of otherwise prohibitively expensive anharmonic frequency analysis. Additionally, it is also possible to restrict the anharmonic treatment to the small part of the total system, directly related to the spectroscopic observable, for example, the most intense bands in the IR spectrum, or the selected large-amplitude motions, without losing the benefits of a unified and comprehensive picture. However, there are still cases in which the underlying assumptions of such static calculations pose severe limitations to a complete vibrational analysis by the so-called "Hessian-based" methods, especially when the vibrational modes involve a complex conformational rearrangement and/or coupling with solvent motions. A possible alternative route is represented by time-dependent approaches based on a classical or quantum treatment of the nuclear dynamics. Indeed, IR spectroscopic data can be obtained by a statistical mechanics formalism that relies on the Fourier transform analysis of the time correlation of atomic velocities or dipole moment. In principle, such approaches can provide a complete description of the experimental spectra, that is, the characterization of the real molecular motion consisting of many degrees of freedom activated at finite temperature, often strongly coupled to each other. In particular, ab-initio and hybrid QM/MM MD make feasible the vibrational analysis of complex system in the condensed phase allowing also a reliable estimate of the possibly induced solvent shifts of fundamental vibrational frequencies [89]. In this case, an important issue concerns the introduction of appropriate quantum corrections to the classical time-correlation functions. Recently, different quantum corrections have been compared on a theoretical basis and with respect to the performance on different kinds of intramolecular and intermolecular motions [90]. However, all the proposed corrections only affect the width and the shape of the IR bands, while the accuracy of the calculated frequencies still relies on the ability of the classical approach to describe the fundamental vibrations. In this regard, it is worth noting that hybrid density functional theory (DFT) functionals do perform reasonably well for a variety of molecular systems and represent the method of choice for large biological systems. Eventually, more sophisticated post-Hartree–Fock methods can be employed to correct the absolute frequencies of specific vibrational modes, while DFT-based approaches can be still used to obtain accurately solvent shifts.

2.3.2. Electronic spectra

To a first approximation level, electronic spectra (UV–vis, photoelectron, X-ray, etc.) can be simulated by computing vertical excitation energies on the geometrical structures optimized for the ground state, with the resulting stick spectra subsequently convoluted by Gaussian or Lorentzian functions, corresponding to inhomogeneous and homogeneous broadening, respectively. Such a treatment completely neglects any dynamic effects on the spectrum shape, but in many cases qualitatively reproduces experimental findings. The simplified scheme is particularly justified for the studies of very large macromolecular systems, for which excited state geometry optimizations and/or frequency computations are still prohibitively expensive. However, for such large systems even computations of reliable vertical excitation energies, particularly when many excited electronic states need to be considered, might be a nontrivial task. In this respect, the QM/MM schemes pave a viable route for studies of large systems where the electronic excitation has a well-defined relatively localized character, and the QM approach can be fully employed for the region of the system relevant to the electronic excitation. Recent developments allow to compute the QM part at the time-dependent DFT (TD-DFT) level and the resulting TD-DFT/MM schemes greatly improves the reliability of the results over the semiempirical approaches. However, in many cases, a more accurate reproduction of bandshapes conveys important insight into structural and electronic features; at this level, the vibrational structure of the electronic band must be taken into account. Within the simplest zero-order harmonic approximation it can be assumed that the PES of the initial and final states do not differ in shape, so that the vibrational levels are identical. Obviously, such an approach can only provide a very rough estimation of the real spectrum, and in general most vibrational transitions are actually missed. A significant improvement is represented by the linear coupling method (LCM) [91]. Here the multidimensional coupling constants are obtained from the ground state frequencies and normal modes, and the excited state energy gradients evaluated at the ground state geometry. Thus, the approach does not require computation of the excited state equilibrium geometry, frequencies and normal modes, which have only recently become feasible for large systems. However, the LCM does not take into account changes in vibrational frequencies and/or in normal modes between the excited and ground state. New models have been recently presented to further improve the quality of the approximation, based on a linear transformation between the normal modes of the initial and final states, as first described by Duschinsky [78]. These models have proven capable to produce very accurate emission and absorption spectra [92–96] in cases where reliable geometries and force fields have been computed for both electronic states. Considering first-principles simulations of vibronic spectrum lineshapes for large systems, the inclusion of vibrational contributions becomes very challenging, since the number of vibrational states to be taken into account increases steeply with the dimension of the molecule and the spectral width. Nonetheless, most of the possible vibronic transitions do not contribute significantly to the spectrum. Thus a crucial aspect is the adoption of effective selection criteria to individuate a priori the most relevant vibronic transitions within the dense bath of possible final states. Several schemes have been proposed [73,83,97–100] ranging from the simplest approach, based solely on the energy window of the spectrum [97,98] up to rigorous prescreening techniques based on analytically derived sum rules [100]. However, in our opinion the fast and effective a priori selection scheme presented in Section 2.2.2 has proven its general applicability for a variety of different systems.

2.3.3. Magnetic properties: electron spin resonance spectroscopy

ESR spectroscopy is widely used to characterize properties of macromolecular systems of biological interest giving access to important information on structural and dynamical properties. As an example we shall recall nitroxide radicals, which are often used as a "spin probes" or "spin labels" [101]. However, the interpretation of ESR spectra is not a trivial task and quantum mechanical computations of magnetic parameters greatly support the analysis of experimental results. In the case of isotropic hcc's of protons, reliable estimates can be obtained from semiempirical relationships, but quantitative evaluation of hcc's for heavier atoms usually requires rather sophisticated computational treatments not accessible for large systems. This is related to the fact that the computation of accurate hcc's requires good description of spin density at the nucleus. Hence, having in mind the computational support of ESR for studying biological systems, it seems reasonable to adopt an efficient QM/MM scheme, where the molecular region surrounding the radical center is described at a high level of theory and with a large basis set. Such an approach allows to define QM/MM schemes well suited for the study of ESR properties of radicals embedded in complex and nonstandard media as proteins, micelles, or cellular membranes.

Here, we briefly sketch the theoretical framework used to compute magnetic properties, invariant with respect to the applied electronic structure method [102]. The interaction between the electron spin (S) of a radical containing magnetic nucleus of spin I with an external magnetic field ($\mathbf{B}$) can be approximated by the spin Hamiltonian H_s:

$$H_\mathrm{s} = \mu_\mathrm{B} S \cdot \mathbf{g} \cdot \mathbf{B} + S \cdot \mathbf{A} \cdot I + \cdots, \tag{28}$$

where the first term is the Zeeman interaction between the electron spin and the external magnetic field through the Bohr magneton, μ_B, and the $\mathbf{g}$-tensor; the second term is the hyperfine interaction between S and the nuclear spin, I, described through the hyperfine coupling tensor $\mathbf{A}$. The latter, which is defined for each nucleus X ($\mathbf{A}_\mathrm{X}$), can be split into three terms: $\mathbf{A}_\mathrm{X} = \mathbf{a}_\mathrm{X}\mathbf{1_3} + \mathbf{T}_\mathrm{X} + \mathbf{\Lambda}_\mathrm{X}$, where $\mathbf{1_3}$ is the 3×3 unit matrix. The first term ($\mathbf{a}_\mathrm{X}$), usually referred to as the Fermi contact interaction, is an isotropic contribution and is related to the spin density at the corresponding nucleus X. The second contribution ($\mathbf{T}_\mathrm{X}$) is anisotropic and can be derived from the classical expression of interacting dipoles. The last term, Λ_X, is due to second-order spin–orbit coupling (SOC) and can be determined by methods similar to those described for the $\mathbf{g}$-tensor. In cases with a strong localization of spin density on first-row atoms and of small SOC constants, the last contribution can be safely neglected and will not be discussed in the following. Because both $\mathbf{a}_\mathrm{X}$ and $\mathbf{T}_\mathrm{X}$ are ruled by one-electron operators, their evaluation is, in principle, quite straightforward. However, hyperfine coupling constants have been among the most challenging quantities for conventional QM approaches for two main reasons [102]. On the one hand, conventional Gaussian basis sets are ill adapted to describe nuclear cusps; on the other hand, the overall result derives from the difference between large quantities of opposite sign. However, the past few years have shown that coupling of some hybrid functionals to specifically tailored basis sets performs a remarkable job for both isotropic and dipolar terms.

The gyromagnetic tensor can be written as follows: $\mathbf{g} = g_e \mathbf{1}_3 + \Delta\, \mathbf{g}_{RM} + \Delta \mathbf{g}_G + \Delta \mathbf{g}_{OZ/SOC}$, where g_e is the free-electron value ($g_e = 2.0023193$). Computation of the relativistic mass (RM) and gauge (G) corrections is quite straightforward because they are first-order contributions [103]. The last term arises from the coupling of the orbital Zeeman (OZ) and the SOC operator. The OZ contribution is computed using the gauge-including atomic orbital approach [103,104], whereas for light atoms, the two-electron SOC operator can be reliably approximated by a one-electron operator involving adjusted effective nuclear charges [105]. Although those charges were optimized for wave function based methods, a number of test computations showed that they are nearly optimal for DFT computations too. Upon complete averaging by rotational motions, only the isotropic part of the **g**-tensor survives, which is given by $g_{iso} = 1/3\ \mathrm{Tr}(\mathbf{g})$. Of course, the corresponding shift from the free electron value is $\Delta g_{iso} = g_{iso} - g_e$. For both hcc's and gyromagnetic tensor calculations, it has been recently shown that B3LYP [106] and EPR-III [107] or N07D [108–110] basis sets provide reliable results [103,111,112].

3. APPLICATIONS

As anticipated in the Introduction, the methodological machinery presented in the above sections can be successfully applied to many computational spectroscopy studies ranging from ESR, IR/Raman, low-resolution UV–Vis up to rovibronic spectra, and to a large variety of systems from small molecules in solution to macrosystems. The examples given below include the UV spectrum of acrolein in the gas phase and aqueous solution, the vibrationally resolved photoelectron spectra of adenine adsorbed on the Si(100) surface, along with computation of ESR magnetic tensors and vibrational frequencies beyond harmonic approximation, and are chosen to illustrate the broad range of computational spectroscopy approaches.

3.1. UV spectra of acrolein in gas phase and in aqueous solution

The UV absorption spectrum of acrolein has attracted significant attention since this molecule exhibits two conjugated chromophores C=C and C=O, a common feature for many natural systems [113]. The spectrum was studied experimentally in different solvents [114–121], as well as in gas phase [121–124], and a solvatochromic blueshift of 0.20–0.25 eV was observed, as a result of water solvation. A simple explanation of such a blueshift is that the electronic ground state has a larger dipole moment with respect to the first excited state and, as a consequence, it is more stabilized in polar solvents, such as water. However, the actual extent of the observed blueshift is the result of subtle and opposite effects, not only polar ones (see, e.g., Ref. [125]). Here, we present a comparative study where time-dependent and time-independent approaches, described in Sections 2.1 and 2.2.2, have been applied to simulate the UV absorption spectrum of acrolein both in gas phase and in aqueous solution aiming at a deeper understanding of the subtle interplay of several different, not easily dissectable and evaluable effects hidden behind the observed blueshift.

Within the time-dependent approach the study of dynamical and solvent effects on acrolein structure and electronic properties has been performed with GLOB model [113]. In particular, an *NVT* QM/MM simulation of acrolein + 134 TIP3P water molecules and a full QM simulation of acrolein in vacuo were performed for 24 ps, including 4 ps of equilibration, using the GLOB/ADMP methodology [126–128] (see Ref. [113] for details). Then the vertical excitation energies and oscillator strengths have been computed within the TD-DFT formalism employing the B3LYP functional and the 6-311++G(2d,2p) basis set. The consistency of such basis set in spectroscopic calculations was validated in a previous work [129]. For the time-independent approach the full geometry optimization, and frequency calculations have been performed for both electronic states in the gas phase and in aqueous solution. For consistency, the DFT/TD-DFT model with B3LYP density functional and 6-311++G(2d,2p) basis set has been applied. In this case, solvent effects have been included implicitly by means of the conductor-like polarizable continuum model (CPCM) [38] within the non-equilibrium limit where only its fast (electronic) degrees of freedom have been equilibrated with the excited state charge density while the slow (nuclear) degrees of freedom remain equilibrated with the ground state. Such an assumption is sufficient to describe the absorption spectrum in solution, due to the different timescales of the electronic and nuclear response components of the solvent reaction field [73].

First we will discuss the nature of the solvent (water) effects on the UV $n \to \pi^*$ transition energy of acrolein in terms of the relative contributions due to direct (solvent polarization and H-bonding) and indirect (solute structural rearrangements) effects. The computed blueshift of the $n \to \pi^*$ vertical transition of acrolein, issuing from the gas- and condensed-phase MD simulations at room temperature, are reported in Table 2.1 while the lower panel of Figure 2.3 shows the corresponding spectra. The overall computed blueshift is 0.26 ± 0.01 eV (last line in Table 2.1), in good agreement with experiments (0.20–0.25 eV). Such a result has been obtained by

Table 2.1 UV n→π* transition energies of acrolein in the gas phase and in aqueous solution, computed at the TD-B3LYP/6-311++G(2d,2p) level of theory

	Energy	Shift
Gas phase	3.58	
Solution		
Acrolein	3.49	−0.08
Acrolein + $2H_2O^{QM}$	3.68	+0.10
Acrolein + $2H_2O^{QM}$ +132 H_2O^{QM} + PCM	3.84	+0.26

Note: Values are in eV, standard error is 0.01 eV.

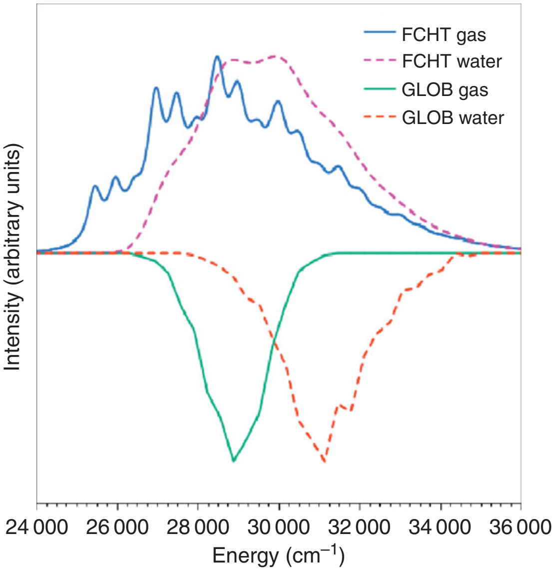

Figure 2.3 UV spectra of n→π* electronic transition of acrolein. Upper panel, time-independent approach, spectra computed with FC–HT approximation, gas phase (solid line), and water solution described by the CPCM model (dashed line). Lower panel, time-dependent approach: spectra obtained from MD simulations with the GLOB model, gas-phase spectrum (solid line), and aqueous solution (dashed line). Please refer online version for color image.

the aqueous solution model with the acrolein molecule and the two closest to the C—O group water molecules treated at QM level (acrolein+$2H_2O^{QM}$+$132H_2O^{MM}$+PCM). Besides, when all water molecules are treated as point charges (acrolein+all H_2O^{MM}+PCM), the blueshift remains unchanged within the statistical noise, 0.25 ± 0.01 eV, in line with a recent study for the case of acetone [130]. This means that solvent effects on the n→π* vertical transition are essentially of electrostatic nature. However, we have also evaluated the separate contributions to the blueshift coming solely from the solute structural changes (second line in Table 2.1) and from the first solvation shell of the C=O group (acrolein+$2H_2O^{QM}$), that is including the two water molecules closest to the carbonyl oxygen. Remarkably, solute geometry distortions lead to a nonnegligible redshift (−0.08 eV) and, hence, the direct solvent effects on the spectroscopic property, once the solute geometry has changed, are of about 0.34 eV. Additionally, more than half of such shift is provided by the first two water molecules surrounding the C=O group (0.18 eV), which means that H-bonding and bulk effects are nearly equal.

The time-independent approach takes into account only the electrostatic part of solute–solvent interaction underlying the solvent shift, but allows a straightforward and relatively inexpensive computation of both the gas-phase and aqueous solution absorption spectra of acrolein. Moreover its advantage stems from the fact that working directly in the frequency domain gives access to the detailed analysis of vibronic contributions. In case of n→π* electronic transition of acrolein assignment of the most intense bands (from stick spectrum, see Figure 2.4) shows that the spectrum is dominated by the progressions into the normal modes, which can be described as a combinations of C=O, C=C, C—C stretching, and C—C—O bending vibrations. To simulate the spectrum lineshape within

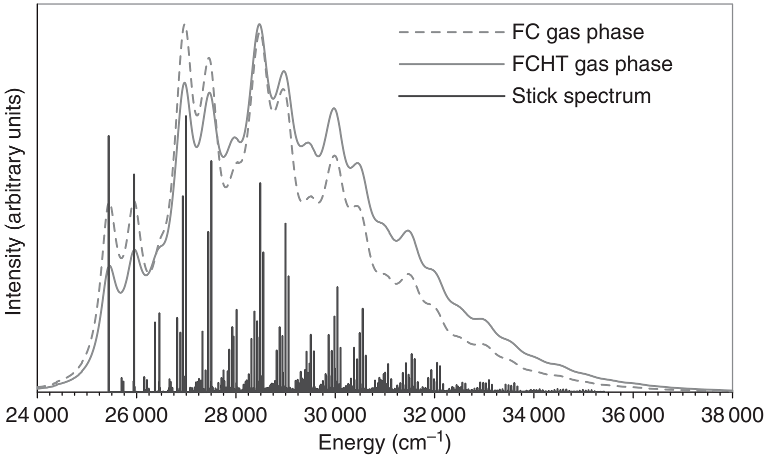

Figure 2.4 OPA spectra of n→π* electronic transition of acrolein computed by time-independent approach. Gas-phase spectra computed with FC approximation (dashed line) and the FC–HT approximation (solid line), convoluted by homogeneous broadening with FWHM of 400 cm^{-1}. The FC–HT stick spectrum is also shown. Please refer online version for color image.

the time-independent framework, it is necessary to convolute the stick spectrum with arbitrarily chosen function and full-width at half-maximum (FWHM). For acrolein in the gas phase, the best comparison with the experiment [121] has been obtained by applying the homogeneous broadening (Lorenzian function) and the FWHM of 400 cm^{-1}, while the inhomogeneous broadening (Gaussian function) with FWHM= 1500 cm^{-1} reproduces well the broad band of the experimental spectrum in solution. The time-independent approach to compute vibrationally resolved electronic spectra presented in Section 2.2.2 allows to go beyond the FC approximation by considering changes of the transition dipole moment with the geometry. It is worth mentioning that such an improvement does not require any additional quantum mechanical computation, since the TD-DFT frequencies are calculated numerically giving direct access to the necessary derivatives of the transition dipole moment with respect to the normal coordinates of the excited electronic state. Inclusion of the HT term is particularly important for the dipole-forbidden or weakly allowed transitions where the FC approximation is less reliable. This is the case of the weakly dipole allowed $n\rightarrow\pi^*$ transition of acrolein ($\mu = 0.0463$ a.u.), where the HT contribution indeed influences significantly the spectrum lineshape, as shown by the comparison of the gas-phase FC and Franck–Condon–Herzberg–Teller (FC–HT) spectra in Figure 2.4. For consistency, the FC–HT approximation has been also applied to simulate the spectrum in aqueous solution, which is compared to its gas-phase counterpart in Figure 2.3. It is quite apparent that the solvent shift is well reproduced by the theory, and also changes in the band shapes agree well with the experimental observations [121].

It is interesting to compare results obtained with the time-dependent and time-independent approaches, and both simulated spectra are shown in Figure 2.3. It is immediately visible that indeed both methodologies accurately predict the absolute position of absorbtion maximum in the gas phase as well as in the aqueous solution. In both cases it is possible to compute solvent shift. However, the time-dependent approach gives direct access to the spectrum lineshape and the band maximum position; thus the solvent shift can be obtained by the comparison of band maximum. In variance, the arbitrary choice of FWHM applied to obtain spectrum shape in case of time-independent approaches influences the position of absorbtion maximum. Thus, in this case, solvent shift has been derived by comparison of electronic transition origins. Nevertheless, the respective solvent shifts of 0.24 and 0.26 eV in case of time-independent and time-dependent approaches, respectively, agree both very well with the experimental value (0.25 eV). Such a good agreement, achieved also for the implicit solvent model, highlights essentially the electrostatic nature of the solute–solvent interaction, which causes a blue shift of the $n\rightarrow\pi^*$ transition. It is worth noting that both the presented approaches allows to study in detail different effects influencing solvent shift and electronic bandshape. From this point of view a combined study applying both time-dependent and time-independent approaches permits to take into account specific and bulk solute–solvent interaction as well as to analyze individual vibronic contributions. Summarizing, we conclude that combined studies which take advantage of both time-dependent and time-independent approaches pave the route toward a better understanding of experimentally observed spectra in condensed phases.

3.2. ESR magnetic tensors of complex radicals in aqueous solution

The combined use of ESR spectroscopy and high-level ab initio calculations represents a very effective tool to probe complex molecular structures and dynamics, due to the high sensitivity of the magnetic tensors to stereoelectronic, dynamical, and environmental effects. In particular, the accurate reproduction of ESR experimental data by sophisticated molecular models allows to unambiguously identify molecular structures that may exist, for example, in a different protonation state or tautomeric form. A very relevant application field for such a combined theoretical/experimental approach is represented by the study of radical species of biological molecules, such as amino acids and nuclear acid bases, which are involved in a variety of important chemical processes, such as enzymatic catalysis, electron transfer, and DNA radiation damage. Among others, two clear examples are provided by glycine and uracil radicals in aqueous solutions. In both cases, all short-time dynamical effects have been taken into account by QM/MM simulations according to the GLOB model, with the radical described at full QM level and the rest of the solvent treated by MM approach. All the simulations and QM calculations of spectroscopic parameters have been performed with a locally modified version of the Gaussian package, according to the methods described in Sections 2.1 and 2.3.3.

Recently, it has been well established that glycine radical prefers a neutral structure in aqueous solution [131,132] (i.e., NH_2—CH—COOH in place of NH_3^+—CH—COO—), whereas the cationic and anionic forms play a negligible role at physiological pH values. However, some of its isotropic hyperfine splittings (especially H^α) show values quite far from those expected for similar radicals or observed for the zwitterionic form of the glycine radical in the solid state [133]. This stimulated a number of theoretical studies, with a satisfactory explanation of the ESR parameters obtained only when intramolecular vibrational averaging and solvent effects were taken into account by an integrated computational procedure [112,134]. The optimized gas-phase structure of the glycine radical (see Figure 2.5), computed at the B3LYP/N07D level, shows that the aminic group is to some degree pyramidal, with $\phi(\mathrm{H1NC^\alpha C}) = -9.5°$ and $\phi(\mathrm{H2NC^\alpha C}) = -165.0°$, whereas H^α is almost on the same plane of the N—C^α—C group ($\phi(\mathrm{NH^\alpha CC^\alpha}) = 1.6°$).

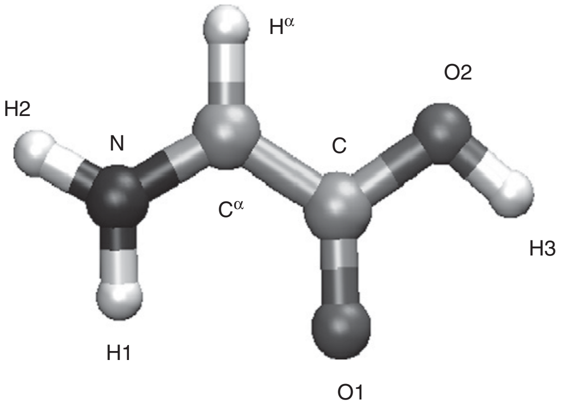

Figure 2.5 Optimized structure of the glycine radical computed at B3LYP/N07D and C-PCM level of theory.

On the other hand, in aqueous solution the glycine radical is, on average, approximately planar: the fluctuations of the above dihedral angles are symmetrically distributed around the planar conformation and the aminic hydrogens show an equal and broader distribution than H$^\alpha$ (see Figure. 2.6).

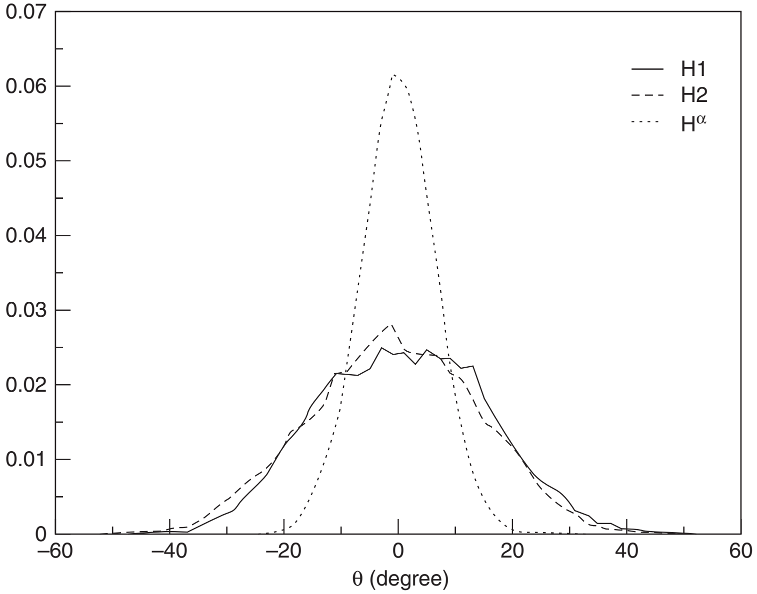

Figure 2.6 Normalized probability distributions of the ϕ(H1NC$^\alpha$C), ϕ(H2NC$^\alpha$C), and ϕ(NH$^\alpha$CC$^\alpha$) dihedral angles of glycine radical in aqueous solution resulting from a QM/MM MD simulation.

Table 2.2 ESR hyperfine coupling constants calculated at B3LYP/EPR-III level of theory for the glycine radical (GlyR) in the gas phase, solvated with four water molecules (GlyR+4H_2O) and by PCM, and in QM/MM aqueous solution simulation (see Figure 2.5 for atom labels)

	GlyR	GlyR + 4H_2O	GlyR + 4H_2O + PCM	GLOB MD	Exp.
a(N)	5.45	4.07	4.19	5.58	6.38
a(H1)	−5.77	−8.95	−9.10	−5.70	−5.59
a(H2)	−3.73	−9.23	−9.39	−5.42	−5.59
a(C^{α})	11.85	6.70	6.22	10.90	
a(H^{α})	−14.54	−12.00	−11.74	−12.12	11.77

Note: Values are in Gauss.

The isotropic hyperfine couplings computed by different models of the glycine radical are compared in Table 2.2 with the results averaged over the QM/MM trajectory. On the one hand, the remarkable agreement between the computed values resulting, from QM/MM simulation and from experiment for all the available hyperfine splittings points out the reliability of the computational approach. On the other hand, the nonnegligible difference between the results of the simulation and those obtained for the isolated glycine radical or the optimized cluster including the whole first solvation shell points out the role of solvent effects both from a static and a dynamic point of view. Starting from the quite disappointing results obtained for the isolated radical, inclusion of the first solvation shell leads to nearly equivalent H1 and H2 atoms, but the quantitative values remain quite far from experiment. Next, inclusion of bulk solvent effects by the PCM [42] has a negligible effect, and only dynamical averaging (both intra- and intermolecular) restores agreement with experiment. Thus, none of the static models is sufficient to provide even semiquantitative results and a dynamical treatment is needed to obtain a coherent picture. While the good results obtained in Ref. [134] suggest that in this case intrasolute dynamics plays a dominant role, in general this is not always the case and more sophisticated theoretical approaches including all the short-time dynamical effects are required (i.e., solute large-amplitude vibrations and solvent librations).

Another significant problem concerning the identifications and characterization of the most stable anionic tautomer of the uracil radical in aqueous solution has been addressed by reviewing recent ESR experimental data [135] in light of the state-of-the-art first-principle calculations. To this end, we have considered five uracil tautomers able to form rather stable valence anions in the gas phase [136]: the canonical tautomer (1) and other tautomers (2–5) obtained by a proton transfer from a nitrogen to a carbon

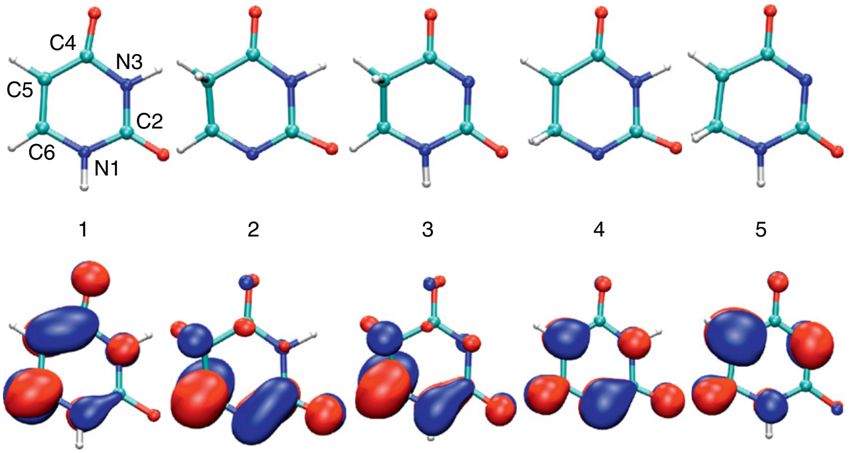

Figure 2.7 Optimized structures and corresponding single occupied molecular orbitals of five tautomers of the uracil radical anion, including the canonical form, obtained at B3LYP/N07D and C-PCM level.

atom. Optimized geometries computed at B3LYP/6-31+G(2d,2p) level, including solvent effects via the effective conductor-like version [137] of the PCM [138–141], are depicted in Figure 2.7, along with the corresponding single-occupied molecular orbitals (SOMOs). All isomers, with the exclusion of 4, show a significant distortion of the molecular framework resulting from the stabilization of the valence π^* state, in line with the gas-phase results. The relative energies span a range of about 7 kcal/mol, with a stability order of the tautomers given by $2 > 3 > 1 > 5 > 4$, thus predicting one of such rare tautomers, not the canonical form, as the most stable in solution. Similarly, a recent theoretical study [142] on the relative free energy of the same uracil radicals reported the following stability: $3 > 5 > 2 > 1 > 4$. However, a thorough comparison of the available ESR isotropic values of the hyperfine coupling tensors of N and H atoms with those computed at quantum mechanical level, provides additional insights for an interpretation of experimental results. In Table 2.3, we report the hcc's parameters as resulting from experiments and theoretical calculations at B3LYP/C-PCM level with specifically tailored EPR-III basis set. It is apparent that the only computed hcc's compatible with experimental data are represented by those belonging to tautomer 1, whereas very significant deviations are observed in all other cases especially considering a(HC5) and a(HC6). Also, we have tested the contributions of both the direct solvent effect and the solvent-mediated intramolecular motions to the magnetic tensors in aqueous solution. Hence, we have performed a hybrid QM/MM MD simulation of tautomer 1 in water and we have computed the same ESR parameters from a posteriori calculations on the sampled

Table 2.3 ESR hyperfine coupling constants calculated at B3LYP/EPR-III and C-PCM level of theory of the five tautomers of the uracil radical as reported in Figure 2.7—Values resulting from a QM/MM MD simulation of tautomer **1** are given in parentheses

	1	2	3	4	5	Exp.
a(N1)	−0.14 (0.21)	−1.03	0.32	0.54	0.21	0.00
a(N3)	0.89 (1.28)	−0.75	−0.04	1.50	1.53	1.46
a(H1)	−1.61 (−0.64)	–	−3.35	–	−0.89	0.84
a(H3)	−1.68 (1.00)	−0.07	–	−3.32	–	0.82
a(H5)	−0.96 (0.18)	15.31, 46.99	−15.20, 50.56	−17.70	−19.20	0.89
a(H6)	−8.17 (10.17)	−16.77	−15.41	57.45, 56.74	43.89, 51.03	12.52

Note: Values are in Gauss.

trajectory. As shown in the first column of Table 2.3 (results in parentheses), small changes of the N and H hcc's are observed (<2 G), with an overall better agreement with experiments. Thus, the overall comparison of computational and experimental data provides a very consistent and clear solution: the canonical form (1) is the anionic tautomer of the uracil radical observed in aqueous solution.

3.3. Vibrational properties beyond harmonic approximation

In this section we will discuss time-independent vibrational computations beyond harmonic approximation. We have chosen in particular the computation of anharmonic frequencies for adenine molecule adsorbed on a Si(100) surface, modeled by Si cluster, and vibrationally averaged nitrogen hyperfine coupling constants of 4-amino-2,2,6,6-tetramethylpiperidine-1-oxyl-4-carboxylic acid (TOAC from now on) in its chair and twisted tautomeric forms.

Recent studies on infrared spectra of isolated adenine molecule have shown excellent agreement between available experimental data [143,144] and anharmonic vibrational frequencies [145,146] computed by perturbative approach [64] with the well-known B3LYP [106] functional and the 6-311++G(df,dp) basis set. Moreover, detailed analysis of the potential energy distribution (PED) from Ref. [145] allowed some revision of the assignment of the experimental results [143,144]. The good accuracy of the results (mean unsigned error lower than 10 cm^{-1}) paves the route toward detailed studies of the IR spectrum changes upon absorbtion on the Si(100) surface. The total system composed of the adenine molecule adsorbed on a Si cluster has been modeled by the ONIOM QM/MM scheme, with QM part corresponding to the adenine molecule calculated at the B3LYP/6-311++G (2df,2pd) level, and the Si_{28} cluster represented at the MM level by the universal force field (UFF) [147]. The total system has 195 normal modes, thus the full-dimensional PT2 anharmonic treatment would require 391 Hessian computations. While such computations are feasible within a QM/MM scheme, they can be still considered rather computationally demanding. On the other hand, it is possible to study anharmonic effects for some selected modes only, for example corresponding to the most intense bands in the IR spectrum. The IR spectrum of adenine can be characterized by two sets of bands in the regions around 1700 and 3500 cm^{-1} (see Figure 2.8), so we have chosen to compute anharmonic frequencies only for the five modes related to the most distinct bands. It is worth recalling that such an approach still takes into account effects of all other vibrations on the computed anharmonic frequencies. Table 2.4 compares results obtained for adenine adsorbed on Si(100) with those from the studies of isolated molecule [146]. The most pronounced blue shift of 20 cm^{-1} is observed for the most intense band related to the NH group

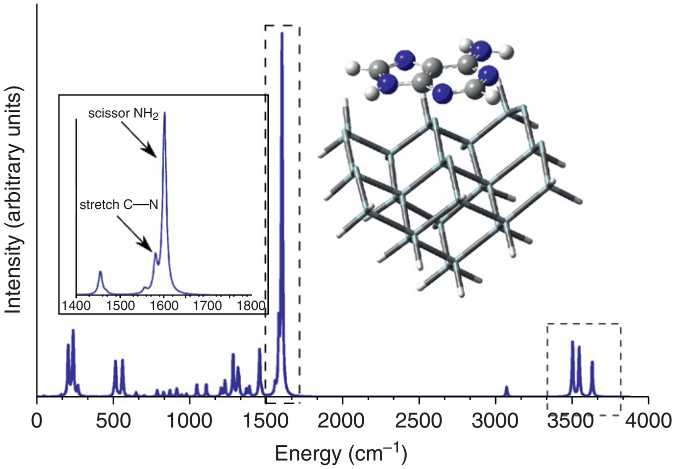

Figure 2.8 IR spectrum of adenine@Si_{28} with five most intense bands included in anharmonic computation.

Table 2.4 Computed PT2 anharmonic frequencies of the five most intense bands in IR spectrum (See Figure 2.8) of isolated adenine molecule and adenine@Si(100), and their shift related to the absorbtion

Mode	Adenine	Adenine@Si(100)	Shift
$\nu(NH_2)_{asym}$	3539	3541	+2
$\nu(N-H)_{stretch}$	3497	3491	−6
$\nu(NH_2)_{sym}$	3432	3441	+9
$\nu(NH_2)_{sciss}$	1616	1636	+20
$\nu(N-C)_{stretch}$	1591	1597	+6

Note: all values in cm^{-1}.

scissor vibration, but also other frequencies change slightly upon absorbtion. Environmental effects of such an order of magnitude have been observed, for example, comparing results from the gas-phase experiments with those from low-temperature matrix or aprotic solution. This is in line with the parallel orientation of the adenine molecule with respect to the surface plane. In variance, much more pronounced frequency shifts would be expected in case of perpendicular orientation due to specific adsorbant–surface interactions. It should be noted that the presented approach makes anharmonic frequency computations for macrosystems feasible, which should greatly improve the understanding of observed experimentally frequency shifts related to environmental effects, absorbtion on a surface, or biomolecule embedding.

Besides frequency computations, the anharmonic analysis gives also insights about vibrational averaging of molecular properties. As already mentioned in Section 2.2.1, vibrational motions often influence strongly the ESR parameters. TOAC is a nitroxide radical which has been largely exploited as a magnetic probe in the studies of macromolecular systems by means of ESR spectroscopy. Its magnetic properties have been evaluated at fully QM level; thus it can stand as a benchmark for less expensive approaches, which would be necessary for studies of large biologically relevant systems. In this respect, we have chosen to compute vibrationally averaged nitrogen hcc's for the chair and twisted forms of TOAC by the QM/MM model. The QM and MM parts are shown as balls and sticks, or tubes, respectively, in Figure 2.9. In QM/MM computations the standard ONIOM model has been applied with QM part computed by the PBE0 functional with the recently developed N07D [108–110] basis set, tailored for accurate studies of radical systems, and the MM part modeled by the UFF force field.

In case of computations of vibrationally averaged properties it is relevant to check the reliability of reduced dimensionality anharmonic models. In fact, at variance with the direct computation of vibrational frequencies one might expect that it is important to include effects of several vibrations, which sum up. In the case of TOAC, we have tested a reduced dimensionality model by taking into account only 11 modes directly coupled with the vibrations of the N—O group, but in this case only about 10% of the total vibrational contribution has been recovered. On the contrary, a full vibrational anharmonic treatment, including all 123 normal modes, led to good agreement with previous QM studies [148]. Table 2.5 shows that also in case of QM/MM study the vibrational contributions are negligible for chair

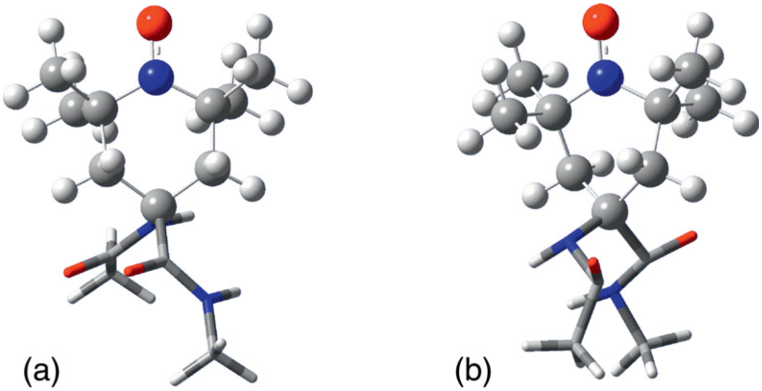

Figure 2.9 The chair (a) and twisted (b) structures of TOAC. The QM part is presented as balls and sticks, while the tubes correspond to the MM part.

Table 2.5 Nitrogen isotropic hyperfine coupling constants (hcc's in Gauss)

Temperature (K)	Equilibrium	Harmonic	Anharmonic	Total
		Chair		
0	16.206	−0.003	0.004	16.207
298		−0.332	0.195	16.069
		Twist		
0	14.326	0.106	0.423	14.856
298		−0.061	0.879	15.145

Note: Equilibrium values, harmonic, and anharmonic contributions and the total hcc's computed at 0 and 298 K.

structure, but become quite significant for the twist structure, especially if temperature effects are also included.

It should be noted that some normal modes have given almost negligible vibronic contribution, so the reduced dimensional anharmonic treatment can be in principle applied also to the computations of vibrationally averaged properties, but in this case the choice of normal modes which must be included is not straightforward. Thus, similar to the TOAC example it might be suggested to apply the QM/MM schemes to evaluate vibrationally averaged properties rather than to reduce the dimensionality of vibrational treatment in order to facilitate computations.

The two examples gathered in the current section in fact highlight two different aspects of approximations to facilitate vibrational property computations beyond the harmonic approximation. In this respect we can distinguish the direct evaluation of some experimentally observable frequencies, which can be most likely performed reducing computational efforts by applying both simplified QM/MM schemes and reduced dimensionality vibrational treatment, from evaluation of frequency-dependent properties like ZPVE or vibrationally averaged hcc's, where it might be important to sum up effects of all vibrations. Summarizing, we have shown that computations of vibrational properties beyond the harmonic approximation within the QM/MM scheme can be successfully applied to rather large systems, and in some cases the computational cost can be further reduced by application of reduced dimensionality anharmonic treatments.

3.4. Photoelectron spectrum of adenine adsorbed on Si(100)

Reliable computational studies of optical properties for large nanosystems in condensed phases can support the design of new materials relevant for optics, photonics, and sensoristics. The approach to compute one-photon electronic spectra presented in Section 2.2.2 is in line with such a demand. The accuracy and effectiveness of our a priori procedure for the selection of the relevant transitions to be computed is of particular relevance to the studies of large macromolecular systems. As an example we compare the photoelectron spectra simulations performed for isolated adenine and for adenine adsorbed on the silicon (100) surface [82]. The full valence photoelectron spectrum of adenine is composed from several overlapping excitations [149], but to show the feasibility of spectra computations for nanosystems we have chosen to study only the ionization from the highest occupied molecular orbital.

Si(100) surface has been modeled by a cluster of 119 silicon atoms, as shown in Figure 2.10, resulting in a total system with 636 normal modes. For computation of geometry structures and frequencies the ONIOM QM/MM scheme has been adopted, with QM part corresponding to the adenine molecule calculated at the B3LYP/6-31+G(d,p) level, and the Si_{119} cluster treated at MM level using the UFF force field [147]. The photoelectron spectra have been calculated for both isolated adenine molecule and adenine@Si(100), implying that the spectrum changes upon adsorption. In Figure 2.10 both spectra are plotted in the range of 8.0–8.7 eV roughly corresponding to the first band of valence shell photoelectron spectrum. It can be

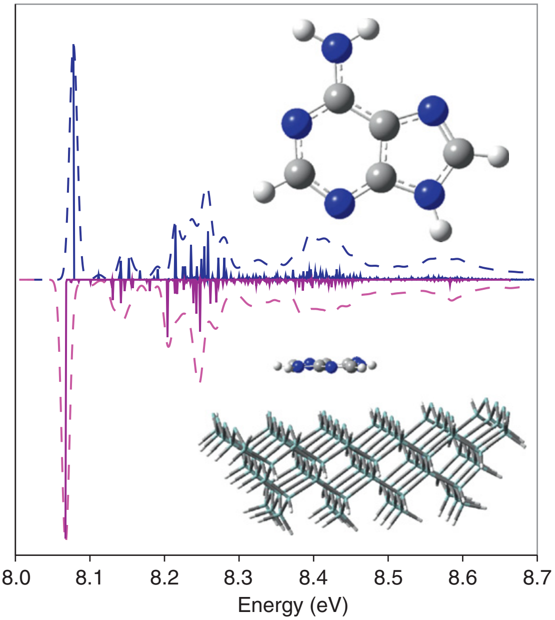

Figure 2.10 Comparison between the theoretical photoionization spectra in gas phase of isolated adenine (upper panel) and adenine adsorbed on a Si(100) surface (lower panel). The spectra in an energy range from 8.0 to 8.7 eV are calculated with FC approximation and with FWHM = 100 cm^{-1}; the stick bands show the most important transitions. Please refer online version for color image.

observed that our model predicts a small red shift of the excitation origin upon adsorption on Si surface, and that new vibronic transitions corresponding to intermolecular vibrations modulate the spectrum lineshape. The analysis of both spectra give insights into the underlying adsorbate–surface interactions, allowing to interpret the rich indirect information provided by the experimental spectra. It can be recalled that the time-independent simulation of spectra works directly in the frequency domain, thus allowing to determine single vibronic contributions even in difficult cases involving relatively broad bands. In a more general context, comparison of experimental and simulated lineshapes supports dissecting and evaluating the role of different effects (environmental, hydrogen bonding, adsorbate–solute interaction, etc.) in determining spectral properties.

The accuracy and effectiveness of our a priori strategy to select only the relevant transitions and discard the less probable ones should be underlined. This will be discussed analyzing the number of combinations for each class C_n for both systems, which is directly related (see Ref. [82] for details) to the number of transitions which stands as an initial pool from which only the relevant ones are chosen to be computed.

Table 2.6 lists ${}_NC_n$ for isolated adenine and adenine@Si(100) along with the spectrum convergence achieved with $N_{\mathrm{I}}^{\max}$ set to the default value of 10^8. Increase of $N_{\mathrm{I}}^{\max}$ limit always yields better spectrum convergence, but also increases computational time and memory requirements. However, all computations with the same $N_{\mathrm{I}}^{\max}$ are equivalent, despite the system size. It is worth noting that in both cases, either an isolated molecule with 39 normal modes or a macrosystem with over 600 modes, almost all spectrum intensity (about 98%), has been recovered at an equivalent computational cost, even if for the cluster, the applied value of $N_{\mathrm{I}}^{\max}$ is not sufficient to consider the whole initial pool even for only three simultaneously excited modes (C_3 class). This particular case shows the ability of the a priori

Table 2.6 Convergence of spectra computations for adenine and adenine@Si(100)

	Adenine		Adenine@Si(100)	
Class (n)	${}_NC_n$	Convergence (%)	${}_NC_n$	Convergence (%)
3	9.14E + 03	84.54	4.27E + 07	87.31
4	8.23E + 04	93.57	6.75E + 09	94.82
5	5.76E + 05	97.48	8.54E + 11	97.37
6	3.26E + 06	98.32	8.98E + 13	97.88
7	1.54E + 07	98.39	8.08E + 15	97.93

Note: For each *classs* C_n the number of combinations of the n excited oscillators ${}_NC_n$ and convergence are listed. The C_1 and C_2 transitions have been computed by analytical formulae allowing a maximum quantum number $v_i = 30$, and $v_1 = v_2 = 20$, respectively. For the *classes* C_n, $n \geq 3$, the transitions to be computed have been selected setting the parameter $N_{\mathrm{I}}^{\mathrm{Max}}$ to 10^8 (the default value).

strategy to select only the relevant transitions and to discard the less probable ones. The efficiency of the procedure can be easily explained by the fact that despite significant difference in the systems size, in both cases, the electronic transition is localized on the adenine molecule. This example confirms the effectiveness of spectra computations within the QM/MM scheme, for systems where electronic transitions are localized on a relatively small QM part.

4. FINAL REMARKS AND CONCLUSIONS

It has been shown that modern computational spectroscopy can be successfully exploited in the study of macromolecular systems and strengths and limitations of the available computational methodologies has been presented.

The time-dependent route is particularly well suited for flexible systems propagating on highly anharmonic PES with large-amplitude motions or solvent librations. In such cases it is necessary to sample larger regions of configurational space and to take into account all its important features. Such computations might be computationally demanding, but it is worth recalling that MD studies can be performed at a relatively lower level of theory which is able to reliably reproduce the overall character of the PES. It is also worth remarking, that one MD simulation stands as a base for a wide range of spectroscopic studies. Then a posteriori computation of spectroscopic properties can be performed by more refined theoretical approaches which can be also appropriately tailored for each property of the interest.

For the semirigid systems accurate results can be obtained by time-independent computations of spectroscopic properties. In such cases it is possible to take into account vibrational effects on the molecular properties or electronic spectra, and to compute vibrational frequencies beyond harmonic approximation. Advantage of time-independent approaches, besides their relatively lower computational cost, stem from the fact that working directly in the frequency domain gives access to the detailed analysis of vibrational contributions. Moreover, time-independent computations allow the reduced dimensionality treatment of the vibrational problem, which paves the route into the better understanding of spectroscopic properties of macromolecular systems.

Moreover both approaches allow to compare directly experimental and theoretical spectra, as well as to evaluate and dissect both dynamic and environmental effects determining spectral properties. Overall, the computational strategies presented here, together with their integration into a computational chemistry package, allow a straightforward but at the same time detailed and accurate computational studies of ESR, IR/Raman, and UV–vis spectra, for macrosystems of direct biological and/or technological interest.

ACKNOWLEDGMENT

The financial support of MIUR and INSTM is gratefully acknowledged. The large-scale computer facilities of the VILLAGE network (http://village.unina.it) are acknowledged for providing computer time.

REFERENCES

[1] V. Barone, A. Polimeno, Chem. Soc. Rev. 36 (2007) 1724.
[2] V. Barone, R. Improta, N. Rega, Acc. Chem. Res. 41 (2008) 605.
[3] D.C. Clary, Science 314 (2006) 5797.
[4] A. Hellman, E.J. Baerends, M. Biczysko, T. Bligaard, C.H. Christensen, D.C. Clary, et al., J. Phys. Chem. B 110 (2006) 17719.
[5] P. Jensen, P.R. Bunker, (Eds.), Computional Molecular Spectroscopy. John Wiley & Sons, UK, 2000.
[6] A. Lami, C. Petrongolo, F. Santoro, Absorption, emission and Photoelectron continuous-wave spectra, in W. Domcke, H. Köppel, D.R. Yarkonyi (Eds.), Conical Intersections, Electronic Structure, Dynamics and Spectroscopy, World Scientific Publishing Co., Singapore, 2004.
[7] S. Grimme, Rev. Comp. Chem. 20 (2004) 153.
[8] O. Christiansen, Phys. Chem. Chem. Phys. 9 (2007) 2942.
[9] J. Bowman, S. Carter, X. Huang, Int. Rev. Phys. Chem. 22 (2003) 533.
[10] J. Vaara, Phys. Chem. Chem. Phys. 9 (2007) 5399.
[11] G. Brancato, V. Barone, N. Rega, Theor. Chem. Acc. 117 (2007) 1001.
[12] V. Barone, M. Brustolon, P. Cimino, A. Polimeno, M. Zerbetto, A. Zoleo, J. Am. Chem. Soc. 128 (2006) 15865.
[13] N. Rega, Theor. Chem. Acc. 116 (2006) 344.
[14] P.E. Smith, B.M. Pettitt, J. Chem. Phys. 95 (1991) 8430.
[15] P.E. Smith, B.M. Pettitt, J. Chem. Phys. 105 (1996) 4289.
[16] P.E. Smith, H.D. Blatt, B.M. Pettitt, J. Phys. Chem. B 101 (1997) 3886.
[17] P.H. Hunenberger, J.A. McCammon, J. Chem. Phys. 110 (1999) 1856.
[18] M. Bergdorf, C. Peter, P.H. Hunenberger, J. Chem. Phys. 119 (2003) 9129.
[19] S. Bogusz, T.E.C. III, B.R. Brooks, J. Chem. Phys. 108 (1998) 7070.
[20] S. Sakane, H.S. Ashbaugh, R.H. Wood, J. Phys. Chem. B 102 (1998) 5673.
[21] G. Hummer, L.R. Pratt, A.E. Garca, J. Chem. Phys. 107 (1997) 9275.
[22] M.A. Kastenholz, P.H. Hünenberger, J. Chem. Phys. 124 (2006) 124108.
[23] G.J. Martyna, M.E. Tuckerman, J. Chem. Phys. 110 (1999) 2810.
[24] A. Lozovoi, A. Alavi, J. Kohanoff, R.M. Lynden-Bell, J. Chem. Phys. 115 (2001) 1661.
[25] S. Dapprich, I. Komaromi, K.S. Byun, K. Morokuma, M.J. Frisch, J. Mol. Struc. (Theochem) 462 (1999) 1.
[26] T. Vreven, K. Morokuma, O. Farkas, H.B. Schlegel, M.J. Frisch, J. Comp. Chem. 24 (2003) 760.
[27] N. Rega, S.S. Iyengar, G.A. Voth, H.B. Schlegel, T. Vreven, M.J. Frisch, J. Phys. Chem. B 108 (2004) 4210.
[28] H. Koeppel, W. Domcke, L. Cederbaum, Adv. Chem. Phys. 57 (1984) 59.
[29] H.D. Meyer, U. Manthe, L.S. Cederbaum, Chem. Phys. Lett. 171 (1990) 97.
[30] A. Raab, G. Worth, H.D. Meyer, J. Chem. Phys. 110 (1999) 936.
[31] N. Rega, G. Brancato, V. Barone, Chem. Phys. Lett. 422 (2006) 367.
[32] G. Brancato, N. Rega, V. Barone, J. Chem. Phys. 128 (2008) 144501.

[33] G. Brancato, A. Di Nola, V. Barone, A. Amadei, J. Chem. Phys. 122 (2005) 154109.
[34] A. Ben-Naim, Solvation Thermodynamics, Plenum Press, New York, 1987.
[35] G. Brancato, N. Rega, V. Barone, J. Chem. Phys. 124 (2006) 214505.
[36] A. Klamt, G. Schüurmann, J. Chem. Soc. Perkin Trans. 2 (1993) 799.
[37] V. Barone, M. Cossi, J. Phys. Chem. A 102 (1998) 1995.
[38] M. Cossi, N. Rega, G. Scalmani, V. Barone, J. Comp. Chem. 24 (2003) 669.
[39] J. Tomasi, M. Persico, Chem. Rev. 94 (1994) 2027.
[40] J. Tomasi, B. Mennucci, R. Cammi, Chem. Rev. 105 (2005) 2999.
[41] C. Benzi, M. Cossi, V. Barone, R. Tarroni, C. Zannoni, J. Phys. Chem. B 109 (2005) 2584.
[42] M. Cossi, G. Scalmani, N. Rega, V. Barone, J. Chem. Phys. 117 (2002) 43.
[43] J.L. Pascual-Ahuir, E. Silla, I. Tũnon, J. Comput. Chem. 15 (1994) 1127.
[44] G. Scalmani, N. Rega, M. Cossi, V. Barone, J. Comput. Meth. Sci. Eng. 2 (2002) 469.
[45] F.M. Floris, J. Tomasi, J. Comput. Chem. 10 (1989) 616.
[46] F.M. Floris, J. Tomasi, J.L. Pascual-Ahuir, J. Comput. Chem. 12 (1991) 784.
[47] J.D. Thompson, C.J. Cramer, D.G. Truhlar, Theor. Chem. Acc. 113 (2005) 107.
[48] C.P. Kelly, C.J. Cramer, D.G. Truhlar, J. Chem. Theory Comp. 1 (2005) 1133.
[49] I. Tuñón, M.F. Ruiz-López, D. Rinaldi, J. Bertrán, J. Comp. Chem. 17 (1996) 148.
[50] C. Curutchet, M. Orozco, F.J. Luque, J. Comp. Chem. 22 (2001) 1180.
[51] C. Curutchet, A. Bidon-Chanal, I. Soteras, M. Orozco, F.J. Luque, J. Phys. Chem. B 109 (2005) 3565.
[52] A. Klamt, V. Jonas, T. Bürger, J.C.W. Lohrenz, J. Phys. Chem. A 102 (1998) 5074.
[53] D. Beglov, B. Roux, J. Chem. Phys. 100 (1994) 9050.
[54] J.W. Essex, W.L. Jorgensen, J. Comput. Chem. 16 (1995) 951.
[55] G. Petraglio, M. Ceccarelli, M. Parrinello, J. Chem. Phys. 123 (2005) 044103.
[56] G.J. Martyna, D.J. Tobias, M.L. Klein, J. Chem. Phys. 101 (1994) 4177.
[57] J.M. Bowman, Science 290 (2000) 724.
[58] S. Carter, N. Handy, J. Chem. Phys. 113 (2000) 987.
[59] G. Chaban, J. Jung, R. Gerber, J. Chem. Phys. 111 (1999) 1823.
[60] G. Rauhut, T. Hrenar, Chem. Phys. 346 (2008).
[61] D. Begue, P. Carbonniere, C. Pouchan, J. Phys. Chem. A 105 (2001) 11379.
[62] S. Tokura, K. Yagi, T. Tsuneda, K. Hirao, Chem. Phys. Lett. 436 (2007) 30.
[63] J.M. Luis, B. Kirtman, O. Christiansen, J. Chem. Phys. 125 (2006) 154114.
[64] V. Barone, J. Chem. Phys. 122 (2005) 014108.
[65] T. Ruden, P.R. Taylor, T. Helgaker, J. Chem. Phys. 119 (2003) 1951.
[66] K. Ruud, P.O. Astrand, P. Taylor, J. Chem. Phys. 112 (2000) 2668.
[67] J.F. Gaw, A. Willetts, W.H. Green, N.C. Handy, Advances in Molecular Vibrations and Collision Dynamics, JAI Press, Greenwich, CT, 1990.
[68] A.D. Boese, J. Martin, J. Phys. Chem. A 108 (2004) 3085.
[69] V. Barone, G. Festa, A. Grandi, N. Rega, N. Sanna, Chem. Phys. Lett. 388 (2004) 279.
[70] J. Franck, Trans. Faraday Soc. 21 (1926) 536.
[71] E. Condon, Phys. Rev. 28 (1926) 1182.
[72] E. Condon, Phys. Rev. 32 (1928) 858.
[73] F. Santoro, R. Improta, A. Lami, J. Bloino, V. Barone, J. Chem. Phys. 126 (2007) 084509.
[74] F. Santoro, R. Improta, A. Lami, J. Bloino, V. Barone, J. Chem. Phys. 128 (2008) 224311.
[75] N. Lin, F. Santoro, X. Zhao, A. Rizzo, V. Barone, J. Phys. Chem. A 112 (2008) 12401.
[76] C. Eckart, Phys. Rev. 47 (1935) 552.
[77] P.M. Johnson, H. Xu, T.J. Sears, J. Chem. Phys. 125 (2006) 164330.
[78] F. Duschinsky, Acta Physicochim. URSS 7 (1937) 551.
[79] T.E. Sharp, H.M. Rosenstock, J. Chem. Phys. 41 (1964) 3453.
[80] J.L. Chang, J. Chem. Phys. 128 (2008) 174111.
[81] P.T. Ruhoff, Chem. Phys. 186 (1994) 355.
[82] V. Barone, J. Bloino, M. Biczysko, F. Santoro, J. Chem. Theory Comput. 5 (2009) 540.

[83] F. Santoro, R. Improta, A. Lami, J. Bloino, V. Barone, J. Chem. Phys. 126 (2007) 184102.
[84] J. Bloino, M. Biczysko, O. Crescenzi, V. Barone, J. Chem. Phys. 128 (2008) 244105.
[85] V. Barone, C. Adamo, Y. Brunel, R. Subra, J. Chem. Phys. 105 (1996) 3168.
[86] S. Carter, S. Culik, J. Bowman, J. Chem. Phys. 107 (1997) 10458.
[87] J. Koput, S. Carter, N. Handy, J. Chem. Phys. 115 (2001) 8345.
[88] P. Cassam-Chenai, J. Lievin, J. Quantum Chem. 93 (2003) 245.
[89] N. Rega, Theor. Chem. Acc. 116 (2006) 347.
[90] R. Ramirez, T. Lopez-Ciudad, P. Kumar, D. Marx, J. Chem. Phys. 121 (2004) 3973.
[91] P. Macak, Y. Luo, H. Ågren, Chem. Phys. Lett. 330 (2000) 447.
[92] M. de Groot, W.J. Buma, Chem. Phys. Lett. 420 (2006) 459.
[93] M. de Groot, W.J. Buma, Chem. Phys. Lett. 435 (2006) 224.
[94] M. Dierksen, S. Grimme, J. Chem. Phys. 120 (2004) 3544.
[95] I. Pugliesi, N.M. Tonge, K.E. Hornsby, M.C.R. Cockett, M.J. Watkins, Phys. Chem. Chem. Phys. 9 (2007) 5436.
[96] N.M. Tonge, E.C. MacMahon, I. Pugliesi, M.C.R. Cockett, J. Chem. Phys. 126 (2007) 154319.
[97] M. Kemper, J. Van Dijk, H. Buck, Chem. Phys. Lett. 53 (1978) 121.
[98] R. Berger, C. Fischer, M. Klessinger, J. Phys. Chem. A 102 (1998) 7157.
[99] M. Dierksen, S. Grimme, J. Chem. Phys. 122 (2005) 244101.
[100] H.C. Jankowiak, J.L. Stuber, R. Berger, J. Chem. Phys. 127 (2007) 234101.
[101] R. Improta, V. Barone, Chem. Rev. 104 (2004) 1231.
[102] V. Barone, R. Improta, Chem. Rev. 104 (2004) 1231.
[103] I. Ciofini, C. Adamo, V. Barone, J. Chem. Phys. 121 (2004) 6710.
[104] J.R. Cheeseman, G.W. Trucks, T.A. Keith, M.J. Frisch, J. Chem. Phys. 104 (1996) 5497.
[105] S. Koseki, M.W. Schmidt, M.S. Gordon, J. Phys. Chem. 96 (1992) 10768.
[106] D. Becke, J. Chem. Phys. 98 (1993) 5648.
[107] N. Rega, M. Cossi, V. Barone, J. Chem. Phys. 105 (1996) 11060.
[108] V. Barone, P. Cimino, E. Stendardo, J. Chem. Theory Comput. 4 (2008) 751.
[109] V. Barone, P. Cimino, Chem. Phys. Lett. 454 (2008) 139.
[110] V. Barone, P. Cimino, J. Chem. Theory Comput. 5 (2009) 192.
[111] S. Kaprzac, R. Reviakine, M. Kaupp, J. Phys. Chem. B 111 (2007) 811.
[112] G. Brancato, N. Rega, V. Barone, J. Am. Chem. Soc. 129 (2007) 15380.
[113] G. Brancato, N. Rega, V. Barone, J. Chem. Phys. 125 (2006) 164515.
[114] A.M. Buswell, E.C. Dunlop, W.H. Rodebush, J.B. Swartz, J. Am. Chem. Soc. 62 (1940) 325.
[115] A.D. Walsh, Trans. Faraday Soc. 41 (1945) 498.
[116] G. Mackinney, O. Temmer, J. Am. Chem. Soc. 70 (1948) 3586.
[117] K. Inuzuka, Bull. Chem. Soc. Jpn. 34 (1961) 6.
[118] R.S. Becker, K. Inuzuka, J. King, J. Chem. Phys. 52 (1970) 5164.
[119] E.J. Bair, W. Goietz, D.A. Ramsay, Can. J. Chem. 49 (1971) 2710.
[120] G.A. Osborne, D.A. Ramsay, Can. J. Chem. 51 (1973) 1170.
[121] K. Aidas, A. Møgelhøj, E.J.K. Nilsson, M.S. Johnson, K.V. Mikkelsen, O. Christiansen, P. Soderhjelm, J. Kongsted, J. Chem. Phys. 128 (2008) 194503.
[122] A. Luthy, Z. Phys. Chem. 107 (1923) 284.
[123] F.E. Blacet, W.G. Young, J.G. Roof, J. Am. Chem. Soc. 59 (1937) 608.
[124] K. Inuzuka, Bull. Chem. Soc. Jpn. 33 (1960) 678.
[125] N.S. Bayliss, E.G. McRae, J. Phys. Chem. 58 (1954) 1002.
[126] H.B. Schlegel, J.M. Millam, S.S. Iyengar, G.A. Voth, A.D. Daniels, G.E. Scuseria, et al., J. Chem. Phys. 114 (2001) 9758.
[127] S.S. Iyengar, H.B. Schlegel, J.M. Millam, G.A. Voth, G.E. Scuseria, M.J. Frisch, J. Chem. Phys. 115 (2001) 10291.
[128] H.B. Schlegel, S.S. Iyengar, X. Li, J.M. Millam, G.A. Voth, G.E. Scuseria, et al., J. Chem. Phys. 117 (2002) 8694.

[129] O. Crescenzi, M. Pavone, F.D. Angelis, V. Barone, J. Phys. Chem. B 109 (2005) 445.
[130] M. Pavone, G. Brancato, G. Morelli, V. Barone, ChemPhysChem 7 (2006) 148.
[131] H. von Paul, H. Fisher, Helv. Chim. Acta 54 (1971) 485.
[132] P. Neta, R.W. Fessenden, J. Phys. Chem. 75 (1971) 738.
[133] D.K. Ghosh, D.H. Wiffen, J. Chem. Soc. (1960) 1869.
[134] N. Rega, M. Cossi, V. Barone, J. Am. Chem. Soc. 119 (1997) 12962.
[135] J.M. Lu, J. Geimer, S. Naumov, D. Beckert, Phys. Chem. Chem. Phys. 3 (2001) 952.
[136] S. Naumov, B. Reinhold, D. Beckert, Phys. Chem. Chem. Phys. 5 (2003) 64.
[137] M. Cossi, G. Scalmani, N. Rega, V. Barone, J. Comput. Chem. 24 (2003) 669.
[138] M. Cossi, N. Rega, G. Scalmani, V. Barone, J. Chem. Phys. 114 (2001) 5691.
[139] M. Cossi, G. Scalmani, N. Rega, V. Barone, J. Chem. Phys. 117 (2002) 43.
[140] M. Cossi, G. Scalmani, N. Rega, V. Barone, J. Comput. Chem. 24 (2003) 669.
[141] E. Cances, B. Mennucci, J. Chem. Phys. 114 (2001) 4744.
[142] M. Haranczyk, M. Gutiwski, A. Warshel, Phys. Chem. Chem. Phys. 10 (2008) 4442.
[143] M. Nowak, L. Lapinski, J. Leszczynski, J. Phys. Chem. 100 (1996) 3527.
[144] P. Colarusso, K. Zhang, B. Guo, P.F. Bernath, Chem. Phys. Lett. 269 (1997) 39.
[145] W. Zierkiewicz, L. Komorowski, D. Michalska, J. Černy, P. Hobza, 112 (2008) 16734.
[146] M. Biczysko, P. Panek, V. Barone, Chem. Phys. Lett. 475 (2009) 105.
[147] A.K. Rappè, C.J. Casewit, K.S. Colwell, W.A. Goddard III, W.M. Skiff, J. Am. Chem. Soc. 114 (1992) 10024.
[148] S. Carlotto, P. Cimino, M. Zerbetto, L. Franco, C. Corvaja, M. Crisma, et al., J. Am. Chem. Soc. 129 (2007) 11248.
[149] A.B. Trofimov, J. Schirmer, V.B. Kobychev, A.W. Potts, D.M.P. Holland, L. Karlsson, J. Phys. B 39 (2006) 305.

CHAPTER 3

Use of the Average Solvent Potential Approach in the Study of Solvent Effects

Ignacio Fdez. Galván[a], **Aurora Muñoz-Losa**[a], **Catalina Soriano-Correa**[b], **M. Luz Sánchez**[a], **M. Elena Martín**[a] and **Manuel A. Aguilar**[a]

Contents

[a] Área de Química Física, Universidad de Extremadura, Avda. de Elvas s/n, 06071 Badajoz, Spain
[b] Laboratorio de Química Computacional. FES-Zaragoza, Universidad Nacional Autónoma de México, 09230 Iztapalapa, México D.F., Mexico

---

Advances in Quantum Chemistry, Vol. 59
ISSN: 0065-3276, DOI: 10.1016/S0065-3276(10)59003-8

© 2010 Elsevier Inc.
All rights reserved

1. INTRODUCTION

In the last decades the search for environmentally friendlier solvents [1] has been accompanied on the theoretical side by a renewed interest in the development of methods oriented to understanding and predicting how the structure, properties, and reactivity of molecules are affected by the presence of a surrounding medium [2], with the hope that this knowledge will serve as a guide in the development of new solvents. In contrast to the pioneering works of Born [3], Kirkwood [4], Onsager [5], and so on, which were based on a classical description of the solute, the new methods use quantum mechanics (QM), which permits a more detailed description of the changes that the solute molecule suffers during the solvation process. The high level of calculation and accuracy that has been achieved in the quantum description of molecules and processes in vacuo is widely known; consequently, an additional objective of current solvent theories is to achieve a similar level for molecules and processes in solution. From a practical point of view, the ultimate goal is to have available effective methods that permit to calculate the geometry and energy of minima, saddle points, conical intersections (CIs), and so on, of molecules in solution and that include the contribution of dynamical electron correlation or the possible multiconfigurational character of the solute wave function.

The medium that surrounds the solute can be of diverse natures: a solid, a liquid, a glassy solid, a liquid drop, a membrane, or even an enzyme; however, the vast majority of biological or chemical transformations takes place in the presence of a solvent. Because of this, most of the examples presented here are referred to systems and processes in the presence of a liquid solvent, even if many of the ideas developed could be easily applied to other media.

The solvent can have very different effects on the solute molecules [6], it can modify the frequency and intensity of the solute spectral bands, the thermodynamics and kinetics of chemical reactions, the strength of molecular interactions or the fate of solute excited states. A change of solvent can drastically alter the behavior of a chemical system, and the choice of a proper solvent is one of the first decisions that a chemist must take when facing a spectroscopic, kinetic, or thermodynamic problem. For all these reasons, it is very interesting to have theoretical methods that can guide chemists in their choices. Unfortunately, the theoretical study of solvent effects is quite complicated, since the presence of the solvent introduces additional difficulties with respect to the study of analogous problems in gas phase. Among these difficulties, we can remark the following:

(1) Firstly, the great number of molecules involved in the description of bulk solvent polarization effects. Molecules placed at long distances have a nonnegligible effect on the solute properties. In general, in the

study of solvent effects, and depending on the type of solute–solvent interactions involved, it is necessary to include several solvent shells in the calculations.

(2) Secondly, the possible presence of specific interactions, mainly hydrogen bonds (HBs), between the solute and the solvent molecules located in the first solvation shell. The correct description of these interactions makes the use of microscopic solvent models compulsory.
(3) Finally, in solution there are a great number of solute–solvent configurations that are thermally accessible. Different solute molecules will have different environments and, consequently, slightly different properties. To obtain statistically significant results, it is necessary to include hundreds or thousands of solute–solvent configurations.

An additional complication comes from the fact that, in solution, the relevant energy to consider is the free energy and we must hence have at our disposal methods that permit the calculation of this quantity in an effective and computationally feasible way.

All these complications, large number of solvent molecules, possible existence of specific interactions, great number of solvent configurations, the necessity of determining free energy differences, and so on, have as a consequence a very large computational cost associated to the calculation of solvent effects. Along the years, researchers have developed different strategies to reduce the computational cost while trying to keep the accuracy of the calculations at an acceptable level. One of the most successful strategies has been the introduction of the mean field approximation (MFA) [7,8] that permits to replace the configurational average of a given solute property with the value obtained for this property when the solute is affected by an average solvent perturbation. In the next sections, we treat different aspects of the practical implementation of the MFA, paying especial attention to a method developed in our laboratory and that combines the MFA with molecular dynamics (MD) simulations.

2. THE MEAN FIELD APPROXIMATION

Whereas the increase of computational power in the last decades has permitted to tackle the study of certain solvent effects using a brute force strategy, as in ab initio dynamics, its application to most chemical and biological problems is far from being routine. In ab initio dynamics [9], one combines the quantum mechanical description of both the solute and the solvent electron distributions with the classical or quantum description of the nuclei movements. Consequently, it becomes necessary to solve the Schrödinger equation of several hundreds of molecules for several thousands of configurations. The computational cost of this strategy is so high that in almost all the studies performed to date, it has been compulsory to reduce the description level of the wave functions, the number of molecules, or the number of solvent configurations.

In the search for theoretical methods that facilitate the study of solvent effects, two main strategies have been followed:

(1) Focused methods. The computational cost associated to the large number of solvent molecules can be reduced using focused methods; here, we center our attention on a small part of the system, in general, the solute or the solute and a reduced number of solvent molecules, which is described using high-level quantum mechanical methods. The description of the rest of the system, generally the solvent, is simplified using for instance dielectric continuum models, Langevin dipoles, molecular mechanics (MM) force fields, or a combination of them. Focused methods are valid when there is a clear separation between the solute and solvent wave functions and they fail when charge transfer between the solute and the solvent is not negligible. In this case, the solvent molecules closer to the solute should be included in the quantum part.

(2) MFA. The computational cost associated to the large number of thermally accessible solvent configurations, and hence of quantum calculations to perform, can be reduced using the MFA. In this approximation, one does not consider the effect of specific configurations, instead, the solvent perturbation enters into the solute molecular Hamiltonian in an averaged way.

These two approximations can be used independently or jointly. Thus, QM/MM [10] or ONIOM-type methods [11] are examples of focused methods, whereas dielectric continuum [12–14], reference interaction site model (RISM)–self-consistent field (SCF) [15–17], or averaged solvent electrostatic potential (ASEP)/MD [18–21] methods use simultaneously both strategies. To our knowledge there are no methods that use exclusively the MFA.

A measure of the success of the MFA is the great number of solvent theories where it is explicitly or implicitly used. Table 3.1 displays a classification of some solvent theories where this approximation is applied. The various theories differ in the description of the solvent. Thus, if the solvent is described as a dielectric, we get different continuum theories. They can, in turn, be classified according to the representation of the solvent perturbation: monocentric multipole [14], multicentric monopole [13,22,23], effective charges [12,24], and so on. Other descriptions of the solvent are also possible: as a conductor [25,26], using Langevin dipoles [27], or MM force fields. In the latter case, the solvent structure can be obtained using RISM theory [15–17], MD [18–21,28,29], or Monte Carlo simulations [30]. In the model proposed in our laboratory, named ASEP/MD, the solvent

Table 3.1 Classification of some of the most commonly used solvent theories that use the mean field approximation

	Conductor	Dielectric	Langevin dipoles	Molecular mechanics	
				RISM	MD
Monopole multicentric		SMx		RISM–SCF	
Multipole monocentric		Rivail, Mikkelsen			
No multipole	COSMO	PCM	Warshel	3D-RISM–SCF	ASEP/MD

structure is obtained from MD simulations and the solvent perturbation is described using potential fitted charges.

The great advantage of the MFA, and what partly explains its success, is that it permits to reduce the number of quantum calculations from several thousands to a single quantum calculation. The price that one must pay is the complete neglect of the correlation energy associated with the response of the solute charge distribution to the instantaneous changes in the solvent structure as a consequence of thermal agitation. Obviously, the MFA will be valid only if the contribution of this energy, known as Stark component [31,32], to the total solute–solvent interaction energy remains negligible. It has been shown, both theoretically [20] and experimentally [33], that this is usually the case. A recent study [34] of the errors introduced by the MFA in the calculation of free energy profiles of S_N2 Menshutkin reactions has concluded that these are lower than 0.5 kcal/mol.

3. THE ASEP/MD METHOD

Any theoretical method devoted to the study of solvent effects and intending to be of application to chemical problems of general interest must provide solution to, at least, the following problems: (1) the description of the mutual polarization of the solute and the solvent, (2) the location of critical points on free energy surfaces, and (3) the calculation of free energy differences between different solute–solvent geometries. In the following, we will show how ASEP/MD solves each one of these problems.

3.1. The mutual solute–solvent polarization

The ASEP/MD method is a focused method that makes use of the MFA. Since the solute is described quantum mechanically and the solvent by using MM force fields, it could also be classified into the QM/MM methods, more specifically, as a sequential QM/MM method [35] where QM and MD calculations are performed alternately and not simultaneously. As usual in focused methods [24], the ASEP/MD Hamiltonian is partitioned into three terms

$$\hat{H} = \hat{H}_{\mathrm{QM}} + \hat{H}_{\mathrm{class}} + \hat{H}_{\mathrm{int}}, \tag{1}$$

corresponding to the quantum part, $\hat{H}_{\mathrm{QM}}$, the classical part, $\hat{H}_{\mathrm{class}}$, and the interaction between them, $\hat{H}_{\mathrm{int}}$.

The energy and the wave function of the solvated solute molecule are obtained by solving the effective Schrödinger equation:

$$\left(\hat{H}_{\mathrm{QM}} + \hat{H}_{\mathrm{int}}\right) |\Psi\rangle = E|\Psi\rangle. \tag{2}$$

In general, in QM/MM methods this equation is solved for each solute–solvent configuration, which means several hundreds or thousands of times. The final value of the energy (or any other property) is calculated by averaging over all considered configurations.

From a computational point of view, it is convenient to split the interaction term into two components associated to the electrostatic and van der Waals contributions:

$$\hat{H}_{\mathrm{int}} = \hat{H}_{\mathrm{int}}^{\mathrm{elect}} + \hat{H}_{\mathrm{int}}^{\mathrm{vdw}}. \tag{3}$$

In many cases, it is supposed that $\hat{H}_{\mathrm{int}}^{\mathrm{vdw}}$ has little effect on the solute wave function and therefore it is usual to represent it through a classical potential that depends only on the solute–solvent nuclear coordinates. Obviously, it will contribute to the final value of the energy, and energy derivatives.

In this point the MFA is introduced. So, we define the MFA electrostatic interaction term, $\left\langle \hat{H}_{\mathrm{int}}^{\mathrm{elect}} \right\rangle$, as follows [7,8,18]:

$$\left\langle \hat{H}_{\mathrm{int}}^{\mathrm{elect}} \right\rangle = \int dr \cdot \hat{\rho} \cdot \langle V_S(r) \rangle, \tag{4}$$

where $\hat{\rho}$ is the solute charge density operator, and $\langle V_S(r) \rangle$, named ASEP, is the average electrostatic potential generated by the solvent at the position r. The brackets denote a statistical average over configurations in equilibrium.

The MFA energy is obtained by solving the following equation:

$$\left(\hat{H}_{\mathrm{QM}} + \langle \hat{H}_{\mathrm{int}} \rangle\right)|\Psi\rangle = \bar{E}|\Psi\rangle. \tag{5}$$

Note, that in the MFA we replace the average value of the energies obtained from Eq. (2) with the energy obtained in presence of the average solvent perturbation, that is, $\langle E \rangle \approx \bar{E}$.

Different solvation methods can be obtained depending on the way the term $\langle V_S(r) \rangle$ is calculated. For instance, in dielectric continuum models $\langle V_S(r) \rangle$ is a function of the solvent dielectric constant and of the geometric parameters that define the molecular cavity where the solute molecule is placed [12]. In ASEP/MD, the information necessary to calculate $\langle V_S(r) \rangle$ is obtained from MD simulations. In this way, $\langle V_S(r) \rangle$ incorporates information about the microscopic structure of the solvent around the solute, furthermore, specific solute–solvent interactions can be properly accounted for.

The basic scheme of the ASEP/MD method is very simple, see Figure 3.1. One begins by performing a quantum calculation of the solute molecule in gas phase. From this one can obtain the solute charge distribution that is introduced as input into an MD simulation. The rest of the simulation parameters can be obtained from suitable force fields. From the MD calculation, one gets the solvent structure, which permits to calculate the ASEP by averaging over the solvent configurations, the ASEP is then introduced into the solute molecular Hamiltonian. By solving the associated Schrödinger equation (5), we get the solute wave function but now perturbed by the solvent. The new solute charge distribution is again introduced into another MD simulation. The procedure is repeated until convergence is attained,

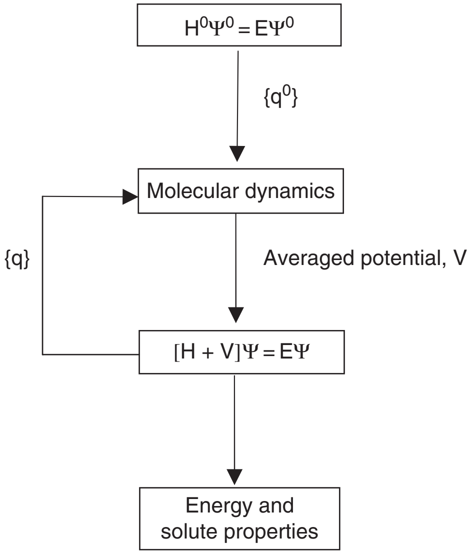

Figure 3.1 Flow chart of the ASEP/MD method.

something that occurs in a few cycles (less than ten, in general). Given that in our method quantum calculations and MD simulations are not simultaneous, there is a certain freedom to decide which configurations to include in the calculation of the ASEP. So, to decrease the statistical correlation between the selected configurations, we include only configurations separated by 0.05 ps or more. It is also important to remember that only the electrostatic term enters into the electron Hamiltonian.

The information that we get at the end of the ASEP/MD cycle is the energy, geometry, and wave function of the solute molecule polarized by the solvent and the solvent structure around it. Figure 3.2 displays how the solute charge distribution, which is represented by its dipole moment, and the solvent structure become mutually equilibrated during the ASEP/MD procedure. At the same time, the free energy of the system decreases until the system reaches the equilibrium and then it begins to fluctuate. The size of the fluctuations is a consequence of the finite size of the simulations.

One important point to clarify is the way in which the ASEP is calculated and introduced into the solute molecular Hamiltonian. We have checked several possibilities. The electrostatic solvent perturbation can be described through multipole expansions or using a set of point charges. In this last case, the charges can be determined in several ways. In general, especially when solute–solvent HBs are present, a representation using point charges is more adequate because the use of multipole expansions can introduce appreciable errors in the solute–solvent interaction energy. The simplest way to get the charges is to use for them the same values and positions used during the MD and then to divide the value of each charge by the number of solvent configurations included in the ASEP. The problem then is that the number of charges increases very quickly as the number of solvent molecules or system configurations gets higher. This approximation has been used, for instance, by Coutinho et al. [36]. To keep the number of charges tractable, we follow a somewhat more elaborated procedure: we consider explicitly only those charges associated to molecules that belong to the first solvation shell, the effect of the remaining solvent molecules is described by using potential-fitted charges.

The set of charges $\{q_i\}$ is obtained in three steps. The details are as follows [21]:

(1) Each selected configuration is translated and rotated in such a way that all of the solvent coordinates can be referred to a reference system centered on the center of mass of the solute with the coordinate axes parallel to its principal axes of inertia. This procedure is needed to get all the charges' coordinates referring to the same coordinate system.

(2) Next, one explicitly includes in the ASEP the charges belonging to solvent molecules that, in any of the MD configurations selected, lie inside a sphere of a given radius and that includes at least the first

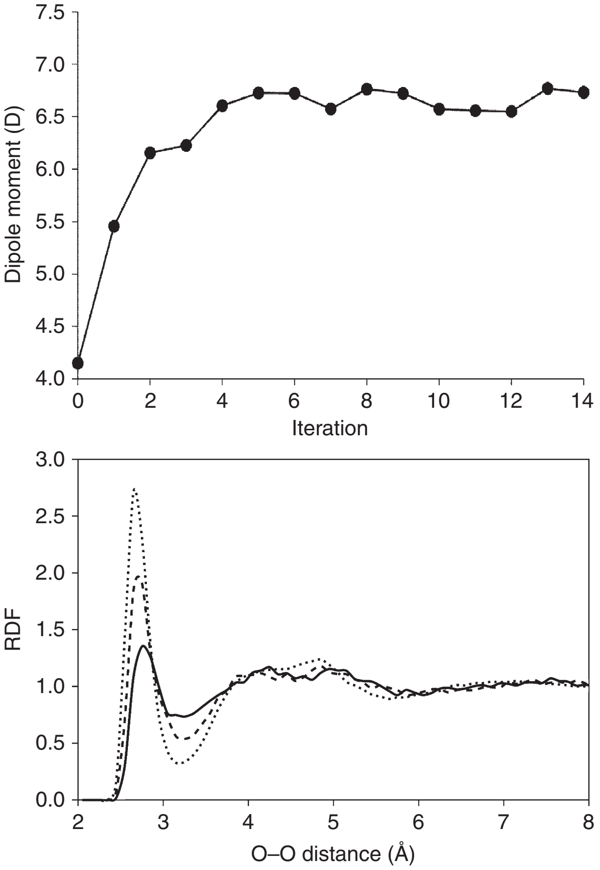

Figure 3.2 Mutual equilibration of solute and solvent during an ASEP calculation of formamide in water. Top: evolution of the solute dipole moment. Bottom: O—O RDF after the 1st (solid), 2nd (dashed), and 10th (dotted) iteration.

solvation shell. The value of every charge is then divided by the number of solvent configurations included in the determination of the ASEP. Next, to reduce the number of charges, one adds together all the charges lying less than a certain distance from each other, this distance is generally taken as 0.5 a_0.

(3) Finally, one includes a second set of charges representing the effect of the solvent molecules lying outside the first solvation shell. These charges are obtained by a least squares fit to the values of the ASEP originated by the outer solvent molecules in a three-dimensional grid

defined inside the volume occupied by the solute molecule. The solute volume is defined through a set of interlocking spheres of radius $f \cdot R_{\mathrm{vdw}}$, where f is a numerical factor close to one, and R_{vdw} are the Bondi radii of the solute atoms. These charges are obtained in such a way that they reproduce the electrostatic potential generated by the outer solvent molecules in the volume occupied by the solute.

The total number of charges introduced into the perturbation Hamiltonian varies generally between 25 000 and 35 000 depending on the size of the system.

3.2. Location of critical points on free energy surfaces

ASEP/MD uses a variant of the free energy gradient method [37–40] for the calculation of the gradients that drive the optimization process. In this method, the average force, $\langle F \rangle$, and Hessian, $\langle G \rangle$, felt by the solute atoms are used to optimize the geometry. The average force is defined as the derivative of the free energy (with a minus sign), and can be calculated as the average value of the potential energy derivative. The average Hessian takes a more complicated form, see below. In the original proposal of Okuyama-Yoshida et al. [37], these average values were obtained from QM/MM calculations where the solute molecule had a fixed geometry. The main advantage of this method is that it permits to obtain both stable and transition states. The main drawback is that the computational cost of calculating $\langle F \rangle$ and $\langle G \rangle$ is usually high. However, as we will show below, it is possible to reduce this cost by using again the MFA in the calculation of the gradient and Hessian.

The basis of the free energy gradient method is the following: Let $G = -kT \ln Z_{\mathrm{NVT}}$ be the Helmholtz free energy of a system formed by one solute molecule and N–1 solvent molecules and Z_{NVT} the quasi-classical canonical partition function. The force on the free energy surface (the force felt by the solute molecule) is

$$\langle F(R) \rangle = -\frac{\partial G(R)}{\partial R} = -\left\langle \frac{\partial E}{\partial R} \right\rangle = -\left\langle \frac{\partial E_{\mathrm{QM}}}{\partial R} \right\rangle - \left\langle \frac{\partial E_{\mathrm{int}}}{\partial R} \right\rangle, \tag{6}$$

R being the nuclear coordinates of the solute, E the energy obtained as the solution of the Schrödinger equation (2), and where we have assumed that E_{class} does not explicitly depend on the solute nuclear coordinates R. As before, the brackets denote a configurational average. Note that E incorporates both intra-, E_{QM}, and intermolecular, E_{int}, contributions.

In the same way the Hessian reads

$$\langle G(R,R')\rangle = \left\langle \frac{\partial^2 E}{\partial R \partial R'} \right\rangle - \beta \left\langle \frac{\partial E}{\partial R} \frac{\partial E^{\mathrm{t}}}{\partial R'} \right\rangle + \beta \left\langle \frac{\partial E}{\partial R} \right\rangle \left\langle \frac{\partial E}{\partial R} \right\rangle^{\mathrm{t}}$$
$$= \left\langle \frac{\partial^2 E}{\partial R \partial R'} \right\rangle - \beta \left[\langle F^2 \rangle - \beta \langle F \rangle^2 \right], \tag{7}$$

where the superscript t denotes the transposition and $\beta = 1/kT$. The last term in Eq. (7) is related to the thermal fluctuations of the force.

As for the energy, it is convenient to split the interaction term into two components associated to the electrostatic and van der Waals contributions:

$$\langle F(R)\rangle = -\left\langle \frac{\partial E_{QM}}{\partial R} \right\rangle - \left\langle \frac{\partial E_{\mathrm{int}}^{\mathrm{elect}}}{\partial R} \right\rangle - \left\langle \frac{\partial E_{\mathrm{int}}^{\mathrm{vdw}}}{\partial R} \right\rangle. \tag{8}$$

Next, we use the MFA to simplify the gradient and Hessian expressions. Given that our final aim is to reduce the number of quantum calculations, this approximation is used for the two first terms of the R.H.S. of Eq. (8), but not for the van der Waals term that does not depend on the electron coordinates. Thus, we replace the configurational average of the derivatives with the derivative of the MFA energies obtained with Eq. (5), furthermore we neglect the force fluctuation term in Eq. (7) (since the Hessian is used only to accelerate the optimization procedure, this approximation has no effect on the optimized geometries but it can affect the harmonic frequencies evaluation). The validity of these approximations has been checked elsewhere [41]. The force now reads as follows:

$$\langle F(R)\rangle = -\frac{\partial \bar{E}_{\mathrm{QM}}}{\partial R} - \frac{\partial \bar{E}_{\mathrm{int}}^{\mathrm{elect}}}{\partial R} - \left\langle \frac{\partial E_{\mathrm{int}}^{\mathrm{vdw}}}{\partial R} \right\rangle, \tag{9}$$

with an analogous expression for the Hessian:

$$\langle G(R,R')\rangle = -\frac{\partial^2 \bar{E}_{\mathrm{QM}}}{\partial R \partial R'} - \frac{\partial^2 \bar{E}_{\mathrm{int}}^{\mathrm{elect}}}{\partial R \partial R'} - \left\langle \frac{\partial^2 E_{\mathrm{int}}^{\mathrm{vdw}}}{\partial R \partial R'} \right\rangle. \tag{10}$$

The advantages of the introduction of the MFA in the calculation of gradients and Hessians are evident, it permits to reduce the computational cost of these quantities in solution; in fact, the cost is similar to that of an isolated molecule.

3.3. Calculation of free energy differences

For most practical applications, one is interested in the free energy (FE) difference between different structures, states, or species, such as the ground and excited state in a photophysical process, and reactants, products, and transition state in a chemical reaction. Within the ASEP/MD methodology, the free energy difference in solution between two given states is approximated as follows [42]:

$$\Delta G_s = \Delta E_{\text{solute}} + \Delta G_{\text{int}} + \Delta ZPE_{\text{solute}}, \tag{11}$$

where ΔE_{solute} is the internal energy difference between the two solute states at QM level, ΔG_{int} is the difference in the solute–solvent interaction free energy, and $\Delta ZPE_{\text{solute}}$ includes the difference in zero-point energy as well as entropy and thermal contributions to the solute QM free energy. Although formally this equation takes the same form as in the QM-FE approach of Jorgensen [43], the meaning of the ΔE term is different. First, because the geometry of the two species involved are optimized in solution. Second, because the internal energy and charge distribution of the solute are determined in the presence of the solvent.

In Eq. (11), the internal energy difference between the two QM states is defined as

$$\Delta E_{\text{solute}} = E_{\text{B}} - E_{\text{A}} = \left\langle \Psi_{\text{B}} | \hat{H}^0_{\text{B}} | \Psi_{\text{B}} \right\rangle - \left\langle \Psi_{\text{A}} | \hat{H}^0_{\text{A}} | \Psi_{\text{A}} \right\rangle, \tag{12}$$

where, $\hat{H}^0_{\text{X}}$ is the in vacuo Hamiltonian for the state X, and Ψ_{X} is the electronic wave function of the state X in solution, that is, calculated in the presence of the perturbation caused by the solvent. Ψ_{X} is obtained by solving the effective Schrödinger equation, Eq. (5). E_{B} and E_{A} are calculated using the geometries optimized in solution and do not include the solute–solvent interaction energy.

The ΔG_{int} term is calculated with the free energy perturbation (FEP) method [44], and takes into account the ensemble of thermally accessible solute–solvent configurations. To obtain ΔG_{int}, the solute geometry, charges, and Lennard-Jones parameters are considered as a function of the perturbation parameter λ: when $\lambda = 0$ they correspond to the initial state and when $\lambda = 1$ to the final state. A series of intermediate arbitrary states are defined by linear interpolation of the solute properties and for each of them a fully classical MD simulation is performed. The free energy difference is calculated from these simulations in the usual FEP way. It must be noted that, although geometries and charges for the initial and final states of the solute are calculated quantum mechanically with the ASEP/MD method, the ΔG_{int} term is obtained through classical simulations. This approximation does not introduce significant errors if a sufficiently good solute charge distribution is used and it permits an important saving in computational effort. A more detailed discussion of this point can be found in Ref. [45]. For a comparison of several strategies based on the MFA for the calculation of solvation free energies in solution and protein environment, see Ref. [46].

Finally, the $\Delta ZPE_{\text{solute}}$ term is calculated in the same way as usually done for in vacuo calculations, using the harmonic approximation for vibrational modes. The only specific consideration in solution is that the molecular geometry and vibrational frequencies of the solute are obtained in solution, using the approximate in solution Hessian matrix. Rotational and translational degrees of freedom are transformed into low-frequency vibrational modes in solution, and must be treated accordingly.

4. VALIDITY OF THE MEAN FIELD APPROXIMATION

The main source of error associated to the use of the MFA is the complete neglect of the Stark component of the solute–solvent interaction energy. In this section, we present some results that permit to estimate the magnitude of this error in several quantities. More specifically, we discuss three types of errors: errors on the energy and dipole moment of molecules in the ground state, errors on the solvent shift in electron transitions, and errors on the energy gradients.

In Table 3.2, the values for the energy and dipole moment of several alcohols and carbonyl compounds in water solution calculated with the MFA or as an average of QM calculations are compared [20]. $\langle A \rangle$ represents the value of the A property calculated as the mean value of 100 quantum calculations; A_{MFA} represents the value obtained when the MFA is used, and has been obtained by calculating the ASEP with the same 100 solvent configurations and performing only one quantum calculation. W_{Stark} is the

Table 3.2 Interaction energy, solvent Stark component (in kcal/mol), and dipole moments (in debyes) in the liquid state calculated as a mean value $\langle E \rangle$ or with the mean field approximation E_{MFA}

	$\langle E \rangle$	E_{MFA}	W_{Stark}	$\langle \mu \rangle$	μ_{MFA}	$\langle \mu \rangle - \mu_{\text{MFA}}$
CASSCF						
Formaldehyde	–9.2	–8.8	0.4 (4.3%)	2.99	2.99	0.00 (0.0%)
Acetaldehyde	–8.9	–8.5	0.4 (4.5%)	3.46	3.46	0.00 (0.0%)
Acetone	–21.9	–21.1	0.8 (3.6 %)	4.48	4.47	0.01 (0.2%)
MP2						
Methanol	–18.3	–17.9	0.4 (2.2%)	2.46	2.45	0.01 (0.4%)
Ethanol	–15.8	–15.4	0.4 (2.5%)	2.27	2.25	0.02 (0.9%)
Propanol	–13.7	–13.5	0.2 (1.5%)	2.15	2.13	0.02 (0.9%)

difference between these two quantities for the energy. As we can see W_{Stark} is in all cases lower than 5% and the errors introduced by the MFA in the dipole moments are lower than 1%. Percentually, the errors are very similar along each series of molecules. The errors are somewhat higher in the carbonyls because of their larger polarizabilities.

For the determination of the error introduced by the MFA in the calculation of the solvent shift of electron transitions, we must compare the transition energy when the MFA is used and when it is not. In Table 3.3, we compared the errors introduced by the MFA in the calculation of the transition energy in several chromophores and different solvents: water, methanol, and cyclohexane. In this study electronic transitions to the first (n–π^*) excited state were studied for acrolein and formaldehyde, whereas (π–π^*) transitions were studied for *p*-difluorobenzene (*p*-DFB) and *trans*-difluoroethene (*trans*-DFE). A practical coincidence is observed between the in solution transition energies obtained using the MFA and those achieved as the average of the transition energies resulting from 100 quantum calculations corresponding to as many solvent configurations. A similar trend can be noted in solvent shift values,

Table 3.3 Transition energies in vacuo, ΔE^0, and in solution calculated as a mean value $\langle \Delta E^d \rangle$ or with the mean field approximation $\Delta E^d_{\mathrm{MFA}}$. δ stands for the solvent shift. W_{Starrk} is the solvent Stark component of the solute–solvent interaction energy. All the quantities in kcal/mol

	ΔE^0	$\langle \Delta E^d \rangle$	$\Delta E^d_{\mathrm{MFA}}$	$\langle \delta \rangle$	δ_{MFA}	$W_{\mathrm{Stark}}(\delta)$
Water						
Acroleine; CASPT2(6,5)//CASSCF(6,5)	83.08	88.26	88.60	5.18	5.51	0.34
Formaldehyde; CASPT2(4,2)//CASSCF(4,2)	92.30	95.79	95.73	3.49	3.43	–0.06
p-DFB; CASPT2(6,6)//MP2	110.02	111.18	111.17	1.16	1.14	–0.02
trans-DFE; CASPT2(2,2)//MP2	190.62	192.34	189.68	1.72	1.67	–0.05
Methanol						
p-DFB; CASPT2(6,6)//MP2	110.02	110.66	110.75	0.64	0.72	0.08
trans-DFE; CASPT2(2,2)//MP2	190.62	191.60	191.42	0.98	0.80	–0.18
Cyclohexane						
p-DFB; CASPT2(6,6)//MP2	110.02	110.22	110.18	0.16	0.19	–0.03

calculated as the difference of electronic transition energies obtained in vacuo and in solution. Consequently, and as a first conclusion, we can state the absence of solvent Stark effect and the validity of the MFA in the study of the solvent effect on the position of the absorption bands in electronic spectra.

Finally, in Table 3.4 we compare the values of the different components of the free energy gradient for a molecule of formamide in aqueous solution [41]. The error introduced by the MFA in the gradient root mean square (RMS) is close to 1%, very similar to the errors introduced in the energy or in dipole moment. This implies that the MFA can provide good optimized geometries of molecules in solution. In the gradient we have included only the electrostatic component of the solute–solvent interaction energy because the MFA affects only this component, the contribution of the van der Waals component to the gradient is evaluated directly from the MD simulations (vide supra).

Table 3.4 Cartesian gradient of the free energy (in 10^{-3} E_h/a_0) of a molecule of formamide in aqueous solution. Only the electrostatic contribution is included

		Mean of 1000 configurations	Average configuration	Difference
N1	x	12.914	12.827	0.087
	y	3.858	3.831	0.027
	z	0.084	0.085	–0.001
H2	x	–3.365	–3.132	–0.233
	y	3.049	2.928	0.121
	z	0.053	0.049	0.004
H3	x	–1.116	–1.081	–0.035
	y	–5.347	–5.081	–0.266
	z	–0.006	–0.004	–0.002
C4	x	–26.864	–26.816	–0.048
	y	5.473	5.487	–0.014
	z	–0.002	–0.010	0.008
O5	x	18.255	17.862	0.393
	y	–10.052	–9.788	–0.264
	z	–0.041	–0.026	–0.015
H6	x	1.567	1.571	–0.004
	y	–2.136	–2.240	0.104
	z	–0.004	0.002	–0.006
r.m.s.		8.898	8.807	0.091

5. EXAMPLES OF APPLICATIONS

In this section we present some examples of application of ASEP/MD. These examples comprise solvent effects on conformational and configurational equilibria, chemical kinetics, UV/Vis spectra and nonradiative de-excitation of excited states. In all of them, the use of the MFA permits to reduce the computational cost associated to the great number of thermally accessible solvent configurations; this makes it possible to increase the description level of the solute and the use of quantum methods similar to those commonly used in gas-phase calculations: density functional theory (DFT), Møller-Plesset perturbation theory (MP2), complete active space self consistent field (CASSCF), complete active space perturbation theory (CASPT2), and so on. Along this discussion, the results obtained with ASEP/MD will be compared with those obtained with other methods. The final aim is to establish the validity of the MFA and to determine the possible importance of solute–solvent specific interactions on the calculated properties.

5.1. Conformational and configurational equilibria

5.1.1. Anomeric effect in xylopyranose and glucopyranose

The anomeric effect describes the axial preference for an electronegative substituent on the pyranose ring adjacent to the ring oxygen. This effect makes the β-anomer—with all the hydroxyl groups in the equatorial orientation with respect to the ring (in D-glucopyranose)—less stable than the α-anomer—which differs from the β-anomer in the axial orientation of the hydroxyl group on C_1—in vacuo. However, the reverse behavior has been observed in aqueous solution. So, for instance, in D-glucopyranose in water solution, the ratio between α- and β-anomers is 36:64. A similar behavior has been observed in xylopyranose.

In the study of D-xylopyranose [47], the energy and wave functions were calculated using DFT with the Becke three-parameter Lee–Yang–Parr (B3LYP) functional [48] and the 6-311G++G(2d,2p) basis set [49]. For each anomer, there are several possible arrangements of the hydroxyl groups. In general, for the isolated molecule, the hydroxyl groups prefer to orient in such a way as to yield a cooperative hydrogen bonding as efficiently as possible. The two preferred arrangements of the intramolecular hydrogen bonds (IHBs) are clockwise or counterclockwise, the counterclockwise orientation being somewhat more stable. The main results obtained are displayed in Figure 3.3. For comparison, we also give the results obtained with the polarizable continuum model (PCM) [12] as implemented in Gaussian 98 [50] and with a scale factor for the radius of each atomic sphere of 1.2. The continuum model erroneously predicts that solvation favors the α-anomer; in fact, the solvation free energy is 1.1 kcal/mol larger in the α-anomer than in the β. On the contrary, ASEP/MD, which includes specific

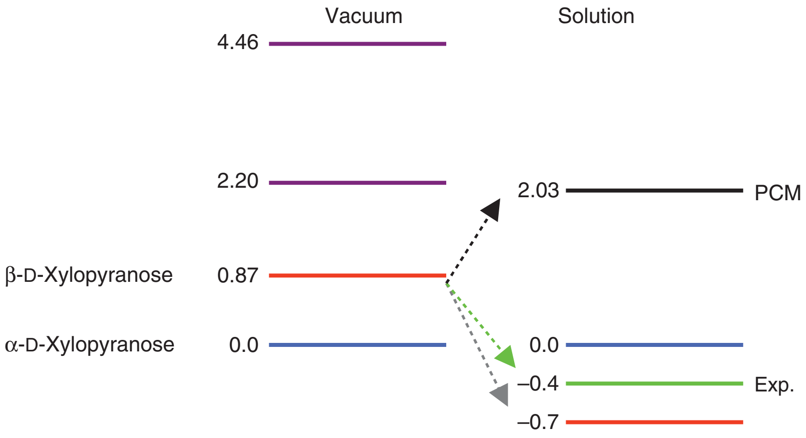

Figure 3.3 Relative free energies (with counterclockwise α-D-xylopyranose as the reference) of α- and β-D-xylopyranose, in vacuo and in solution.

solute–solvent interactions, predicts the correct trend: in solution the more stable form is the β-anomer. Given that in vacuo the anomeric effect favors the α-anomer, the greater stability in solution of the β-anomer must be due to a more favorable solvent interaction term. The relative stability predicted by ASEP/MD, 0.6 kcal/mol, agrees very well with the experimental value, 0.4 kcal/mol [51].

The study of the D-glucopyranose molecule [52] is somewhat more complicated because the hydroxymethyl group can adopt different orientations (see Figure 3.4) with different values of the dihedral angle

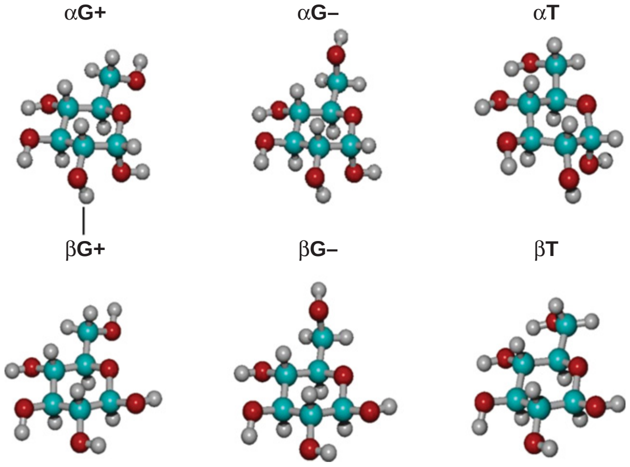

Figure 3.4 Structures of the different rotamers of α- and β-D-glucopyranose.

O_R—C_5—C_6—O_6. In our study we considered the three most important rotamers (T, G+, G–) of counterclockwise D-glucopyranose, which were studied in vacuo and in water solution at the B3LYP/6-31+G(d,p) level and with the ASEP/MD method.

Figure 3.5 shows the relative energies of the six studied conformers of D-glucopyranose in vacuo and in aqueous solution. The energy of the most stable conformer in vacuo, αT, is arbitrarily taken as the reference value. The most significant effect of the solvation of D-glucopyranose is the larger stabilization of the β-conformers relative to the α ones. As a result, we found that while in vacuo the α-conformers are more stable than their β counterparts; in aqueous solution any of the β-conformers is preferred to any of the α-conformers. The difference in energy in solution between the most stable β-conformer, βG+, and the most stable α-conformer, αT, is 0.9 kcal/mol. Experimental evidence [53,54] suggest that the difference in free energy between α- and β-conformers of D-glucopyranose in aqueous solution is around 0.4 kcal/mol (a ratio between α- and β-abundances of 36:64). Our results slightly overestimate these differences in energy (we obtain a ratio between α and β of 20:80), but, given the approximations made in our study, this result is very encouraging.

In order to gain a deeper insight into the solvation effects, in Figure 3.6 we plot the radial distribution function (RDF) for the distances between the anomeric oxygen, O_1, and the water solvent oxygen, O_w, for the six

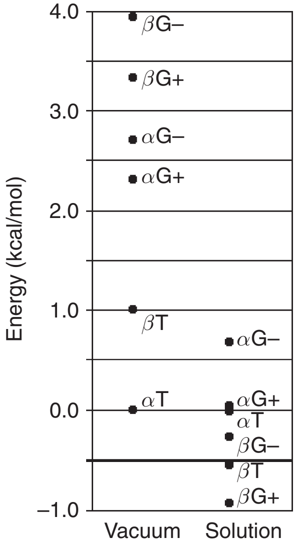

Figure 3.5 Relative free energies (with αT as the reference) of the different rotamers of α- and β-D-glucopyranose, in vacuo and in solution.

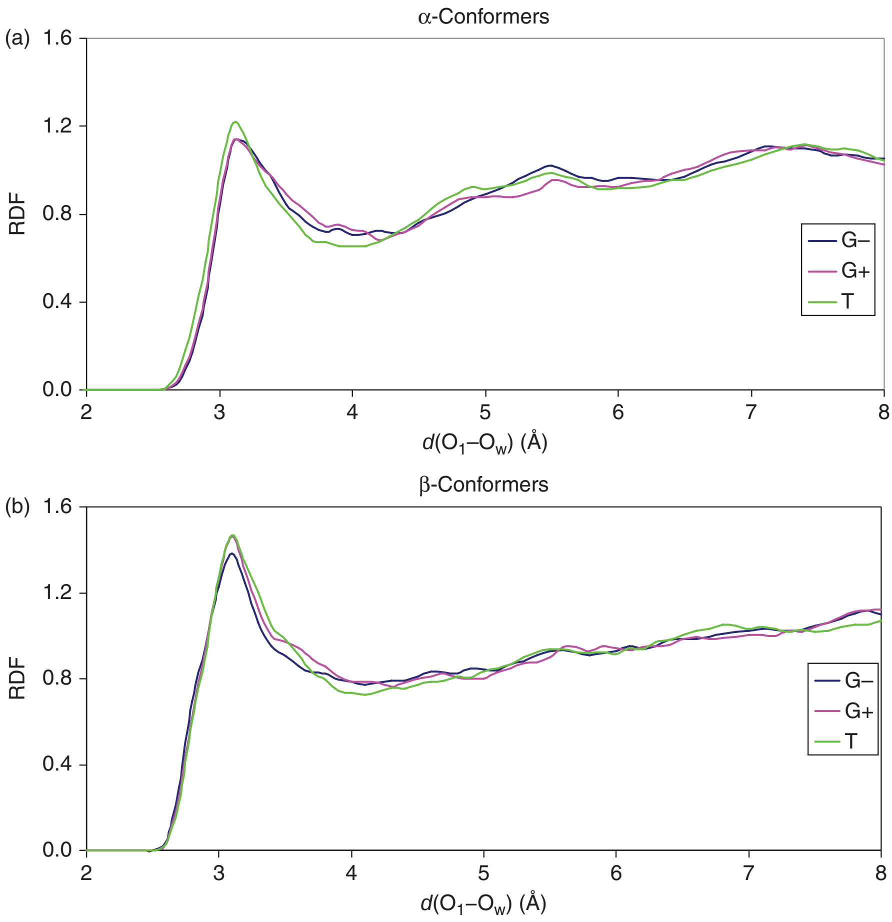

Figure 3.6 O(anomeric)—O(water) RDFs of the different rotamers of α- and β-D-glucopyranose.

conformers. Figure 3.6a shows the RDF for the α conformers and Figure 3.6b for the β-conformers. The main conclusion is that, as we noted above, solvation is more effective for the β-conformers, which shows a peak (at around 3.1 Å) that is higher than for the α-conformers. One can therefore expect the β-conformers to be more stabilized by solvation than the α-conformers, the solvent molecules being more tightly bonded to the anomeric oxygen in the β-conformers. The solvation of the rest of the OH groups of the pyranose ring hardly depends at all on the type of conformer, and hence has no influence on the relative stability of the α- and β-forms.

In sum, the most significant effect of the solvation of D-xylopyranose and D-glucopyranose is the greater stabilization of the β-conformers relative to the α-conformers. The explanation is that the anomeric effect, which makes α-conformers more stable in the gas phase, is not powerful enough to compete with the effect of a stronger interaction between the solvent and the free electron pairs of the anomeric oxygen in the β-conformers than in the α-conformers, where this interaction is hindered by the rest of the pyranose ring.

5.1.2. Conformational equilibrium in a tripeptide

In recent years, small peptides have been used as model systems for the study of the conformational behavior of more complex biomolecules. In an effort to gain insight on the solvent influence on the structure and stability of peptides, we undertook the study of the electronic structure, the geometric parameters, and the physicochemical properties of the tripeptide Cys-Asn-Ser (Figure 3.7) both in gaseous and in acidic aqueous solutions [55]. The study was performed with ASEP/MD and at the B3LYP/6-311+G(d) level. The Cys-Asn-Ser tripeptide can form several IHBs that involve groups of very different nature [56]. It is hence a good model to check the solvent influence on the geometry and energy of the different groups. We are especially interested in the study of the IHB formed by the oxygen (O25) of the side chain of Asn with the two hydrogens (H2 and H19) bonded to the

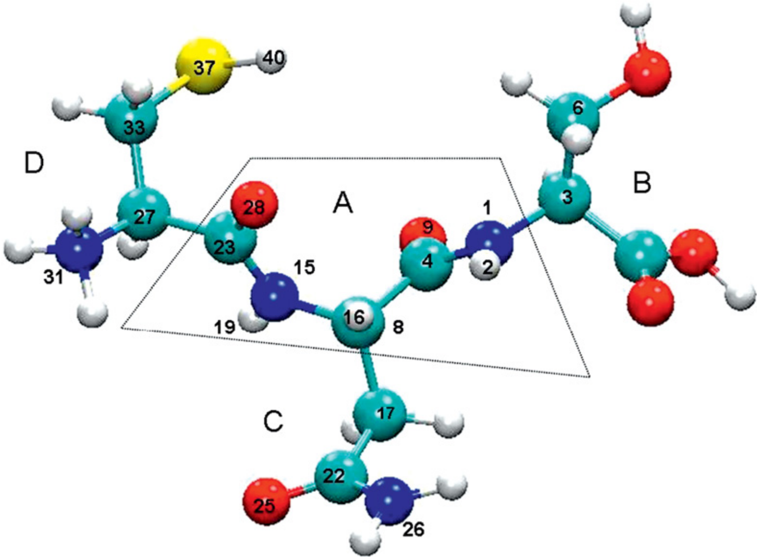

Figure 3.7 Structure and labeling of the Cys-Asn-Ser tripeptide.

nitrogens (N1 and N15) of the peptide bonds, because they can provide stiffness to the main chain of the tripeptide. We named these IHBs as HB1a (N1—H2—O25) and HB1b (N15—H19—O25), respectively.

In gas phase we found three minima, see Figure 3.8. The two more stable structures are Vac-2 and Vac-3, the free energy difference between these two structures is only 0.3 kcal/mol. In both structures, O25 is involved in the formation of an IHB. Somewhat higher in energy (2 kcal/mol), we find Vac-1, in this structure the O25 IHB is missing.

Next, we analyzed the in solution results. Figure 3.9 displays the six more stable structures, for the sake of simplicity other structures at higher energies have not been included. The structures of Sol-1–Sol-3 conformers are equivalent to those obtained in vacuo (Vac-1–Vac-3), in the sense that they are characterized by the same number of IHBs and display a similar orientation of the side groups. Sol-4–Sol-6 are extended structures without IHB. The first conclusion is that the number of local minima is greater in solution than in vacuo. The solvent stabilizes extended structures without IHB that are not stable in vacuo. These results confirm previous studies on the relative stability of amino acids and peptides, where it was found that

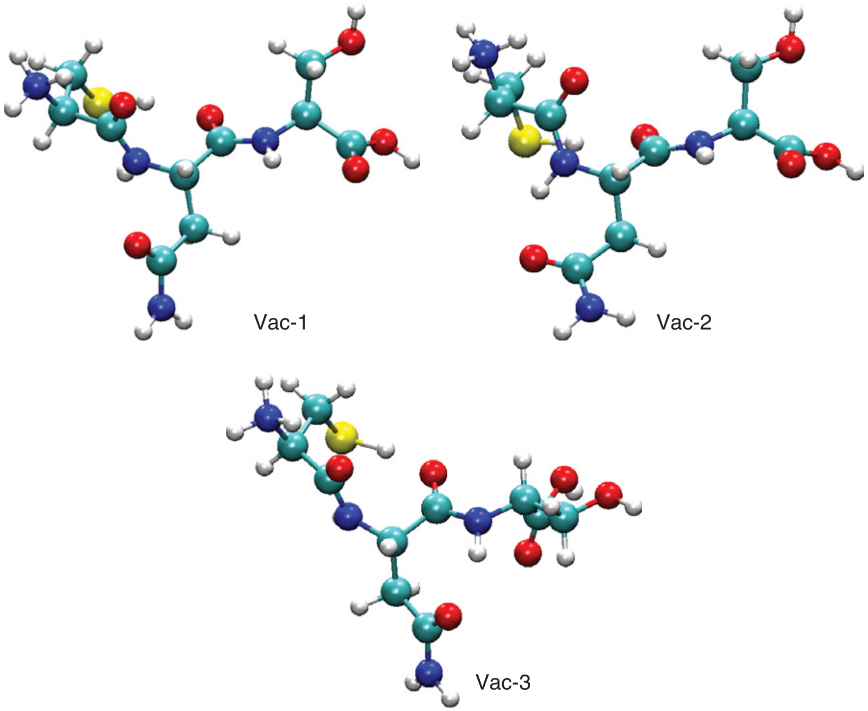

Figure 3.8 Stable conformations of the tripeptide in vacuo.

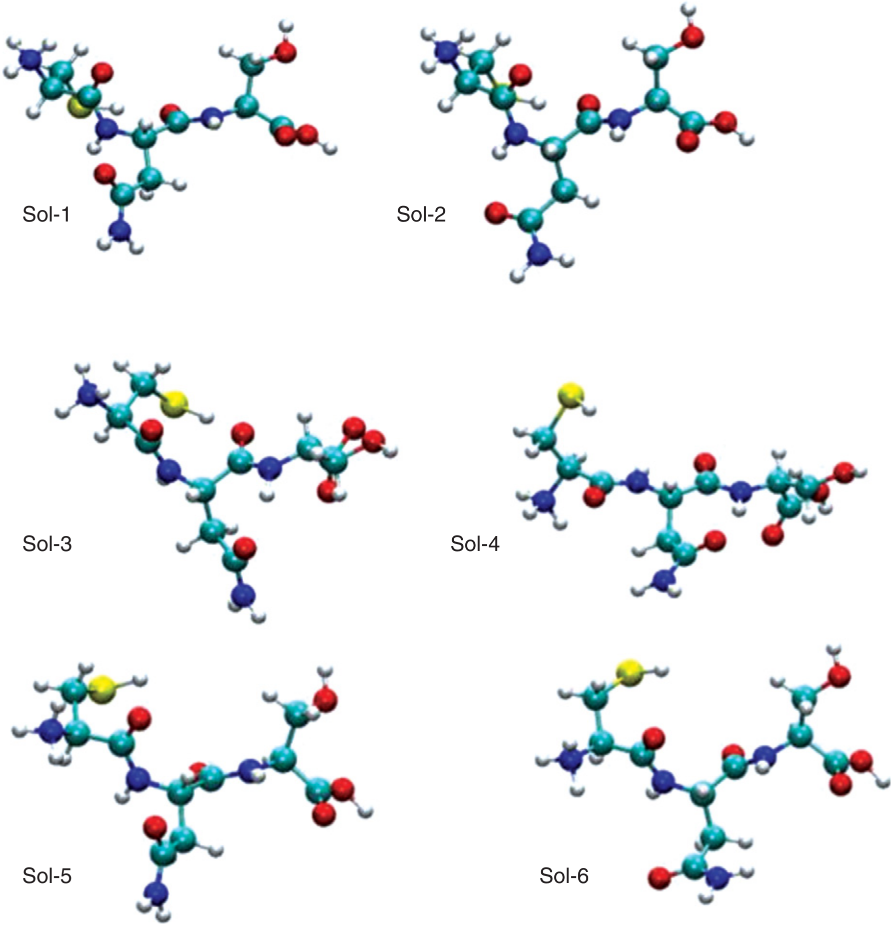

Figure 3.9 Stable conformations of the tripeptide in solution.

some structures that do not exist in gas phase become stable in solution because of their ability to form strong intermolecular HBs with water. So, for instance, in solution, the most stable structures are Sol-1, Sol-5, and Sol-6; in these three conformers, O25 forms an intermolecular HB with the water molecules. Higher in energy are Sol-2 and Sol-3, characterized by the presence of HB1b and HB1a, respectively. Consequently, in solution there is an equilibrium between several structures, with the structures where O25 forms intermolecular HBs strongly favored.

Another fact to emphasize is that, in solution, the stability order is reversed with respect to the situation found in vacuo, here the order is Vac-3 > Vac-2 > Vac-1 whereas in solution the stability order of the equivalent structures is Sol-1 > Sol-2 > Sol-3. The study of the different

Table 3.5 Free energy difference and its components, in kcal/mol, for the six most stable minima found in solution

	ΔE_{solute}	ΔG_{int}	ΔG
Sol-1	–8.0	3.1	–4.9
Sol-2	–11.0	7.4	–3.6
Sol-3	–11.8	9.8	–2.0
Sol-4	0.0	0.0	0.0
Sol-5	4.1	–8.8	–4.7
Sol-6	8.2	–13.0	–4.8

contributions to the free energy, Table 3.5, permits us to clarify the origin of the inversion in the differential stability of the conformers when we pass from gas phase to solution. ΔG is the sum of two contributions: the internal energy, ΔE_{solute}, and the solvation energy, ΔG_{int}, as indicated in Eq. (11) neglecting the $\Delta ZPE_{\text{solute}}$ term. It is interesting to note that there exists a strong negative correlation between the internal energy and the solvation energy: the less stable the internal structure of the conformer, the greater the solvation energy. The internal energy is stabilized by the presence of IHBs, consequently, the most negative values of the internal energy correspond to those structures with the larger number of IHB (Sol-2 and Sol-3). On the contrary, the solvation energy is larger in those structures where there is a better exposure of the polar groups of the peptide to the water molecules, that is, in those structures in which the tripeptide adopts a more extended conformation without IHB (Sol-5 and Sol-6). The stability order results from the interplay of these two factors: internal energy and solvation that, in turn, are determined by the competition between intra- and intermolecular HBs.

The study of the shape of RDF and of the coordination numbers also reveals the competition between IHBs and intermolecular HBs, see Figure 3.10. If one fixes the attention on the O25(tripeptide)—H(water) RDF, it can be noted that the height of the RDF and the coordination number decreases as we pass from a conformation with intermolecular HB to one with intramolecular HB. So, for instance, the O25 coordination number decreases from 2.5 to 2.2 when one passes from Sol-1 to Sol-2, and to 1.8 in Sol-3. However, the most dramatic effects are displayed by H2 and H19. In Sol-1, both hydrogen atoms show well-defined peaks at 2 Å in the H(tripeptide)—O(water) RDFs. In the two cases, the coordination numbers are close to 1. In Sol-2, H2 displays also a very well-defined peak but the RDF associated to H19 has completely lost its structure, evidencing the existence of an IHB between O25 and H19. Something similar is found in Sol-3, in this case the H19—O(water) RDF displays a very well-defined peak but the H2—O(water) RDF loses its structure as a consequence of the H2—O25 IHB.

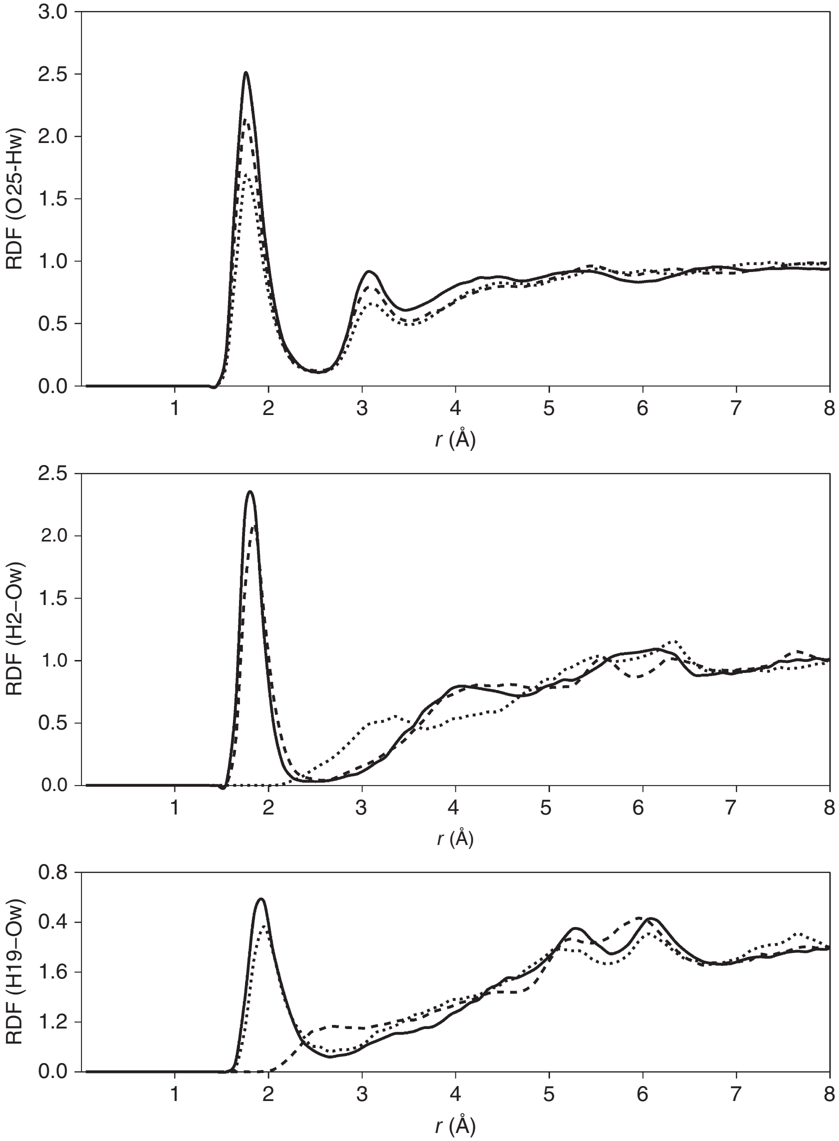

Figure 3.10 O25—H, H2—O, and H19—O RDFs for the tripeptide in solution. Solid: Sol-1. Dashed: Sol-2. Dotted: Sol-3.

5.2. Chemical reactions

An example of application of the ASEP/MD methodology to chemical reactions was the study of the 1,3-proton shift in triazene (N_3H_3) [57]. The ASEP/MD method was used to optimize the geometries of the triazene

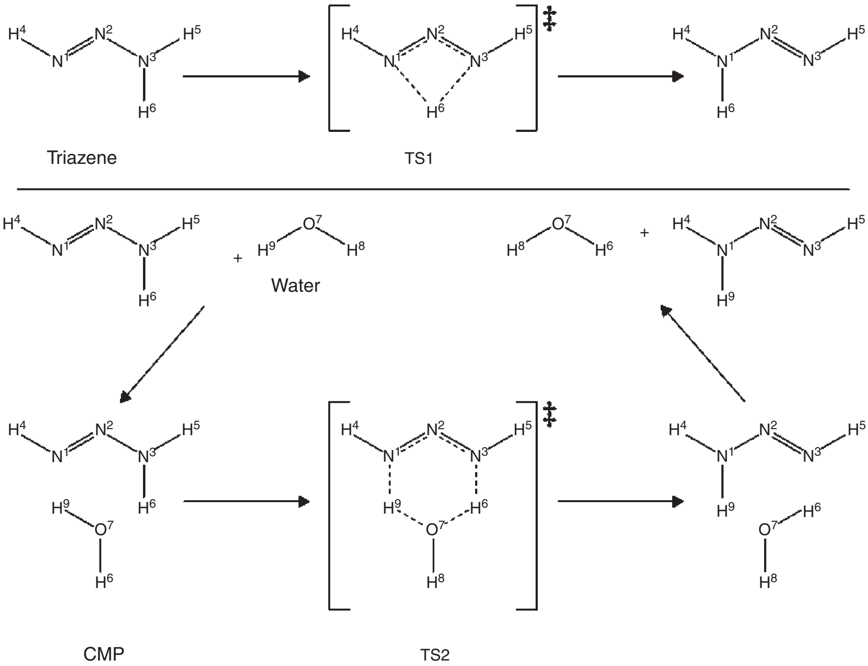

Figure 3.11 Scheme of 1,3 proton shift of triazene. Top: unimolecular reaction. Bottom: bimolecular reaction with the aid of a water molecule.

molecule in water, as well as the transition states of two possible reaction mechanisms: a unimolecular shift (TS1) and a bimolecular reaction aided by a water molecule (TS2, see Figure 3.11) in aqueous solution. A DFT method with a BP86 functional [58,59] was used for the quantum calculations with a triple-zeta basis set. Concerning the structure of the transition states, it was found that TS2 in solution resembles a $N_3H_4^+ + OH^-$ ionic pair in solution more than in gas phase, which accounts for a part of the stabilization of this transition state in solution (see Table 3.6). While the activation energy for the unimolecular reaction increases from 32.0 kcal/mol in gas phase to 34.9 kcal/mol in solution, for the bimolecular reaction it decreases from

Table 3.6 Energy barriers (in kcal/mol) of the two activation processes for the 1,3 proton shift in triazene. See Figure 3.11 for the structures

	In vacuo	In solution
$N_3H_3 \rightarrow TS1$	32.03	34.91
$N_3H_3 + H_2O \rightarrow TS2$	10.07	5.46

10.1 kcal/mol to 5.5 kcal/mol. Not only the bimolecular path is preferred, but the preference is much stronger in solution.

As a complementary application, the optimized TS2 structure obtained in water with the ASEP/MD method was used as the initial solute geometry for trajectory calculations with a standard QM/MM method (DFMM) [60–62], using the "rare event" approach for the dynamical study of the bimolecular reaction. Starting with the transition state, 50 different QM/MM trajectories, with Boltzmann-distributed initial velocities, were run both forward and backward in time. This allowed us to observe the behavior of the transition state structure in solution and the course of the reaction. The main conclusions were (1) the hydrogen-bonded complex (CMP) is maintained before and after the reaction takes place; (2) a transition-state-like structure, which resembles an ionic pair, is relatively long-lived (an average life of 85 fs); (3) the calculated transmission coefficient was 0.73, indicative of a good initial representation of the transition state, which was the aim of the ASEP/MD method, and at the same time of a nonnegligible influence of dynamical effects and recrossings, as suggested by the long-lived TS2-like structure.

5.2.1. Electron transitions

In the study of solvent effects on electron spectra, it is very usual to consider two time scales: a fast one, associated with the motion of the electrons, and a slow one, related to the nuclear motion. During an electron transition, the Franck–Condon (FC) principle establishes that the nuclear geometries of the solute and solvent remain fixed. That means that for an absorption process the solvent structure will be in equilibrium with the ground-state solute charge distribution, but not with the solute charge distribution of the excited state (the contrary is valid for the emission process). However, the response of the electron distribution of the solvent is in general fast enough to adapt to the change in the solute charge distribution during the transition. In our group we have developed a polarizable solvent version [63,64] of the ASEP/MD method that permits the electronic degrees of freedom of the solvent to respond instantaneously to the change in the solute charge distribution during the transition, that is, the electron solvent polarization is always in equilibrium with the solute charge distribution. To this end an additional self-consistent process is performed. Using the solvent structure and solute geometry obtained in the first self-consistent ASEP/MD process, we couple the quantum mechanical solute and the electron polarization of the solvent. We assign a molecular polarizability to every solvent molecule, and simultaneously, we replace the effective solvent charge distribution used in the MD simulation with the gas-phase values for the solvent molecule. The induced dipole moment on each solvent molecule is a function of the induced dipole moments on the rest of the molecules and of the solute charge distribution, and hence the electrostatic equation has to be solved self-consistently. The process finishes when convergence in the solute and solvent charge distributions is achieved.

In our method, the solvatochromic or solvent shift of an electron transition is the sum of several contributions [65] corresponding to the change in the internal energy of the solute when polarized, the distortion energy of the solvent, that is, the energy spent in the reorganization of the solvent during the excitation, and several terms associated to the interactions between the solute charge distribution, Q, and the permanent, q, and induced, p, charges in the solvent.

$$\delta = U_{\mathrm{ex}} - U_{\mathrm{g}} = \frac{1}{2}\delta_{pq} + \delta_{Qq} + \frac{1}{2}\delta_{Qp} + \delta_{\mathrm{dist}}^{\mathrm{solute}} + \delta_{\mathrm{dist}}^{\mathrm{solvent}}. \tag{13}$$

The last term of Eq. (13), the distortion energy of the solvent, vanishes in a vertical transition where the solvent structure is kept fixed but takes a nonnull value in adiabatic transitions.

As an example of application of the method, the transition energy of dimethylaniline (DMA) in several solvents is presented [66]. The geometry of DMA was optimized at CASSCF(8,7)/6-311G** level, and the transition energies calculated with second-order perturbation theory (CASPT2) as implemented in MOLCAS-6 [67]. The solvents, water, cyclohexane, and tetrahydrofuran, were represented as rigid molecules with the OPLS-AA force field. In vacuo, the ground-state dipole moment is 1.33 D and 1.66 D in the excited state. When the molecule is introduced into a solvent, it is expected that the excited state will be more stabilized than the ground state, consequently the transition energy will decrease and we will have a red solvent shift. In Figure 3.12 white circles represent the experimental values. As one can see, the decrease of the transition energy becomes larger when the solvent polarity increases. Water, however, presents an anomalous behavior. In water, the transition energy increases. We will try to explain the reasons of this anomalous behavior later. First, we will describe the prediction of continuum models, blue circles. As we can see, PCM reproduces the experimental trend in nonprotic solvents, but fails in the water case. On the contrary, ASEP/MD, red circles, reproduces correctly the experimental trend, both in protic and nonprotic solvents. The systematic deviation of our results from the experimental values is due to the neglect of the contribution of the dispersion component. This component is a function of the refraction index of the solvent and hence it hardly depends on the solvent nature (the refraction index varies very little among the different solvents studied) and its contribution can be eliminated by considering the differences between solvents instead of the absolute transition energy, see Figure 3.13. The agreement with the experiment is very good.

Turning to the motives of the anomalous behavior of water, in Figure 3.14 we represent the occupancy map of water oxygen atoms. Because of the formation of HBs, most of the water molecules concentrate close to the free

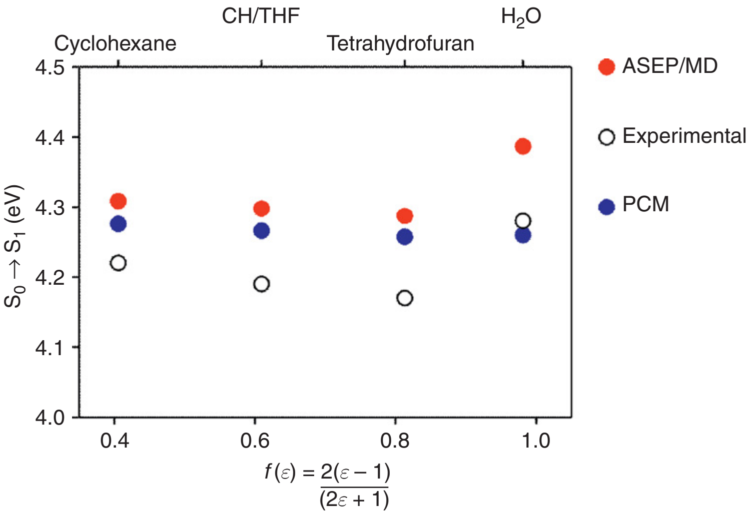

Figure 3.12 Absorption energies of DMA in solvents of different polarity.

electron pair of the nitrogen atom. There are also high concentrations above and below the aromatic ring. When the molecule is excited, part of the charge is transferred from the nitrogen atom to the ring, and the HBs are broken, as a consequence the solvation energy decreases in the excited state. In reality, this is only a partial view of the problem. When the solute molecule is placed in

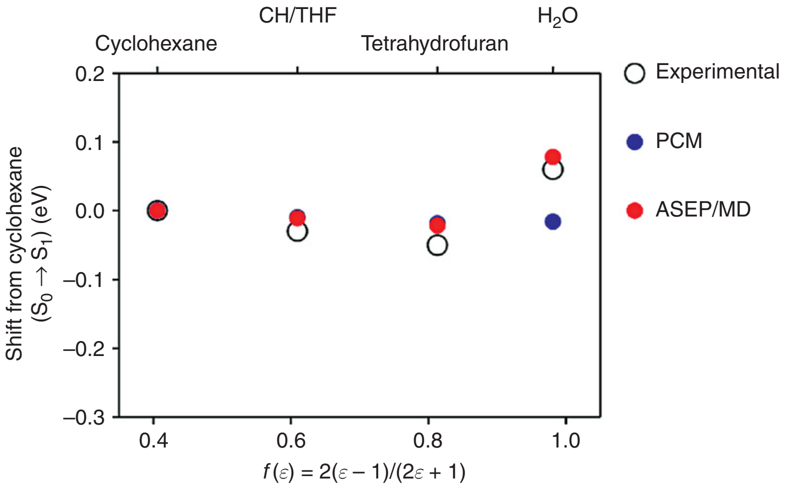

Figure 3.13 Relative absorption energies of DMA in solvents of different polarity, with cyclohexane as the reference.

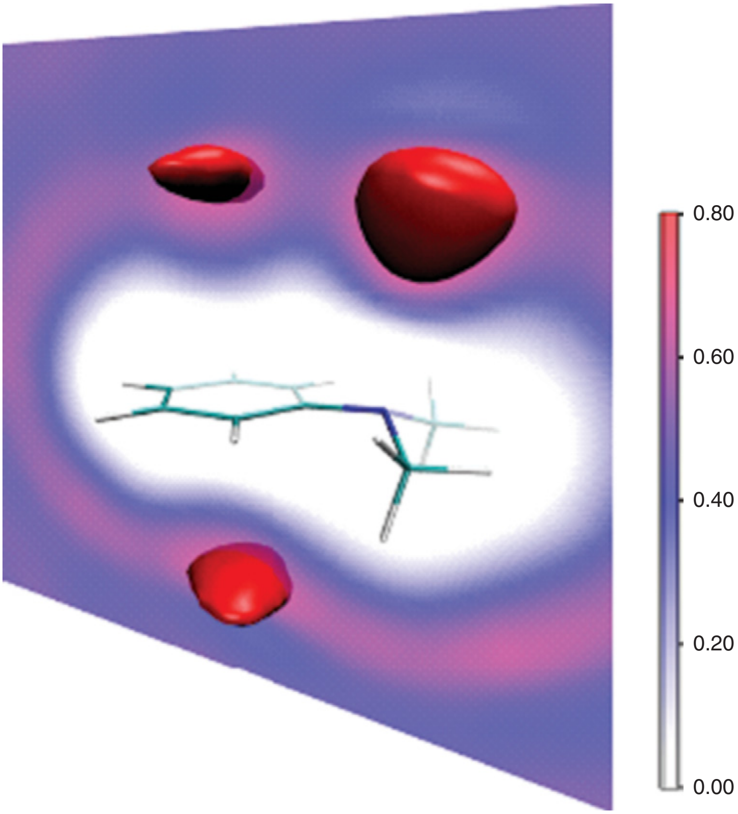

Figure 3.14 Occupancy map of oxygen atoms around the ground state of DMA. Solid isosurface at a density value of 0.64.

water, the wagging angle between the dimethylamino and phenyl moieties increases, see Table 3.7, something that does not occur with the other solvents. Almost half of the solvent shift comes from this distortion of the geometry, the rest is explained by the breaking of the HBs mentioned before.

Table 3.7 Twisting angle (in degrees) for optimized geometries of DMA in several solvents

	Angle
Gas	28.4
Cyclohexane	28.7
CH/THF (0.5)	28.5
Tetrahydrofuran	28.5
Water	34.0

Another interesting case is the study of the solvent effects on the electron transitions in retinal [68,69]. Retinal is a very interesting molecule because it is the chromophore of rhodopsin, the visual pigment in vertebrates. The (π–π^*) electron transitions to the first two excited states of 11-*cis*-retinal protonated Schiff base (PSB) and several simplified models that have been profusely used in the bibliography (see Figure 3.15) were calculated in vacuo and in methanol solutions. The ASEP/MD method was employed for the in solution calculations. Full ground-state geometry optimizations were performed in both conditions, allowing the total relaxation of all the degrees of freedom at MP2 and/or CASSCF level of calculation with the split-valence 6-31G* basis set. Nevertheless, the transition energies were always obtained at CASSCF/6-31G* level of calculation using in each case the complete active π space (10e, 10o), or (12e, 12o) depending on the model used. To improve the energy results, the dynamic electron correlation energy was included with second-order perturbation theory (CASPT2).

In vacuo, the first transition gives rise to a very strong band, while the transition to the second state is almost forbidden. In the ground and second excited states, the positive charge is localized close to the nitrogen atom (covalent states); however, in the first excited state the charge is spread out on the entire molecule (ionic state), see Figure 3.16. Consequently, the second excited state will solvate better than the first and one expects that the energy gap between the two states decreases. In fact, we find that in methanol solution, both states become almost degenerate. Furthermore, the oscillator strength of the transition to the second state increases. This behavior agrees with the experimental spectra [70–72], where, in gas-phase conditions two bands are found, one weak and the other strong but only a single very broad band appears in methanol solution.

Table 3.8 collects vertical transition energies in solution and the corresponding solvent shifts obtained for different models of retinal. At first sight, the interaction with the solvent seems to produce the inversion in the relative position of the first two excited states, the covalent state becoming lower in energy with respect to the ionic one. The nature of the different states was corroborated by the dominant configuration participating in each state, that is, doubly excited for the covalent and a highest occupied molecular orbital (HOMO)–lowest unoccupied molecular orbital (LUMO) transition for the ionic. Oscillator strengths were also calculated, being the transition to the upper excited state the optically allowed transition (f value close to 1). The energy difference between the covalent and ionic states varies between 0.7 eV and 0.3 eV at CASSCF//MP2 level of calculation. The scene changes substantially when dynamic correlation is taken into account. Under these conditions, both states become practically degenerate, and we find an energy gap between them of about 0.1 eV. The proximity between these electron transitions gives rise to the fact that, contrary to the in vacuo conditions, the in solution theoretical absorption spectrum shows

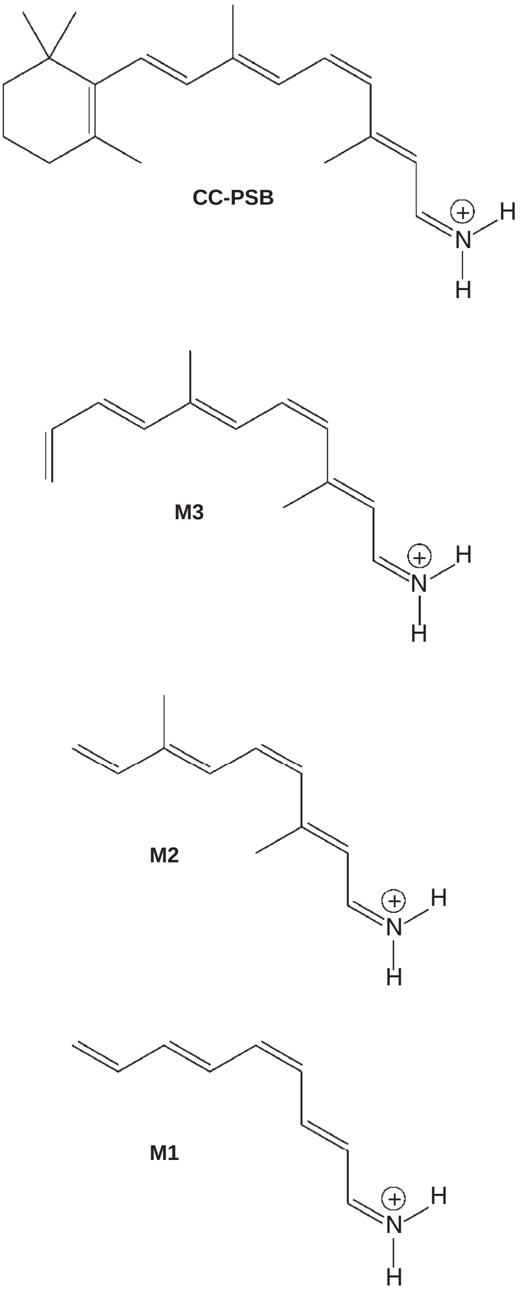

Figure 3.15 Structures of the 11-*cis*-retinal protonated Schiff Base (CC-PSB), and their models used in the study.

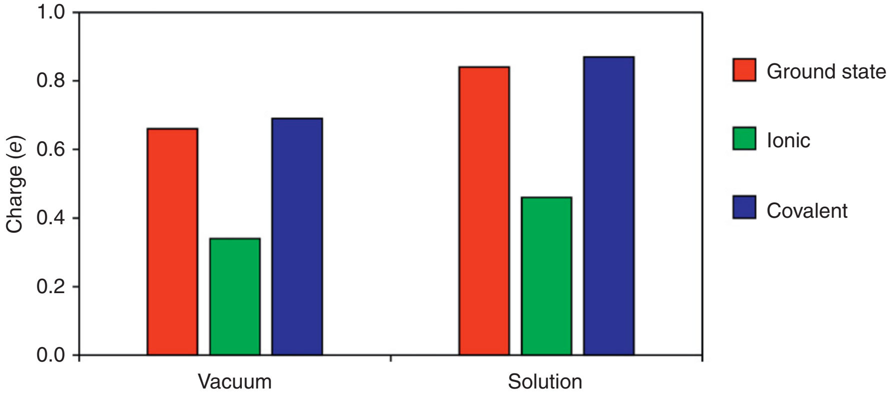

Figure 3.16 Localization of the molecular charge on the iminium half of the retinal molecule (M1 model) in vacuo and in solution, for the three lower electronic states.

Table 3.8 Calculated vertical transition energies (eV), oscillator strengths, and solvent shifts values (eV) for the M1, M2, M3, and CC-PSB models

	S_0→Ionic			S_0→Covalent	
	Vacuo	Solution	δ	Vacuo	Solution
M1					
CASSCF/CASSCF	3.55	5.22	1.67	4.61	4.62
CASPT2/CASSCF	2.56	3.82	1.26	3.58	3.78
CASPT2/MP2	2.40	3.51	1.11	3.16	3.61
Oscillator strength	1.15	1.00		0.09	0.01
M2					
CASSCF/CASSCF	3.34	4.93	1.59	4.34	4.44
CASPT2/CASSCF	2.56	3.68	1.12	3.64	3.45
Oscillator strength	0.97	0.87		0.21	0.23
M3					
CASSCF/MP2	3.03	4.08	1.05	4.05	3.78
CASPT2/MP2	2.28	2.99	0.71	3.27	2.88
Oscillator strength	0.95	0.91		0.22	0.21
CC-PSB					
CASSCF/MP2	2.54	4.19	1.65	3.42	3.87
CASPT2/MP2	1.93	3.00	1.07	2.77	2.95
Oscillator strength	1.20	0.93		0.06	0.15
Experimental	2.03	2.79		3.18	

two poorly resolved bands. Our results confirm the recent experimental study published by Nielsen et al. [72]. In this study, the authors provide the in vacuo and the in solution electronic absorption spectra of the all-*trans* *n*-butyl PSB in methanol solution and also the in vacuo spectrum for the 11-*cis* dimethyl Schiff base. The in solution registered spectra for the two isomers are said to be identical. The experimental gas-phase spectrum shows a band at 390 nm corresponding to the S_2 absorption band maximum and another at 610 nm corresponding to the transition to the S_1 state. When the spectrum is recorded in methanol solution, the S_1 band maximum is blue-shifted by more than 150 nm and what is more important, no resolved S_1 and S_2 bands were found. The spectrum shows only a broad band centered at around 450 nm (2.76 eV). Independently of the model used in the calculations, our theoretical results completely reproduce the appearance of the experimental spectra.

Another interesting quantity to evaluate is the predicted solvent shift. These values are also collected in Table 3.8 and were calculated as the shift suffered by the ionic band as a consequence of the solvent effect. Surprisingly, CASPT2 calculations supply practically the same solvent shift (around 1.1 eV) value independently of the system complexity, except for the M3 model where the value is slightly lower. In all cases the calculated value is larger than the experimental one, estimated in 0.72 eV (2.76 eV, the electronic transition energy in methanol solution, minus 2.03 eV, in vacuo). The fact that the complete chromophore (CC)-PSB system shows the same solvent shift overestimation as most simplified models (M1 or M2) is due to a structural characteristic of the system shared by all of them. Most of the solvation energy comes from the interaction between the iminium group and the methanol molecules. In all the systems here considered, the N atom is bonded to two hydrogen atoms; however, the experiments have been performed with molecules where the N is bonded to methyl or bulkier groups. In order to get more details, new calculations were performed. In particular a new model (M4) was built replacing the hydrogen atoms linked to the N atom in M1 with two methyl groups. Both CASSCF and MP2 geometry optimizations were performed in vacuo and in methanol solution keeping the same conditions as in previous calculations. The solvent shift obtained for this model was 0.84 eV and 0.64 eV at CASPT2//CASSCF and CASPT2//MP2 level of calculation, respectively. Comparison with the equivalent results for M1 shows that the methyl groups' incorporation decreases the solvent shift value in around 0.45 eV. If this decrease is directly applied to the CC-PSB solvent shift, the final value becomes 0.65 eV, in very good agreement with experimental data (0.72 eV).

5.3. Nonradiative de-excitations in retinal

Even if the very first step of the visual process can be considered the light-induced promotion of one electron from a π-type orbital to a π^* one in the chromophore of the protein rhodopsin, its biological activity starts with the *cis–trans* isomerization that this chromophore suffers in the excited state. This conformational inversion causes in turn a conformational change in the protein and starts the rest of the reactions taking place in the visual process. Inside the protein pocket, this isomerization step is very fast, taking only 200 fs, and no significant fluorescence is usually observed. These properties are characteristic of nonradiative processes involving crossings between potential energy surfaces. These crossings can take place through CIs or singlet–triplet crossings (STC) depending on the identical of different spin symmetry of the involved states, respectively.

In the last decade, there have been quite exhaustive studies on the isomerization of the rhodopsin chromophore through a CI between its covalent ground state and the ionic first excited state in vacuo conditions. Different models for the chromophore representation and more and more accurate methods have been used in these studies. It has been only in the last years when the development of the computational resources has permitted the study of this process in a more realistic way, that is, considering the possible effect of the environment. In our case, we have used an extended version of the ASEP/MD method that allows the location of CIs and STCs of systems in solution. The algorithm implemented in the method is due to Bearpark et al. [73] and simultaneously minimizes the in solution energy difference between the two intersecting states and the energy of the crossing seam between the two potential energy surfaces. See Ref. [74] for more details.

We started our study with the location of the in vacuo minimum energy conical intersection (MECI) structure for the simplest model used in the previous study devoted to the solvent effect on the UV absorption spectrum. The main structural characteristic of this CI is a twist of ~90° showed by the central original double bond. In order to permit this change in the dihedral angle, it is necessary the inversion in the nature of the single and double bonds with respect to the FC structure, which is clearly observed in Table 3.9. Next, our objective was the study of the solvent influence (methanol, in particular) on the structure and position of the MECI. In this point, two strategies were followed depending on whether the solvent is considered as a frozen solvent or it is allowed to equilibrate with the solute electronic distribution. The first corresponds to an infinitely slow solvent response and the second to an infinitely fast solvent reorganization.

In the equilibrium case, it is possible to locate the MECI in solution, and from a structural viewpoint, the solvent modifies bond distances and slightly the twist of the dihedral angle. What is worth noting is that the solvent suffers an important restructuring around the solute molecule to respond to the torsion of almost 90° of its central dihedral angle from the FC structure. Figure 3.17 displays the occupancy maps of methanol oxygen atoms around the FC and MECI structures. As it can be seen, at the FC point the solvent is mainly concentrated around the iminium end, where the

Table 3.9 Optimized geometries of a retinal model at the Franck–Condon point and at the conical intersection. Bond lengths in ångström, angles in degrees

	FC		MECI S_0/S_1	
	Vacuo	Methanol	Vacuo	Methanol
C_1C_2	1.35	1.34	1.36	1.36
C_2C_3	1.46	1.47	1.42	1.40
C_3C_4	1.35	1.36	1.41	1.41
C_4C_5	1.45	1.45	1.38	1.36
C_5C_6	1.36	1.36	1.47	1.46
C_6C_7	1.45	1.46	1.37	1.41
C_7C_8	1.35	1.36	1.42	1.39
C_8C_9	1.44	1.43	1.39	1.44
$C9{=}N$	1.28	1.28	1.32	1.30
Dihedral	Planar	Planar	91.0	85.9

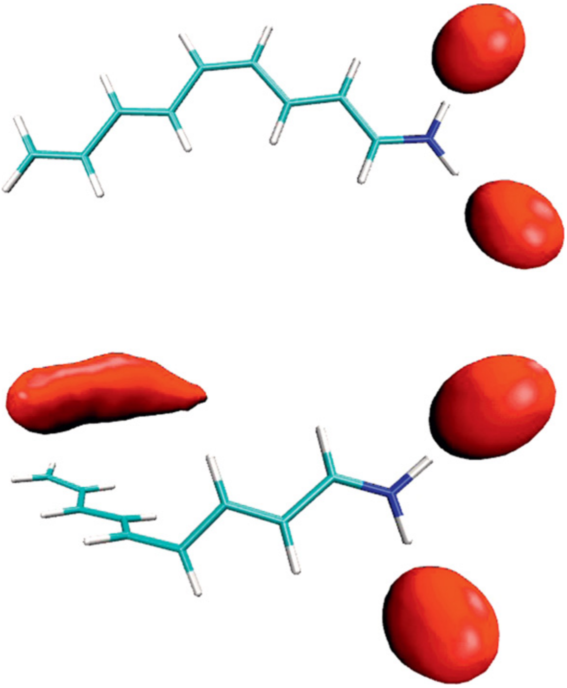

Figure 3.17 Maximum occupancy regions of oxygen atoms around the ground state (top) and the MECI (bottom) of the M1 retinal model.

molecular charge is predominantly located, as at the FC the solvent is in equilibrium with the ground state covalent electronic distribution. At the MECI, one finds solvent molecules around the iminium end but also around the carbon skeleton along which at the excited state the charge is spread out. It can be concluded that in the equilibrium situation solvent molecules stabilize the delocalization of the charge in the excited state and the two states involved in the CI can cross. In frozen solvent conditions, the location of the MECI has been impossible. If the solvation shells are considered fixed and in equilibrium with the ground-state electronic distribution, when the central dihedral angle rotates, part of the solute molecule will overlap with the solvent. In addition, if the solvent can in some way equilibrate with the solute, the great restructuring that it should suffer must take several picoseconds and the isomerization in solution should be slower than in vacuo or inside the protein pocket. This fact agrees with somewhat more persistent fluorescence found for the rhodopsin chromophore in methanol solution [75].

6. SUMMARY

The theoretical study of solvent effects is, in general, very demanding because it requires extensive sampling of the configurational space of the solute–solvent system. The MFA provides a practical and effective approach that opens the possibility of studying chemical equilibria, spectroscopic transitions, kinetic problems, and so on, using computational levels similar to those used for gas-phase systems. The study of different systems and processes in solution has permitted us to conclude that the MFA works very well, even in those cases where the solvent is represented in a simplified way, a dielectric for instance. Obviously, in this case, we must restrict ourselves to systems where specific solute–solvent interactions are not present. If these interactions are present, it is compulsory the use of more sophisticated solvent descriptions that allow accounting for the effect of bulk and specific interactions. ASEP/MD is a method that permits to combine a high-level quantum mechanical description of the solute with a detailed, microscopic, description of the solvent.

The following are the main characteristics of ASEP/MD: (1) A reduced number of quantum calculations that permits to increase the description level of the solute molecule which, in fact, can be described at the same level as in isolated conditions. (2) Since the solvent is described through MM force fields, there exists a great flexibility to include both bulk and specific interactions into the calculations. (3) At the end of the procedure, the solute wave function and the solvent structure become mutually equilibrated, that is, the solute is polarized by the solvent and the solvent structure is in equilibrium with the polarized solute charge distribution. (4) Finally, the method permits to find in an efficient way the geometry of critical points. With critical points we refer to minima, transition states, CIs, and so on.

In the last section of this chapter, we have presented an overview of applications of the ASEP/MD method to different systems and phenomena. The approximations and methodology used have been validated through comparisons with other studies and accepted methods and, in general, it has been shown that ASEP/MD is a powerful and efficient method that does not introduce significant errors but, in contrast, makes it possible to consistently introduce the solvent influence on high-level quantum calculations. Conformational equilibria, chemical reactivity, and electron transitions are just three areas where solvent effects play an important role and where ASEP/MD has proved to be a valuable tool.

REFERENCES

[1] C. Reichardt, Org. Process Res. Dev. 11 (2007) 105.
[2] S. Canuto (Ed.), Solvation Effects on Molecules and Biomolecules. Computational Methods and Applications, Springer, Berlin, 2008.
[3] M. Born, Z. Phys. 1 (1920) 45.
[4] G.J. Kirkwood, J. Chem. Phys. 2 (1934) 351.
[5] L. Onsager, J. Am. Chem. Soc. 58 (1936) 1486.
[6] C. Reichardt, Solvent and Solvent effects in Organic Chemistry, third ed., Wiley-VHC, Weinheim, 2003.
[7] O. Tapia, in: Z.B. Maksic (Ed.), Theoretical Treatment of Large Molecules and Their Interactions, vol. 4, Springer-Verlag, Berlin, 1991, p. 435.
[8] J.G. Angyán, J. Math. Chem. 10 (1992) 93.
[9] R. Car, M. Parrinello, Phys. Rev. Lett. 55 (1985) 2471.
[10] A. Warshel, M. Levitt, J. Mol. Biol. 103 (1976) 227.
[11] S. Humbel, S. Sieber, K. Morokuma, J. Chem. Phys. 105 (1996) 1959.
[12] J. Tomasi, M. Persico, Chem. Rev. 94 (1994) 2027.
[13] J.L. Rivail, D. Rinaldi, in: J. Leszczynski (Ed.), Computational Chemistry: Review of Current Trends, World Scientific Publishing, Singapore, 1995.
[14] C.J. Cramer, G.D. Truhlar, in: K.B. Lipkowitz, D.B. Boyd (Eds.), Reviews in Computational Chemistry, vol. VI, VCH Publishers, New York, 1995, p. 1.
[15] S. Ten-no, F. Hirata, S. Kato, Chem. Phys. Lett. 214 (1993) 391.
[16] H. Sato, F. Hirata, S. Kato, J. Chem. Phys. 105 (1996) 1546.
[17] F. Hirata (Ed.), Molecular Theory of Solvation (Understanding Chemical Reactivity), Springer, Berlin, 2003.
[18] M.L. Sánchez, M.A. Aguilar, F.J. Olivares del Valle, J. Comput. Chem. 18 (1997) 313.
[19] M.L. Sánchez, M.E. Martín, M.A. Aguilar, F.J. Olivares del Valle, J. Comput. Chem. 21 (2000) 705.
[20] M.L. Sánchez, M.E. Martín, I. Fdez. Galván, F.J. Olivares del Valle, M.A. Aguilar, J. Phys. Chem. B 106 (2002) 4813.
[21] I. Fdez. Galván, M.L. Sánchez, M.E. Martín, F.J. Olivares del Valle, M.A. Aguilar, Comput. Phys. Commun. 155 (2003) 244.
[22] K.V. Mikkelsen, H. Agren, H.J.A. Jensen, T. Helgaker, J. Chem. Phys. 89 (1988) 3086.
[23] K.V. Mikkelsen, A. Cesar, H. Agren, A.J.H. Jensen, J. Chem. Phys. 103 (1995) 9010.
[24] J. Tomasi, B. Mennuci, R. Cammi, Chem. Rev. 105 (2005) 2999.

[25] A. Klamt, G. Shüürmann, J. Chem. Soc., Perkin Trans. 2 (1993) 799.
[26] T.N. Truong, V.E. Stefanovich, Chem. Phys. Lett. 240 (1995) 253.
[27] A. Warshel, Computer Modelling of Chemical Reactions in Enzymes and Solutions, Wiley, New York, 1991.
[28] H. Hu, Z. Lu, J. Yang, J. Chem. Theory Comput. 3 (2007) 390.
[29] H. Hu, Z. Lu, J.M. Parks, S.K. Burger, J. Yang, J. Chem. Phys. 128 (2008) 034105.
[30] H.C. Georg, K. Coutinho, S. Canuto, Chem. Phys. Lett. 429 (2006) 119.
[31] B. Linder, Adv. Chem. Phys. 12 (1967) 225.
[32] G. Karlström, B. Halle, J. Chem. Phys. 99 (1993) 8056.
[33] N. Ghoneim, P. Suppan, Spectrochim Acta, 51 (1995) 1043.
[34] T. Yamamoto, J. Chem. Phys. 129 (2008) 244104.
[35] K. Coutinho, R. Rivelino, H.C. Georg, S. Canuto, in: S. Canuto (Ed.), Solvation Effects on Molecules and Biomolecules. Computational Methods and Applications, Springer, Berlin, 2008, p. 159.
[36] K. Coutinho, H.C. Georg, T.L. Fonseca, V. Ludwig, S. Canuto, Chem. Phys. Lett. 437 (2007) 148.
[37] N. Okuyama-Yoshida, M. Nagaoka, T. Yamabe, Int. J. Quantum Chem. 70 (1998) 95.
[38] N. Okuyama-Yoshida, K. Kataoka, M. Nagaoka, T. Yamabe, J. Chem. Phys. 113 (2000) 3519.
[39] H. Hirao, Y. Nagae, M. Nagaoka, Chem. Phys. Lett. 348 (2001) 350.
[40] Y. Zhang, H. Liu, W. Yang, J. Chem. Phys. 112 (2000) 3483.
[41] I. Fdez. Galván, M.L. Sánchez, M.E. Martín, F.J. Olivares del Valle, M.A. Aguilar, J. Chem. Phys. 118 (2003) 255.
[42] I. Fdez. Galván, M.E. Martín, M.A. Aguilar, J. Comput. Chem. 25 (2004) 1227.
[43] L.W. Jorgensen, Acc. Chem. Res. 22 (1989) 184.
[44] W.R. Zwanzig, J. Chem. Phys. 22 (1954) 1420.
[45] I. Fdez. Galván, M.E. Martín, M.A. Aguilar, J. Chem. Phys. 124 (2006) 214504.
[46] E. Rosta, M. Haranczyk, Z.T. Chu, A. Warshel, J. Phys. Chem. B 112 (2008) 5680.
[47] I. Fdez. Galván, F.J. Olivares del Valle, M.E. Martín, M.A. Aguilar, Theor. Chem. Acc. 111 (2004) 96.
[48] D.A. Becke, J. Chem. Phys. 98 (1993) 5648.
[49] R. Krishnan, J.S. Binkley, R. Seeger, A.J. Pople, J. Chem. Phys. 72 (1980) 650.
[50] J.M. Frisch, G.W. Trucks, H.B. Schlegel, G.E. Scuseria, M.A. Robb, J.R. Cheeseman, et al., Gaussian 98, Gaussian, Pittsburgh, PA, 1998.
[51] C. Höög, G. Widmalm, J. Phys. Chem. B 105 (2001) 6375.
[52] J.C. Corchado, M.L. Sánchez, M.A. Aguilar, J. Am. Chem. Soc. 126 (2004) 7311.
[53] J.S. Angyal, Aust. J. Chem. 21 (1968) 2737.
[54] J.S. Angyal, Angew. Chem. 81 (1969) 172.
[55] C. Soriano-Correa, F.J. Olivares del Valle, A. Muñoz-Losa, I. Fdez. Galván, M.E. Martín, M.A. Aguilar (2010) to be published.
[56] C. Soriano-Correa, J.F. Sánchez-Ruiz, G. Rico-Rosillo, J.A. Giménez-Scherer, J. Velázquez-Rodríguez, R. Kretschmer-Schmid, J. Mol. Struct. (Theochem) 769 (2006) 91.
[57] I. Fdez. Galván, M.A. Aguilar, M.F. Ruiz-López, J. Phys. Chem. B 109 (2005) 23024.
[58] P.J. Perdew, Phys. Rev. B 33 (1986) 8822.
[59] D.A. Becke, Phys. Rev. A 38 (1988) 3098.
[60] I. Tuñón, M.T.C. Martins-Costa, C. Millot, M.F. Ruiz-López, J. Mol. Mod. 1 (1995) 196.
[61] I. Tuñón, M.T.C. Martins-Costa, C. Millot, M.F. Ruiz-López, L.J. Rivail, J. Comput. Chem. 17 (1996) 19.
[62] I. Tuñón, M.T.C. Martins-Costa, C. Millot, M.F. Ruiz-López, J. Chem. Phys. 106 (1997) 3633.
[63] M.E. Martín, M.L. Sánchez, F.J. Olivares del Valle, M.A. Aguilar, J. Chem. Phys. 113 (2000) 6308.
[64] M.E. Martín, M.L. Sánchez, M.A. Aguilar, F.J. Olivares del Valle, J. Mol. Struct. (Theochem) 537 (2001) 213.
[65] M.E. Martín, A. Muñoz-Losa, I. Fdez. Galván, M.A. Aguilar, J. Chem. Phys. 121 (2004) 3710.

[66] I. Fdez. Galván, M.E. Martín, A. Muñoz-Losa, M.A. Aguilar, J. Chem. Theory Comput. 5 (2009) 341.
[67] G. Karlström, R. Lindh, P.-Å. Malmqvist, B.O. Roos, U. Ryde, V. Veryazov, et al., Comput. Mater. Sci. 28 (2003) 222.
[68] A. Muñoz-Losa, I. Fdez. Galván, E. Martín, M.A. Aguilar, J. Phys. Chem. B 110 (2006) 18064.
[69] A. Muñoz-Losa, I. Fdez. Galván, M.A. Aguilar, E. Martín, J. Phys. Chem. B 112 (2008) 8815.
[70] K.A. Freedman, S.R. Becker, J. Am. Chem. Soc. 108 (1986) 1245.
[71] L.H. Andersen, I.B. Nielsen, M.B. Kristensen, M.O.A. El Ghazaly, S. Haacke, M.B. Nielsen, Å.M. Petersen, J. Am. Chem. Soc. 127 (2005) 12347.
[72] I.B. Nielsen, L. Lammich, H.L. Andersen, Phys. Rev. Lett. 96 (2006) 018304.
[73] M.J. Bearpark, M.A. Robb, B.H. Schlegel, Chem. Phys. Lett. 223 (1994) 269.
[74] A. Muñoz-Losa, I. Fdez. Galván, M.L. Sánchez, E. Martín, M.A. Aguilar, J. Phys. Chem. B 112 (2008) 877.
[75] H. Kandori, Y. Katsuta, M. Ito, H. Sasabe, J. Am. Chem. Soc. 117 (1995) 2669.

CHAPTER 4

QM/MM Approaches to the Electronic Spectra of Hydrogen-Bonding Systems with Connection to Many-Body Decomposition Schemes

Ricardo A. Mata[a] and **B.J. Costa Cabral**[a]

Contents

[a] Grupo de Física-Matemática da Universidade de Lisboa, Avenue Professor Gama Pinto 2, 1649-003 Lisboa, Portugal

---

Advances in Quantum Chemistry, Vol. 59
ISSN: 0065-3276, DOI: 10.1016/S0065-3276(10)59004-X

© 2010 Elsevier Inc.
All rights reserved

1. INTRODUCTION

Important methodological developments for investigating the structure, thermodynamics, and electronic properties of many-body interacting systems in condensed phase have been accomplished in the last decades [1–4]. Several sophisticated approaches including first-principles molecular dynamics [2], combined quantum mechanics/molecular mechanics (QM/MM) [5–9], and sequential statistical mechanics/quantum mechanical (SM/QM) [10,11], became fundamental tools for studying condensed phase properties. On the other hand, it is of general acceptance that a deeper knowledge of the molecular mechanisms controlling the energetic and dynamics of complex chemical and biochemical processes in solution relies on the understanding of their electronic properties [12]. However, it is also recognized that this fundamental aspect is not very well understood. Specifically, although chemical reactions in solution are considered as dynamic processes assisted by the solvent [13,14] the relationship between the electronic properties of the solvent and its role for assisting chemical reactions remains unclear. The reasons that, at least partially, explain the theoretical difficulties for accurate predictions of electronic properties in condensed phases are well known and are basically related to the complex nature of many-body interactions in disordered media. Thus, although first-principles molecular dynamics based on density functional theory (DFT) represents a fundamental tool for investigating condensed phase properties, some limitations of DFT for predicting the structure and dynamics of liquids, particularly those of liquid water, have been extensively discussed in the literature [15–17]. It should be stressed, however, that many recent improvements of DFT, with specific implications on its adequacy for investigating hydrogen-bonding (HB) systems have been reported and are extremely promising [18,19]. Moreover, DFT-based first-principles simulations are of fundamental importance for studying bond forming and breaking in solution and has opened the way for relevant theoretical studies of chemical reactions in condensed phases [2]. Another classical route for describing complex processes in solution is combined QM/MM [9]. This method relies on the definition of a quantum system (QM) for which the dynamics is coupled to the dynamics of an environment (MM) usually treated by a simplified theoretical approach. Some methodological issues inherent to this approach, which introduces a QM/MM interface, are the correct representation of the interactions between the quantum system and the environment and the treatment of the dynamics for particles close to the QM/MM interface.

In close relationship with the QM/MM formulation is the sequential SM/QM methodology [10,11]. In this approach, a set of configurations generated by Monte Carlo (MC) or Molecular Dynamics (MD) is selected for a posteriori analysis of its electronic properties. The QM calculations are performed by defining a quantum system (QM) with a few molecules. The most common procedure in sequential QM/MM for describing the interactions between quantum system and the environment takes into account, essentially, Coulombic interactions. Therefore, a simple representation of the environment as an embedding background is usually adopted. On the other hand, there is no coupling between the dynamics and the a posteriori QM calculations. However, the definition of a quantum system with a significant number of molecules and the application of high-level ab initio methods for the accurate calculation of the electronic properties make this approach very convenient in many cases of interest.

Although the application of high-level ab initio procedures to systems with a large number of molecules is still not possible, some recent approaches based on energy-partitioning schemes have been proposed [20–24] and represent an attractive possibility for investigating the electronic properties of complex molecular systems in condensed phase [25]. In this chapter we present an overview of recent developments and applications of sequential SM/QM to the study of electronic spectra of hydrogen bond liquids and anionic species in solution with particular emphasis on the connections between QM/MM methodologies and some recently proposed many-body partitioning expansions [23].

2. THEORETICAL METHODS

2.1. Statistical mechanics sampling for many-body interacting systems in condensed phases

Monte Carlo and molecular dynamics simulations of liquids and solutions are standard techniques for the study of condensed phase properties [26,27]. Both techniques depend on the calculation of the energy for a many-body interacting system. This system can be defined by a Hamiltonian operator $\hat{H}$, a set of nuclear coordinates $[\mathbf{R}_\mathrm{A}, A=1,\ldots, a,\ldots, M]$, and a wavefunction $[\,|\Psi(\mathbf{r_i};\mathbf{R_A};\mathbf{X})>, i=1,N]$. N is the number of electrons and $[\mathbf{X}]$ represents an additional set of coupling variables. Let $\mathbf{P}=(P_1,\ldots, P_a,\ldots, P_\mathrm{M})$ and $\hat{\mathbf{p}}=(\hat{p}_1,\ldots,\hat{p}_i,\ldots,\hat{p}_N)$ the set of momenta corresponding, respectively, to the (classical) nuclear and electronic coordinates. The Hamiltonian of the system is

$$\hat{H}=\sum_{a=1}^{M}\frac{P_a{}^2}{2m_a}+\sum_{i=1}^{N}\frac{\hat{p}_i^2}{2m_i}+V(\mathbf{r_i};\mathbf{R_A};\mathbf{X}), \tag{1}$$

where $V(\mathbf{r_i};\mathbf{R_A};\mathbf{X})$ defines the interactions between the different degrees of freedom. The expectation value for the energy is given by

$$E(\mathbf{R_A};\mathbf{X})=\ \langle\Psi(\mathbf{r_i};\mathbf{R_A};\mathbf{X})|\hat{H}|\Psi(\mathbf{r_i};\mathbf{R_A};\mathbf{X})\rangle. \tag{2}$$

The Monte Carlo method generates a Markov chain over the configurational space that can be sampled according to an arbitrary distribution $\rho(\mathbf{R_A};\mathbf{X})$. Specifically, Metropolis Monte Carlo with Boltzmann sampling relies on the acceptance of a new configuration $[\mathbf{R}^*_\mathbf{A};\mathbf{X}]$ over the chain with a probability $\eta = \mathrm{Min}[1, \rho(\mathbf{R}^*_\mathbf{A};\mathbf{X})/\rho(\mathbf{R_A};\mathbf{X})]$, where

$$\frac{\rho(\mathbf{R}^*_\mathbf{A};\mathbf{X})}{\rho(\mathbf{R_A};\mathbf{X})} = \frac{\exp[-\beta E(\mathbf{R}^*_\mathbf{A};\mathbf{X})]}{\exp[-\beta E(\mathbf{R_A};\mathbf{X})]}, \tag{3}$$

$\beta = 1/k_\mathrm{B}T$, k_B is the Boltzmann's constant and T the temperature.

Phase space sampling through Born–Oppenheimer molecular dynamics [2,3] is carried out by the numerical integration of the equations of motion

$$\frac{\mathrm{d}R_a}{\mathrm{d}t} = \frac{\partial \hat{H}}{\partial P_a}, \tag{4}$$

$$\frac{\mathrm{d}P_a}{\mathrm{d}t} = -\nabla_{R_a} E(\mathbf{R_A};\mathbf{X}) = \mathbf{F}_a. \tag{5}$$

For wavefunctions that are eigenstates of the Hamiltonian operator $\hat{H}$, the forces can be calculated by the Hellman–Feynman theorem [28–30] and are given by

$$\mathbf{F}_a = -\langle \Psi(\mathbf{r_i};\mathbf{R_A};\mathbf{X})|\nabla_{R_a}\hat{H}|\Psi(\mathbf{r_i};\mathbf{R_A};\mathbf{X})\rangle. \tag{6}$$

Two main reasons make extremely difficult the general application of statistical sampling methods for a many-body interacting system through the ab initio calculation of the energy given by expression (2). Firstly, the computational cost of correlated post-Hartree–Fock (HF) methods scales at best as N^5 (e.g., MP2), where N is a measure of the system size. Although several recent developments have been reported in order to significantly reduce the scaling of ab initio methods with N, including density fitting or local approximation procedures, full ab initio calculations for large systems demand enormous computational costs, and are in many cases of interest, simply not affordable. Therefore, the most widely used methods for first principles statistical mechanics sampling in condensed phases relies on the application of Hartree–Fock [31] or DFT methods [32], which scales as $\sim N^4$ or better (down to linear scaling). However, it is well known that the presently available DFT methods are not adequate for dealing with dispersion interactions or for accurate predictions of conformational energetics. The second reason is related to the statistical convergence of the samplings that depends on the generation of a very large Markov chain or of a molecular dynamics trajectory during several picoseconds.

2.2. Electronic spectra in QM/MM

Alternative approaches allowing the application of accurate ab initio procedures for energy calculation and statistical mechanics sampling in condensed phases rely on QM/MM partitioning. The dynamics of the QM sub-system is in general coupled to the MM environment. However, in some cases, a QM/MM approach can be defined through the analysis of the configurations generated by Markovian or dynamic sampling, using HF or DFT energy calculations for a whole QM system, or even by adopting a simplified force-field representation between the interactions of a complete MM system. This alternative approach corresponds to a sequential methodology, where all QM calculations are carried out a posteriori and it is usually known as sequential SM/QM method. Actually, (SM/QM) can be seen as a particular case of QM/MM. However, in contrast with the classical QM/MM methodology, there is no coupling between the QM and the MM subsystems in the sampling procedure. The adequacy of a sequential methodology is strongly dependent on the reliability of sophisticated force-field representations for the interactions of many-body systems. Moreover, the MC or MD generation of a large number of configurations by using a force field allows for a careful convergence analysis of the electronic properties a posteriori calculated with high-level ab initio methods.

A fundamental aspect in the application of QM/MM procedures for investigating electronic properties concerns the dependence of the results on the size of the quantum system, the force-field representation of the MM environment, and the coupling protocol between the QM and the MM partitions. The following sections discuss all these aspects under the specific subject of electronic spectra. Some of these discussions will be later recovered in the applications featured in Section 3.

2.2.1. The QM/MM coupling schemes

From the various models available today for the QM/MM partitioning of a system, we will restrict our discussion to the additive scheme. In this approach, the QM and MM calculations are performed on (mostly) nonoverlapping sections of the system, with the interaction between the two regions added through coupling terms. In this work, we will be focusing on the QM/MM energy for a system composed of a QM solute M, embedded in a large number of MM solvent molecules $\{I\}$. There are no covalent bonds connecting the two regions. The additive QM/MM energy can be split down into three terms

$$E_{\mathrm{QM/MM}}[M] = E[M] = E_{\mathrm{QM}}(M) + E_{\mathrm{MM}}(\{I\}) + E_{\mathrm{int}}, \tag{7}$$

where the first term is the QM energy of the solute

$$E_{\mathrm{QM}}(M) = \langle \Psi(\mathbf{r_i}; \mathbf{R_A}; \mathbf{X}) | \hat{H} | \Psi(\mathbf{r_i}; \mathbf{R_A}; \mathbf{X}) \rangle. \tag{8}$$

The QM wavefunction Ψ depends on the solute electron coordinates $\mathbf{r_i}$, the solute nuclei coordinates $\mathbf{R_A}$, and additional parameters $\mathbf{X}$, which depend on the coupling method used. The second term in Eq. (7) represents the molecular mechanics energy of the solvent molecules and the last term gives the interaction energy between both regions. The interaction term is also often given in the form of an added Hamiltonian. However, we prefer referring to it as an extra energy contribution. This is more in line with the structure of a program, where Eq. (8) and the interaction contributions are computed at different steps. The notation $E[X]$ (using square brackets) will be used throughout this chapter to denote a QM/MM energy, with X being the region represented in the QM section. We will now concentrate our discussion in explicit forms for the coupling and its influence on the solute excitation energies.

Since we are splitting the system into two regions without covalent bonding, the coupling should strictly include nonbonded interactions. Although simplistic, one commonly considers two main effects: electrostatic and dispersion. The latter is most commonly computed by taking the atom positions of both regions, and computing an energy contribution with parameterized van der Waals (vdW) potentials, for both solute and solvent. Such an approach seems to be generally reasonable since these are short-range forces, and therefore there is no large error accumulation. The electrostatic effects, on the other hand, are of vital importance, and several different approaches have been used in the literature to compute them.

The most basic form of coupling in QM/MM methods is known as *mechanical coupling*. In the case at hand, the E_{int} term will only include electrostatic interaction terms given by a molecular mechanics parameterization of the solute, just as the vdW forces

$$E_{\mathrm{int}}(\mathrm{el}) = \sum_{A\alpha} \frac{q_A q_\alpha}{r_{A\alpha}}. \tag{9}$$

The A and α indices stand for nuclei in the QM and MM regions, respectively. The charges of each center are given by q and distances by r. Although such a form will account for steric effects, the MM system does not influence the solute wavefunction ($\mathbf{X} = 0$). When calculating a QM/MM vertical excitation energy, the coupling term will be the same for both ground and excited states. As a result, one simply obtains the gas value [the first term in Eq. (7) will be the only equation to change]. One could, however, change the charge of the QM atoms for the excited state. One possibility would be to compute these charges by a population analysis scheme applied to the densities of both states. This type of approach poses several problems, since there is no univocal method to translate an electron density to atom-centered point charges. The Mulliken scheme, for example, has several shortcomings [33,34]. We refer the reader to the discussion in the literature about this subject, which is out of the scope of this chapter. In short, mechanical coupling is of very limited interest in the study of electronic spectra in solution.

If one is interested in describing the excitation energy of a solute in a polar medium such as water, the polarization effect of the surrounding molecules should be taken into account. The next step is, therefore, to create a dependence of the QM wavefunction on the surrounding charges of the MM atoms. If we consider an all-atom molecular mechanics potential for the solvent, QM polarization can be included by using

$$E_{\text{int}}(\text{el}) = \langle \Psi(\mathbf{r_i}; \mathbf{R_A}; \mathbf{q}_\alpha) | \sum_{\alpha} \frac{q_\alpha}{r_{i\alpha}} | \Psi(\mathbf{r_i}; \mathbf{R_A}; \mathbf{q}_\alpha) \rangle + \sum_{A\alpha} \frac{Z_A q_\alpha}{r_{A\alpha}}, \tag{10}$$

where the first term is the MM charge–QM electron interaction and the second is the MM charge–QM nucleus interaction. In Eq. (10), the wavefunction bears a dependence on the MM point charges. This is commonly referred to as *electrostatic coupling*. The QM calculation on the solute is performed with additional Coulomb operators, and as a result, there is an interaction between the solute electrons and the electrostatic field of the environment. In this coupling, only the "pure" MM energy of the solvent is kept when changing the electronic state of the solute. This is by far the most popular coupling scheme in QM/MM applications to date. It is quite straightforward to use and to implement. In a QM code, one only needs to add the environment charges in the zeroth-order Hamiltonian, which are in practice the same as atomic centers without basis functions. The changes are equivalent for an HF or DFT implementation, and all post-HF code is kept unchanged (the only difference in the calculation is that the wavefunction is polarized, and there are no additional terms). The most commonly used QM codes to date have the possibility of adding a lattice of point charges and are therefore elegible to be used in QM/MM applications with electrostatic coupling.

The next step in improving the QM/MM coupling is to allow for a "back-polarization" of the solvent. This is commonly referred to as *polarization coupling* [35]. A change in the QM wavefunction could, for instance, induce a dipole on the MM atoms. This is, of course, only possible when the MM force field in use is itself polarizable. The extra energy terms can be considered as part of $E_{\text{int}}(\text{el})$ [36], or by defining an extra term, exclusively for polarization, such as in Ref. [37]. For clarity, we will introduce an extra $E_{\text{int}}(\text{pol})$ term, which gives the interaction energy of the electronic density with the induced dipoles.

The fact that the solvent electrostatic field is influenced by the QM wavefunction leads to several technical complications. Usually, two main schemes are available to include this "back-polarization" effect [36]. One possibility is to change the MM charge distribution, but without propagating the effect back to the QM region. This has the drawback of defining an inconsistent polarization. The second scheme mends the problem by solving self-consistently the QM wavefunction and the MM charge distribution. This can be done in several ways, either by taking effect between QM self-consistent field (SCF) cycles or by updating the MM field after each SCF run. Things become even more elaborate in the case of post-HF calculations, since one needs to extract the electric field generated by a correlated wavefunction. The polarization coupling can, therefore, lead to significantly added computational effort. This is one of the reasons why this coupling form has not found more widespread use. The other reason has already been mentioned above, the fact that the MM potential has to be polarizable. There is a rather limited number of force fields available for these types of calculations. Most applications of this coupling scheme have been found in hydration studies [38–46].

A short summary of the above discussed coupling schemes is presented in Table 4.1. The vdW contribution is not included since it has little weight in spectra calculation and also because the same formulation is used for all of the three approaches.

2.2.2. Choosing the QM system

The choice of the QM system is determining for the success of a QM/MM calculation. In the study of a solute electronic spectra, the obvious choice would be to take the solute molecule, and represent the remaining solvent environment with MM. Even if this setup is adequate for many cases, the underlying assumptions should be reviewed. For the specific case of electronic spectra, these can be summarized as follows:

- The density difference between the states under study is significant *only* in the strict vicinity of the QM region.
- The influence of the environment is fundamentally electrostatic and can be well approximated by the MM potential chosen.

The first item depends strongly on the type of excitation one is interested in. In Rydberg-type excitations the excited electron is promoted to a diffuse orbital, and the final state will therefore be much more delocalized than the one of reference. Choosing a small quantum system can lead to an

Table 4.1 Common-use QM/MM coupling methods

Coupling scheme	$E_{\text{int}}(\text{el})$	$E_{\text{int}}(\text{pol})$	$\mathbf{X}$
Mechanical	Charge–charge	0	0
Electrostatic	Density–charge	0	q_α
Polarization	Density–charge	density-induced dipole	$q_\alpha;\mu_\alpha(\Psi)$

unbalanced description (the reference state being more accurately described). Some studies, however, have shown that even more important than expanding the QM system in itself, the basis space should be flexible, and that a small system can reproduce rather well the excitation energies as long as the AO basis is carefully chosen [47]. Charge-transfer excitations, on the other hand, will necessarily require an expanded QM system, including the molecule to which the excited electron is transferred. This is a particularly hard task when dealing with molecules in solution, since there is no straightforward way of distinguishing a priori which solvent molecules will take part in the excitation. This is a topic discussed in further detail in Section 3.3.

The second item is a rather general problem of QM/MM studies. Even if the MM field is adequate to describe the average electrostatic influence of the environment, effects such as Pauli repulsion and electron correlation are left out. Fortunately, all of these effects are more short ranged than Coulombic interactions and, therefore, defining a large QM system where the regions of transferred density are far away from the QM/MM frontier should guarantee well-converged results. If this is not feasible, the states should be treated as much as possible in an equal footing to guarantee some error compensation. Among the most complicated cases we again find the Rydberg-type excitations since they can span large regions of space, significantly overlapping with the multipoles used to describe the MM environment.

2.2.3. Truncating the MM system

Although the cost of a single-point QM/MM calculation is not significantly affected by the size of the MM system, large MM regions still present serious problems. In order to obtain an accurate explicit solvent description, the sampling must consider all degrees of freedom in the total system. This conformational space search will scale at least linearly with the system size. This can become an obstacle, since more conformations have to be computed and/or the simulation time preceding the quantum chemical calculations will have to be increased. It is therefore necessary to make decisions based on the nature of the problem and to adjust the size of the environment around the chromophore of interest.

In this chapter we are concerned with electronic excitation (or ionization) phenomena and the influence of the environment will be of electrostatic nature. In the following, we restrict ourselves to the electrostatic coupling approach. However, we would like to note that on increasing the MM system size, the effect of the outer fringes will be similar in the electrostatic or in the polarization embedding case. The electric field generated by the QM system will decay with r^{-2} or faster, due to charge shielding, and the outer MM atoms will stop feeling its influence after a given distance. In fact, based on this observation, a recently developed polarized coupling scheme only accounts for polarization in the vicinity of the QM region [48,49].

It is a nontrivial task to converge the energy of a QM molecule embedded in the polarization field of an explicit solvent. One needs to resort to periodic boundary conditions [26], which are also available in the context of QM/MM [50]. This is due to the non-convergent behavior of the Coulombic interaction. However, one is rarely interested in the total energy, and rather in an energy difference, which only needs to be computed up to a given accuracy. It is therefore reasonable to truncate the embedding environment, as long as the effect on the energy difference is kept at a minimum. Let us consider an electronic excitation on a given solute molecule. We are interested in computing the QM/MM energy difference between the excited and the ground state of the solute. To better understand the effect of the environment, we extend the excitation energy expression on the basis of perturbation theory. The perturbation will be the MM environment, through the E_{int} term. In the case of electrostatic embedding, this corresponds to the effect of the MM point charges ($\mathbf{X} = q_\alpha$). The reference Hamiltonian is the gas-phase Hamiltonian of the solute ($\mathbf{X} = 0$). The wavefunctions for both ground and excited states are given by the expansion

$$\Psi^0 = \Phi^0_{(0)} + \Phi^0_{(1)} + \Phi^0_{(2)} + \cdots, \tag{11}$$

$$\Psi^* = \Phi^*_{(0)} + \Phi^*_{(1)} + \Phi^*_{(2)} + \cdots. \tag{12}$$

Excited states will be denoted with the "$*$" superscript, while for reference states the "0" will be used. The zeroth-order value for the excitation energy $\omega(0)$ will be given by the QM value in the gas phase

$$\omega_{(0)} = \left\langle \Phi^*_{(0)} | \hat{H} | \Phi^*_{(0)} \right\rangle - \left\langle \Phi^0_{(0)} | \hat{H} | \Phi^0_{(0)} \right\rangle. \tag{13}$$

The corrections to the QM expectation value due to the environment will be given by

$$\begin{aligned}
\omega_{(1)} &= \left\langle \Phi^*_{(0)} \Big| \sum_\alpha \frac{q_\alpha}{r_{i\alpha}} \Big| \Phi^*_{(0)} \right\rangle - \left\langle \Phi^0_{(0)} \Big| \sum_\alpha \frac{q_\alpha}{r_{i\alpha}} \Big| \Phi^0_{(0)} \right\rangle, \\
\omega_{(2)} &= \left\langle \Phi^*_{(0)} \Big| \sum_\alpha \frac{q_\alpha}{r_{i\alpha}} \Big| \Phi^*_{(1)} \right\rangle - \left\langle \Phi^0_{(0)} \Big| \sum_\alpha \frac{q_\alpha}{r_{i\alpha}} \Big| \Phi^0_{(1)} \right\rangle, \\
&\vdots
\end{aligned} \tag{14}$$

$$\omega_{(n)} = \left\langle \Phi^*_{(0)} \Big| \sum_\alpha \frac{q_\alpha}{r_{i\alpha}} \Big| \Phi^*_{(n-1)} \right\rangle - \left\langle \Phi^0_{(0)} \Big| \sum_\alpha \frac{q_\alpha}{r_{i\alpha}} \Big| \Phi^0_{(n-1)} \right\rangle. \tag{15}$$

The first-order correction is then the differential interaction of the QM wavefunctions with the perturbing electrostatic field. Higher-order terms [given by Eq. (15) for any general value of n] include corrections due to the relaxation of the wavefunction in the perturbing field.

The effect of adding MM atoms far away from the chromophore should be particularly dominated by $\omega_{(1)}$. Even in polar solvents, the solute wavefunction is only significantly affected by the first and second solvation shells. Therefore, the effect of solvent molecules beyond the first shells will be of a rather simple electrostatic nature. If we consider an electronic excitation within the solute, the only difference between $\Phi^{*}_{(0)}$ and $\Phi^{0}_{(0)}$ will be the QM charge distribution. The $\omega_{(1)}$ term can be approximated as a dipole interacting with the MM electrostatic field, which holds (at most) a r^{-2} distance dependence (but mostly r^{-3}, since the solvent is usually not charged). The number of necessary solvent molecules will then be drastically smaller than the ones needed to converge the total energy of each isolated system. This also explains why many microsolvation studies of electronic excitations tend to converge rather quickly to the bulk value [51,52]. One should note that the convergence pattern actually depends on the excitation under study. If the charge is significantly moved (raising a higher dipole), the number of MM atoms needed to obtain a converged electrostatic environment will have to be necessarily larger.

We now turn to the case of ionization. This is rather different from the previous example. Since the total charge of the QM system changes, the differential stabilization of excited and ground states is now closer to the case of a charge interacting with the surrounding environment. This is slow converging (although not as serious as the total energy) and the size of the MM system will have to be significantly larger. This is again observable in cluster studies, where the ionization potential is hardly attainable [52].

2.2.4. Beyond QM/MM: many-body expansions

A way to improve over the classical QM/MM energy expression is to write the total energy of the system as a many-body expansion. The original QM/MM expression presented in Eq. (7) with electrostatic coupling can be rewritten as

$$E_{\mathrm{QM/MM}} = \left\langle \Psi \middle| \hat{H} + \sum_{\alpha} \frac{q_\alpha}{r_i r_\alpha} \middle| \Psi \right\rangle + E_{\mathrm{MM}}(\text{solvent}) + E_{\mathrm{int}}(\text{vdW}), \tag{16}$$

where the electrostatic interaction term has been joined with the solute QM Hamiltonian, and the wavefunction dependence has been dropped for clarity.

Let us now look at the full system, including solvent molecules. One can expand the total energy by a many-body expansion of the form

$$E = \sum_{A} E(A) + \sum_{A>B} \Delta E(AB) + \sum_{A>B>C} \Delta E(ABC) + \cdots, \tag{17}$$

with

$$\begin{aligned}\Delta E(AB) &= E(AB) - E(A) - E(B)\\ \Delta E(ABC) &= E(ABC) - \Delta E(AB) - \Delta E(AC) - \Delta E(BC) - E(A) - E(B) - E(C)\\ &\vdots\end{aligned}$$

We have made no distinction between the species being computed. The energy terms stand for the energy of the given molecules A, B, and/or C in vacuo. The series can be expanded up to level N, where N stands for the number of molecules present in the system.

The problem with such an expansion, for the electronic energy of a system, is that the series is known to converge rather slowly. As an example, we have divided the total energy of an eight-water molecule cluster into the constituting many-body contributions. The results at the HF/cc-pVDZ level of theory are shown in Figure 4.1. It is seen that even with three-body terms, the energy is far from being converged. One should be critical of the error, since it is particularly sensible to the conformation under study. One would have to go even beyond four-body terms to reach chemical accuracy (1 kcal/mol). This has two sources. One is a basis set superposition effect (BSSE), which is actually desireable to leave out of the calculation. Higher-body terms of the expansion are known to be contaminated with BSSE

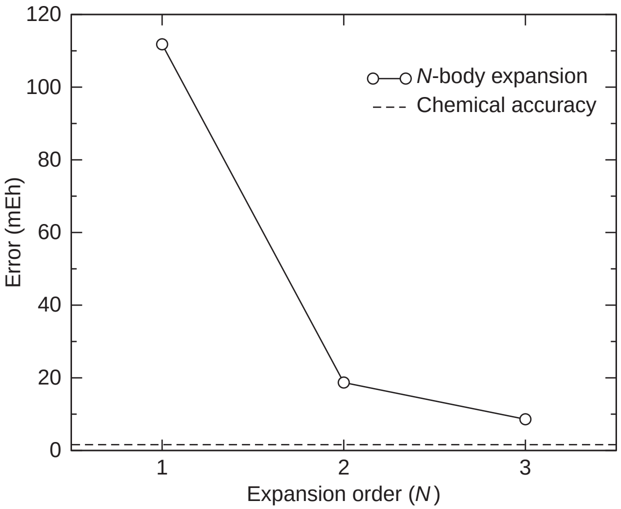

Figure 4.1 Error in the total energy (in milliHartree) of a N-body expansion of a water octamer. The results are given for HF/cc-pVDZ calculations.

[23,53]. However, it is also due to the underestimation of cooperative effects, in which case the expansion will be biased against aggregation. This will be the major effect in the case of water, the lack of higher-order polarization effects. The interaction energy of a water dimer embedded in a cluster is influenced by the hydrogen bonding network; neglecting this effect leads to a slow convergence. Since a many-body approach scales with $O(N^X)$, where X is the level at which the series is truncated, it becomes impractical to use high orders ($X > 2$) for larger systems.

A possible solution around the problem would be to compute each of the energy terms in Eq. (17) not as a molecule in vacuo, but to already include some approximate higher-order terms. On the basis of our previous discussion, one could perform a QM/MM calculation for each monomer, dimer, trimer, etc. defining the given molecules as the QM system and the remaining species as the MM environment. If we truncate the series up to two-body terms, and make a distinction between the solute M and the solvent molecules $\{I\}$, the total system energy expression is given by

$$\begin{aligned} E = E[M] + \sum_{I \neq M} E[I] + \sum_{I \neq M} (E[MI] - E[M] - E[I]) \\ + \sum_{\substack{I<J \\ I,J \neq M}} (E[IJ] - E[I] - E[J]), \end{aligned} \tag{18}$$

where we have purposefully separated terms involving the solute molecule from those involving exclusively solvent molecules. The use of square brackets highlights the fact that we are no longer working with monomers in the gas phase, but instead computing a QM/MM energy for each term. The first term of the expansion is defined with the use of Eqs. (7 and 10). Since each term already includes the energy of the other particles, as well as interaction contributions, there could be a double-counting problem. However, if one expands Eq. (18), all extra terms do cancel out [20,23]. This would also be the case if the expansion would be performed to a higher-order, but not for the one-body truncation. For ease of discussion, we will in the following text only consider the first term of the r.h.s. of Eq. (16). That is, we will no longer discuss the MM "pure" energy terms or the vdW interactions, since these are kept constant. We are interested in the vertical excitation energies, so the quantity to compute will be the energy difference between the system where the solute is found in the electronic ground state, and the one after excitation. Equation (18) can be generally used for any given electronic state of the solute. By computing the difference between the ground and a specific excited state, one arrives at the following result for the vertical excitation energy:

$$\Delta E = E[M^*] - E[M^0] + \sum_{I \neq M} \Delta E[I] + \sum_{I \neq M} (E[M^* I] - E[M^0 I] - E[M^*] + E[M^0] - \Delta E[I]) + \sum_{\substack{I<J \\ I,J \neq M}} (\Delta E[IJ] - \Delta E[I] - \Delta E[J]), \tag{19}$$

where

$$\Delta E[I] = E[I]_{(M^*)} - E[I]_{(M^0)}$$

represents the energy difference between the solvent molecule I in a point charge field where the solute is found in the excited state (M^*), or in the ground state (M^0). All other terms are self-explanatory.

A further change which one could operate would be to leave out all terms describing the polarization change in the solvent due to the excitation in the solute. This simplifies Eq. (19) to

$$\Delta E = (N-1)(E[M] - E[M^*]) + \sum_{I \neq M} (E[M^* I] - E[MI]). \tag{20}$$

The formulation above only requires a monomer calculation, and a dimer calculation for each solvent molecule present in the system. The one-body result is the QM/MM value with electrostatic embedding. The two-body terms will give further contributions, although it might not be quite clear at this time which. However, it should be noted that since the solute is always present in the QM region there is no need to define potential parameters for the solute molecule.

Let us return to the question of solvent polarization. As the solute wavefunction changes, it is expectable to observe a change in the energy of the solvent molecules. In fact, this is the motivation behind the polarization coupling which we presented in Section 2.2.1. If we expand the polarization effect also in a many-body formulation, we obtain

$$\Delta E(\{I\}) = \sum_{I \neq M} \Delta E[I] + \sum_{\substack{I<J \\ I,J \neq M}} (\Delta E[IJ] - \Delta E[I] - \Delta E[J]) + \dots, \tag{21}$$

which can be taken up to order N. One can see that the difference between Eqs. (20,19) is the two-body polarization energy. The one-body polarization energy, which is represented by the first sum, is already included through the $E[M^* I] - E[M^0 I]$ difference. In fact, it is not even obtained by computing point charges to approximate the density of the solute, the polarization effect is instead computed fully quantum-mechanically. This holds a definite advantage over a single QM/MM calculation with polarization coupling. Equation (20) has already been previously used for computing the solvatochromic shift of the n → π* excitation of formaldehyde [54]. It also holds relation to fragment-based approaches, such as the fragment molecular orbital (FMO) method [21]. The main difference is in the approximate treatment of the intermonomer terms. The equation can be seen as a particular case of the FMO expression.

2.3. QM methods for the calculation of electronic spectra

In any QM/MM or related application, the choice of high-level method is of utmost importance. In the limit, any of the above-discussed methodologies will obtain the same result as the QM method chosen and this will, therefore, establish the reference accuracy. Due to computational limitations, and the high-order scaling of some of these methods, a compromise must be found between cost and accuracy. As such, it is useful to have some acquaintance with the many approaches available today, and the new developments being made in QM theory. The following sections give a superficial overview of the methods which will be later referred to in Section 3, and is not intended to be a thorough review of the subject. More detailed information on the methods can be found in the cited works and references therein.

2.3.1. Wavefunction-based methods

In *ab initio* wavefunction theory, the reference is commonly defined as the Hartree–Fock solution, a normalized Slater determinant for the $N/2$ lowest energy orbitals of an N-electron system. These orbitals are built as a linear combination of M atomic orbitals, with optimized coefficients according to the variational principle. The most straightforward way to compute an excited state, relative to this configuration, is to build another Slater determinant, replacing one of the occupied orbitals by one of the remaining $M - N/2$ virtual orbitals

$$|\Phi_i^a\rangle = \hat{e}_i^a|\Phi^0\rangle = |\ldots\phi_{i-1}\phi_a\phi_{i+1}\cdots\rangle, \tag{22}$$

where the operator $\hat{e}_i^a$ is a spin-adapted excitation operator. Since the molecular orbital space is built as orthonormal, the determinant built in this way is a valid excited state, orthogonal to the reference HF wavefunction.

In order to find the lowest lying excited state, one needs to optimize the linear combination of all possible single excited determinants

$$|\Phi^*\rangle = \sum_{ia} C_{ia}|\Phi_i^a\rangle, \tag{23}$$

where C_{ia} are the optimization coefficients, under the constraint $\Sigma_{ia}C_{ia}^2 = 1$. These are also commonly referred to as CI coefficients. This is the procedure followed in configuration interaction singles (CIS). Since single excitations do not interact directly with the HF wavefunction, the CIS states $|\Phi^{*}\rangle$ are in equal footing with the HF reference, and excitation energies can be computed by simply calculating the energy difference. In order to include correlation effects, one needs to go up the CI series, and include in Eq. (23) higher-order excitations. However, the CI series is slow converging, and in many cases one would need to build a higher-order series (even beyond quadruple excitations) to achieve convergence.

The coupled cluster (CC) series, although not variational, is a valuable alternative to the CI formalism. The CC singles and doubles with perturbative triples [CCSD(T)] method has established itself as a gold standard for ground-state calculations. Time-dependent formalisms of CC have been proposed, and are currently the state-of-the-art approach to electronic excitations in small molecular systems. Contrary to CI, the CC formalism does not build a linear combination of excited configurations [such as the one in Eq. (23)]. An exponential operator is used, which by acting on the HF wavefunction gives the correlated CC ground state

$$|\Phi^{\mathrm{CC}}\rangle = \exp(\hat{T})|\Phi^{\mathrm{HF}}\rangle, \tag{24}$$

where the $\hat{T}$ operator holds the amplitudes and excitation operators up to a given order. If we consider the CC singles and doubles model (CCSD), it will be defined as

$$\hat{T} = \sum_{ia} t_i^a \, \hat{e}_i^a + \sum_{ijab} t_{ij}^{ab} \, \hat{e}_{ij}^{ab}, \tag{25}$$

with a new labeling for the coefficients (t), which in the CC theory are most commonly referred to as amplitudes. The advantage of using an exponential ansatz is that higher-order excitations are approximately included as products of lower operators. In the CCSD model, for example, quadruple excitations are also included as products of two double excitation terms. The eigenvalue equation

$$\exp(-\hat{T}) H \exp(\hat{T})|\Phi^{\mathrm{HF}}\rangle = E|\Phi^{\mathrm{HF}}\rangle \tag{26}$$

is valid, and projection from the left with the reference HF wavefunction yields the CC energy.

Moving from the static to the time-dependent case, there are two possible formulations, namely linear response (LR-CC) [55] or equation of motion coupled cluster (EOM-CC) [55–58]. Both approaches give identical excitation energies, the major difference being that the latter approach does not scale correctly for transition moments and polarizabilities. We now briefly review both extensions to CC theory.

In LR-CC, the linear response functions are derived for the given CC model, and the excitation energies are computed as poles for the latter functions. The main drawback of this approach is that noniterative perturbation corrections cannot be included. As an example, the poles derived from CCSD(T) will be the same as those from CCSD. Therefore, it can only be successfully applied to fully iterative CC approaches. Due to the steep increase in computational cost on moving from HF [$O(N^4)$] to CCSD [$O(N^6)$] and CCSDT [$O(N^8)$], intermediate models have gained some attention in the last few years. The second-order approximate CC singles and doubles model (CC2) is an approximation to the CCSD method proposed by Christiansen et al. [59] In this model, the doubles equations (obtained by projecting from the left Eq. (26) with the double excitation manifold) are approximated, but keeping the singles effect, which are of relevance to the description of orbital relaxation. A similar model (CC3) has been proposed as an approximation to CCSDT [60]. This allows to define a more complete CC series as

$$\mathrm{CC2} < \mathrm{CCSD} < \mathrm{CC3} < \mathrm{CCSDT} < \ldots$$

ordered according to the accuracy and computational cost. Both CC2 and CC3 have been extensively applied in the last few years to problems of electronic excitations in solution by Christiansen and coworkers [61–66]. These include calculations using a QM/MM polarized embedding scheme, whereby the CC equations are solved through a quasienergy Lagrangian approach. The interested reader should refer to Refs. [55] and [37,67], for the derivation of the response functions under the influence of a self-consistent polarized field.

In the EOM-CC theory, one proceeds in a similar fashion as in CI-type methods. In order to build the excited states, a linear expansion is used, where the CC ground state is contained

$$|\Phi^{\mathrm{EOM-CC}}\rangle = \sum_{\mu} C_\mu \hat{e}_\mu |\Phi^{\mathrm{CC}}\rangle = \exp(\hat{T}) \sum_{\mu} C_\mu \hat{e}_\mu |\Phi^{\mathrm{HF}}\rangle. \tag{27}$$

In the equation above, the orbital indices have been replaced by a general index μ, since these can refer to single or higher-order excitations. Compared to a CI expansion, the EOM-CC formulation has the advantage of including both a linear and an exponential expansion. Although the divide is not so clear, one can think of the C_μ coefficients as defining the states, and the CC amplitudes responsible for the dynamical correlation treatment of each. The drawback is that the amplitudes were optimized for the ground state, and these are not changed in the EOM-CC treatment (the only variational parameters are the C_μ). This would mean that the ground state is better described, but in fact the linear expansion compensates for this problem. The excitation energies under the EOM-CC formalism are computed as the energy difference between states. Orthogonality is imposed by means of a variational principle, and size-extensivity is kept (even though a linear expansion is used). The most commonly used method is EOM-CCSD, which works remarkably well for singly excited states, with errors around 0.2 eV (see Ref. [68] and references therein).

Both linear response and EOM-CC models hold significant promise in application to QM/MM problems, with new developments such as improved parallel algorithms bringing the limit of treatable quantum atoms to already over 30 atoms [69]. Other present developments include density-fitting approximations [70,71], which reduce the cost of calculation with increasing basis sets and lower the computational prefactor, as well as local approximations [72–74], with the LCC2 [75,76], and EOM-LCCSD [68] methods. Other approaches to reduce the computational cost may work by limiting the correlation calculation to a specific region of the QM system, just as in Ref. [77].

2.3.2. Time-dependent density functional theory

Kohn–Sham (KS) density functional theory has established itself as a standard quantum chemical method for the computation of ground-state properties. By replacing the high-dimensional wavefunction for the three-dimensional electronic density, significant savings can be achieved, while keeping with a reasonable description of both exchange and correlation effects. Every year, new developments on functional forms have been put forward, and DFT can nowadays rival with higher-level correlated wave-function methods in a wide variety of applications.

Owing to the Runge–Gross theorem [78], a time dependent formulation of DFT (TD-DFT) has also become available. Just as in the time independent case [79], a univocal relation between the external potential and the density (both time dependent) is established, although lacking a variational principle. We would like to mention the ongoing debate on the foundations of TD-DFT [80–84], but for practical purposes (and since this is not the subject of this chapter), the Runge–Gross theorem will be accepted as is. The interested reader should refer to the above cited works and references therein.

In the context of TD-DFT, it is possible to investigate electronic transitions by computing the linear response of the system to an external time-dependent perturbing potential $v_1(\mathbf{r},t)$ [85,86]. The total external potential $v_{\text{ext}}(\mathbf{r},t)$ can be written as

$$v_{\text{ext}}(\mathbf{r},t) = v_0(\mathbf{r}) + v_1(\mathbf{r},t), \tag{28}$$

where $v_0(\mathbf{r})$ represents the Coulomb potential between electrons and nuclei in the absence of the perturbation. If the perturbing potential $v_1(\mathbf{r},t)$ is small in comparison with $v_0(\mathbf{r})$, the time-dependent density of the perturbed system $\rho(\mathbf{r},t)$ can be expanded as

$$\rho(\mathbf{r},t) = \rho^{(0)}(\mathbf{r}) + \rho^{(1)}(\mathbf{r},t) + \cdots. \tag{29}$$

Therefore, the deviation of the time-dependent density from the unperturbed density can be written as

$$\rho(\mathbf{r},t)-\rho^{(0)}(\mathbf{r})\cong\rho^{(1)}(\mathbf{r},t)=\int\mathrm{d}t'\int\mathrm{d}\mathbf{r}'\chi(\mathbf{r},t,\mathbf{r}',t')v_1(\mathbf{r},t),\tag{30}$$

where $\chi(\mathbf{r},t,\mathbf{r}',t')$ is the linear density–density response function and can be expressed as a functional derivative

$$\chi(\mathbf{r},t,\mathbf{r}',t')=\left[\frac{\delta\rho[v_{\mathrm{ext}}](\mathbf{r},t)}{\delta\rho[v_{\mathrm{ext}}](\mathbf{r}',t')}\right]_{v_{\mathrm{ext}}[\rho_0]},\tag{31}$$

which is calculated at the time-independent external potential $v_0=v_{\mathrm{ext}}[\rho_0]$ for the unperturbed ground-state density ρ_0. On the other hand, the density–density response function for the KS reference system of non-interacting electrons can be written as

$$\chi_{\mathrm{KS}}(\mathbf{r},t,\mathbf{r}',t')=\left[\frac{\delta\rho[v_{\mathrm{KS}}](\mathbf{r},t)}{\delta\rho[v_{\mathrm{KS}}](\mathbf{r}',t')}\right]_{v_{\mathrm{KS}}[\rho_0]}.\tag{32}$$

The potential $v_{\mathrm{KS}}(\mathbf{r},t)$ of the KS system related to $v_{\mathrm{ext}}(\mathbf{r},t)$ is given by $v_{\mathrm{KS}}(\mathbf{r},t)=v_{\mathrm{ext}}(\mathbf{r},t)+v_{\mathrm{H}}(\mathbf{r},t)+v_{\mathrm{xc}}(\mathbf{r},t)$, where $v_{\mathrm{H}}(\mathbf{r},t)$ is the time-dependent Hartree potential and $v_{\mathrm{xc}}(\mathbf{r},t)$ is the time-dependent exchange–correlation (xc) potential. Introduction of a time-dependent xc kernel $f_{\mathrm{xc}}(\mathbf{r},t,\mathbf{r}',t')=v_{\mathrm{xc}}[\rho](\mathbf{r},t)/\delta\rho(\mathbf{r}',t')$ and application of functional chain rules and derivatives leads to the following fundamental equation relating density–density response functions of interacting and noninteracting systems:

$$\begin{aligned}\chi(\mathbf{r},t,\mathbf{r}',t')={}&\chi_{\mathrm{KS}}(\mathbf{r},t,\mathbf{r}',t')+\int\mathrm{d}\mathbf{x}\int\mathrm{d}\tau\int\mathrm{d}\mathbf{x}'\int\mathrm{d}\tau'\chi_{\mathrm{KS}}(\mathbf{r},t,\mathbf{x}',\tau)\\&\times\left[\frac{\delta(\tau-\tau')}{|\mathbf{x}-\mathbf{x}'}+f_{\mathrm{xc}}[\rho_0](\mathbf{x},\tau,\mathbf{x}',\tau')\right]\chi(\mathbf{x}',\tau',\mathbf{r}',t').\end{aligned}\tag{33}$$

Further elementary operations then lead to

$$\rho^{(1)}(\mathbf{r},t)=\int\mathrm{d}t'\int\mathrm{d}\mathbf{r}'\chi_{\mathrm{KS}}(\mathbf{r},t,\mathbf{r}',t')v_{1,\mathrm{KS}}(\mathbf{r}',t')\tag{34}$$

with

$$v_{1,\mathrm{KS}}(\mathbf{r},t)=v_1(\mathbf{r},t)+\int\mathrm{d}\mathbf{r}'\frac{\rho^{(1)}(\mathbf{r}',t)}{|\mathbf{r}-\mathbf{r}'}+\int\mathrm{d}\mathbf{r}'\int\mathrm{d}t'f_{\mathrm{xc}}[\rho_0](\mathbf{r},t,\mathbf{r}',t')\rho^{(1)}(\mathbf{r}',t').\tag{35}$$

By Fourier transformation with respect to time one arrives at the frequency-dependent expression

$$\rho^{(1)}(\mathbf{r},\omega)=\int\mathrm{d}\mathbf{r}'\chi_{\mathrm{KS}}(\mathbf{r},\mathbf{r}',\omega)\left[v_1(\mathbf{r}',\omega)+\int\mathrm{d}\mathbf{x}\left[\frac{1}{|\mathbf{r}'-\mathbf{x}|}+f_{\mathrm{xc}}[\rho_0](\mathbf{r}',\mathbf{x},\omega)\right]\rho^{(1)}(\mathbf{x},\omega)\right],\tag{36}$$

where $\chi_{\mathrm{KS}}(\mathbf{r},\mathbf{r}';\omega)$ is the density–density response function for a KS reference system of noninteracting electrons and can be calculated in terms of the unperturbed set $\{\phi_j(\mathbf{r})\}$ of KS orbitals as

$$\chi_{\mathrm{KS}}(\mathbf{r},\mathbf{r}';\omega) = \lim_{(\Gamma\to 0^+)}\sum_{jk}^{\infty}(n_k - n_j)\frac{\phi_j(\mathbf{r})\phi_j^*(\mathbf{r}')\phi_k(\mathbf{r}')\phi_k^*(\mathbf{r})}{\omega-(\epsilon_j-\epsilon_k)+i\Gamma} \tag{37}$$

and n_j is the occupation number of the jth ground-state KS orbital.

From Eq. (30 and 36) we obtain

$$\chi(\mathbf{r},\mathbf{r}';\omega) = \chi_{\mathrm{KS}}(\mathbf{r},\mathbf{r}';\omega) + \int \mathbf{dxdx}'\chi(\mathbf{r},\mathbf{x};\omega)\left[\frac{1}{|\mathbf{x}'-\mathbf{x}|}+f_{\mathrm{xc}}(\mathbf{x},\mathbf{x}',\omega)\right]\chi_{\mathrm{KS}}(\mathbf{x}',\mathbf{r}';\omega). \tag{38}$$

The density response function can be determined by a self-consistent solution of the previous equation [85,86]. One of the main difficulties lies in the exact definition of the XC kernel, which depends on a time-evolving density $\rho(\mathbf{r},t)$.

However, if one considers the density as slowly-varying in time, the kernel at time t can be defined as depending solely on the density at the same time, removing the need for any explicit treatment of time dependence in the kernel itself. This is known as the adiabatic local density approximation, and allows for the use of any “ground-state” XC functional for TD-DFT calculations. Although as promising as its static relatives, the TD-DFT method has its own particular issues which should be cautioned

- Most TD-DFT functionals to date fail to accurately describe nonlocal excitations, such as Rydberg and charge-transfer states [87].
- Since TD-DFT works as a correction to the orbital energies of the underlying ground-state calculation, the errors are carried from the latter to the final result.
- The adiabatic approximation does not allow for the computation of double excitations, and may also fail if any is found close to the single-excited state of interest.

The first fault noted above is linked to the local approximations used in building the XC functionals. It can also to some extent be related to the second item in the list. A nonlocal potential would have to be used, and a straightforward correction to the problem is yet to be presented. New functionals have significantly decreased the problem, such as CAM-B3LYP [88], where the r_{12}^{-1} operator is split into short- and long-range parts, allowing for a reparameterization and correction of the long-range behavior of the DFT potential. A general observation is that for hybrid functionals, increasing the amount of exchange reduces the error. A diagnostic tool has also been recently proposed [89].

Other problems pertaining to the ground-state description is the incorrect asymptotic behavior of the KS potential. The true dependence should be $1/r$, while DFT functionals have an exponential decay. This has a destabilizing effect on the orbital energies, in turn making ionization energies systematically too low. This error can be corrected through the use of optimized effective potential DFT [84].

The problem in describing double excitations is, for the problems at hand, the least serious, and is also shared by some wavefunction-based alternatives, as noted above. In the CC case, it is necessary to include up to triple excitations [90] to obtain reliable results for such states. In short, although several issues may be raised in the use of TD-DFT, careful validation and/or correct use of new functional forms may prevent most of these issues. The new functionals referred above are not a simple reappreciation of a set of parameters. They introduce new physics directly related to the shortcomings of the method. Important review works illustrating the importance of time-dependent density functional response theory for the calculation of excitation energies and polarizabilities have been published [84,91].

3. APPLICATIONS

3.1. Electronic properties of water

3.1.1. UV spectra of water clusters

Somewhat naturally, the first system under discussion is water, the most commonly occurring solvent in chemical applications. We start by looking into water clusters, building up to the liquid. The condensed phase is only discussed in the next section. By looking at clusters, we will have an opportunity to evaluate a many-body formalism, as well as to analyze the behavior of the spectra with increasing cluster sizes. This is a common strategy in the study of condensed phases, since clusters bridge the gas and liquid phases, helping to a better understanding of cooperative effects in solution [92].

We examine in this section the first electronic absorption band of water. Since under several electrostatic environments the energy difference between the first and the second excited state is known to be kept around 2 eV, a many-body expansion should be viable. By truncating the series at the one-body terms, one obtains the following expressions for ground and excited states of a specific water molecule M:

$$E^{1B}(M^*) = E[M^*] + \sum_{I \neq M}^{N-1} E[I]_{M^*} - C^*, \tag{39}$$

$$E^{1B}(M^0) = E[M^0] + \sum_{I \neq M}^{N-1} E[I]_{M^0} - C^0, \tag{40}$$

where subscripts have been added to remind the fact that the QM/MM energy of each I is computed in a specific environment, with fragment M in the excited [Eq. (39)] or ground state [Eq. (40)]. The C^* and C^0 terms correct for double counting of the interactions between each fragment. If the crude approximation $E[I]_{M^*} = E[I]_{M^0}$ is made, the excitation energies are simply the QM/MM electrostatically embedded values $\omega(M^0 \rightarrow M^*) = E[M^0] - E[M^*]$, since the correction terms also cancel out. This is the same expression used for the FMO1 excitation energies [21]. It neglects one-body polarization effects due to the excitation.

In Figure 4.2, three sets of diagrams are shown, depicting the spectra of four selected water tetramers. The top diagrams depict the results for the

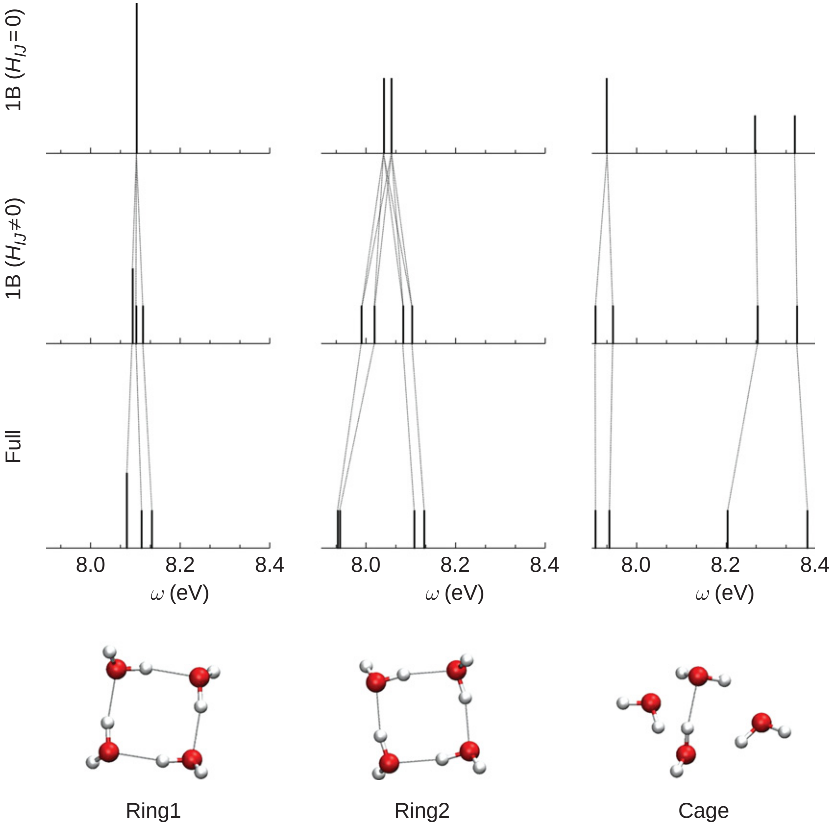

Figure 4.2 Computed spectra for selected water tetramers. The top graphs have been computed with a one-body approach without excitonic coupling, the second set includes coupling, and the last graphs are the full results (EOM-CCSD/aug-cc-pVTZ). The connection between the peaks are given by the eigenvectors of the coupling and/or EOM-CC coefficients.

computed excitation values, using the above formulae for the one-body excitation energy. The reference level of theory was EOM-CCSD/aug-cc-pVTZ. The full results are shown at the bottom. The peaks are all normalized to an arbitrary scale. Degenerate excited states are shown in the combined height of all respective peaks. In the case of ring1, for example, there is a single excitation energy value for the one-body treatment, corresponding to four degenerate states.

Comparison of the spectra shows marked differences between the two sets. Although the energy differences are rather small (below 0.1 eV), the one-body states are highly degenerate. This is understandable, taking into account the symmetry of the optimized clusters. In the case of ring1, for example, all four water molecules are identical. By applying a many-body scheme to the energy of each individual excited state, the same energy will be obtained, independently of the order up to which the expansion is built. The degeneracy can only be lifted by allowing the excited states to couple.

We have recently proposed a small modification to this many-body expansion in which excitonic coupling is explicitly included [25]. One builds an Hamiltonian for all excitonic states, where the diagonal elements H_{II} are given by Eq. (39), and the coupling is defined as the transition dipole moment interaction of the two excitations

$$H_{IJ} = \frac{1}{R_{IJ}^3}[\mathbf{d}_{01}^I.\mathbf{d}_{01}^J - 3(\mathbf{d}_{01}^I.\mathbf{R}_{IJ})(\mathbf{d}_{01}^J.\mathbf{R}_{IJ})], \tag{41}$$

where R_{IJ} is the distance between the centers of mass of the two molecules I and J. The transition dipoles $\mathbf{d}_{01}^I$ are also placed at the centers of mass. The same procedure was used by Harvey et al. [93] to introduce excitonic coupling, but their dipoles were of the analytical form while the ones used in Eq. (41) are taken as a subproduct from computing the diagonal terms. The approximation $E[I]_{M^*} = E[I]_{M^0}$ can also be used, and in this case, after diagonalizing the Hamiltonian

$$\mathbf{H} = \begin{pmatrix} H_{11} & H_{12} & \cdots & \\ H_{12} & H_{22} & & \\ \vdots & & \ddots & \vdots \\ & & \cdots & H_{NN} \end{pmatrix}, \tag{42}$$

the excitation energies are given by the difference between the eigenvalues and Eq. (40), which is the ground state energy.

The results computed including excitonic coupling are given in Figure 4.2. Also in the figure we have depicted with dotted lines the connection between the decoupled one-body states and the coupled states. The states have been connected according to the respective eigenvector values. Finally, we have compared our state decomposition to the information from the full calculation. As exemplified in Eq. (23) for the CIS case, an excited state is built by a combination of determinants weighted by the CI coefficients. In the EOM-CCSD method, the energy is invariant relative to a unitary transformation of the occupied space, so one can localize the occupied orbitals, and thereby identify from which occupied orbital the electron has been excited. Comparison of the configuration coefficients of our EOM-CCSD results for the full system compare well to the one-body coupled procedure, and allow us to establish the lower connection to the full results. It is clear that a simple one-body expansion with approximate coupling of the excitonic states already reproduces rather accurately the spectra for these clusters. Calculations have been performed for three other pentamer structures, with similar results. The lowest excitation for a set of hexamers was also compared (at this point we approach the computational limit for the level of theory chosen). Our results show an average absolute deviation of about 0.03 eV. This is about an order of magnitude lower than the expected accuracy of EOM-CCSD for single excitations.

In Figure 4.3, we show averaged results for 100 configurations of $(H_2O)_N$ clusters ($N = 40, 60, 80$). Further details on the cluster structures are found in Ref. [25]. Two sets of values are available for each system size, one without coupling (H_{IJ}) and the other with excitonic coupling. The greatest differences between the two sets are in the higher energy regime, where the neglect of coupling leads to a sharper peak around 8.6–8.7 eV. The other sets are somewhat broader, which is expectable due to coupling. The largest

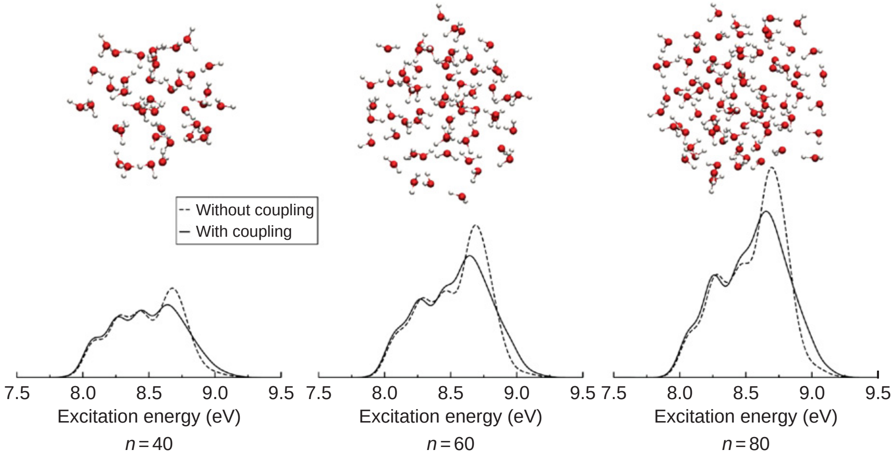

Figure 4.3 First excited band for water clusters of varying size ($N = 40,60,80$). The dotted lines represent the results without coupling between states and the solid line represents the results diagonalizing the matrix of Eq. (42). Each value has been represented by a normalized Gaussian ($\sigma^2 = 0.0025\,\text{eV}^{-2}$).

peak for $N = 80$ is also shifted to the red, but only by less than 0.1 eV. The size effect on the spectra is mainly visible on the proportionality of the bands. The most dominant band at $N = 80$, which will correspond to the one in the bulk phase, slowly grows in size with increasing N. A study of the states eigenvectors show that the higher excitations are more delocalized and with larger contributions from core one-particle states [25]. The excitations to the red are mainly due to localized surface states and, therefore, are not visible in the liquid phase. The liquid-phase spectra is the subject of the next section.

3.1.2. Absorption spectra of liquid water

Several experimental works on the absorption spectrum of liquid water have been reported [94–99]. These works also provide some general background on absorption processes in liquid phase. From the theoretical point-of-view [100–102], the calculation of the absorption spectrum of liquid water represents a considerable challenge. Firstly, an adequate description of the liquid state structure and electronic density fluctuations is needed. Moreover, light absorption by liquid water in the ultraviolet region leads to some specific difficulties related with the description of high energy-lying excited states.

A sequential molecular dynamics/QM approach for investigating the absorption spectrum of liquid water in the 6–15 eV energy range has been recently reported [103]. For completeness, an overview of the adopted methodology is described as follows: Initially, a 2 ns molecular dynamics run using a polarizable model [104] for liquid water was carried out. Then, 100 configurations saved every 20 ps were selected for the calculation of electronic properties. For each configuration a QM/MM partition was defined, where the QM system includes explicitly a few water molecules and the MM environment is represented by a charge distribution of 100 water molecules. Polarization effects lead to a nonuniform charge background, which is represented by a set of point charges that reproduces the induced dipole moments of the polarizable model [105]. Some issues are of particular relevance. The dependence of the results on (1) the basis set representation of the quantum system for describing higher excitations; (2) the size of the quantum system (N_{w}), and (3) the charge background. Moreover, a comparison of the theoretical results with experimental information on the liquid water absorption spectrum is of crucial interest for assessing the adequacy of the adopted theoretical procedures.

The water absorption spectrum is related to the complex dynamic dipole polarizability, $\alpha(\omega) = \alpha_1(\omega) + \alpha_2(\omega)$, where $\alpha_1(\omega)$ and $\alpha_2(\omega)$ are, respectively, the real and imaginary parts of $\alpha(\omega)$. The dynamic polarizability $\alpha(\omega)$ can be calculated through a sum-over-states (SOS), according to:

$$\alpha(\omega) = \sum_{k=0}^{\infty} f_k \left\{ \frac{\Delta E_k^2 - \omega^2}{(\Delta E_k^2 - \omega^2)^2 + \omega^2 \Gamma_k^2} + \frac{i \Gamma_k \omega}{(\Delta E_k^2 - \omega^2)^2 + \omega^2 \Gamma_k^2} \right\}, \tag{43}$$

where ΔE_k's and f_k's are transition energies and oscillator strengths, respectively, and $1/\Gamma_k$ is a decay time describing the radiative relaxation of transition k. Γ_k can be estimated as $\Gamma_k = \hbar/\tau = 6.582 \times 10^{-16}\,\mathrm{eV\,s}/\tau$, where the decay time is on the femtosecond timescale [106]. For the calculation of $\alpha(\omega)$ using the SOS expression Γ_k has been set to a single arbitrary and small value.

At high frequencies, the relationship between the dielectric constant $\epsilon(\omega) = \epsilon_1(\omega) + i\epsilon_2(\omega)$ and the dynamic polarizability $\alpha(\omega)$ is given by the Lorenz-Lorentz equation [107],

$$\frac{\epsilon(\omega) - 1}{\epsilon(\omega) + 2} = \frac{4\pi}{3}\rho\alpha(\omega), \tag{44}$$

where the number density $\rho = N/V$, N is the number of particles and V its volume.

The basis set dependence of the imaginary part of the dielectric constant $\epsilon_2(\omega)$ calculated with the Dunning's hierarchical d-aug-cc-pVxZ (x = D,T,Q) basis sets [108–110] is illustrated in Figure 4.4. No significant dependence is observed for excitation energies below 15 eV. However, as expected, for higher excitation energies, at least a d-aug-cc-pVTZ basis set should be used. This dependence reflects excitations to a quasi-continuum set of unoccupied orbitals.

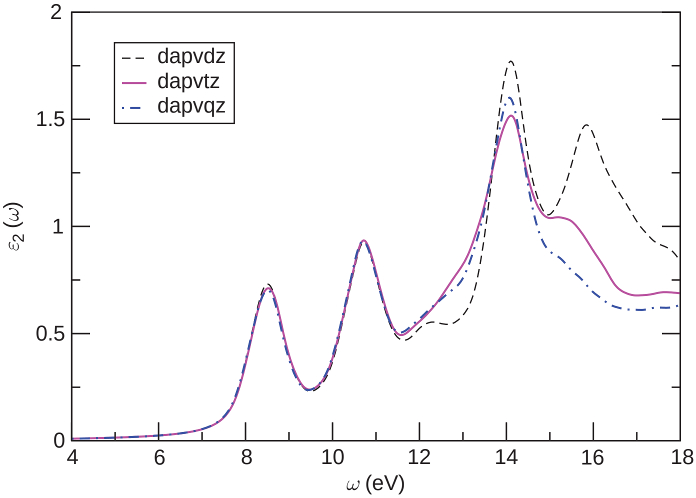

Figure 4.4 Basis set dependence of the imaginary part of the dielectric constant of liquid water [$\epsilon_2(\omega)$]. Calculations were carried out with the BH and HLYP functional and a single water molecule in the quantum system. Results are shown for dapvdz, dapvtz, and dapvqz basis sets.

The dependence of the results on the number of water molecules explicitly included in the quantum system is illustrated in Figure 4.5 (bottom panel). Although some differences can be observed when we compare results for $N_w = 1$ and 2, no significant dependence of $\epsilon_2(\omega)$ on the number of water molecules is observed for $N_w > 3$ [103]. However, we notice that this can only be verified for statistically converged calculations carried out with the adequate basis set for the energy range of interest. Therefore, a significant number of weakly correlated configurations should be included in the calculation of average properties (100 in the present calculations). As previously discussed, the convergence of the SOS procedure for calculating dynamic polarizabilities should also be checked. Although in many cases, full SOS calculations are possible, they become not affordable for large quantum systems and basis sets. Therefore, for many cases of interest, the SOS is truncated. The top panel of Figure 4.5 illustrates the behavior of $\epsilon_2(\omega)$ with the number of states (NStates) included in the SOS. For this particular case, a weak dependence on NStates is observed, suggesting that calculations for larger systems are affordable by using a truncated SOS. Another attractive route for the calculation of polarizabilities and therefore for investigating absorption properties in condensed phase relies on the polarization propagator (PP) approach [111]. The PP approach leads to results quite

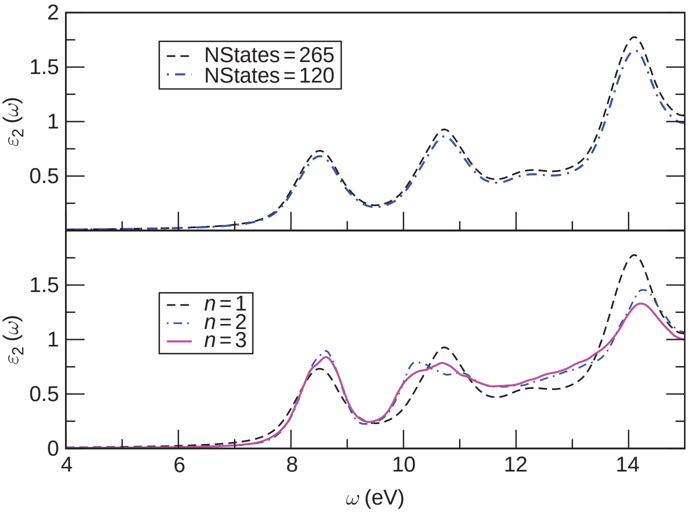

Figure 4.5 Bottom: dependence of the imaginary part of the dielectric constant of liquid water [$\epsilon_2(\omega)$] on the number of water molecules in the quantum system. Results are from TDDFT BH and HLYP/dapvdz calculations; top: behavior of $\epsilon_2(\omega)$ with the number of states (NStates) included in the SOS for a system with $N_w = 1$. Reprinted with permission from J. Chem. Phys. 130 (2009) 014505. Copyright 2009, AIP.

similar to the SOS calculations [103]. However, in contrast with the SOS procedure there is no truncation of the number of excited states [111].

A sequential QM/MM partition is usually based on the representation of environment (the MM part) by a charge background. Therefore, it is of crucial importance to discuss how the results depend on the choice of the embedding charge background. In principle, a general procedure based on the SCF determination of the quantum electronic density and charge background should be adopted [37]. SCF determination of embedding charges can be carried out in different ways. One possibility is to define a large quantum system and to estimate the charges by fitting to the electrostatic potential at a given theoretical level. Then, a smaller quantum system is used for the calculation of the electronic properties at the same theoretical level with the embedding charges previously estimated. The following procedure has been recently applied to investigate the influence of self-consistent charge relaxation in the first hydration shell on the calculation of the water absorption spectrum [103]. A quantum system or QM partition including explicitly six water molecules was embedded in the frozen charge distribution of 100 water molecules represented by NCC charges. The charges of the QM partition were determined by fitting to the electrostatic potential [112]. Then, calculations of electronic properties at the same theoretical level were carried out for one quantum molecule surrounded by the SCF charges of the nearest five water molecules and this system was embedded in the background of the remaining water molecules represented by the nonuniform charge distribution that reproduces the induced dipoles of the NCC model. On the other hand, a much simpler procedure relies on the assumption that the charge background that defines the MM system is frozen. A frozen charge background can be defined by adopting a polarizable (NCC) or nonpolarizable (TIP3P) model for the charge distribution of the surrounding water molecules. The dependence of $\epsilon_2(\omega)$ on the choice of different charge backgrounds is illustrated in Figure 4.6. In agreement with previous studies [100,101], no significant dependence of the results for the absorption spectrum on the charge background is observed.

3.1.3. Ionization of liquid water

Electronic properties of water, in particular, electron binding energies in liquid phase, were investigated by several experimental [12,113,114] and theoretical [115–117] works. A review on experimental techniques for assessing electron binding energies of liquid and solutions has been recently reported [114]. In contrast with results for the gas-phase water molecule, the electronic structure in liquid phase is characterized by electronic and thermal broadening [115]. Electronic broadening in liquid water is related to hydrogen bond interactions and are a fingerprint of the electronic density of states (DOS) of water clusters at low temperatures. Thermal broadening is associated with the different configurations of the HB network that

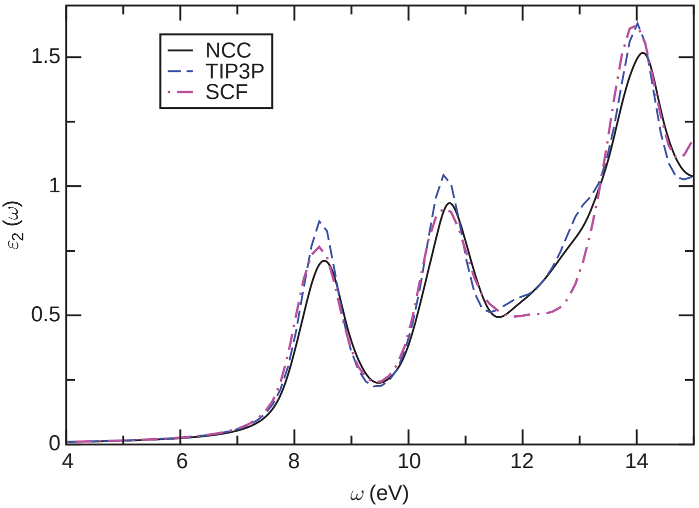

Figure 4.6 Dependence of the imaginary part of the dielectric constant of liquid water [$\epsilon_2(\omega)$] on the choice of the charge background. Results for TIP3P, NCC, and SCF charges are from TDDFT BH and HLYP/dapvdz calculations with $N_w = 1$.

characterizes liquid water at a finite temperature T. Usually, the symmetry species associated with the ground-state electronic configuration $(1a_1)^2(2a_1)^2(1b_2)^2(3a_1)^2(1b_1)^2$ are used to label the distribution of electron binding energies and "band" formation in liquid water. Hydrogen bond interactions lead to orbital mixing and splitting defining orbital energy ranges that can be associated with a given symmetry species of the water monomer.

Electronic broadening can be illustrated by the results for electron binding energies of water clusters [117]. This is shown in Figure 4.7, where pole strengths versus orbital energies (eV) from Green's function or electron propagator theory calculations [118–121] for $(H_2O)_{1-8}$ are reported. Besides orbital mixing and energy broadening, these results also indicate that the orbital energy of the highest occupied molecular orbital (HOMO) in small water clusters is red shifted relative to the HOMO of the water molecule. This is in trend with experimental data indicating a ~1.4 eV red shift of the $1b_1$ energy from the water monomer to the liquid phase [113].

Although calculations of electron binding energies based on electron propagator theory can be carried out for small clusters, they are not affordable for larger systems. In these cases, an attractive possibility for investigating electronic properties in condensed phases is DFT. However, applications of DFT for the calculation of EBEs are limited by the self-interaction error, which is inherent to many approximations for the XC functional (see Section 2.3.2). Although the meaning of DFT orbital energies

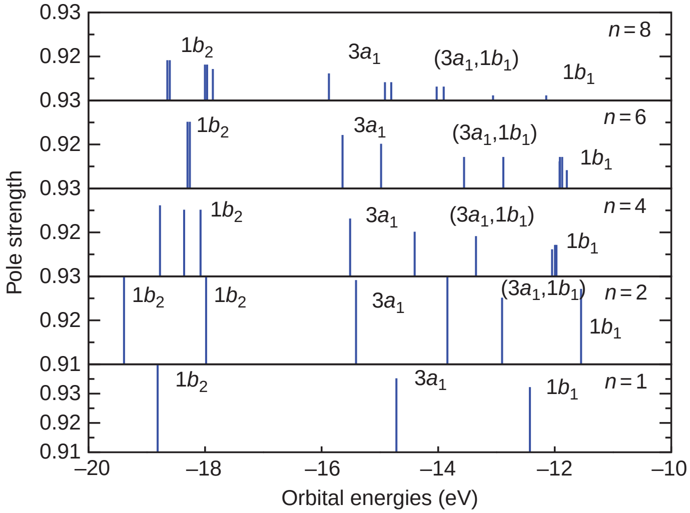

Figure 4.7 Outer valence orbital energies (eV) for water clusters from Green's function calculations with the dapvdz basis set. Results are for $(H_2O)_{2-8}$ clusters. Reprinted from Chem. Phys. Lett. 429 (2006) 129–135, P.C. do Couto, B.J.C. Cabral, S. Canuto, Electron binding energies of water clusters: Implications for the electronic properties of liquid water, Copyright 2006, with permission from Elsevier.

remains a controversial issue in the literature [122], several works provided evidence on the reliability of specific parameterizations of DFT for predicting orbital energies [117,122,123]. The electronic DOS of liquid water based on a reparameterized MPW1PW91 XC energy [52] is shown in Figure 4.8.

On the other hand, there is a strong interest in the calculation of the first vertical ionization energy (VIP) and electron affinity (VEA) because these electronic properties are intimately connected to charge transfer and chemical reactivity in solution. The average VIP, for example, can be estimated through the following ΔE calculation:

$$\mathrm{VIP}_{N_\mathrm{w}} = \frac{1}{N}\sum_{i=1}^{N}[E^{+}_{N_\mathrm{w}}(i) - E_{N_\mathrm{w}}(i)], \tag{45}$$

where N is the number of selected configurations, N_w the number of water molecules in QM system, and $E_{N_\mathrm{w}}(i)$ and $E^{+}_{N_\mathrm{w}}(i)$ are the energies of the ionized and neutral systems, respectively. Sequential QM/MM calculations of the VIP and VEA of liquid water were recently reported. The set of configurations for the calculation of the VIP and VEA of liquid water was generated by molecular dynamics for a polarizable model of the water [105]. The behavior of VIP and VEA with the number of water molecules in the

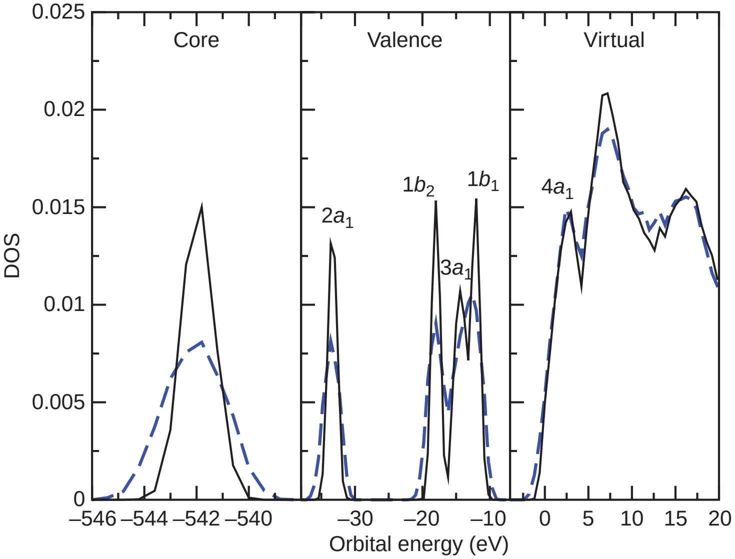

Figure 4.8 Average electronic DOS of liquid water at $T = 298$ K from sequential Monte Carlo/DFT calculations. The average DOS was calculated over 50 configurations. The QM system includes 30 water molecules. The surrounding water molecules (200) are represented by TIP5P charges. Results for a nonembedded QM system are also shown (dashed lines). Reprinted with permission from J. Chem. Phys. 123 (2005), 054510, Copyright 2005, AIP.

quantum system is illustrated in Figure 4.9. A significant dependence of the results on the size of the quantum system can be observed. Our best estimate for the first ionization potential of liquid water (9.71 ± 0.06 eV) is based on a MPW1PW91/apvdz calculation with $N_w = 20$. This prediction is in good agreement with the experimental result reported by Winter and Faubel (9.9 eV). The calculated VEA can be compared with minus the conduction band edge of water ($-V_0$) [124]. Our best estimate of VEA is 0.44 ± 0.05 eV, which is significantly smaller than the typical literature value for $-V_0$ (1.2 ± 0.1 eV) [125]. However, it is in keeping with a more recent prediction by Coe et al. [124] that points to a value close to zero.

3.2. Electron binding energies of liquid ammonia

In contrast with water, electronic properties of liquid ammonia are much less known from both the experimental and the theoretical points of view, despite the fact that several studies on the ammoniated electron [126,127] have been reported. A sequential QM/MM approach to the electronic properties of liquid ammonia has been recently reported [128]. The results

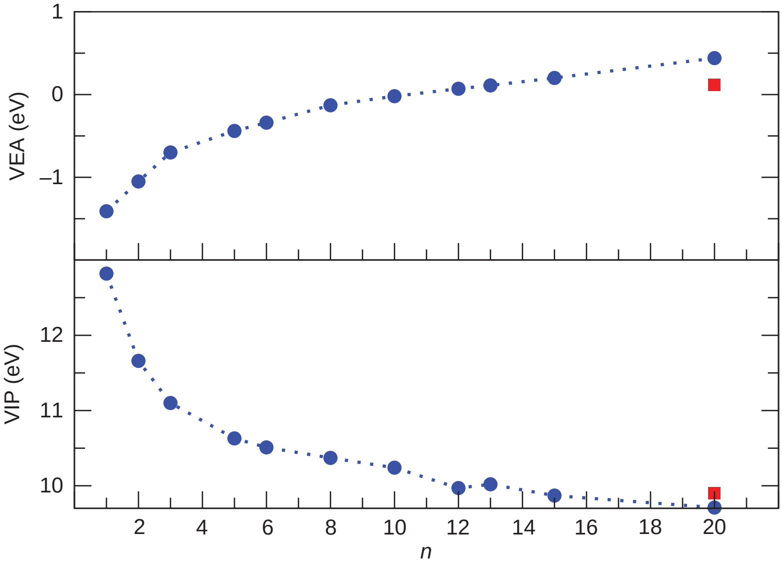

Figure 4.9 Behavior of the VIP and VEA with the number of water molecules (N_w) in the quantum system. Squares represent experimental values.

are for liquid ammonia at $d = 0.73\,\mathrm{g/cm^3}$ and $T = 197.2\,\mathrm{K}$. A first issue concerns the analysis of polarization effects in liquid ammonia. This is important because the attachment of an electron to a molecular structure or aggregate depends on its multipolar moments [129]. In comparison with water, in which the dipole moment increases from the gas-phase value of 1.85 to ~2.7 D in the liquid phase, polarization effects in liquid ammonia are weaker. The QM/MM calculations predict that the dipole moment of liquid ammonia is 2.05 D, which means an increase of 27% relative to the gas-phase value. We are not aware of experimental data for the electron binding energies of liquid ammonia. Recent QM/MM results for the density of states of liquid ammonia with different number of molecules ($n = 5$, 8, 10, and 14) in the quantum system (Figure 4.10) indicate that the edge of the $3a_1$ band can be placed at ~9.8 eV.

This value can be associated with the ionization energy of liquid ammonia and it is ~1.05 eV below the ionization energy of the gas-phase ammonia molecule. The predicted red shift for the first ionization energy of liquid ammonia relative to the gas phase is, therefore, smaller than the experimental prediction for liquid water of 1.7 eV. As previously discussed for liquid water, this red shift can be related to electronic and thermal broadening [115]. The previous QM/MM predictions rely on a reparameterized XC functional that reproduce Green's function electron binding energies of

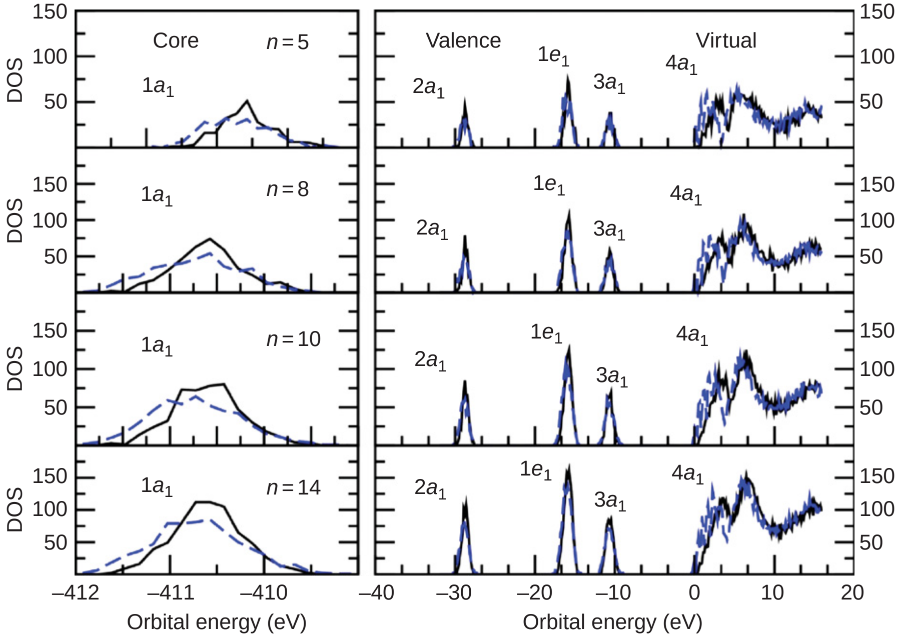

Figure 4.10 Electronic DOS of ammonia clusters ($n = 5$, 8, 10, and 14) in the presence (solid line) and absence (dashed line) of an embedding background. Reprinted with permission from J. Chem. Phys. 128 (2008) 014506, Copyright 2008, AIP.

small ammonia clusters (see Ref. [128] for details). The same approach was used to estimate the VEA in liquid ammonia. It was found that the VEA is negative for quantum systems embedded in a charge background representing the surrounding ammonia molecules. However, as illustrated in Figure 4.11, VEAs become positive for nonembedded quantum systems.

These results indicate that no *vertical* electron attachment via internal states is observed in liquid ammonia, at least for the adopted interaction model and thermodynamic conditions of the QM/MM approach. Interestingly, positive VEAs for nonembedded quantum systems are positive for $n \geq 10$. This can be interpreted as an indication on the stabilization of an excess electron via surface states. In other words, and in agreement with theoretical predictions of Barnett et al. [130] small ammonia clusters can stabilize an excess electron by localizing the extra charge on the surface. Figure 4.11 also indicates that in small ammonia clusters the VEAs are correlated with the total dipole moment of the clusters. This correlation is observed for both embedded and nonembedded clusters.

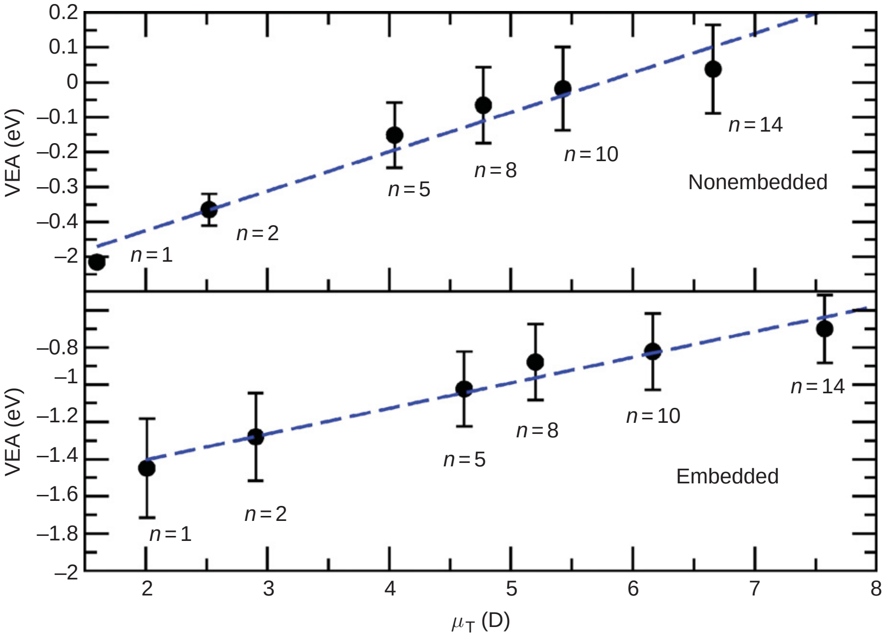

Figure 4.11 Average VEA (in eV) versus average total dipole moment (μ_T in D) of ammonia clusters. Dashed lines are fitting to raw data with correlation coefficients $r = 0.977$ (nonembedded) and $r = 0.983$ (embedded clusters). Reprinted with permission from J. Chem. Phys. 128 (2008) 014506, Copyright 2008, AIP.

3.3. Charge transfer to solvent in halide aqueous solutions

The electronic spectra of halide ions in aqueous solution is a topic of intense experimental and theoretical work [114,131–133]. A distinguishing trait of their spectra is the existence of intense absorption bands in the deep ultraviolet which is otherwise absent in the gas phase. These bound excited states are, therefore, due to interactions with the surrounding solvent. For this reason, the computational study of halides is a challenging but likewise interesting case for QM/MM and related approaches.

The maximum absorption peaks for the halides in solution have been measured: 7.10 (Cl^-), 6.29 (Br^-), and 5.47 (I^-) [134]. In order to discuss the trends in these values, one has to take into account the various states in question. These are namely the ground state (X^-, X = F, Cl, Br, I), the excited state (X^{-*}) and the ionized state (X). The stability of the excited state can be defined relative either to the ground state, in which case the determining quantity is the excitation energy ω, or the ionized state. In the latter case, the question is whether the excited state is bound, the same is to say, whether the excited state is lower in energy than the neutral halogen atom. If not, the excitation will not be observed. A comment should be made at this point. The question of whether an excitation is observed or not is only valid in experiment. In QM calculations, it is possible to compute any given excited state, even if energetically unstable relative to ionization. This is simply due to the constraints placed on the wavefunction.

A short diagram has been sketched in Figure 4.12 for three possible environments. The example is rather general and can be applied to any of the halogens. On the left side, the energy levels for all states have been sketched for the halide in vacuo. The energetic ordering is in this case ground, ionized, and excited states. The latter state is therefore not bound, since the system will rather lose the electron than to remain on that given electronic configuration. The electronic spectra of halides will be featureless, up till the ionization threshold. In the middle diagram, a halide is surrounded by a few water molecules. All states are stabilized, but on different degrees. The most favored by the solvent environment is the ground state. Given that water is a polar solvent, this should come as no surprise. This ground state is negatively charged with a well-localized electron. Electrostatic interactions are, therefore, particularly favorable. The excited state is also stabilized, but not so significantly, since the excess electron is delocalized in the process, smearing the charge and reducing the electrostatic interaction with the environment. The relative positions of ionized and excited states are undetermined, since the crossover between the two will depend on the specific halide and the number of water molecules. However, in solution (right-hand side), there will be a bound state for all halides. We will in the following text refer to as excitation energy (ω) the difference between $E[X^{-*}] - E[X^{-}]$ and as excited state vertical detachment energy the difference $E[X] - E[X^{-*}]$.

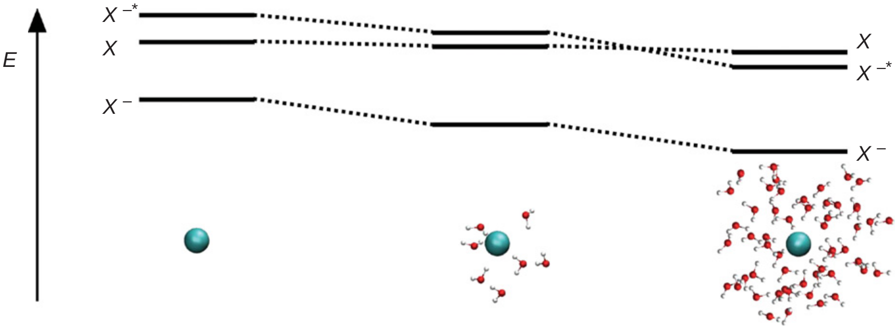

Figure 4.12 Energy diagram for three electronic states of the halide—ground state (X^{-}), excited state (X^{-*}), and ionized state (X). The ordering is given according to the environment (from left to right, gas, cluster, and aqueous solution).

Several theoretical studies have focused on small water-halide clusters [135–137]. These showed, in general, that the excitation values slowly rised with the number of solvent molecules to the experimental estimates in a close to scalable manner. Different correlations between environmental effects and the rise in the excitation energy have been proposed. Serxner et al. [138] have searched for a semiquantitative correlation between the dipole of the waters around the halide and the solvatochromic shift. This has been later contested by Majumdar et al. [135], who considered the resulting electric field. In our recent study of chloride in aqueous solution [139], we confirmed a correlation between the electric field generated by the surrounding solvent and the excitation energy value. For this purpose, we used 50 configuration from a Born–Oppenheimer MD/DFT simulation of Cl^- in a small periodic water box (64 water molecules). For each of these configurations, we chose as QM system the anion and the nearest-neighbor water molecule, representing the remaining waters as SPC/E point charges. We then reduced the number of MM waters, computing at each step the excitation energy, as well as the electrostatic field of the solvent at the chloride site. The two sets of values are given in Figure 4.13. Bradforth and Jungwirth [140] have also pointed out the importance of including a

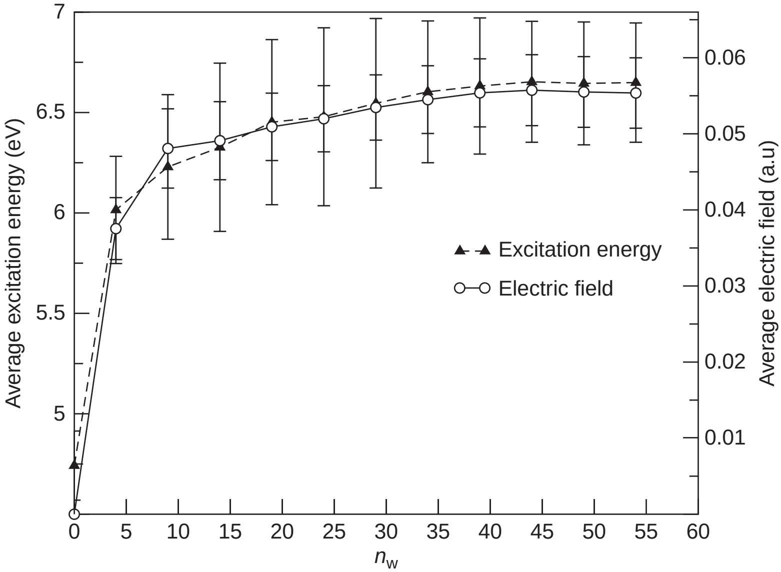

Figure 4.13 Average excitation energies (in eV) and solvent electrostatic field (in a.u.) for 50 configurations of Cl^- immersed in a simulation box with 64 water molecules (EOM-CCSD/aug-cc-pVDZ values). The QM system includes the anion and the nearest water molecule. Both values are given as a function of the embedding water molecules (n_w).

very large electrostatic field around the halide for the description of the excited state. Their calculations were focused not only on determining excitation energies but also vertical detachment energies for the ground and first excited states. The two studies indicate that a modest field is enough to predict the excitation energy, while the detachment energy has a very slow convergence. This is in line with the discussion of Section 2.2.3, as the ionization process requires a very large MM environment.

Perhaps the most relevant question in the study of halides in solution is the nature of the excitation. The vertical excitation is a precursor to the charge-transfer-to-solvent (CTTS) state, where a solvated electron is created. Most cluster studies argue that the excited electron is promoted to a virtual orbital directed toward the surface of the cluster, in what would be a dipole-bound electron [141,142]. The solution studies on chloride and iodide, however, show that upon including a sufficiently large embedding system, the excited electron is instead delocalized in a solvent cavity and the surrounding waters [139,140].

Just as in the case of the water study, it is relevant to examine the dependence of the above cited results with the number of quantum water molecules. Due to the charge-transfer nature of the excitation, a many-body expansion such as the one used in Eq. (20) is not feasible. In Eq. (20) it is implied that the same excitation is computed for each of the energy terms. This will not be the case if CTTS occurs (the one-body term will not be consistent with the two-body expansion). The only possibility is to compute brute force with larger QM regions. This has been done in both studies referenced above. The conclusion is that ω holds a slight dependence on the number of QM waters. In the case of chloride, up to six water molecules have been included and the effect is seen to be around 0.8 eV [139]. In the case of iodide, only a few single point calculations were performed, but again differences of up to 0.6 eV could be observed [140]. The maximum quantum size, in this case, included seven water molecules. The other conclusion, however, is that around three water molecules seem to suffice for a well-converged result. The number is not related to any of the solvation shells. Observing the individual values, the reason behind the number is manifold. First, the electron will not be necessarily transferred to the closest water molecule. The orientation of the water solvation shell is an issue. Second, as referred above, the electron is somewhat delocalized over a number of water molecules and the space around them, so the quantum region of a single molecule is, in some cases, not a good enough description. A last issue concerns the basis set effect. Calculations with a small quantum system show a large basis set dependence, especially diffuse functions, hinting at the need to include basis functions close to the point charge water molecules or even in between the solvent. As such, one could to some extent improve the result by adding diffuse basis functions instead of augmenting the QM region. However, even if the excitation energy is converged, it is questionable whether such a description, where the electronic density is significantly overlapping with MM point charges, would be physically reasonable. In fact, it should be avoided, since it leads to a large dependence on the choice of charges describing the embedding field.

3.4. Solvatochromic shifts of small organic molecules

The solvent effect on the excitation energies (or solvatochromic shift) of organic species is fundamental to the understanding of life mechanisms. A wide variety of processes have been developed by all kinds of life forms, from bacteria to the human being, in order to sense and regulate exposure to light. These processes can only be fully understood by looking at the molecular level. The study of solvatochromic shifts also gives insight into specific solute–solvent interactions and opens way to interesting applications, such as the tailoring of new materials with specific absorption properties in solution. However, computing this value is far from being a trivial task.

One of the often cited problems is related to the description of the molecule itself. Some of the excitations, even in the gas phase, are remarkably sensitive to the geometry. A typical example is the $n \rightarrow \pi^*$ excitation in carbonyl groups, where the value depends strongly on the C=O distance [143]. However, in predicting a shift in solution, the most determining factor will be the description of the environment, since effects pertaining to the solute will partly cancel out.

The first excitation energy of formaldehyde in aqueous solution has been the subject of many theoretical studies. Several have relied on a QM/MM calculation, including only the chromophore in the QM region. Hirata et al. [54] have used the same expansion as Eq. (20), but with the embedding environment described by dipoles centered on the surrounding water molecules. Results for small clusters (formaldehyde + two water molecules) showed good agreement with full calculations. In order to predict the solvatochromic shift, they used large water clusters (up to 81 molecules) and a variety of QM methods. The EOM-CCSD results indicated a shift of 0.17 eV, in close agreement with the QM(CASSCF)/MM results of Martín et al. [144] (0.18 eV). Even though the two procedures widely differ, this seems to hint at a very small two-body correction term. The main contribution would be connected to the electrostatic influence of the water molecules, and their explicit quantum description can be considered unnecessary. We now turn to other cases where the QM/MM approximations apparently fail.

In aqueous solution, the $\pi \rightarrow \pi^*$ excitation energy of uracil is known to suffer a red shift. Previous computational studies have shown that a large number of solvent molecules have to be included explicitly into the quantum system when making use of a QM/MM hybrid scheme. The experimental estimate is around −0.3 eV. The results of Ludwig et al. [145], using a QM/MM scheme with TD-B3LYP and including only the solute molecule in the quantum region, show almost no change relative to the gas phase (−0.02 eV). By introducing nine explicit water molecules, the shift increases to −0.20. However, semiempirical calculations show that the result for nine water molecules (which make up for the first solvation shell) is not converged relative to the quantum system size.

A similar observation has been made in the case of acrolein. With the use of TD-DFT (CAM-B3LYP) as the quantum level of theory, Aidas et al. [66] identified changes in the solvatochromic shift above 0.2 eV on increasing the number of water molecules in the quantum system. This is in line with previous results on the system which made use of continuum solvent approaches. The experimental estimate in the case of acrolein is of a −0.52 eV shift. The values obtained by Iwata and Morokuma [146] (QM = HF: −0.25), do Monte et al. [147] (QM = MR − CISD + Q: −0.40), and Aquilante et al. [148] (QM = MS − CASPT2: −0.10 and QM = PBE0: −0.22) were all consistently too low, independently of the quantum method used. We present in Table 4.2 a small review of computed solvatochromic shift values for the two systems, together with the experimental estimates.

The problem seems more or less analog to both systems. The approximate treatment of the solvent, reducing it to a simple electrostatic effect, is unable to describe the shift. It should be pointed out that some of these studies were performed with polarized coupling, including the effect of back-polarization in the solvent. This seems to give little to no improvement

Table 4.2 Literature values for several QM/MM theoretical studies and experimental estimates for the $\pi \rightarrow \pi^*$ solvatochromic shifts in water of some small organic molecules

Molecule	Level of theory	n_w	Shift	Ref.
Acrolein	SCF/EHP	0	−0.25	[146]
	CASPT2/PCM	0	−0.22	[148]
	MR-CISD + Q/COSMO	0	−0.40	[147]
	LR-CCSD/SPCpol	3	−0.26	[66]
	CAM-B3LYP/SPCpol	0	−0.26	[66]
	CAM-B3LYP/SPCpol	12	−0.46	[66]
	experiment		−0.52	
Uracil	PBE0/PCM	4	−0.10	[149]
	B97-1/PCM	0	−0.08	[150]
	PBE0(PMM)	0	−0.10	[151]
	B3LYP/SPC	0	−0.02	[145]
	B3LYP/SPC	9	−0.20	[145]
	experiment		−0.28/−0.31	

relative to a simple electrostatic embedding. The error seems to stem exclusively from the quantum treatment. As a test system, we opted to use the acrolein molecule in analyzing the many-body effects responsible for the slow convergence of this value. The uracil case is somewhat more complicated, since the $\pi \rightarrow \pi^*$ excited state is expected to cross below the $n \rightarrow \pi^*$ state, on going from the gas to the solution. The problem of state crossing is a severe limitation to the use of many-body schemes.

In order to compare the gas and the solution spectra, we optimized the acrolein molecule at the MP2/aug-cc-pVTZ level, with and without the PCM continuum correction. The MP2(PCM)/aug-cc-pVTZ geometry was then used in a fixed-body MD simulation immersed in a water (TIP3P) box with periodic conditions. The intermolecular terms for acrolein were taken from Ref. [66]. After an equilibration time of 50 ps, 10 snapshots were taken in 5 ps intervals, and were later used for the calculation of the ground and the excited states. For the single point calculations, the simulation box was replicated in all three dimensions, and a sphere was cut, with the acrolein oxygen as the geometric center, and including all water molecules with a distance of up to 20 Å from the same atom. A depiction of one of these snapshots is shown in Figure 4.14. The excitation energies were computed at the EOM-CCSD/aug-cc-pVDZ level of theory. The solvatochromic shift is defined as the energy difference between the excitation energy of the MP2 (PCM)/aug-cc-pVTZ optimized structure, dipped in the solvent box, and of the gas-phase optimized molecule. The EOM-CCSD/aug-cc-pVDZ has been confirmed as a suitable theoretical level for computing the $\pi \rightarrow \pi^*$ excitation energy. Further details on the system preparation and single point calculations will be published elsewhere [152].

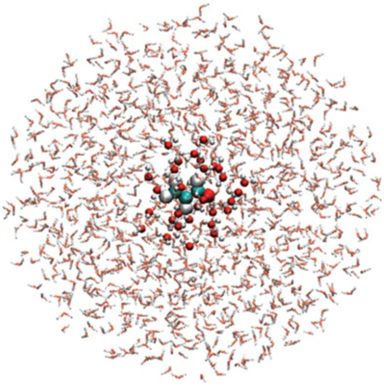

Figure 4.14 MD snapshot of an acrolein molecule (vdW representation) surrounded by water molecules. The closest 32 water molecules are depicted as balls and sticks, which is the largest quantum system considered in the study.

In order to compute the excitation energy in the case of the solvated acrolein molecule, we make use of Eq. (20). The excitation energy is calculated according to the reduced two-body expression, including a variable number of water molecules into the expansion. As it can be easily gathered from Figure 4.15, the inclusion of water molecules in the QM region has a dramatic effect on the solvatochromic shift. The QM/MM estimate, with only the solute as quantum system ($n_w = 0$), is only -0.24 eV, about 50% of the experimental value. This is in line with the previous results for the system (see Table 4.2). Including the first solvation shell ($n_w = 12$), one is still at -0.45 eV, an error of about 10%. This is only recovered by including as much as 32 water molecules. Such a quantum system size is computationally prohibitive, even for lower levels of theory such as TD-DFT. A remarkable agreement with experiment is obtained, when comparing the converged result.

Besides the possibility of achieving such large system sizes, one of the positive aspects of a many-body formulation is the amount of information available in the decomposition. The values presented in Figure 4.15 are estimated as a by-product of the two-body calculation with $n_w = 32$. Contrary to what was performed in Sections 3.1.2 and 3.3, there is no need to

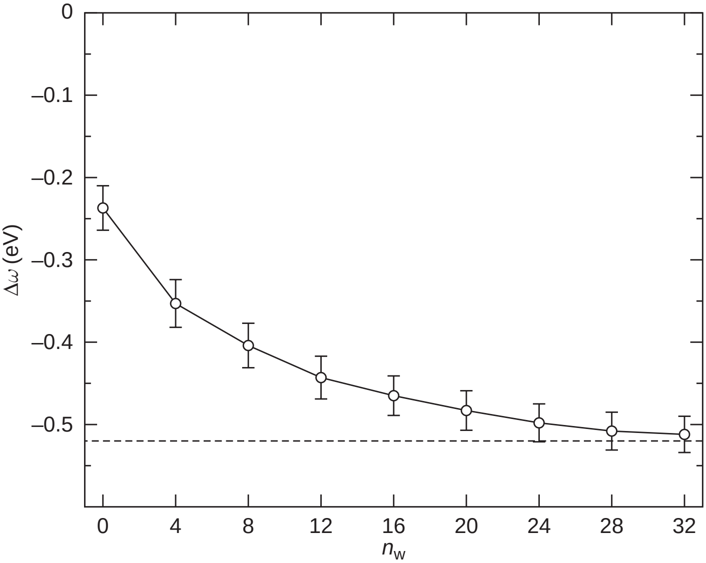

Figure 4.15 Solvatochromic shift $\Delta\omega$ of the $\pi \rightarrow \pi^*$ excitation of the acrolein molecule (in eV), embedded in a solvent sphere with a 20 Å radius. The shift is computed with use of Eq. (20), and shown as a function of the number of water molecules treated quantum mechanically (n_w).

repeat the calculation for different sizes in order to check for convergence of the QM system. The two-body value is obtained in an incremental fashion and, therefore, has inherent diagnostic capabilities. One can start by computing the QM/MM value and then add the effect of dimers. If the two-body effect is found to be small, one can, with some certainty, confirm the convergence of the calculation. The contrary is, however, not applicable.

4. FINAL REMARKS AND CONCLUSIONS

The application of sequential QM/MM method for the calculation of the electronic spectra of hydrogen bond systems was reviewed. In contrast with the conventional QM/MM approach, there is no coupling between the QM and the MM partitions in the dynamic or stochastic sampling procedures for studying many-body interacting systems in condensed phase. However, the sequential approach can be seen as a particular case of a more general QM/MM formulation. Particular emphasis was placed on the possibility of exploiting the coupling between many-body energy decomposition schemes and the QM/MM partition. In this sense, the present results for the absorption spectrum of water clusters illustrate how a simple one-body decomposition scheme for the total energy can be successfully applied to carry out ab initio calculations for large water clusters. We have also presented an analysis of the merits and limitations of an application of the sequential QM/MM approach to study the liquid water absorption spectrum in the 6–15 eV range. This analysis indicated that some aspects for assessing the reliability of a QM/MM partition should be taken into consideration. Specifically, the dependence of the results on the size of the quantum system and the representation of the embedding charge background should be investigated. Several other applications of the sequential QM/MM approach were also reviewed and include ionization of liquid water and ammonia, charge transfer to solvent in halide aqueous solutions, and solvatochromic shifts of small organic molecules. The last application, namely, the calculation of the excitation energy of the acrolein molecule in liquid water, clearly illustrates how the coupling of a many-body decomposition scheme to a QM/MM partition makes possible an accurate ab initio approach to the solvatochromic shift for a system where a strong dependence of the results on the number of solvent molecules explicitly included in the QM system has been observed. In conclusion, the application of a many-body decomposition scheme to the energy representation of a QM/MM partition leads to a new and powerful formulation that is beyond the conventional QM/MM methodology.

ACKNOWLEDGMENTS

The authors would like to thank their collaborators in the above-referenced studies. This work was partially supported by Fundação para a Ciência e a Tecnologia (FCT), Portugal (Grant No. PTDC/QUI/68226/2006). R.A.M. gratefully acknowledges the FCT (Portugal) (Grant No. SFRH/BPD/38447/2007).

REFERENCES

[1] M.E. Tuckerman, P.J. Ungar, T. vonRosenvinge, M.L. Klein, J. Phys. Chem. 100 (1996) 12878.
[2] M.E. Tuckerman, G.J. Martyna, J. Phys. Chem. B 104 (2000) 150.
[3] I.F.W. Kuo, C.J. Mundy, M.J. McGrath, J.I. Siepmann, J. Van-deVondele, M. Sprik, et al., J. Phys. Chem. B 108 (2004) 12990.
[4] D. Prendergast, J.C. Grossman, G. Galli, J. Chem. Phys. 123 (2005) 014501.
[5] I. Tunon, M.T.C.M. Costa, C. Millot, M.F. Ruiz-Lopez, J. Chem. Phys. 106 (1997) 3633.
[6] M. Eichinger, P. Tavan, J. Hutter, M. Parrinello, J. Chem. Phys. 110 (1999) 10452.
[7] N. Reuter, A. Dejaegere, B. Maigret, M. Karplus, J. Phys. Chem. A 104 (2000) 1720.
[8] J.L. Gao, D.G. Truhlar, Annu. Rev. Phys. Chem. 53 (2002) 467.
[9] H. Lin, D.G. Truhlar, Theor. Chim. Acta 117 (2007) 185.
[10] K. Coutinho, S. Canuto, Adv. Quantum. Chem. 28 (1997) 89.
[11] K. Coutinho, S. Canuto, J. Chem. Phys. 113 (2000) 9132.
[12] B. Winter, M. Faubel, Chem. Rev. 106 (2006) 1176.
[13] C. Kobayashi, K. Iwahashi, S. Saito, I. Ohmine, J. Chem. Phys. 105 (1996) 6358.
[14] I. Ohmine, S. Saito, Acc. Chem. Res. 32 (1999) 741.
[15] D. Asthagiri, L.R. Pratt, J.D. Kress, Phys. Rev. E 68 (2003) 041505.
[16] P.H.-L. Sit, N.J. Marzari, J. Chem. Phys. 122 (2005) 204510.
[17] M. Guidon, F. Schiffmann, J. Hutter, J. VandeVondele, J. Chem. Phys. 128 (2008) 214104.
[18] Y. Zhao, D.G. Truhlar, Theor. Chim. Acta 120 (2008) 215.
[19] Y. Zhao, D.G. Truhlar, J. Chem. Phys. 125 (2006) 194191.
[20] E.E. Dahlke, D.G. Truhlar, J. Chem. Theory Comput. 3 (2007) 46.
[21] M. Chiba, D.G. Fedorov, K. Kitaura, J. Chem. Phys. 127 (2007) 104108.
[22] A. Sorkin, E.E. Dahlke, D.G. Truhlar, J. Chem. Theory Comput. 4 (2008) 683.
[23] R.A. Mata, H. Stoll, Chem. Phys. Lett. 465 (2008) 136.
[24] H.R. Leverentz, D.G. Truhlar, J. Chem. Theory Comput. 5 (2009) 1573.
[25] R.A. Mata, H. Stoll, B.J.C. Cabral, J. Chem. Theory Comput. 5 (2009) 1829.
[26] M.P. Allen, D.J. Tildesley, Computer Simulation of Liquids, Oxford Science Publications, New York, 1987.
[27] D. Frenkel, B. Smit, Understanding Molecular Simulations. From Algorithms to Applications, Academic Press, San Diego, 1996.
[28] H. Hellmann, Einfuhring in die Quantemchemie, F. Deuticke, Leipzig, 1937.
[29] R.P. Feynman, Phys. Rev. 56 (1939) 340.
[30] R.E. Stanton, J. Chem. Phys. 36 (1962) 1298.
[31] A. Szabo, N. Ostlund, Modern Quantum Chemistry, McGraw-Hill, New York, 1989.
[32] R.G. Parr, W. Yang, Density-Functional Theory of Atoms and Molecules, Oxford University Press, Oxford, 1989.
[33] A.E. Reed, R.B. Weinstock, F. Weinhold, J. Chem. Phys. 83 (1985) 735.

[34] F.M. Bickelhaupt, N.J.R. van Eikema Hommes, C.F. Guerra, E.J. Baerends, Organometallics 15 (1996) 2923.

[35] I. Antes, W. Thiel, Combined Quantum Mechanical and Molecular Mechanical Methods, vol. 712, p. 50, ACS Symposium Series, 1998.

[36] D. Bakowies, W. Thiel, J. Phys. Chem. 100 (1996) 10580.

[37] J. Kongsted, A. Osted, K.V. Mikkelsen, O. Christiansen, J. Chem. Phys. 118 (2003) 1620.

[38] M.A. Thompson, J. Phys. Chem. 100 (1996) 14492.

[39] J. Gao, J. Comput. Chem. 18 (1997) 1061.

[40] J.L. Gao, K. Byun, Theor. Chem. Acc. 96 (1997) 151.

[41] J.L. Gao, C. Alhambra, J. Am. Chem. Soc. 119 (1997) 2962.

[42] R.A. Bryce, M.A. Vincent, N.O.J. Malcolm, I.H. Hillier, N.A. Burton, J. Chem. Phys. 109 (1998) 3077.

[43] L. Jensen, P.T. van Duijnen, J.G. Snijders, J. Chem. Phys. 118 (2003) 514.

[44] Y.-L. Lin, J. Gao, J. Chem. Theory Comput. 3 (2007) 1484.

[45] D.P. Geerke, S. Thiel, W. Thiel, W.F. van Gunsteren, J. Chem. Theory Comput. 3 (2007) 1499.

[46] C. Curutchet, A. Muñoz-Losa, S. Monti, J. Kongsted, G.D. Scholes, B. Mennucci, J. Chem. Theory Comput. 5 (2009) 1838.

[47] C.B. Nielsen, O. Christiansen, K.V. Mikkelsen, J. Kongsted, J. Chem. Phys. 126 (2007) 154112.

[48] Y. Zhang, H. Lin, D.G. Truhlar, J. Chem. Theory Comput. 3 (2007) 1378.

[49] Y. Zhang, H. Lin, J. Chem. Theory Comput. 4 (2008) 414.

[50] K. Nam, J. Gao, D.M. York, J. Chem. Theory Comput. 1 (2005) 2.

[51] Y. Kawashima, M. Dupuis, K. Hirao, J. Chem. Phys. 117 (2002) 248.

[52] S.G. Estácio, P.C. do Couto, B.J.C. Cabral, J. Chem. Phys. 123 (2005) 054510.

[53] M. Kamiya, S. Hirata, M. Valiev, J. Chem. Phys. 128 (2008) 074103.

[54] S. Hirata, M. Valiev, M. Dupuis, S.S. Xantheas, S. Sugiki, H. Sekino, Mol. Phys. 103 (2005) 2255.

[55] O. Christiansen, P. Jørgensen, C. Hättig, Int. J. Quantum Chem. 68 (1998) 1.

[56] J. Geertsen, M. Rittby, R.J. Bartlett, Chem. Phys. Lett. 164 (1989) 57.

[57] J.F. Stanton, R.J. Bartlett, J. Chem. Phys. 98 (1993) 7029.

[58] D.C. Comeau, R.J. Bartlett, Chem. Phys. Lett. 207 (1993) 414.

[59] O. Christiansen, H. Koch, P. Jørgensen, Chem. Phys. Lett. 243 (1995) 409.

[60] H. Koch, O. Christiansen, P. Jørgensen, A.M.S. de Merás, T. Helgaker, J. Chem. Phys. 106 (1997) 1808.

[61] J. Kongsted, A. Osted, K.V. Mikkelsen, O. Christiansen, J. Phys. Chem. A 107 (2003) 2578.

[62] J. Kongsted, A. Osted, K.V. Mikkelsen, P.-O. Åstrand, O. Christiansen, J. Chem. Phys. 121 (2004) 8435.

[63] J. Kongsted, A. Osted, T.B. Pedersen, K.V. Mikkelsen, O. Christiansen, J. Phys. Chem. A 108 (2004) 8624.

[64] A. Osted, J. Kongsted, K.V. Mikkelsen, O. Christiansen, J. Phys. Chem. A 108 (2004) 8646.

[65] K. Aidas, J. Kongsted, A. Osted, K.V. Mikkelsen, O. Christiansen, J. Phys. Chem. A 109 (2005) 8001.

[66] K. Aidas, A. Møgelhøj, E.J.K. Nilsson, M.S. Johnson, K.V. Mikkelsen, O. Christiansen, et al., J. Chem. Phys. 128 (2008) 194503.

[67] J. Kongsted, A. Osted, K.V. Mikkelsen, O. Christiansen, Mol. Phys. 100 (2002) 181.

[68] T. Korona, H.-J. Werner, J. Chem. Phys. 118 (2003) 3006–3019.

[69] P.-D. Fan, M. Valiev, K. Kowalski, Chem. Phys. Lett. 458 (2008) 205.

[70] F. Weigend, M. Häser, Theor. Chim. Acta 97 (1997) 331.

[71] F. Weigend, Phys. Chem. Chem. Phys. 4 (2002) 4285.

[72] P. Pulay, Chem. Phys. Lett. 100 (1983) 151–154.

[73] S. Saebø, P. Pulay, Chem. Phys. Lett. 113 (1985) 13–18.

[74] C. Hampel, H.-J. Werner, J. Chem. Phys. 104 (1996) 6286–6297.
[75] D. Kats, T. Korona, M. Schütz, J. Chem. Phys. 125 (2006) 104106.
[76] D. Kats, T. Korona, M. Schütz, J. Chem. Phys. 127 (2007) 064107.
[77] R.A. Mata, M. Schütz, H.-J. Werner, J. Chem. Phys. 128 (2008) 144106.
[78] E. Runge, E.K.U. Gross, Phys. Rev. Lett. 52 (1984) 997.
[79] P. Hohenberg, W. Kohn, Phys. Rev. 136 (1964) B864.
[80] J. Schirmer, A. Dreuw, Phys. Rev. A 75 (2007) 022513.
[81] N.T. Maitra, R. van Leeuwen, K. Burke, Phys. Rev. A 78 (2008) 056501.
[82] J. Schirmer, A. Dreuw, Phys. Rev. A 78 (2008) 056502.
[83] A. Holas, M. Cinal, N.H. March, Phys. Rev. A 78 (2008) 016501.
[84] S. Kummel, L. Kronik, Rev. Mod. Phys. 80 (2008) 3.
[85] M. Petersilka, U.J. Gossman, E.K.U. Gross, Phys. Rev. Lett. 76 (1996) 1212.
[86] M.A.L. Marques, E.K.U. Gross, Ann. Rev. Phys. Chem. 55 (2004) 427.
[87] D.J. Tozer, J. Chem. Phys. (2003) 119.
[88] T. Yanai, D.P. Tew, N.C. Handy, Chem. Phys. Lett. 393 (2004) 51.
[89] M.J.G. Peach, P. Benfield, T. Helgaker, D.J. Tozer, J. Chem. Phys. 128 (2008) 044118.
[90] K. Kowalski, P. Piecuch, J. Chem. Phys. 120 (2004) 1715.
[91] S.J.A. Gisbergen, C.F. Guerra, E.J. Baerends, J. Comput. Chem. 21 (2000) 1511.
[92] F.N. Keutsch, R.J. Saykally, Proc. Nat. Acad. Sci. 98 (2001) 10533.
[93] J.N. Harvey, J.O. Jung, R.B. Gerber, J. Chem. Phys. 109 (1998) 8747.
[94] R.E. Verral, W.A. Senior, J. Chem. Phys. 50 (1969) 2746.
[95] J.M. Heller Jr., R.N. Hamm, R.D. Birkhoff, L.R. Painter, J. Chem. Phys. 60 (1974) 3483.
[96] J.M. Heller Jr., R.D. Birkhoff, L.R. Painter, J. Chem. Phys. 67 (1977) 1858.
[97] T.I. Quickenden, J.A. Irvin, J. Chem. Phys. 72 (1980) 4416.
[98] H. Hayashi, N. Watanabe, Y. Udagawa, C.-C. Kao, J. Chem. Phys. 108 (1998) 823.
[99] R.R. Dagastine, D.C. Prieve, L.R. White, J. Colloid Interface Sci. 231 (2000) 351.
[100] V. Garbuio, M. Cascella, L. Reining, R. Del Sole, O. Pulci, Phys. Rev. Lett. 97 (2006) 137402.
[101] G. Brancato, N. Rega, V. Barone, Phys. Rev. Lett. 100 (2008) 107401.
[102] D. Lu, F. Gygi, G. Galli, Phys. Rev. Lett. 100 (2008) 147601.
[103] R.A. Mata, B.J.C. Cabral, C. Millot, K. Coutinho, S. Canuto, J. Chem. Phys. 130 (2009) 014505.
[104] U. Niesar, G. Corongiu, E. Clementi, G.R. Kneller, D.K. Bhatacharya, J. Phys. Chem. 94 (1990) 7949.
[105] C. Millot, B.J.C. Cabral, Chem. Phys. Lett. 460 (2008) 466.
[106] A.N. Brito, R. Feifel, A. Mocelin, A.B. Machado, S. Sundin, I. Hjelte, et al., Chem. Phys. Lett. 309 (1999) 377.
[107] C.J.F. Bøttcher, Theory of Electric Polarization, Elsevier, Amsterdam, 1973.
[108] T.H. Dunning Jr., J. Chem. Phys. 90 (1989) 1007.
[109] R.A. Kendall, T.H. Dunning Jr., R.J Harrison, J. Chem. Phys. 96 (1992) 6796.
[110] D.E. Woon, T.H. Dunning Jr., J. Chem. Phys. 98 (1993) 1358.
[111] P. Norman, D.M. Bishop, H.J. Aa, J. Oddershede, J. Chem. Phys. 115 (2001) 10323.
[112] C.M. Breneman, K.B. Wiberg, J. Comput. Chem. 11 (1990) 361.
[113] B. Winter, R. Weber, W. Widdra, M. Dittmar, M. Faubel, I.V. Hertel, J. Phys. Chem. A 108 (2004) 2625.
[114] B. Winter, Nucl. Instrum. Methods Phys. Res. Sect. A 601 (2009) 139.
[115] P. Hunt, M. Sprik, R. Vuilleumier, Chem. Phys. Lett. 376 (2003) 68.
[116] P.C. do Couto, R.C. Guedes, B.J.C. Cabral, J.A.M. Simoes, J. Chem. Phys. 119 (2003) 7344.
[117] P.C. do Couto, B.J.C. Cabral, S. Canuto, Chem. Phys. Lett. 429 (2006) 129.
[118] B.T. Pickup, O. Goscinsky, Mol. Phys. 26 (1973) 1013.
[119] J. Linderberg, Y. Öhrn, Propagators in Quantum Chemistry, John Wiley, New Jersey, 1973.
[120] L.S. Cederbaum, W. Domcke, Adv. Chem. Phys. 26 (1977) 206.

[121] J.V. Ortiz, J. Chem. Phys. 104 (1996) 7599.
[122] D.P. Chong, O.V. Gritsenko, E.J. Baerends, J. Chem. Phys. 116 (2002) 1760.
[123] S. Hamel, P. Duffy, M.E. Casida, D.R. Salahub, J. Electron Spectrosc. Relat. Phenom. 123 (2002) 345.
[124] J.V. Coe, A.D. Earhart, M.H. Cohen, G.J. Hoffman, H.W. Sarkas, K.H. Bowen, J. Chem. Phys. 107 (1997) 6023.
[125] D. Grand, A. Bernas, E. Amouyal, Chem. Phys. 44 (1979) 73.
[126] J.C. Thompson, Electrons in Liquid Ammonia, Oxford University, London, 1976.
[127] E.J. Hart, M. Anbar, The Hydrated Electron, John Wiley, New York, 1970.
[128] T.S. Almeida, K. Coutinho, B.J.C. Cabral, S. Canuto, J. Chem. Phys. 128 (2008) 014506.
[129] M. Seydou, A. Modelli, B. Lucas, K. Konate, C. Desfrançois, J.P. Schermann, Eur. Phys. J. D 35 (2005) 199.
[130] R.N. Barnett, U. Landman, C.L. Cleveland, N.R. Kestner, J. Jortner, Chem. Phys. Lett. 148 (1988) 249.
[131] M.J. Blandamer, M.F. Fox, Chem. Rev. 70 (1970) 59.
[132] C. Dessent, J.J. Kim, M.A. Johnson, Acc. Chem. Res. 31 (1998) 527.
[133] X. Chen, E. Bradforth, Annu. Rev. Phys. Chem. 59 (2008) 203.
[134] N. Takahashi, K. Sakai, T. Tanida, I. Watanabe, Chem. Phys. Lett. 183 (1995) 246.
[135] D. Majumdar, J. Kim, K.S. Kim, J. Chem. Phys. 112 (2000) 101.
[136] J. Kim, H.M. Lee, S.B. Suh, D. Majumdar, K.S. Kim, J. Chem. Phys. 113 (2000) 5259.
[137] W.-S. Sheu, Y.-T. Liu, Chem. Phys. Lett. 374 (2003) 620.
[138] D. Serxner, C.E.H. Dessent, M.A. Johnson, J. Chem. Phys. 105 (1996) 7231.
[139] N. Galamba, R.A. Mata, B.J.C. Cabral, J. Phys. Chem. A 113 (2009) 14684.
[140] S.E. Bradforth, P. Jungwirth, J. Phys. Chem. A 106 (2002) 1286.
[141] W.H. Robertson, M.A. Johnson, Ann. Rev. Phys. Chem. 54 (2003) 173.
[142] S.S.M.C. Godinho, P.C. do Couto, B.J.C. Cabral, Chem. Phys. Lett. 419 (2006) 340.
[143] G. Brancato, N. Rega, V. Barone, J. Chem. Phys. 125 (2006) 164515.
[144] M.E. Martín, M.L. Sánchez, F.J. Olivares del Valle, M.A. Aguilar, J. Chem. Phys. 113 (2000) 6308.
[145] V. Ludwig, K. Coutinho, S. Canuto, Phys. Chem. Chem. Phys. 9 (2007) 4907.
[146] S. Iwata, K. Morokuma, J. Am. Chem. Soc. 97 (1975) 966.
[147] S.A. do Monte, T. Müller, M. Dallos, H. Lischka, M. Diedenhofen, A. Klamt, Theor. Chim. Acta 111 (2004) 78.
[148] F. Aquilante, V. Barone, B.O. Roos, J. Chem. Phys. 119 (2003) 12323.
[149] R. Improta, V. Barone, J. Am. Chem. Soc. 126 (2004) 14320.
[150] S. Millefiori, A. Alparone, Chem. Phys. 303 (2004) 27.
[151] C. Zazza, A. Amadei, N. Sanna, A. Grandi, G. Chillemi, A. Di Nola, et al., Phys. Chem. Chem. Phys. 8 (2006) 1385.
[152] R.A. Mata, Mol. Phys. in press (2009).

CHAPTER 5

Molecular Dynamics of Polypeptides and Their Inclusion Compounds with β-Cyclodextrin in Aqueous Solution Using DC–SCC–DFTB/UFF Approach

Guilherme Ferreira de Lima[a], **Thomas Heine**[b] and **Hélio Anderson Duarte**[a]

Contents

[a] Departamento de Química, ICEx, Universidade Federal de Minas Gerais, UFMG, 31270-901 Belo Horizonte, MG, Brazil
[b] School of Engineering and Science, Jacobs University, Bremen, 28759 Bremen, Germany
E-mail address: duarteh@ufmg.br (H.A. Duarte)

Advances in Quantum Chemistry, Vol. 59
ISSN: 0065-3276, DOI: 10.1016/S0065-3276(10)59005-1

© 2010 Elsevier Inc.
All rights reserved

1. INTRODUCTION

Water plays an important role for most chemical processes that are relevant for the environment, biology, and technology. Water-assisted reactions in catalysis [1,2] and biochemistry [3], chemical speciation [4,5], mineralogy [6–8], supramolecular chemistry [9–11], and nanoreactors [12,13] are some of the areas for which water is an active medium creating the environment necessary for the favorableness of chemical processes. Understanding the role of water in the chemical phenomena is the crucial point for bringing up new breakthroughs in many frontier fields of chemistry and physics. Many sophisticated techniques such as nuclear magnetic resonance (NMR) spectroscopy and nuclear overhauser effects (NOE) [14], spectroscopic and ultrafast electronic excitation techniques [15] are now used to acquire fundamental knowledge about the influence of water in different phenomena providing new perspectives on a wide range of reactions and processes [16].

The intermolecular interactions leading to association species and inclusion compounds in aqueous solution are of particular interest. Computer simulation of such challenging systems is very important to understand the intrinsic interactions involved, the dynamics, and the driving forces that govern the phenomena. An example of such system is the polypeptides in aqueous solution and their interaction with macromolecules forming inclusion and association compounds.

The heptapeptide Angiotensin-(1–7) [17]—(Ang-(1–7)—in aqueous solution has attracted our attention because of its great potential to treat cardiovascular diseases due to its activity in the rennin–angiotensin systems (RAS) [17,18]. NMR technique has been applied and a majority of the resonances were accomplished by rotating frame overhauser enhancement spectroscopy (ROESY), total correlation spectroscopy (TOCSY), and correlation spectroscopy (COSY) peak coordinates, and have permitted a detailed analysis of the conformation and their inclusion to β-Cyd [14]. Bradykinin potentiating peptides (BPPs) [19] have also attracted our attention, as these compounds were the first naturally occurring angiotensin-converting enzyme (ACE) inhibitors described in the literature [19]. The BPPs activity is related to the potentiation of the hypotensive effects of Bradykinin, and also by inhibition of the conversion of Angiotensin-I into Angiotensin-II [20]. These classes of peptides were essential for the development of the Captopril®, the first commercial ACE inhibitor, used nowadays clinically for cardiovascular dysfunction treatment [21–23]. Particularly, the inclusion compound of Ang-(1–7):β-Cyd is of great interest because of its technological importance.

The self-consistent charge–density functional tight-binding (SCC–DFTB) method has been extensively used with remarkable success to describe large organic molecules such as those found in the biological field. Elstner and collaborators [24] were the first to propose the strategy of using SCC–DFTB combined with molecular mechanics to treat large biologically relevant molecules [24,25]. Rhodopsin, relative p*K*a's of proteins, enzymes, proton transfer, ATP hydrolysis in myosin, and dizinc β-lactamase are some of the systems that have been successfully treated using the SCC–DFTB/MM method [26–33]. In most of these systems, part of the protein was treated quantum mechanically, whereas the remaining structure was described by an appropriate force field. Water molecules were included in some of these systems, and they have usually been treated classically.

In the present work, we explore the simulation of polypeptides and their inclusion compounds with the β-cyclodextrin (β-Cyd) in aqueous solution using the combined QM/MM method where the QM is the SCC–DFTB method including empirical London dispersion correction (DC), and MM is described by the universal force field (UFF), augmented by Coulomb interactions which are in-line with the quantum method. This is a good compromise between a first-principle method and an empirical force field. The aim is to establish the method which is able to describe systems of larger complexity such as those involved in self-assembly and nanoreactors. Cyclodextrins have been extensively studied because of their technological and biological importance that is used as drug delivery device and, more recently, as nanoreactors [34]. In the last decade, many reviews [34–45] have been dedicated to the dynamics and thermodynamics of cyclodextrins in aqueous solution and their inclusion compounds with biologically relevant molecules.

2. THEORETICAL APPROACH

This section is organized as follows. A brief review of the SCC–DFTB method will be given. A posteriori treatment of London dispersion interactions will be discussed followed by the presentation of QM/MM implementation with mechanical and with electrostatic embedding will be discussed. All methods are implemented in an experimental version of the deMon computer code [46].

2.1. Density functional tight-binding method

DFTB uses density functional theory (DFT) as basis for the establishment of a tight-binding method. Many reviews about DFTB and its extensions are now available [47–49]. We will limit ourselves to the practical part of the SCC–DFTB method and its implementation.

In the Kohn–Sham (KS) formalism, the total energy can be calculated as follows:

$$E[\rho] = \sum_i n_i \varepsilon_i - \frac{1}{2}\int \frac{\rho(\vec{r})\rho(\vec{r}\,')}{|\vec{r}-\vec{r}\,'|}\mathrm{d}^3r\mathrm{d}^3r' + E_{xc}[\rho] - \int v_{xc}(\vec{r})\rho(\vec{r})\mathrm{d}^3r. \tag{1}$$

n_i denotes the occupation number of the orbital. The basic idea of DFTB is to write the electronic density as a reference density ρ_0 plus a small fluctuation $\delta\rho$ [50],

$$\rho(\vec{r}\,') = \rho_0(\vec{r}) + \delta\rho(\vec{r}). \tag{2}$$

Inserting Eq. (2) in (1), and after some arrangements, we write the total energy equation according to Eq. (3):

$$E = \underbrace{\sum_i n_i \left\langle \psi_i \middle| \hat{H}^0 \middle| \psi_i \right\rangle}_{E_{\mathrm{bnd}}} + E_{\mathrm{rep}}[\rho_0] + E_{\mathrm{2nd}}[\delta\rho, \rho_0]. \tag{3}$$

The first term contains a reference Hamiltonian $\hat{H}^0$ that depends only on the reference density ρ_0:

$$\hat{H}^0 = -\frac{1}{2}\nabla^2 + \underbrace{v_{\mathrm{ext}}(\vec{r}) + \int \frac{\rho'_0}{|\vec{r}-\vec{r}\,'|}\mathrm{d}\vec{r}\,' + v_{\mathrm{xc}}[\rho_0]}_{v_{\mathrm{KS}}[\rho_o]}. \tag{4}$$

The sum in the first term of Eq. (3), E_{bnd}, is the sum over the energies of all occupied orbitals. The second term of Eq. (3) defines the repulsive contribution,

$$E_{\mathrm{rep}}[\rho_0] = -\frac{1}{2}\iint \frac{\rho'_0\rho_0}{|\vec{r}-\vec{r}\,'|}\mathrm{d}\vec{r}\mathrm{d}\vec{r}\,' + E_{\mathrm{xc}}[\rho_0] - \int v_{\mathrm{xc}}[\rho_0]\rho_0\mathrm{d}\vec{r} + E_{\mathrm{nn}}. \tag{5}$$

Note that E_{rep}, as defined in Eq. (5), includes the nucleus–nucleus repulsion energy, a quantity of similar magnitude than the first term, the electron–electron repulsion, but with different sign. Finally, the last term in Eq. (3) includes the corrections related to the fluctuations in the electronic density. This term is defined as

$$E_{\mathrm{2nd}}[\rho_0, \delta\rho] = \frac{1}{2}\iint \left(\frac{1}{|\vec{r}-\vec{r}\,'|} + \left.\frac{\delta^2 E_{\mathrm{xc}}}{\delta\rho\delta\rho'}\right|_{\rho_0} \right)\mathrm{d}\vec{r}\mathrm{d}\vec{r}\,'. \tag{6}$$

In order to obtain a good estimate of the reference, electronic density, ρ_0, is written as a superposition of atom-like densities, centered on the nuclei α,

$$\rho_0(\vec{r}) = \sum_{\alpha}^{N} \rho_0^{\alpha}(\vec{r}_\alpha), \qquad \vec{r}_\alpha = \vec{r} - \vec{R}_\alpha. \tag{7}$$

With this approximation, it is assured that E_{rep} does not depend on the electronic-density fluctuations. Furthermore, because of the neutrality of ρ_0^α, the Coulomb contributions become negligible for long distances. Therefore, E_{rep} can be expanded, and because of the screening of terms of more than two centers, one can assume the two-center contributions to be short ranged. However, the repulsion energy does not decay to 0 for long interatomic distances. Instead, it decays to a constant value given by the atomic contributions:

$$\lim_{R_{\alpha\beta}\to\infty} E_{\text{rep}}[\rho_0] = \sum_{\alpha}^{N} E_{\text{rep}}[\rho_0^\alpha]. \tag{8}$$

Thus, $\Sigma_\alpha^N E_{\text{rep}}[\rho_0^\alpha] = 0$ is assumed in order to make E_{rep} dependent only on two-center contributions:

$$E_{\text{rep}}[\rho_0] \approx \frac{1}{2}\sum_{\alpha,\beta}^{N} U[\rho_0^\alpha, \rho_0^\beta]. \tag{9}$$

Although it would be possible to calculate E_{rep} for known values of ρ_0^α, it is more convenient to adjust E_{rep} to ab initio reference calculations. This is in particular motivated by the imbalance in the terms of Eq. (5), where the electron–electron repulsion is approximated and large in magnitude, and is to be compensated by the exact nucleus–nucleus repulsion energy. Thus, E_{rep} is fitted to the difference between the DFT energy and E_{bnd}, as a function of the interatomic distance $R_{\alpha\beta}$ using a suitable reference structure, that is,

$$E_{\text{rep}}[\rho_0] \equiv E_{\text{rep}}(R_{\alpha\beta}) = \{E_{\text{DFT}}(R_{\alpha\beta}) - E_{\text{bnd}}(R_{\alpha\beta})\}|_{\text{ref. struct.}}. \tag{10}$$

In DFTB, the KS orbitals are represented by a linear combination of atomic orbitals (LCAO) centered on the nuclei. Denoting the basis functions by ϕ_ν and the expansion coefficients by $C_{i\nu}$, one can write the KS orbitals in the form

$$\psi_i(\vec{r}) = \sum_{\nu}^{N} C_{i\nu}\phi_\nu(\vec{r} - \vec{R}_\alpha). \tag{11}$$

From this LCAO model, one obtains the secular problem

$$\sum_{\nu}^{N} C_{i\nu}\left(H_{\mu\nu}^0 - \varepsilon_i S_{\mu\nu}\right) = 0,\ \forall \mu, \nu, \tag{12}$$

where the elements $H_{\mu\nu}^0$ of the Hamiltonian matrix and $S_{\mu\nu}$ of the overlap matrix are defined as follows:

$$\begin{aligned} H_{\mu\nu}^0 &= \left\langle \phi_\mu \middle| \hat{H}^0 \middle| \phi_\nu \right\rangle; \\ S_{\mu\nu} &= \left\langle \phi_\mu \middle| \phi_\nu \right\rangle; \end{aligned} \qquad \forall \mu \in \alpha, \nu \in \beta. \tag{13}$$

The second term of Eq. (3) can be transformed, with Eq. (11), into

$$\sum_i n_i \left\langle \psi_i \middle| \hat{H}^0 \middle| \psi_i \right\rangle = \sum_i \sum_{\mu,\nu}^{N} n_i C_{i\mu} C_{i\nu} \left\langle \phi_\mu \middle| -\frac{1}{2}\nabla^2 + v_{\mathrm{KS}}[\rho_0] \middle| \phi_\nu \right\rangle = \mathrm{tr}(P \cdot H^0); \tag{14}$$

in which the elements of the density matrix P are defined as

$$P_{\mu\upsilon} = \sum_i n_i C_{i\mu} C_{i\upsilon}. \tag{15}$$

In 1998, Elstner and coworkers [51] presented an approach to derive the DFTB equations through a second-order expansion of the DFT total energy with respect to the electron density. As a result, the Hamiltonian matrix elements are calculated as density superpositions, according to the following equation:

$$H^0_{\mu\nu} = \left(\phi_\mu \middle| -\frac{1}{2}\nabla^2 + v_{\mathrm{KS}}[\rho_0^\alpha + \rho_0^\beta] \middle| \phi_\nu \right), \; \mu \in \{\alpha\}, \nu \in \{\beta\}. \tag{16}$$

This approach is extensively used for SCC–DFTB. It is, however, also possible to superpose atomic potentials in the Hamiltonian elements, following closer the original tight-binding concept. For more details, the interested reader is referred to reference [49].

The ϕ_ν basis functions and the reference atom-like densities ρ_0^α are obtained by solving the Schrödinger equation

$$\left[-\frac{1}{2}\nabla^2 + v_{\mathrm{KS}}[\rho_0^\alpha] + \left(\frac{r}{r_0}\right)^2 \right] \phi_\nu(\vec{r}\,) = \varepsilon_\nu \phi_\nu(\vec{r}\,), \tag{17}$$

for the free atom within a self-consistent DFT method. The contraction potential $(r/r_0)^2$ in Eq. (17) confines the atomic orbitals and hence their densities, and results in better basis sets for the study of condensed-phase systems and free molecules as well. The value for the parameter r_0 is normally chosen as approximately $2r_{\mathrm{cov}}$, with r_{cov} being the atomic covalent radius [52]. In some cases, r_{cov} has been treated as parameter to improve the accuracy of the method.

In practice, the Hamiltonian matrix elements are calculated as follows: For the diagonal elements, the energy level of the free atom is chosen, which ensures correct dissociation limits. Because of the orthogonality of the basis functions, the off-diagonal elements of the intra-atomic blocks are 0. The interatomic blocks are computed as given in Eq. (16), depending on the choice of potential generation. Within the density superposition approach, the Hamiltonian matrix elements unfold as follows:

$$H^0_{\mu\nu} = \begin{cases} \varepsilon_\mu^{\text{free atom}}, & \mu = \nu, \\ \left\langle \phi_\mu \middle| \hat{T} + v_{\mathrm{KS}}[\rho_0^\alpha + \rho_0^\beta] \middle| \phi_\nu \right\rangle, & \mu \in \{\alpha\}, \nu \in \{\beta\}, \alpha \neq \beta, \\ 0, & \text{otherwise.} \end{cases} \tag{18}$$

It should be noted that the Hamiltonian elements $H^0_{\mu\nu}$ depend only on atoms α and β and, therefore, only the two-center matrix elements are explicitly calculated, as well as two-center elements of the overlap matrix. According to Eq. (18), the free atom eigenvalues form the diagonal of the Hamiltonian matrix, which assure the correct limit for free atoms.

By using ϕ_ν and ρ^α_0, the Hamiltonian and overlap matrix elements can be calculated and tabulated as a function of the distance between atomic pairs. Thus, it is not necessary to recalculate any integrals during, for example, a geometry optimization or molecular dynamics simulation.

2.2. Self-consistent charge–density functional tight-binding

It is well known that the accuracy of the DFTB method decreases when the chemical bonds in the system are controlled by a more delicate charge balance between atoms, especially in the case of heteronuclear molecules and polar semiconductors [51]. It is, therefore, natural to correct the electronic density through inclusion of the second-order contributions E_{2nd} of Eq. (3), which are neglected in DFTB. The SCC–DFTB is an extension of DFTB that improves the description of electronic systems and the transferability of DFTB in the cases where long-range Coulomb interactions are significant.

In order to include the density fluctuations in a simple, yet efficient, way according to a tight-binding approach, $\delta\rho$ is written as the superposition of atom-like contributions $\delta\rho_\alpha$, which fast decays along the distance from the corresponding atomic center,

$$\delta\rho = \sum_{\alpha}^{N} \delta\rho_\alpha, \tag{19}$$

where the atom-like contributions can be simplified with the monopole approximation:

$$\delta\rho_\alpha \approx q_\alpha F^\alpha_{00} Y_{00}. \tag{20}$$

Here q_α is the Mulliken charge, the difference between the atomic Mulliken population p_α[53] and the number of valence electrons of the neutral free atom p^0_α ($q_\alpha = p_\alpha - p^0_\alpha$); F^α_{00} denotes the normalized radial dependence of the density fluctuation in atom α, approximated to spherical by the angular function Y_{00}. In other words, the effects of charge transfer are included, but changes in the shape of the electronic density are neglected. Equation (6) then becomes

$$E_{\text{2nd}} \approx \frac{1}{2}\sum_{\alpha,\beta}^{N} q_\alpha q_\beta \underbrace{\iint \left(\frac{1}{|\vec{r} - \vec{r}'|} + \left.\frac{\delta^2 E_{\text{xc}}}{\delta\rho\delta\rho'}\right|_{\rho_0} \right) F^\alpha_{00} F^\beta_{00} Y^2_{00} \mathrm{d}\vec{r}\mathrm{d}\vec{r}'}_{\gamma_{\alpha\beta}}, \tag{21}$$

in which the notation $\gamma_{\alpha\beta}$ was introduced merely for convenience.

In order to solve Eq. (21), $\gamma_{\alpha\beta}$ must be analyzed. In the limit case where the interatomic separation is very large ($|\vec{R}_\alpha - \vec{R}_\beta| = |\vec{r} - \vec{r}\,'| \to \infty$), one finds, by GGA-DFT, that the exchange-correlation term goes to 0 and $\gamma_{\alpha\beta}$ describes the interaction of two normalized spherical electronic densities, basically reducing to $1/|\vec{R}_\alpha - \vec{R}_\beta|$, thus,

$$E_{\text{2nd}} \approx \sum_{\alpha,\beta}^{N} \frac{q_\alpha q_\beta}{|\vec{R}_\alpha - \vec{R}_\beta|}. \tag{22}$$

In the opposite case, for which the interatomic distance tends to 0 ($|\vec{R}_\alpha - \vec{R}_\beta| = |\vec{r} - \vec{r}\,'| \to 0$), $\gamma_{\alpha\beta}$ describes the electron–electron interaction within the atom α and can be related with the chemical hardness η_α [54], or Hubbard parameter $\gamma_{\alpha\alpha} = 2\eta_\alpha = U_\alpha$. Within the monopole approximation, U_α can be calculated—using a DFT procedure—as the second derivative of the total atomic energy of atom α with respect to its atomic population:

$$E_{\text{2nd}} \approx \frac{1}{2}\frac{\partial^2 E_\alpha[\rho_0]}{\partial p_\alpha^2} q_\alpha^2 = \frac{1}{2} U_\alpha q_\alpha^2. \tag{23}$$

In order to obtain a well-defined and useful expression for systems in all scales, and still keep consistence with the aforementioned approximations, an analytical expression was developed [51] to approximate the density fluctuations with spherical electronic densities.

Then, the total energy within SCC–DFTB is written as

$$E_{\text{SCC}} = \sum_i n_i \left\langle \psi_i \middle| \hat{H}^0 \middle| \psi_i \right\rangle + \frac{1}{2}\sum_{\alpha,\beta}^{N} \gamma_{\alpha\beta} q_\alpha q_\beta + E_{\text{rep}}, \tag{24}$$

with $\gamma_{\alpha\beta} = \gamma_{\alpha\beta}(U_\alpha, U_\beta, |\vec{R}_\alpha - \vec{R}_\beta|)$. Here, the contribution owing to the Hamiltonian $\hat{H}^0$ is exactly the same as in standard DFTB scheme. Note that the first term in Eq. (24) does only simplify to the sum of molecular orbitals (MO) energies—the convenient notation for DFTB—if all charges are 0. Like in the non-self-consistent method, the wave functions ψ_i are expanded in an LCAO model—Eq. (11)—and Eq. (24) gives Eq. (25) as follows:

$$E_{\text{SCC}} = \text{tr}(P \cdot H^0) + \frac{1}{2}\sum_{\alpha,\beta}^{N} \gamma_{\alpha\beta} q_\alpha q_\beta + E_{\text{rep}}. \tag{25}$$

The charge fluctuations are calculated by Mulliken population analysis [53]:

$$p_\alpha = \frac{1}{2}\sum_i n_i \sum_{\mu\in\alpha} \sum_\nu (C_{i\mu} C_{i\nu} S_{\mu\nu} + C_{i\nu} C_{i\mu} S_{\nu\mu}), \tag{26}$$

and secular equations similar to those in Eq. (12) can be obtained, with modified elements in the Hamiltonian matrix:

$$H_{\mu\nu} = \left\langle \phi_\mu \middle| \hat{H}^0 \middle| \phi_\nu \right\rangle + \frac{1}{2} S_{\mu\nu} \sum_{\xi}^{N} (\gamma_{\alpha\xi} + \gamma_{\beta\xi}) q_\xi = H^0_{\mu\nu} + H^1_{\mu\nu}, \qquad \forall \mu \in \alpha, \nu \in \beta. \tag{27}$$

The matrix elements $H^0_{\mu\nu}$ and $S_{\mu\nu}$ are identical to those defined in the standard DFTB method, in Eq. (13). Since the atomic charges depend on the monatomic wave functions ψ_i, it is necessary to use a self-consistent procedure. Once the elements $S_{\mu\nu}$ extend to some neighboring atoms, multiparticle interactions are introduced. The second-order correction is achieved by introducing the elements $H^1_{\mu\nu}$, which depend on the Mulliken charges.

Identically to the standard DFTB, the repulsive potential is fitted according to Eq. (10), using a suitable reference system.

As the SCC correction allows for the explicit treatment of charge–transfer effects, the transferability of E_{rep} is considerably better, in comparison to the non-self-consistent scheme.

As in standard DFTB, a simple analytic expression for the atomic forces can be derived accordingly:

$$\vec{F}_\alpha = -\sum_i n_i \sum_{\mu,\nu}^{N} C_{i\mu} C_{i\nu} \left[\frac{\partial H^0_{\mu\nu}}{\partial \vec{R}_\alpha} - \left(\varepsilon_i - \frac{H^1_{\mu\nu}}{S_{\mu\nu}} \right) \frac{\partial S_{\mu\nu}}{\partial \vec{R}_\alpha} \right] - q_\alpha \sum_{\xi}^{N} \frac{\partial \gamma_{\alpha\beta}}{\partial \vec{R}_\alpha} q_\xi - \frac{\partial E_{\mathrm{rep}}}{\partial \vec{R}_\alpha}. \tag{28}$$

2.3. A posteriori treatment for London dispersion in SCC–DFTB

Despite their weak nature, London interactions—also called dispersion interactions—affect many fundamental processes in chemistry, physics, and biology. They influence, for example, the formation of molecular crystals, the structure of biological molecules such as proteins and DNA, adsorption processes, and π–π stacking interactions.

However, DFTB and also SCC–DFTB treat only short-range atomic potentials, resulting in a short-range Hamiltonian $H^0_{\mu\nu}$. Moreover, long-range electronic interactions, only accounted for in SCC–DFTB, are multiplied with the overlap matrix and hence also effectively short-ranged. Indeed, the matrix elements approach 0 usually at distances closer than the van der Waals minimum. Hence, DFTB completely disregards London dispersion forces [55].

Two treatments meant to include dispersion interactions a posteriori have been proposed [55,56]. In both cases, the dispersion energy E_{disp} is calculated separately using empirical potentials, and then added to the DFTB total energy expression. Since London dispersion forces are totally absent in DFTB, the addition of E_{disp} does not introduce any double-counting errors to the energy.

Since both treatments are somewhat similar, we describe the one we have used in the present work [55]. This correction was implemented in an experimental version of the deMon code [46] and makes use of the UFF force field [57], already available in deMon. The dispersion interaction $U_{\alpha\beta}$ between atoms α and β at a distance R is given in Lennard-Jones-type form, which includes two parameters: van der Waals distance ($R_{\alpha\beta}$) and well depth ($d_{\alpha\beta}$):

$$U_{\alpha\beta}(R) = d_{\alpha\beta}\left[-2\left(\frac{R_{\alpha\beta}}{R}\right)^{6} + \left(\frac{R_{\alpha\beta}}{R}\right)^{12}\right]. \tag{29}$$

The $R_{\alpha\beta}$ and $d_{\alpha\beta}$ parameters are reported in the original UFF paper [57] and are available from H to Lw in the periodic table of elements. In UFF, the diverging short-range part of the van der Waals term is set to 0 according to an adjacency criterion: the calculation of van der Waals interactions are omitted between the atoms and their first and second neighbors according to the bonding map. This imposes an inflexible topology of the system, which is not desirable in a quantum mechanical method. To overcome this problem, Eq. (29) is used only when $U_{\alpha\beta}$ is attractive (London interactions are never repulsive), that is, $R < 2^{-1/6}R_{\alpha\beta}$. In addition, a short-range potential is derived using the polynomial

$$U_{\alpha\beta}^{\text{short-range}}(R) = U_0 - U_1R^n - U_2R^{2n}, \tag{30}$$

where U_0, U_1, and U_2 are calculated to make the interaction energy and their first and second derivatives match Eq. (29) at $R = 2^{-1/6}R_{\alpha\beta}$. The best value suggested for n is 5, which gives the following U_0, U_1, and U_2 parameters [55]:

$$U_0 = \frac{396}{25}d_{\alpha\beta}, \tag{31}$$

$$U_1 = 2^{5/6}\frac{672}{25}\frac{d_{\alpha\beta}}{R_{\alpha\beta}^5}, \tag{32}$$

$$U_2 = -2^{2/3}\frac{552}{25}\frac{d_{\alpha\beta}}{R_{\alpha\beta}^{10}}. \tag{33}$$

Therefore, the dispersion potential for the DFTB method can be written as

$$U_{\alpha\beta}(R) = \begin{cases} d_{\alpha\beta}\left[-2\left(\frac{R_{\alpha\beta}}{R}\right)^{6} + \left(\frac{R_{\alpha\beta}}{R}\right)^{12}\right], & \forall R \geq 2^{-1/6}R_{\alpha\beta}, \\ \frac{396}{25}d_{\alpha\beta} - 2^{5/6}\frac{672}{25}\frac{d_{\alpha\beta}}{R_{\alpha\beta}^5}R^5 + 2^{2/3}\frac{552}{25}\frac{d_{\alpha\beta}}{R_{\alpha\beta}^{10}}R^{10}, & \forall R < 2^{-1/6}R_{\alpha\beta}, \end{cases} \tag{34}$$

and the dispersion energy is given by

$$E_{\mathrm{disp}} = \frac{1}{2}\sum_{\alpha,\beta}^{N} U_{\alpha\beta}(R). \tag{35}$$

This term is then added to the total DFTB energy calculated using standard DC–SCC–DFTB.

2.4. Universal force field implemented in deMon

The implementation of the UFF follows closely the original work of Rappé and coworkers [57]. As noted in Rappé's seminal paper, it is important to provide some additional information of the system to achieve a reasonable performance of the method. In particular, these are bond orders and atomic charges. For the simulation of water, we apply TIP3P charges ($Q_O = -0.842$ and $Q_H = 0.421$). This way, the description of water is very similar to the TIP3P force field [58], but physically more rigorous in several ways: (i) the water molecules are not restricted in their motion, that is, also the three internal degrees of freedom are unconstrained; and (ii) the London dispersion interactions include O—O, O—H, and H—H terms, in contrast to only O—O terms in original TIP3P. With these minor modifications, the water diffusion constant is somewhat lower than that of TIP3P and therefore closer to the experimental value [59].

The UFF implementation in deMon works both for periodic and for finite systems. This way, it is straightforward to control temperature and pressure using adequate thermo- and barostats.

2.5. QM/MM approach

The strategy of using the DC–SCC–DFTB/UFF hybrid method is particularly interesting because of its practical implementation and for the accuracy of SCC–DFTB to treat systems of biological interest. The modified version of deMon contains a QM/MM scheme [60] with mechanical and with electrostatic embedding.

For mechanical embedding, we apply a straightforward subtraction scheme. The system (S) is separated into a core region (C) and its environment (E). The aim of a QM/MM treatment is to describe the core region using QM, while the environment is described at the MM level. Total energy and gradients are then calculated by calculating the full system S at the MM level, and then computing the core area once at the MM and at the QM level. The MM contribution of region C is then subtracted from the quantity describing the full system, while the QM contribution is added to it:

$$\begin{aligned} E &= E_{\mathrm{MM}}(S) - E_{\mathrm{MM}}(C) + E_{\mathrm{QM}}(C) \\ \vec{F} &= \vec{F}_{\mathrm{MM}}(S) + \vec{F}_{\mathrm{MM}}(C) + \vec{F}_{\mathrm{QM}}(C). \end{aligned} \tag{36}$$

The interaction between environment and core region is obviously described by MM and includes both electrostatic and London dispersion interactions. In order to allow a reasonable electrostatic interaction, the charges in the MM region need to be well balanced. In SCC–DFTB/UFF, we use SCC–DFTB Mulliken charges for the UFF Coulomb interactions.

The treatment of electrostatic embedding is a little bit more involved. Here, also the electrostatic polarization of the core region by the environment is respected. To achieve this, the quantum mechanical calculation has to be carried out in the electrostatic field of the environment, which is given by the distribution of point charges present in the MM region. It has to be noted that the total energy of the QM calculation includes the electrostatic interaction with external point charges. As the subtraction scheme used for mechanical embedding already includes the Coulomb interaction between charges in regions S and E, the term needs to be omitted in the energy and gradient contribution of the QM region in Eq. (36). The resulting equations are equivalent to those of Ref [24], but leave the general appearance of the mechanical embedding subtraction scheme untouched.

2.6. Periodic boundary conditions

It is desirable to carry out molecular dynamics simulations in a simulation box. A first reason is the fact that there are no artificial phase boundaries which are found in a finite "drop" model of a solvated biological molecule. Such boundaries usually imply undesirable technical consequences, such as the "evaporation" of water molecules from the "drop" to "vacuum." A further advantage of a simulation box is the accessibility of thermodynamically important quantities like volume, mass density, and pressure. However, the implementation of periodic boundary conditions (PBC) also comes with potential pitfalls, in particular in the computation of long-range interactions.

Our implementation of PBC is aiming at large structures, as various things simplify in this case. First of all, for large unit cell it is not necessary to calculate the band structure, we can work in the Γ point approximation. Furthermore, we will choose unit cells that have translation vectors always exceeding the maximum range of electronic interactions between the atoms of the QM region. Within DFTB, this is easily achieved, as overlap- and Kohn–Sham matrix elements approach 0 usually at a distance of about 5 Å. Our box size shall therefore always exceed 10 Å, and in this case it is justified to use the minimum image convention (for details, see, e.g., Ref. [61]). The minimum image convention is applied to all short-range interactions, which include the electronic interaction in the QM region as well as the bonded interactions in the MM region.

The long-range treatments, that are the London dispersion and electrostatic contributions, require special treatment. The electrostatic contributions are conveniently calculated using the Ewald summation technique. Several implementations are available in the literature and we have decided for a straightforward implementation of the physical equations as given in Ref. [62], which contribute significantly (25%) to the total computer time, but do not dominate. More sophisticated approaches, for example, the particle mesh Ewald summation [63], are also common in modern computer codes. The London dispersion relation is, if cohesion energies are concerned, surprisingly long-ranged. Indeed, as the long-range tail is always attractive, and as it dies off with R^{-4} (if the increase of particles in a growing sphere is respected), interaction radii of up to 100 Å need to be respected if the total energy shall be computed with a final accuracy on the kJ/mol scale. Obviously, the London dispersion influences of such large systems are usually not contributing to any physical effect. They are, however, important if energetics of simulations in unit cells of different size have to be compared. We have therefore approximated the London-dispersion interactions in the long range in order to achieve a size-consistent treatment: One may use the minimum image representation, which is computationally cheap and robust and gives accurate gradients for large enough super cells. For a more accurate treatment, we add a "productive zero" to the Lennard-Jones interaction potential that describes the London dispersion interaction:

$$U_{\alpha\beta}(R) = \max\left(d_{\alpha\beta}\left(\frac{R_{\alpha\beta}}{R}\right)^{12} - \varepsilon, 0\right) - \min\left(-2d_{\alpha\beta}\left(\frac{R_{\alpha\beta}}{R}\right)^{6} + \varepsilon, 0\right), \quad (37)$$

with a reasonable choice of ε, for example, about 0.05 kJ/mol. Here, the minimum of the potential is not touched, and the potential is continuous until it dies off at much shorter distance. Consequently, a much shorter interaction range has to be considered, and the results are size-consistent.

3. POLYPEPTIDES AND THEIR INCLUSION COMPOUNDS WITH β-CYCLODEXTRIN IN AQUEOUS SOLUTION

3.1. β-Cyclodextrin in aqueous solution

Cyclodextrins are probably among the most studied molecules in the last decades because of their large range of technological applications, mainly in the multibillionaire dollar pharmaceutical industries. Many formulations are now available with cyclodextrins working as a drug delivery system enhancing the bioavailability of drugs or providing a way for oral administration [64,65] by increasing its solubility. The chemical properties and their cyclic structures called attention of many researchers which tried to probe their macrocycle properties and the ability to protect hydrophobic molecules or groups in their cavities. The task to assess that an inclusion compound, and not only an association compound, has actually been formed seems to be quite difficult. NMR, neutron scattering diffraction, ultrafast laser microscopy, circular dichroism, and isothermal calorimetry titration [15,16,66–69] have been applied to try to understand the mechanism of inclusion formation.

Notwithstanding, computational chemistry has been applied intensively trying to verify the favorableness of the inclusion compound formation from the thermodynamic point of view. We advance that the use of oversimplified gas-phase models cannot give such information. The water has an important role, which cannot be neglected in any approximation. For instance, in gas phase, any reasonable model will predict that two molecules which can make hydrogen bonds (HBs) and local dipole interactions remain bounded. Understanding and predicting the inclusion compound formation means, invariably, that the model has to take into account explicitly the solvent effects and the dynamics. The entropy is probably the most important contribution and cannot be neglected. We present here the progress of taking into account the solvent effects explicitly for investigating the chemical behavior of β-Cyd in aqueous solution.

β-Cyds are starch-derived cyclic oligomers with seven glucose units. β-Cyd has the shape of a truncated cone enclosing a hydrophobic cavity (Figure 5.1) . The "top" and "bottom" orifice diameters of, respectively, 6.0 Å and 6.5 Å, and a depth of 7.9 Å make the cavity large enough for hosting many biologically active molecules. About seven water molecules are included in the β-Cyd, which have been assessed by X-ray diffraction [70] and neutron diffraction [66,67,71].

Molecular dynamics of β-Cyd in aqueous solution has been performed using the DC–SCC–DFTB/UFF method in our laboratories [59]. The simulation used a 34.9 Å cubic box, containing 1385 water molecules. The trajectories were initially heated up, followed by 20 ps equilibration run using Berendsen thermostat [72] with a coupling parameter of $\tau = 0.1, \ldots, 1.0$ ps. For the microcanonical NVE (constant number of particles, volume, and energy) production run of 0.16 ns, a time step of 0.5 fs was chosen. The total energy remained constant within 0.001 Hartree during the whole simulation. The average temperature during the production run was 303 ± 3 K.

The optimized gas phase geometry calculated using DC–SCC–DFTB and PBE/DZVP method [73] has been compared. The results are in very good agreement with the X-ray diffraction results. The maximum deviation is about 6°. The structural parameters presented in Table 5.1 are related to the distortion of β-Cyd out-of-plane and in-plane with respect to the plan that

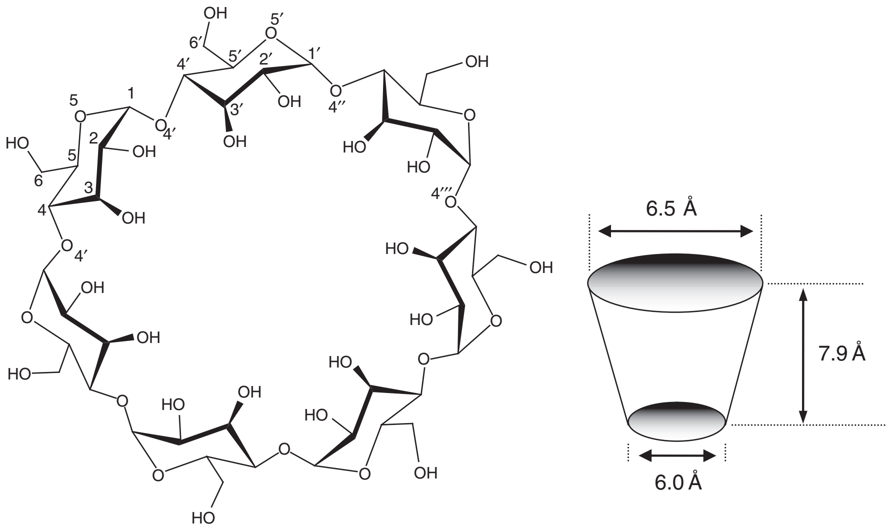

Figure 5.1 Structure of the β-Cyd including the numbering scheme used to define the structural parameters.

crosses the cone. As it is expected, the results of the molecular dynamics show larger deviations. The standard deviation is taken over all equivalent sites and over several snapshots of the trajectory in the case of molecular dynamics (MD).

The O4O4′O4″O4‴ dihedral angle provides information about the deformation of the cavity. It has a minimum at 0°. At gas-phase molecular dynamics, the temperature effect on the geometry can be inferred. It is observed that this dihedral angle is about 27 ± 16° and 14 ± 9° at the DC–SCC–DFTB and UFF levels, respectively. It turns out to be important

Table 5.1 Structural parameters calculated for β-Cyd at DC–SCC–DFTB and PBE/DZVP levels of theory

Angles[a]	DC–SCC–DFTB	PBE/DZVP	DC–SCC–DFTB/UFF MD	Exp[b]
C2C3C4C5	53 ± 1	54 ± 2	36 ± 11	55 ± 3
O4O4′O4″O4‴	–0.2 ± 14	0 ± 5	4.6 ± 19	0.2 ± 9
C1O4′C4′	123 ± 17	116.9 ± 0.9	114 ± 3	118 ± 1
O4O4′O4″	128 ± 3	129 ± 3	126 ± 9	128 ± 2

[a] See Figure 5.1 for the definitions of structural parameters.
[b] Refs. [70,71].

to note that UFF predicts a much harder structure compared to the quantum mechanical DC–SCC–DFTB calculations. The increase of the standard deviations in the case of MD indicates larger degree of fluxionality.

The solvent-induced changes in the β-Cyd structure can be quantified by the root-mean-square deviations (RMSD) of the coordinates between two snapshots of a MD trajectory, as proposed by Lawtrakul et al. [74].

$$\left\langle RMSD \right\rangle = \frac{1}{N_{\{C,O\}}} \sqrt{\sum_{k \in \{C,O\}} \left\langle \left| \vec{r}_k(t) - \vec{r}_k(0) \right|^2 \right\rangle}. \tag{38}$$

In Eq. (38), N denotes the number of nonhydrogen atoms of β-Cyd.

Figure 5.2 shows that RMSD of the coordinates between two snapshots of a MD trajectory (in angstrom) at gas phase and aqueous phase. While for the gas-phase molecular dynamics at 300 K, the RMSD converged to 2 Å, the β-Cyd in solution converged to the RMSD about 1.2 Å. The water surrounding the β-Cyd acts as a cushion, decreasing its free motion. Interestingly, this effect cannot be seen in pure MM calculations using the UFF force field. Obviously, the low energy region of the potential energy surface (PES) for this force field is restricted to the area close to the experimental structure of the sugar, resulting in an excessively rigid sugar framework. As a result, UFF is not able to describe structures that change with temperature or environment, such as β-Cyd, at high precision. This highlights the potential of quantum mechanical methods to describe molecules of biological interest, even if no chemical reaction takes place, as QM methods tend to show a much better transferability than

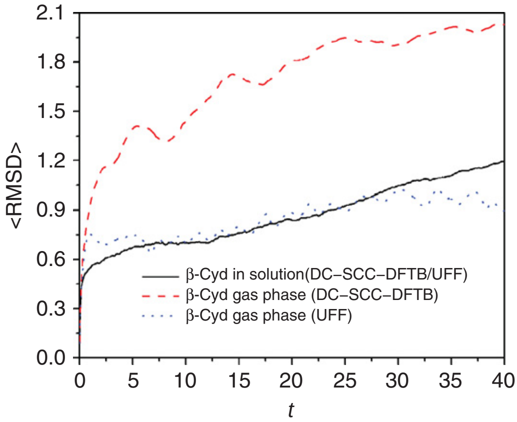

Figure 5.2 Root-mean-square deviation, $\langle RMSD \rangle$, see Eq. (38), of the coordinates between two snapshots of an MD trajectory (in Å) (gas phase in dashed line) against simulation time t (in ps). The simulation in solution is given as black solid line, the DFTB and MM gas phase simulation as dashed line and dotted line, respectively. Please refer online version for color image.

an MM method. A similar increase in flexibility could be expected from a classical force field which is more specialized for biological applications. The average values of dihedrals, angles, and distances are very similar to those of optimized structures. However, the standard deviations are much larger because of the flexibility of the molecule at high temperature. The intramolecular HBs are well described; however, it has observed an increase of the O—O and OH—O distances for the β-Cyd in solution.

The radial distribution function (RDF) of the centers of mass of water with respect to the center of mass of β-Cyd (see Figure 5.3) shows clearly the features because of the water inside and outside of the molecule. The first minimum about 4 Å corresponds to the encapsulated water molecules. The two outer minima, at 10.9 Å and 13.8 Å, arise from the first and second solvation shells of β-Cyd, respectively. The integration of the RDF shows that on average seven water molecules are inside the cavity, in good agreement with X-ray [70] and neutron diffraction [66,67,71]. The features of the RDF between 4.0 Å and 7.3 Å are related to water molecules that are weakly bonded to the primary and secondary OH groups at the rim of the cavity. The 7.0 water molecules inside of the cavity are interacting mostly with the glycosidic oxygens. Figure 5.4 illustrates the motion of the water molecules inside of the cavity and of the β-Cyd structure during the dynamics.

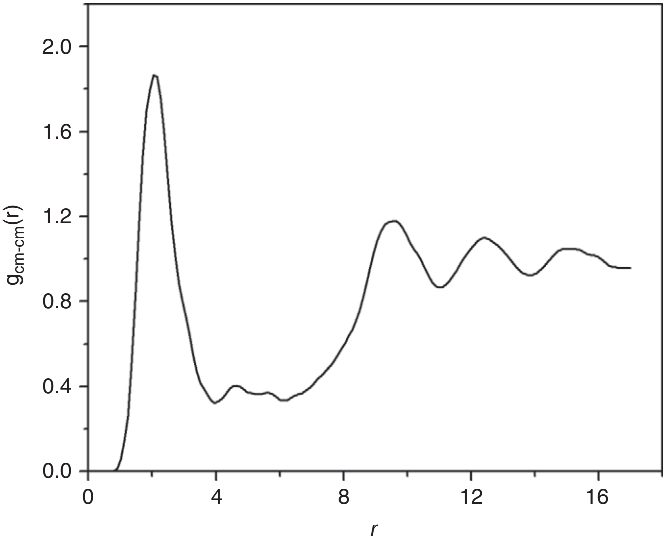

Figure 5.3 Radial distribution function for the distance (in Å) between the centers of mass of β-Cyd and water molecules.

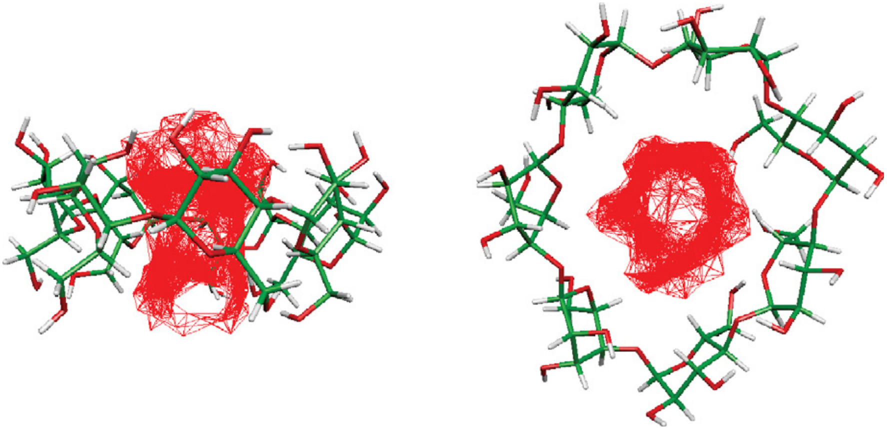

Figure 5.4 Configurational space taken by the water molecules encapsulated in β-Cyd. For sake of clarity, only the initial structure of β-Cyd is shown.

Certainly if one wants to understand the chemical behavior of β-Cyd in solution, it is necessary to investigate the role of the hydrogen bonding of the water molecules with β-Cyd. Following Lawtrakul et al. [74], we define the criterion for the existence of a HB between donor (D) and acceptor (A) that (1) the D—A distance is less than the value corresponding to the first minimum of the respective D–A distance RDF, and (2) the DH—A distance is less than 2.8 Å. The proton acceptor or donor sites are those related to the oxygen sites, namely the primary alcohol O6, secondary alcohols O2 and O3, pyranoids O5, and the glycosidic oxygens O4. About 83 and 27% of the HBs of the glycosidic (O4) and pyranoid (O5) oxygens, respectively, are formed with the encapsulated waters. More than 92% of the HBs of the primary and secondary hydroxyls are formed with water molecules of the outer solvent. About 36% of the seven encapsulated waters form HBs with the glycosidic oxygens, and 25% with the pyranoid oxygens. It is important to note that 8% of HBs of the primary and secondary hydroxyls be formed with the encapsulated water molecules, this is only possible because the solvated β-Cyd at ambient conditions is extremely flexible, allowing the pyranoid rings to undergo major distortions which are needed to form these HBs. The results are in qualitative agreement with the findings based on a quasi-elastic neutron scattering study of β-Cyd, which showed that at room temperature the inner water molecules undergo an extensive positional disorder with only three water positions fully occupied.

The dwell time distribution of the water molecules in the cavity has strong peak at 70 ps with a very wide distribution, indicating that many water molecules remain in the cavity much longer about a few hundreds of picoseconds. It is important to highlight that, roughly, 64% of the water molecules enter the cavity through the 17% larger bottom opening. This effect may arise due to synergy of two factors: (1) approximately one-third of the HBs in solvated β-Cyd is formed by the primary hydroxyl groups at O6 and these HBs are involved in an interlocked network, reducing water mobility at the "top" (smaller) aperture; (2) the flexible sugar backbone allows the "bottom" orifice to distort, accommodating solvent dynamics and increasing water mobility in this area. These factors lead to a more pronounced difference in water dynamics than one might expect from the purely geometrical difference of the bottom and top apertures.

3.2. BPP7a

The BPP7a presents a primary sequence with seven amino acid residues, similar to other BPPs (Figure 5.5), which hold similar features as a high content of proline residues and the tripeptide Ile-Pro-Pro at the C-terminus portion [20]. Numerous challenges must be addressed before peptides and proteins can be fully implemented successfully in pharmaceutical formulations. The challenges include poor bioavailability after oral administration and intestinal membrane permeability, solubility and principally its chemical and enzimatic instability, in function of their degradation by the stomach, and the intestine digestive enzymes [75]. The inclusion compound

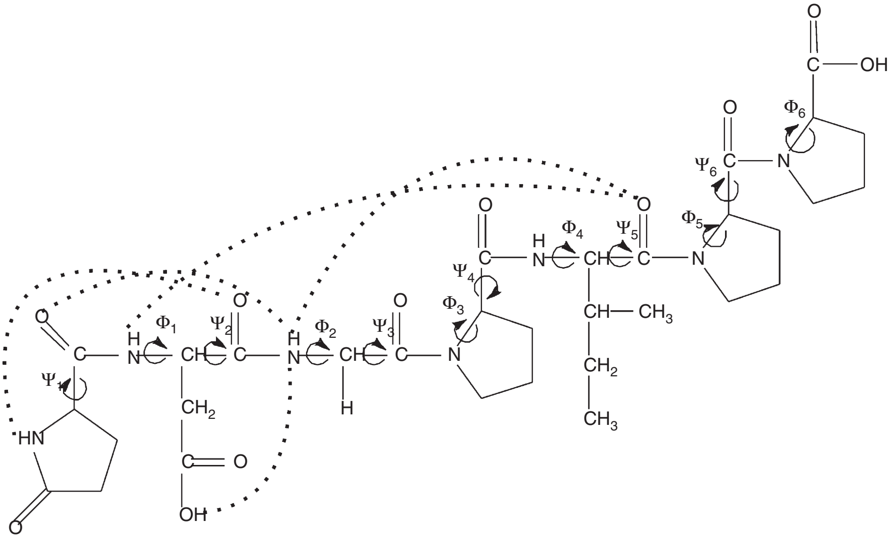

Figure 5.5 The chemical structure of BPP7a, [p-Glu^{1}Asp^{2}Gly^{3}Pro^{4}Ile^{5}Pro^{6}Pro^7]. For clarity, dihedral angles and intramolecular HBs are indicated.

of the polypeptide with β-Cyd has been envisaged to overcome the problem of solubility and bioavailability. However, recent investigations showed that the β-Cyd and BPP7a interacts forming association compounds [76]. The encapsulation of the BPP7a or one of the residues has not been observed.

The behavior of BPP7a in aqueous solution has been investigated through molecular dynamics using DC–SCC–DFTB/UFF method in our laboratory. The simulation used a 36 Å cubic box, containing 1300 water molecules. The trajectories were initially heated up, followed by 20 ps equilibration run using Berendsen thermostat [72] with a coupling parameter of $t = 0.1, \ldots, 1.0$ ps. For the microcanonical NVE production run of 0.1 ns, a time step of 0.5 fs was chosen. The total energy remained constant within 0.05 Hartree during the whole simulation. The average temperature during the production run was 300.3 ± 2.7 K.

Figure 5.6 shows $\langle RMSD \rangle$, plotted against simulation time for BPP7a in gas phase and in solution. In solution, $\langle RMSD \rangle$ converges to an asymptotic value of approximately 1.9 Å. The $\langle RMSD \rangle$ was also estimated for the BPP7a in gas phase at the DC–SCC–DFTB and UFF levels of theory, for comparison. At DC–SCC–DFTB, the $\langle RMSD \rangle$ converges to 1.1 Å, indicating a less flexible molecule. In fact, BPP7a yarns maximizing the intramolecular HBs and decreasing its flexibility. It is important to highlight that, using

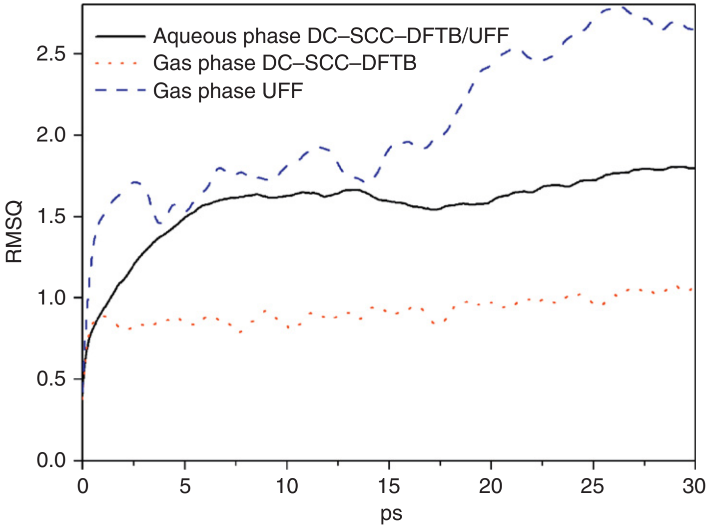

Figure 5.6 Root-mean-square deviation, $\langle RMSD \rangle$, see Eq. (38), of the coordinates between two snapshots of an MD trajectory (in Å) against simulation t (in ps). The simulation in solution is given as black solid line, the DFTB and UFF gas-phase simulation as dotted line and dashed line, respectively.

the force field UFF to describe the BPP7a, the molecule is much more flexible, increasing the $\langle RMSD \rangle$ to 2.20 Å. This highlights the limitations of the force fields for describing correctly the whole potential energy surface. In spite of the predominant presence of hydrophobic proline and isoleucine residues in BPP7a, the intermolecular HBs of the backbone, the *p*-glutamic and aspartate residues with the water solvent weak the intramolecular HBs enhancing its flexibility in aqueous solution.

In Table 5.2, structural parameters of the optimized BPP7a are compared with those in aqueous solution. The latter ones are the time averages of the mean values, as discussed above. The differences with the gas phase DC–SCC–DFTB results are not larger than 30°. The exception is for Φ_2 (asp-gly), Ψ_3 (gly-pro), and Φ_4 (pro-ile) dihedral angles that are larger than 70° difference from the gas-phase result. This is probably due to the lack of steric hindrance of glycine and isoleucine residues. The backbone of the polypeptide is relatively rigid and the residues are flipping around the equilibrium geometry. The configurational space taken by BPP7a in aqueous solution is shown in Figure 5.7. Because of the steric hindrance, proline is not a good candidate to be included in β-Cyd. On the other side, the isoleucine and aspartate residues can be good candidates. However, the DC–SCC–DFTB/UFF simulation in aqueous solution shows that these residues are much flexible with large standard deviations of the dihedral

Table 5.2 Structural parameters calculated for BPP7a at the DC–SCC–DFTB and DFT/PBE levels of theory

Angle	B3LYP/6-31 + G(d)	DC–SCC–DFTB	DC–SCC–DFTB/ UFF MD
Ψ_1 (glu-asp)	27.0	46.4	29 ± 22
Φ_1 (glu-asp)	–118.6	–73.2	–56 ± 89
Ψ_2 (asp-gly)	27.9	38.0	43 ± 29
Φ_2 (asp-gly)	–176.7	130.4	59 ± 134
Ψ_3 (gly-pro)	166.6	–148.2	13 ± 169
Φ_3 (gly-pro)	–86.7	–80.6	–47 ± 70
Ψ_4 (pro-ile)	61.5	80.5	60 ± 17
Φ_4 (pro-ile)	–114.1	–134.3	–70 ± 113
Ψ_5 (ile-pro)	96.3	133.8	130 ± 44
Φ_5 (ile-pro)	–71.2	–66.1	–39 ± 64
Ψ_6 (pro-pro)	127.0	129.9	130 ± 60
Φ_6 (pro-pro)	–83.3	–75.2	–38 ± 61

Note: Angles are given in degrees (°). HB distances are in Angstrom (Å). See Figure 5.5 for the definitions of structural parameters.

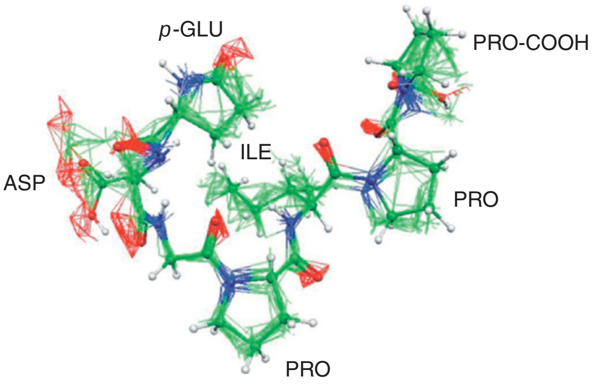

Figure 5.7 Configurational space spawned by BPP7a based on DC–SCC–DFTB/UFF molecular dynamics simulation.

angles (see Table 5.2). This reinforces the unfavorableness of the isoleucine and aspartate residues to form guest:host inclusion compound since it would be accompanied by a decrease of entropy due to the loss of flexibility. Therefore, the formation of association through intermolecular HBs between β-Cyd and BPP7a is more plausible as it was observed experimentally [76].

As a final structural property, we analyze the formation of HBs between BPP7a and water. The terminal GLU residue has about 3.9 ± 1.3 HB's and ASP residue with its carboxylic group presents about 4.8 ± 1.1 HB's. The terminal carboxylic group has an average number of HB's about 4.8 ± 1.5. Figure 5.5 shows that the most prominent intramolecular HB's in the BPP7a, which are mostly involved with the ASP residue and the peptide backbone.

The RDFs of the water surrounding the different residue for the BPP7a have been calculated and the number of water molecules in the first solvation shell estimated. The RDFs are related to the distances of the residue center of mass and the water. On average, the first solvation shell around the residues is about 6 Å from its center of mass with about 16 water molecules in good agreement with the results for the residues of Ang-(1–7) in aqueous solution using the same methodology [14]. The proline residues have in its first solvation sphere about 19 water molecules with the exception of pro2, that have only 14 water molecules, probably due to its proximity to the nonpolar ILE residue. ASP, GLU, and ILE residues have about 16, 14, and 12 water molecules, respectively, and the small GLY residue only 6 water molecules in the first solvation shell. The terminal group —COOH has 14 water molecules in the first solvation shell.

3.3. Angiotensin-(1–7) in aqueous solution

The biologically active heptapeptide Ang-(1–7), with the amino acid sequence AspArgValTyrIleHisPro, Ang-(1–7) (Figure 5.8) inhibits vascular smooth muscle cell growth and contributes to the regulation of blood pressure. Ang-(1–7) belongs to the angiotensin family of peptides, and evidence suggests that it could be used to treat cardiovascular diseases [77,78].

Recently, inclusion compounds of Ang-(1–7) and β-Cyd (CD) have been proposed as a formulation to overcome the problem of degradation of the drug due to the digestive enzymes of the stomach [14]. It has been studied recently the heptapeptide Ang-(1–7) with the amino acid sequence AspArgValTyrIleHisPro and its β-Cyd inclusion compound by using different physical–chemical techniques and the complete attribution of their NMR signal [14].

The flexibility of the backbone and the different residues of the heptapeptide Ang-(1–7) is important for the understanding the chemical behavior of this molecule in solution and its interaction with cyclodextrins. The solvent water has an important role in stabilizing the different conformations.

The structure and the dynamics of Ang-(1–7) at aqueous solution using the DC–SCC–DFTB/UFF method have been analyzed. For Ang-(1–7), the simulation box is cubic with an adequate lattice vector length of 55.15 Å, including 5564 water molecules and solute. All trajectories have been carefully heated up and finally equilibrated for 90 ps using the Berendsen thermostat [72] with a coupling parameter of $\tau = 0.1, \ldots, 1$ ps. For the production run of 80 ps, a time step of 0.5 fs was chosen. The microcanonical

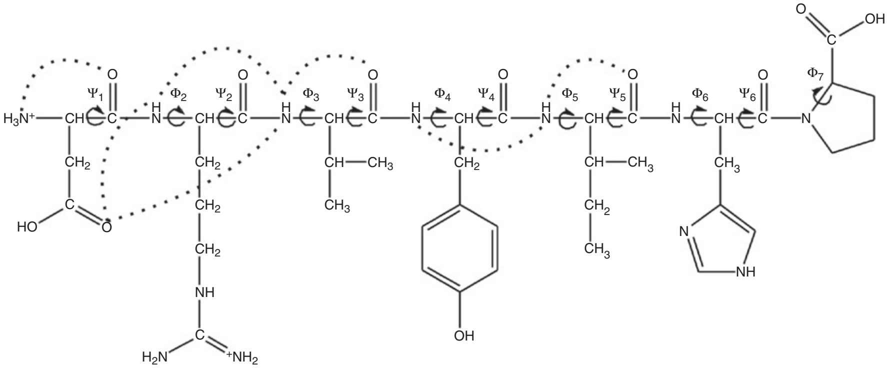

Figure 5.8 The chemical structure of angiotensin-(1–7), [AspArgValTyrIleHisPro]. Dashed lines show the intramolecular HBs present during the simulation of Ang-(1–7) in aqueous solution. See text for detail.

NVE ensemble was used during the production run. The total energy remained constant within 0.001 Hartree during the whole simulation and did not show a drift. The average temperature during the production run was 300.4 ± 1.3 K.

The Ang-(1–7) was firstly optimized in the gas phase as a benchmark for the DC–SCC–DFTB method. The optimized parameters of the Ang-(1–7) gas-phase structure are compared to a PBE/DFT calculation and the results are shown in Table 5.3. The backbone dihedral angles are well described compared to the PBE/DFT results. The largest difference is for Ψ_3, which is related to the valine residue. The differences in the backbone dihedral angles are not larger than 30°.

Structural parameters of the optimized Ang-(1–7) have been compared with those of Ang-(1–7) in aqueous solution. The differences with the gas phase DC–SCC–DFTB results are not larger than 80°. The exceptions are the Φ_2 (arg-val) and Ψ_4 (tyr-ile) dihedral angle, which are about 100° difference from the gas-phase result. This is probably due to the tradeoff between the intra- and intermolecular HBs. The backbone of the polypeptide is relatively rigid and the residues are flipping around the equilibrium geometry.

Figure 5.9 shows $\langle RMSD \rangle$, plotted against simulation time for Ang-(1–7) in gas phase and in solution. In solution, $\langle RMSD \rangle$ converges to an

Table 5.3 Structural parameters calculated for Ang-(1–7) at the DC–SCC–DFTB and DFT/PBE levels of theory

Angle	DC–SCC–DFTB	PBE/DZVP	DC–SCC–DFTB/UFF MD	
	Ang-(1–7)	Ang-(1–7)	Ang-(1–7)	Ang-(1–7):β-Cyd
Ψ_1 (asp-arg)	76.0	65.0	137 ± 57	–60 ± 115
Ψ_2 (arg-val)	28.9	38.3	70 ± 29	–71 ± 129
Φ_2 (arg-val)	–132.4	–148.0	–34 ± 151	94 ± 139
Ψ_3 (val-tyr)	109.5	72.4	143 ± 38	130 ± 22
Φ_3 (val-tyr)	–67.5	–80.7	–67 ± 109	–34 ± 60
Ψ_4 (tyr-ile)	–42.5	–45.3	60 ± 36	–35 ± 67
Φ_4 (tyr-ile)	–60.9	–64.5	–56 ± 85	–74 ± 135
Ψ_5 (ile-his)	63.6	40.3	144 ± 28	–8 ± 38
Φ_5 (ile-his)	27.3	53.2	–53 ± 94	–66 ± 97
Ψ_6 (his-pro)	156.1	167.5	61 ± 25	–22 ± 52
Φ_6 (his-pro)	60.1	65.2	47 ± 15	–62 ± 106
Φ_7 (pro)	–89.3	–93.4	–43 ± 62	–34 ± 59

Note: Angles are given in degrees (°). HB distances are in Angstrom (Å). See Figure 5.8 for the definitions of structural parameters.

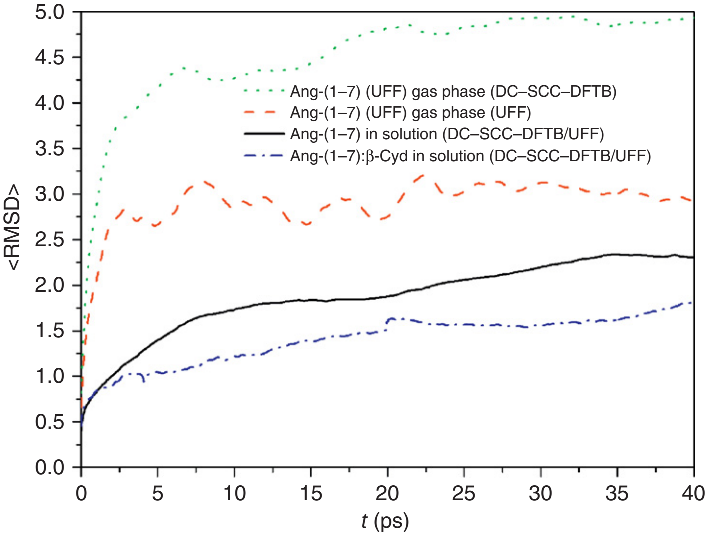

Figure 5.9 Root-mean-square deviation, $\langle RMSD \rangle$, see Eq. (38), of the coordinates between two snapshots of an MD trajectory (in Å) against simulation time t (in ps). The Ang-(1–7) and Ang-(1–7):β-Cyd in solution simulations are given as solid and dashed-dotted lines, respectively. The DC–SCC–DFTB and UFF Ang-(1–7) gas-phase simulations are given as dotted and dashed lines, respectively. Please refer online version for color image.

asymptotic value of approximately 1.8 Å. In gas phase, the molecule completely changes its geometry during the simulation at 300 K, converging to the value around 4.5 Å at the DC–SCC–DFTB level of theory. Actually, the water surrounding the Ang-(1–7) acts as a cushion, decreasing its free motion. As it has been pointed out elsewhere [14], this effect cannot be seen in pure MM calculations using the UFF force field.

The configurational space taken by Ang-(1–7) in aqueous solution is shown at Figure 5.10. The peptide dihedral angles—Ψ's and Φ's—have averages with large standard deviations of about 80°. The Ψ_3 and Ψ_4 dihedral angles that are related to the tyrosine motion present the smallest standard deviations of about 37°. Tyrosine is relatively rigid in comparison to the other residues along the simulation. This can have important consequences for the inclusion compound. Decrease of entropy is normally accompanied by the interaction of the guest:host inclusion compound due to the loss of flexibility. However, if the tyrosine is included, the loss of entropy is minimized. This is in agreement with the NMR-based structure that shows small flexibility of the tyrosine and arginine residues [14].

As a final structural property, we analyze the formation of HBs between Ang-(1–7) and water. Table 5.4 shows the average number of water molecules forming HBs with the proton acceptor sites in each

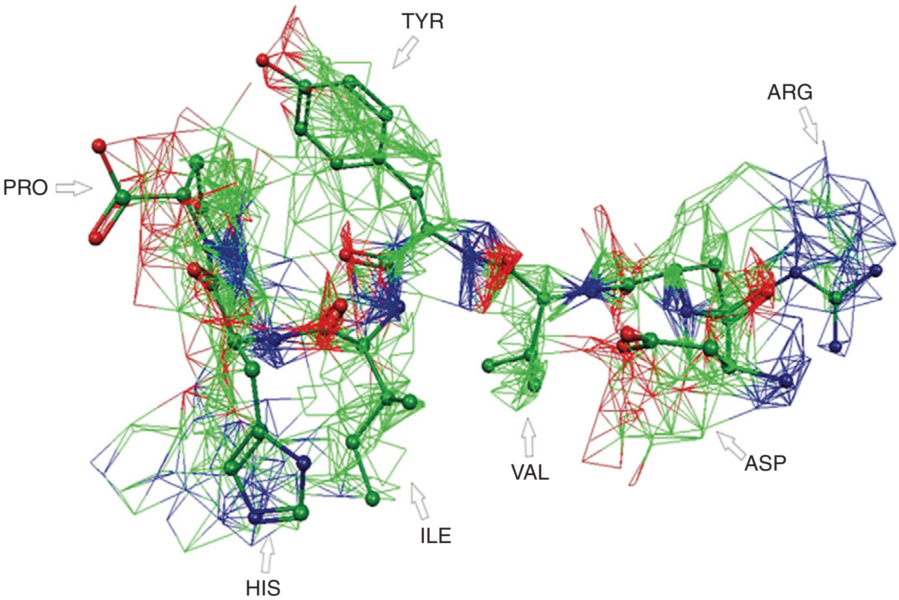

Figure 5.10 Configurational space taken by Ang-(1–7) in aqueous solution.

of the Ang-(1–7) residues. The average A–D bond distances are also shown. Arginine with its three proton acceptor sites has the largest average number of HBs, about 5.3 ± 0.9. Aspartate with its carboxyl group has about 4.8 ± 1.3 HBs, followed by histidine and tyrosine with 5.5 ± 1.0 and 3.0 ± 1.2 HBs, respectively. The terminal carboxylic and amine groups have an average number of HBs about 5.6 ± 1.1 and 2.6 ± 0.8, respectively. The intramolecular HBs have also been estimated. The intramolecular HBs correspond about 25% of the total number of HBs. Figure 5.8 shows that most prominent intramolecular HBs in the Ang-(1–7), which are mostly involved with the aspartate and valine residues. It has also been observed intramolecular HBs in the peptide backbone.

RDFs related to the distances of the residue center of mass and the H_2O have been calculated. On average, the first solvation shell around the residues is about 6 Å from its center of mass with about 16 water molecules. The bulky tyrosine residue has in its first solvation sphere about 20 water molecules. The histidine residue has about 18 water molecules. The residues lacking of proton acceptor sites—Val, Ile, Pro—have less water molecules in the first solvation shell, as it is expected. The terminal groups —NH_3^+ and —COOH have about 7 and 14 water molecules in the first solvation shell, respectively.

Table 5.4 Average number of HBs and corresponding donor–acceptor distances between water and Ang-(1–7) residues

Residue	Average number of HBs		Bond distance (Å)	First sphere radii (Å)	Number of water molecules
	With solvent	Intramolecular			
Asp	4.8 ± 1.3	1.65 ± 0.70	3.14 ± 0.24	5.5	16
Arg	5.3 ± 0.9	5.05 ± 0.37	3.14 ± 0.33	5.2	15
Val	–		–	5.9	15
Tyr	3.0 ± 1.2	0.0 ± 0.0	3.15 ± 0.17	6.0	20
Ile	–		–	5.9	16
His	5.5 ± 1.0	0.29 ± 0.63	3.34 ± 0.31	5.8	18
Pro	–		–	5.6	12
Backbone[a]	17.7 ± 1.6	4.5 ± 1.4	3.30 ± 0.20	–	–
NH_3^+	2.6 ± 0.8	0.87 ± 0.45	3.03 ± 0.18	4.1	7
COOH	5.6 ± 1.1	0.0 ± 0.0	3.13 ± 0.23	5.2	14

[a] The terminal groups —NH_3^+ and —COOH have not been taken into account.

Note: The first solvation sphere radii and the corresponding number of water molecules are also given.

Finally, it is important to note that the residues are flipping around the minimum energy and the tyrosine presents the smallest flexibility in good agreement with the NMR results [14]. The tyrosine residue also presents the largest number of water molecules in its first solvation shell. These results are coherent with the observation that tyrosine is the preferred residue to be included by β-Cyd [14].

3.4. Angiotensin-(1–7):β-Cyclodextrin inclusion compound

Recently, inclusion compounds of Ang-(1–7) and β-Cyd have been proposed as a formulation to overcome the problem of degradation of the drug because of the digestive enzymes of the stomach [14]. Ang-(1–7) and its β-Cyd inclusion compounds have been investigated employing different physical–chemical techniques and the complete attribution of their NMR signals [14]. According to the NOE effects, the β-Cyd prefers to make inclusion compound with the tyrosine residue of Ang(1–7).

For Ang-(1–7): β-Cyd inclusion compound, the simulation box is also cubic with lattice vector length of 61.0 Å, including 7381 water molecules and solute. All trajectories have been carefully heated up and finally equilibrated for 20 ps using the Berendsen thermostat [72] with a coupling parameter of $\tau = 0.1, \ldots, 1$ ps. In the microcanonical NVE (i.e., no energy transfer from or to the medium) production run of 90 ps, a time step of 0.5 ps was chosen. The total energy remained constant within 0.001 Hartree during the whole simulation and did not show a drift. The average temperature during the production run was 300.4 ± 1.2 K.

At Figure 5.11, the view of the box with the whole molecule is shown and the inclusion compound is highlighted. In Table 5.3, the structural parameters of Ang-(1–7) in the Ang-(1–7):β-Cyd inclusion compound in aqueous solution are also shown. The backbone dihedral angles can be compared with those of the Ang-(1–7) in aqueous solution and in gas phase. The complex formation leads to substantial changes in the backbone of the Ang-(1–7) probably because of the changes in the HBs network with the presence of β-Cyd.

The $\langle RMSD \rangle$ of the Ang-(1–7) fragment in the Ang-(1–7):β-Cyd complex is also plotted against the simulation time in aqueous solution at Figure 5.9. In solution, $\langle RMSD \rangle$ converges to an asymptotic value of approximately 1.5 Å. This value must be compared with the Ang-(1–7) in aqueous solution which is about 1.8 Å. Comparison of the $\langle RMSD \rangle$ curves of Ang-(1–7) alone and in the inclusion compound with β-Cyd shows clearly that this polypeptide is much more rigid, decreasing its flexibility. The configurational space taken by Ang-(1–7):β-Cyd in aqueous solution is shown at Figure 5.12.

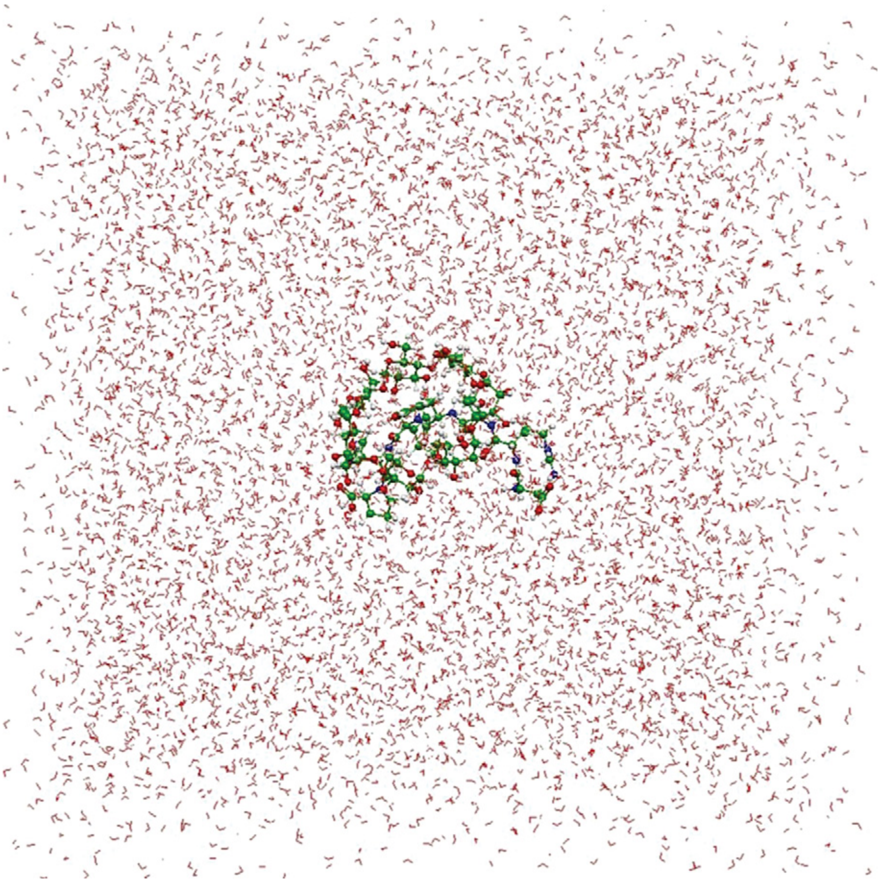

Figure 5.11 Box of water used to simulate Ang-(1–7):β-Cyd in solution.

Table 5.5 shows the average number of water molecules forming HBs with the proton acceptor sites in each of the residues present in Ang-(1–7):β-Cyd. These values can be compared directly to those estimated for Ang-(1–7). Arginine is still the proton acceptor site with largest average number of HBs, about 3.1 ± 1.4, which must be compared to the value of 5.3 ± 0.9 of Ang-(1–7) in aqueous solution. Aspartate and histidine have about 2.0 ± 1.2 and 2.36 ± 1.2 HBs, respectively. These values must be compared with 4.8 ± 1.3 and 5.5 ± 1.0 HBs for aspartate and histidine in the Ang-(1–7) structure in solution, respectively. It is clear that the number of HBs decreased with the formation of inclusion compound with β-Cyd through the tyrosine residue. For the tyrosine residue, the number of HBs decreased from 3.0 ± 1.2 to 0.08 ± 0.40 HBs because of hindrance caused by the β-Cyd. Isoleucine and valine residues present hydrophobic tails and, consequently,

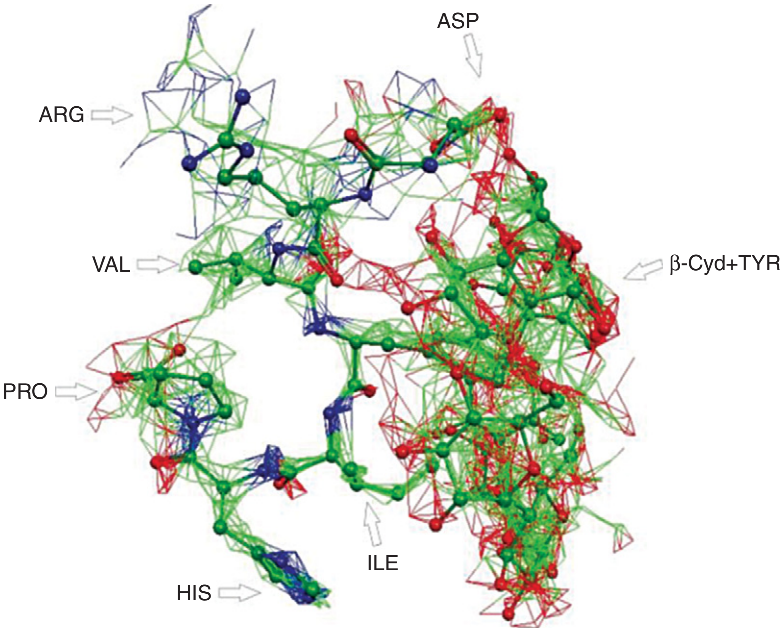

Figure 5.12 Configurational space taken by Ang-(1–7):β-Cyd in aqueous solution.

rather large first sphere radii. In fact, the proximity of β-Cyd results in a distortion of the solvent structure. Actually, a solvation shell cannot be identified for isoleucine residue. The proline residue presented similar number of HBs and number of water molecules in the first solvation shell compared to the Ang-(1–7), probably due to the fact that β-Cyd is included far from this site. For the backbone, the intermolecular HBs decreased with the inclusion compounds formation. However, the number of intramolecular HBs increased in the same extent leading to a less flexible Ang-(1–7) when included in the β-Cyd.

The RDFs of the water surrounding the tyrosine residue for the Ang-(1–7) and its inclusion compound with the β-Cyd are shown in Figure 5.13. The first solvation shell around the tyrosine is about 6 Å from its center of mass with about 20 water molecules. The RDF for the Ang-(1–7):β-Cyd shows clearly that the first solvation shell has only one water molecule mostly surrounding the rim of the β-Cyd and the hydroxyl group of the tyrosine residue (see Figure 5.14). The average distances between the tyrosine H2/H3 and H6 of β-Cyd are about 3.55 ± 0.48 Å. For the tyrosine H3/H5 and H5 of β-Cyd distances, the average is about 2.74 ± 0.35 Å corroborating with the NMR results that revealed NOE effect for those interactions [14].

Table 5.5 Average number of HBs and corresponding donor–acceptor distances between water and Ang-(1–7) residues for the Ang-(1–7):β-Cyd inclusion compound

Residue	Average number of HB's		Bond distance (Å)	First sphere radii (Å)	Number of water molecules
	With solvent	Intramolecular			
Asp	2.0 ± 1.2	0.51 ± 0.81	3.20 ± 0.50	5.92	18
Arg	3.1 ± 1.4	0.44 ± 0.92	2.97 ± 0.30	6.48	21
Val	–	–	–	7.92	43
Tyr	0.08 ± 0.40	0.02 ± 0.17	3.47 ± 0.19	3.68	1
Ile	–	–	–	–	–
His	2.36 ± 1.2	1.06 ± 1.1	3.17 ± 0.25	5.52	11
Pro	–	–	–	5.36	9
Backbone[a]	12.9 ± 2.9	8.7 ± 2.2	3.12 ± 0.21	–	–
NH_3^+	0.14 ± 0.57	0.04 ± 0.30	3.26 ± 0.30	3.44	1
COOH	3.05 ± 1.5	0.8 ± 1.0	3.12 ± 0.21	3.84	3

[a] The terminal groups —NH_3^+ and —COOH have not been taken into account.

Note: The first solvation sphere radii and the corresponding number of water molecules are also given.

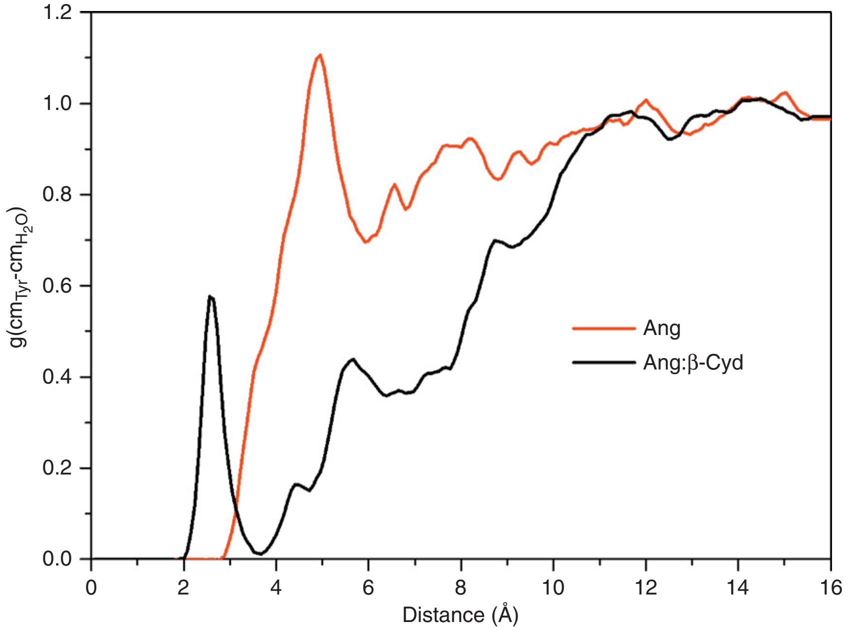

Figure 5.13 Radial distribution functions of the water around the tyrosine residue in the Ang-(1–7).

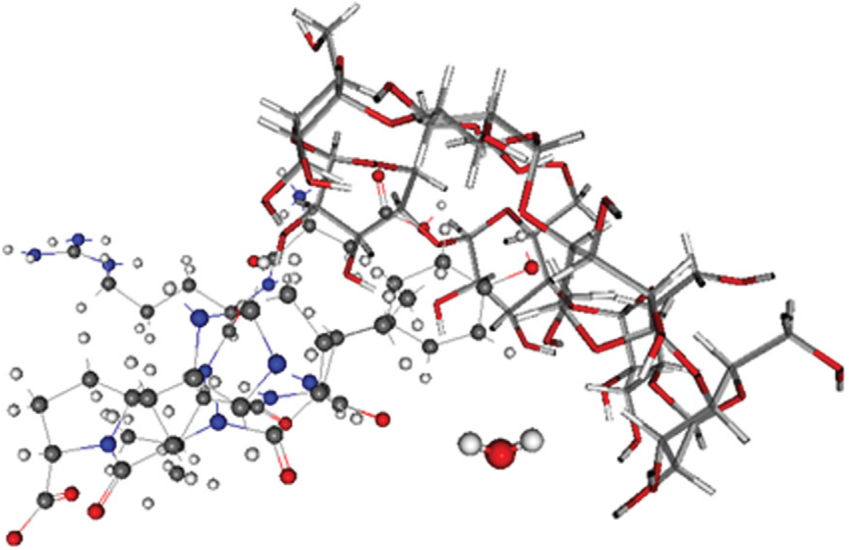

Figure 5.14 Snapshot of the Ang-(1–7): β-CD with 1 water molecule (ball-stick) closest to the tyrosine center of mass.

It is important to note that the inclusion of Ang-(1–7) in the β-Cyd leads to more rigid structure. The intermolecular HBs with water solvent decrease upon the inclusion formation due to the hindrance caused by the β-Cyd. Consequently, intramolecular HBs are increased including between Ang-(1–7) and β-Cyd. In spite of the presence of β-Cyd in the tyrosine, one water molecule still remains in the vicinity of this residue.

4. FINAL REMARKS

The strategy of using DC–SCC–DFTB and UFF in a QM/MM approach to investigate polypeptides in solution has been successful. It is a good compromise between computational cost and precision. This approach can be easily extended to investigate complex systems such as those related to enzymatic catalysis and self-assembly systems. The posteriori treatment for London dispersion has demonstrated to be important for studying such systems in which weak interactions are present. β-Cyd in solution and its inclusion compounds with polypeptides have been investigated through Born–Oppenheimer molecular dynamics. The results show clearly the phenomena of the inclusion are not only guided by geometrical aspects, but they are much affected by the solvent. The water acts creating a cushion in which the molecules with high fluxionality decreases its motion. Furthermore, water molecules are involved in the complex intermolecular hydrogen bonding network that competes with the intramolecular HBs. This HB network can favor or prevent the inclusion compound to form. It correlates with the balance of enthalpy and entropy in the process. As it was pointed out elsewhere [16], the entropy change due to the water rearrangement surrounding the β-Cyd and the guest molecule is very important and must be taken into account in a suitable model. For instance, many calculations have been performed using gas-phase models to justify the inclusion compound formation from thermodynamic analysis [69,79]. We understand that these models lack information of the solvent that has to be taken explicitly. Weak interaction between the host and guest inclusion compounds will always make the gas-phase calculations to predict its formation. Special attention should be done when molecular dynamics are carried out at gas phase. Most of the force fields predict more rigid structure as it has been shown in the present work.

The correct description of the inclusion compound in solution is the first step to model more complex processes such as those related to self-assembly and nanoreactors. The DC–SCC–DFTB/UFF, as it was presented here, is very attractive for such endeavor due to its simplicity, easy implementation, and low computational cost and precision.

ACKNOWLEDGMENTS

We would like to thank the following Brazilian agencies for the steady funding and fellowships during the last 10 years: Fundação de Amparo a Pesquisa do Estado de Minas Gerais—FAPEMIG, Conselho Nacional para o Desenvolvimento Científico e Tecnológico—CNPq, and Coordenação de Aperfeiçoamento de Pessoal do Ensino Superior—CAPES.

REFERENCES

[1] H. Gunaydin, K.N. Houk, J. Am. Chem. Soc. 130(46) (2008) 15232.
[2] Y. Yang, Q. Cui, J. Phys. Chem. B 113(14) (2009), 4930.
[3] L. Ramirezsilva, M.T. Degomezpuyou, A. Gomezpuyou, Biochem. 32(20) (1993), 5332.
[4] M.L. Farquhar, D.J. Vaughan, C.R. Hughes, J.M. Charnock, K.E.R. England, Geochim. Cosmochim. Acta 61(15), (1997) 3051.
[5] O. Gustafsson, P.M. Gschwend, Limnol. Oceanogr. 42(3) (1997), 519.
[6] G.E. Brown, Science 294 (5540) (2001) 67.
[7] M.A. Henderson, Surf. Sci. Rep. 46(1–8) (2002) 5.
[8] P.A. Thiel, T.E. Madey, Surf. Sci. Rep. 7(6–8) (1987) 211.
[9] S. Kubik, C. Reyheller, S. Stuwe, J. Incl. Phenom. Macrocycl. Chem. 52(3–4) (2005) 137.
[10] A.T. Wright, E.V. Anslyn, Chem. Soc. Rev. 35(1) (2006) 14.
[11] L.X. Song, L. Bai, X.M. Xu, J. He, S.Z. Pan, Coord. Chem. Rev. 253(9–10) (2009) 1276.
[12] B. Karimi, D. Zareyee, Org. Lett. 10(18) (2008) 3989.
[13] P.K. Singh, A.K. Satpati, M. Kumbhakar, H. Pal, S. Nath, J. Phys. Chem. B 112(37) (2008) 11447.
[14] I. Lula, A.L. Denadai, J.M. Resende, F.B. de Sousa, G.F. de Lima, D. Pilo-Veloso, et al., Peptides 28(11) (2007) 2199.
[15] A. Douhal, Chem. Rev. 104(4) (2004) 1955.
[16] K.A. Connors, Chem. Rev. 97(5) (1997) 1325.
[17] R.A.S. Santos, A. Silva, C. Maric, D.M.R. Silva, R.P. Machado, I. de Buhr, et al., Proc. Nat. Acad. Sci. USA 100(14) (2003) 8258.
[18] R.A.S. Santos, A.J. Ferreira, S.V.B. Pinheiro, W.O. Sampaio, R. Touyz, M.J. Campagnole-Santos, Expert Opin. Investig. Drugs 14(8) (2005) 1019.
[19] D. Regoli, J. Barabe, Pharmacol. Rev. 32(1) (1980) 1.
[20] D. Ianzer, K. Konno, R. Marques-Porto, F.C.V. Portaro, R. Stocklin, A.C.M. de Camargo, et al., Peptides 25(7) (2004) 1085.
[21] D.W. Cushman, H.S. Cheung, E.F. Sabo, M.A. Ondetti, Biochem. 16(25) (1977) 5484.
[22] D.W. Cushman, H.S. Cheung, E.F. Sabo, M.A. Ondetti, Prog. Cardiovasc. Dis. 21(3) (1978) 176.
[23] M.A. Ondetti, D.W. Cushman, Science 196(4288) (1977) 441.
[24] Q. Cui, M. Elstner, E. Kaxiras, T. Frauenheim, M. Karplus, J. Phys. Chem. B 105(2) (2001) 569.
[25] D. Riccardi, P. Schaefer, Y. Yang, H.B. Yu, N. Ghosh, X. Prat-Resina, et al., J. Phys. Chem. B 110(13) (2006) 6458.
[26] M. Hoffmann, M. Wanko, P. Strodel, P.H. Konig, T. Frauenheim, K. Schulten, et al., J. Am. Chem. Soc. 128(33) (2006) 10808.
[27] P.H. Konig, N. Ghosh, M. Hoffmann, M. Elstner, E. Tajkhorshid, T. Frauenheim, et al., J. Phys. Chem. A 110(2) (2006) 548.
[28] M. Wanko, M. Hoffmann, J. Frahmcke, T. Frauenheim, M. Elstner, J. Phys. Chem. B 112(37) (2008) 11468.

[29] M. Wanko, M. Hoffmann, T. Frauenheim, M. Elstner, J. Comput. Aided Mol. Des. 20(7–8) (2006) 511.

[30] M. Wanko, M. Hoffmann, T. Frauenheim, M. Elstner, J. Phys. Chem. B 112((37) (2008) 11462.

[31] M. Wanko, M. Hoffmann, P. Strodel, A. Koslowski, W. Thiel, F. Neese, et al., J. Phys. Chem. B 109(8) (2005) 3606.

[32] A.N. Bondar, J. Baudry, S. Suhai, S. Fischer, J.C. Smith, J. Phys. Chem. B 112(47) (2008) 14729.

[33] A.N. Bondar, S. Fischer, S. Suhai, J.C. Smith, J. Phys. Chem. B 109(31) (2005) 14786.

[34] D.M. Vriezema, M.C. Aragones, J. Elemans, J. Cornelissen, A.E. Rowan, R.J.M. Nolte, Chem. Rev. 105(4) (2005) 1445.

[35] E. Engeldinger, D. Armspach, D. Matt, Chem. Rev. 103(11) (2003) 4147.

[36] F. Hapiot, S. Tilloy, E. Monflier, Chem. Rev. 106(3) (2006) 767.

[37] R. Villalonga, R. Cao, A. Fragoso, Chem. Rev. 107(7) (2007) 3088.

[38] G. Wenz, B.H. Han, A. Muller, Chem. Rev. 106(3) (2006) 782.

[39] V.T. D'Souza, K.B. Lipkowitz, Chem. Rev. 98(5) (1998) 1741.

[40] A.R. Hedges, Chem. Rev. 98(5) (1998) 2035.

[41] K.B. Lipkowitz, Chem. Rev. 98(5) (1998) 1829.

[42] W.R. Saenger, J. Jacob, K. Gessler, T. Steiner, D. Hoffmann, H. Sanbe, et al., Chem. Rev. 98(5) (1998) 1787.

[43] H.J. Schneider, F. Hacket, V. Rudiger, H. Ikeda, Chem. Rev. 98(5) (1998), 1755.

[44] J. Szejtli, Chem. Rev. 98(5) (1998) 1743.

[45] K. Uekama, F. Hirayama, T. Irie, Chem. Rev. 98(5) (1998) 2045.

[46] A.M. Koester, R. Flores, G. Geudtner, A. Goursot, T. Heine, S. Patchkovskii, et al., deMon vs. 1.1, NRC, Ottawa, Canada, 2004.

[47] M. Elstner, Theor. Chem. Acc. 116(1–3) (2006) 316.

[48] P.H. Konig, M. Hoffmann, T. Frauenheim, Q. Cui, J. Phys. Chem. B 109(18) (2005) 9082.

[49] A.F. Oliveira, G. Seifert, T. Heine, H.A. Duarte, J. Braz. Chem. Soc. 20(7) (2009) 1193.

[50] W.M.C. Foulkes, R. Haydock, Phys. Rev. B 39(17) (1989) 12520.

[51] M. Elstner, D. Porezag, G. Jungnickel, J. Elsner, M. Haugk, T. Frauenheim, et al., Phys. Rev. B 58(11) (1998) 7260.

[52] T. Frauenheim, G. Seifert, M. Elstner, Z. Hajnal, G. Jungnickel, D. Porezag, et al., Physica Status Solidi B-Basic Res. 217(1) (2000) 41.

[53] R.S. Mulliken, J. Chem. Phys. 23(10) (1955) 1833.

[54] R.G. Parr, R.G. Pearson, J. Am. Chem. Soc. 105(26) (1983) 7512.

[55] L. Zhechkov, T. Heine, S. Patchkovskii, G. Seifert, H.A. Duarte, J. Chem. Theor. Computat. 1(5) (2005) 841.

[56] M. Elstner, P. Hobza, T. Frauenheim, S. Suhai, E. Kaxiras, J. Chem. Phys. 114 (12) (2001) 5149.

[57] A.K. Rappe, C.J. Casewit, K.S. Colwell, W.A. Goddard, W.M. Skiff, J. Am. Chem. Soc. 114(25) (1992) 10024.

[58] W.L. Jorgensen, J. Chandrasekhar, J.D. Madura, R.W. Impey, M.L. Klein, J. Chem. Phys. 79(2) (1983) 926.

[59] T. Heine, H.F. dos Santos, S. Patchkovskii, H.A. Duarte, J. Phys. Chem. A 111(26) (2007) 5648.

[60] A. Warshel, M. Levitt, J. Mol. Biol. 103(2) (1976) 227.

[61] M.P. Allen, D.J. Tildesley, Computer Simulation of Liquids, Oxford Science Publications, Bristol, 2004.

[62] D. Frenkel, B. Smit, Academic Press, New York, 2002.

[63] T. Darden, D. York, L. Pedersen, J. Chem. Phys. 98(12) (1993) 10089.

[64] M.K. Chourasia, S.K. Jain, J. Pharm. Pharm. Sci. 6(1) (2003) 33.

[65] A. Vyas, S. Saraf, J. Incl. Phenom. Macrocycl. Chem. 62(1–2) (2008) 23.

[66] T. Steiner, G. Koellner, J. Am. Chem. Soc. 116(12) (1994) 5122.

[67] T. Steiner, W. Saenger, R.E. Lechner, Mol. Phys. 72(6) (1991) 1211.

[68] L. Ivan, M.F. Gomes, D. Pilo-Veloso, A.L.O. De Noronha, H.A. Duarte, R.A.S. Santos, et al., J. Incl. Phenom. Macrocycl. Chem. 56(3–4) (2006) 293.

[69] L.M.A. Pinto, M.B. de Jesus, E. de Paula, A.C.S. Lino, J.B. Alderete, H.A. Duarte, et al., J. Mol. Struct. (Theochem) 678(1–3) (2004) 63.
[70] K. Lindner, W. Saenger, Carbohydr. Res. 99(2) (1982) 103.
[71] V. Zabel, W. Saenger, S.A. Mason, J. Am. Chem. Soc. 108(13) (1986) 3664.
[72] H.J.C. Berendsen, J.P.M. Postma, W.F. Vangunsteren, A. Dinola, J.R. Haak, J. Chem. Phys. 81(8) (1984) 3684.
[73] J.P. Perdew, K. Burke, M. Ernzerhof, Phys. Rev. Lett. 77(18) (1996) 3865.
[74] L. Lawtrakul, H. Viernstein, P. Wolschann, Int. J. Pharm. 256(1–2) (2003) 33.
[75] D.B.M. Malik, S. Baboota, A. Ahuja, S. Hasan, J. Ali, Curr. Drug Deliv. 4(2) (2007) 141.
[76] I. Lula, F.B. De Sousa, A.L. Denadai, D. Ianzer, R.D. Sinisterra, non published results.
[77] R.A.S. Santos, M.J. Campagnole-Santos, S.P. Andrade, Regul. Pept. 91(1–3) (2000) 45.
[78] R.D. Paula, C.V. Lima, R.R. Britto, M.J. Campagnole-Santos, M.C. Khosla, R.A.S. Santos, Peptides 20(4) (1999) 493.
[79] L.M.A. Pinto, L.F. Fraceto, M.H.A. Santana, T.A. Pertinhez, S.O. Junior, E. de Paula, J. Pharm. Biomed. Anal. 39(5) (2005) 956.

CHAPTER 6

Computer Simulations of Photobiological Processes: The Effect of the Protein Environment

Gerrit Groenhof[a], **Martial Boggio-Pasqua**[b], **Lars V. Schäfer**[c] and **Michael A. Robb**[d]

Contents

---

[a] Computational Biomolecular Chemistry, Department of Computational and Theoretical Biophysics, Max-Planck-Institute for Biophysical Chemistry, Am Fassberg 11, D-37077, Göttingen, Germany
[b] Laboratoire de Chimie et Physique Quantiques, IRSAMC, CNRS et Université de Toulouse, 118 Route de Narbonne, 31062 Toulouse, France
[c] Department of Biophysical Chemistry, University of Groningen, Nijenborg 4, 9747 AG Groningen, The Netherlands
[d] Department of Chemistry, Imperial College London, London SW7 2AZ, UK

Advances in Quantum Chemistry, Vol. 59
ISSN: 0065-3276, DOI: 10.1016/S0065-3276(10)59006-3

© 2010 Elsevier Inc.
All rights reserved

1. INTRODUCTION

Interaction between biology, physics, and chemistry is presently providing a window into an exciting new era of bioinspired nanotechnology. In particular, photobiological processes, like vision or photosynthesis, in which sunlight is used as the source of energy to bring about a chemical reaction, provide valuable templates to create tools for biomolecular imaging, information technology, and renewable energy. Mimicking photobiological processes requires a complete understanding of the underlying molecular dynamics (MD). As the relevant time and spatial resolution are notoriously hard to access experimentally, computer simulations are the methods of choice to deepen our understanding of how proteins have evolved to mediate photochemical reactions and to use these insights to create devices that mimic biological functions. In this chapter, we present the approach we use to perform excited state MD simulations of photoinduced processes in biological systems. We start by reviewing the theoretical concepts of photochemical reactions. We then discuss how we have used these concepts to create a practical simulation methodology. We conclude this chapter with a short review of selected applications on photobiological systems. These simulations not only reveal the detailed sequence of events that follow photon absorption, but also demonstrate how the biological environment controls the excited state dynamics.

2. THEORY

The size and complexity of a typical photobiological system, together with the timescales that must be reached, necessitate the use of classical MD for the nuclear degrees of freedom. In MD simulations Newton's equations of motion are solved numerically to obtain a trajectory of the dynamics of a molecule over a period of time. To model the electronic rearrangement upon excitation, a quantum mechanical (QM) description is required for those parts of the system that are involved in photon absorption. For the remainder, a simple molecular mechanics (MM) forcefield model suffices. The interactions in the systems are thus computed within a hybrid QM/MM framework.

To model the dynamics of a photoactivated process, the ground and excited state potential energy surfaces must be described accurately. As we show schematically in Figure 6.1, a photochemical reaction starts in the excited state (S_1) but ends in the ground state (S_0) after radiationless decay via the conical intersection seam. To model the deactivation process, we use a diabatic surface-hopping algorithm in our MD simulations that allows the trajectory to hop between the surfaces when the intersection seam is reached.

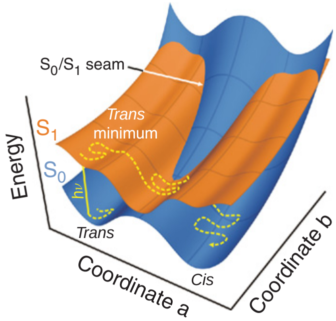

Figure 6.1 Schematic overview of a photochemical reaction pathway (dashed line). After photon absorption, evolution takes place on the excited state potential energy surface (red) until the system hits the S_1/S_0 intersection seam. At the intersection, a radiationless transition to the ground state occurs (blue). After the decay, the system continues evolving in the ground state. Please refer online version for color image.

2.1. Born–Oppenheimer approximation

The aim in computational chemistry is to find and interpret the solution for the many-body Schrödinger equation of chemical systems:

$$H\Psi = E\Psi, \tag{1}$$

with H the system's Hamilton operator, or Hamiltonian, that returns the total energy E of the system when operating on the many-body wavefunction Ψ. As in classical mechanics, the Hamiltonian is defined as the sum of the kinetic T and potential energy V:

$$H = T + V. \tag{2}$$

From the wavefunction Ψ, all static properties of the system can be derived.

Dynamic information is obtained by integrating the time-dependent Schrödinger equation:

$$i\hbar\frac{\partial}{\partial t}\Psi = H\Psi, \tag{3}$$

with $\hbar$ the Planck constant divided by 2π. Unfortunately, an exact solution exists only if there are at most two interacting particles in the system. Solving the equations for any larger system requires approximations.

Since biological molecules are mainly composed of first and second row elements, the electronic velocities are sufficiently low for relativistic effects to be ignored. Within this approximation, the nonrelativistic Hamiltonian is given by

$$H = T_{\mathrm{N}} + T_{\mathrm{e}} + U(\mathbf{r}, \mathbf{R}), \tag{4}$$

where T_{e} and T_{N} are the operators of the kinetic energy of the electrons and the nuclei, respectively, and $U(\mathbf{r},\mathbf{R})$ is the total potential energy of the electrons and nuclei together. The vector $\mathbf{r}$ denotes the set of electronic coordinates and the vector $\mathbf{R}$ stands for the nuclear coordinates.

The next step in reducing the complexity is to assume that the dynamics of the electrons on the one hand and nuclei on the other are decoupled. This approximation, proposed by Born and Oppenheimer, is based on the large mass difference between electrons and nuclei. As a consequence, the much lighter electrons adapt instantaneously to displacements of the nuclei. Electrons "see" nuclei standing still, whereas nuclei move on potential energy landscapes created instantly by the faster electrons. Within the Born–Oppenheimer approximation, the electronic and nuclear degrees of freedom can thus be treated independently.

First, the Schrödinger equation is solved for electrons moving in a framework of fixed nuclei. Thus, the nuclear kinetic energy operator (T_{N}) is omitted from the full Hamiltonian [Eq. (4)] to yield

$$H^{\mathrm{e}} = T_{\mathrm{e}} + U(\mathbf{r},\mathbf{R}), \tag{5}$$

where the superscript e indicates the *electronic* Hamiltonian. The electronic wavefunctions are the eigenfunctions of this Hamiltonian

$$H^{\mathrm{e}}\psi_i(\mathbf{r};\mathbf{R}) = V_i(\mathbf{R})\psi_i(\mathbf{r};\mathbf{R}), \tag{6}$$

with $\psi_i(\mathbf{r};\mathbf{R})$ and $V_i(\mathbf{R})$ as the electronic wavefunctions and their electronic energies, respectively, that both depend *parametrically* on the nuclear coordinates. The wavefunctions are the adiabatic electronic states, representing the electronic ground state ($i=0$), excited state ($i=1$), second excited state ($i=2$), and so on. How these wavefunctions are obtained in practical computations is the subject of modern quantum chemistry [1] and is briefly discussed below in Section 2.5.

The adiabatic wavefunctions can be made *orthonormal*, that is,

$$\langle\psi_i|\psi_j\rangle = \int_{-\infty}^{\infty}\psi_i(\mathbf{r},\mathbf{R})^*\psi_j(\mathbf{r},\mathbf{R})d\mathbf{r} = \delta_{ij}, \tag{7}$$

where the Dirac bracket notation ($\langle|\rangle$) has been introduced that will be used throughout the text and where δ_{ij} is the Kronecker delta function, which is 1 if $i=j$ and 0 otherwise.

Within the Born–Oppenheimer approximation, the adiabatic electronic states provide a complete basis to expand the molecular wavefunction in

$$\Psi(\mathbf{r},\mathbf{R}) = \sum_n \chi_n(\mathbf{R})\psi_n(\mathbf{r};\mathbf{R}), \tag{8}$$

where the expansion coefficients $\chi_n(\mathbf{R})$ are the nuclear wavefunctions. Substituting the expression for the molecular wavefunction in the time-independent Schrödinger equation [Eq. (1)] and multiplying by the adiabatic electronic wavefunction $\psi_i^*(\mathbf{r};\mathbf{R})$ from the left, followed by integration over the electronic coordinates $\mathbf{r}$ leads to the following set of coupled equations:

$$\sum_j H_{ij}(\mathbf{R})\chi_j(\mathbf{R}) = E(\mathbf{R})\chi_i(\mathbf{R}), \tag{9}$$

with

$$H_{ij}(\mathbf{R}) = \langle\psi_i(\mathbf{r};\mathbf{R})|H|\psi_j(\mathbf{r};\mathbf{R})\rangle = \langle\psi_i(\mathbf{r};\mathbf{R})|T_\mathrm{N}|\psi_j(\mathbf{r};\mathbf{R})\rangle + V_i(\mathbf{R})\delta_{ij}. \tag{10}$$

The nuclear kinetic energy operator is defined as

$$T_\mathrm{N} = -\sum_k \frac{\hbar^2}{2M_k}\nabla^2_{\mathbf{R}_k}, \tag{11}$$

in which M_k is the mass of nucleus k and the sum runs over all nuclei. Using this relation, Eq. (10) can be rewritten as follows [2]:

$$H_{ij}(\mathbf{R}) = [T_\mathrm{N} + V_i(\mathbf{R})]\delta_{ij} - \Lambda_{ij}(\mathbf{R}). \tag{12}$$

The *nonadiabatic* operator elements $\Lambda_{ij}(\mathbf{R})$ are defined as

$$\Lambda_{ij}(\mathbf{R}) = \sum_k F^k_{ij}(\mathbf{R})\nabla_{\mathbf{R}_k} + G_{ij}(\mathbf{R}), \tag{13}$$

$$F^k_{ij}(\mathbf{R}) = \frac{\hbar^2}{M_k}\langle\psi_i(\mathbf{r};\mathbf{R})|\nabla_{\mathbf{R}_k}|\psi_j(\mathbf{r};\mathbf{R})\rangle, \tag{14}$$

$$G_{ij}(\mathbf{R}) = \sum_k \frac{\hbar^2}{2M_k}\langle\psi_i(\mathbf{r};\mathbf{R})|\nabla^2_{\mathbf{R}_k}|\psi_j(\mathbf{r};\mathbf{R})\rangle. \tag{15}$$

In contrast to H^e [Eq. (5)], in which T_N was omitted, H_{ij} is *not* diagonal on the basis of the adiabatic electronic wavefunctions (ψ_i). The individual electronic states are thus coupled *via* nuclear motions. Nonadiabatic coupling is the key player in a photochemical reaction, as we will show below.

In the limit that the electronic wavefunctions vary very slowly with the nuclear dynamics, the nonadiabatic operators $F^k_{ij}(\mathbf{R})$ and $G_{ij}(\mathbf{R})$ are vanishingly small and can be safely neglected. Thus, the crux of the Born–Oppenheimer approximation is that H_{ij} is assumed to be diagonal:

$$H_{ij}(\mathbf{R}) = [T_\mathrm{N} + V_i(\mathbf{R})]\delta_{ij}. \tag{16}$$

Under this assumption, the total molecular wavefunction becomes a product of a *single* nuclear and a *single* electronic wavefunction:

$$\Psi_i^{\mathrm{tot}}(\mathbf{R},\mathbf{r}) = \chi_i(\mathbf{R})\psi_i(\mathbf{r};\mathbf{R}), \tag{17}$$

which implies that the nuclei move on a *single* electronic potential energy surface $V_i(\mathbf{R})$ of a given electronic state i, and the electronic wavefunction remains in that state. The Born–Oppenheimer approximation not only reduces the computational complexity of the equations that have to be solved, but also provides a conceptually intuitive picture of molecular structure and dynamics.

2.2. Conical intersections

The Born–Oppenheimer is valid as long as the separation between the electronic energy levels is large compared to the separation between the vibrational energy levels. Since this is true for almost all ground state chemical processes, the Born–Oppenheimer provides the basis for modern quantum chemistry. For photochemical processes, however, this is usually not true.

During a photochemical reaction, the system samples regions of configuration space, where the energy gaps between electronic states are of the same magnitude as the energy gaps between the vibrational states of the nuclei. Under such conditions, resonance will occur between nuclear vibrations and electronic transitions. The populations of the adiabatic wavefunctions become strongly dependent on the nuclear dynamics and the nonadiabatic coupling operator [Λ, Eq. (13)] can no longer be ignored. Thus, in regions of strong non-adiabatic coupling the Born–Oppenheimer approximation breaks down. Nuclear dynamics induces population transfer between different electronic states. Furthermore, if the coupling is strong enough, the adiabatic potential energy surfaces can even intersect. These surface crossings provide efficient funnels for radiationless deactivation of the excited state and therefore play a crucial role in photochemistry.

In theory, *all* electronic states $\psi_i(\mathbf{r};\mathbf{R})$ are involved in the nonadiabatic coupling. In practice, however, there is only significant coupling between electronic states that have comparable energies. Therefore, only a small number of states needs to be included in the nonadiabatic coupling matrix Λ, which considerably reduces its dimensionality.

The nonadiabatic coupling operators Λ_{ij} are nonlocal derivative operators that depend inversely on the energy gap between the coupled adiabatic states [3]:

$$F_{ij}^{k}(\mathbf{R}) = \frac{\hbar^2}{M_k}\langle\psi_i(\mathbf{r};\mathbf{R})|\nabla_{\mathbf{R}_k}|\psi_j(\mathbf{r};\mathbf{R})\rangle = \frac{\hbar^2}{M_k}\frac{\langle\psi_i(\mathbf{r};\mathbf{R})|\nabla_{\mathbf{R}_k}H^{\mathrm{e}}|\psi_j(\mathbf{r};\mathbf{R})\rangle}{V_j - V_i}. \tag{18}$$

When the gap ($V_j - V_i$) gets smaller, the coupling increases, and the nuclear wavefunction that is initially on one surface will spread to the other surface without losing energy. The coupling thus induces a radiationless transition between the electronic states.

If the gap vanishes, that is, $V_j - V_i = 0$, the coupling becomes infinite. Due to the nonlocal nature of the coupling matrix elements in the adiabatic representation, it is more convenient to switch to a diabatic representation, in which the nonadiabatic coupling operator is a local, potential-like operator. The switch to the diabatic wavefunctions φ is achieved by a unitary transformation of the adiabatic wavefunctions ψ at each point in space [3]:

$$\varphi = \mathbf{S}(\mathbf{R})\psi. \tag{19}$$

In the diabatic representation the complete Hamiltonian [Eq. (12)] becomes

$$H_{ij}(\mathbf{R}) = T_\mathrm{N}\delta_{ij} + W_{ij}(\mathbf{R}), \tag{20}$$

and the molecular Schrödinger equation [Eq. (12)] can be written in matrix notation as

$$\mathbf{H}\boldsymbol{\chi} = [T_\mathrm{N}\mathbf{1} + \mathbf{W}(\mathbf{R})]\boldsymbol{\chi} = \mathbf{E}\boldsymbol{\chi}, \tag{21}$$

in which $\mathbf{1}$ is the identity matrix and $\mathbf{W}(\mathbf{R})$ is the diabatic potential energy matrix, which, in contrast to the adiabatic potential matrix $\mathbf{V}(\mathbf{R})$, contains only *local* terms.

To illustrate the concept of the surface crossing, we consider a molecule in which there is coupling between two diabatic states A and B, but not to any other state. We can expand the potential matrix elements in a Taylor series around an arbitrary point $\mathbf{R}_0$:

$$\mathbf{W}(\mathbf{R} - \mathbf{R}_0) = \mathbf{W}^{(0)} + \mathbf{W}^{(1)} + \mathbf{W}^{(2)} + \cdots, \tag{22}$$

At $\mathbf{R}_0$, we can choose the diabatic and adiabatic states to be equal. Then, the zeroth-order matrix, $\mathbf{W}^{(0)}$, is a diagonal matrix in which the elements correspond to the energies E_A and E_B of the diabatic states ψ_A and ψ_B at $\mathbf{R}_0$, which, by our choice of origin, are identical to the *adiabatic* energies V_1 and V_2:

$$\mathbf{W}^{(0)} = \frac{E_\mathrm{A} + E_\mathrm{B}}{2}\mathbf{1} + \begin{pmatrix} -\dfrac{E_\mathrm{B} - E_\mathrm{A}}{2} & 0 \\ 0 & \dfrac{E_\mathrm{B} - E_\mathrm{A}}{2} \end{pmatrix} = \mathbf{V}(\mathbf{R}_0). \tag{23}$$

For very small displacements $\Delta\mathbf{R}$ around $\mathbf{R}_0$, the Taylor expansion in Eq. (22) can be truncated after the first-order term

$$\mathbf{W}^{(1)} = \frac{\lambda \cdot \Delta\mathbf{R}}{2}\mathbf{1} + \begin{pmatrix} -\frac{1}{2}\boldsymbol{\delta\kappa} \cdot \Delta\mathbf{R} & \boldsymbol{\kappa}^{\mathrm{AB}} \cdot \Delta\mathbf{R} \\ \boldsymbol{\kappa}^{\mathrm{AB}} \cdot \Delta\mathbf{R} & \frac{1}{2}\boldsymbol{\delta\kappa} \cdot \Delta\mathbf{R} \end{pmatrix}, \tag{24}$$

in which we have introduced linear potential constants that are defined as

$$\begin{aligned} \boldsymbol{\delta\kappa} &\equiv \nabla_{\mathbf{R}}(E_{\mathrm{B}} - E_{\mathrm{A}})|_{\mathbf{R}_0,} \\ \boldsymbol{\kappa}^{\mathrm{AB}} &\equiv \nabla_{\mathbf{R}}\langle\varphi_A|H^{\mathrm{e}}|\varphi_B\rangle|_{\mathbf{R}_0}, \\ \lambda &\equiv \nabla_{\mathbf{R}}(E_{\mathrm{A}} + E_{\mathrm{B}})|_{\mathbf{R}_0}. \end{aligned} \tag{25}$$

We can choose $\mathbf{R}_0$ to be the point of degeneracy, so that E_{A} and E_{B} are equal at $\mathbf{R}_0$ and $\mathbf{W}^{(0)}$ is 0. The adiabatic potential energy surfaces V_1 and V_2 are obtained by diagonalizing the diabatic potential matrix $\mathbf{W}$. Thus, for the two-state system considered here,

$$V_{1,2} = \frac{1}{2}\lambda \cdot \Delta\mathbf{R} \pm \frac{1}{2}\sqrt{[\boldsymbol{\delta\kappa} \cdot \Delta\mathbf{R}]^2 + 4[\boldsymbol{\kappa}^{\mathrm{AB}} \cdot \Delta\mathbf{R}]}. \tag{26}$$

The necessary condition for a crossing between the two potential energy surfaces at $\mathbf{R}_0$ is that the two electronic energies are identical. Therefore, two conditions need to be fulfilled simultaneously:

$$\begin{aligned} \boldsymbol{\delta\kappa} \cdot \Delta\mathbf{R} &= 0, \\ \boldsymbol{\kappa}^{\mathrm{AB}} \cdot \Delta\mathbf{R} &= 0. \end{aligned} \tag{27}$$

Thus, to first order, the degeneracy is lifted in the two-dimensional space spanned by the vectors $\delta\boldsymbol{\kappa}$ and $\boldsymbol{\kappa}^{\mathrm{AB}}$, which are the gradient difference vector and derivative coupling vector, respectively. The space spanned by these two vectors is often referred to as the branching space, or g–h plane. Furthermore, as is evident from Eq. (26) and illustrated in Figure 6.2, the topology of the surfaces is that of a double cone, with the point of degeneracy at the apex. Orthogonal to the two-dimensional branching space exists the so-called intersection space (or seam space), in which the energies of the two states remain degenerate to first order. In a molecule with N internal degrees of freedom, the intersection space thus forms an $N-2$-dimensional seam, each point of which is a conical intersection. If a molecule has less than two degrees of freedom, the two conditions for degeneracy [Eq. (27)] cannot be simultaneously fulfilled. In diatomic molecules, for example, electronic states of same symmetry cannot cross, which led Von Neumann and Wigner to propose their famous noncrossing rule [4].

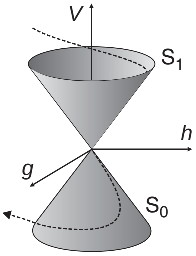

Figure 6.2 A conical intersection plotted in the two-dimensional branching space that is spanned by the gradient difference vector (*g*) and the derivative coupling vector (*h*). Motion away from the intersection in the *g*–*h* plane lifts the degeneracy between the two electronic states S_1 and S_0. The dotted line shows a path of a nuclear trajectory passing from one electronic state (S_1) to another (S_0) through the intersection funnel.

The concept of the intersection seam is illustrated in Figure 6.3 for a hypothetical triatomic molecule. In this molecule there are three internal degrees of freedom: two bond lengths (x_1 and x_2) and one angle (α). Since *two* degrees of freedom are required to span the branching space, there is only *one* degree of freedom available for the intersection seam. For the sake of simplicity, we let the branching space coordinates (i.e., the gradient difference and derivative coupling vectors) coincide with the two bond length variables x_1 and x_2 in our molecule. Note that in real triatomic molecules, the branching space coordinates can be linear combinations of the three internal degrees of freedom.

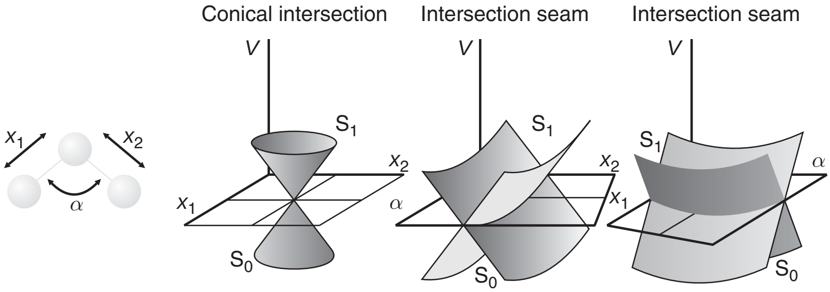

Figure 6.3 Surface crossing between two potential energy surfaces S_1 and S_0 in a hypothetical triatomic molecule (left). We let x_1 and x_2 be parallel to the gradient difference vector and the derivative coupling vector, respectively, and α be the remaining degree of freedom. When projected onto the branching space spanned by x_1 and x_2, the surfaces of S_0 and S_1 intersect in a single point, the conical intersection. In the two other subspaces, spanned by either x_2 and α, or by x_1 and α, there is an intersection line between the surfaces. In the second plot x_1 and in the third x_2 are assumed to be at their conical intersection coordinates.

In the first plot of Figure 6.3 the two adiabatic potential energy surfaces (denoted S_0 and S_1) are projected onto the branching space. The surfaces adopt a double cone shape with a single intersection point at the apex. Any displacement away from the apex in either the x_1 or x_2 coordinate lifts the degeneracy.

The second plot shows the two surfaces in the subspace spanned by the derivative coupling vector x_2 and the third independent degree of freedom, the bond angle α. The gradient difference vector x_1 is kept fixed at the conical intersection. Therefore, the only coordinate left to lift the degeneracy is x_2. If the latter is at the conical intersection as well, the surfaces intersect irrespective of the value of the angle variable (α). The intersection seam is thus a one-dimensional line that is parallel to α.

The third plot shows the projection of the two surfaces onto the subspace spanned by the gradient difference vector x_1 and the bond angle variable α. Now the derivative coupling vector x_2 is constrained to be at the conical intersection. Under this condition, only x_1 can lift the degeneracy and the surfaces intersect along a seam parallel to α.

The conical intersection has a number of peculiar characteristics. For instance, if we consider a small displacement $\mathbf{q}$ away from the cone tip in the branching plane, the diabatic energy matrix $U_{\mathrm{A,B}}$ becomes

$$U_{\mathrm{A,B}}(\mathbf{q}) = \begin{pmatrix} H_{\mathrm{AA}}(\mathbf{q}) & H_{\mathrm{AB}}(\mathbf{q}) \\ H_{\mathrm{AB}}(\mathbf{q}) & H_{\mathrm{BB}}(\mathbf{q}) \end{pmatrix} = S(\mathbf{q})\mathbf{1} + \begin{pmatrix} -\Delta H(\mathbf{q}) & H_{\mathrm{AB}}(\mathbf{q}) \\ H_{\mathrm{AB}}(\mathbf{q}) & \Delta H(\mathbf{q}) \end{pmatrix}, \tag{28}$$

with [see Eq. (24)]

$$\begin{aligned} \Delta H(\mathbf{q}) &= \frac{H_{\mathrm{BB}}(\mathbf{q}) - H_{\mathrm{AA}}(\mathbf{q})}{2} = \boldsymbol{\delta\kappa} \cdot \mathbf{q}, \\ H_{\mathrm{AB}}(\mathbf{q}) &= \boldsymbol{\kappa}^{\mathrm{AB}} \cdot \mathbf{q}, \\ S(\mathbf{q}) &= \frac{H_{\mathrm{BB}}(\mathbf{q}) + H_{\mathrm{AA}}(\mathbf{q}).}{2} \end{aligned} \tag{29}$$

The matrix $U_{\mathrm{A,B}}(\mathbf{q})$ is the two-state Hamiltonian matrix defined on the basis of the eigenvectors at the reference point $\mathbf{R}_0$, at which the diabatic and adiabatic bases are identical. The diabatic potential matrix $U_{\mathrm{A,B}}(\mathbf{q})$ can be diagonalized by the rotation matrix $\mathbf{T}(\mathbf{q})$ [5], to obtain the adiabatic energies $V_{1,2}$

$$\mathbf{T}(\mathbf{q}) = \begin{pmatrix} \cos[\theta(\mathbf{q})] & -\sin[\theta(\mathbf{q})] \\ \sin[\theta(\mathbf{q})] & \cos[\theta(\mathbf{q})] \end{pmatrix}. \tag{30}$$

From Eq. (29), the rotation angle $\theta(\mathbf{q})$ is defined as [5–10]:

$$\begin{aligned}\theta(\mathbf{q}) &= \frac{1}{2}\arctan\left[\frac{2H_{\mathrm{AB}}(\mathbf{q})}{\Delta H(\mathbf{q})}\right] \\ &= \frac{1}{2}\arctan\left[\frac{2\boldsymbol{\kappa}^{\mathrm{AB}}\cdot\mathbf{q}}{\delta\boldsymbol{\kappa}\cdot\mathbf{q}}\right] \\ &= \frac{1}{2}\arctan\left[\frac{y}{x}\right],\end{aligned} \tag{31}$$

where we have introduced the *scaled* coordinates x and y. Replacing these scaled coordinates by polar coordinates r and ϕ

$$\begin{aligned} r &= \sqrt{x^2+y^2}, \\ \phi &= \arctan\left[\frac{2y}{x}\right], \end{aligned} \tag{32}$$

yields the following expression for the rotation angle:

$$\theta(H_{\mathrm{AB}},\ \Delta H) = \frac{\phi}{2}. \tag{33}$$

Thus, a simple relationship exists between the polar angle (ϕ), which defines a rotation around the apex of the cone in the branching space, and the *mixing* angle (θ) for the diabatic states (φ_{A},φ_{B}). Since the extent of mixing depends *only* on the polar angle ϕ and *not* on the radius r, it is constant along any straight line that starts from the apex of the double cone.

Because of this relationship, the adiabatic wavefunction changes sign upon a complete rotation around the apex of the cone in the branching space. This is demonstrated by comparing the wavefunctions at $\phi = \phi_0$ and $\phi_0 + 2\pi$. Substituting Eq. (33) into the rotation matrix [Eq. (30)] gives the following expression for the adiabatic states:

$$\psi_1 = \cos\left[\frac{\phi_0}{2}\right]\varphi_{\mathrm{A}} - \sin\left[\frac{\phi_0}{2}\right]\varphi_{\mathrm{B}} \tag{34}$$

and

$$\psi_2 = \sin\left[\frac{\phi_0}{2}\right]\varphi_\mathrm{A} + \cos\left[\frac{\phi_0}{2}\right]\varphi_\mathrm{B}. \tag{35}$$

If we substitute $\phi = \phi_0 + 2\pi$, we see that the adiabatic wavefunction has indeed changed sign after the 360° rotation:

$$\begin{aligned}\psi_1 &= \cos\left[\frac{\phi_0 + 2\pi}{2}\right]\varphi_\mathrm{A} - \sin\left[\frac{\phi_0 + 2\pi}{2}\right]\varphi_\mathrm{B} \\ &= \sin\left[\frac{\phi_0}{2}\right]\varphi_\mathrm{A} - \cos\left[\frac{\phi_0}{2}\right]\varphi_\mathrm{B} \\ &= -\psi_1.\end{aligned} \tag{36}$$

Because single valuedness of the wavefunction is one of the basic postulates of quantum mechanics, this result implies that the conical intersection is a singularity. This singularity is a consequence of the separation between electronic and nuclear degrees of freedom, which, as we have seen, is not valid near a surface crossing. Thus, the singularity only exists for the adiabatic electronic wavefunction and must be remedied by the nuclear wavefunction, so that the total molecular wavefunction is a single-valued function. Furthermore, as illustrated schematically in Figure 6.4, rotation

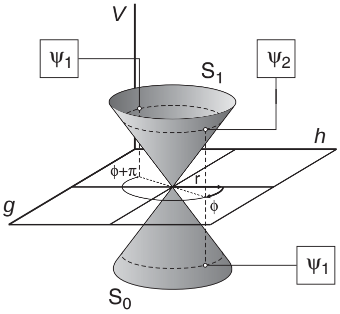

Figure 6.4 In the branching space (*x*,*y*), points lying on a circle centered at the apex of the double cone and with a small radius *r* are *diabatically* related. If we select a point on one of the surfaces and move it to the opposite side of the circle ($\phi \rightarrow \phi + \pi$), its wavefunction becomes equal to the wavefunction of the other surface at the original position. If we complete the circle, the point is back at its original position, but its wavefunction has changed sign (not shown, see text).

by 90° permutes the order of the electronic states, as is demonstrated by substituting $\theta+\pi$ into Eq. (33):

$$\begin{aligned}\psi_1 &= \cos\left[\frac{\phi_0+\pi}{2}\right]\varphi_A - \sin\left[\frac{\phi_0+\pi}{2}\right]\varphi_B \\ &= \sin\left[\frac{\phi_0}{2}\right]\varphi_A - \cos\left[\frac{\phi_0}{2}\right]\varphi_B \\ &= -\psi_2.\end{aligned} \tag{37}$$

As we will show in Section 2.3, this characteristic of the conical intersection can be used to detect the time step at which the seam is passed in a classical MD simulation of a photochemical reaction.

The conical intersection seam is the central mechanistic feature in a photochemical reaction. The conical intersection provides a funnel for efficient radiationless decay between electronic states (Figure 6.2). To illustrate the relationship between the surface crossing and photochemical reactivity, we draw a parallel with the transition state in ground state chemistry. The transition state forms the bottleneck through which the reaction must pass on its way from reactants to products. A transition state separates the reactant and product energy minima along the reaction path. A conical intersection also forms a bottleneck that separates the excited state branch of the reaction path from the ground state branch. The crucial difference between conical intersections and transition states is that, while the transition state must connect the reactant minimum to a single product minimum *via* a single reaction path, an intersection is a spike on the ground state energy surface and thus connects the excited state reactant to two or more products on the ground state *via* several reaction paths.

2.3. Excited state molecular dynamics

Photochemical reactions start in the excited state (S_1) but end in the ground state (S_0, Figure 6.1). To model the dynamics of such processes, we need a method to accurately compute the ground and excited state potential energy surfaces. In addition, we need an algorithm that models the radiationless transitions between the surfaces in a manner that is consistent with quantum mechanics.

If a sufficiently accurate description of the adiabatic Born–Oppenheimer potential energy surfaces is available, nuclear dynamics can be computed by numerically integrating either the time-dependent Schrödinger equation [Eq. (3)] or Newton's equations of motion. In the first case, quantum mechanics is used to follow the dynamics of nuclear wavepackets [$\chi_n(\mathbf{R})$, Eq. (9)], evolving on the electronic potential energy surfaces. With this approach transitions between surfaces near or at conical intersections can be described correctly. A wavepacket traveling through or near an intersection spawns new packets on both surfaces. The transfer probability is controlled by the nonadiabatic coupling elements. At the conical intersection, the coupling has its maximal strength, resulting in an efficient transfer of the complete wavepacket to the lower surface.

A requirement for wavepacket dynamics is that the relevant potential energy surfaces have been computed beforehand. As the computational costs associated with precomputing these surfaces increases rapidly with the number of coordinates in the system, wavepacket dynamics is restricted to small isolated molecules. Alternatively, the multidimensional configuration space can be reduced to a lower dimensional subspace in which quantum dynamics is possible [11]. However, choosing suitable coordinates is difficult and requires averaging over the remaining degrees of freedom. Furthermore, the choice of the coordinates can strongly bias the outcome of a simulation. Therefore, for photobiological problems, the size and complexity of the systems involved severely limit the applicability of wavepacket simulations.

Alternatively, we can decide to ignore the QM character of the nuclei altogether and use Newton's equations of motion to compute MD trajectories. In terms of computational effort, classical MD is orders of magnitude more efficient than wavepacket dynamics and is therefore routinely used for computing the time evolution of large biomolecular systems. Classical mechanics has the additional advantage that the potential energy surface can be computed on the fly. Forces are evaluated for the geometry at time step t and used to compute the geometry at the next time step $t + \Delta t$. Thus, only at the configurations sampled by the classical trajectory, electronic structure calculations are required. For systems with many degrees of freedom, for which computing potential energy surfaces beforehand is not possible, the on-the-fly strategy is the only option for performing MD simulations.

Classical mechanics provides a computationally cheap alternative to wavepacket dynamics. However, because quantum effects are ignored, population transfer cannot occur and classical trajectories are restricted to a single potential energy surface. Therefore, in contrast to wavepacket dynamics, radiationless transitions do not take place spontaneously. Instead, a binary decision to jump to a different electronic surface must be made at every time step in a single trajectory. The criterion for switching between electronic states must result in a distribution of state populations over very many trajectories that reflects the populations of a full QM treatment. Furthermore, in contrast to wavepacket dynamics, classical trajectories do not capture coherence effects. When a nuclear wavepacket originally traveling on a single adiabatic potential energy surface encounters a crossing, it typically produces two subpackets, or offsprings, one on each surface [12]. After such spawning event, the new wavepackets will still interfere with each other. However, as these subpackets travel on different surfaces and often have different initial velocities on their respective surfaces, they are well separated in phase space and it is highly unlikely that they will encounter each other again, especially in high-dimensional systems, such as solvated biomolecules. Therefore, the spawned wavepackets are effectively incoherent [12,13], and the classical trajectory approximation is justified in most situations.

2.4. Diabatic surface hopping

The interest in understanding photochemical processes has prompted the development of methods for the treatment of nonadiabatic effects in classical MD. Most, if not all of these methods are based on surface hopping: nuclei move on a single potential energy surface and nonadiabatic transitions are included by allowing the trajectory to hop from one surface to another. The size and complexity of biomolecular systems necessitate the use of computationally cheap surface-hopping algorithms. In this section we present the hopping procedure that we use in our simulations of photochemical processes in biological systems.

Our so-called diabatic hopping algorithm is based on the one-dimensional Landau and Zener equation, which relates the probability of a transition between two electronic states ψ_2 and ψ_1, to the nonadiabatic coupling, via:

$$P_{2\to 1} = \exp\left[-\frac{1}{4}\pi\xi\right]. \tag{38}$$

In this equation ξ is the Massey parameter defined as [14]

$$\xi = \frac{\Delta E}{\hbar \frac{\partial \mathbf{Q}}{\partial t} \cdot \mathbf{g}(\mathbf{Q})}, \tag{39}$$

where ΔE is the energy gap between the adiabatic states, $\mathbf{Q}$ represents a one-dimensional nuclear reaction coordinate, and

$$\mathrm{g}(\mathbf{Q}) = \langle \psi_1 | \nabla_{\mathbf{Q}} \psi_2 \rangle. \tag{40}$$

If we differentiate ψ_2 with respect to t *via* $\frac{\partial}{\partial t}(\mathbf{Q})$, we can rewrite ξ as

$$\xi = \frac{\Delta E}{\hbar \left\langle \psi_1 \middle| \frac{\partial \psi_2}{\partial t} \right\rangle}. \tag{41}$$

To decide when to undergo a transition to a different potential energy surface, one would in principle need to compute $\langle \psi_1 | \frac{\partial}{\partial t} \psi_2 \rangle$ at every time step of the simulation. In practice, however, it is possible to approximate $\langle\psi_1|\frac{\partial}{\partial t}\psi_2\rangle$ as follows.

If we integrate the classical equations of motion for the nuclei with a small time step Δt, we have at t:

$$\begin{aligned} \psi_1(t) &= \varphi_{\mathrm{A}}, \\ \psi_2(t) &= \varphi_{\mathrm{B}}, \end{aligned} \tag{42}$$

where the $\varphi_{\mathrm{A,B}}$ are the diabatic electronic states. At $t+\Delta t$, the states will have become mixed due to the nonadiabatic coupling. In the limit of an infinitesimally small time step, the change in the wavefunctions can be approximated by

$$\begin{aligned} \psi_1(t+\Delta t) &= \varphi_{\mathrm{A}} + \beta\varphi_{\mathrm{B}}, \\ \psi_2(t+\Delta t) &= -\beta\varphi_{\mathrm{A}} + \varphi_{\mathrm{B}}, \end{aligned} \tag{43}$$

where β is a mixing coefficient. Numerical differentiation (finite differences) of the wavefunction gives

$$\frac{\partial}{\partial t}\psi_2 = -\beta\frac{\varphi_{\mathrm{A}}}{\Delta t}, \tag{44}$$

and yields the following expression:

$$\left\langle \psi_1 \middle| \frac{\partial}{\partial t}\psi_2 \right\rangle \approx -\frac{\beta}{\Delta t}. \tag{45}$$

Since

$$\langle\psi_1(t)|\psi_2(t+\Delta t)\rangle = -\beta, \tag{46}$$

we can compute $\langle\psi_1(t)|\psi_2(t+\Delta t)\rangle$ as a numerical approximation for $\langle\psi_1|\frac{\partial}{\partial t}\psi_2\rangle$ in the Massey parameter [Eq. (41)].

Calculating the energy gap ΔE and $\langle\psi_1(t)|\psi_2(t+\Delta t)\rangle$ at every time step is straightforward, and we can use the Landau–Zener formula [Eq. (38)] to calculate the probability of a transition to the other surface. In principle, the transition probability can be used to spawn a new trajectory on the other surface. However, since this procedure would lead to multiple trajectories that have to be computed simultaneously, spawning is too demanding in practice. We therefore restrict hopping to situations where the transition probability approaches unity. This happens at the conical intersection seam, where $\Delta E \approx 0$ and $\|\langle\psi_1(t)|\psi_2(t+\Delta t)\rangle\| \approx 1$. The former is trivially true by the definition of an intersection. The latter follows from Eq. (37) and is illustrated in the branching space projection of Figure 6.4: passing through the intersection during a single time step (Δt), leads to geometries at t and $t+\Delta t$ that are opposite to each other with respect to the apex. Thus, crossing the seam is equivalent to rotating the wavefunction by a half of a circle in the branching space (Figure 6.4):

$$\begin{aligned}\langle\psi_1(t)|\psi_2(t+\Delta t)\rangle &= \langle\psi_1(\phi)|\psi_2(\phi+\pi)\rangle\\ &= -\langle\psi_1(\phi)|\psi_1(\phi)\rangle\\ &= -\langle\psi_1(t)|\psi_1(t)\rangle\\ &= -1.\end{aligned}\tag{47}$$

Because we allow hopping only at the conical intersection seam, our classical trajectories never leave the diabatic surface. Therefore, energy and momentum are obviously conserved. In principle, this strict diabatic hopping criterion could lead to an underestimation of the population transfer probability, because a surface hop in regions with strong nonadiabatic coupling far from the intersection is prohibited. In practice, however, the high dimensionality of the seam ensures that all trajectories encounter such regions of high transfer probability. The Landau–Zener model is clearly an approximation but helps one to keep a proper physical insight, which is crucial in understanding complex systems.

2.5. Excited state quantum chemistry

Although highly accurate methods for computing excited state electronic wavefunctions have become available over the past years, they are usually too time-consuming for systems larger than a few atoms. Therefore, most of these methods are not yet applicable in on-the-fly MD simulations of large biomolecular systems. Alternatively, simple forcefields or existing semi empirical methods that are computationally efficient may be used, but their applicability is limited, unless properly reparameterized [15,16]. Therefore, for on-the-fly MD, a compromise between cost and accuracy has to be made.

A computationally feasible approach to describe excited state electronic structure is the equation of motion coupled cluster (EOM-CCSD) method and ab initio dynamics simulations of small isolated molecules have been performed at the EOM-CCSD level [17]. However, EOM-CCSD can only work well if the underlying CCSD method provides a good description of the ground electronic state. This can cause problems when bonds are being broken or formed and the ground electronic state has a significant multiconfigurational character. The description of electronic states with a strong double excitation character also causes problems [18].

Time-dependent density functional theory (TD-DFT) also offers a computationally very efficient approach to describe excited states and consequently has been used in excited state MD simulations [19]. Similar to

EOM-CCSD, TD-DFT suffers from the deficiencies of the underlying monoconfigurational DFT description of the ground state in regions of bond breaking and bond formation. Moreover, TD-DFT is known to encounter severe problems in describing valence states of molecules exhibiting extended π systems, doubly excited states, and charge transfer excited states [20].

The problems associated with methods that are based on a single reference configuration, such as EOM-CCSD and TD-DFT, demonstrate that for computing excited states, multiconfigurational methods are required to provide wavefunctions that are sufficiently flexible to describe bond rearrangements, electronic state mixing, and electronic reorganizations. In addition, to calculate MD trajectories, analytical energy gradients are necessary. Since the complete active space self-consistent field (CASSCF) method fulfills these requirements, it has often been used in the framework of excited state dynamics simulations [21–25]. In CASSCF, a judicious set of occupied and virtual orbitals is chosen, the so-called active space orbitals. In this active space, a full configuration interaction calculation is performed, while the other orbitals are being kept doubly occupied or empty in all configurations. The active orbitals are optimized such that the electronic energy of the state considered is minimal. Alternatively, the average energy of the states under study is minimized (state-averaged approach), if state bias or root-flipping problems [26] have to be avoided that occur near surface crossing regions [27].

The CASSCF method captures to a large extent so-called *static* electron correlation. However, due to the necessary truncation of the active space, it does not recover *dynamic* electron correlation completely. Dynamic correlation is known to play a key role in the quantitative description of barrier heights and excitation energies. Thus, a higher level treatment that includes dynamic electron correlation effects is desirable. Unfortunately, methods that resolve both static and dynamic correlations tend to be computationally too demanding and furthermore often lack the required analytical energy gradients. Because in most cases CASSCF describes the topology of the potential energy surfaces of the involved states sufficiently accurate, it is widely used for mechanistic studies of photochemical reactions [28].

Dynamic correlation is accounted for in multireference perturbation theory approaches, such as CASPT2 [29]. CASPT2 provides a means of including dynamic correlation, while simultaneously describing static correlation. Recently, analytical CASPT2 energy gradients [30] have become available, which has opened the way for MD simulations. Coe et al. have already used these gradients to perform an ab initio MD simulation on the excited state proton transfer reaction in methyl salicylate [31]. However, the computational cost of this method still prevents its use for larger biomolecular systems, in which the number of correlated electrons is too large.

Alternatively, dynamic electron correlation is included to some extent in the restricted active space self-consistent field (RASSCF) method [29]. RASSCF allows larger active spaces and thus provides more flexibility in the choice of the active orbitals than CASSCF [32]. The larger active space is subdivided into three classes: orbitals with a limited number of valences, a fully active orbital set, and orbitals with a limited number of electrons. By eliminating the redundant configurations, the size of the configuration interaction problem can be greatly reduced in RASSCF compared to CASSCF without compromising accuracy. Because analytical gradients are available, the RASSCF method can be expected to be used in excited state dynamics simulations in the future. Unfortunately, however, it remains a difficult task even in RASSCF to select the correct orbital set for a given photochemical problem.

A promising alternative that circumvents the choice of active orbitals lies in the use of semi empirical configuration interaction methods. These methods offer a lower cost alternative, while still taking into account the correlation effects necessary to describe excited states. For example, the recently developed semi empirical OM2 method has been shown to describe accurately the well-known conical intersections of small molecules [33]. Thus, the use of new semiempirical methods, such as OM2, could hold great promise for nonadiabatic MD simulations of very large molecular systems in the near future.

Due to inaccuracy of approaches that are based on a single reference configuration, lack of validation of the semi empirical alternatives, and prohibitive computational demands of multireference perturbation methods, CASSCF is at present the most attractive option for excited state MD simulations. However, even at the CASSCF level of theory, the calculation of energies and gradients at every step of the simulation places a severe demand on computational resources. We are therefore forced to use minimal active spaces. These minimal spaces have to be calibrated against higher level methods before the simulations can be performed. Validation is usually done by comparing the energies of stationary points on the CASSCF potential energy surfaces to the single-point CASPT2 energies at these geometries.

2.6. Mixed quantum classical molecular dynamics

MD computer simulations of biological systems have come of age. Since the first application of MD on a small protein in vacuum more than three decades ago [34], advances in computer power, algorithmic developments, and improvements in the accuracy of the used interaction functions have established MD as an important and predictive technique to study dynamic processes at atomic resolution [35]. In the interaction functions, the so-called

MM forcefield, simple chemical concepts are used to describe the potential energy of the system [36]:

$$
\begin{aligned}
V_{\mathrm{MM}} \quad = \quad & \sum_{i}^{N_{\mathrm{bonds}}} V_i^{\mathrm{bond}} + \sum_{j}^{N_{\mathrm{angles}}} V_j^{\mathrm{angle}} + \sum_{l}^{N_{\mathrm{torsions}}} V_l^{\mathrm{torsion}} \\
& \sum_{i}^{N_{\mathrm{MM}}} \sum_{j>i}^{N_{\mathrm{MM}}} V_{ij}^{\mathrm{Coul}} + \sum_{i}^{N_{\mathrm{MM}}} \sum_{j>i}^{N_{\mathrm{MM}}} V_{ij}^{\mathrm{LJ}}, \qquad (48)
\end{aligned}
$$

where N_{MM} is the number of atoms in the system. Bonds and angles (V^{bond}, V^{angle}) are normally modeled by harmonic functions, and torsions by periodic functions (V^{torsion}). The pairwise electrostatic interaction between atoms with a partial charge (Q_i) is given by Coulomb's law:

$$
V_{ij}^{\mathrm{Coul}} = \frac{e^2 Q_i Q_j}{4\pi\epsilon_0 R_{ij}}, \qquad (49)
$$

in which R_{ij} denotes the interatomic distance, e the unit charge, and ϵ_0 the electric constant. Short-range Pauli repulsion and long-range dispersion attraction are most often described by a single Lennard-Jones potential:

$$
V_{ij}^{\mathrm{LJ}} = \left(\frac{C_{12}^{ij}}{R_{ij}}\right)^{12} - \left(\frac{C_6^{ij}}{R_{ij}}\right)^{6}, \qquad (50)
$$

with C_{12}^{ij} and C_6^{ij} a repulsion and attraction parameter, respectively, that depend on the atom types involved.

Electrons are thus ignored in molecular mechanics forcefields. Their influence is expressed by empirical parameters that are valid for the ground state of a given covalent structure. Therefore, processes that involve electronic rearrangements, such as photochemical reactions, cannot be described at the MM level. Instead, these processes require a quantum mechanics description. As we have discussed above, the computational effort associated with computing excited state electronic structure puts severe constraints on the size of the system that can be studied. To overcome this limitation for biological systems, which are typically orders of magnitude too large for a complete quantum chemical treatment, methods have been developed that treat a small part of the system at an appropriate QM level, while retaining the computationally cheaper forcefield (MM) for the remainder. This hybrid QM/MM strategy was originally introduced by Warshel and Levitt [37] and is illustrated in Figure 6.5.

The justification for dividing a system into regions that are described at different levels of theory is the local character of chemical reactions in condensed phases. A distinction can usually be made between a "reaction

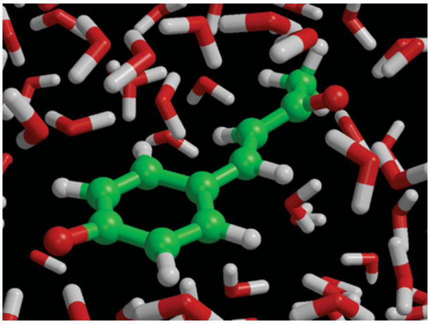

Figure 6.5 The QM/MM partitioning scheme used in recent simulations of a photoactive yellow protein chromophore analog in water. The atoms of the QM subsystem are shown in ball-and-stick representation and MM atoms are shown as thick sticks. The CASSCF method was employed to model the electronic structure of the chromophore, while the SPCE model [38] was used for the water molecules.

center" with atoms that are directly involved in the reaction and a "spectator" region, in which the atoms do not directly participate in the reaction. For example, most reactions in solution involve the reactants and the first few solvation shells. The bulk solvent is hardly affected by the reaction, but can influence the reaction *via* long-range interactions. The same is true for most enzymes, in which the catalytic process is restricted to an active site. The rest of the protein provides an electrostatic background that may or may not facilitate the reaction.

The hybrid QM/MM Hamiltonian contains three classes of interactions: interactions between atoms in the QM region, between atoms in the MM region, and interactions between QM and MM atoms

$$H^{\text{hybrid}} = H_{\text{QM}} + H_{\text{MM}} + H_{\text{QM/MM}}. \tag{51}$$

The interactions within the QM and MM regions are relatively straightforward to describe, that is, at the QM and MM level, respectively. The interactions between the two subsystems are more difficult to describe and several approaches have been proposed.

In the most simple approach, the QM subsystem is mechanically embedded in the MM system and kept in place by forcefield interactions, that is, bonds, angles, torsions, and Lennard-Jones. With the exception of these interactions, the two systems are treated independently. Thus a quantum chemistry calculation is performed on an isolated QM subsystem, while a forcefield calculation is performed on the MM region. An improvement of the model is to use the isolated electronic wavefunction to derive partial atomic charges for the QM atoms and use these charges to compute the electrostatic QM/MM interactions with the MM atoms.

In the more popular electronic embedding scheme of Field and coworkers [39], the MM atoms enter the electronic Hamiltonian, as if they were QM nuclei:

$$\begin{aligned} H^{\mathrm{e}}_{\mathrm{QM/MM}} &= H^{\mathrm{e}} + \sum_{i}^{n_{\mathrm{e}}}\sum_{K}^{N_{\mathrm{MM}}} \frac{Q_i}{4\pi\epsilon_0 r_{iK}} \\ &= -\frac{\hbar^2}{2m_{\mathrm{e}}}\sum_{i}^{n_{\mathrm{e}}}\nabla_i^2 + \sum_{i}^{n_{\mathrm{e}}}\sum_{j>i}^{n_{\mathrm{e}}}\frac{e^2}{4\pi\epsilon_0 r_{ij}} \\ &\quad -\sum_{i}^{n_{\mathrm{e}}}\sum_{A}^{N_{\mathrm{QM}}}\frac{e^2 Z_A}{4\pi\epsilon_0 r_{iA}} + \sum_{K}^{N_{\mathrm{MM}}}\frac{e^2 Q_K}{4\pi\epsilon_0 r_{iK}}, \end{aligned} \tag{52}$$

where H^{e} is the original electronic Hamiltonian for the isolated QM system, defined in Eq. (5); n_{e} is the number of electrons, N_{QM} the number of QM nuclei and N_{MM} the number of MM atoms; Z_A and Q_K are the nuclear and partial charges of QM nucleus A and MM atom K, respectively; and m_{e} denotes the electron mass. Because the MM atoms enter the Hamiltonian, the electronic wavefunction is polarized by the environment. Simultaneously, the electrons are exerting electrostatic forces on both QM nuclei and MM atoms. Problems may arise if the MM atoms near the QM region have high partial charges. In this case, the electrons are strongly attracted by such MM atoms, and the wavefunction can become overpolarized. Penetration of electron density into the MM region is an artefact of ignoring the electrons of the MM atoms. A remedy for this spill-out effect is to use Gaussian-shaped charge densities rather than point charges to represent partially charged MM atoms [40].

Interactions between the nuclei in the QM region, and between QM nuclei and MM atoms are described by Coulomb's law:

$$H^{\mathrm{nuc}}_{\mathrm{QM/MM}} = \sum_{A}^{N_{\mathrm{QM}}}\sum_{B>A}^{N_{\mathrm{QM}}}\frac{Z_A Z_B}{4\pi\epsilon_0 R_{AB}} + \sum_{A}^{N_{\mathrm{QM}}}\sum_{K}^{N_{\mathrm{MM}}}\frac{Z_A Q_K}{4\pi\epsilon_0 R_{AK}}. \tag{53}$$

In addition to electrostatics, there are also van der Waals interactions between the subsystems that are handled at the forcefield level [Eq. (50)], as if the QM nuclei were MM atoms. Similar to the previous model, bonded interactions, such as bonds, angles, and torsions involving both QM and MM atoms, are described by the respective forcefield functions.

If the QM and MM subsystems are connected by chemical bonds, care has to be taken when evaluating the QM wavefunction. Cutting the QM/MM bond creates one or more unpaired electrons in the QM subsystem. In reality, these electrons are paired in a bonding orbital with electrons belonging to the atoms on the MM side. A number of approaches to remedy the artifact of such open valences have been proposed. The most easy solution is to introduce a monovalent link atom at an appropriate position along the bond vector between the QM and MM atoms. Hydrogen is most often used, but there is no restriction on the type of the link atom and even complete fragments, such as methyl groups, can be used to cap the QM subsystem. The link atoms are present only in the QM calculation and are invisible for the MM atoms. Alternative approaches for capping the QM region are the frozen orbital approach [41] and the generalized hybrid orbital method [42]. In all of our simulation studies to date, we have used hydrogen link atoms for capping the QM subsystem.

The QM/MM scheme of Field and coworkers provides a conceptually intuitive way of including the effect of an environment on a chemical reaction. However, unless polarization is treated explicitly at the forcefield level, this QM/MM model is not internally consistent. In most forcefields polarization is not explicitly included, but is implicitly accounted for *via* the parameters in the other terms, most notably, in the nonbonded interactions. Thus, although the MM region can induce polarization of the QM subsystem, the latter cannot back-polarize the MM region. A related problem arises from the use of standard Lennard-Jones and charge parameters, which implicitly contain polarization. When using these parameters without modification, there is both explicit and implicit polarization of the QM region. Therefore, the total polarization can be overestimated. To avoid such possible artifact, the nonbonded parameters in principle should be reparameterized for use in QM/MM simulations. However, this procedure requires the optimization of very many parameters that also depend on the level of theory employed for the QM subsystem and is most often skipped in practice.

3. APPLICATIONS

In this section we discuss some of our recent applications of excited state dynamics simulations on photobiological systems. We will show that in these systems, the protein environment controls the photochemical properties of the chromophore and steers the excited state dynamics.

3.1. Photoactive yellow protein

Photoactive yellow protein (PYP) is believed to be the primary photoreceptor for the photoavoidance response of the salt-tolerant bacterium *Halorhodospira halophila* [43]. PYP contains a deprotonated 4-hydroxy-cinnamic acid (or *p*-coumaric acid, pca) chromophore linked covalently to the γ-sulfur of Cys69 via a thioester bond (Figure 6.6). Upon absorbing a blue-light photon,

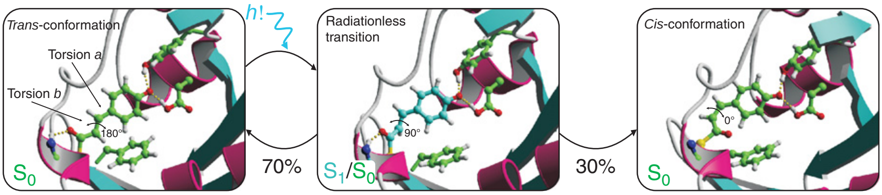

Figure 6.6 Snapshots from excited state trajectories of wild-type PYP showing the chromophore (pca) in the active site pocket. The first snapshot is at the excitation. The second shows the configuration at the radiationless transition from S_1 to S_0. The third snapshot shows the photoproduct, in which the carbonyl oxygen of the thioester linkage has flipped and is no longer hydrogen bonded to the backbone of Cys69.

PYP enters a fully reversible photocycle involving several intermediates on timescales ranging from a few hundred femtoseconds to seconds [43].

To understand the intrinsic photochemical properties of the PYP chromophore, we have performed geometry optimizations of an isolated chromophore analog [44]. In these optimizations, the complete π system of the chromophore was included in the active space, which thus consisted of 12 electrons in 11 π orbitals. In addition to optimizing the local minima on the S_1 potential energy surface and the barriers that separate them, we also located conical intersections in the vicinity of these mimima. The optimizations revealed that there are two minima on S_1: the single bond twisted minimum, in which the bond adjacent to the phenol ring is rotated by 90°; and the double bond twisted minimum, in which the ethylenic bond is twisted at 90° (Figure 6.7). In the isolated chromophore, there is almost no barrier for reaching the single bond twisted S_1 minimum from the Franck–Condon region, whereas there is a significant barrier to double bond

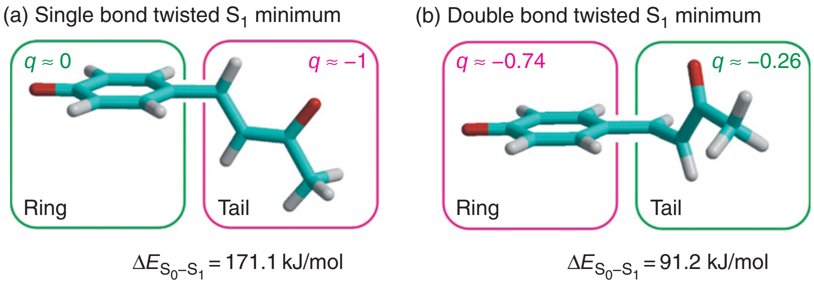
(a) Single bond twisted S_1 minimum

(b) Double bond twisted S_1 minimum

Figure 6.7 Excited state minimum energy configurations of a chromophore analog. In both the single bond twisted S_1 minimum (a) and the double bond twisted S_1 minimum (b), there is a substantial energy gap between the ground and excited states. The distribution of the negative charge in these minima is opposite.

rotation. Thus, after photon absorption in vacuum, the main relaxation channel on S_1 involves rotation of the single bond to 90°. We furthermore found that the S_1/S_0 intersection seam lies very far away from this minimum. As a consequence, radiationless decay is not very likely to occur in vacuum. In subsequent QM/MM simulations, we have probed the effect of different environments on the photochemistry of the chromophore.

To examine the effect of an aqueous environment, we have performed 91 QM/MM excited state dynamics simulations of a chromophore analog in water [44]. The chromophore was described at the CASSCF(6,6)/3-21G level of theory, while the water molecules were modeled by the SPCE forcefield [38]. The results of these simulations demonstrate that in water radiationless decay is very efficient [44]. The predominant excited state decay channel involves twisting of the single bond (88%) rather than the double bond (12%). In contrast to vacuum, decay takes place very near these minima. Inspection of the trajectories revealed that decay is mediated by specific hydrogen bond interactions with water molecules. These hydrogen bonds are different for the single and double twisted S_1 minima, which reflects the difference in charge distribution between these minima [45]. In the single bond twisted S_1 minimum, the negative charge resides on the alkene moiety of the chromophore (Figure 6.7). Three strong hydrogen bonds to the carbonyl oxygen stabilize this charge distribution to such an extent that the seam almost coincides with the single bond twisted S_1 minimum (Figure 6.8). In the double bond twisted S_1 minimum, the negative charge is localized on the phenolate ring (Figure 6.7). Transient stabilization of this charge distribution by two or more strong hydrogen bonds to the phenolate oxygen brings the seam very close to this S_1 minimum (Figure 6.8). Thus, in water the ultrafast excited state decay is mediated by hydrogen bonds.

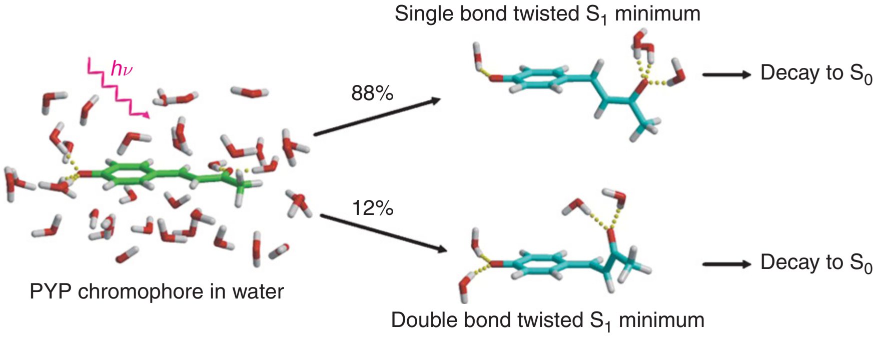

Figure 6.8 In water the chromophore undergoes both single and double bond isomerization. Excited state decay from these minima is very efficient due to stabilization of the chromophore's S_1 charge distribution by specific hydrogen bond interactions.

To find out how the protein mediates the photochemical process, we also carried out a series of QM/MM simulations of wild-type PYP. Figure 6.6 shows the primary events after photoexcitation in the simulation. The chromophore rapidly decays to the ground state *via* a 90° rotation of the double bond (Figure 6.6), rather than the single bond. During this photoisomerization process, the hydrogen bonds between the chromophore's phenolate oxygen atom and the side chains of the highly conserved Tyr42 and Glu46 residues remain intact. Just as in water, these hydrogen bonds enhance excited state decay from the double bond twisted minimum.

Upon returning to the ground state, the chromophore either relaxes back to the original *trans* conformation (180°), or it continues isomerizing to a *cis* conformation (0°). In the latter case, the relaxation also involves a flip of the thioester linkage, which causes the carbonyl group to rotate 180°. During this rotation, the hydrogen bond between the carbonyl oxygen and the Cys69 backbone amino group is broken (Figure 6.6). In total, 14 MD simulations were carried out, initiated from different snapshots from a classical ground state trajectory. The fluorescence lifetime (200 fs) and isomerization quantum yield (30%) in the simulations agree well with experiments (400 fs [46] and 35% [43], respectively).

In the wild-type protein no single bond isomerization was observed. Thus, the protein not only provides the hydrogen bonds required for ultrafast decay, but also controls which of the chromophore's bond isomerizes upon photoexcitation. We identified the positive guanidinium moiety of Arg52 located just above the chromophore ring, as the "catalytic" residue that enforces double bond isomerization. The preferential electrostatic stabilization of the double bond twisted S_1 minimum by the positive Arg52 strongly favors double bond isomerization over single bond isomerization.

To elucidate the role of this arginine in the activation process in more detail, we performed excited state dynamics simulations on the Arg52Gln mutant of PYP [47]. This mutant can still enter the photocycle, albeit with a lower rate and quantum yield [48,49]. Without the positive Arg52, the predominant excited state reaction in the mutant involves isomerization of a single bond in the chromophore, rather than the double bond (Figure 6.9) [50]. This observation confirms that the role of Arg52 is to steer the initial events after photoabsorption to ensure rotation of the double bond rather than the single bond in the chromophore.

During rotation of the single bond, the hydrogen bond between the carbonyl oxygen and Cys69 backbone amino group is broken. As shown in Figure 6.10, new hydrogen bonds are rapidly formed between the carbonyl oxygen atom and the backbone amino groups of Tyr98 and Asp97. A water molecule from outside enters the chromophore pocket to donate a third hydrogen bond. With these three hydrogen bonds stabilizing the negative charge on the alkene moiety, the chromophore rapidly decays to S_0. Thus, the decay mechanism in the Arg52Gln mutant and in water are essentially the same.

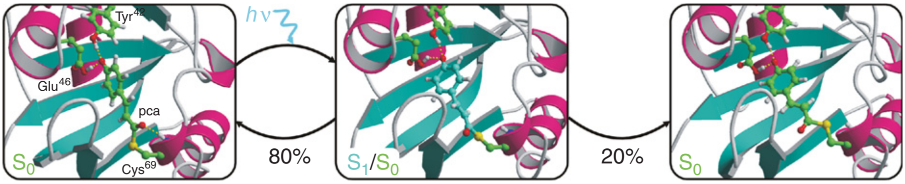

Figure 6.9 Snapshots from an excited state trajectory of the Arg52Gln mutant of PYP, showing the chromophore (pca) in the active site pocket. The first snapshot is at the excitation. The second shows the configuration at the radiationless transition from S_1 to S_0. The third snapshot shows the photoproduct. In the mutant isomerization takes place around the single bond. Like in the wild-type protein, the carbonyl oxygen of the thioester linkage flips, causing the break of the hydrogen bond to the backbone of Cys69.

Although single bond isomerization does not result in the formation of the *cis* chromophore, a 180° flip of the thioester group and a rupture of the hydrogen bond to Cys69 was observed with a 20% quantum yield (Figure 6.9). Together with the experimental observation that the mutant has a photoactivation quantum yield of about 21% [49], this suggests that the key step to enter the photocycle is the oxygen flip rather than the double bond isomerization.

To summarize, the simulations are consistent with experimental observations and have provided detailed structural and dynamic information at a resolution well beyond that achievable by other means. From the simulations, key amino acids have been identified as well as the mechanism by which they control the primary events in the photocycle of PYP. These are (1) double bond photoisomerization and (2) the break of a hydrogen bond

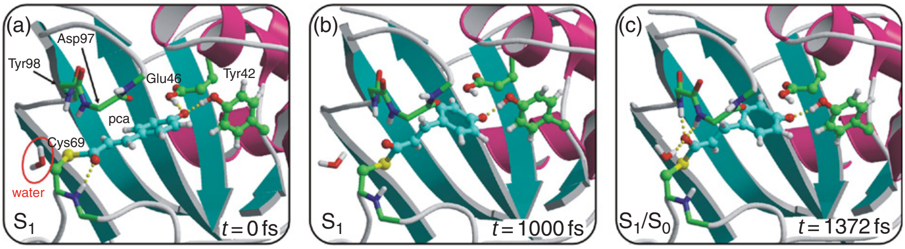

Figure 6.10 Snapshots from an excited state trajectory of the Arg52Gln mutant of PYP, demonstrating that three hydrogen bonds to the carbonyl moiety are essential for S_1 decay at the single bond twisted minimum. The first snapshot is at the excitation to S_1. The second snapshot shows the twisted configuration without hydrogen bonds to the carbonyl. The gap between S_1 and S_0 is far too high for decay at this configuration. However, as the third snapshot shows two backbone amino groups and a bulk water, that has moved into the chromophore pocket during the excited state dynamics, donate the three hydrogen bonds that are required for efficient decay from the S_1 minimum.

between the chromophore and the protein backbone. These events trigger a proton transfer from the protein to the chromophore, which ultimately leads to the signaling state of PYP [51].

3.2. Reversibly switchable fluorescent proteins

Photochromic, or reversibly switchable fluorescent proteins (RSFPs) that can be photoswitched between a fluorescent and a nonfluorescent state have proven to be crucial for new innovative microscopy schemes. However, despite the availability of X-ray structures of fluorescent and nonfluorescent states of several RSFPs, there is as yet no consensus about how these protein achieve the switching. To reveal the molecular basis of the switching process we have carried out a two-step QM/MM study of asFP595, a natural occurring RSFP from the sea anemone *Anemonia sulcata* (Figure 6.11).

The first step was to locate the protons in the chromophore binding pocket, because these protons were not resolved in the available X-ray structures. For this purpose, simulated UV/Vis spectra were compared to the available experimental data. This comparison was backed up by continuum electrostatics calculations, and enabled to unambiguously determine the protonation of the *on* and *off* states of asFP595 [52]. These calculations ascertained that the neutral chromophore form is dominant in the *cis* conformation (*on*-state), whereas the zwitterionic and the anionic chromophores predominate in the *trans* conformation (*off*-state) (Figure 6.11b). These results reveal that the photoinduced *trans*–*cis* isomerization of the chromophore is accompanied by proton transfer events. As shown in Figure 6.11a, these proton transfers are mediated by the ionizable residues

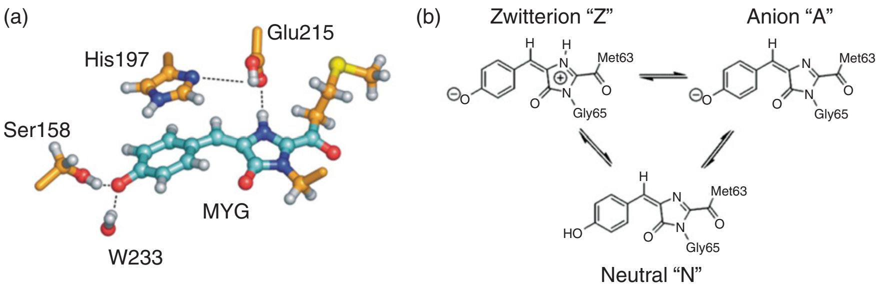

Figure 6.11 (a) Active site of the reversibly switchable fluorescent protein asFP595, showing the asFP595 chromophore (MYG) in the *trans* conformation and adjacent amino acid side chains. Dashed lines represent hydrogen bonds between MYG and Ser158, Glu215, and a crystallographic water molecule (W233), respectively. His197 is π stacked to the MYG phenoxy moiety and forms a hydrogen bond to Glu215. The carbon skeleton of the QM subsystem is shown in cyan, and the carbon atoms modeled by MM are shown in orange. (b) Schematic drawings of the important MYG protonation states.

Ser158, His197, and Glu215 in the chromophore pocket. His197 is connected through an extended hydrogen bonding network to the exterior interface between the protein and the surrounding solution (not shown in Figure 6.11).

In the second step of the study, nonadiabatic QM/MM MD simulations were carried out to elucidate the photochemistry of each of the previously identified protonation states of the chromophore [53]. In these simulations, energies and gradients on the ground and excited states were calculated on the fly at the CASSCF(6,6)/3-21G level of theory. Prior to the dynamics simulations, minima and conical intersections were characterized in vacuo at the RASSCF(18,7+4+5)[2,2]/6-31G* level of theory, that is, including all π orbitals of the chromophore in the active space. The final six-electron, six-orbital active space used in the QM/MM dynamics simulations was selected from these RASSCF calculations such as to enable the simultaneous description of the ground state and the first excited state.

The quantum yields and excited state lifetimes from the QM/MM dynamics simulations agree well with experimental measurements [54]. In addition, the simulations enable to predict the structures of the hitherto unknown photochemical intermediates and the irreversibly fluorescent state. Furthermore, the simulations revealed how the proton distribution in the active site of the asFP595 controls the photochemical conversion pathways of the chromophore in the protein matrix. The suggested mechanism in Figure 6.12 shows that changes in the protonation state of the chromophore and some proximal amino acids lead to different photochemical states, which all turn out to be essential for the photoswitching mechanism. These photochemical states are (1) a neutral chromophore, which can photoisomerize back and forth between the *trans* and *cis* configuration on a subpicosecond timescale, (2) an anionic chromophore, which rapidly undergoes radiationless decay after excitation in both the *cis* and *trans* configuration, and (3) a long-lived and therefore putatively fluorescent zwitterionic chromophore. The *trans* zwitterion can rapidly return to the ground state through proton transfer to the neighboring Glu215 (Figure 6.11a). This alternative de-excitation pathway is not accessible for the *cis* isomer, thus explaining why only the *cis* form fluoresces. The overall stability (and thus the relative population) of the different protonation states is controlled by the isomeric state of the chromophore.

On the basis of the simulations, it was proposed that radiation-induced decarboxylation of the glutamic acid Glu215 could block the proton transfer pathways that enable the deactivation of the zwitterions and thus leads to irreversible fluorescence (Figure 6.12). Recent experiments on the structurally similar protein Dronpa [55,56] also provide strong support for the proposed protonation/deprotonation mechanism. The similarity between the chromophores in a variety of fluoroproteins suggests that during molecular evolution, the (*p*-hydroxybenzylidene)imidazolinone chromophoric

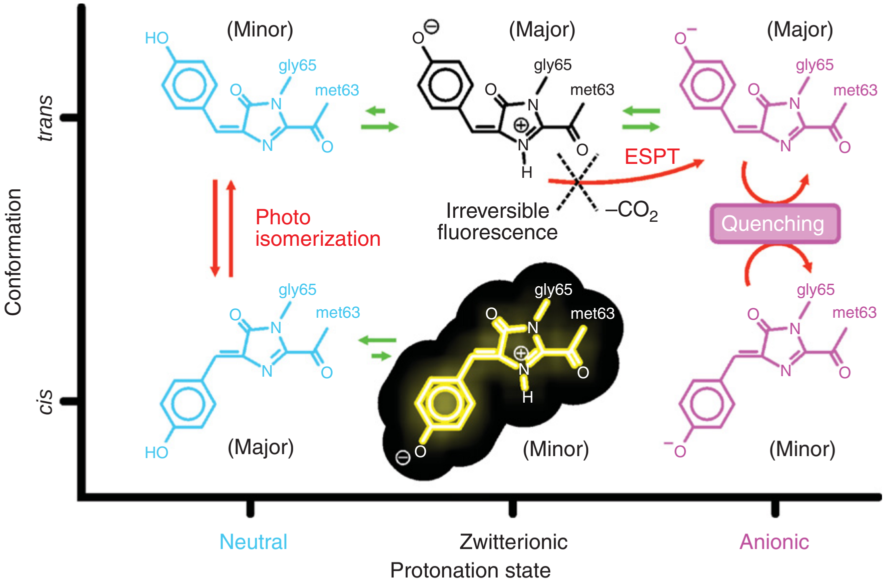

Figure 6.12 Scheme of the reversible photoswitching mechanism of asFP595. The fluorescent state Z_{cis} is highlighted. The green arrows indicate ground state equilibria, whereas the red arrows indicate excited state processes. The major protonation states are the zwitterionic and the anionic chromophores in the *trans* conformation, and the neutral chromophore in the *cis* conformation, as indicated in the square brackets.

moiety served as a template and that the photochromic properties—and thus the function—was fine-tuned by the protein environment.

4. FINAL REMARKS AND CONCLUSIONS

Understanding light-driven processes is one of the major goals of the bio- and nanosciences. The underlying molecular mechanisms are typically governed by subpicosecond atomic motions. Mechanisms on such ultrafast timescales are very challenging to probe by experiment. Here, MD simulations have become an invaluable tool to understand such processes in atomic detail.

In this contribution, we have reviewed our approach for excited state MD simulations. In the applications that we have selected here, the simulations have provided detailed structural and dynamical information of the photobiological process at a resolution well beyond what is achievable experimentally. The applications also demonstrate what is feasible today with on-the-fly MD simulations, and where the limits are. These limits are predominantly imposed by the current state of computer technology, which restricts both system size and timescale of the processes we can study today. However, the expected increase of computer power, complemented by the development of more efficient electronic structure methods and new algorithms, will enable the study of larger systems and longer timescales in the near future. Therefore, excited state MD simulation has the potential to lead to a better understanding of photobiological reactions. Ultimately, we expect these simulations to enable accurate predictions of photochemical properties and to become a standard tool for rational design of new photoactive systems.

REFERENCES

[1] A. Szabo, N.S. Ostlund, Modern Quantum Chemistry, Dover Publications, New York, 1989.
[2] H. Köppel, W. Domcke, L.S. Cederbaum, Adv. Chem. Phys. 57 (1984) 59.
[3] G.A. Worth, L.S. Cederbaum, Annu. Rev. Phys. Chem. 55 (2004) 127.
[4] J. von Neumann, E. Wigner, Z. Physik 30 (1929) 467.
[5] G.J. Atchity, S.S. Xantheas, K. Ruedenberg, J. Chem. Phys. 95 (1991) 1862.
[6] G.J. Atchity, K. Ruedenberg, J. Chem. Phys. 111 (1999) 2910.
[7] D.R. Yarkony, J. Chem. Phys. 112 (2000) 2111.
[8] H. Koppel, J. Gronki, S. Mahapatra, J. Chem. Phys. 115 (2001) 2377.
[9] H. Muller, H. Koppel, L.S. Cederbaum, New J. Chem. 17 (1993) 7.
[10] S. Matsika, D.R. Yarkony, J. Phys. Chem. A 106 (2002) 2580.
[11] I. Burghardt, J. Chem. Phys. 114 (2001) 89.
[12] M. Thachuk, M.Y. Ivanov, D.M. Wardlaw, J. Chem. Phys. 109 (1998) 5747.
[13] J. Onuchic, P. Wolynes, J. Phys. Chem. 92 (1998) 6495.
[14] M. Desouter-Lecomte, J. Lorquet, J. Chem. Phys. 71 (1979) 4391.
[15] A. Warshel, Nature 260 (1976) 679.
[16] A. Toniolo, S. Olsen, L. Manohar, T.J. Martinez, Faraday Discuss. 127 (2004) 149.
[17] K.K. Baeck, T.J. Martinez, Chem. Phys. Lett. 375 (2003) 299.
[18] R.J. Bartlett, M. Musial, Rev. Mod. Phys. 79 (2007) 291.
[19] I. Tavernelli, U.F. Rohrig, U. Rothlisberger, Mol. Phys. 103 (2005) 963.
[20] A. Dreuw, M. Head-Gordon, Chem. Rev. 105 (2005) 4009.
[21] J.D. Coe, T.J. Martinez, J. Phys. Chem. A. 110 (2006) 618.
[22] J.D. Coe, T.J. Martinez, J. Am. Chem. Soc. 127 (2005) 4560.
[23] O. Weingart, A. Migani, M. Olivucci, M.A. Robb, V. Buss, P. Hunt, J. Phys. Chem. A 108 (2004) 4685.
[24] M. Boggio-Pasqua, M.J. Bearpark, P.A. Hunt, M.A. Robb, J. Am. Chem. Soc. 124 (2002) 1456.
[25] A. Sanchez-Galvez, P. Hunt, M.A. Robb, M. Olivucci, T. Vreven, H.B. Schlegel, J. Am. Chem. Soc. 122 (2000) 2911.
[26] H.J. Werner, W. Meyer, J. Chem. Phys. 74 (1981) 5794.
[27] G.A. Worth, M.A. Robb, Adv. Chem. Phys. 124 (2002) 355.
[28] M.K.B. Lipkowitz, D.B. Boyd (Eds.), Reviews in Computational Chemistry, Wiley, New York, 2000.
[29] B.O. Roos, Acc. Chem. Res. 32 (1999) 137.
[30] P. Celani, H.J. Werner, J. Chem. Phys. 119 (2003) 5044.

[31] J.D. Coe, B.G. Levine, T.J. Martinez, J. Phys. Chem. A 111 (2007) 11302.
[32] M. Boggio-Pasqua, M.J. Bearpark, M. Klene, M.A. Robb, J. Chem. Phys. 120 (2004) 7849.
[33] T.W. Keal, A. Koslowski, W. Thiel, Theor. Chem. Acc. 118 (2007) 837.
[34] J.A. McCammon, B.R. Gelin, M. Karplus, P.G. Wolynes, Nature 262 (1976) 325.
[35] H.J.C. Berendsen, Science 271 (2001) 954.
[36] F. Jensen, Introduction to Computational Chemistry, Wiley, New York, 2001.
[37] A. Warshel, M. Levitt, J. Mol. Biol. 103 (1976) 227.
[38] H.J.C. Berendsen, J.R. Grigera, T.P. Straatsma, J. Phys. Chem. 91 (1987) 6269.
[39] M.J. Field, P.A. Bash, M. Karplus, J. Comp. Chem. 11 (1990) 700.
[40] P. Amara, M.J. Field, Theor. Chem. Acc. 109 (2003) 43.
[41] D.M. Philipp, R.A. Friesner, J. Comput. Chem. 20 (1999) 1468.
[42] J. Gao, P. Amara, C. Alhambra, M.J. Field, J. Phys. Chem. A 102 (1998) 4714.
[43] K.J. Hellingwerf, J. Hendriks, T. Gensch, J. Phys. Chem. A 107 (2003) 1082.
[44] M. Boggio-Pasqua, M.A. Robb, G. Groenhof, J. Am. Chem. Soc. 131 (2009) 13580.
[45] E.V. Gromov, I. Burghardt, J.T. Hynes, H. Köppel, L.S. Cederbaum, J. Photochem. Photobiol. A 190 (2007) 241.
[46] N. Mataga, H. Chosrowjan, Y. Shibata, Y. Imamoto, F. Tokunaga, J. Phys. Chem. B 104 (2000) 5191.
[47] N. Shimizu, H. Kamikubo, Y. Yamazaki, Y. Imamoto, M. Kataoka, Biochemistry 45 (2006) 3542.
[48] P. Changenet-Barret, P. Plaza, M.M. Martin, H. Chosrowjan, S. Taniguchi, N. Mataga, et al., Chem. Phys. Lett. 434 (2007) 320.
[49] K. Takeshita, Y. Imamoto, M. Kataoka, K. Mihara, F. Tokunaga, M. Terazima, Biophys. J. 83 (2002) 1567.
[50] G. Groenhof, L.V. Schäfer, M. Boggio-Pasqua, H. Grubmüller, M.A. Robb, J. Am. Chem. Soc. 130 (2008) 3250.
[51] G. Groenhof, M.F. Lensink, H.J.C. Berendsen, A.E. Mark, Proteins 48 (2002) 212.
[52] L.V. Schäfer, G. Groenhof, A.R. Klingen, G.M. Ullmann, M. Boggio-Pasqua, M.A. Robb, H. Grubmüller, Angew. Chem. Int. Ed. 46 (2007) 530.
[53] L.V. Schäfer, G. Groenhof, M. Boggio-Pasqua, M.A. Robb, H. Grubmüller, PLoS Comput. Biol. 4 (2008) e1000034.
[54] T.A. Schüttrigkeit, T. von Feilitzsch, C.K. Kompa, K.A. Lukyanov, A.P. Savitsky, A.A. Voityuk, M.E. Michel-Beyerle, Chem. Phys. 323 (2006) 149.
[55] S. Habuchi, P. Dedecker, J.I. Hotta, C. Flors, R. Ando, H. Mizuno, A. Miyawaki, J. Hofkens, Photochem. Photobiol. Sci. 5 (2006) 567.
[56] E. Fron, C. Flors, G. Schweitzer, S. Habuchi, R. Ando, H. Mizuno, J. Am. Chem. Soc. 129 (2007) 4870.

CHAPTER 7

Ab Initio Quantum Mechanical Charge Field Molecular Dynamics—A Nonparametrized First-Principle Approach to Liquids and Solutions

Thomas S. Hofer[a], **Andreas B. Pribil**[a],
Bernhard R. Randolf[a] and **Bernd M. Rode**[a]

Contents

[a] Theoretical Chemistry Division, Institute of General, Inorganic and Theoretical Chemistry, University of Innsbruck, Innrain 52a, A-6020 Innsbruck, Austria
E-mail address: t.hofer@uibk.ac.at (T.S. Hofer)

Advances in Quantum Chemistry, Vol. 59
ISSN: 0065-3276, DOI: 10.1016/S0065-3276(10)59007-5

© 2010 Elsevier Inc.
All rights reserved

1. INTRODUCTION

There is no doubt about the dominant importance of the liquid state in chemistry and also in all biological processes. However, any theoretical treatment of the liquid state encounters numerous problems, in particular because of its complexity, as it combines the mobility of molecules encountered in the gaseous state with the density of solids. Therefore, the number of interacting particles is large and the nature and strength of these interactions make it difficult to describe them with simple potentials. In particular, when hydrogen bonding is involved—which is an essential feature of all aqueous and many nonaqueous solutions—sophisticated interaction potentials have to be developed in order to describe the physical behavior of liquids. Whenever solutions are considered still other types of interactions are present, which usually require complicated potential functions to be taken into account.

The modern theoretical treatment of liquids and solutions started with statistical methods of Monte Carlo (MC) or molecular dynamics (MD) type [1] which both were developed in the second half of the 20th century. Based on potential functions that were derived either from empirical data or from increasingly accurate ab initio calculations of energy hypersurfaces the behavior of particles in the liquid systems is evaluated in these methods by means of classical statistical thermodynamics [2]. The potential functions were usually assumed to be pairwise additive, but it was soon recognized that wherever interactions became stronger this approximation is not justified [3,4]. As a consequence, three- or even four-body interaction potentials had to be added. The development of such functions based on ab initio calculated energy hypersurfaces encounters problems both in terms of accuracy of the energy surface calculations and in finding appropriate analytical potential functions to be fitted to these three- and four-body terms. In addition, the classical approach makes it difficult to include further important features in the interactions, in particular polarization and charge transfer, and the existence of numerous "polarizable" models for water, almost none of them sufficiently describing all properties of this most essential liquid [5], illustrate this difficulty.

The logical consequence for further improvement of these simulation methods was, therefore, the inclusion of quantum mechanics into the classical molecular mechanics treatment. The enormous numerical computational tasks of calculating interaction energies or forces acting on the molecules by means of quantum mechanics have for a long time made such an approach nearly impossible. Even nowadays with all the advanced computational facilities, a treatment of a representative simulation box with several hundred particles by means of quantum mechanics is beyond the capabilities of contemporary computational equipment. The solution for this problem was sought in two ways: first, in the use of simplified density functional methods and in the restriction of the system to a number of 30–60 molecules in the quantum mechanical (QM) treatment. This type of treatment is known under the name Car–Parrinello (CP) simulations and it has presently become a popular way to proceed with the simulation of systems where a QM treatment seems inevitable in order to achieve a better accuracy for the description of the liquid systems [6]. The second approach divides the system within the simulation box into two regions: one containing the most relevant subsystem, for example, a solvated molecule with its first or even second solvation layer; and the other one dealing with the remaining part of the simulation box by means of classical potentials [quantum mechanical and molecular mechanical (QM/MM) approach]. The latter methodology also encounters some problems, first of all with respect to the size of the quantum mechanical region, but also with respect to particle transitions between QM/MM region.

Both approaches, namely CP and QM/MM approach have not only technical problems but also a number of inherent methodical error sources that demand much care in the performance of the simulations and sometimes do not allow an unambiguous interpretation of the results.

The main problems of CP simulations [6] are the size of the system that is often not representative for a "real" liquid system, in particular if a far-reaching order is present. In particular, this refers to the need of considering a second or even third solvation shell of a molecule or ion when interactions are strong. In this case, the number of solvent molecules considered in typical CP simulations is insufficient to describe the solvation completely and embedding in bulk is not considered at all. On the contrary, the use of simple density functionals—for example, the most commonly used Becke-Lee-Yang-Parr (BLYP) [7] or Perdew, Burke, Ernzerhof (PBE) [8,9] functionals—includes further error sources. These functions imply all simplifications of the general gradient approximation formalism and, besides that, the other problems, common to virtually all contemporary density functional theory (DFT) methods, namely, the wrong treatment of kinetic energy, the semiempirical parameterization of some of the terms [10–13], and the attempt to compensate errors by empirical formulae, make the interpretation of the results to a certain extent ambiguous.

In the QM/MM formalism, embedding in sufficient bulk is not a problem [14,15] but the aforementioned question of the transition between QM and MM region poses some serious problems, in particular if the QM zone is small and thus the transition occurs within a region of strong interactions. As an example for this problem, any ion can serve [16–19], which forms a distinct second or even third hydration shell in water, and where the structure of the second shell is still strongly determined by quantum effects, but due to the size of the QM region this shell is not included in the quantum mechanical treatment. This problem can be overcome by increasing the size of the QM region, which is of course connected to a drastic increase in the computational effort of the method. Another problem is the choice of the MM model for the solvent. Only flexible solvent models can be accepted in such simulations; otherwise, a molecule with full flexibility in the QM region would suddenly "freeze" to a rigid (and often very different) configuration upon entering into the MM region, with all the energetic inconsistencies related to such a process.

The other problem of conventional QM/MM methods is the need of describing the QM region also by classical molecular mechanics, in order to work out the quantum effects in this region and obtain the differences to the classical treatment. This means that despite of the quantum mechanical treatment of the forces or energies in the QM region one still has to know or construct all the interaction potentials between solute and solvent species by means of classical potential functions. In particular, for composite solutes with no symmetry, this causes serious problems in the development of suitable analytical potential functions. The related evaluation of a highly asymmetric energy surface is a tedious and sometimes almost unmanageable process. For many systems almost unsurmountable difficulties will be encountered in the construction of appropriate analytical potential functions, making thus the QM/MM approach a very difficult and sometimes ambiguous procedure.

While it still seems very difficult—despite some promising approaches to improve the density functional procedure toward an ab initio approach [11–13,20]—to overcome DFT-inherent problems, the QM/MM methodology could be recently improved to an extent that overcomes most of the aforementioned methodical difficulties and eventual error sources. In the next chapter, this new approach named quantum mechanical charge field molecular dynamics (QMCF MD) [21–22] will be outlined in detail and it will be shown how this method improves the QM/MM formalism, avoiding the major technical and physical problems associated with it.

2. METHODOLOGY

2.1. Definition of subregions and the respective forces

The basic approach of conventional QM/MM methodologies [23–27], the separation of the system into a quantum mechanical (QM) region containing the most relevant part and an MM region, is retained in the QMCF framework [21,22]. The forces in the subregions are treated according to the respective methodologies, that is, on the quantum mechanical level and via application of the respective potential model.

For coupling purposes, the QM particles are separated into two groups—those located close to the QM/MM border and those which are near the QM center. For the latter the intermolecular distances to MM particles are large, typically beyond the non-Coulombic cutoff distances.

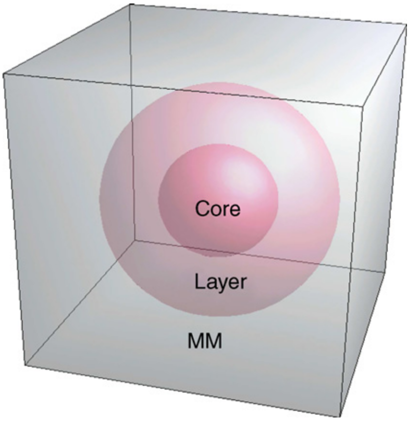

Figure 7.1 Scheme of a QMCF simulation: the chemical most relevant region is treated by quantum mechanics (QM), the remaining part by molecular mechanics (MM). For coupling purposes the QM region is again separated into two zones, namely, the "QM core" and the "solvation layer."

Therefore, these species only require a Coulombic interaction term (including a correction compensating for the Coulombic cutoff such as an Ewald summation or a reaction field) to account for the coupling between the QM and the MM particles. For QM atoms close to the region interface, the intermolecular distances are small and in addition to the Coulombic forces the non-Coulombic interactions have to be included to achieve a proper coupling. Following these consideration, the system is divided into three subregions as depicted in Figure 7.1. The inner part of the QM region is termed the QM core zone, whereas the outer part is referred to as the QM layer region. Solutes located in the QM core region do not require the application of potential functions, thus composite species which would require complex potentials for classical and conventional QM/MM simulations can be treated in a straightforward way. The interaction of the solute with solvent molecules at close range is treated by quantum mechanics (automatically including polarization, charge transfer, as well as many-body interactions), whereas the interaction with the solvent beyond the QM region is treated by Coulombics.

This approach requires all atoms of the solute to remain near the QM center—whenever a solute particle moves too close to the QM/MM interface, non-Coulombic potentials would be required and the advantage of this approach is lost. This consideration also implies that only those species for which non-Coulombic potentials have been supplied are allowed to be located in the "QM layer" region. The second QM zone is referred to as the "solvation layer" as only particles of the solvent are allowed in this region.

Besides solvent molecules this also applies to other species such as ions assuming that non-Coulombics are implemented for these species as well.

The size assigned to the individual regions is a crucial setting for such simulations. The minimum size of the “core region” is determined by the solute, but it is often necessary to include also the first layer of hydration, for example, in the case of hydrated ions. The distance of all “core” particles to the QM border should exceed the non-Coulombic cutoffs of all involved species. For aqueous systems, the critical minimum size of the layer region is about 2.5–3.0 Å. In that case, the entire QM region should contain at least two layers of hydration. For composite solutes, this condition leads to an enormous computational effort. However, as these species are in general less polarizing than ions, the size of the core zone is chosen to include the solute and eventually a part of the first hydration layer only.

As an additional improvement of the interaction between QM and MM particles, quantum mechanically derived point charges are assigned to all QM atoms by population analysis performed in every step of the simulation. This treatment reflects the influence of polarization, charge-transfer and many-body effects as well as all geometrical changes and incorporates this information into the QM/MM coupling. In various comparative studies, this procedure was found to be advantageous over the assignment of fixed partial charges. For example, the effective charge of an Al(III) ion was found to be in the order of +2.0 to +2.5 instead of the formal +3.0 charge, as a consequence of the polarization and charge-transfer effects between the ion and the solvent. QM/MM simulations utilizing the fixed formal charge lead to a too strong interaction between the ion and the MM solute molecules resulting in artifacts near the QM/MM interface. As a consequence, the MM region contracted and exerted a “stress” on the QM region. The QM particles had to adapt to this contraction and deformations in the ligands’ arrangement around the solute occurred. Application of quantum mechanically derived charges as realized in the QMCF framework significantly reduced these shortcomings. As the re-evaluation of the charges in every subsequent step takes into account all changes in the electron density in the course of a simulation, this procedure is considered superior over the assignment of fixed charges and, hence, is the standard mode in QMCF MD simulations.

According to this discussion the forces in the respective regions are defined as follows:

$$F_{\mathrm{J}}^{\mathrm{core}} = F_{\mathrm{J}}^{\mathrm{QM}} + \sum_{I=1}^{\mathrm{M}} \frac{q_{\mathrm{J}}^{\mathrm{QM}} \cdot q_{\mathrm{I}}^{\mathrm{MM}}}{r_{\mathrm{IJ}}^{2}} \cdot \left[1 + 2 \cdot \frac{\varepsilon + 1}{2\varepsilon - 1} \cdot \left(\frac{r_{\mathrm{IJ}}}{r_{\mathrm{c}}}\right)^{3}\right]. \tag{1}$$

$F_{\mathrm{J}}^{\mathrm{core}}$, the force acting on the particle J in the core region, is composed of the force resulting from the quantum mechanical treatment $F_{\mathrm{J}}^{\mathrm{QM}}$ plus the Coulombic interactions between particle J and all MM atoms (M) according to their respective partial charges. The charges of the QM atoms are derived by means of a population analysis as discussed earlier, whereas the partial charges of the MM particles are defined by the respective MM model. In this formulation, a reaction field [1] was used to correct the error resulting from the limited box size and the associated Coulombic cutoff is given as r_c. ε corresponds to the dielectric constant of the surrounding medium beyond the cutoff distance. Ewald summation techniques [28] could be applied as an alternative approach instead.

The force acting on a particle J in the layer region F_J^{layer} is obtained in a similar way. In addition to the contributions derived for core particles non-Coulombic interactions F_{IJ}^{nC} between the target particle J and all MM atoms have to be considered because of the short internuclear distances as discussed earlier.

$$F_J^{\text{layer}} = F_J^{\text{QM}} + \sum_{I=1}^{M} \left\{ \frac{q_J^{\text{QM}} \cdot q_I^{\text{MM}}}{r_{IJ}^2} \cdot \left[1 + 2 \cdot \frac{\varepsilon + 1}{2\varepsilon - 1} \cdot \left(\frac{r_{IJ}}{r_c} \right)^3 \right] + F_{IJ}^{\text{nC}} \right\}. \tag{2}$$

The force of a particle J situated in the MM region is composed of the interactions with the remaining (M − 1) MM atoms plus the QM/MM coupling contributions. The force associated to MM interactions is in general composed of a Coulombic term (plus an appropriate long-range correction), non-Coulombic contributions (a simple example are Lennard-Jones 6–12 type potentials), and intramolecular force field contributions. The QM/MM coupling terms consist of the Coulombic interactions with all core (N_1) and layer (N_2) atoms and the non-Coulombic forces with all layer atoms (N_2). The latter contributions are consistent with the coupling terms in the core and layer regions and no violation of force consistency and momentum conservation occurs.

$$F_J^{\text{MM}} = \sum_{\substack{I=1 \\ I \neq J}}^{M} F_{IJ}^{\text{MM}} + \sum_{I=1}^{N_1+N_2} \frac{q_I^{\text{QM}} \cdot q_J^{\text{MM}}}{r_{IJ}^2} \cdot \left[1 + 2 \cdot \frac{\varepsilon + 1}{2\varepsilon - 1} \cdot \left(\frac{r_{IJ}}{r_c} \right)^3 \right] + \sum_{I=1}^{N_2} F_{IJ}^{\text{nC}}. \tag{3}$$

The force contributions between the core zone and the MM region are composed of Coulombic interactions only. As the partial charges of the quantum mechanical region vary according to the geometrical changes, these contributions are considered as a fluctuating field of charges, which determined the name of the methodology "QMCF" in order to distinguish the framework from other QM/MM approaches.

2.2. Electrostatic embedding and the periodic box

The difficulties observed in the Coulombic coupling between the QM and MM region discussed above are not the only source of QM/MM transition artifacts—the quantum mechanical description itself leads to an artificial behavior close to the QM/MM interface. According to the assignment of the molecules to the respective regions, the QM region is “unaware” of its surrounding. This virtual vacuum environment leads to an extension of the molecular orbitals and thus the electron density into this empty region of space [22]. This description is a bad representation of the system within the bulk of a liquid, as the electron density should be confined within the QM region, and modifies its shape according to the surrounding charge distribution. As the arrangement of these charges results in an inhomogeneous electric field, simplistic approaches like implicit solvation models [29] [e.g., polarizable continuum model (PCM)] mimicking the surrounding solvent by a homogeneous potential are not expected to yield a satisfactory consideration of all effects.

A common way to tackle this problem is the electrostatic embedding technique [23,30–32]. Effective atomic point charges representing the MM particles are included in the Hamiltonian as a perturbation potential, which influence the formation of the molecular orbitals. Negative point charges lead to a repulsion of the electron density, whereas positive charges result in an attraction. This approach leads to a significant improvement of the quantum mechanical treatment in the context of the QM/MM framework and at the same time does not increase the computational effort significantly, as the point charge interactions are included in the less demanding one-electron contributions.

A typical example for the improved description is the hydrogen bonds crossing the QM/MM interface—the electron density is modified according to the surrounding point charges, which leads to variations of the partial charges of respective atoms. The partial charges reflecting the shift of the electron density are utilized in the QM/MM coupling as discussed earlier. Hence, a significant improvement of the QM/MM coupling can be achieved with a modest increase of the computational effort.

Although the execution of quantum chemical computations utilizing electrostatic embedding technique is straightforward and implementations of this method are included in numerous quantum chemistry packages, the application of this framework in QM/MM approaches creates some difficulties [22]. The problems arise in the derivation of forces in connection with the periodic environment, which is utilized to ensure that the system corresponds to the bulk of a liquid/crystal/gaseous state. The application of the periodic boundary condition assumes the system to extend periodically in selected (in the majority of cases all) directions of space. Particles leaving the system on one side re-enter the simulation box through the opposite side. To avoid artifacts resulting from double counting, interactions are computed utilizing the closest image, that is, either the original particle or a respective image in an adjacent box. This condition is known as the minimum image convention (cf., Figure 7.2a) [1].

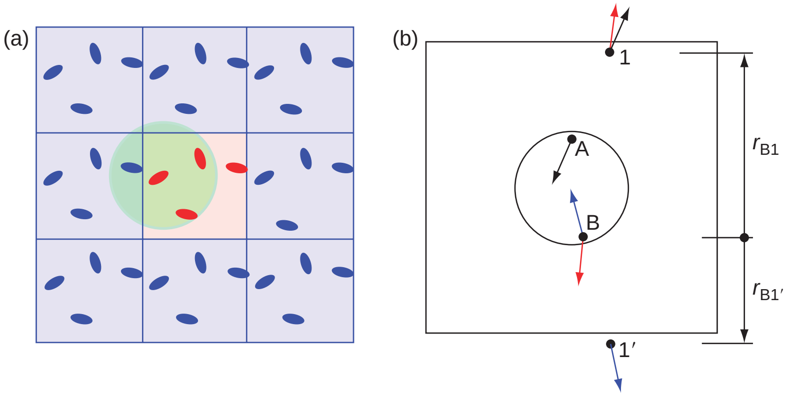

Figure 7.2 (a) Periodic images surrounding the simulation box. Interactions are computed with respect to the nearest image that is indicated by the circle. (b) Violation of the minimum image convention resulting from the interaction of QM particle B with point charge 1.

Figure 7.2b depicts a typical situation arising in the course of a quantum mechanical treatment utilizing electrostatic embedding. While the interaction of QM particle A with point charge 1 does not pose any problems, the minimum image convention is violated for QM particle B, as it should interact with the periodic image 1′. This wrong inclusion of the interaction leads to three errors of increasing significance. First, the distance between particle 1 and B is too large. Second, the resulting force is pointing in the wrong direction. The third error arises when particle 1 is imaged through the box boundary in the course of an MD simulation. Suddenly all forces are pointing in another direction and sudden changes are observed in the interparticle distances. These discontinuities in the forces result from a violation of the minimum image convention and pose severe problems in simulation studies. Therefore, this embedding scheme cannot be utilized to derive forces in a periodic system.

However, there exists the possibility to include the point charges during the energy calculation and to discard the embedding during the force computation [22]. This leads to a modification of the molecular orbitals associated to the external field of charges, which results in different forces between the QM atoms and the modified QM partial charges. The coupling between the QM and MM region is then realized via application of Coulomb's law as discussed in the previous chapter. All requirements connected to the correct periodic treatment such as Coulombic cutoffs, long-range corrections, and the minimum image convention can be satisfied by this procedure.

Consequently, the QM energy does not reflect the correct energy of the QM region, as it contains nuclei–point charge and electron–point charge interactions. These contributions have to be subtracted to obtain the proper result. As some quantum chemical packages do not explicitly output the latter contributions, it is sometimes necessary to evaluate the energy via a separate computation. The molecular orbitals derived during the energy calculation with embedding have to be read in as initial orbitals. The so-called "guess-only" run enables the computation of the energy without embedding, but at the same time does not modify the electron density according to the virtual vacuum environment resulting from the absence of the MM point charges. Afterward, the QM forces and atomic populations can be computed in the normal way.

This methodology has been successfully applied in QMCF MD simulation of various hydrated systems [33–38]. The embedding technique and the improvements of the QM/MM coupling lead to some significant improvements of the description of the systems compared to a conventional QM/MM MD procedure. This framework is compatible with any affordable quantum chemical level, thus enabling the application of correlated ab initio methods such as MP/2 or better in the near future.

2.3. Smoothing of particle migrations between the QM and MM region

Whenever particles are to be exchanged between the QM and MM region, a special treatment is required to avoid discontinuities. As molecular vibrations are accessible in the QM region, the force field model describing the solute in the MM region has to account for molecular flexibility as well. Rigid models are, therefore, not acceptable as molecules could freeze in unfavorable geometries upon migration from the QM to the MM region.

A small layer with a typical thickness of 0.2 Å is defined at the QM/MM interface region. The forces of particles located in this region are computed twice, first according to the normal definition of the region (F^{layer}) and a second time assuming that the respective particles were already in the MM region (F_{J}^{MM}). Based on the center of mass of a respective molecule, a smoothing factor *S(r)* is derived, which is utilized to compute the resulting force $F_{\text{J}}^{\text{Smooth}}$.

$$F_{\text{J}}^{\text{Smooth}} = S(r) \cdot (F_{\text{J}}^{\text{layer}} - F_{\text{J}}^{\text{MM}}) + F_{\text{J}}^{\text{MM}}. \tag{4}$$

The smoothing factor *S(r)* is defined by a continuous function gradually increasing from 0 to 1:

$$\begin{aligned} S(r) &= 1, \text{ for } r \leq r_1, \\ S(r) &= \frac{(r_0^2 - r^2)^2 (r_0^2 + 2r^2 - 3r_1^2)}{(r_0^2 - r_1^2)^3}, \text{ for } r_1 < r \leq r_0, \\ S(r) &= 0, \text{ for } r > r_0. \end{aligned} \tag{5}$$

r defines the distance of a molecule's center of mass from the QM center, r_0 and r_1 define the upper and lower limits of the smoothing region. Usually a thickness of 0.2 Å is employed. This value was found to be the optimal choice ensuring smooth transitions of molecules and at the same time avoiding the occurrence of significant transition artifacts. It should be mentioned that although the forces of the exchanging particles are continuously changed from the QM to the MM force, a slight violation of momentum conservation can be observed. It has been shown that long simulation trajectories (a few nanoseconds) will lead to artificial diffusion effects [39]. Considering the high computational demand of the quantum mechanical evaluation of energy and forces and thus, the limited time span achievable within a QMCF MD simulation study, the deviations are too small to have a noticeable effect. Very large smoothing areas such as a thickness of 0.5 Å [39] result in a significant violation of momentum conservation, however.

More advanced smoothing procedures have been designed [39,40], but the strongly increased demand of the computational effort (up to N^2 energy and force evaluations per step with N being the number of molecules in the smoothing regions) makes those schemes unfeasible for investigations utilizing hybrid QM/MM approaches. While the calculation time is dramatically increased, a noticeable improvement of the accuracy is not achieved, as long as the simulation time is significantly below the nanosecond scale. These approaches appear useful, however, for hybrid MM/MM approaches such as the combination of reactive and nonreactive force fields [41].

2.4. Computational effort and accuracy considerations

In MD studies, different elements influence the computational effort. The system size specifying the number of particles N, which is one of the most crucial factors, as the number of intermolecular interactions typically increases with N^2. If quantum chemical methods are applied such as in CP simulations, the dependence of the computational effort on the system size is even more pronounced. In the context of hybrid QM/MM studies for hydrated systems up to 40 quantum mechanically treated solvent molecules are embedded in 500–1000 MM solvent molecules in order to ensure a proper description of the solution with a sufficient number of bulk molecules. In CP-type simulations, the number of particles typically employed ranges between 30 and 60 water molecules, which are all treated by the DFT formalism.

The simulation time required to study all relevant processes is another important factor that influences the computational effort linearly. As explicit hydrogen movements are accessible in QMCF MD simulations, the time step is determined by the fast-moving hydrogens. The period of an O—H vibration in water is in the order of 10 fs and hence, time steps on the sub-femtosecond scale are compulsory: in order to achieve about 50 energy and force evaluations per vibrational cycle, a time step of 0.2 fs is required.

The minimum simulation time to study hydration structures of solvated ions is 10 ps plus 2 ps for equilibration purposes if the system is properly pre-equilibrated (e.g., by classical simulations). In cases of complex solute species, the equilibration time needs to be extended, thus leading to a further increase of the required number of steps. Utilizing a time step of 0.2 fs, the total number of energy and force computations amount to at least 60 000. Longer trajectories are required if the solvate is labile and if ligand exchange reactions are to be evaluated. In these cases, the typical range of the required simulation time is between 20 and 50 ps, corresponding to 110 000 and 250 000 steps, respectively.

The most influential choice, however, is the level of accuracy of the energy and force evaluation, which strongly correlates with the computational effort. Force field methods utilizing parameterized potential functions are less demanding—simulations of a few thousand molecules can be easily carried out within a few hours, reaching one million steps or more.

Whenever hybrid quantum mechanical methods are used, considerations regarding the computational level, the basis sets, and the size of the QM region are crucial. These choices strongly determine the accuracy of results and the computational effort. The treatment of an entire simulation box with several hundred molecules by ab initio methods is far beyond the present computational capability. In the CP framework, the compromise between accuracy and computational effort is achieved by a reduction of the system size and the usage of simple density functionals of the generalized gradient approximation type. Such simulations have been widely employed in numerous computational studies, but various error sources such as the fictive electron mass, usage of plane wave functions, or the inherent methodical problems associated with DFT (unphysical self-interaction, wrong kinetic energy, dependence on parameterizations) [11–13] require empirical corrections of the framework in order to obtain results in agreement with experiment.

In hybrid QM/MM simulations, the size of the high-level region as well as the employed methodology in that region is crucial for their quality. Methods with lower accuracy enable the usage of larger regions and vice versa. In most cases the quantum mechanical region should be chosen as large as possible, thereby restricting the applicable theoretical level to the single determinantal level, that is, DFT or ab initio Hartree–Fock (HF) method. Density functional methods have become increasingly popular within the last decade, although they imply several methodical limitations. One of the most significant findings associated with DFT is the need for a calibration source which is discussed in detail in recent literature [11]. Therefore, a cautious evaluation of the method of choice has to be carried out prior to a simulation in order to assess whether the functional's parameterization is appropriate for the specific system of interest. Solvated ions are strongly dominated by Coulombic interactions and a significant polarization of the surrounding solvent results from the presence of the charged solute. For these cases, the unphysical self-interaction inherent to DFT is a striking disadvantage. Furthermore, the parameterization of the functionals is aimed at molecular systems instead of charged atomic systems. Comparative optimization studies of ion–water clusters utilizing DFT and correlated ab initio methods have confirmed these conclusions [18,42–48].

The other alternative, the HF level, suffers from the error resulting from the neglect of electron correlation. This methodical shortcoming can lead to considerable errors in some applications, mostly when dealing with weak interactions, whereas it is less important for strongly interacting systems as, for example, ion–water interactions. Again, studies of cation–water clusters utilizing various levels of theory demonstrate the magnitude of this error [18,42–48]. An extreme case is the strongly polarizing ion Al(III) [18]. The average ion–water bond lengths and energies of $[Al(H_2O)_n]^{3+}$ ($n = 1$–4, 6, 8) clusters predicted by the HF method are in much better agreement with correlated methods (Moeller Plesset 4th order single double quadrupel (MP/4 SDQ), coupled cluster double substitution (CCD), quadratic configuration interaction calculation including single and double substitution (QCISD)) than those from popular density functionals such as Becke, three-parameter, Lee-Yang-Parr (B3LYP). For less polarizing systems, the differences are less pronounced but still significant.

The application of DFT methods in a QM/MM MD simulation of pure water, whose intermolecular interaction is considered moderate [49], demonstrated that DFT methods are not very suitable to describe the forces of this system. Although they seem to describe the water–water interaction energy and H-bond distances more reliably, they fail with respect to the dynamical aspects. A comparative QM/MM MD study [50,51] demonstrated that DFT predicts a too rigid structure for water. The HF method yields too long and weak H-bonds, but the dynamical data are in better agreement with experiments. QM/MM MD simulation studies at correlated MP/2 level are presently restricted to a one-shell treatment because of the strongly increased computational effort, which does not produce experimental data satisfactorily. It has been concluded that the treatment of a larger region at lower quantum mechanical level is more important than the partial correction of electron correlation in a smaller region.

For these reasons, the ab initio HF level presently seems the best compromise between computational effort and accuracy for solvated ionic systems. Despite the general weakness related to the single determinantal treatment, the inclusion of many-body, polarization, and charge-transfer effects near the solute and the possibility to provide systems containing hundreds of solvent molecules are important features for a reliable representation of the solution. However, the technological improvements of software and hardware resources will enable the application of more advanced quantum chemical methodologies in the near future. One example for improvements in theoretical approaches is the “resolution of identity” (RI) approximation [52], which has gained increasing interest in recent years.

Utilizing balanced auxiliary functions, quantum chemical methods such as MP/2 can be significantly accelerated, but the respective methodical accuracy is retained in the majority of cases.

Further considerations related to accuracy and computational effort involve the inclusion of relativistic effects, which are important in the case of heavy atoms. Core electrons reach high velocities and effects resulting from special relativity become significant, leading to a contraction of bond lengths and shifts of energy levels. Effective core potentials (ECP) resembling a preset number of core electrons are efficient tools to include a large fraction of relativistic effects and at the same time to reduce the computational effort. A full relativistic treatment utilizing advanced quantum chemical methodologies is still too time consuming for hybrid QM/MM approaches.

The chosen basis set has also a strong influence on the accuracy/effort relation—minimum basis sets have been shown to yield significantly wrong data [53], while double-zeta plus polarization basis sets have been shown to be a reasonable compromise leading in many cases to data comparable with experimental results. For correlated methods, larger basis sets have to be utilized to capture an appropriate fraction of the electron correlation. Thus, the application of these methods implies not only the inherently higher computational demand but an additional increase of this demand due to the requirement of larger basis sets.

All these aspects need to be balanced considering the available computational equipment. Although it is possible to execute quantum chemical computations in parallel by distribution of parts of the computation to several processors, parallelization is limited depending on the architecture of the computational equipment and the efficiency of QM programs. Highly optimized programs reach this limit at about 8–20 processors depending on the level of theory and the system size. The time required for the evaluation of the classical potentials as well as the routines for thermostatization, integration of the equations of motions, and so on are negligible in these considerations. Assuming a computation time of 5 minutes for energy, force, and charge evaluation, the minimum of 60 000 steps amounts to a total net computation time of 5000 h corresponding to 7 months. These dimensions of computation time make an application of correlated methods still prohibitive. As the comparison of ion–water clusters treated at different levels of theory has shown that the computational effort for correlated treatment leads only to marginal improvements in energies and geometries, the treatment of charged systems in polar solvents at the HF level appears justified. However, systems with weak interactions as, for example, hydrophobic solutes in aqueous solution or apolar solvents will require the inclusion of electron correlation for a proper description. For them DFT methods could provide an alternative, as the common parameterization of the functionals appears more suitable for this class of molecules.

3. APPLICATION OF THE QMCF MD METHODOLOGY

In the following a few selected examples are presented demonstrating the advanced capabilities of the QMCF framework. It was of special interest to investigate systems where previous QM/MM data are available in order to perform a detailed comparison of the different approaches. Other applications focus on systems posing difficulties for solute–solvent potential-based QM/MM studies.

In particular, the hydration of monoatomic ions in solution could be utilized to compare methodologies due to numerous existing data [14,15]. In these examples the ions and their first and second hydration shells were included in the QM region, the respective “core region” defined in the QMCF framework included the ion and the first hydration layer, and the layer region the second shell. Because of the formulation of the QMCF framework, no ion–water potentials were required, which is one particular benefit of this methodology, as the construction of these potentials is a tedious and time-consuming task. Especially in the case of strongly polarizing systems such as Al(III) [18], this construction process encounters numerous obstacles, for example, unphysical charge transfer and the accuracy of the resulting potentials is limited even if three-body correction terms are included.

Figures 7.3a and b depict the ion–oxygen radial distribution functions (RDFs) of Na(I) and Al(III) in aqueous solution obtained from a QMCF and a conventional QM/MM MD simulation. The main difference in the RDFs of Na(I) is visible near the weak second shell in the region between 4.0 and 5.0 Å and in the bulk region between 6.0 Å and 7.0 Å. The first shell peak’s location and intensity as well as its integration corresponding to the coordination number are similar.

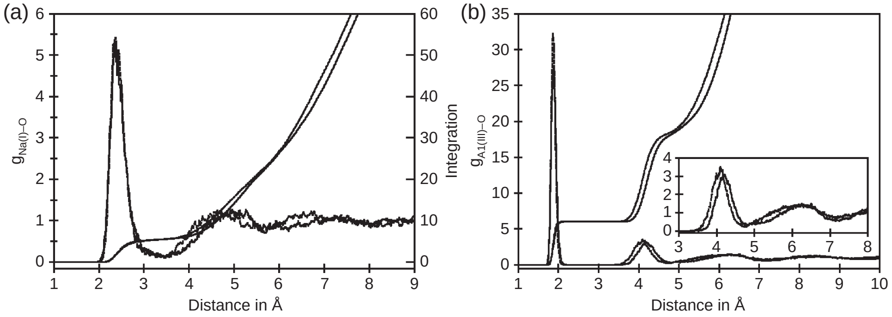

Figure 7.3 Comparison of the ion–water radial distribution function for (a) Na(I) and (b) Al(III) in aqueous solution obtained from a QMCF (solid line) and a conventional QM/MM (dashed line) MD simulation.

In the case of Al(III), the differences are much more pronounced. The first shell peak's intensity is significantly decreased, whereas its location and the first shell coordination number remain unchanged. The second shell is significantly shifted to a larger distance when the QMCF framework is utilized, but the coordination numbers are nearly identical. A closer look at the second shell peak obtained from the conventional QM/MM MD simulation reveals a pronounced asymmetry of the peak. The slope pointing toward the third shell is steeper than the slope pointing toward the ion, whereas the second shell peak is more symmetric when the QMCF scheme is applied. The third shell also shows significant differences, although the maxima of both plots are coinciding. A higher population can be identified, which is clearly shifted toward lower distances when the conventional QM/MM scheme is applied. A plateau is found in the region from 5.8 Å to 6.4 Å rather than a distinct peak maximum. In contrast to that, a well-defined third shell results from the QMCF MD treatment. As in the case of Na(I), the most pronounced differences are found near the QM/MM interface that was set to 5.0 Å.

The explanation of the observed differences in the structural description of the system is related to the improved QM/MM coupling realized in the QMCF framework. In the "classical" QM/MM approach, the interactions between QM and MM particles are evaluated utilizing empirical MM potentials. Thus, even for Al(III) that is located in the QM region, such a potential is applied. These potentials consist of Coulombic and non-Coulombic terms and are in most cases constructed by scanning the energy surface of the interaction via ab initio calculations. The MM partial charge of a single atomic species such as an ion corresponds to the formal charge, that is, to +3 for an Al(III) ion. Hence, all MM particles experience the formal charge of the ion, although it should be reduced due to charge transfer resulting from the binding of the surrounding ligands. The QM treatment on the other hand does account for all polarization and charge transfer as well as many-body effects, and hence all QM atoms are subject to interactions including these influences. MM solvent particles on the other hand experience too strong interactions, which in many cases result in a contraction of the MM hydration sphere toward the ion, explaining the increased intensities in the RDFs observed for the MM region near the QM/MM interface. This contraction exerts a "stress" on all QM molecules, forcing them to migrate closer to the QM center. In the case of Na(I), the first shell is unaffected as polarization effects are rather small, but they are pronounced in the case of the strongly polarizing ion Al(III), where the artificial "pressure" is so strong that even the first shell is affected. As a further contraction is not possible, the motion of the first shell ligands is hindered leading to an increase of the first shell peak intensity.

Application of the QMCF framework does reduce these artifacts by utilizing quantum mechanically derived point charges for the QM/MM coupling. As these partial charges are re-evaluated in every step, any change of the electron density resulting from geometrical changes is taken into account. The average partial charges for Na(I) and Al(III) were found to be +0.75 and +2.5 unit charges, respectively, employing Mulliken population analysis [54]. Despite some known shortcomings, this population scheme yields partial charges compatible with the charges defined in the BJH-CF2 water model [55,56], which was employed to describe the solvent in the MM region. This criterion of compatibility of charges is the central consideration when choosing the method to derive the QM charges.

Electrostatic embedding further improves the description of the system. As discussed earlier, the embedded point charges prevent the electron density to expand into a virtual vacuum environment but confine it to the QM region. This leads to an improved representation of the system that results in more reliable forces acting on the QM atoms.

These (and other [21,22]) examples demonstrate the advantages of the QMCF procedure: first, a substantial improvement of the accuracy of results is achieved with a modest increase of the computational effort of the quantum mechanical treatment related to the electrostatic embedding method and the employment of the population analysis. Second, the QMCF approach does not rely on solute–solvent potential parameters as non-Coulombics are not required due to the large distances, and the Coulombic interactions are based on quantum mechanically derived partial charges. This gives the opportunity to study systems that are difficult to represent by empirical or ab initio generated force fields.

The construction of potential functions for polarizing systems such as Mg(II) or Al(III) is a highly delicate task [57]. All of these ions require at least a three-body correction term. Difficulties arise in the ab initio scanning of the hypersurface, that is, the evaluation of the binding energy utilizing different geometrical arrangements. Artificial charge transfer is likely to occur and as basis sets are typically constructed for non-charged species, a reoptimization is in many cases mandatory to provide a better description of the ionic species. The resulting data set is afterwards fitted to an analytical representation. For these extreme cases, the formulation of the potential functions as well as the fitting procedure itself is difficult and time consuming, sometimes ambiguous. For some systems, the procedure does not lead to an appropriate representation of the entire energy hypersurface. One particular example is the U(IV) ion for which all problems encountered with polarizing systems are present to an extreme extent. Besides difficulties occurring in the scanning of the energy hypersurface, the definition of a suitable potential form is by no means trivial. The treatment of this system is straightforward, however, when the QMCF MD method is applied. Figure 7.4 depicts the U(IV)–water RDFs and a snapshot of the first shell structure. The U(IV)–oxygen RDF indicates a rigid first shell structure located at 2.45 Å, which is composed of nine water molecules. This value

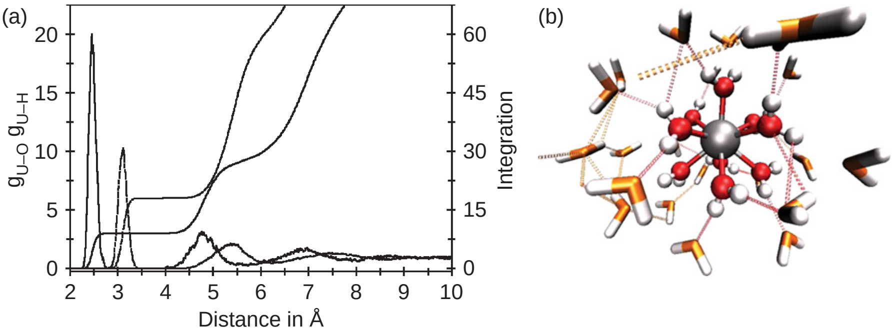

Figure 7.4 (a) Ion–oxygen (solid line) and ion–hydrogen (dashed line) radial distribution function obtained from a QMCF MD simulation of U(IV) in aqueous solution. (b) Snapshot of the simulation.

coincides well with experimentally determined data—the ion–oxygen distance was measured as 2.42 Å [X-ray scattering (XS] [58] and 2.44 Å [extended X-ray absorption fine structure (EXAFS)] [59], the coordination numbers were determined as 8 and 10 ± 1 by XS and EXAFS, respectively. Computational studies of U(IV)–water clusters have also suggested nine as the first shell coordination number [60]. The average spatial arrangement of the first shell ligands was identified as a capped square antiprism (also known as gyroelongated square pyramid). The agreement of the simulation results with experimental data is an encouraging verification of the reliability of the QMCF MD framework. No exchange of the first shell ligands was observed during the simulation time of 10 ps. The second shell contains in average ~19 ligands and still shows a considerable rigidity—coordination number 19 has an occurrence of about 40%, the distribution of the second shell coordination ranges from 17 to 21 only. The corresponding mean ligand residence time was determined as 8.1 ps.

Although highly polarizing systems like Al(III) and U(IV) pose serious difficulties in the construction of empirical potentials, these systems are still considered simple, due to the fact that the potentials are spherically symmetric. There are, however, systems which show, in addition to the radial, an angular dependence of the potential. Thus, ligands approaching the ion from different directions experience different intermolecular forces and consequently, different ion–ligand bonds are observed. Two prominent examples are the Pd(II) and Pt(II) ions. For a long time, the hydration of these ions was assumed to be square planar, but the interpretation of kinetic data suggested the participation of axial ligands in exchange reactions [61]. Recent theoretical and experimental data observed the existence of these axial ligands [35,62,63]. Figure 7.5a–b depicts the ion–water RDFs of Pd(II) and Pt(II), respectively, obtained from QMCF MD simulations. After the

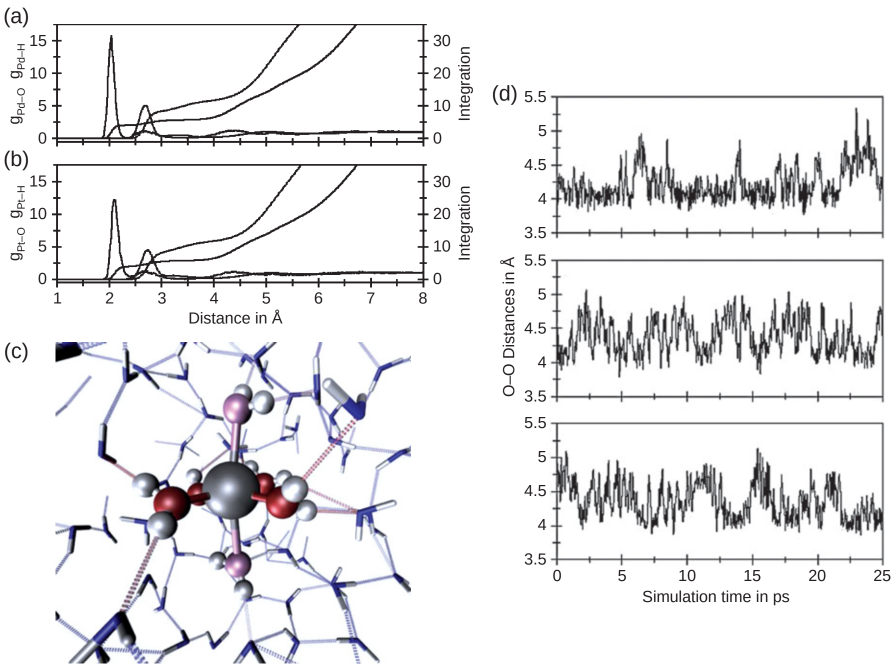

Figure 7.5 Ion–oxygen (solid line) and ion–hydrogen (dashed line) radial distribution function obtained from a QMCF MD simulation of (a) Pd(II) and (b) Pt(II) in aqueous solution. (b) Snapshot of the Pt(II) simulation. (c) O—O distances of water molecules in trans-position observed in the course of a QMCF MD simulation of hydrated Cu(II).

main peak found at 2.0 Å and 2.1 Å, resulting from the four ligands located in a square-planar arrangement, a broad peak can be identified at about 2.7–2.75 Å, which shows an average coordination number of 1.6 and 1.5 for Pd(II) and Pt(II), respectively. The snapshot of the simulation (cf., Figure 7.5c) clearly indicates that these ligands are located in axial positions above and below the plane formed by the four first shell ligands. The term "mesoshell" was proposed to classify this peak [63], as it is found in between the first and second shell. However, as this peak is not situated exactly halfway in between these shells and the respective molecules clearly belong to the first layer of ligands directly bound to the ion, the term "extended first shell" appears more appropriate. Recent EXAFS investigations of Pd(II) and Pt(II) in aqueous solution have confirmed the predictions obtained from the simulation [35,64].

The low peak intensity and the noninteger coordination number of this extended first shell peak indicate that these ligands are weakly bound and ligand exchange reactions occur along the simulation. Evaluation of the mean ligand residence times yielded values of 2.8 and 3.9 ps for Pd(II) and Pt(II), respectively. The experimental determined exchange rates of first shell ligands [61] given as 5.6×10^2 [Pd(II)] and $3.9 \times 10^{-4}\,\mathrm{s}^{-1}$ [Pt(II)] do not correspond to these values, but to exchanges of the equatorial ligands. However, the experimental exchange rates as well as the mean ligand residence times deduced from the simulation indicate that the Pt(II) hydrate is more stable than that of Pd(II) with respect to both axial and equatorial ligands.

A potential function representing the ion–water interactions of these ions exhibits several difficulties, not only in the construction but also in its application in a simulation environment. The first problem is the sampling of the energy hypersurface: an ion–water pair-scan does not reproduce any angular dependence, hence the axial scanning has to include the in-plane ligands. Any functional formulation of the potential has, thus, to account for the relative position of the ligands with respect to a predefined plane typically evaluating the angle between its associated normal vector and the ion–ligand vector. This reference plane must not be fixed in space, however, but should be connected to the plane defined by the four equatorial ligands. Otherwise, a rotation of the entire hydrate would be prevented, which would lead to wrong results. Hence, the average plane defined by the four oxygens and the ion needs to be defined, but the out-of-plane vibrations of the planar ligands are likely to impose perturbations which lead to fluctuations of the plane's normal vector.

An alternative approach employing the hydrated-ion model [63] has been utilized, treating the axial and equatorial ligands by different potential functions, thus "biasing" the result. This approach leads to an appropriate description of the hydrate's structure in classical simulations [63], but it imposes restraints on the flexibility of the equatorial ligands. In particular cases of Pd(II) and Pt(II) this might not be relevant, but other systems showing faster interconversion and exchange rates cannot be treated in this way. An example is the distorted octahedral hydration of the Cu(II) ion [65,66]. Similar to the structure of Pd(II) and Pt(II) ligands in axial positions are found at longer bond distances than the remaining four ligands arranged in a plane. However, this structure is not persistent but highly dynamic as depicted in Figure 7.5d. The initially elongated molecules move closer to the ion while other ligands move to larger distances. These dynamic Jahn–Teller distortions were found to occur on the picosecond scale and involve not only ligand pairs in opposite positions but also molecules in cis-position. The formulation of empirical potential functions to properly reflect the ion–water interaction in this case encounters almost unsurmountable difficulties. Even a conventional QM/MM simulation including the ion and its first hydration shell only yielded a quite inaccurate description of the system [65]. Only after the ion and its first plus second hydration shell were treated quantum mechanically a proper description could be obtained [66], and a further improvement was obtained upon application of the QMCF MD framework [21].

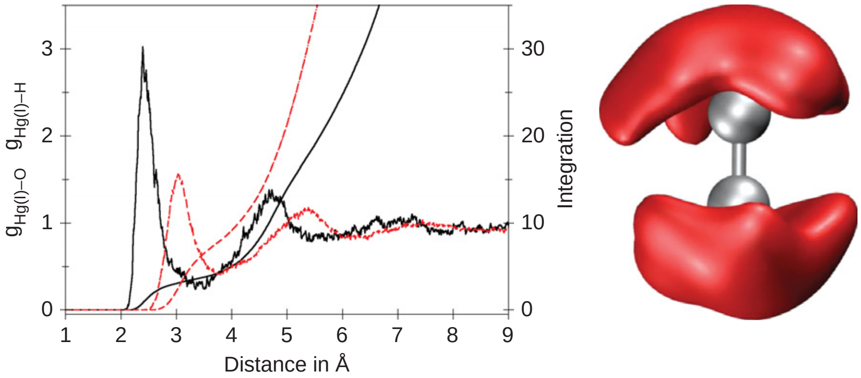

Figure 7.6 Hg(I)—O (solid line) and Hg(I)—H (dashed line) radial distribution function (left side). Spatial distribution of the first shell oxygen atoms (right side).

Despite the complications and peculiarities observed in these examples of monoatomic ionic species, these systems have to be considered simple compared to solvates composed of multiple atoms. A simulation study of Hg_2^{2+} in aqueous solution serves as example [34] of the QMCF MD capabilities. Figure 7.6 depicts the Hg(I)–water RDFs and the spatial density of the first shell oxygens. It can be clearly seen that the first shell ligands are located in distinct hemispheres whereas no ligands are found near the Hg(I)—Hg(I) bond, as the electron density repels the oxygen atoms while the positive charge of the ion repels the hydrogen atoms of the solvent. The Hg(I)—Hg(I) and Hg(I)—O distances obtained from the simulation as 2.6 and 2.4 Å are in good agreement with the experimental values [67] given as 2.24–2.53 Å, respectively. Considering the methodical error bars as well as the different conditions of experiment [0.5 M $Hg_2(ClO_4)_2$ in 30% perchloric acid] and theory (dilute environment), some deviations are to be expected. The high amount of acid utilized in the experimental structure determination is required to suppress hydrolysis of the Hg(I) dimer [67], but it is expected to considerably influence the properties of the hydrate. The number of water molecules freely available at this concentration is too low to enable the formation of a distinct second hydration shell, and the associated change of the dielectric properties of the solution will also influence the characteristics of the hydration.

Classical simulations of this particular hydrated Hg_2^{2+} system applying standard Coulombic plus Lennard-Jones 6–12 potentials would yield an erroneous description of this system. In this case the global minimum forms a ring surrounding the Hg(I)—Hg(I) bond (cf., Figure 7.7) leading to a stable coordination of ligands at that site. In order to prevent the binding of solvent molecules, an artificial interaction site would be required located

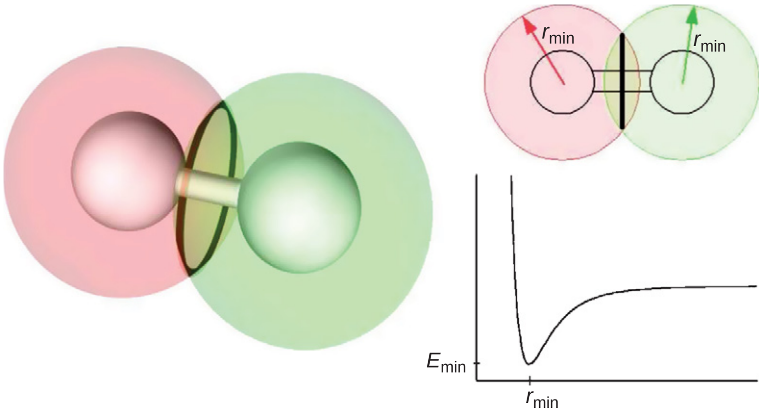

Figure 7.7 Application of standard MM potentials (e.g., Lennard-Jones 6–12 plus Coulomb potential) to Hg_2^{2+} predicts the favored ligand position at the intersection of the spheres with a radius r_{min}. Data obtained from experiments and the QMCF simulation indicate that these positions are unfavored, however.

at the center of the Hg(I)—Hg(I) bond. Alternatively, in addition to the radial dependence the angle between the Hg(I)—Hg(I) and the ion–ligand vectors could be incorporated in the potential function. However, it is still questionable whether these corrections could achieve an appropriate description of the system, as further complications arise from charge shifts within the ion.

Figure 7.8 depicts the charges of the individual mercury atoms and their sum. While the total charge displays only minor oscillations with a mean value of 1.45, the individual charges of the Hg(I) atoms fluctuate widely with minimum and maximum charges of 0.3 and 1.1, respectively. Electronic structure calculations are capable to cover these effects as all shifts of the electron density due to polarization and charge transfer are taken into account. The accuracy is only determined by the applied level of theory, that is, the chosen quantum chemical method and the size of the basis sets. Classical models on the contrary do not appropriately account for such effects even if the effects of polarization are incorporated into the potential functions. Various methods for an approximate treatment of polarization and charge transfer have been developed, with different strengths and weaknesses [68], but the incorporation of all relevant contributions is an almost impossible task. In the case of the Hg_2^{2+} ion, the possibility of disproportionation to Hg^{2+} and Hg^0 further complicates this situation, as the majority of classical models are not capable to describe the formation and cleavage of chemical bonds. Quantum chemical methods do account for bond formation and breaking and as disproportionation and hydrolysis occurring in aqueous medium are not expected to change the spin state of

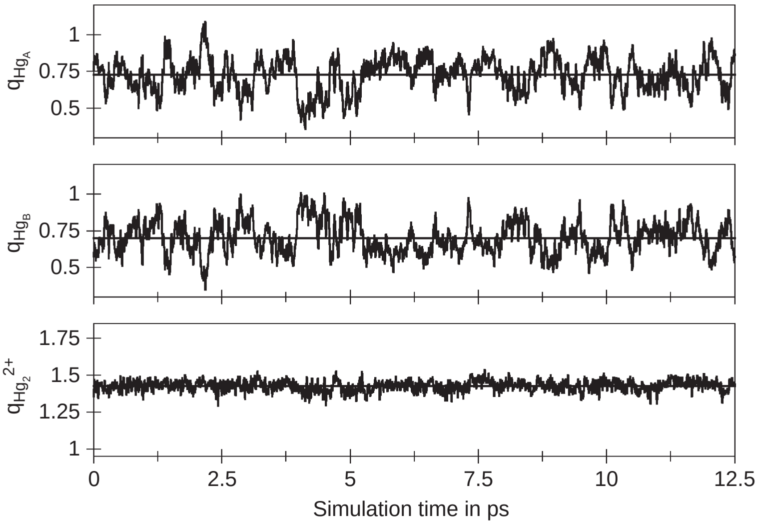

Figure 7.8 Partial charges of the individual Hg(I) atoms and the respective sum (same scaling for all plots).

the systems, the treatment of such processes can be realized with standard quantum chemical methods. Recent developments of reactive force field approaches [69,70] have demonstrated that some limitations of classical models can be overcome, but the construction of these models is a very sophisticated and time-consuming task, and the computing time is considerably increased compared to nonreactive force field methods.

A detailed analysis of the topology of the Hg(I) dimer reveals some ambiguities. It is seen from the spatial distribution depicted in Figure 7.6 that the first shell water molecules are arranged in the respective hemispheres of the Hg(I) atoms. The RDFs take spherical volume elements into account, thereby considering also the unpopulated region near the Hg(I)—Hg(I) bond. The corresponding volume is utilized in the normalization of the RDF and it can be concluded that the first shell peak appears too low and does not properly reflect the bond strength of the first shell ligands. For larger regions such as the second shell, it is apparent from Figure 7.9 that the distance to the first shell ligands of the opposite mercury atom B is within the same range as the second shell ligands of mercury atom A. Hence, the second shell peak in the RDF includes the entire first shell and part of the second shell of the opposite mercury atom. Bond distances, peak heights, and also the coordination numbers are thus wrongly predicted by this full sphere treatment and do not properly reflect the arrangement of molecules.

To obtain a more reliable representation of the hydration, the system was cut into two halves by defining a plane perpendicular to the Hg(I)—Hg(I)

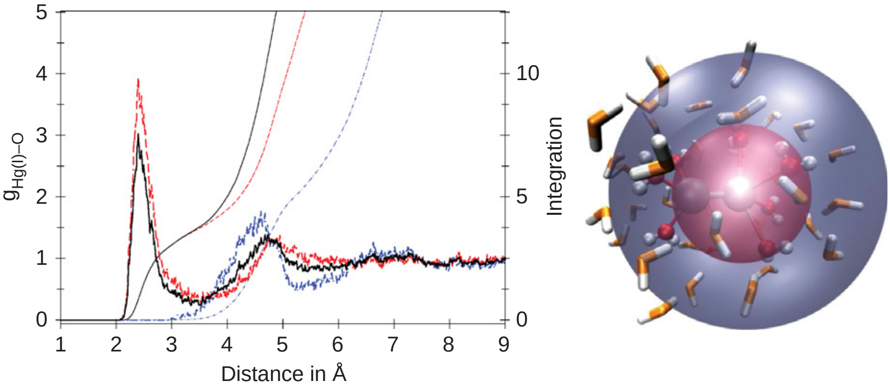

Figure 7.9 Hg(I)—O RDFs considering full spherical (solid line) and hemispherical volumes [dashed line—Hg(I) and O on the same side; dash-dotted line—Hg(I) and O on opposite sides; left side]. Analysis of the second shell utilizing a spherical volume includes first and second shell ligands of the other Hg(I) atom (right side).

bond. The center of mass of the Hg_2^{2+} ion defined the center of this plane. This treatment enables the investigation of RDFs between Hg(I) and ligands located on either side of the plane. The resulting Hg—O RDFs are depicted in Figure 7.9. The intensity of the first shell peak has increased, whereas the Hg—O distance and the coordination number remained unchanged. The second shell obtained via the hemisphere analysis differs significantly from the result of the full sphere RDF. The peak is located at a slightly larger distance of 4.85 Å with reduced height and the coordination number has become significantly lower.

Simulation data can also be utilized to investigate the distribution of microspecies. Figure 7.10 depicts the first shell coordination number distributions as well as the associated exchange plots for both Hg(I) atoms obtained from the simulation. It can be seen that a distinct coordination number is not determinable, as a large number of exchanges of first shell ligands are observed for both atoms, but the obtained picture of the probability of various microspecies being formed is a valuable information hardly obtainable by experimental measurement.

In addition to the structural information, dynamical data can be obtained from MD trajectories. The time evolution of the Hg—O distances depicted in Figure 10 indicates that a large number of exchanges occur at both Hg atoms, and a distinct exchange mechanism (such as an "associative" or "dissociative" mechanism) cannot be deduced. The mean ligand residence time of the first shell ligands was determined as 3.0 ps by the direct method [71], reflecting the weak ion–ligand bond strength. The ion–oxygen stretching frequency was calculated as 160 cm^{-1} (165 cm^{-1} at the halfwidth). These values are only insignificantly lower than the experimental one of 171 cm^{-1} [67].

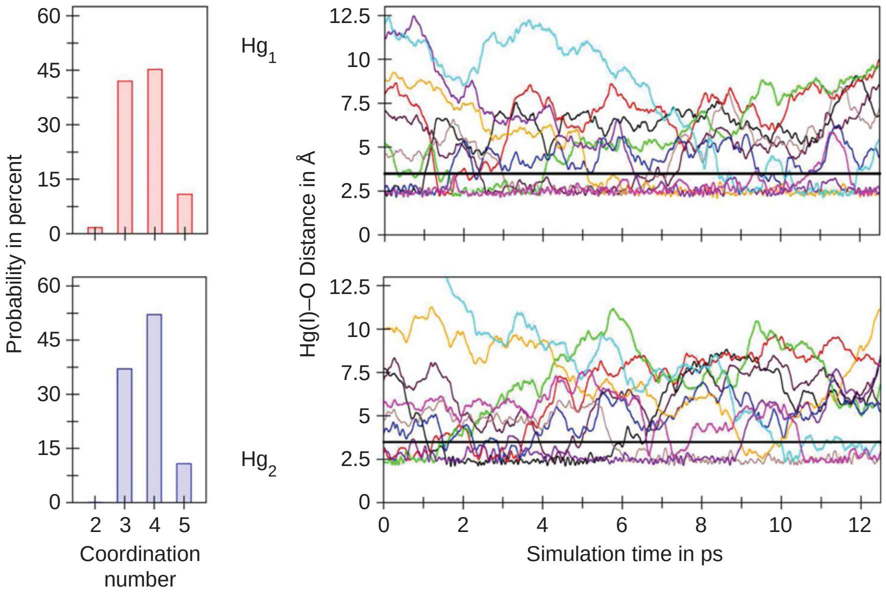

Figure 7.10 Coordination number distribution (left side) and distance plots of exchanging first shell ligands (right side) of the individual Hg(I) atoms.

The experimental hydration energy of −1148 kJ/mol based on the tetraphenylarsonium tetraphenylborate (TATB) assumption [72] is reproduced in excellent agreement by the QMCF MD simulation yielding a value of −1137 kJ/mol. The good agreement of the simulation results with various experimental data gives confidence that the QMCF MD approach is an adequate tool for the description of the solvation of composite species as well.

As another example of a composite ion the triatomic UO_2^{2+} ion in aqueous solution is discussed. Similar as in the case of the Hg(I) dimer atom–centered spherical potentials are not capable of representing the energy hypersurface for hydration, whereas the treatment is straightforward when the QMCF method is applied.

Figure 7.11 depicts the U—water and O_U—water RDFs obtained from the QMCF MD simulation. A tall first shell peak located at 2.5 Å indicates a rigid first hydration layer composed of five water molecules surrounding the U(VI) atom. As the RDF reaches zero after the first shell, no exchange events between first and second hydration layer took place during the simulation. The corresponding peak in the U—H RDF is found at a distance of 3.1 Å. Both first shell peaks are not overlapping indicating a strong dipole orientation as expected.

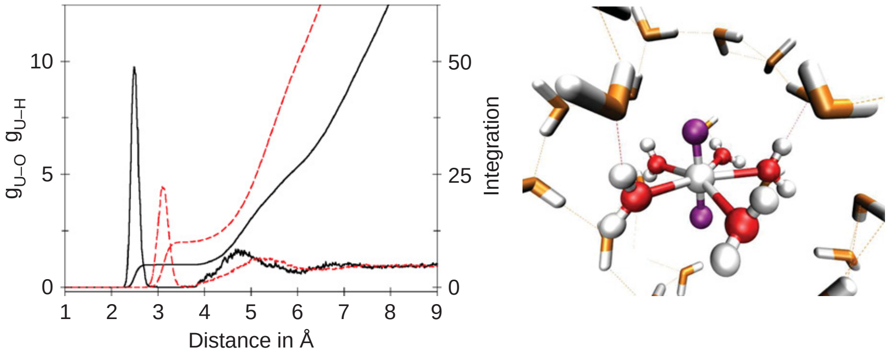

Figure 7.11 U—O (solid line) and U–H (dashed line) radial distribution functions (left side). Snapshot of the simulation (right side).

The broad second shell peak in the U—O RDF found at 4.75 Å shows a significant tailing. The overlap between this peak and the second shell peak of the U—H RDF located at 5.3 Å is a result of different solute–solvent interactions: While the uranium ion is attractive for water oxygens, the uranyl–oxygens attract the hydrogen atoms of the solvent. A continuous reorientation of the dipole of the ligands occurs when moving along the UO_2^{2+} ion. A spherical analysis of a common RDF does not account for this behavior. Therefore, as in the case of the previous examples, a plane is defined including the positions of the uranium atom and the oxygen atoms of its five first shell ligands. According to the respective normal vector, conical regions are defined enabling a selective analysis of the radial distributions within selected spatial regions.

Typical settings for the cones are 30°, 60°, and the remaining part of the system (cf., Figure 7.12). The corresponding RDFs are depicted in Figure 7.12. An increase of the first shell peak intensity accompanied by a broadening of the peak's halfwidth is noticed when moving from the equatorial (30°) to the axial cone (60°–90°). Consequently, the axial ligands show an increased mobility compared to the first and second shell molecules in equatorial positions. A strong dipole orientation is observed in the region perpendicular to the cone vectors, while the dipole character is reduced for the axial ligands.

The analysis of segmented RDFs provides detailed data on the hydration of solvates with lower symmetry. Longer simulation trajectories enable the reduction of the angle regions leading to smaller cones and thus a more refined picture of the surrounding of a composite solute system. Figure 7.13 depicts a combined radial–angular density distribution surrounding the UO_2^{2+} ion. This plot has been generated by probing the uranyl hydrate in terms of overlapping cones with an aperture of 22.5°. The hydration is

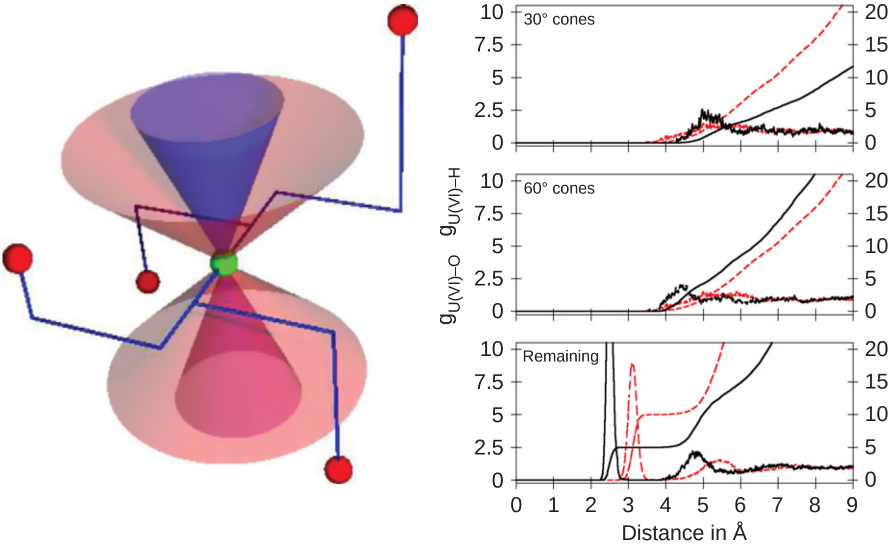

Figure 7.12 Scheme depicting the different angle regions set to 30° and 60° (left side). U(VI)—O (solid line) and U(VI)—H (dashed line) evaluated for the respective angular regions (right side).

dominated by the peaks of the first shell ligands which had to be truncated in order to observe the structure of less strongly bound ligands. This plot, therefore, allows to quantify the second shell ligands of the uranium atoms as well as the first shell ligands of the oxo atoms combining radial and

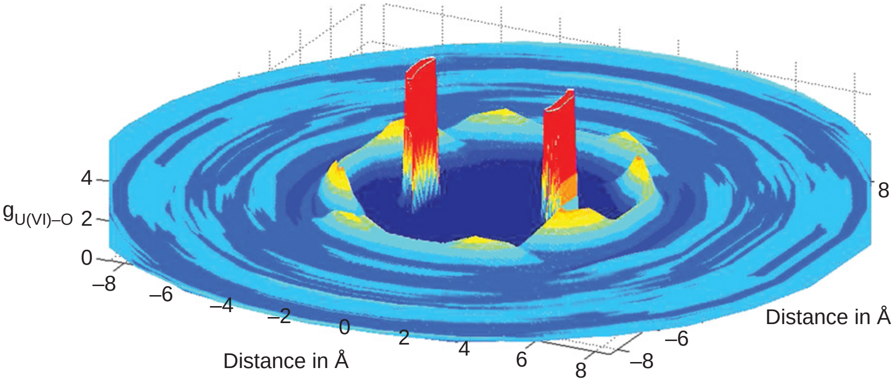

Figure 7.13 Two-dimensional U(VI)—O pair correlation plot. The second shell of the U(VI) atom as well as the first shell of the oxo atoms can be easily identified, which is not possible by an unspecific full sphere radial distribution function.

angular dependencies. The second shell ligands are found at an average distance of 4.3 Å and an angle of 60° with respect to the average cone vector. The ligands bound to the oxygen atoms are located at a distance of 4.7 Å from the uranium atom at an angle of 27°. This results in an average O_U—O distance of 3.3 Å. The corresponding value obtained from the spherical O_U—O RDF is 3.0 Å. This difference is another example for the difficulties encountered when analyzing hydrated composite species and demonstrates that geometrically adopted analysis schemes have to be applied in order to obtain an appropriate structural description of solvation.

Anions mostly bind to the water molecules through hydrogen bonds, but the strength of these hydrogen bonds can vary considerably, thus leading to specific characteristics of different anions. Table 7.1 lists the data for two halogenide ions, namely, chloride and fluoride [73,74] and the three previously mentioned oxo anions, phosphate [75], sulfate [37], and perchlorate [76], in water with respect to their structural details and coordination number distributions. The corresponding RDFs evaluated between the center atom and all water oxygens are depicted in Figure 7.14. The distance of the ion to the nearest oxygen is a function of the strength of the hydrogen bond and one can see, therefore, already from the r_1 value that the strength of hydrogen bonds varies considerably within this series. A distinct second hydration shell is not well defined in all cases and will, therefore, not be discussed in detail.

Concerning the first shell coordination number distribution, one observes a remarkable variation, in particular in the case of chloride and even more in the case of the oxo anions, for which one can specifically compare ions with identical structure but different charge. A good measure for this comparison is the number of water ligands per coordination site being in average 2.2 for phosphate, 1.7 for sulfate, and 1.5 for perchlorate, respectively. It is quite evident that the number of stable hydrogen bonds depends on the charge of the anion. The structure-breaking activity of the anions can be estimated from the H-bond distance, which is larger than the

Table 7.1 Ion–oxygen distance r_1 and r_2 in angstrom, distribution of coordination number CND_1, CND_2, and average first shell coordination number $CN_{1,av}$ of hydrated cations obtained from QM/MM MD or QMCF MD simulations

Ion	r_1	r_2	CND_1	$CN_{1,av}$	CND_2	Refs.
Cl^-	3.24	–	4–7	5.6	–	[73,74]
F^-	2.68	–	4–6	4.6	–	[73,74]
PO_4^{3-}	3.7	5.7	11–16	13	23–33	[75,76]
SO_4^{2-}	3.8	5.5	8–14	11	–	[37]
ClO_4^-	4.2	5.5	4–16	10	–	[76]

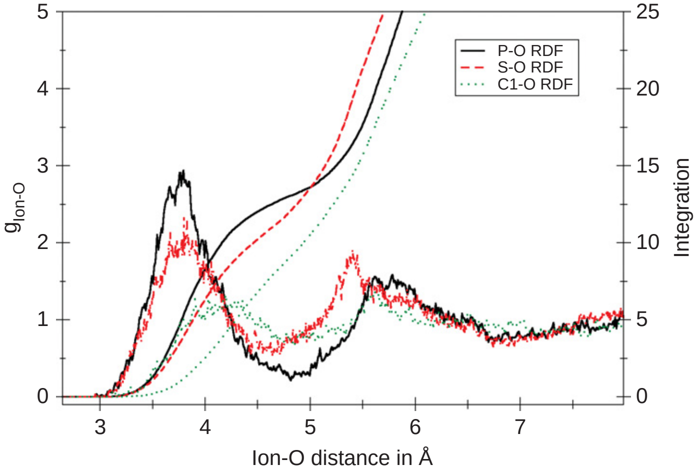

Figure 7.14 Ion–O radial distribution functions for PO_4^{3-}, SO_4^{2-}, and ClO_4^- obtained from QMCF MD simulations.

value for pure water for all anions except fluoride, and hence one could consider fluoride as the only structure forming anion among our examples.

Table 7.2 lists the values for the RDF halfwidth and the mean residence time of water molecules in the first shell as well as its normalized value based on the average coordination number of the first shell. Also the R_{ex} values are listed which refer to the number of required attempts to achieve one persistent (i.e., longer than 0.5 ps) ligand exchange. Considering the halfwidth of the first shell peak, only perchlorate [76] shows a value considerably larger than that of water, sulfate [37] a slightly higher value, and chloride [73,74] and phosphate [75] a halfwidth that is smaller but not too

Table 7.2 Halfwidth $b_{1/2}$ in angstrom, intensity and respective ration of the first shell peak of the ion–oxygen RDF, mean ligand residence time τ_1 ($t^* = 0.5$ ps) in picoseconds of the first shell, ratio between τ_1 and the $CN_{1,av}$, and the ratio of exchange of ligands of hydrated ions obtained from QM/MM MD or QMCF MD simulations

Ion	$b_{1/2}$	h_1	$\frac{h}{b_{1/2}}$	τ_1	$\frac{\tau_1}{CN_{1,av}}$	R_{ex}	Refs.
H_2O	0.68	2.0	2.9	1.5	0.36	11.2	[51,77]
Cl^-	0.57	2.4	4.2	2.0	0.36	9.4	[73,74]
F^-	0.38	3.4	8.9	2.5	0.53	6.2	[73,74]
PO_4^{3-}	0.60	2.9	4.8	3.9	0.34	3.1	[75]
SO_4^{2-}	0.70	2.3	3.3	2.5	0.22	7.4	[37]
ClO_4^-	~1.1	1.3	1.2	1.5	0.15	5.2	[76]

different from that of water. On the contrary, the fluoride [73,74] RDF has a much shorter halfwidth of its first peak and thus confirms this ion's classification as a structure-making ion. The mean residence times again give a value identical to that of water in the case of perchlorate, and for all other anions they are slightly higher. In this aspect the trivalent phosphate delivers a larger mean residence time than any other of these ions following a clear charge-dependent order ($PO_4^{3-} > SO_4^{2-} > ClO_4^{-}$).

Once the normalized values are considered, the picture changes and in this case fluoride [73,74] results again as the strongest structure former whereas all other ions are similar or even less stable with respect to their exchange time compared to pure water. These data are of particular interest, as all ligands are coordinated via hydrogen bonds, and thus the normalized mean residence times correspond to the average lifetime of these hydrogen bonds. This lifetime, which exceeds that of water only in the case of fluoride, is almost identical with that of water for chloride [73,74] and the triply charged phosphate [75], but considerably shorter for the divalent and monovalent oxo anions sulfate [37] and perchlorate [76].

The discussed values reflect different aspects of the structure-breaking or structure-forming property and any consideration of these properties of the ions would have to take into account not only the cavity needed to be formed in the solvent in order to place the ions but also various other data such as the structure and composition of the ion. A simple comparison as in the case of the cations seems only possible for the comparison of the monoatomic ions fluoride and chloride. The R_{ex} values display a quite unexpected order at the first glance, not showing any systematic trends, even for the oxo anions. What is observed, however, is that in general they are much higher than the values for the cations and that the charge seems to have only a secondary influence on the number of attempts needed to produce a ligand exchange event. This different behavior can be attributed to the lack of a second hydration shell even in the case of higher charged anions, and to a different exchange mechanism compared to the cations, mostly related to hydrogen bond formation and breaking, both between anion and solvent and between solvent molecules in their surrounding.

4. OUTLOOK

The methodical discussion and the application examples presented so far enable an outlook toward possible and desirable future developments of the simulation framework presented here. This refers to two major topics, namely, the further methodical development and the extensions of applications in chemistry.

4.1. Methodical developments

It is clear that a methodical improvement would refer first of all to the inclusion of effects neglected in the HF ab initio calculations. Numerous tests of the methodology in general, that is, the application of DFT–QM/MM schemes and CP simulations to liquid systems have made it clear that the inclusion of correlation in a semiempirical way as in common density functional methods is not the solution for this purpose. None of the generalised gradient approxiamation (GGA) and hybrid density functionals implemented in presently used techniques appear suitable to describe with sufficient accuracy the liquid state, in particular of hydrogen-bonded systems, and hence will not offer an appropriate way to improve the simulation by (partial) inclusion of electron correlation effects. However, recent developments toward ab initio density functional methods that would finally allow to include both the exchange and the correlation term in an exact way into a one-determinant description could lead to an economic and favorable solution of this problem [11–13]. At present, however, one cannot yet foresee when such methods will become available for general implementation.

Among the conventional multideterminantal approaches for the inclusion of electron correlation, MP/2 does not seem to be a satisfactory way either. Based on a perturbational calculation of electron correlation effects, MP/2 can easily overestimate these effects and thus also lead to erroneous results. The desirable extension to correlated methods is to be seen in coupled-cluster methods, at least at CCSD(T) level. However, it is obvious that such an expansion of the methodical framework is extremely costly and hence not feasible for larger systems in the near future, especially as this would also imply the usage of larger basis sets.

Another methodical development refers to the treatment of larger solutes and solvent molecules. This will eventually require cutting through covalent bonds which is not necessary in the case of small solutes embedded in layers consisting of small solvent molecules. This cutting through bonds will lead to the same problems as already encountered and partially solved in the case of numerous QM/MM simulations of biomolecules [78,79]. However, the method of embedding and of taking into account Coulombic forces in the QMCF MD method could lead to new promising approaches also in this topic.

Last but not least, improvement of the solvent models for the MM region of the simulations is an important task that should not be neglected. This refers not only to water, where such improvements have been achieved recently [80,81], but to all kinds of relevant solvents in chemistry. Further search for suitable classical models for these solvents is essential for a very general applicability of any simulation framework in solution chemistry.

4.2. Applications

With the present method any extension of the framework to larger solutes is straightforward. These will be on the one hand complexes of metal ions with larger ligands or a number of different ligands, where the construction of potential functions is almost not feasible. On the other hand, this will refer to biomolecules and biological complexes as encountered in a number of enzymes and many other biochemically reactive species. Besides the aforementioned problem of cutting through covalent bonds in such molecules, the treatment of complexes will also create further methodical problems, in particular when one deals with fast-migrating ligands. Once these ligands move from the core zone into the layer zone, the problem of considering non-Coulombic forces between these ligands and the solvent in the MM region arises. The straightforward way to avoid this problem is to extend the layer zone further or to add a third QM zone to the system. The extension of the core zone as well as the related increase of the layer zone will inevitably lead to an exponentially increasing computational effort.

It is obvious that all of these developments will mainly depend on the availability of computational power. So far the development of computational facilities in the past decades allows a quite optimistic view of this aspect, computations becoming increasingly cheaper and processors increasingly faster. Parallelization is not a general remedy for this problem, as parts of the quantum mechanical framework cannot be arbitrarily parallelized. The scalar speed of the processors is, therefore, the most relevant parameter for the future development of such simulations. One can expect that also in the years to come advances in computer technology will grant a continuously increasing applicability of accurate simulation methods based on quantum mechanics and hence provide a deeper insight into reactivity and properties of solutions at molecular level. The inclusion of counterions and the treatment of larger ligands will further expand the range of such studies far beyond present limits. In general, these theoretical methods will provide a flexible and universal tool to analyze and understand chemical processes, often at much less cost than experimental work, and in several aspects exceeding the capabilities of experimental methods. Therefore, computational chemistry is on the way to become a front-runner in solution chemistry and related chemical and biological processes.

REFERENCES

[1] M.P. Allen, D.J. Tildesley, Computer Simulation of Liquids, Oxford Science Publications, Oxford, 1990.
[2] D.A. McQuarrie, Statistical Mechanics, Harper & Row, New York, 1976.
[3] E. Clementi, G. Corongui, Int. J. Quant. Chem., Symp. 10 (1983) 31.

[4] J.H. Detrich, E. Clementi, G. Corongui, Chem. Phys. Lett. 112 (1984) 426.
[5] B.Guillot, J. Mol. Liq. 101 (2002) 219.
[6] R. Car, M. Parrinello, Phys. Rev. Lett. 55 (22) (1985) 2471–2474.
[7] A.D. Becke, Phys. Rev. A 38 (1988) 3098.
[8] J.P. Perdew, K. Burke, M. Ernzerhof, Phys. Rev. Lett. 77 (1996) 3865.
[9] J.P. Perdew, K. Burke, M. Ernzerhof, Phys. Rev. Lett. 78 (1997) 1396.
[10] A.D. Becke, J. Chem. Phys. 98 (1993) 5648–5652.
[11] W. Kutzelnigg, in: G. Maroulis, T. Simos (Eds.), Trends and Perspectives in Modern Computational Science, International Science Publishers (VSP), Leiden, 2006, p. 23.
[12] R.J. Bartlett, I.V. Schweigert, V.F. Lotrich, J. Mol. Struct. (Theochem) 764 (2006) 33.
[13] R.J. Bartlett, V.F. Lotrich, I.V. Schweigert, J. Chem. Phys. 06 (2005) 2205.
[14] C.F. Schwenk, A. Tongraar, B.M. Rode, J. Mol. Liq. 110 (2004) 105.
[15] B.M. Rode, C.F. Schwenk, T.S. Hofer, B.R. Randolf, Coord. Chem. Rev. 249 (2005) 2993.
[16] C.F. Schwenk, B.M. Rode, J. Am. Chem. Soc. 126 (2004) 12786–12787.
[17] C. Kritayakornupong, K. Plankensteiner, B.M. Rode, ChemPhysChem 5 (2004) 1499–1506.
[18] T.S. Hofer, B.R. Randolf, B.M. Rode, PhysChemChemPhys 7 (2005) 1382.
[19] M.Q. Fatmi, T.S. Hofer, B.R. Randolf, B.M. Rode, J. Chem. Phys. 123 (2005) 4514.
[20] A.J. Cohen, P. Mori-Sánchez, W. Yang, Science 321 (2008) 792.
[21] B.M. Rode, T.S. Hofer, B.R. Randolf, C.F. Schwenk, D. Xenides, V. Vchirawongkwin, Theor. Chem. Acc. 115 (2006) 77.
[22] T.S. Hofer, B.R. Randolf, B.M. Rode, Challenges and Advances in Computational Chemistry and Physics, vol. 6, Springer, Heidelberg, 2008, pp. 247–278 (Chapter Molecular Dynamics Simulation Methods including Quantum Effects).
[23] H. Lin, D.G. Truhlar, Theor. Chem. Acc. 117 (2007) 185.
[24] A. Warshel, M. Levitt, J. Mol. Biol. 103 (1976) 227.
[25] M.J. Field, P.A. Bash, M. Karplus, J. Comput. Chem. 11 (6) (1990) 700–733.
[26] J. Gao, J. Am. Chem. Soc. 115 (1993) 2930–2935.
[27] D. Bakowies, W. Thiel, J. Phys. Chem. 100 (25) (1996) 10580–10594.
[28] R. Hockney, J.W. Eastwood, Computer Simulation using Particles, Taylor & Francis, New York, 1988.
[29] C.J. Cramer, D.G. Truhlar, Chem. Rev. 99 (1999) 2161.
[30] A. Laio, J. VandeVondele, U. Rothlisberger, J. Chem. Phys. 116 (2002) 6941.
[31] E. Voloshina, N. Gaston, B. Paulus, J. Chem. Phys. 126 (2007) 134115.
[32] J. Kästner, S. Thiel, H.M. Senn, P. Sherwood, W. Thiel, J. Chem. Theory Comput. 3 (2007) 1064.
[33] M.Q. Fatmi, T.S. Hofer, B.R. Randolf, B.M. Rode, J. Comput. Chem. 28 (2007) 1704.
[34] T.S. Hofer, B.R. Randolf, B.M. Rode, Chem. Phys. 349 (2008) 210.
[35] T.S. Hofer, B.R. Randolf, S.A.A. Shah, B.M. Rode, I. Persson, Chem. Phys. Lett. 445 (2007) 193.
[36] T.S. Hofer, B.R. Randolf, B.M. Rode, Chem. Phys. 346 (2008) 182.
[37] V. Vchirawongkwin, I. Persson, B.M. Rode, J. Phys. Chem. B 111 (2007) 4150.
[38] V. Vchirawongkwin, B.M. Rode, J. Phys. Chem. 10 (2007) 1016.
[39] A. Heyden, H. Lin, D.G. Truhlar, J. Phys. Chem. B 111 (2007) 2231.
[40] T. Kerdcharoen, K. Morokuma, Chem. Phys. Lett. 335 (2002) 257.
[41] M.J. Buehler, A.C.T. van Duin, W.A. Goddard III, Phys. Rev. Lett. 96 (2006) 095505.
[42] T.S. Hofer, B.R. Randolf, B.M. Rode, J. Comput. Chem. 26 (2005) 949.
[43] T.S. Hofer, B.M. Rode, J. Chem. Phys. 121 (2004) 6406.
[44] T.S. Hofer, B.M. Rode, B.R. Randolf, Chem. Phys. 312 (2005) 81.
[45] T.S. Hofer, A.B. Pribil, B.R. Randolf, B.M. Rode, J. Am. Chem. Soc. 127 (2005) 14231.
[46] C.F. Schwenk, T.S. Hofer, B.M. Rode, J. Phys. Chem. A 108 (2004) 1509.
[47] T.S. Hofer, H. Scharnagl, B.R. Randolf, B.M. Rode, Chem. Phys. 327 (2006) 31.
[48] T.S. Hofer, B.R. Randolf, B.M. Rode, J. Phys. Chem. B 110 (2006) 20409.

[49] A.J. Stone, The Theory of Intermolecular Forces, Oxford University Press, Oxford, 1995.
[50] D. Xenides, B.R. Randolf, B.M. Rode, J. Chem. Phys. 122 (2005) 4506.
[51] D. Xenides, B.R. Randolf, B.M. Rode, J. Mol. Liq. 123 (2006) 61.
[52] R. Ahlrichs, S.D. Elliot, U. Huniar, Ber. Bunsen. Phys. Chem. 102 (1998) 795.
[53] T. Kerdcharoen, K.R. Liedl, B.M. Rode, Chem. Phys. 211 (1996) 313–323.
[54] R.S. Mulliken, J. Chem. Phys. 36 (1962) 3428.
[55] F.H. Stillinger, A. Rahman, J. Chem. Phys. 68 (2) (1978) 666.
[56] P. Bopp, G. Janscó, K. Heinzinger, Chem. Phys. Lett. 98 (2) (1983) 129.
[57] D. Spångberg, K. Hermansson, J. Chem. Phys. 120 (2004) 4829.
[58] S. Pocev, G. Johansson, Acta Chem. Scand. 23 (1973) 2146.
[59] H. Moll, M.A. Denecke, F. Jalilehvand, M. Sandström, I. Grenthe, Inorg. Chem. 38 (1999) 1795.
[60] Z. Szabó, T. Toraishi, V. Valle, I. Grenthea, Coord. Chem. Rev. 250 (2006) 784.
[61] L. Helm, A.E. Merbach, Coord. Chem. Rev. 187 (1999) 151.
[62] J. Purans, B. Fourest, C. Cannes, V. Sladkov, F. David, L. Venault, et al., J. Phys. Chem. B 109 (2005) 11074.
[63] J.M. Martinez, F. Torrico, R.R. Pappalardo, E.S. Marcos, J. Phys. Chem. A 108 (2004) 15851.
[64] T.S. Hofer, B.R. Randolf, B.M. Rode, I. Persson, Dalton Trans. 9 (2009) 1512.
[65] C.F. Schwenk, B.M. Rode, ChemPhysChem 4 (2003) 931.
[66] C.F. Schwenk, B.M. Rode, J. Chem. Phys. 119 (18) (2003) 9523–9531.
[67] J. Rosdahl, I. Persson, L. Kloo, K. Stahl, Inorg. Chim. Acta 357 (2004) 2624.
[68] H. Yu, W.F. van Gunsteren, Comp. Phys. Commun. 172 (2005) 69.
[69] A.C.T. van Duin, S. Dasgupta, W.A. Goddard III, J. Phys. Chem. A 105 (2001) 9396.
[70] T.S. Mahadevan, S.H. Garofalini, J. Phys. Chem. B 111 (2007) 8919.
[71] T.S. Hofer, H.T. Tran, C.F. Schwenk, B.M. Rode, J. Comput. Chem. 25 (2004) 211–217.
[72] M. Yizhak, Ion Properties, Marcel Dekker, Inc., New York, 1997.
[73] A. Tongraar, B.M. Rode, PhysChemChemPhys 5 (2003) 357–362.
[74] A. Tongraar, B.M. Rode, Chem. Phys. Lett. 409 (2005) 304–309.
[75] A.B. Pribil, T.S. Hofer, B.R. Randolf, B.M. Rode, J. Comput. Chem. 29 (14) (2008) 2330–2334.
[76] T.E. Simos (Ed.), Structure and Dynamics of Composite Anions in Aqueous Solution, American Institute of Physcs (AIP), New York, 2007.
[77] D. Xenides, B.R. Randolf, B.M. Rode, J. Chem. Phys. 122 (17) (2005) 17450601–17450610.
[78] N. Reuter, A. Dejaegere, B. Maigret, M. Karplus, J. Phys. Chem. A 104 (2000) 1720.
[79] P.H. Koenig, M. Hoffmann, T. Frauenheim, J. Phys. Chem. B 109 (2005) 9082.
[80] G.S. Fanourgakis, S. Xantheas, J. Chem. Phys. 128 (2008) 11328.
[81] S. Lammers, S. Lutz, M. Meuwly, J. Comput. Chem. 29 (2008) 1048.

CHAPTER 8

Applications of Mixed-Quantum/Classical Trajectories to the Study of Nuclear Quantum Effects in Chemical Reactions and Vibrational Relaxation Processes

Gustavo Pierdominici-Sottile[a], **Sebastián Fernández Alberti**[a] and **Juliana Palma**[a]

Contents

1. INTRODUCTION

The description of many processes which are relevant to Chemistry and Biology, such as proton and electron transfer, photodissociation, and vibrational energy relaxation, requires the use of quantum mechanics. However,

[a] Universidad Nacional de Quilmes, Sáenz Peña 352, Bernal, B1876BXD, Bs. As., Argentina

Advances in Quantum Chemistry, Vol. 59
ISSN: 0065-3276, DOI: 10.1016/S0065-3276(10)59008-7

© 2010 Elsevier Inc.
All rights reserved

in many cases, these processes take place within large and complex systems, where a full-quantum description cannot be afforded. To cope with such situations, several approximate methods have been developed, each of them having its own strengths and weaknesses. Among them, methods combining quantum and classical mechanics stand out because of their conceptual simplicity and relatively low computational cost.

In this chapter we will concentrate on methods that make explicit use of mixed-quantum/classical (mixed-Q/C) trajectories, designed to analyze processes in real time. Thus, very valuable and highly used approaches such as semiclassical dynamics, Gaussian wave packet propagation (WPP), and path integral will not be reviewed here. Instead, the reader is referred to Refs. [1–4], and the references cited there, for discussions about their characteristics, scope, and applications. Furthermore, this chapter is restricted to electronically adiabatic processes requiring a Q/C treatment because of the presence of nuclear quantum effects, such as the effect of tunneling on a rate constant, or the effect of having discrete energy levels on energy transfer processes. Some of these methods, however, can also be adapted to analyze electronically nonadiabatic processes.

By mixed-Q/C trajectories we mean trajectories in which the evolution of the system is determined through the joint application of the time-dependent Schrödinger equation to some selected degrees of freedom, and the Newton equations to the others. In order to make possible the flow of energy between the two partitions, while maintaining the total energy of the combined system, both quantum and classical equations need to be properly modified. As there is not a single way to do this, different procedures have been proposed which can be distinguished by the strategy used to connect the quantum and the classical subsystems.

One of the most useful features of the methods based on mixed-Q/C trajectories is that they allow observing processes in real time. Thus, a clear picture of their dynamics can be readily appreciated. This is particularly helpful in studies of vibrational energy relaxation and intramolecular energy redistribution. Besides, statistical results such as reaction probabilities or canonical rate constants can also be obtained through averaging over a large number of trajectories.

In the following section we briefly present the basic equations of the most used mixed-Q/C propagation schemes. This is mainly done to introduce the terminology and equations employed in the discussions given in the rest of the chapter. For more detailed descriptions, as well as comparisons between the different schemes, the reader is referred to Refs. [5–7]. Then, we discuss the application of mixed-Q/C trajectories to the study of three different kinds of processes, selected among the large variety that can be analyzed with this methodology. These processes are (1) hydrogen transfer reactions in gas phase; (2) hydride/proton transfer reactions in condensed phase; and (3) vibrational energy relaxation of small solutes in van der Waals clusters and condensed phase. We believe that, by discussing the applications of mixed-Q/C trajectories to these selected cases, the capabilities and limitations of the approach will be clearly exemplified. We conclude this chapter with a discussion on prospective implementations of this methodology.

2. MIXED-Q/C PROPAGATIONS SCHEMES

For the sake of simplicity we will consider a 2D Hamiltonian in the form,

$$\hat{H} = -\frac{\hbar^2}{2m}\frac{\partial^2}{\partial r^2} - \frac{\hbar^2}{2M}\frac{\partial^2}{\partial R^2} + V(r,R), \tag{1}$$

as this greatly simplifies the notation. Nevertheless, the equations derived with this Hamiltonian can be easily extended to treat systems with more degrees of freedom, for which some kind of approximation is actually needed. Without loss of generality, the potential $V(r,R)$ can be partitioned as

$$V(r,R) = V_r(r) + V_R(R) + V_{\mathrm{int}}(r,R),$$

where $V_{\mathrm{int}}(r, R)$ gives the interaction between the quantum and the classical subsystems and renders the Hamiltonian of Eq. (1) nonseparable. It is assumed that $m \ll M$. Therefore, the coordinate r requires a quantum treatment, while R behaves classically.

In Q/C-trajectories, the state of the quantum subsystem is usually described by a wave function in the coordinate representation, $\psi(r,t)$, while the state of the classical subsystem is given by its coordinate and momentum $[R(t),P(t)]$. Accordingly, the evolution of the quantum system is calculated from the time-dependent Schrödinger equation, while the classical subsystem evolves according to the Hamilton equations. In both cases, effective Hamiltonians must be defined in order to allow the coupling between the subsystems. Thus, the differential equations to be solved are

$$i\hbar\dot{\psi} = \hat{H}_r^{\mathrm{eff}}\psi, \tag{2}$$

$$\dot{R} = \frac{\partial H_R^{\mathrm{eff}}}{\partial P}, \tag{3}$$

$$\dot{P} = -\frac{\partial H_R^{\mathrm{eff}}}{\partial R}, \tag{4}$$

with $\hat{H}_r^{\text{eff}}$ and H_R^{eff} defined as

$$\hat{H}_r^{\text{eff}} = -\frac{\hbar^2}{2m}\frac{\partial^2}{\partial r^2} + V_r(r) + V_{\text{int}}(r,R), \tag{5}$$

$$H_R^{\text{eff}} = \frac{P^2}{2M} + V_R(R) + \langle\psi(r,t)|V_{\text{int}}(r,R)|\psi(r,t)\rangle_r. \tag{6}$$

The symbol $\langle\ \rangle_r$, in Eq. (6) denotes integration over the full range of the quantum coordinate, r.

One possibility to differentiate the various Q/C-propagation schemes is by the way in which they represent the wave function that indicates the state of the quantum subsystem. In some methods, the focus is on the spatial characteristics of $\psi(r, t)$. Therefore, the information to be obtained from a trajectory is how the position and the shape of the initial wave packet evolve with time. In such cases, it is customary to expand $\psi(r, t)$ on a grid representation. In some other cases, a basis set representation is employed, through the use of the eigenfunctions of an appropriate zero-order Hamiltonian, or the adiabatic Hamiltonian. In this instance, the information to be obtained from the trajectories is how the coefficients of the expansion evolve with time. In principle, the two representations are equivalent and the use of one or the other is just a matter of computational advantage. However, each of them leads to rather different propagation schemes when the basic algorithms are modified in order to improve the performance of the mixed-Q/C method.

In approaches dealing with a grid representation, ψ and R are both independent dynamical variables. Therefore, in Eq. (5), $V_{\text{int}}(r, R)$ is a fluctuating potential that depends on time through the motion of the classical coordinate. Accordingly, R is not an adiabatic parameter for $\psi(r, t)$ and there should be no ambiguity in the application of Eq. (4):

$$\dot{P} = -\frac{\partial V_R}{\partial R} - \frac{\partial}{\partial R}\langle\psi(r,t)|V_{\text{int}}(r,R)|\psi(r,t)\rangle_r,$$

$$\dot{P} = -\frac{\partial V_R}{\partial R} - \left\langle \psi(r,t)\left|\frac{\partial V_{\text{int}}(r,R)}{R}\right|\psi(r,t)\right\rangle_r.$$

The second term on the right-hand side of these equations is the Hellman–Feynman force [8]. It accounts for the effect of the quantum subsystem on the classical trajectory. The following alternate expression can also be obtained invoking the same reason:

$$\dot{P} = -\frac{\partial V_R}{\partial R} - \frac{\partial}{\partial R}\left\langle \psi(r,t)\left|\hat{H}_r^{\text{eff}}\right|\psi(r,t)\right\rangle_r. \tag{7}$$

It has been shown [8,9] that the propagation scheme described by Eqs. (2–6) can be derived from the full time-dependent Schrödinger equation using

$$\Psi(r,R,t) = \psi(r,t)\ \varphi(R,t), \tag{8}$$

with

$$\varphi(R,t) = a(R,t)\ e^{iS(R,t)/\hbar}, \tag{9}$$

where $a(R,t)$ and $S(R,t)$ are real-valued functions. Bornemann et al. [8] proved that, if the mass of the classical particle is large enough and $|\varphi(R,t=0)|^2$ can be approximated by a δ function of variance ε^2, the product given in Eq. (8) approximates the full-quantum wave function with an error of order ε/L, where L is a characteristic length of the system. Similarly, the error in the classical trajectories computed by Eqs. (3 and 4) is of order $(\varepsilon/L)^2 + \sqrt{m/M}$. Finally, a subtle but important remark is that the procedure remains valid as long as the propagation time does not exceed a maximum time $t_{\max}$, at which the system gets to a focal point (i.e., a point where two nearby trajectories intersect). A nice example of this problem is discussed in Ref. [8] for a model representing the collision of a heavy particle with a harmonic oscillator. Unfortunately, for larger and more complex systems it is not easy to establish, a priori, where the focal points are. Among the methods that typically employ a grid representation of the wave function we can mention the Q/C-time dependent self-consistent field (Q/C-TDSCF) approach [9] used in simulations of inelastic and reactive collisions in gas phase, and the quantum classical molecular dynamics (QCMD) algorithm [8] used in studies of proton transfer in condensed phase.

Several numerical algorithms have been proposed to integrate the equations of motion corresponding to a grid representation of the wave function. The simplest one, usually called the hybrid method, combines a classical MD integrator, such as Verlet, with a quantum wave packet propagator, such as the split operator. However more sophisticated algorithms which employ symplectic and nonsymplectic integrators [10,11], as well as others involving multiple timescales, have been proposed [12]. They have proven to conserve the energy of the whole system with higher accuracy than the hybrid approach. For details about this specialized topic the reader is referred to Refs. [10–12].

Alternatively, other propagation schemes can be derived from Eqs. (2–4) by using a basis set expansion for $\psi(r,t)$,

$$\psi(r,t) = \sum_{j=1}^{N} c_j(t)\Phi_{\mathrm{j}}(\mathrm{r};\mathrm{R}). \tag{10}$$

Here the coefficients, $c_j(t)$, are complex variables that do not depend on R. Inserting this expansion into Eq. (2), the following set of differential equations is obtained for the coefficients:

$$i\hbar\dot{c}_j = \sum_{k=1}^{N} c_k\left(\left\langle \hat{H}_r^{\text{eff}}(r,R)\right\rangle_{jk} - i\hbar\dot{R}d_{jk}\right), \tag{11}$$

where

$$\left\langle \hat{H}_r^{\text{eff}}(r,R)\right\rangle_{jk} = \left\langle \Phi_j \middle| \hat{H}_r^{\text{eff}}(r,R)|\Phi_k\right\rangle_r$$

and

$$d_{jk} = \left\langle \Phi_j \middle| \frac{\partial\Phi_k}{\partial R}\right\rangle_r .$$

It is important to note that introducing the expansion of Eq. (10) into the propagation equations is equivalent to make a variable change. The dynamical variables are now the coefficients c_j, R, and P (instead of ψ, R, and P). Accordingly, the time evolution of the system is obtained by integrating the set of coupled differential equations [Eq. (11)], along with the classical equations [Eqs. (3,4)].

Equation (11) shows that the rate of change of $c_j(t)$ depends on two terms: the potential couplings, $\langle \hat{H}_r^{\text{eff}}(r,R)\rangle_{jk}$, and the kinetics couplings, $\dot{R}d_{jk}$. The first of these terms vanishes for $j \neq k$ if $\psi(r,t)$ is expanded in the adiabatic basis set $\{\Phi_j^a(r;R)\}$, which is composed of the orthonormal eigenfunctions of $\hat{H}_r^{\text{eff}}$ for the given value of R,

$$\hat{H}_r^{\text{eff}}(r;R)\ \Phi_j^a(r;R) = \epsilon_j(R)\Phi_j^a(r;R). \tag{12}$$

In this case, the set of differential equations for the coefficients is

$$i\hbar\dot{c}_j = c_j\epsilon_j(R) - i\hbar\dot{R}\sum_{k=1}^{N} d_{jk}c_k, \tag{13}$$

and $\dot{R}d_{jk}$ measures the strength of the nonadiabatic coupling between the adiabatic states j and k. Using the nondiagonal Hellman–Feynman theorem, d_{jk} can be calculated as

$$d_{jk} = \frac{\left\langle \Phi_j^a \middle| \partial\hat{H}_r^{\text{eff}}/\partial R \middle| \Phi_k^a\right\rangle}{(\epsilon_k - \epsilon_j)}. \tag{14}$$

On the contrary, the kinetic couplings vanish when $\psi(r,t)$ is expressed in a diabatic basis set $\{\Phi_j^d(r)\}$, which is formed by a set of orthonormal eigenfunctions calculated as

$$\hat{H}_r(r)\Phi_j^d(r) = \epsilon_j \Phi_j^d(r),$$

with

$$\hat{H}_r = -\frac{\hbar^2}{2m}\frac{\partial^2}{\partial r^2} + V_r(r).$$

The functions of this basis set do not depend on the position of the classical particle. Therefore Eq. (11) reduces to

$$i\hbar\dot{c}_j = \sum_{k=1}^{N} c_k \left\langle \hat{H}_r^{\text{eff}}(r,R) \right\rangle_{jk}. \tag{15}$$

Even after deciding by the use of an adiabatic or a diabatic basis set, multiple possibilities exist for carrying out the propagation. A relatively simple algorithm is obtained if the propagation is performed employing just a single function of the adiabatic basis set. In so doing, the system is forced to remain in the same state and the propagation is said to be adiabatic. Equation (13) shows that this procedure can be justified if the motion of the classical degrees of freedom is slow (i.e., in the limit of $\dot{R} \rightarrow 0$). Besides, as implied by Eq. (14), the energy gap between quantum states must remain large during the whole propagation.

The application of the adiabatic algorithm is relatively simple. First, Eq. (12) is solved for the appropriate initial values of the classical variables. Then, using the wave function corresponding to the selected adiabatic state, the effective force on the classical system is calculated as

$$\dot{P} = -\frac{\partial V_R}{\partial R} - \frac{\partial}{\partial R}\left\langle \Phi_j(r;R) \middle| \hat{H}_r^{\text{eff}} \middle| \Phi_j(r;R) \right\rangle_r.$$

Afterward, Eqs. (3 and 4) are employed to update the classical coordinate and momentum, respectively. The new coordinate is then used to update the adiabatic wave function, starting a new cycle. As, by assumption, $c_j = 1$ and $c_{k\neq j} = 0$, there is no need to propagate Eq. (13) and the nonadiabatic couplings do not have to be calculated. This greatly reduces the computational cost of the approach. However, in many studies of nuclear quantum effects, the conditions required to have an adiabatic process are not fulfilled, or rather, it is not known whether they are fulfilled or not. Therefore, the use of more than one function should be preferred, whenever it is affordable. Anyhow, if the process is actually adiabatic, the algorithm will tell by itself that the coefficients associated to other states remain close to zero.

Two different propagation schemes are possible when more than one function is used in the expansion of $\psi(r,t)$. In the "mean field" or Ehrenfest approach, the effective force on the classical subsystem is obtained through direct application of Eqs. (7 and 10) to give

$$\dot{P} = -\frac{\partial V_R}{\partial R} - \frac{\partial}{\partial R}\sum_{j=1}^{N}|c_j|^2\epsilon_j(R).$$

Alternatively, the Hellman–Feynman theorem affords the more operative expression,

$$\dot{P} = -\frac{\partial V_R}{\partial R} - \sum_{j=1}^{N}|c_j|^2\left\langle \Phi_{\mathrm{j}} \left| \frac{\partial H_r^{\mathrm{eff}}}{\partial R} \right| \Phi_{\mathrm{j}} \right\rangle. \tag{16}$$

The last equation clearly shows that the force exerted by the quantum subsystem on the classical subsystem is an average of those generated by each individual quantum state. As a result, problems arise when these individual forces are significantly disparate to each other. In this case, the average of the second term of Eq. (16) does not resemble any actual force experienced by the classical system when it interacts with a single quantum state.

Surface hopping methods have been designed to cope with situations like this. In this approach, the quantum system is prepared into a single state j by initially setting $c_j = 1, \{c_k = 0\}_{k \neq j}$. Moreover, it is assumed that the system remains in the same state until a sudden transition occurs. Accordingly, the forces on the classical subsystem are evaluated as in the adiabatic approximation. At the same time, Eq. (13) is propagated to monitor the evolution of the coefficients $c_j(t)$, which are used to evaluate the transition probability between the current quantum state and the others. Different procedures have been proposed to decide when and how a quantum transition should be made.

A widely used procedure to do this is given by Tully's "Fewest Switches" method. This algorithm distributes trajectories among quantum states in proportion to their probabilities $|c_j|^2$, using the minimum required number of quantum transitions. Lets $a_{jk} = c_j c_k^*$ be the elements of a Hermitian matrix whose diagonal elements give the occupation probabilities of the states included in the expansion of $\psi(r, t)$. Then, $\dot{a}_{jj}$ measures the rate of change of the occupation probability of state j. Using Eq. (13) it is found that

$$\dot{a}_{jj} = -\sum_{k \neq j}^{N} b_{jk}.$$

Here,

$$b_{jk} = 2\dot{R}d_{jk}Re\left(a_{jk}^*\right)$$

measures the rate of change in the occupation probability for state j due to its coupling with state k. So, a value of b_{jk} greater than zero indicates an increase in the occupation probability of state k at the expense of the occupation of state j. Consequently, if for a short time interval δt, a_{jj} and b_{jk} can be considered as constants, the relative change in the occupation probability of state j due to its coupling to state k is given by $b_{jk}\delta t/a_{jj}$. This relative change is assumed to measure the probability of transitions between the current state j and the new state k. If this value is positive, random numbers are used to allow transitions in accordance with their probabilities; if it is negative, the transition is not performed.

When the algorithm indicates that a transition between states j and k must take place, but $\epsilon_j \neq \epsilon_k$, the classical velocities are adjusted in order to conserve the total energy of the composed system. This adjustment is performed as if the classical coordinates were subjected to a force in the direction of the coupling, as explained in Ref. [13]. However, it may occur that there is no enough energy in the direction of the nonadiabatic coupling to maintain the energy. These events are called "classically forbidden transitions." When they occur, it is assumed that the system remains in the original quantum state and the direction of the classical velocities is reversed [14]. The existence of classically forbidden transitions leads to a disagreement between $|c_j|^2$ and the fraction of trajectories at state j. For that reason, improvements to the basic algorithm have been proposed in order to eliminate these kind of events [15,16]. The surface hopping with fewest switching approach has been extensively used in studies of nuclear quantum effects in vibrational relaxation and proton transfer processes, usually under the name of molecular dynamics with quantum transitions (MDQT).

Basis sets different than the adiabatic and diabatic ones can also be used to expand $\psi(r, t)$. In this way, propagation schemes slightly different than the ones discussed above are obtained. Nevertheless, they involve the same principles. For example, when simulating the transference of a light particle between the wells of a bistable system, vibrational functions centered on each well can be used, as well as distributed Gaussians. In these cases, additional computations must be done because the basis set is not orthonormal [17].

3. HYDROGEN TRANSFER IN GAS PHASE

The application of mixed-Q/C trajectories to the study of gas-phase reactions is commonly referred to as Q/C-TDSCF. However, Billing and his coworkers, who extensively contributed to the growth of this field, used the name of "semiclassical approach." In most of the early applications, the processes studied were three atomic reactions of the type $A + BC \rightarrow AB + C/AC + B$. Moreover, in many instances, further simplifications were made in order to allow the computation of exact full-quantum magnitudes so that meaningful comparisons, intended to assess the accuracy of the mixed approach, could be done. Among these, we can mention the use of collinear, planar, and zero total angular momentum approximations. In general, the quality of mixed-Q/C approaches improves by increasing the size of the system. Therefore, these small, low-dimensionality systems represented a rather stringent test. Thus several limitations were readily noticed, which provided useful insights into the very nature of the approach. More importantly, they stimulated new developments aimed to improve its reliability.

Neuhauser and Judson [18] studied the collinear $T+HT \rightarrow TH+T$ reaction in two different ways. In the "particle-based" approximation the Hamiltonian was expressed in atomic Cartesian coordinates. The coordinates corresponding to the T atoms were treated classically while the one corresponding to the H atom was treated quantally. In the second method, labeled as "bond-based," the Hamiltonian was expressed in Jacobi coordinates. One of these coordinates describes the vibration of the initial H—T bond while the other one accounts for the relative motion between T and the center of mass of the HT molecule. In this case, the H—T bond was treated quantally while the relative motion was treated classically. By using absorbing potentials placed at the exit of the products channel, Neuhauser managed to evaluate reaction probabilities as a function of the kinetic energy. He found that the two Q/C approaches performed significantly better than a full classical calculation, both being able to predict tunneling. However, differences between full quantum (full-QM) and mixed-Q/C results were important at the whole energy range.

The "particle-based" approximation is usually employed in the study of reactions that occur in condensed phases. However, as discussed by Newhauser, it produces some ambiguities at the time of initializing the Q/C trajectories. This is because one of the atoms that form the bond being broken belongs to the classical subsystem, while the other one belongs to the quantum subsystem. The "bond-based" approach, on the other hand, is of choice in studies of inelastic and reactive scattering involving a handful of atoms. This is due to the fact that the approach relies on the use of Jacobi coordinates which allow for an accurate treatment of the vibrational states of the bonds being broken/formed. Besides, the Jacobi coordinates minimize the number of degrees of freedom that need to be propagated. Nevertheless, this advantage is not so critical in mixed-Q/C applications as it is in full-quantum calculations.

The collinear $Cl+HCl \rightarrow ClH+Cl$ [19] and $O(^3P)+HCl \rightarrow OH+Cl$ [20] reactions, which are prototypes of heavy–light–heavy systems, were studied with the "bond-based" approach. For the Cl + HCl reaction, two different Q/C-propagation schemes were evaluated. One of them was the standard single-trajectory Q/C-TDSCF approach. The second one involved multiple

Q/C trajectories in which the initial classical coordinate and momentum were selected according to a Wigner distribution function. In this case the final results were obtained by averaging the outcomes over several individual trajectories. Reasonable agreement was found between both the Q/C approaches and the full-quantum results, except for energies close to resonances. The results obtained with multiple trajectories were closer to the quantum ones than those obtained with a single trajectory, but the improvement was just moderate.

The most serious limitation of the Q/C-TDSCF method becomes evident when the wave packet, that is initially concentrated in a small region of the configurational space, splits into two or more parts. In this case, the force corresponding to the second term of Eq. (7) (which is a mean field force), does not correspond to the actual forces exerted by each part of the wave packet, but to an average of them. To solve this problem, Wang and Clary proposed the "Quenching" method based on physical intuition [21,22]. Later on, Wang demonstrated that the method could be derived from the time-dependent Schrödinger equation by using a Q/C-multiconfiguration time-dependent self-consistent field approach (MC-TDSCF) [23].

Several, slightly different implementations of the MC-TDSCF method have been proposed, but all of them are based on the same idea. The simulations start with a single Q/C-trajectory which is propagated until the wave packet shows a clear bifurcation. After that, two different trajectories are propagated, each of them representing the interaction of the classical subsystem with a single part of the wave packet. The main difference between alternative procedures is the criterion used to detect the bifurcation and the way in which the wave function is decomposed to produce the independent trajectories.

The MC-TDSCF approach was applied to the collinear $O(^3P) + HCl$ [20] reaction, on two different potential energy surfaces. Standard single configuration computations (SC-TDSCF) and full-QM computations were also performed. It was found that the SC-TDSCF algorithm afforded reasonably accurate results for one of the surfaces but not for the other. More importantly, it was shown that for both surfaces, the accuracy of the results could be significantly improved by introducing just a second configuration into the Q/C simulation. The conclusion was that the MC-TDSCF approach was able to produce fairly accurate results except at very high energies where, probably, more than just two configurations should be used. The drawbacks of the SC-TDSCF algorithm were attributed to the asymmetry of the surface at the strong interaction region, since the derivative $\partial V/\partial R$ taken at the reactants' channel bears significant differences with the derivative taken at the products' one. This leads to an artificial correlation between the dynamics of the reactants and the products channels [20]. On the other hand, when the surface is highly symmetrical, the derivative $\partial V/\partial R$ is similar in both channels and there is no harm in taking the average implied by the Hellman–Feynman forces.

Later on, the MC-TDSCF approach was used to describe the collisions between O(^{3}P) and the van der Waals complex Ar–HCl [24]. The study of the O(^{3}P) + Ar–HCl system is a good example of the possibilities offered by this method that allows observing individual reactive events. Thus, the analysis of the Q/C trajectories revealed that the rare gas atom was able to focus the wave packet on a small part of the configurational space, producing a more thorough sampling of the transition state (TS) region. This leads to an increase in the reaction probability, in comparison with the simple O (^{3}P) + HCl reaction, in agreement with the experimental results [25].

Billing and coworkers performed Q/C studies of gas-phase reactions not restricted to the collinear geometry. The theory to treat three atomic reactions was introduced [26] and employed to investigate the $D + H_2 \rightarrow DH + H$ reaction [27–29], as well as other nonadiabatic reactions [30], with a planar approximation [27] and also in 3D [28,29]. One interesting feature of Billing's approach is that he formulated the reactive scattering problem in hyperspherical coordinates, which consider all the reactive channels on the same footing [31]. In the first model, the Euler angles that describe the rotation of the whole system and the hyperradious that describes the relative motion of the colliding fragments were treated classically. The vibrational and rotational degrees of freedom of the diatomic were treated quantally [29]. In a second study, the hyperradious was also included in the quantum subsystem just leaving the classical treatment for the degrees of freedom associated with the rotational motion [28]. It was found that only the latest model compared well with the available exact quantum results, giving reasonable accurate vibrationally resolved cross sections over a large range of translational energy. It was concluded that a quantum treatment of the hyperradious was needed in order to obtain a fairly good description of the dynamics. Billing and coworkers also studied the $OH + H_2 \rightarrow H_2O + H$ reaction [32,33]. In the first of these studies [33], the quantum subsystem was composed by the vibrational degrees of freedom of the diatomic molecules, while all the rotations plus the translational motion were part of the classical subsystem. The comparison between full-QM and mixed-Q/C rate constants was satisfactory at temperatures above 400 K, but not good below that temperature where the Q/C results underestimated the full-QM values. In a second paper, the translational motion was also included in the quantum subsystem and the comparison with full-QM computations improved significantly.

An important step forward in the application of the mixed Q/C-TDSCF approximation to more complex systems was given by Zhang and coworkers, who analyzed a series of reactions that involve methane as a reactant. In particular, they implemented a Q/C version of the reduced dimensionality semirigid vibrating rotor target (SVRT) model [34]. When applied to the study of reactions of a single atom with methane ($X + CH_4 \rightarrow XH + CH_3$), the basic version of the SVRT model has four degrees of freedom. Two of them are the radial Jacobi coordinates for the reactants channel: one describes the vibration of the bond being broken and the other one describes the translational motion. The other two degrees of freedom are angles. One of them is associated with the orbital motion of the colliding atom, the other one with the rotation of the CH_3 moiety.

In the Q/C version of the model, the translation is treated classically while the rest of the Hamiltonian is treated quantally. This procedure is justified for collisions in which the reduced mass for the translational motion is large, as in the case of the $O(^3P) + CH_4 \rightarrow OH + CH_3$ reaction. Fortunately, it is just in these cases where a classical treatment becomes convenient, or needed, because of the large number of basis set functions required by the full-quantum calculation. Thus, for the $O(^3P) + CH_4 \rightarrow OH$ CH_3 reaction, the comparison of results obtained with the Q/C-SVRT approach and the full-quantum version of the model gave encouraging results [35].

A more thorough evaluation of the approximation was given in a later study in which the comparison between quantum and Q/C computations was performed for the isotopic reactions $H(D,T) + CH_4 \rightarrow HH(D,T) + CH_3$ [36]. For the three cases, the full-quantum reaction probabilities presented oscillations which were attributed to dynamical resonances. In accordance with the previous conclusions of Wang and Mc Coy, it was found that Q/C computations were unable to reproduce this effect. As these resonances were more pronounced for the reaction with H than with T, the agreement was worst in the former case. A second important trend detected in this work appeared in the analysis of the reaction probabilities out of the ground vibrational state of CH_4. The results showed that the threshold of the Q/C-probabilities was smaller than the one corresponding to full-QM ones. This was explained in terms of the vibrationally adiabatic barriers for the mixed-Q/C and full-QM computations.

The translational motion, which has no frequency when the reactants are far apart to each other, becomes a vibration at the TS. In the full-QM computations there is a zero point energy associated with this TS-vibration while in the mixed-Q/C computations there are no restrictions on the amount of energy associated with this mode. Accordingly, the vibrationally adiabatic barrier observed in the full-QM computations is higher than the one observed in the mixed approach. This effect is well known from the comparisons between the results of full-quantum and quasi-classical trajectory calculations [37]. As the zero point energy associated with the lacking vibration is larger for the $H + CH_4$ reaction than for the $T + CH_4$ one, the disagreement in the thresholds is larger in the former case.

More disturbing results were obtained from the analysis of reaction probabilities out of the first excited vibrational state of the C—H bond. In this case, significant differences in the thresholds to reaction were observed for the three isotopes. The problem was attributed to the fact that all the computations used just a single configuration, instead of the minimum number of two required to account for the splitting of the wave packet. As the results of MC-TDSCF computations have not been reported yet, this must be considered just as a putative explanation. The Q/C version of the SVRT model was also used to study the collisions between a molecule of methane and a Ni surface [38].

In the discussion so far we have just included time-dependent calculations for which, at $t = 0$, the reactants are well separated to each other, as correspond to the initial conditions of the scattering problems. However, the mixed-Q/C approach can also be used in direct computations of rate constants by using the flux–flux correlation function formalism [39]. In this case the propagation is initiated at the TS, and the trajectory is followed for a short interval until the flux–flux correlation function goes to zero. Although the method has been mainly used to study reactions in condensed phases, a recent study on model systems indicates that it could work fairly well for gas-phase reactions [40].

Before leaving this section we summarize the main conclusions. First, the SC-TDSCF approach can give reasonably accurate results in the case of symmetric potentials. In all the cases, however, it is preferable to introduce at least a second configuration (MC-TDSCF), to take into account the splitting of the wave packet after getting to the strong interaction region. The MC-TDSCF method is always needed in the case of asymmetric potentials. Second, when the mass associated with the translational motion is small, a quantum treatment of this motion is required in order to get the correct threshold to reaction. This is an important issue in the calculation of rate constants.

4. PROTON AND HYDRIDE TRANSFER IN CONDENSED PHASE

Proton transfer is an important class of reaction in Chemistry, Biochemistry, and Biology [41–45]. In particular, it is an essential and ubiquitous step in enzyme catalysis [46–52], where the role of nuclear quantum effects is currently a matter of intense debate [53–55]. Classical MD has been used to analyze some aspects of proton transfer in condensed phases [56]. However, due to the light mass of the hydrogen atom, tunneling and zero point energies are significant and the use of quantum mechanics becomes mandatory [57]. The number of methods that have been designed and applied to describe H^+/H^- transfer in condensed phases is huge. Among them, the "ensemble averaged-variational transition state theory" (EA-VTST) stands up because of the large number of processes studied with it (see Ref. [58]). The algorithm is an extension of the VTST method widely used to calculate rate constants in the gas phase. The EA-VTST approach takes into account the participation of the environment in the reaction coordinate and allows a sampling of the TS region without a previous knowledge of the stationary points. However, a thorough discussion of EA-VTST is beyond the scope of this chapter, so the interested reader is referred to Ref. [58] and the references cited there. In the following section, as in the rest of this chapter, we restrict ourselves to the description of approaches based on a separation of the whole system into a quantum and a classical part, followed by the joint propagation of the equations of motion for each part (as discussed in Section 2).

An example that nicely illustrates the ability of mixed-Q/C trajectories to describe the real-time dynamics of reactions in complex environments is given in a series of works on phospholipase A2 by Bala et al. [59–61]. This enzyme, that hydrolyzes phospholipids, consists of three connected α-helices. The active site, located between two parallel α-helices, is composed of a histidine residue and a water molecule. According to the accepted mechanism, the catalyzed reaction starts with a proton transfer from the water molecule to the histidine residue, forming the OH^- group that performs the nucleophilic attack on the carbonyl carbon of the substrate. The most complete of these studies [60], in which the proton was treated as a 3D Gaussian wave packet, was able to demonstrate that the transfer takes place only when it is accompanied by the nucleophilic attack on the substrate. In other words, the simulation indicated that the mechanism is not sequential, but concerted.

The effect of fluctuations of the protein environment was revealed by analyzing the time evolution of the formal charges of the atoms in the active site. It was noted that the transfer is triggered by an increase in the charge of the carbon atom that suffers the nucleophilic attack. At the same time, this atom changes its hybridization from sp^2 to sp^3, as indicated by a variation in its geometry from planar to tetrahedral. Interestingly, it was observed that the transfer is associated with a slight increase in the donor–acceptor distance. This is contrary to the common belief that the shortening of this distance promotes the transfer [62]. By comparing mixed-Q/C and full-classical simulations it was noted that the effective barriers were significantly smaller when the proton was treated quantum-dynamically. This phenomenon was attributed to the zero point energy and to the delocalization of the quantum particle. A similar behavior was also observed in comparisons between quantum (path integrals) and classical simulations of the proton shared in a hydrogen bond [63].

Other lesson to be gained from these studies is how sensitive are the results to the potential used to run the computations. Thus, the simulations of Refs. [59 and 60] used valence bond parameterizations, similar to the empirical valence bond (EVB) method [64], to calculate the potential that describes the transfer. The first of these studies [59] included eight valence bond structures in the parameterization while the last one used fourteen [60]. In the first work, the transference of the proton was observed only in mixed-Q/C simulations, but not in the full-classical ones. However, in the most complete study, the transfer was observed in both instances. Also, the simultaneous proton transfer/nucleophilic attack mechanism was only detected in the latter case.

Another approach used to calculate the rate of proton transfer in condensed phases is the density matrix evolution (DME) method of Mavri et al. [65]. The method combines the Liouville–von Neumann equation for the quantum subsystem, with the Hamilton equations for the classical one. Numerical tests on the approach were done with nonreactive systems such as the collision between a quantum harmonic oscillator and a classical particle or a quantum harmonic oscillator embedded in a classical noble gas bath [66,67].

In the DME method, the wave function of the proton is expanded in a basis set,

$$\psi = \sum_{i=1}^{N} c_i \phi_i,$$

and then an $N \times N$ density matrix is defined as $\rho_{ij} = c_i c_j^*$. Note that this matrix is not an average over an ensemble but an instantaneous property of an individual quantum subsystem. The density matrix is propagated in time according to

$$\dot{\rho} = \frac{i}{\hbar}[\rho, H],$$

where

$$H_{ij} = \left\langle \phi_i \middle| \hat{H}_r^{\text{eff}} \middle| \phi_j \right\rangle.$$

The DME method was applied to calculate the rate of proton tunneling in hydrogen malonate in aqueous solution. In a first work [66], the proton wave function was expanded in a basis set consisting of two orthonormalized Gaussian functions, one centered at the reactants well and the other at the products well. In this representation, ρ_{11} indicates the population of the reactants. Accordingly, the rate constant was obtained from the time dependence of ρ_{11} evaluated with a coarse-grained timescale,

$$k = \frac{\langle \Delta \rho_{11} \rangle}{\Delta t},$$

where Δt is small in the timescale of the reaction but large in a molecular time scale. Here the symbol $< >$ denotes average over a canonical ensemble of initial conditions, which were taken from MD simulations in which the proton was located at the reactant well. It should be noted that, with this procedure, the solvent is organized to stabilize the reactant state. Therefore, configurations for which the energies of reactants and products are nearly the same, occur scarcely. Since these configurations are the most important ones (the transfer is more likely in these cases), the sampling cannot be appropriate unless long-enough MD simulations are performed. To analyze the effect of the sampling on the results, a biased sampling was then introduced in the DME procedure [65]. In this case, the initial configurations were taken from a MD simulation in which the proton was fixed at the middle point between the donor and the acceptor. Accordingly, the solvent accommodates so as to stabilize the TS and the potential for the instantaneous proton transfer becomes (nearly) symmetric. By using these potentials in the DME propagation, and analyzing the average population decay of the reactants, a rate constant about 20 times larger than the previous one was obtained. However this is not the final value of $k(T)$, as it has to be multiplied by a Boltzman factor that takes into account the energy required to reorganize the solvent. When this factor is introduced, the values of the rates determined with the two procedures were found to be approximately the same.

In a latter study, a more flexible basis set consisting of five displaced Gaussians was employed. This set is computationally convenient to evaluate the integrals needed to propagate the DME equations of motion. However, it was not the basis set used to define the density matrix. Instead, ρ was written in terms of the eigenfunctions of a reference Hamiltonian, $\hat{H}_0$, which was defined as the one associated with the average proton potential. One important difference between the two basis sets is that the eigenfunctions of $\hat{H}_0$ are orthogonal, while the displaced Gaussians are not. Besides, the eigenfunctions of $\hat{H}_0$ have a clearer physical meaning. The initial state of the proton in all the propagations was taken as the ground state of $\hat{H}_0$. The DME equations of motion were propagated using the orthogonal basis, but calculating the required integrals with the nonorthogonal one. The algorithm used to do this is described in detail in Ref. [17]. The rate constant was calculated from the initial population increase of the products state, giving a value of $k(T)$ about 30 times larger than that obtained using only two basis set functions. These results remark the importance of employing a large-enough basis set to describe the state of the quantum system.

In a more recent article, Mavri et al. applied the WPP approach to calculate the kinetic isotope effect in the proton transfer step that determines the rate of the reaction catalyzed by soybean lipoxygenase-1 [68]. The WPP approach is closely related to the DME method. The main difference between them is that the WPP procedure uses a grid representation of the state of the proton, which is initially considered to be a Gaussian wave packet located at the reactant well, with a width given by the ground vibrational state. Good agreement was found between the results obtained with the WPP method and other more established approaches, such as the quantized classical path (QCP) method of Olsson et al. [69]. Lately, the WPP approach was applied to study the proton transfer step that determines the rate of oxidation of methylamine, catalyzed by enzyme methylamine dehydrogenase [70]. A rather good agreement was found between the calculated kinetic isotope effect and the experimental value. Altogether, these results suggest that the WPP is a valid alternative to analyze nuclear quantum effect in enzymes.

A different insight into the dynamics of the transfer can be obtained if the state of the proton is expressed in terms of the eigenfunctions of the adiabatic Hamiltonian. As explained in Section 2, two options are available in this case. In the simplest one, the proton is assumed to remain in the ground vibrational state during the whole process. This assumption is valid when the energy gap between the ground and the first excited states is larger than k_BT, a feature that is characteristic of strong hydrogen bonds. The second and more involved option requires the application of a surface-hopping algorithm, in order to allow for nonadiabatic transitions.

The first mixed-Q/C computational simulations of realistic proton transfer models, in the adiabatic regime, were presented by Borgis et al. [71,72] and Laría et al. [73] in 1992. The model used by Borgis et al. consisted of a collinear complex AH^+–A, with a fixed A–A distance, immersed in an ensemble of 255 polar aprotic molecules. The coordinate that describes the position of the proton along the donor–acceptor segment was treated by quantum mechanics while the solvent and the other coordinates of the complex were treated classically. Laría et al. [73] modeled a system composed of a proton, two fixed ions of charge $-e$, and 342 molecules of a polar aprotic solvent. The three Cartesian coordinates of the proton were treated by quantum mechanics while the rest of the system was considered classically. In both cases, the bare proton potential (i.e., the potential for the proton motion in the absence of the solvent) was designed to give a relatively low barrier and an energy gap between the first two states higher than k_BT. In both cases, too, the solvent–solvent and solvent–solute interactions were modeled by the sum of Lennard-Jones and Coulomb interactions.

A distinctive aspect of the model introduced by Borgis et al. is that the charge distribution within the complex was dependent on the proton position. Because of this feature, the change in the dipole moment $\Delta\mu$ associated with the transfer could be made larger than the one corresponding to the mere displacement of a single charge. *Ab initio* computations have demonstrated that this effect, known as Zundel polarization [74], is indeed observed in hydrogen-bonded complexes. In this way, models with $\Delta\mu = 2.4$, 5.2, and 7.0 D could be analyzed.

The two computations used the flux–flux correlation function formula [75–77] to calculate the rate constant. This formulation requires the definition of an appropriate reaction coordinate. Laría et al. discussed the use of the mean value of the proton position along the internuclear axis $\bar{z}_P = \langle\psi|z_P|\psi\rangle$, as well as the difference of solvent electrical potential, ΔE, between the two points located at the global minima of the total proton-ion potential. They verified that the two magnitudes evolve in phase so that they should produce similar results. Nevertheless, they decided to employ ΔE because it is an analytical function of the solvent coordinates and this facilitates the application of the holonomic constraints needed to initiate the trajectories at the transition state. Borgis et al., on the other hand, initiated their trajectories at the reactant well. Therefore, they could use $\bar{z}_{\mathrm{P}}$ as the reaction coordinate. They also tested the use of a slightly different ΔE, which was defined as the instantaneous energy splitting between the protonic diabatic states associated with the product and reactant configurations. Finally, they used an expression for the rate constant in terms of the expectation value of the product population [78,79].

A rate constant could not be defined for the models of Borgis et al. with $\Delta\mu = 2.4$, and 5.2 D. In these cases, as the free energy barrier for the transfer is small, the proton does not get trapped in either well for long enough. Instead, it moves forward and backward and therefore $k(T)$, as a function of time, does not show the required plateau. However, for the model with $\Delta\mu = 7.0\,\mathrm{D}$ the rate constant could be calculated and the values obtained with the three definitions of the reaction coordinate produced similar results. Laría et al. were also able to evaluate $k(T)$. In both cases the value of $k(T)$ determined with the flux–flux correlation function was compared against the TST one, detecting important deviations in the TST results. Moreover, by evaluating the transmission coefficients, the computations of Laría et al. also highlighted the shortcomings of the two-level approximation, which is commonly used to discuss quantum dynamics in condensed phases. In addition to these quantitative results, the two calculations presented a clear qualitative picture of the proton transfer in the adiabatic regime, illustrating how the transference is driven by the fluctuations of the environment. They also had the very important role of demonstrating the feasibility of rate constants computations for proton transfer in condensed phases, using multidimensional realistic models.

More recently, Thompson used mixed-Q/C trajectories in the adiabatic regime to reveal the mechanism for proton transfer in polar solvents confined within nanocavities [80]. Although the models analyzed in this work did not explicitly represent any particular experimental system, they provided important insights on the chemistry occurring in a diverse range of nanoscale confining frameworks. Previously, Monte Carlo (MC) simulations on the same models had determined that the reactants were preferentially located near the walls of the cavity while the products were in the interior. However, the MC simulations could not indicate if the movement from the walls to the interior occurred before or after the solvent reorganization that triggers the proton transfer. By analyzing mixed-Q/C trajectories in real time Thompson noted that the dominant mechanism involved a solvent reorganization followed by the diffusion of the nascent products into the cavity interior. Nevertheless, the opposite sequence was also observed. Moreover, the ratio between the two mechanisms was found to depend on the size of the cavity. Rate constants were evaluated from the average population decay of the reactants, while the equilibrium constants and free energy changes were computed from the values of the forward and backward rates. All these values were found to depend on the size of the cavity.

When the barrier for the transference is relatively large, the energy gap between the two lowest states is small and quantum transitions between them become feasible. Moreover, since the tunneling rate depends on this energy difference, including at least the first two states is crucial to properly account for tunneling. The application of the adiabatic approach in situations like these severely overestimates the rate constants. This is because any fluctuation of the solvent that stabilizes the products state over the reactants state induces an instantaneous transition. To address the study of systems with these characteristics, Hammes–Schiffer and Tully adapted the surface-hopping method known as molecular dynamics with electronic transitions [13], in which the quantum degrees of freedom are electronic while the nuclei move classically, so that it could be used to simulate the quantum nature of the proton. The new approach was named as molecular dynamics with quantum transitions (MDQT). In the application of MDQT to proton transfer processes, the Born–Oppenheimer approximation is assumed to be valid for the electrons, a few nuclear degrees of freedom are treated by Quantum Mechanics and the rest of the system is modeled classically. The basic propagation equations for MDQT have been presented and discussed in Section 2.

The first application of MDQT to proton transfer processes in condensed phase [14] used a model previously developed by Azzouz and Borgis [81]. The model corresponds to an intramolecular reaction of the type AH—B $\rightarrow$ A^{-}—H^{+}B in liquid methyl chloride, whose parameters were set to represent a typical OH—N asymmetrical hydrogen-bonded complex. The rates of proton and deuterium transfer were calculated in the adiabatic and nonadiabatic regimes. In order to do so, the system was considered to be a reactant if the classical coordinates stabilize the reactants and the H atom is in the ground state. Similarly, it was considered to be a product if the classical coordinates stabilize the products and the H atom is in the ground state. A reactive event was defined as one in which the system starts as a reactant and ends as a product. In order to perform meaningful comparisons, adiabatic and nonadiabatic trajectories were initiated from the same configurations. Finally, the rate constants were calculated by adding up the number of reactive events and dividing this sum by the total time of the trajectories. It was found that, in the adiabatic limit, the rate constants for H and D were nearly the same, and that the inclusion of quantum transitions decreased $k(T)$ in both cases. However, the reduction was larger for D than for H, giving a kinetic isotope effect of 3.85 in the nonadiabatic regime. This is consistent with the fact that tunneling, which is taken into account by the nonadiabatic simulations, is larger for H than for D.

The necessity of using different timescales for the integration of the quantum and classical equations of motion was also discussed, as well as the possibility of doing this only in the region of strong nonadiabatic coupling. Finally, the advantages of the MDQT methodology were highlighted. Among these we have: the possibility of analyzing the transfer by doing full-MD simulations, the self-consistent treatment given to the quantum and classical degrees of freedom and the absence of *ad hoc* tunneling corrections. Probably more important is the fact that the method can be used either in the adiabatic and nondiabatic limits, or in the intermediate regime, with no previous assumptions about which of them should be applied. This is very valuable in the study of proton transfer in solution and enzymes because the barrier height depends on the donor–acceptor distance. Therefore, the same system can be in any of either limit depending on the value of this distance.

In a subsequent work, the effect of the excitation of the proton vibration on the transfer probabilities was investigated [82]. Thus, the MDQT methodology was applied to the same model system, but the trajectories were initiated with the reactants at the first excited state. The mechanisms of vibrational relaxation and assisted tunneling were discussed, establishing that MDQT is a valuable method to analyze photoinduced and photoassisted reactions. Finally, a more involved MDQT treatment, called 2D-MDQT, was given to the same system by also treating quantum-mechanically the donor–acceptor distance [83]. The results showed that the quantum treatment of this vibration was not critical in this case, as the rate constants obtained with 2D-MDQT were the same, within the statistical uncertainty, as the ones calculated previously with 1D-MDQT. This behavior was explained by comparing the characteristics of the 1D and 2D dynamics. It was detected that the two approaches only presented differences outside the strong coupling region, where the first excited state of the 2D-MDQT corresponds to a donor–acceptor vibration, while it corresponds to a proton vibration in 1D-MDQT. Accordingly, the energy splitting between the two lowest vibrational states is smaller in 2D-MDQT. However, as the nonadiabatic couplings are negligible in this region, the difference has no relevance. On the other hand, in the strong coupling region, the first excited state corresponds to a proton vibration in both calculations. Therefore, the energy splitting and nonadiabatic couplings are similar and this leads to a similar number of nonadiabatic transitions. Nevertheless, the fact that the quantum treatment of the donor–acceptor vibration was found to be irrelevant in this case does not preclude the possibility that it could be important for other systems.

Subsequently, MDQT was used to analyze dynamical quantum effects in liver alcohol dehydrogenase [84] and dihydrofolate reductase [85]. These two enzymes catalyze reactions that involve a hydride transfer. In both cases, too, the experimental evidence suggests that the transferences occur by tunneling. Rate constants were calculated as the product of a quantum adiabatic TST constant and a transmission factor that was estimated using a MDQT version of the reactive flux method [86]. In the study of liver alcohol dehydrogenase, it was found that the recrossings did not affect significantly the rate constant. However, they showed a high degree of correlation with the donor–acceptor distance. As this distance decreases, the number of recrossings grows and the transmission coefficient diminishes. However, the activation free energy also decreases. Since this effect generally dominates, the result is that the rate constant gets higher as the donor–acceptor distance decreases. On the other hand, in the case of the dihydrofolate reductase, the transmission coefficient showed considerable deviations from unity indicating that dynamical effects are significant.

Multiple proton transfer reactions play a critical role in many important biological processes like the double proton transfer that takes place in DNA base pairs [87] and the ones that occur in enzymes such as serine proteases [74], alcohol dehydrogenases [88], and carbonic anhydrases [89]. In order to allow the study of this sort of processes, Hammes–Schiffer combined the MDQT algorithm with a multiconfigurational self-consistent field evaluation of the adiabatic states of the protons. The methodology received the name of MC-MDQT [90]. In this approach, the quantum subsystem is composed of several protons, and its adiabatic states are expanded as linear combinations of single configuration wave functions. In turn, these functions are obtained as the product of the one-particle adiabatic states for each particle. Since the one-particle states and the multiconfigurational states are dependent on each other, the equations must be solved iteratively until a self-consistent result is obtained. For a detailed description of the MC-SCF algorithm the reader is referred to Ref. [91]. The methodology was applied to simulate multiple proton transfer reactions along water chains of three and four molecules in an electric field [92]. Finally, the versatile MDQT algorithm was extended to treat processes that involve transitions between nuclear states and electronic states [93,94].

A decade ago, Kapral and Ciccotti derived the mixed-Q/C equations of motion for a quantum subsystem composed of light particles, which evolves coupled to a classical bath of heavy particles [95]. The derivation started with a partial Wigner transformation of the Liouville equation over the bath degrees of freedom, followed by an expansion in the small parameter $\mu = (m/M)^{1/2}$. By retaining only the linear terms, the mixed-Q/C Liouville equation was obtained [96],

$$\frac{\partial \hat{\rho}_{\mathrm{W}}}{\partial t} = -\frac{i}{\hbar}[\hat{H}_{\mathrm{W}}, \hat{\rho}_{\mathrm{W}}] - \frac{1}{2}\left(\left\{\hat{H}_{\mathrm{W}}, \hat{\rho}_{\mathrm{W}}\right\} - \left\{\hat{\rho}_{\mathrm{W}}, \hat{H}_{\mathrm{W}}\right\}\right).$$

Here $\hat{H}_{\mathrm{W}} = \hat{H}_{\mathrm{W}}(R, r)$ and $\hat{\rho}_{\mathrm{W}} = \hat{\rho}_{\mathrm{W}}(R, r)$ are the partial Wigner transforms of the full Hamiltonian and the density matrix, respectively. This formalism provided a framework to simulate nonadiabatic dynamics [97] and allowed the investigation of the statistical mechanics of mixed-quantum/classical systems [98]. Besides, an expression for the rate constant, based on the reactive flux formalism, was derived by invoking the linear response approximation [99]. This development afforded algorithms which can be used to calculate Q/C-rate constants in terms of an ensemble of surface-hopping trajectories [100].

These algorithms were employed to calculate the rate constant for proton transfer in a model system designed by Azzouz and Borgis [81]. The first two adiabatic states of the proton were included in the propagation, because the energy gap between the first and the second excited states was found to be large. The reaction coordinate was defined as the energy difference ΔE, already used in the adiabatic computations of Laría et al. In order to calculate $k(T)$, the time evolution of the product species operator,

$$\hat{N}_{\mathrm{B}}(R, P, t) = \Theta(\Delta E\# - \Delta E(R))$$

was determined from its Q/C Liouville equation by simulating an ensemble of surface-hopping trajectories. These trajectories differ in character from those used in the standard surface-hopping methods (such as MDQT). In this case, each single stochastic trajectory evolves by classical segments, in which the potential is calculated as the mean of two adiabatic surfaces. These segments are interspersed with quantum transitions that change one of the quantum states of the pair and induce momentum changes in the bath. If the two states of the pair are the same, the classical evolution takes place on a single adiabatic surface. On the other hand, if the classical evolution occurs on the mean surface between two states, a phase factor is introduced to account for coherent coupling between the two surfaces.

It was found that the rate constant for proton transfer, calculated with the mixed-Q/C Liouville equation, agreed rather well with the MDQT ones reported by Hammes–Schiffer and coworkers. The value of the kinetic isotope effect (KIE) was also close to the MDQT one. It is interesting to note, however, that many other approximate methods have been implemented on the model of Azzouz and Borgis with disparate results. The rate constants obtained with different methodologies vary by two orders of magnitude, while the KIE ranges from 3.9 to 47. As discussed in Ref. [101], it is difficult to identify the source of these discrepancies because the approaches applied have rather disparate theoretical origins. Having these differences in mind, it is worth noting that the results obtained with algorithms based on mixed-Q/C trajectories agree with each other. Unfortunately, exact computations for this model system have not been reported yet, so the accuracy of the individual approaches cannot be evaluated.

Numerically exact results have been obtained for a model in which the proton transfer is represented as a symmetric double-well coupled to a bath of harmonic oscillators. This model has been extensively used to evaluate approximate methods intended to treat reactions in condensed phase. Among them, the MDQT approach was used to calculate the transmission coefficients giving good agreement with the exact results for high values of the friction parameter (but not for low values). Wang et al. [39] also applied a mixed-Q/C approach to evaluate the transmission coefficients, but they used a mean field approximation to compute the flux–flux correlation function. It was found that, at 300 K, the Q/C-transmission coefficients differed from the exact ones by a factor between 0.6 and 1.8 approximately. The comparison deteriorated at lower temperatures.

At any rate, discrepancies between the results computed with different approximate methods, or between approximate and numerically exact results, clearly indicate that there is a great deal to be learned about the simulation of proton/hydride transfer in condensed phase. Certainly, in this regard, approaches based on mixed-Q/C trajectories, such as MDQT or the mixed-Q/C Liouville methods, will pave the road to get the required knowledge.

5. VIBRATIONAL ENERGY RELAXATION

The correct simulation of the vibrational energy relaxation of small solutes, in van der Waals clusters and condensed phases, requires the consideration of quantum effects such as the existence of discrete energy levels in the solute, as well as their zero point energies [7,102–105]. These features become especially important when the spacing between levels is significantly larger than k_BT. As with other cases already discussed in this chapter, a full quantum description is usually prohibitive due to the large number of particles involved. Fortunately, a particular characteristic of vibrational energy relaxation processes is that the degrees of freedom that require a quantum description are suitably localized on the solute molecule. Therefore, the definition of the quantum and classical subsystem presents no ambiguities and the use of Q/C trajectories turns out to be a highly intuitive tool for their study. By simultaneously analyzing the quantum state of the solute, and the trajectory of the solvent, a deep understanding on the molecular mechanism of the relaxation can be obtained. In this way, for example, solvent motions that couple to the quantum states of the solute can be identified.

Both surface-hopping and mean field methods have been applied to the study of vibrational relaxation and intramolecular vibrational-energy redistribution in van der Waals clusters and condensed phases with dissimilar results. In general, it has been found that the accuracy of the two approaches strongly depends on the system being considered [2,106,107]. Therefore, whenever possible, it is advisable to check both methods against accurate quantum results using simplified models that retain the basic characteristics of the system of interest [108]. Comparisons against experiments are also extremely valuable. In this regard, the contribution of recent developments on ultrafast infrared and Raman spectroscopies must be remarked, as these techniques have produced a large amount of experimental information on the vibrational dynamics of solutes in clusters and condensed phases.

5.1. van der Waals clusters

The MDQT method was adapted to study vibrational energy relaxation processes receiving the name of vibrational MDQT. In particular, the method has been used to analyze vibrational predissociation, intramolecular vibrational energy redistribution, and fragmentation dynamics of van der Waals clusters consisting of a dihalogen molecule and a varying number of rare gas atoms [109–113]. Lifetimes and final state distributions, as well as their dependence on the size of the cluster, were calculated and analyzed in terms of kinetic schemes. The vibration of the diatomics was treated by quantum mechanics, while a classical treatment was given to the other variables. The quantum degree of freedom was represented in the diabatic basis set corresponding to the isolated diatomic molecule. The functions of this set describe the state of the molecule once all the rare gas atoms have been ejected, a feature that is useful at the time of analyzing new kinetic mechanisms for vibrational predissociation. Furthermore, the diabatic or potential couplings decrease as the rare gas atoms sequentially leave the cluster. This is not the case for the adiabatic or kinetic couplings which are influenced by the velocities of the ejected atoms.

The success of the vibrational MDQT method applied to the predissociation of van der Waals clusters was remarkable, as it predicted final vibrational state distributions in close agreement with the experimental results. In particular, the highly specific and nonstatistical character of these distributions, as well as the strong contribution of dissociation channels that involve large amounts of vibrational energy transfer, were accurately reproduced. The improvements achieved by giving a quantum treatment to the vibrational motion of the dihalogen molecule are readily noted by analyzing the results of intramolecular vibrational-energy redistribution and fragmentation dynamics of $I_2(B,\nu=21,22)\cdots Ne_n$ clusters. For the smallest cluster, $I_2 \ldots Ne$, the product state distribution shows a very strong propensity to the ejection of the Ne atom accompanied by the loss of one quantum of the I_2 vibration. For the following cluster in the series, $I_2 \ldots Ne_2$, the transference of two quanta would be enough to eject the two Ne atoms. However, it is observed that the dissociation channel that corresponds to the loss of three quanta accounts for more than 40% of the final state distribution. For higher clusters, the channels in which the I_2 loses more quanta than what would be necessary become predominant [109,111]. It has been found that a classical treatment of the I_2 vibration cannot account for these facts. On the contrary, in classical simulations the Ne atoms are ejected by taking the minimum fraction of the I_2 vibrational quantum required to conserve the total energy of the system. As a consequence, the main channel predicted by classical trajectories corresponds to $\Delta\nu = E_{\mathrm{diss}}/\hbar\omega_{I_2}$ in strong disagreement with the experimental results.

Another example is given by the dissociation of the $Br_2(\nu)\cdots$ Ne complex [112]. In this case, vibrational MDQT results were compared against accurate quantum calculations and experimental measurements. Very good agreement was found for the decay lifetimes and for the final rovibrational-state distributions. The only important differences occurred for the $\Delta\nu = -2$ channel of $\nu = 27$. In this case, a significant intramolecular vibrational-energy redistribution takes place after the transfer of the first quantum of Br_2 vibration. In the quantum mechanical computations a highly structured rotational distribution was observed. This was attributed to interferences between the direct dissociation and the dissociation via a long-lived state in the v-1 continuum. This structure was not observed in the vibrational MDQT simulations since the rotation of the Br_2 was treated classically.

5.2. Condensed phase

The mean field method produces rather accurate results when applied to nearly harmonic systems [107,114]. However, one of its limitations when applied to the description of vibrational dynamics in condensed phases is that it does not provide the correct equilibrium Boltzmann quantum state populations [114–125]. In particular, in ergodic systems, the method overestimates the energy of the quantum subsystem [117,119,121]. Tully and coworkers derived an analytical expression for the equilibrium mean energy attained by a two-level quantum system connected to an infinite number of classical particles, using both the mean field and the MDQT methods [121]. Their analysis indicated that, when the energy gap between vibrational states, ΔE, is larger than $k_B T$, the mean field equilibrium quantum populations deviate dramatically from the Boltzman distribution. This failure was attributed to the partial neglect of correlation between the classical and the quantum subsystems. Specifically, in the mean field approach, the motion of the classical subsystem is not determined by the full density matrix of the quantum subsystem but only by an expectation value calculated from this matrix [i.e., the Hellman–Feynman forces of Eq. (16)]. Therefore, the method is not suitable for systems with large couplings and strong dependence of the classical forces on the quantum state.

In order to clarify the shortcomings of the mean field approach, when applied to the simulation of vibrational energy transfer in liquids, Günter Käb analyzed its performance under different initial conditions of the quantum subsystem, which were varied from coherent to delocalized wavepackets [119]. The coherent states are well localized. Therefore, they are classical-like quantum states that properly relax toward thermal equilibrium. On the contrary, delocalized wavepackets, such as the eigenfunctions of the harmonic oscillator, experience an unphysical heating. The author suggested that further improvements in the method could be achieved by increasing the correlation between the classical and the quantum parts.

The surface-hopping method addresses this problem by using state-specific forces on the classical degrees of freedom. Therefore, even though in general the approach does not exactly reproduce the equilibrium Boltzman distributions, the deviations observed are not large [126]. Actually, the method gives the correct equilibrium Boltzman populations in the limit of small adiabatic splitting and in the limit of large nonadiabatic couplings. These conditions are fulfilled by electronically nonadiabatic processes, which typically present a well-localized region of strong nonadiabatic coupling. However, in the analysis of vibrational energy relaxation of small molecules in condensed phase, the couplings are not localized in a small region of the classical phase space and their strength oscillates in time throughout the course of the simulation [124,127,128]. These conditions are not the most convenient ones for the application of the MDQT approach [5,107,114,129]. The accuracy of surface-hopping methods applied to problems involving long interaction times or with repeated entrances into the interaction region was tested using a model consisting of harmonic oscillators for both, the quantum and the classical subsystems, with a bilinear coupling between them [107]. The results showed damped oscillations in the populations which were attributed to the independent trajectory approximation. After a significant time, a loss of the correct phase coherence was observed.

At this point, it is interesting to analyze the way in which quantum decoherence is treated by the different mixed-Q/C methods. The times for quantum decoherence are in the order of a few femtoseconds for condensed phase chemical systems, and they play a direct role in determining nonadiabatic transition rates [130]. In the MDQT method [13,131], the phases of the quantum coefficients are retained at all time steps, so that the dynamics of the individual trajectories is completely coherent. Decoherence can be taken into account by running a swarm of trajectories with the same initial condition. These trajectories differ on the sequences of random number used to decide transitions between the adiabatic states. Therefore, quantum hops occur at different times and the trajectories differentiate from one another. The interference between all of them, when summed up together, provides the quantum decoherence for the mixed-Q/C trajectory associated with the initial state considered. Finally, the results of different initial states must be added in order to obtain the ensemble averages. Thus, the procedure requires a double summation which produces an important increase in the computational costs of the algorithm.

The stationary phase surface-hopping (SPSH) method, originally proposed by Webster et al. [132–135], represents an alternative to the calculation of the swarm of trajectories needed by the MDQT approach. The SPSH method combines surface hoppings with the stationary phase semiclassical force devised by Pechukas [136]. The classical dynamics is propagated under the influence of a mixed-quantum state, avoiding the restriction of MDQT that propagates it adiabatically. This represents a more accurate choice in the regions of strong nonadiabatic couplings. Furthermore, complete quantum coherence is provided by the selection of a single adiabatic eigenstate at the end of each step. The SPSH transition probabilities computed over a given time step are equivalent to those produced by the swarm of trajectories with the MDQT approach. However, an iterative procedure is required to calculate the nonlocal-in-time quantum forces. This can represent a too high computational cost and convergence problems may arise. If nonadiabatic transitions are not highly localized, as in the case of vibrational relaxation in condensed phase, SPSH becomes equivalent to MDQT [137].

A more drastic procedure consists of systematically removing the coherence of the quantum amplitudes during the MDQT trajectories. This procedure, which has been applied using different recipes [15,130,138], contributes to eliminate the internal inconsistency between the quantum and the classical populations observed in many systems [15,114]. Nevertheless, changing the decoherence time can lead to dramatic differences in nonadiabatic rate constants and the overall population dynamics of the system [130,139]. Therefore, extensions to MDQT that provide a smooth decay of quantum coherence have been proposed [139]. Other methods, like the "mean field molecular dynamics with surface hopping" [140] and the "mean field approximation to the stochastic Schrödinger equation" [137], were also developed to improve the treatment of decoherence in the quantum subsystem.

Another promising tool in the treatment of decoherence is given by the hybrid-Q/C propagation scheme based on Bohmian quantum trajectories [141,142]. The method was successfully applied to the description of the vibrational revivals of I_2 in rare gas environments and its damping by decoherence induced by atomic collisions. In this case, a grid representation is used for the quantum degrees of freedom. In spite of this, the method does not present problems derived from the delocalization produced by the anharmonicities of the potential energy surface. Therefore, it can be applied in studies of the coherence properties of the wave packets for long times.

The performance of MDQT to simulate the vibrational relaxation of an I_2 molecule in xenon fluid was tested by comparisons against the conventional perturbation theory approach and nonequilibrium classical MD [143]. Differences in the relaxation time T_1 and in the state-to-state vibrational-transition rate constants $k_{0\leftarrow1}$, calculated by the three methods, were between 10 and 50%. The relaxation times were found to be 10 times shorter than the experimental values. Later on, this discrepancy was solved by changing the potential used in the classical simulations [144]. However, the validity of the classical approach to describe the vibrational motion of the solute should be questioned, since the molecule is allowed to transfer amounts of energy which are smaller than its vibrational quantum. The solvent, whose translational frequencies are $<120\,\mathrm{cm}^{-1}$, can accommodate these smaller amounts of energy more easily than the $\approx 200\,\mathrm{cm}^{-1}$ associated with the I_2 vibration. Therefore, the relaxation becomes artificially more efficient.

A different algorithm for surface-hopping calculations, proposed by Bastida et al. [145] was also used to analyze the vibrational relaxation of I_2 in liquid Xenon [138]. These simulations showed a slower I_2 vibrational energy decay than the classical MD simulations, in agreement with experimental measurements performed at different solvent densities and temperatures. The algorithm, called the collective probabilities algorithm, assures the identity between the quantum populations of the vibrational states and the fraction of trajectories occupying those states (the so-called classical populations).

The lack of coincidence between the classical and the quantum populations in the MDQT method has been recognized by different authors [15,114,146–148]. Two features of the MDQT algorithm can explain these differences. First, in order to conserve the energy, classically forbidden transitions are not allowed. Modifications on the MDQT procedure have been proposed in order to overcome this problem [15,16,147]. Nevertheless, in the vibrational relaxation of I_2 in liquid xenon, classically forbidden transitions are expected to be infrequent because the energy transferred to the solvent is quickly dissipated through atomic collisions in the solvent. The second feature is the assumption that the quantum populations for different trajectories are the same [13]. The collective probabilites algorithm overcomes this problem by assuming the dependence of the transition probabilities on the average populations corresponding to the whole set of trajectories.

Beyond the quantitative differences, all the surface-hopping algorithms agree in the qualitative description of the mechanism observed for the vibrational relaxation of I_2 in liquid xenon [138,143]. The collisions of the I_2 molecule with a single or two xenon atoms, mainly aligned with the I—I bond, are responsible for the highest changes in the quantum populations. According to this, Liu and Guo [149] proposed a more realistic Q/C model that included the symmetric vibration of the two nearest rare gas atoms in the quantum subsystem. The model was tested on the ultrafast photodissociation/recombination dynamics of $I_2(A)$ in rare gas matrices, a process that involves two adiabatic electronic surfaces corresponding to the X and A states of the I_2 molecule. A coupled wave packet was propagated using a 2D spatial grid representation and the mean field approximation. It was noted that the validity of the approach deteriorated with time. Therefore, the long-time dynamics required for the study of vibrational relaxation was unreliable. In spite of this limitation, the comparison with the model that only considers the I–I distance as the quantum coordinate revealed a feature that should be taken into account in future implementations of Q/C-trajectories. While both models showed coherent wave packet motion after the energy transfer, the model with a 2D quantum subsystem showed a much faster dephasing. Accordingly, the study suggested that the mean field treatment of the quantum coherence could be systematically improved by including in the quantum subsystem bath modes that are strongly coupled to the solute vibrational motion. In this regard, we note that a model with a classical bath coupled to a multidimensional quantum subsystem, has been proposed to simulate photodynamical process of triatomic molecules in condensed phase [150]

The quantum treatment of the solvent vibrational modes was introduced in the simulation of the relaxation of the cyanide ion in water [151]. The propagation was performed using the "mean-field method with quantum transitions." The state of the quantum subsystem was expanded in a diabatic basis set, whose terms were products of a vibrational wave function for the isolated CN^- molecule and harmonic wave functions for the normal modes of the water molecules. The frequency of the bending mode of the water molecule ($\omega_b = 1643\,\mathrm{cm}^{-1}$) is lower than the CN^- vibrational frequency ($\omega_{CN^-} = 2080\,\mathrm{cm}^{-1}$), but significantly higher than the thermal energy ($k_bT \approx 210\,\mathrm{cm}^{-1}$ at room temperature). Accordingly, the bending of water can be excited by energy transfer from the cyanide ion and the quantum treatment of this mode can lead to different relaxation pathways than those observed with a classical treatment. In fact, it was found that the pathway that involved the participation of the bending mode of water molecules was the fastest and most important one, accounting for more than 80% of the relaxation process.

In another study of the vibrational relaxation of the cyanide ion in liquid water [152], deviations of the mean field method from the Boltzman quantum distributions were observed. This was attributed to the time evolution of the nonadiabatic couplings which causes strong oscillations on the populations for each trajectory. These shortcomings can be partially solved by considering a unique quantum subsystem interacting with a bundle of trajectories at the same time. In the mixed-Q/C algorithms discussed so far, the state of the quantum subsystem is propagated along with a single trajectory for the classical system [125]. An alternative procedure consists on propagating the state of the quantum subsystem interacting with an ensemble of classical trajectories. When using this alternative, the effective Hamiltonian for the quantum part becomes [9,153]:

$$\hat{H}_r^{\mathrm{eff}} = -\frac{\hbar^2}{2m}\frac{\partial^2}{\partial r^2} + V_r(r) + \overline{V}_{\mathrm{int}}\left(r, \{R^{(i)}\}_{i=1}^{N}\right)$$

with

$$\overline{V}_{\mathrm{int}}\left(r,\{R^{(i)}\}_{i=1}^{N}\right)=\frac{1}{N}\sum_{i=1}^{N}V\left(r,R^{(i)}(t)\right).$$

Simulations of CN^- in liquid water [152] proved that this procedure greatly decreases the magnitude of the oscillations of the nonadiabatic couplings. Consequently, an improvement is observed in the equilibrium quantum populations. Nevertheless, at high temperatures, the "bundle of trajectories" approach does not strictly reproduce the Boltzman distribution.

A modification of the mean field method that definitely guarantees the achievement of the Boltzmann quantum state population was proposed by Bastida et al. [115]. Based on strategies previously developed in the perturbative hybrid-Q/C method, quantum corrections were introduced into the matrix elements that couple the quantum states of the solute. The final quantum corrected nonadiabatic coupling matrix elements, d_{jk}^{qc}, are calculated as

$$d_{jk}^{\mathrm{qc}}=\left(\frac{2}{1+e^{-\hbar\omega_{jk}/k_BT}}\right)^{1/2}d_{jk}.$$

This approach, named "Ehrenfest method with quantum corrections", not only allows the achievement of the equilibrium Boltzmann quantum state populations in the long time limit, but also makes the magnitudes of the d_{jk}^{qc} couplings to decrease in time, particularly when it is used in combination with the "bundle of trajectories" approach.

A final aspect to discuss about the implementation of Q/C trajectories to deal with vibrational relaxation processes in condensed phase is the choice of the quantum representation. Typically, the differences between the diabatic and the adiabatic vibrational states of a molecule in solution are small. Therefore, the two representations usually lead to very similar equilibrium populations at room temperatures. These similarities have been observed in systems as different as I_2 in liquid xenon and CN^- in water [115,124,152]. Moreover, in the latter case, it was found that the potential energy that governs the movement of the solvent had little dependence on the vibrational quantum state of the solute [124]. Thus, the difference,

$$|\langle\psi_1|V_{\mathrm{int}}|\psi_1\rangle-\langle\psi_0|V_{\mathrm{int}}|\psi_0\rangle|$$

is more than one order of magnitude smaller than the thermal energy. Furthermore, the classical degrees of freedom lose their structural memory before the changes on the quantum state of the solute can significantly affect their trajectories. Therefore, the choice of the diabatic or the adiabatic representations does not significantly alter the timescale of the relaxation.

Summarizing, a significant experience has been gained during the last years on the application of mixed-Q/C trajectories to the analysis of vibrational relaxation processes. The vibrational MDQT method, in which the quantum degrees of freedom are represented in the diabatic spectral basis set, has shown to be very convenient and accurate in studies of vibrational predissociation processes in van der Waals clusters. On the other hand, some shortcomings were detected in the application of both mean field and MDQT methods to the study of vibrational relaxation in condensed phase. A variety of modifications on the two techniques are now available to overcome these shortcomings.

6. CONCLUDING REMARKS

During the last two decades enormous progresses have been made in the implementation of techniques based on mixed-Q/C trajectories. Studies with small or relatively simple models were used to evaluate the accuracy of the approach, establishing the conditions in which mixed-Q/C trajectories produce reliable results. Also, these evaluations served to stimulate new developments aimed to overcome the drawbacks detected in the early applications. Now, a variety of techniques are available. They have already proven to be useful to include nuclear quantum effects in simulations of chemical reactions and energy relaxation processes occurring in large systems.

Mixed-Q/C trajectories provide a detailed description of processes at a molecular level. Besides, the computational cost of the approach is usually not an impediment to its implementation. Therefore, it is to be expected that mixed-Q/C trajectories will be increasingly used to analyze processes relevant in Chemistry and Biology, which take place within large and complex molecular environments.

ACKNOWLEDGMENTS

This work was supported by the Universidad Nacional de Quilmes and the CONICET. G.P.S. especially thanks CONICET for his doctoral fellowship.

REFERENCES

[1] B.J. Berne, D. Thirumalai, Annu. Rev. Phys. Chem. 37 (1986) 401.
[2] N. Makri, Annu. Rev. Phys. Chem. 50 (1999) 167.
[3] W.H. Miller, Proc. Natl. Acad. Sco. USA 102 (2005) 6660.
[4] M. Thoss, H. Wang, Annu. Rev. Phys. Chem. 55 (2004) 299.

[5] J.C. Tully, Faraday Discuss. 110 (1998) 407.
[6] L.E. Ballentine, Y. Yang, J.P. Zibin, Phys. Rev. A 50 (1994) 2854.
[7] D.F. Coker, in: B.J. Berne, G. Ciccotti, D.F. Coker (Eds.), Classical and Quantum Dynamics in Condensed Phase Simulations, World Scientific, Singapore, 1998, p. 539.
[8] F.A. Bornemann, P. Nettesheim, C. Schútte, J. Chem. Phys. 105 (1996) 1074.
[9] R.B. Gerber, V. Buch, M.A. Ratner, J. Chem. Phys. 77 (1982) 3022.
[10] P. Nettesheim, F.A. Bornemann, B. Schmidt, C. Schútte, Chem. Phys. Letters 256 (1996) 581.
[11] P. Grochowski, B. Lesyng, J. Chem. Phys. 119 (2003) 11541.
[12] H. Jiang, X.S. Zhao, J. Chem. Phys. 113 (2000) 930.
[13] J.C. Tully, J. Chem. Phys. 93 (1990) 1061.
[14] S. Hammes-Schiffer, J.C. Tully, J. Chem. Phys. 101 (1994) 4657.
[15] J.-Y. Fang, S. Hammes-Schiffer, J. Phys. Chem. A 103 (1999) 9399.
[16] J.-Y. Fang, S. Hammes-Schiffer, J. Chem. Phys. 110 (1999) 11166.
[17] J. Mavri, H.J.C. Berendsen, J. Phys. Chem. 99 (1995) 12711.
[18] D. Neuhauser, R.S. Judson, Chem. Phys. Lett. 179 (1991) 385.
[19] L. Wang, A.B. McCoy, Phys. Chem. Chem. Phys. 1 (1999) 1227.
[20] L. Wang, W.J. Meurer, A.B. McCoy, J. Chem. Phys. 113 (2000) 10605.
[21] L. Wang, D.C. Clary, Chem. Phys. Lett. 262 (1996) 284.
[22] L. Wang, J. Chem. Phys. 108 (1998) 7538.
[23] L. Wang, Phys. Chem. Chem. Phys. 2 (2000) 2883.
[24] L. Wang, A.B. McCoy, J. Chem. Phys. 119 (2003) 1996.
[25] Y. Hurwitz, P.S. Stern, R. Naaman, A.B. McCoy, J. Chem. Phys. 106 (1997) 2627.
[26] N. Markovic, G.D. Billing, Chem. Phys. Lett. 195 (1992) 53.
[27] N. Markovic, G.D. Billing, Chem. Phys. 173 (1993) 385.
[28] N. Markovc, G.D. Billing, Chem. Phys. 224 (1997) 53.
[29] G.D. Billing, N. Markovic, Chem. Phys. 209 (1996) 377.
[30] N. Markovic, G.D. Billing, Chem. Phys. Lett. 248 (1996) 420.
[31] B.R. Johnson, J. Chem. Phys. 79 (1983) 1906.
[32] N. Balakrishnan, G.D. Billing, Chem. Phys. 189 (1994) 499.
[33] N. Balakrishnan, G.D. Billing, J. Chem. Phys. 101 (1994) 2785.
[34] J.Z.H. Zhang, J. Chem. Phys. 111 (1999) 3929.
[35] M. Wang, J. Zhang, J. Theor. Comp. Chem. 2 (2003) 3516.
[36] Q. Cui, X. He, M.-L. Wang, J.Z.H. Zhang, J. Chem. Phys. 119 (2003) 9455.
[37] W. Hu, G.C. Schatz, J. Chem. Phys. 125 (2006) 132301.
[38] Y. Xiang, J.Z.H. Zhang, J. Chem. Phys. 118 (2003) 8954.
[39] H.B. Wang, X. Sun, W.H. Miller, J. Chem. Phys. 108 (1998) 9726.
[40] J. Palma, J. Chem. Phys. 130 (2009) 124119.
[41] C.H. Bamford, Proton Transfer, Elsevier Scientific Publisher, Amsterdam and New York, 1978.
[42] R.P. Bell, The Tunnel Effect in Chemistry, Chapman & Hall, New York, 1980.
[43] T. Bountis, Proton Transfer in Hydrogen-Bonded Systems, Vol. 291, Plenum Press, New York, 1992.
[44] V. Gold, E. Caldin, Proton transfer Reactions, Chapman & Hall, London, New York, 1975.
[45] A. Warshel, Computer Modeling of Chemical Reactions in Enzymes and Solutions, Wiley, New York, 1991.
[46] A. Warshel, M. Levitt, J. Mol. Biol. 103 (1976) 227.
[47] C. Alhambra, J. Gao, J.C. Corchado, J. Villa, D.G. Truhlar, J. Am. Chem. Soc. 121 (1999) 2253.
[48] B.J. Bahnson, J.P. Klinman, Methods Enzymol. 249 (1995) 373.
[49] W.E. Karsten, C.-C. Hwang, P.F. Cook, Biochemistry 38 (1999) 4398.
[50] J.P. Klinman, Trends Bioch. Scie. 14 (1989) 368.

[51] J. Rucker, Y. Cha, T. Jonsson, K.L. Grant, J.P. Klinman, Biochemistry 31 (1992) 11489.
[52] J. Rucker, J.P. Klinman, J. Am. Chem. Soc. 121 (1999) 1997.
[53] A. Kohen, J.P. Klinman, Acc. Chem. Res. 31 (1998) 397.
[54] M.J. Sutcliffe, N.S. Scrutton, Philos. Trans. R Soc. Lond. A358 (2000) 367.
[55] P. Ball, Nature 431 (2004) 396.
[56] A. Warshel, J. Phys. Chem. 86 (1982) 2218.
[57] R.P. Bell, The Proton in Chemistry, Cornell University, Ithaca, 1973.
[58] D.G. Truhlar, J. Gao, M. García-Viloca, C. Alhambra, J. Corchado, M.L. Sánchez, et al., Int. J. Quantum Chem. 100 (2004) 1136.
[59] P. Bala, P. Grochowski, B. Lesyng, J.A. McCammon, J. Phys. Chem. 100 (1996) 2535.
[60] P. Bala, P. Grochowski, K. Nowidski, B. Lesyng, J.A. McCammon, Biophys. J. 79 (2000) 1253.
[61] P. Grochowski, B. Lesyng, P. Bala, J.A. McCammon, Int. J. Quantum Chem. 60 (1996) 1143.
[62] W.J. Bruno, W. Bialek, Biophys. J. 63 (1992) 689.
[63] M.E. Tuckerman, D. Marx, M.L. Klein, M. Parrinello, Science 275 (1997) 817.
[64] A. Warshel, R.M. Weiss, J. Am. Chem. Soc. 102 (1980) 6218.
[65] J. Mavri, H.J.C. Berendsen, W.F. van Gunsteren, J. Phys. Chem. 97 (1993) 13469.
[66] H.J.C. Berendsen, J. Mavri, J. Phys. Chem. 97 (1993) 13464.
[67] J. Mavri, H.J.C. Berendsen, Phys. Rev. E 50 (1994) 198.
[68] J. Mavri, H. Liu, M.H.M. Olsson, A. Warshel, J. Phys. Chem. B 112 (2008) 5950.
[69] M.H.M. Olsson, P.E.M. Siegbahn, A. Warshel, J. Am. Chem. Soc. 126 (2004) 2820.
[70] G. Pierdominici-Sottile, J. Palma, Chem. Phys. 363 (2009) 59.
[71] D. Borgis, G. Tarjus, H. Azzouz, J. Chem. Phys. 97 (1992) 1390.
[72] D. Borgis, G. Tarjus, H. Azzouz, J. Phys. Chem. 96 (1992) 3188.
[73] D. Laria, G. Ciccotti, M. Ferrario, R. Kapral, J. Chem. Phys. 97 (1992) 378.
[74] G. Zundel, J. Mol. Struct. 177 (1988) 43.
[75] T. Yamamoto, J. Chem. Phys. 33 (1960) 281.
[76] D. Chandler, J. Chem. Phys. 68 (1978) 2959.
[77] W.H. Miller, S.D. Schwartz, J.W. Tromp, J. Chem. Phys. 79 (1983) 4889.
[78] G.A. Voth, D. Chandler, W.H. Miller, J. Chem. Phys. 91 (1989) 7749.
[79] G.A. Voth, D. Chandler, W.H. Miller, J. Phys. Chem. 93 (1989) 7009.
[80] W.H. Thompson, J. Phys. Chem. B 109 (2005) 18201.
[81] H. Azzouz, D. Borgis, J. Chem. Phys. 98 (1993) 7361.
[82] S. Hammes-Schiffer, J.C. Tully, J. Phys. Chem. 99 (1995) 5793.
[83] D.C. Borgis, S. Lee, J.T. Hynes, Chem. Phys. Lett. 162 (1989) 19.
[84] S.R. Billeter, S.P. Webb, P.K. Agarwal, T. Iordanov, S. Hammes-Schiffer, J. Am. Chem. Soc. 123 (2001) 11262.
[85] P.K. Agarwal, S.R. Billeter, S. Hammes-Schiffer, J. Phys. Chem. B 106 (2002) 3283.
[86] S. Hammes-Schiffer, J.C. Tully, J. Chem. Phys. 103 (1995) 8528.
[87] J. Florian, V. Hrouda, P. Hobza, J. Am. Chem. Soc. 116 (1994) 1457.
[88] V.C. Sekhar, B.V. Plapp, Biochemistry 27 (1988) 5082.
[89] X. Ren, C. Tu, P.J. Laipis, D.N. Silverman, Biochemistry 34 (1995) 8492.
[90] S. Hammes-Schiffer, J. Chem. Phys. 105 (1996) 2236.
[91] K. Drukker, S. Hammes-Schiffer, J. Chem. Phys. 107 (1997) 363.
[92] K. Drukker, S.W. de Leeuw, S. Hammes-Schiffer, J. Chem. Phys. 108 (1998) 6799.
[93] J.-Y. Fang, S. Hammes-Schiffer, J. Chem. Phys. 106 (1997) 8442.
[94] J.-Y. Fang, S. Hammes-Schiffer, J. Chem. Phys. 107 (1997) 5727.
[95] R. Kapral, G. Ciccotti, J. Chem. Phys. 110 (1999) 8919.
[96] R. Kapral, Annu. Rev. Phys. Chem. 57 (2006) 129.
[97] S. Nielsen, R. Kapral, G. Ciccotti, J. Chem. Phys. 112 (2000) 6543.
[98] S. Nielsen, R. Kapral, G. Ciccotti, J. Chem. Phys. 115 (2001) 5805.
[99] A. Sergi, R. Kapral, J. Chem. Phys. 118 (2003) 8566.

[100] G. Hanna, R. Kapral, J. Chem. Phys. 122 (2005) 244505.
[101] G. Hanna, R. Kapral, J. Chem. Phys. 128 (2008) 164520.
[102] R. Alimi, R.B. Gerber, A.D. Hammerich, R. Kosloff, M.A. Ratner, J. Chem. Phys. 93 (1990) 6484.
[103] P.J. Rossky, in: B.J. Berne, G. Ciccotti, D.F. Coker (Eds.), Classical and Quantum Dynamics in Condensed Phase Simulations, World Scientific, Singapore, 1998, p. 515.
[104] J.C. Tully, in: B.J. Berne, G. Ciccotti, D.F. Coker (Eds.), Classical and Quantum Dynamics in Condensed Phase Simulations, World Scientific, Singapore, 1998, p. 489.
[105] Susumu Okazaki, in: I. Prigogine, S.A. Rice (Eds.), Advances in Chemical Physics, Vol. 118, John Wiley & sons inc, New York, 2007, p.191.
[106] M.D. Hack, D.G. Truhlar, J. Phys. Chem. A 104 (2000) 7917.
[107] D. Kohen, F.H. Stillinger, J.C. Tully, J. Chem. Phys. 109 (1998) 4713.
[108] J.S. Bader, B.J. Berne, J. Chem. Phys. 100 (1994) 8359.
[109] S.F. Alberti, N. Halberstadt, J.A. Beswick, A. Bastida, J. Zúñiga, A. Requena, J. Chem. Phys. 111 (1999) 239.
[110] A. Bastida, B. Miguel, J. Zúñiga, A. Requena, N. Halberstadt, K.C. Janda, J. Chem. Phys. 111 (1999) 4577.
[111] A. Bastida, J. Zúñiga, A. Requena, N. Halberstadt, J.A. Beswick, J. Chem. Phys. 109 (1998) 6320.
[112] B. Miguel, A. Bastida, J. Zúñiga, A. Requena, N. Halberstadt, J. Chem. Phys. 113 (2000) 10130.
[113] A. Bastida, B. Miguel, J. Zúñiga, A. Requena, Halberstadt, Faraday Discuss. 118 (2001) 257.
[114] U. Muller, G. Stock, J. Chem. Phys. 107 (1997) 6230.
[115] A. Bastida, C. Cruz, J. Zúñiga, A. Requena, B. Miguel, Chem. Phys. Lett. 417 (2006) 53.
[116] R.C.F. Mauri, E. Tosatti, Europhys. Lett. 24 (1993) 431.
[117] G. Käb, J. Phys. Chem. A 108 (2004) 8866.
[118] G. Käb, J. Phys. Chem. A 110 (2006) 3197.
[119] G. Käb, Phys. Review E 66 (2002) 046117.
[120] A.A. Neufeld, D. Schwarzer, J. Schroeder, J. Troe, J. Chem. Phys. 119 (2003) 2502.
[121] P.V. Parandekar, J.C. Tully, J. Chem. Phys. 122 (2005) 094102.
[122] P.V. Parandekar, J.C. Tully, J. Chem. Theory and Comput. 2 (2006) 229.
[123] M. Sato, S. Okazaki, J. Chem. Phys. 123 (2005) 124508.
[124] T. Terashima, M. Shiga, S. Okazaki, J. Chem. Phys. 114 (2001) 5663.
[125] J.C. Tully, in: D.L. Thompson, (Ed.), Modern Methods for Multidimensional Dynamics Computations in Chemistry, World Scientific, Singapore, 1998, p. 34.
[126] J.R. Schmidt, P.V. Parandekar, J.C. Tully, J. Chem. Phys. 129 (2008) 044104.
[127] M. Sato, S. Okazaki, J. Mol. Liq. 119 (2005) 15.
[128] W.H. Thompson, J. Chem. Phys. 118 (2003) 1059.
[129] E. Neria, A. Nitzan, J. Chem. Phys. 99 (1993) 1109.
[130] B.J. Schwartz, E.R. Bittner, O.V. Prezhdo, P.J. Rossky, J. Chem. Phys. 104 (1996) 5942.
[131] D.F. Coker, L. Xiao, J. Chem. Phys. 102 (1995) 496.
[132] T.H. Murphrey, P.J. Rossky, J. Chem. Phys. 103 (1995) 6665.
[133] F. Webster, P.J. Rossky, R.A. Friesner, Comput. Phys. Commun. 63 (1991) 494.
[134] F. Webster, E.T. Wang, P.J. Rossky, R.A. Friesner, J. Chem. Phys. 100 (1994) 4835.
[135] F.J. Webster, J. Schnitker, M.S. Friedrichs, R.A. Friesner, P.J. Rossky, Phys. Rev. Lett. 66 (1991) 3172.
[136] P. Pechukas, Phys. Rev. 181 (1969) 174.
[137] O.V. Prezhdo, P.J. Rossky, J. Chem. Phys. 107 (1997) 825.
[138] A. Bastida, C. Cruz, J. Zúñiga, A. Requena, B. Miguel, J. Chem. Phys. 121 (2004) 10611.
[139] E.R. Bittner, P.J. Rossky, J. Chem. Phys. 103 (1995) 8130.
[140] O.V. Prezhdo, J. Chem. Phys. 111 (1999) 8366.
[141] E. Gindensperger, C. Meier, J.A. Beswick, J. Chem. Phys. 113 (2000) 9369.
[142] C. Meier, J.A. Beswick, J. Chem. Phys. 121 (2004) 4550.

[143] S. Li, W.H. Thompson, J. Phys. Chem. A 107 (2003) 8696.
[144] S. Li, W.H. Thompson, Chem. Phys. Lett. 383 (2004) 326.
[145] A. Bastida, C. Cruz, J. Zúñiga, A. Requena, J. Chem. Phys. 119 (2003) 6489.
[146] M.D. Hack, D.G. Truhlar, J. Chem. Phys. 114 (2001) 9305.
[147] A.W. Jasper, S.N. Stechmann, D.G. Truhlar, J. Chem. Phys. 116 (2002) 5424.
[148] M. Thachuk, M.Y. Ivanov, D.M. Wardlaw, J. Chem. Phys. 109 (1998) 5747.
[149] L. Liu, H. Guo, J. Chem. Phys. 104 (1996) 528.
[150] S.F. Alberti, J. Echave, V. Engel, N. Halberstadt, J.A. Beswick, J. Chem. Phys. 113 (2000) 1027.
[151] A. Bastida, J. Zúñiga, A. Requena, B. Miguel, J. Chem. Phys. 129 (2008) 154501.
[152] A. Bastida, C. Cruz, J. Zúñiga, A. Requena, B. Miguel, J. Chem. Phys. 126 (2007) 014503.
[153] R.B. Gerber, M.A. Ratner, in: I. Prigogine, S.A. Rice (Eds.), Advances in Chemical Physics, Vol. 70, John Wiley & sons inc, New York, 1998, p. 97.

CHAPTER 9

Development of a Quantum Chemical Method Combined with a Theory of Solutions—Free-Energy Calculation for Chemical Reactions by Condensed Phase Simulations

Hideaki Takahashi[a], **Nobuyuki Matubayasi**[b] and **Masayoshi Nakano**[c]

Contents

[a] Division of Chemical Engineering, Department of Materials Engineering Science, Graduate School of Engineering Science, Osaka University, Toyonaka, Osaka 560-8531, Japan
[b] Institute for Chemical Research, Kyoto University, Uji, Kyoto 611-0011, Japan
[c] Department of Materials Engineering Science, Graduate School of Engineering Science, Osaka University, Toyonaka, Osaka 560-8531, Japan
E-mail addresses: takahasi@cheng.es.osaka-u.ac.jp (H. Takahashi), nobuyuki@scl.kyoto-u.ac.jp (N. Matubayasi)

Advances in Quantum Chemistry, Vol. 59
ISSN: 0065-3276, DOI: 10.1016/S0065-3276(10)59009-9

© 2010 Elsevier Inc.
All rights reserved

1. INTRODUCTION

It is one of the major subjects in theoretical and computational chemistry to predict the dominant reaction path for reactants under a given thermodynamic condition. In 1935 by Evans and Polanyi [1] and by Eyring [2], great strides were made for such a problem by formulating the absolute reaction rate for small molecules with the assumption that the activated complex is being in equilibrium with the reactant. The theory, termed as the transition-state theory (TST), is described in terms of the molecular partition functions as well as the energy difference between the transition state and the reactant. The efficiency and the robustness of the theory have, so far, been well established by a number of successful applications. However, it should be reminded that it is only several decades ago that the TST became a practical tool to predict the reaction rate. The book of Fueno [3] states in its Opening Remarks that the researchers in 1960s were still less optimistic about the accurate prediction of the rates even of the simplest reactions besides the usefulness of the concept of the transition state in understanding complex reactions. Such a situation was, of course, due to the lack of capability at that time to locate the TS geometries. Indeed, it is also noted in the above book [3] that one cannot find even single example of explicit geometry of TS in the volume of proceedings entitled “The Transition State” published for a symposium held in 1962 [4].

In the field of quantum chemistry [5], substantial efforts have been devoted to the development of efficient methodologies to construct the electronic structures of molecules in terms of the molecular orbitals (MO). The concept of MO provides us with a useful picture for understanding the complicated many-electron systems on the basis of the approximation that constituent electrons are independent. In the Hartree–Fock (HF) method in the MO theory, the wave function is constructed on the basis of the mean-field approximation and the electron correlations because of the repulsive Coulomb interactions are completely neglected. With more sophisticated approaches such as configuration interaction (CI), it is possible to take into account the electron correlation by involving the electronically excited configurations generated from the HF reference state. Such a procedure allows systematic improvements on the wave functions, however, the computational cost increases drastically as the number of electrons being correlated increases. Hence, the application of the MO theories has been limited to relatively small-sized systems. During the past several decades, a breakthrough was made in the methods of constructing electronic ground states. The density functional theory (DFT) [6], more specifically the Kohn–Sham (KS)-DFT [7,8], enables one to perform accurate calculations with much less computational costs as compared with the MO approaches. It achieved a great success in describing the total energy as well as the electron density of the electronic ground state by projecting the nonlocal exchange and correlation potential onto a local potential as a functional of the electron density. There have been a lot of theoretical developments to refine the exchange-correlation functionals that dominate the quality of the DFT calculations. Mainly because of the success in the MO and DFT approaches, supported by the rapid growth in the computer technologies, the TST is now a powerful tool to predict the absolute reaction rates, which deserve for the direct comparisons with experimental data. Nowadays even experimental chemists find almost no difficulties in determining the TS geometries in the gas phase and their statistical mechanical properties by utilizing (non) commercial program packages equipped with sophisticated algorithms to search TSs.

It is a matter of course that general interests of theoretical chemists move from the gas-phase reactions to the studies of the chemical events occurring in more realistic systems such as solutions or biological molecules. There are, however, two major difficulties in determining the reaction pathway in many-particle systems. The theoretical investigation of the chemical reaction essentially necessitates the use of the quantum chemical approach and it gives rise to a serious problem because of the computational cost, which scales $N^3 \sim N^4$ with respect to the number N of electrons involved in the system even when we rely on the lowest levels of theories [5]. Another obstacle is related to the computation of a statistical mechanical property. For a system of which structure undergoes serious fluctuation under a given temperature, it is essential to consider the free-energy change associated with the chemical event of interest for the discussions on the quantitative basis. Unfortunately, the free-energy calculation with the method of molecular simulation is also known as a heavy task [9,10]. The difficulty arises mainly from the fact that a huge number of configuration samplings are needed for many intermediate points along an arbitrary path connecting the reactant and the product. In the following, we make a review for the methodologies relevant to these problems for the purpose to clarify the position in this field of our work introduced later.

The ab initio molecular dynamics simulation developed by Car and Parrinello (CP) [11] opened a way to the study of chemical reactions involving many atoms or molecules. In the CP approach, it circumvents the explicit diagonalization of the electronic Hamiltonian, which is the most time-consuming part at each time step of molecular dynamics, by propagating the KS wave functions in the same time step with the nuclear motion, for which a fictitious mass is introduced for electrons. Then, the electronic wave function is being loosely bound to the solution given by the Born–Oppenheimer approximation during the CP molecular dynamics. Although the CP method is a robust technique, it necessitates rather small time step in the numerical propagation as compared with the classical molecular dynamics simulation. Hence, its execution for a practical application is still rather difficult at least under ordinary computational environments. The order-*N* approach [12] provides an effective framework for computing electronic states of which computational costs scale linearly with respect to the size of the system. The underlying concept for such a method is the “near-sightedness principle” postulated by Prodan and Kohn [13] and it seems to constitute the common basis of the order-*N* approaches. The principle states that the element in the density matrix in real space decays rapidly as the distance of the two sites increases, which practically ensures the order-*N* scaling in the electronic structure calculations with DFT or tight-binding Hamiltonians. Directly along this line, Yang proposed a method referred to as “divide and conquer” [14], where the whole system is divided into overlapping regions and the norm conservation for the total electron density is imposed by introducing a common chemical potential for the domains. Then, the total energy is obtained as the sum of the eigenvalues of the Hamiltonians of the constituent domains. Substantial efforts have been made to develop efficient and rigorous algorithms of the order-*N* scaling. However, it seems there is no outstanding method that can be generally used in practical applications with satisfying reliability.

An alternative route to reduce the computational cost is to take a hybrid approach. It is often the case that only the small part of the whole system participates in the chemical event and the rest of the system serves as a static environment. The quantum mechanical/molecular mechanical (QM/MM) approach provides us with a promising framework to handle such a system by dividing the whole system into two subsystems [15,16]. The chemically active site is described by the method of quantum chemistry, while the electronically static region is represented by a classical force field. The notable advantage of the method is that the effect of the electrostatic field constructed by the fractional charges in the MM subsystem on the reaction is efficiently taken into consideration by putting the electrostatic field in the Hamiltonian of the QM subsystem. So far the QM/MM method has been widely applied to various systems and its efficiency has been well established. Recently, we originally developed a QM/MM code [17–23] that utilizes the real-space grids to represent the one-electron wave functions in the QM region described by the KS-DFT. The advantage of the use of the real-space grids approach resides in its efficiency in the parallel computation due to the fact that the Hamiltonian matrix in the real-space representation is almost diagonal within the framework of the KS-DFT.

The quantity that plays an essential role in determining the reaction path in a condensed system is the free-energy change associated with the path. Hence, the free-energy calculation is an issue of crucial importance for the study of the chemical reactions in many-particle system. However, the evaluation of the free energy on the basis of the molecular theory is computationally very demanding [9,10]. The free-energy perturbation (FEP) or thermodynamic integration (TI) method is based on the Kirkwood's charging formula and it introduces a set of intermediate points on an arbitrary path that connects the initial and final states of the chemical reaction of interest. Then, the free-energy changes between the adjacent points are accumulated along the path to compute total free-energy change. The FEP or TI is numerically rigorous, however, it should be noted that a sufficient number of intermediate points, which are physically of no importance, must be prepared to avoid being ill-sampled for the molecular configurations. It is also required for the convergence in the free energy to sample a large number of molecular configurations at each intermediate point. Therefore, the free-energy calculation by the FEP or TI approach along with the quantum chemical calculation becomes almost intractable since the number of the intermediate states typically amounts to several tens. The quest is, thus, required for the development of an efficient methodology to compute free energy in combination with the quantum chemical calculations.

Based on above discussions, we focus our interest in this chapter on the combination of the method of quantum chemistry and the theory of solutions majorly described in terms of the statistical mechanics. First, we present an overview of prevailing approaches. The polarizable continuum model (PCM) [24,25] approximates the solvent, an aggregate consisting of molecules, by a continuum with a uniform dielectric constant. Due mainly to the numerical convenience the PCM approach has, so far, been extensively utilized in the field of quantum chemistry by combining it with the self-consistent field (SCF) calculation. The deficiency of the approach is that it completely neglects the explicit structure of the constituent molecules of the solvent, and hence, it cannot realize the short-range interactions such as hydrogen bonds. It is, then, desirable to incorporate the solvation structure on the molecular level through a quantum–classical-coupled calculation. Within the framework of the DFT of solutions, the solvation free energy can be described in terms of the spatial distribution function of the solvent molecules around the solute. In general, the configuration of a solvent molecule with respect to the solute is specified by the multidimensional coordinate. In practice, the reference interaction site model (RISM) [26,27] is often used, where the distribution function is reduced to a set of site–site radial distribution functions (RDFs). Then, an approximate set of integral equations are introduced to solve the site–site RDFs by adopting the closure relations such as Percus–Yevick (PY) or hypernetted-chain (HNC) approximation [28]. A remarkable advance, referred to as RISM-SCF method [29], was made by combining the SCF procedure in quantum chemical calculation with the RISM equations. An important aspect of the RISM-SCF is that it soundly incorporates the effect of the solvent as a structured environment into the quantum chemical calculation. This is definitely more advantageous than the PCM approach. On the other hand, the RISM-SCF has a drawback that the electron density of the solute molecule is reduced to a set of point charges placed on the nuclei in the procedure to construct the RDFs. This indicates that the spatial diffuseness of the electron density, inherent nature of the QM object, is spoiled in the evaluation of the free energy.

In this literature, we review our recent approach to compute efficiently the free-energy change [30]. Our strategy to overcome the difficulties is to employ the hybrid quantum mechanical/molecular mechanical (QM/MM) approach in combination with a novel theory of solutions [31–33], termed as the theory of energy representation (QM/MM-ER) [30]. Within the framework of the ER, the solvent distribution function is constructed with respect to the solute–solvent interaction potential instead of the spatial distribution and it serves as a fundamental variable to describe the free energy. We emphasize that the concept of the interaction site is no longer needed in the construction of the distribution functions, and therefore, diffuseness of the electron density as well as its fluctuation can be straightforwardly taken into consideration without introducing special devices for it. In the previous works [34–41], we applied the method to various chemical events in aqueous solutions to examine the efficiency and reliability of the method and found that it reproduces the free-energy changes in excellent agreement with experimental results. The extension of the method is now in progress to construct an integrated methodology to compute free energies for various sorts of chemical reactions in biological systems, such as ligand bindings, redox reactions in cofactor, proton affinities of the amino acid residues, and chemical bond rearrangements.

The organization of this chapter is as follows. In Sections 2 and 3, we will make reviews, respectively, for the QM/MM approach and the theory of ER along with their related issues. Section 4 will be devoted to describe several methodologies that combine the quantum chemical approach with some solution theories, where an emphasis will be placed on the development of QM/MM-ER. Sections 3 and 4 will include the descriptions for applications utilizing the theory of ER as well as QM/MM-ER. In Section 4, we also describe a novel implementation of QM/MM-ER to compute reduction free energy of a cofactor immersed in water, where the excess charge to be attached on the cofactor is regarded as a single solute [40,41]. We give conclusions and perspectives in Section 5.

2. QUANTUM CHEMICAL APPROACH

As described in Introduction, DFT played a crucial role in the recent advances in quantum chemistry especially for the electronic structure calculations for large systems. In Subsection 2.1, we shall survey the framework of the KS-DFT, the workhorse in the methods categorized as DFT. We introduce, in Subsection 2.2, the real-space grids used as a basis to express the one-electron wave functions in the KS-DFT for the purpose to achieve high efficiencies in parallel computations. Methodological details will be presented with a particular emphasis on the parallel implementations. Subsection 2.3 will be devoted to describe the hybrid QM/MM approach, a simple and efficient quantum chemical approach to handle the reaction in the presence of environment.

2.1. Kohn–Sham density functional theory

In this section we present a concise review for the KS-DFT [6–8], which have made a large contribution to the today's great success in the theoretical and computational molecular science. The start was given by the Hohenberg–Kohn (HK) [7] theorem which proved that there exists one-to-one correspondence between the set of external potentials and that of the electron densities of the nondegenerate ground states. The HK theorem ensures that all physical properties of the system can be described in terms of the electron density instead of the wave function. In the framework of HK, however, we have to remind that the variational search of the electron density is constrained within the set of the v-representable electron densities by its construction. This is obviously an unpleasant situation since we cannot specify the explicit boundary of the set of v-representable densities. The Levy's constraint search [6,42,43] successfully circumvents this shortcoming inherent in the HK theorem. In the Levy's approach, the universal functional is introduced for an N-representable electron density, which is defined as

$$F[n^N] = \min_{\Psi \to n^N} \langle \Psi | T + V_{\mathrm{ee}} | \Psi \rangle. \tag{1}$$

The functional F is universal in the sense that it is independent of the external potential v in the system of interest. The superscript N in Eq. (1)

is to place an emphasis that only N-representability is required for the density as an argument of the functional. In Eq. (1) T and V_{ee} express, respectively, the electron kinetic energy operator and sum of the repulsive potentials between electrons. And Ψ is the antisymmetric total wave function for N electrons of which density becomes n^N. By using this functional, we can formulate the DFT for the ground-state energy E_{g} as the variational search within the set of the N-representable densities, thus,

$$\begin{aligned} E_g &= \min_{\Psi}\langle\Psi|\mathrm{H}|\Psi\rangle, \\ &= \min_{n^N}\left[\min_{\Psi\to n^N}\langle\Psi|\mathrm{T}+\mathrm{V}_{\mathrm{ee}}|\Psi\rangle + \int d\mathbf{r}v(\mathbf{r})n^N(\mathbf{r})\right], \\ &= \min_{n^N}[F[n^N] + \int d\mathbf{r}v(\mathbf{r})n^N(\mathbf{r})]. \end{aligned} \tag{2}$$

v stands for the external potential and its expectation value is dependent only on the electron density. Importantly, the explicit criterion is available to distinguish the N-representable density. Hence, Eq. (2) makes sense as a formulation for the density functional. Here, we note that the variational search in the method proposed by Kohn and Sham is also outlined by Eq. (2). The KS-DFT is based on the fundamental assumption that the ground-state electron density of a system can be constructed by that of a noninteracting reference system, and then the search of the electron density is carried out by the variation of the Slater determinant of one electron wave functions. It should be kept in mind, however, that in some cases the electron densities corresponding to the ground states of the noninteracting systems constitute merely a subset of the v-representable densities [6]. In such a case, the KS procedure possibly cannot achieve the ground state energy or density even if the explicit form of the universal functional $F[n]$ is known. In the following, we take a closer look for the KS-DFT.

The notable feature of the KS approach is that most of the electronic kinetic energy $T[n]$ in the functional $F[n]$ is to be explicitly evaluated by sum of the one-electron kinetic energies $T_{\mathrm{s}}[n]$ of the non-interacting system. $T_{\mathrm{s}}[n]$ is simply given as

$$T_{\mathrm{s}}[n] = \min_{\{\varphi_i\}\to n}\sum_i^N\left\langle\varphi_i\middle|-\frac{1}{2}\nabla^2\middle|\varphi_i\right\rangle, \tag{3}$$

where $\{\varphi_i\}$ is a set of one-electron wave functions giving the density n and it minimizes the value of T_{s}. By subtracting $T_{\mathrm{s}}[n]$ as well as the classical electron repulsion energy $J[n]$ from $F[n]$ of Eq. (1), we define the exchange-correlation energy functional $E_{\mathrm{xc}}[n]$ as follows,

$$\begin{aligned} E_{\mathrm{xc}}[n] &= F[n] - T_{\mathrm{s}}[n] - J[n] \\ &= (T[n] - T_{\mathrm{s}}[n]) + (V_{\mathrm{ee}}[n] - J[n]). \end{aligned} \tag{4}$$

Here we note that the kinetic correlation energy $T[n]–T_s[n]$ can be naturally incorporated into the functional by the adiabatic connection method [6]. It is, then, possible to derive the variational equation by supposing the variation of the total energy with respect to the density is equal to 0 at the stationary point, thus,

$$\delta\left\{T_s[n]+\int d\mathbf{r}d\mathbf{r}'\frac{n(\mathbf{r})n(\mathbf{r}')}{|\mathbf{r}-\mathbf{r}'|}+E_{xc}[n]+\int d\mathbf{r}\nu(\mathbf{r})n(\mathbf{r})-\mu\left[\int d\mathbf{r}n(\mathbf{r})-N\right]\right\}=0, \tag{5}$$

where μ is the Lagrange's multiplier introduced to impose the norm conservation for electron density. It is easy to see that Eq. (5) leads to an Euler equation,

$$\frac{\delta T_s[n]}{\delta n(\mathbf{r})}+v_{\text{eff}}(\mathbf{r})=\mu, \tag{6}$$

with the definition of

$$v_{\text{eff}}(\mathbf{r})=\int d\mathbf{r}'\frac{n(\mathbf{r}')}{|\mathbf{r}-\mathbf{r}'|}+\frac{\delta E_{xc}[n]}{\delta n}+V(\mathbf{r}). \tag{7}$$

Furthermore, the functional derivative of $T_s[n]$ in Eq. (6) can be reformulated in terms of one-electron orbitals $\{\varphi_i\}$ by virtue of Eq. (3), thus,

$$\left(-\frac{1}{2}\nabla^2+v_{\text{eff}}(\mathbf{r})\right)\varphi_i(\mathbf{r})=\varepsilon_i\varphi_i(\mathbf{r}) \qquad (i{=}1,\ldots,N). \tag{8}$$

Equation (8) is called the KS equation and it plays a central role in the KS-DFT.

2.2. Real-space grids approach

In the field of quantum chemistry, of which major targets are atoms or molecules, the linear combination of atomic orbitals (LCAO) method [5] has been extensively utilized to expand the one-electron wave function in the numerical implementation of the MO and the DFT. It is known that the Slater-type orbital is more appropriate than the Gaussian orbital as a component atomic orbital to reproduce the realistic behaviors of MO near the atomic core regions and in the outer regions of molecules. However, the Gaussian-type orbitals are commonly used instead of Slater-type ones because of the numerical convenience. In practice, a basis function used in the LCAO approach is constructed from a linear combination of primitive Gaussians with fixed contraction coefficients so that it mimics the whole behavior of a Slater-type orbital. As a result, a huge number of two-electron integrals with respect to primitive basis functions are to be computed and stored in preparation for the SCF calculations. The adequacy of the LCAO approach is well established by a number of numerical applications. A critical drawback in the LCAO approach is that the effective Hamiltonian represented by atomic orbitals has nonzero elements in its off-diagonal part, which gives rise to a large amount of data communications among the processors in the parallel computations. In the study for the electronic structures of infinite systems such as crystals, on the other hand, plane wave basis set is often employed to make use of its periodicity. The matrix for the kinetic energy operator in the effective Hamiltonian is completely diagonal in the plane wave representation, which is obviously advantageous for the parallel computation. However, other operators in the Hamiltonian are not diagonal in the momentum space. Moreover, the approximate exchange-correlation potential which appears in the KS equation can be evaluated only after the total electron density is obtained in the real space. It means that the transformations are necessitated for one-electron wave functions from the momentum space to the real space and vice versa, where the fast Fourier transformation (FFT) algorithm is often utilized to expedite the transformations. The computational cost of FFT for each orbital scale as $N \log_2 N$ where N is the number of discrete points taken in the momentum (real) space and FFT is the most time-consuming part in the method of the plane wave basis. It should also be noted that FFT is never suitable for the parallel computing especially at least when one uses a parallel computer with a distributed memory architecture.

In a recent development, Chelikowsky et al. proposed to express a one-electron wave function by means of the real-space grids [44–46]. Since most of the operators in the KS equation are local in the real-space representation, it is quite natural to express the one-electron orbitals by a set of probability amplitudes defined on the discrete grid points that are uniformly distributed over a real-space cell. In the parallel implementation, we divide the real-space cell into subdomains and allocate each subdomain to a processor, for which we give an illustration in Figure 9.1. Then, the values of the wave functions on the subdomain are distributed to the processor. The Hamiltonian matrix has nonzero elements only in the vicinity of diagonal part, and hence, the data communication among the processors can be suppressed minimally, which benefits the high performance in the parallel computation. Moreover, the real-space grids approach has several advantages as follows [47,48]. At first the local augmentation of the basis can be done straightforwardly by introducing dense grids around atomic cores for instance. Second, the periodic and the nonperiodic boundary conditions are available without serious modifications of the code. Third, the overlap matrix of the real-space grids basis becomes an identity matrix and no additional procedure is needed for orthogonalization of the basis set. It should be noted, however, that the drawbacks also exist in the real-space approach. It is well recognized that

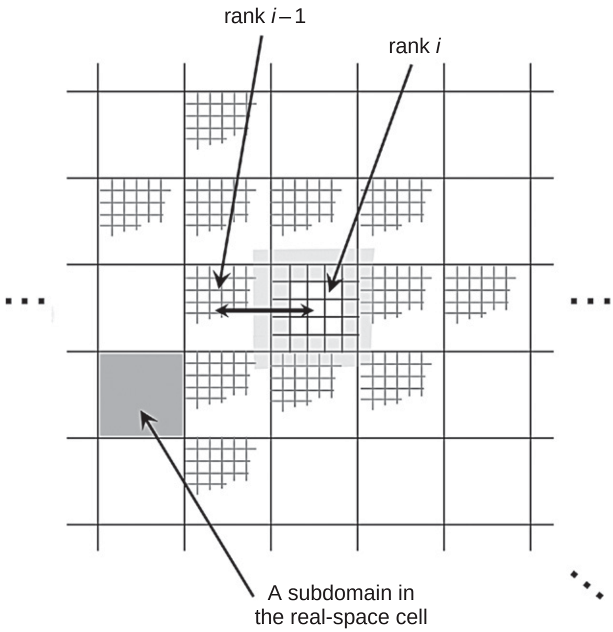

Figure 9.1 Illustration of the division of the real-space cell in the parallel implementation. Each core processor (rank) is charged with the computation for a subdomain. The area of which data must be communicated is colored in the figure. The line with arrows at both ends represents the data exchange between neighboring cores [rank i and rank (i − 1)].

the electronic energy of an atom varies seriously for the shift of the relative position of the atom with respect to the grid points. Such an erroneous situation can be substantially alleviated by the use of the dense grids near the atomic core regions. Furthermore, the numerical integration in the real-space approach is less accurate as compared to the atomic orbital basis. The major difficulty in the real-space approach arises from the evaluation of the nonlocal operator such as HF exchange operator. Actually, one may find a difficulty in computing integrals associated with a nonlocal operator when its nonlocality is serious in the real space. Fortunately, most of the operators in KS-DFT are local or semilocal except for the hybrid-type functional that includes the HF exchange. In the following paragraphs, we describe the real-space approach for the implementation of the KS-DFT. An emphasis will be placed on the efficiency in the parallel computations.

A notable feature of the real-space grids approach is that the kinetic energy operator in Eq. (8) is expressed by the finite-difference method. Here, we formulate the matrix elements for the wave function on a one-dimensional coordinate x for the sake of simplicity. The Taylor series expansions of the wave function φ at a grid point i lead to

$$\begin{aligned}\varphi(i+1) &= \varphi(i)+\frac{1}{1!}\varphi'(i)\cdot\Delta x+\frac{1}{2!}\varphi''(i)\cdot\Delta x^2+\frac{1}{3!}\varphi''(i)\cdot\Delta x^3+O(\Delta x^4),\\ \varphi(i-1) &= \varphi(i)-\frac{1}{1!}\varphi'(i)\cdot\Delta x+\frac{1}{2!}\varphi''(i)\cdot\Delta x^2-\frac{1}{3!}\varphi''(i)\cdot\Delta x^3+O(\Delta x^4),\end{aligned} \tag{9}$$

where Δx is the width of the grid. We obtain the first-order finite-difference expression for the second derivative $\varphi''(i)$ by the sum of above two equations as

$$\varphi''(i)=\frac{1}{\Delta x^2}\{\varphi(i+1)-2\varphi(i)+\varphi(i-1)\}+O(\Delta x^4). \tag{10}$$

It is worth noting that the numerical error can be suppressed to fourth power of the grid spacing even for the first-order finite-difference. The higher order expression can also be formulated by considering the higher order terms in the Taylor series expansion. Equation (10) can be generalized to the Lth-order finite-difference representation for the grids in three-dimensional space, thus,

$$\begin{aligned}-\frac{1}{2}\nabla^2\varphi(i,j,k) = -\frac{1}{2h^2}\Bigg[&\sum_{l_1=-L}^{L}C_{l_1}\varphi(i+l_1,j,k)\\ &+\sum_{l_2=-L}^{L}C_{l_2}\varphi(i,j+l_2,k)\\ &+\sum_{l_3=-L}^{L}C_{l_3}\varphi(i,j,k+l_3)\Bigg]+O(h^{2N+2}),\end{aligned} \tag{11}$$

where C are the expansion coefficients of which values are presented for $L=1\sim6$ in Ref. [45]. h is the grid spacing that is common to all directions. By performing the preliminary calculations, we found that $L=4$ is sufficient enough to achieve the desired accuracy for usual purposes. Let us consider here the parallel efficiency for a CPU that is assigned to a subdomain yielded by the division of the real-space cell. In the case of $L=4$, evaluation of the kinetic energy at a grid point necessitates the values of the wave functions on the neighboring eight grid points for each axis. It suggests that the wave functions at a boundary with the thickness of four grids in the subdomain must be exported to another CPU that corresponds to the neighboring subdomain. In Figure 9.1 such a part is colored. It is recognized in Figure 9.1 that the amount of the data communication is confined within a small region of space.

The use of the uniform grids necessitates the employment of the pseudopotentials [49] V_{ps} for the nuclei to realize the smooth behaviors of the wave functions for valence electrons. For clarity, we rewrite the effective potential v_{eff} of Eq. (7) for the noninteracting electrons as

$$v_{\text{eff}}(\mathbf{r}) = \int d\mathbf{r}' \frac{n(\mathbf{r}')}{|\mathbf{r}-\mathbf{r}'|} + \frac{\delta E_{\text{xc}}[n]}{\delta n} + V_{\text{ps}}(\mathbf{r}). \tag{12}$$

Our purpose here is to describe the outline to compute each term in Eq. (12). The first term in the right-hand side of Eq. (12) is usually termed as Hartree potential $V_{\text{H}}(\text{r})$ and it represents the classical Coulomb potential provided by the electron density $n(\text{r})$. As for the periodic system, we compute the Hartree potential $V_{\text{H}}(\mathbf{g})$ in the momentum space, which can be easily evaluated in the reciprocal space, thus,

$$V_{\text{H}}(\mathbf{g}) = \frac{4\pi}{|\mathbf{g}|^2} n(\mathbf{g}), \tag{13}$$

where $n(\text{g})$ is the electron density in momentum space and constructed from $n(\mathbf{r})$ by an FFT transformation. $V_{\text{H}}(\mathbf{r})$ is, then, obtained by the backward transformation of $V_{\text{H}}(\mathbf{g})$. In the nonperiodic system, on the other hand, $V_{\text{H}}(\mathbf{r})$ can be determined by performing the integration in Eq. (12) directly. However, it is computationally very demanding because it requires two-fold loops for the coordinates $\mathbf{r}$ and $\mathbf{r}'$. Instead, we adopt a method to solve the Poisson equation for the Hartree potential $V_{\text{H}}(\mathbf{r})$ [48],

$$\nabla^2 V_{\text{H}}(\mathbf{r}) = -4\pi n(\mathbf{r}). \tag{14}$$

It is critically important to determine the values of $V_{\text{H}}(\mathbf{r})$ at the boundary of the cell for the solution of the Poisson equation. For this purpose we determine the fractional charge at each nucleus from the electron density $n(\mathbf{r})$. Then, we approximate the electrostatic potential due to $n(\mathbf{r})$ at the boundary by the Coulomb interaction formed by these fractional charges. The fractional charges are determined by the fuzzy cellular partitioning of the electron density [50]. We employ the conjugate gradient (CG) algorithm [51] synchronized with the steepest descent procedure to solve Eq. (14) iteratively. The Laplacian is evaluated by the same method adopted in the kinetic energy operator, which is higher order finite-difference approach. The amount of data communication is much less than that required in the kinetic energy term since only a single function $V_{\text{H}}(\mathbf{r})$ must be communicated among the processors instead of the set of one-electron wave functions.

The second term of Eq. (12) is the exchange-correlation potential, the derivative of E_{xc} with respect to density. The first step to estimate the energy E_{xc} is usually based on the local density approximation (LDA), which assumes that E_{xc} can be expressed as [6]

$$E_{\text{xc}}^{\text{LDA}}[n_\alpha, n_\beta] = \sum_\sigma \int d\mathbf{r} n_\sigma(\mathbf{r}) \varepsilon_{\text{xc}}[n_\sigma(\mathbf{r})], \tag{15}$$

where the suffix σ stands for the electron spins α and β. ε_{xc} in Eq. (15) is the exchange correlation energy per electron in a uniform electron gas. Then, it is easy to see that the exchange-correlation potential is completely local in the real-space representation. Hence, no communication is needed in the parallel computation within the framework of LDA. For the generalized gradient approximation (GGA) functional, the energy E_{xc} is formally written in terms of the gradient $\nabla n_\sigma(\mathbf{r})$ besides the electron density itself, thus,

$$E_{\text{xc}}^{\text{GGA}}\left[n_\alpha, n_\beta\right] = \sum_\sigma \int d\mathbf{r} F\Big(n_\sigma(\mathbf{r}), |\nabla n_\sigma(\mathbf{r})|\Big) \tag{16}$$

The gradient can also be approximated by the finite-difference method, hence, the communication cost in the parallel computation to evaluate the exchange-correlation potential with GGA correction is comparable to that for the Hartree potential.

The last term V_{ps} in Eq. (12) is the pseudopotentials for nuclei and we employ the norm-conserving separable form proposed by Kleinman and Bylander [52] throughout this chapter. For a nucleus it is expressed as,

$$V_{\text{ps}}^{\text{KB}}(\mathbf{r}) = V_{\text{loc}}(r) + \sum_{l,m} \frac{|\Delta V_l \phi_{l,m}\rangle\langle\phi_{l,m}\Delta V_l|}{\langle\phi_{l,m}|\Delta V_l|\phi_{l,m}\rangle}. \tag{17}$$

In Eq. (17) $V_{\text{loc}}(r)$ is the local pseudopotential and it depends only on the radial distance r between $\mathbf{r}$ and the nucleus. Integers l and m stand for the angular momentum quantum number and the magnetic quantum number, respectively. $\Delta V_l(r)$ is the l-dependent local potential $V_l(r)$ subtracted by $V_{\text{loc}}(r)$ and is short range. $\phi_{l,m}$ is the atomic pseudo wave function. The second term of the left-hand side of Eq. (17) involves the projection operator, and hence, it is nonlocal. However, the nonlocality does not make a matter in the parallel computation since $\phi_{l,m}$ as well as $\Delta V_l(r)$ is confined within a small region around the atomic core. Thus, it is demonstrated that the real-space representation is advantageous to the parallel computation of the KS-DFT due to the locality of the operators in the real space.

Here, we introduce a key technique to attain substantial accuracy in the calculations with the real-space grids. As mentioned above, the energy profile of an atom for the variation of the relative position of the atom with respect to a grid shows an erroneous behavior that the energy depends seriously on the relative position. This is a well-known deficiency in the real-space grids method. A promising way to improve this situation is to employ the double-grid technique around the atomic core to refine the resolution of the wave functions. However, it inevitably leads to the undesirable increase in the computational costs. Ono and Hirose proposed a unique approach [53] to solve this problem by taking advantage of the smooth nature of the pseudo wave function. According to their method, the computational overhead associated with the introduction of the double grids can be substantially reduced. In the following we illustrate the method. The major quantity we want to improve its accuracy by using the double grids is the inner product between $\langle\phi_{\mathrm{l,m}}\Delta V_l|$ in Eq. (17) and wave function $|\varphi_{\mathrm{i}}\rangle$. For simplicity we restrict the problem to one-dimensional integration and simplify the notations, thus,

$$\int_\Omega v(x)\varphi(x)\mathrm{d}x, \tag{18}$$

where Ω is the atomic core region which contains the dense grids. The approximate evaluation of Eq. (18) by the double-grid approach can be expressed as

$$\int_\Omega v(x)\varphi(x)\mathrm{d}x \cong \sum_{i\in\Omega} v(i)\varphi(i)\delta x, \tag{19}$$

where i denotes the index for the dense grids of which width is taken as δx. The point of their approach is to estimate the values of the wave function on the dense grids by interpolating those on the coarse (original) grids by virtue of the fact that the pseudo wave function varies smoothly even in the atomic core regions. With the simplest interpolation method such as linear interpolation, the value of $\varphi(i)$ can be expressed in terms of the wave functions $\varphi(I)$ and $\varphi(I+1)$ on the neighboring *coarse* grids I and $I+1$, thus,

$$\varphi(i) = \frac{\Delta x - (x_i - X_I)}{\Delta x}\varphi(I) + \frac{\Delta x - (X_{I+1} - x_i)}{\Delta x}\varphi(I+1) \tag{20}$$

In Eq. (20) Δx is the width of the coarse grid and x_i and X_I denote the coordinates of the grids i and I, respectively. By substituting Eq. (20) to Eq. (19), we obtain the approximate expression for the integration by the discrete sum over the coarse grids I,

$$\int_\Omega v(x)\varphi(x)\mathrm{d}x \cong \sum_{I\in\Omega} \omega_I\varphi(I)\Delta x, \tag{21}$$

where the weight factor ω_I specific for the grid I is given as

$$\omega_I = \sum_{s=-n}^{n} \frac{\Delta x - |x_{nI+s} - X_I|}{n\Delta x} v(nI+s) \tag{22}$$

In Eq. (22) n is an integer that satisfies $\Delta x = n \times \delta x$, and hence nI corresponds to the index assigned for the coarse grid I in the indexing of the dense grids. For the help of understanding, we present an illustration for the wave function φ and pseudopotential v on the double grids in Figure 9.2. Since the pseudopotential is to be given from the outset, evaluation of the values of v on the dense grids does not accompany additional costs. From Eq. (22), it is easy to see that the weight factors ω_I do not change unless the

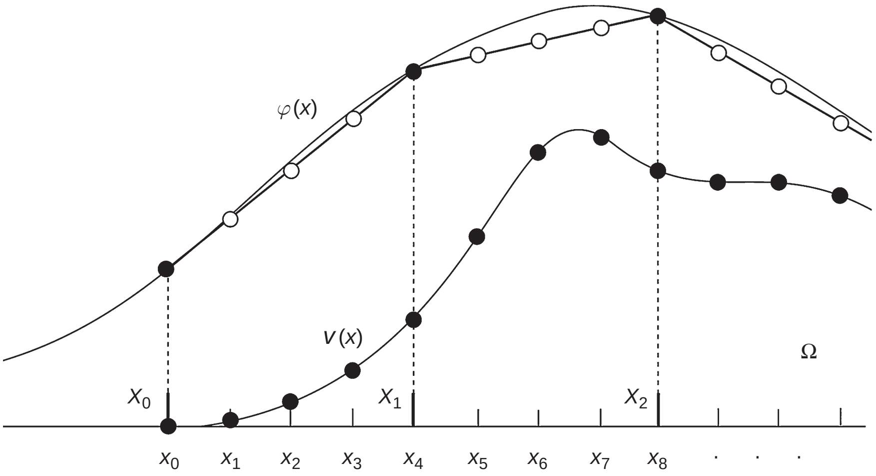

Figure 9.2 Schematic for the one-dimensional double grids in the atomic core region Ω. $\varphi(x)$ and $v(x)$ are the wave function and the nonlocal pseudopotential, respectively. Arrays $\{X_i\}$ and $\{x_i\}$ denote the coarse and dense grids, respectively. The values on the black points are to be evaluated explicitly, while those on the white ones are obtained by an interpolation.

position of the atom is updated. Hence, the same set of ω_I for each atom can be used during an SCF cycle. It is also advantageous that no memory space should be newly allocated for wave functions on the dense grids by virtue of Eq. (21) in contrast to the conventional double-grid approach. We note that we utilize the Lagrange interpolations with $n=5$ in our usual applications. We discuss here the parallel efficiency in the time-saving Ono–Hirose approach. It is apparent that no data communication is needed for the integration of Eq. (21). Thus, what is necessitated for the high efficiency is that the atoms in the system are uniformly distributed over the subdomains to achieve the good load balance among the processors for the computation of the weight factors of Eq. (22) for atoms.

In closing this subsection, we present the results of the preliminary calculations to examine the parallel efficiency in the real-space grids approach [54]. The test system is the pair of aspartic acids embedded in HIV-1pr and a model substrate, which contains 98 valence electrons; 80 grids points were prepared for each axis of the real-space cell. We carried out the KS-DFT calculations that employed 1, 2, 4, and 8 CPUs. The parallel efficiency P_n is defined as the percentage of the rate of the speedup divided by the number n of CPUs used, thus,

$$P_n = \frac{\mathrm{Time(1CPU)}}{\mathrm{Time}(n\mathrm{CPU})} \cdot \frac{100}{n}. \tag{23}$$

The notation of “Time” in Eq. (23) expresses the wall clock time spent to accomplish an SCF step. We obtained P_2, P_4, and P_8 as 90.0, 88.5, and 80.5%, respectively. Thus, we achieved a good performance in parallelization, however, it was also found that the efficiency P is decreasing as the increase in the number of CPUs. This is mainly attributed to the increase in the amount of the communication relative to the net computational cost for each domain. The amount of the communication at the boundaries of the domains scales in the square of the cell size, while the net computational cost scales in the cube of it. Hence, it is possible that the parallel efficiency is recovered when one computes a larger system. Anyway the parallel efficiency P around 80–90% is quite satisfying in the quantum chemical calculations. The present approach can be straightforwardly extended to the massively parallel computations without serious loss of efficiency as far as the computational cost is well balanced with the amount of communications. We note that these calculations were performed on an ordinary cluster system with distributed memory architecture consisting of Pentium 4/3.2 GHz processors connected by a gigabit switch. The data communication was commanded by invoking the standard message-passing interface (MPI) libraries [55]. Lastly let us make an overview of the parallelization in the LCAO approach. A crucial step that should be parallelized in the LCAO calculation is the evaluation of two-electron integrals for a large number of sets of four-centered atomic orbitals. The basic strategy for the parallelization is, then, to divide all sets of four atomic orbitals and to distribute them to CPUs. Each processor may compute corresponding two-electron integrals and construct individual Hamiltonian matrix in terms of the partial sets of the two-electron integrals. The incomplete Hamiltonian held in each processor will be summed up in the master node to form complete one, for which the transfer of the whole matrix with full size to the master processor is necessitated. Importantly, the size of the Hamiltonian is square of the number of atomic basis and it increases rapidly as the number of atoms involved in the system increases. It is, thus, apparent that LCAO approach is disadvantageous for efficient parallelization as compared with the real-space grids, though it may be recovered to a certain extent by making some devices. Since the recent trend in the supercomputer is toward the massively parallel architecture connecting multicore processors, it is desirable to introduce parallel-oriented methodologies in the quantum chemical calculation.

2.3. Hybrid quantum mechanical/molecular mechanical method

It is often the case that only a small part in the whole system takes part in a chemical event in condensed system. The hybrid QM/MM approach provides a reliable computational framework to describe such a situation, where the chemically active part is described by a method of quantum chemistry, while the rest of the system is approximated by a certain coarse model. The PCM combined with the SCF calculation as well as RISM-SCF, of which outlines were given in Introduction, are along the line of the QM/MM method in a broad sense. In the ONIOM approach [56], multiple intermediate layers are introduced to adopt various levels of description according to the importance of the layer for the reaction and it is considered to be the generalization of the concept of QM/MM.

By taking the advantage of the classical molecular simulations, we can explicitly treat the environmental part of the system within the QM/MM scheme. In this case, the total energy of the system E_{tot} can be expressed as

$$E_{\mathrm{tot}} = E_{\mathrm{QM}} + E_{\mathrm{QM/MM}} + E_{\mathrm{MM}}. \tag{24}$$

The first term in the right side of Eq. (24) is the electronic energy of the QM subsystem including the nuclear repulsion energy and the third one is the energy of the MM subsystem represented by a classical force field. The term $E_{\mathrm{QM/MM}}$ denotes the interaction between the QM and MM subsystems. The electronic wave function Ψ with an eigenvalue E under an instantaneous solvent configuration can be defined by the following Schrödinger equation,

$$\left(\mathbf{H}_0 + \mathbf{V}_{\mathrm{ES}}(\mathbf{X})\right)\Psi = E\Psi, \tag{25}$$

where $\mathbf{H}_0$ is the electronic Hamiltonian of the isolated QM subsystem including the nuclear repulsion energies while $\mathbf{V}_{\mathrm{ES}}$ is the electrostatic potential formed by the point charges placed on the interaction sites of the MM molecules of which coordinates are collectively denoted by $\mathbf{X}$. Then, we can define the energy E_{QM} in Eq. (24) as

$$E_{\mathrm{QM}} = \langle \Psi | \mathbf{H}_0 | \Psi \rangle. \tag{26}$$

Here, we introduce the energy termed as distortion energy E_{dist} of the QM subsystem, thus,

$$E_{\mathrm{dist}} = \langle \Psi | \mathbf{H}_0 | \Psi \rangle - E_0 = \langle \Psi | \mathbf{H}_0 | \Psi \rangle - \langle \Psi_0 | \mathbf{H}_0 | \Psi_0 \rangle, \tag{27}$$

where E_0 and Ψ are the energy and the wave function of the isolated solute in the ground state, respectively. The interaction energy $E_{\mathrm{QM/MM}}$ in Eq. (24) consists of three terms, thus,

$$E_{\mathrm{QM/MM}} = E_{\mathrm{ES}} + E_{\mathrm{ns}} + E_{\mathrm{vdW}}, \tag{28}$$

where E_{ES} is the expectation value of $\mathbf{V}_{\mathrm{ES}}(\mathbf{X})$ for the wave function Ψ in Eq. (25), E_{ns} is the Coulomb interaction between the nuclei in the QM molecule and the fractional charges on the MM molecules, and E_{vdW} is the van der Waals interaction between the QM and MM subsystems. The last term E_{MM} of Eq. (24) stands for the potential energy of the MM subsystem and it is usually given by the sum of contributions from electrostatic and van der

Waals energies, which are, respectively, expressed by the point charge representations and Lennard-Jones (LJ) interactions [9,10] as follows,

$$\begin{aligned} E_{\mathrm{MM}} &= E_{\mathrm{pc}} + E_{\mathrm{vdW}} \\ &= \sum_{i<j} \frac{q_i q_j}{r_{ij}} + \sum_{k<l} 4\varepsilon_{kl} \left(\left(\frac{\sigma_{kl}}{r_{kl}} \right)^{12} - \left(\frac{\sigma_{kl}}{r_{kl}} \right)^{6} \right). \end{aligned} \tag{29}$$

In Eq. (29), q_i is the point charge assigned to site i and r_{ij} is the site–site distance. ε_{ij} and σ_{ij} are the empirical parameters in the LJ potential, which are, respectively, related to the interaction energy and the size between two LJ sites. We note that E_{vdW} in Eq. (28) is also given by the LJ form in Eq. (29).

3. THEORY OF SOLUTIONS

The chemical potential is the free-energy change corresponding to the insertion of a unit number of solute molecules in solution. It is actually the most fundamental quantity in the theory of solutions. Indeed, the free-energy change for a physical or chemical process of interest can be readily evaluated once the chemical potentials are known for the species present in the initial and final states of the process. Part of the chemical potential quantifying the solvent effect is the solvation free energy. It is the free-energy change for turning on the solute–solvent interaction. Since the solvent effect is the main focus of solution studies, it is of primary importance in statistical mechanics of solutions to establish a scheme to determine the solvation free energy of a solute in solution.

The purpose of this section is to describe schemes of computing the solvation free energy. The free energy in solution is notorious for its heavy computational demand. We approach this difficulty by combining the molecular simulation and statistical–mechanical theory of solutions. Since the target of solution chemistry expands and now includes quantum–classical-coupled (QM/MM) system, nano-organized systems such micelle, lipid membrane, and protein, and environmentally benign reaction media such as ionic liquid and supercritical fluid, the theory of solutions also needs to be (re-)formulated to treat these frontline subjects. The goal of this section is to introduce a new theory of solutions that is amenable to diverse areas of applications. We first describe the standard scheme of free-energy calculation. We then present the concept of distribution function and the DFT connecting the distribution function and free energy. Finally, we formulate a new method of solutions, the method of ER, and show its application to molecular binding into micelle and lipid membrane.

3.1. Free-energy perturbation and thermodynamic integration methods

Let H_0 and H_1 be, respectively, the Hamiltonians at the initial and final states of a process in solution. When the solvation process is concerned, the initial and final states are typically the pure solvent and solution systems of interest. The corresponding free-energy change ΔF is given by

$$\exp(-\beta\Delta F) = \frac{\int \mathrm{d}\Gamma \exp(-\beta H_1)}{\int \mathrm{d}\Gamma \exp(-\beta H_0)}, \tag{30}$$

where β is the inverse of the product of the Boltzmann constant k_B and the temperature T and Γ is the (collective) coordinate for the phase space. When the classical statistical mechanics is adopted and the Hamiltonian change between the initial and final states does not involve the kinetic part, Eq. (30) reduces to

$$\exp(-\beta\Delta F) = \frac{\int \mathrm{d}\mathbf{X} \exp(-\beta U_1)}{\int \mathrm{d}\mathbf{X} \exp(-\beta U_0)}, \tag{31}$$

where $\mathbf{X}$ is the (collective) coordinate for the configuration and U_0 and U_1 are the potential energies of the system at the initial and final states, respectively. Equation (31) is the starting point of our development. It should be noted that Eq. (31) cannot be used when a quantum fluid is to be treated.

When $U_1 - U_0$ is denoted by ΔU, Eq. (31) is rewritten as

$$\exp(-\beta\Delta F) = \langle \exp(-\beta\Delta U)\rangle_0, \tag{32}$$

where $<\ldots>_0$ is the ensemble average taken at the initial state whose configuration is sampled according to the potential energy U_0. Equation (32) shows that the free-energy change ΔF can be calculated, in principle, by performing only the simulation for the initial state and averaging the Boltzmann factor of the relevant energy change ΔU. Indeed, Eq. (32) is the basis of the particle insertion method for evaluating the solvation free energy (chemical potential) of a solute in solution [9,10,28]. In the particle insertion method, the pure solvent is simulated and the solute molecule of interest is inserted randomly into the pure solvent. The chemical potential is then obtained from

$$\exp(-\beta\Delta F) = \int \mathrm{d}(\Delta U)\exp(-\beta\Delta U)f(\Delta U), \tag{33}$$

where $f(\Delta U)$ is the probability distribution function of ΔU in the pure solvent system. The particle insertion method is convenient and fast since only the pure solvent configurations need to be prepared and the free energy is calculated from a one-step insertion process of the solute. As it is well documented, however, the particle insertion method is applicable only for a small and weakly interacting solute [9,10,28]. When the solute is large and/or interacts strongly with the solvent, the formally exact form of Eq. (33) exhibits a numerical difficulty. See Figure 9.3. When the solute is not small, it almost always overlaps with solvent molecules upon insertion. When the solute does not interact weakly with the solvent, the attractive solute–solvent effect needs to be properly taken into account. The problem is that $f(\Delta U)$ is well sampled only toward large (repulsive) value of ΔU. Although the Boltzmann factor exp $(-\beta\Delta U)$ increases steeply toward small (attractive) ΔU, the small ΔU region, which makes a significant contribution in Eq. (33), is usually ill sampled in the computation of $f(\Delta U)$. Thus, Eq. (33) is not computationally useful and the particle insertion method cannot be used for most of "interesting" systems. Actually, the calculation of the average of the exponential of the energy change is often prohibitive unless the energy change is small in magnitude.

The standard and often used methods to circumvent the difficulty associated with the form of Eq. (33) are the FEP and TI methods [9,10,28]. These methods are generally applicable to free-energy evaluation. In this review, we restrict our development to the solvation process; the initial state is the pure solvent and the final state is the solution system of interest.

The FEP method utilizes the intermediate states connecting the initial and final states of the process of interest. Let V_i $(i = 0, \ldots, n)$ be a sequence of potential energies where the initial and final ones V_0 and V_n are taken to the

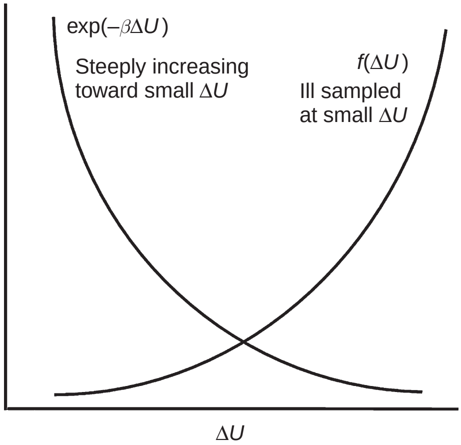

Figure 9.3 A schematic distribution of ΔU value in the particle insertion method.

potential functions U_0 and U_1 for the initial and final states, respectively. For an arbitrary (set of) V_i, Eq. (31) can be expressed as

$$\exp(-\beta\Delta F) = \prod_{i=0}^{n-1} \left\langle \exp\left(-\beta(V_{i+1} - V_i)\right) \right\rangle_i, \tag{34}$$

where $< \ldots >_i$ is the ensemble average taken with respect to the potential function V_i. Equation (34) shows that ΔF is given as the sum of the free-energy change accompanying the energy change from V_i to V_{i+1} ($i = 0, \ldots, n-1$). The states corresponding to V_i ($i = 1, \ldots, N-1$) are called intermediate states. The free energy is a state function and does not depend on the choice of the intermediate states in principle. From the computational viewpoint, the point is to "select" the set of V_i so that the change from V_i to V_{i+1} is "small" in magnitude. When V_i and V_{i+1} are "similar" and the energy change is small, the difficulty encountered in the particle insertion method can be circumvented and the calculation of the free-energy change becomes feasible. The drawback is that a number of intermediate states need to be prepared and that the computational cost is enhanced accordingly.

In the TI method, the intermediate states are introduced with respect to the coupling parameter λ ($0 \leq \lambda \leq 1$). The potential function at the coupling parameter of λ is denoted as U_λ and satisfies $U_\lambda = U_0$ and $U_\lambda = U_1$ at the initial and final states ($\lambda = 0$ and 1), respectively. The intermediate states correspond to $0 < \lambda < 1$. The form of averaging-the-exponential is then avoided by rewriting Eq. (31) as

$$\Delta F = \int_0^1 \mathrm{d}\lambda \left\langle \frac{\partial U_\lambda}{\partial \lambda} \right\rangle_\lambda, \tag{35}$$

where $< \ldots >_\lambda$ is the ensemble average when the potential energy is U_λ. As is the case of the FEP method, ΔF value calculated by Eq. (35) is independent of the choice of the intermediate states in principle. The integrand of Eq. (35) is a preferable average from the computational viewpoint. The exponential average is not involved any more. In practice, the integral of Eq. (35) is replaced by a discretized sum and a finite number of intermediate states are to be treated explicitly. Since a systematic error is introduced by the discretization, a large number of intermediate states need to be prepared and the computational demand increases correspondingly.

In both the FEP and TI methods, the key to the computational accuracy and efficiency is the choice of the intermediate states as a function of the coupling parameter λ. Note that the intermediate states adopted in the FEP method can be considered a finite subset of the intermediate states introduced continuously over $0 < \lambda < 1$. A straightforward implementation of the intermediate states is possible by varying the system potential energy linearly. When the solvation is concerned and the solute–solvent interaction is expressed as the sum of LJ and Coulombic terms, the linear variation is realized by the intermediate solute–solvent interaction given by

$$\lambda\sum_{i,j}\left(4\varepsilon_{ij}\left\{\left(\frac{\sigma_{ij}}{r_{ij}}\right)^{12}-\left(\frac{\sigma_{ij}}{r_{ij}}\right)^{6}\right\}+\frac{q_iq_j}{r_{ij}}\right), \tag{36}$$

where i and j refer to solute and solvent interaction sites, respectively. The first term in the sum expresses the LJ interaction at the distance r_{ij} between the solute and solvent sites, and ε_i and σ_i are the energy and length parameters, respectively. The second term in the sum corresponds to the Coulombic interaction, and q_i and q_j are the charges on the solute and solvent sites, respectively. The linear scaling of the solute–solvent interaction with Eq. (36) is often ill-behaved numerically around $\lambda=0$. This is related to the appearance of $r=0$ singularity at $\lambda=0$. To alleviate the problem, a nonlinear scaling, which is obtained by replacing λ with λ^n ($n\geq 2$) in Eq. (36), can be used [57,58]. The calculation becomes more stable near $\lambda=0$. The $r=0$ singularity is still present in the nonlinear scaling, however, and careful analysis is necessary to determine the λ values actually sampled. Another choice of the intermediate states is provided by

$$4\lambda\varepsilon\left(\left(\frac{\sigma^2}{r^2+(1-\lambda)\delta}\right)^{6}-\left(\frac{\sigma^2}{r^2+(1-\lambda)\delta}\right)^{3}\right), \tag{37}$$

or similar expressions for the LJ part [58,59]. The $r=0$ singularity is then removed and the free-energy calculation on the basis of Eq. (37) is numerically stable.

Although the FEP and TI methods are exact in principle under a given set of potential functions, they are not free from systematic errors in practice. The systematic error most often encountered in the FEP method is the noncoincidence of the free-energy changes ΔF calculated from the forward variation of the coupling parameter λ from 0 to 1 and the backward variation from 1 to 0. The common practice is to average the ΔF from the forward and backward calculations. It is pointed out, however, that the simple averaging is itself a source of systematic error [60]. To achieve the accuracy, the use of Bennett's weighting function is recommended [60,61]. In the TI method, a systematic error is inevitable when the integral over λ in Eq. (35) is discretized. A careful examination of discretization is necessary, especially when the integrand of Eq. (35) exhibits a nonmonotonic dependence on λ and/or varies steeply over some range of λ.

3.2. Distribution function theory

A molecular picture of solutions is established through distribution (correlation) functions. Correspondingly, a molecular description of the solvation free energy can be implemented by formulating a functional which expresses the solvation free energy in terms only of distribution functions in the solution and pure solvent systems of interest. An approximate functional needs to be constructed in practice, however, since the exact functional involves an infinite series of many-body distribution functions [62]. The theories introduced in Subsections 3.4 and 3.5 are formulated to provide the solvation free energy with simple distribution functions in closed form. In this section, a general description of distribution function is provided.

The system of our interest is a dilute solution containing a single solute molecule. Even when the solute concentration is finite, our development is valid by viewing one of the solute molecules as the "solute" and the others as part of mixed solvent. To describe completely the solute–solvent configuration, the position and orientation need to be specified simultaneously. The complete set of the position and orientation is called the full coordinate and is denoted collectively as $\mathbf{x}$ for the solvent molecule. If the solvent molecule is flexible, its intramolecular degrees of freedom are also incorporated into $\mathbf{x}$. Similarly, the full coordinate of the solute molecule is denoted as ψ. In the full coordinate representation, the instantaneous distribution $\hat{\rho}^f$ at an arbitrarily given snapshot configuration is introduced as

$$\hat{\rho}^f(\psi, \mathbf{x}) = \delta(\psi - \hat{\psi}) \sum_i \delta(\mathbf{x} - \hat{\mathbf{x}}_i), \tag{38}$$

where $\hat{\mathbf{x}}_i$ and $\hat{\psi}$ are the full coordinate of the ith solvent molecule and the solute molecule at the snapshot configuration, respectively, and the sum is taken over all the solvent molecules. The superscript f is attached to emphasize that Eq. (38) is in the full coordinate representation. The distribution functions are generated from the averages of products of $\hat{\rho}^f$ in the system of interest.

When the distribution function is generated from $\hat{\rho}^f$, a multidimensional description is inevitable. Indeed, the full coordinate $\mathbf{x}$ is six-dimensional (5 for linear molecule) for rigid species and involves more for flexible species. To implement the full coordinate representation, the expansion in terms of spherical harmonics can be employed [28]. However, the calculation of multidimensional distribution functions is often slow in molecular simulation and the numerical realization is not straightforward. When the coordinate has too "fine" information content, the corresponding distribution function needs additional methodology for handling. Too much information is not desirable both from the computational viewpoint (large memory and slow convergence) and the conceptual viewpoint (unclear perception in mind).

It is then useful to reduce the information content by introducing a "projected" coordinate. With projection, some information of (ψ,$\mathbf{x}$) is retained, while the others are disregarded. When the projection is implemented with respect to a function $P(\psi,\mathbf{x})$, the corresponding distribution functions are generated from the instantaneous distribution given by

$$\sum_i \delta\Big(p - P(\psi,\mathbf{x}_i)\Big), \tag{39}$$

where p is the value of $P(\psi,\mathbf{x})$ and serves as the coordinate for the distribution function.

A typical choice of $P(\psi,\mathbf{x})$ is the radial distance between the atomic sites (interaction sites) of the molecule. When a pair of atomic sites in the solute and solvent molecules is picked up, the histogram of its radial distance is averaged with an appropriate normalization to give the site–site RDF. For example, when the solute and solvent is both H_2O (when one of the molecules in pure water is viewed as the "solute" and the others as the "solvent"), the O—O, O—H, and H—H RDFs are generated by the projections onto O—O, O—H, and H—H distances, respectively. It should be noted that the RDFs do not represent a simultaneous distribution of a set of site–site radial distances. In the case of water, the O—O RDF specifies only the O—O distance and the other distance information such as those for O—H and H—H is disregarded. Similarly, the O—H RDF does not contain explicit information about the O—O and H—H distances. In Figure 9.4, we show the O—O and O—H RDFs of water at 1 g/cm^3 and 25 °C. It is seen from the O—O RDF that the neighboring water molecules stay in the distance of ~2.8 Å. The O—H RDF shows that the intermolecular hydrogen-bonding distance is ~2 Å. The second peak of the O—O RDF is characteristic of water. In simple liquid, the second peak appears at about twice the distance for the first peak. In water, the second-peak position is ~1.6 times of the first-peak

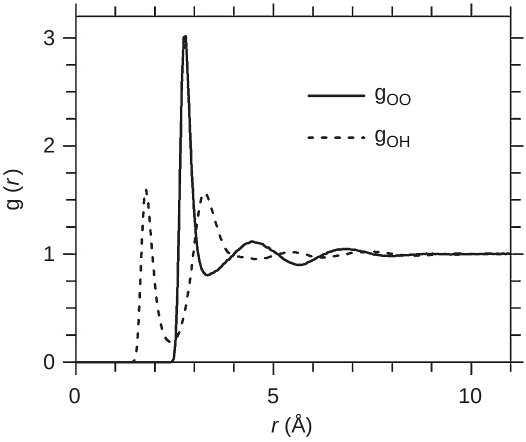

Figure 9.4 O—O and O—H radial distribution functions of water at 1 g/cm^3 and 25 °C.

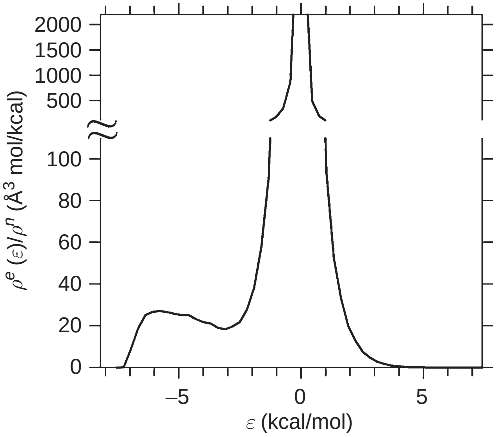

Figure 9.5 The distribution function of the pair interaction energy ε of water at 1 g/cm^3 and 25 °C. ρ^n is the (number) density in the system.

position. This provides a view that the ice-like structure persists even in liquid water.

Another useful distribution function is for the interaction pair energy. An example is shown in Figure 9.5 for water at 1 g/cm^3 and 25 °C. The peak at ~–6 kcal/mol corresponds to the intermolecular hydrogen bonding of water in the liquid state. In the high-energy regime, the distribution function vanishes. This reflects the excluded volume effect and is consistent with the fact the RDFs vanish at short distances.

Of course, the choice of the projecting function $P(\psi,\mathbf{x})$ of Eq. (39) is not unique. The choice depends on the purpose. For example, when the angle of the hydrogen bonding is of interest, it is most useful to adopt the hydrogen-bonding angle itself as $P(\psi,\mathbf{x})$ [63]. In general, no a priori criterion is present for preferable projection. The desirable form of projection can be based only upon the target quantity to be investigated.

3.3. Kirkwood charging formula and density functional theory

A connection between the solvation free energy $\Delta\mu$ and distribution function is provided by the Kirkwood charging formula [9,10,28]. In the present section, we describe the Kirkwood charging formula for a pairwise additive solute–solvent interaction. The Kirkwood formula is then transformed into a density functional form through partial integration. We briefly describe the DFT in the full coordinate representation.

The target quantity of the development is the solvation free energy. The solvation free energy $\Delta\mu$ is the free-energy change corresponding to the gradual insertion process of the solute molecule. In the classical (nonquantum) treatment of $\Delta\mu$, only the contribution from the potential energy is involved and the ideal (kinetic) contribution is excluded. Let ψ and $\mathbf{x}$ be the full coordinates of the solute and solvent molecules, respectively. We suppose that the solute–solvent intermolecular interaction of interest is pairwise additive and is written as $v(\psi,\mathbf{x})$. When the one-body energy of the solute including the intramolecular component is $\Psi(\psi)$ and the total solvent–solvent interaction energy is $U(\mathbf{X})$, $\Delta\mu$ is expressed as

$$\exp(-\beta\Delta\mu) = \frac{\int \mathrm{d}\psi d\mathbf{X} \exp\left(-\beta\left\{\Psi(\psi) + \sum_i v(\psi, \mathbf{x}_i) + U(\mathbf{X})\right\}\right)}{\int \mathrm{d}\psi d\mathbf{X} \exp\left(-\beta\left\{\Psi(\psi) + U(\mathbf{X})\right\}\right)}, \tag{40}$$

where $\mathbf{X}$ represents the solvent configuration collectively and β is the inverse of the product of the Boltzmann constant k_B and the temperature T. A restriction of attention to a certain set of solute intramolecular state can be made simply by the corresponding alteration of the domain of integration over ψ.

To formulate the Kirkwood charging formula, we introduce a set of intermediate states involving pairwise additive solute–solvent interaction. Let λ be the coupling parameter identifying the state and $u_\lambda(\psi,\mathbf{x})$ be the solute–solvent interaction potential at the coupling parameter λ. When $\lambda = 0$, the system is the pure solvent system and $u_0(\psi,\mathbf{x}) = 0$ (no solute–solvent interaction). When $\lambda = 1$, the solute interacts with the solvent at full coupling and $u_1(\psi,\mathbf{x}) = v(\psi,\mathbf{x})$. The form of $u_\lambda(\psi,\mathbf{x})$ at $0 < \lambda < 1$ is arbitrary. The Kirkwood charging formula is an integration over the coupling parameter and is expressed as

$$\Delta\mu = \int_0^1 \mathrm{d}\lambda \int \mathrm{d}\psi \mathrm{d}\mathbf{x} \frac{\partial u_\lambda(\psi, \mathbf{x})}{\partial \lambda} \rho^f(\psi, \mathbf{x}; u_\lambda), \tag{41}$$

where $\rho^f(\psi,\mathbf{x};u_\lambda)$ is the ensemble average of Eq. (38) in the presence of the solute–solvent interaction u_λ. The superscript f means that the function is represented over the full coordinate $(\psi,\mathbf{x})$.

The solvation free energy can be evaluated using the Kirkwood charging formula [9,10,28]. It introduces a set of intermediate states connecting the initial and final states of the gradual insertion process of the solute; the initial and final states correspond to the pure solvent system without the solute and the solution system of interest, respectively. In principle, the Kirkwood charging formula provides the "exact" solvation free energy under a given set of potential functions. Its implementation is expensive in practice, however, since a number of intermediate states need to be introduced. For the purpose of analyzing the solvation free energy on the molecular level, furthermore, it is necessary to express the solvation free energy in terms only of distribution functions in the solution and pure solvent systems of interest. Within the framework of the Kirkwood charging formula, the intermediate states are actually arbitrary and are employed for the convenience of formulation and computation. They are not of physical significance since the free energy is a state function.

A molecular description of the solvation free energy can be implemented by formulating a functional which expresses the solvation free energy in terms of distribution functions in the solution and pure solvent systems of interest. Distribution functions in the other systems should not be involved in the functional in order to assure that the free energy is given as a state function. The exact functional is not useful, however, since it is an infinite series of many-body distribution functions [62]. In practice, an approximate but accurate functional needs to be constructed which is expressed with few-body distribution functions in closed form. When such a functional is formulated and the distribution functions constituting the approximate functional are readily obtained by computer simulation, the solvation free energy can be determined and analyzed with reasonable computational load in terms of exact microscopic information of the systems of interest.

It is a statistical–mechanical theory of solutions to express the solvation free energy as a functional of distribution functions. Traditionally, the theory of solutions is formulated with a diagrammatic approach [28], in which an approximation is provided through a two-step procedure. In the first step, the free energy and/or distribution function is expanded with respect to the solute–solvent interaction potential function or its related function as an infinite, perturbation series. In the second step, a renormalization scheme is applied; a set of functions are defined through partial summation of the series and are employed for substitution to make the infinite series more tractable. An approximation is typically introduced simply by neglecting nontractable diagrams.

We adopt an alternative route to the distribution function theory. The approach is based upon the DFT. In this approach, the change of variables is conducted through Legendre transform from the solute–solvent interaction potential function to the solute–solvent distribution function or the solvent density around the solute. The (solvation) free energy is then expressed approximately by expanding the corresponding Legendre-transformed function with respect to the distribution function to some low order.

The starting point of the density functional treatment is the Kirkwood charging formula. The partial integration of the Kirkwood formula given by Eq. (41) provides

$$\begin{aligned}\Delta\mu &= \int \mathrm{d}\psi \mathrm{d}\mathbf{x} v(\psi,\mathbf{x})\rho^f(\psi,x;v) - \int_0^1 \mathrm{d}\lambda \int \mathrm{d}\psi \mathrm{d}\mathbf{x} u_\lambda(\psi,\mathbf{x}) \frac{\partial\rho^f(\psi,\mathbf{x};u_\lambda)}{\partial\lambda} \\ &\equiv \int \mathrm{d}\psi \mathrm{d}\mathbf{x} v(\psi,\mathbf{x})\rho^f(\psi,x) - F^f\left[\rho^f(\psi,\mathbf{x})\right],\end{aligned} \tag{42}$$

where the density functional F^f is defined in the second line of Eq. (42) and $\rho^f(\psi,\mathbf{x};v)$ at the potential v of interest is simply denotes as $\rho^f(\psi,\mathbf{x})$. $\Delta\mu$ and F^f are related to each other with Legendre transform since the map is proved to be one-to-one from the solute–solvent interaction potential to the distribution function [28]. An approximation can be devised by introducing the indirect part ω^f of the potential of mean force as

$$\rho^f_\lambda(\psi,\mathbf{x}) = \rho^f_0(\psi,\mathbf{x})\exp\left(-\beta\left(u\left(\psi,\mathbf{x};\rho^f_\lambda\right) + \omega^f\left(\psi,\mathbf{x};\rho^f_\lambda\right)\right)\right), \tag{43}$$

where $\rho^f{}_\lambda(\psi,\mathbf{x})$ is the distribution function at the coupling parameter λ. In Eq. (43), the dependence is written in terms of the distribution function $\rho^f{}_\lambda$, instead of the potential u_λ. This is possible due to the property of one-to-one correspondence. When the solvent–solvent correlation is absent (low-density limit), ω^f is zero. In other words, all the "complicated" solvent–solvent correlations are put into ω. Equations (42) and (43) lead exactly to

$$\begin{aligned} F^f[\rho^f(\psi,\mathbf{x})] = k_\mathrm{B}T\int \mathrm{d}\psi\mathrm{d}\mathbf{x}\Bigg[&\left(\rho^f(\psi,\mathbf{x}) - \rho^f_0(\psi,\mathbf{x})\right) - \rho^f(\psi,\mathbf{x})\log\left(\frac{\rho^f(\psi,\mathbf{x})}{\rho^f_0(\psi,\mathbf{x})}\right) \\ &- \beta\left(\rho^f(\psi,\mathbf{x}) - \rho^f_0(\psi,\mathbf{x})\right)\int_0^1 \mathrm{d}\lambda\omega^f(\psi,\mathbf{x};\rho^f_\lambda)\Bigg], \end{aligned} \tag{44}$$

where u_λ is taken so that $\rho^f{}_\lambda$ varies linearly against λ, and $\rho^f(\psi,\mathbf{x})$ and $\rho^f(\psi,\mathbf{x})$ denote the distribution functions at the coupling parameter $\lambda = 0$ and 1, respectively. Equation (44) is exact, and an approximation is introduced to the λ integral of ω^f. When ω^f is taken to vary linearly with λ, the HNC approximation is obtained. When exp $(-\beta\omega^f)$-1 is set to be linear, it is the PY approximation.

The above is the brief introduction to the DFT of solutions. The mathematical development is quite straightforward. The numerical implementation is difficult, however, in the full coordinate representation. As noted in Subsection 3.2, the full coordinate is multidimensional; the solute–solvent distribution is a function over high-dimensional configuration space and cannot be implemented in practice. To overcome the problem of dimensionality, it is necessary to introduce a projected coordinate. In Subsection 3.5, we introduce the ER and formulate the DFT in the ER.

3.4. Site–site radial distribution function and reference interaction site model

The method of RISM is based on the site–site RDFs. It introduces the "direct correlation functions" through the inverses of the correlation matrices for the site–site distance and formulates an approximate set of integral equation for the site–site RDFs by adopting “closure” relationships between the RDFs and direct correlation functions [26–28,64,65]. Compared to the molecular simulation method, the method of integral equation is much faster. The speed is achieved by restricting the attention only to the RDFs and adopting approximate closures. Furthermore, the solvation free energy is expressed in closed form for some types of closure relationships [64,65]. In this case, no reference to the intermediate states of the solute insertion process is required and the solvation free energy can be evaluated directly from the RDFs obtained from the integral equation. When a closed-form functional for the solvation free energy is given in terms of distribution functions, the functional not only provides an efficient route of computation, but also sets a basis for the molecular understanding with respect to the distribution functions.

A basic quantity in the RISM approach is the intermolecular site–site RDF $g_{\alpha\gamma}(r)$, where α and γ denotes interaction sites and r is the radial distance between the sites α and γ. An example is provided in Figure 9.4. Another basic quantity in RISM is the intramolecular correlation function $\omega_{\alpha\gamma}(r)$. This carries information of the molecular structure, and its Fourier-transformed form is expressed over the reciprocal coordinate k as

$$\omega_{\alpha\gamma}(k) = \frac{\delta_{\alpha\gamma} + (1 - \delta_{\alpha\gamma})\sin(kL_{\alpha\gamma})}{kL_{\alpha\gamma}}, \tag{45}$$

where $L_{\alpha\gamma}$ is the intramolecular distance between the sites α and γ. It should be noted that the set of $g_{\alpha\gamma}(r)$ is not a simultaneous distribution of the radial distances for various pairs of sites α and γ. Instead, they are a set of independent distributions over distinct site-site pairs. A similar remark also applies to $\omega_{\alpha\gamma}(r)$. $g_{\alpha\gamma}(r)$ is provided by projecting the full-coordinate distribution function generated from Eq. (38) onto the site–site radial distance between α and γ with appropriate normalization. Similarly, $\omega_{\alpha\gamma}(r)$ is a projection of the one-body distribution function in the full coordinate representation onto the radial distance between a pair of sites α and γ.

The RISM integral equation is formulated in terms of the site–site total correlation function $h_{\alpha\gamma}(r)$ and the site–site direct correlation function $c_{\alpha\gamma}(r)$. $h_{\alpha\gamma}(r)$ is defined from the site–site RDF $g_{\alpha\gamma}(r)$ as

$$h_{\alpha\gamma}(r) = g_{\alpha\gamma}(r) - 1, \tag{46}$$

and $c_{\alpha\gamma}(r)$ is introduced through the site–site Ornstein–Zernike (SSOZ, also called RISM) equation written as

$$h_{\alpha\gamma}(|\mathbf{r}-\mathbf{R}|) = \sum_{\beta,\kappa} \int \mathbf{d}\mathbf{x}\mathbf{d}\mathbf{y}\omega_{\alpha\beta}(|\mathbf{r}-\mathbf{x}|)c_{\beta\kappa}(|\mathbf{x}-\mathbf{y}|)[\omega_{\kappa\gamma}(|\mathbf{y}-\mathbf{R}|) + \rho h_{\kappa\gamma}(|\mathbf{y}-\mathbf{R}|)], \tag{47}$$

where the system is supposed to be a one-component, homogeneous fluid for simplicity and r is the density of the fluid. Equation (47) was first derived from the Ornstein–Zernike equation in the full coordinate representation by adopting the assumption that the direct correlation function in the full coordinate representation is given as a sum of the site–site direct correlation functions. Instead, Eq. (47) can be viewed as a definition of the site–site direct correlation functions [66,67]. In any case, another set of equations, called "closure" relationship, is necessary to obtain $h_{\alpha\gamma}(r)$ and $c_{\alpha\gamma}(r)$ with Eq. (47). In the original formulation [26], the PY-type form was adopted as

$$c_{\alpha\gamma}(r) = [h_{\alpha\gamma}(r) + 1]\left[1 - \exp\left(\beta v_{\alpha\gamma}(r)\right)\right], \tag{48}$$

where $v_{\alpha\gamma}(r)$ is the interaction potential between the sites α and γ and β is the inverse of the product of the Boltzmann constant and the temperature. In the extended version [27], the HNC-type approximation was employed with

$$h_{\alpha\gamma}(r) + 1 = \exp\left(-\beta v_{\alpha\gamma}(r) + h_{\alpha\gamma}(r) - c_{\alpha\gamma}(r)\right). \tag{49}$$

Equation (47) with Eq. (48) or (49) constitutes a self-consistent set of integral equations for $h_{\alpha\gamma}(r)$ and $c_{\alpha\gamma}(r)$. With the site–site potential $v_{\alpha\gamma}(r)$ and the intramolecular correlation function $\omega_{\alpha\gamma}(r)$ as inputs, the correlation functions $h_{\alpha\gamma}(r)$ and $c_{\alpha\gamma}(r)$ are given as outputs in the RISM treatment. Furthermore, the solvation free energy is expressed in closed form for certain types of closure relationships [64,65]. In this case, the integral equation provides not only the structural information $h_{\alpha\gamma}(r)$ but also the solvation free energy in an efficient manner. The RISM integral equation with PY-type or HNC-type closure can be solved with a variational procedure [26,27], though it is not of sound character from the standpoint of the DFT [67].

A drawback is present, of course, in any approximate method of solutions. Under a given set of potential functions, the molecular simulation gives the exact distribution functions when it is done long enough. In contrast, since the closure relationship is approximate, the RDF obtained from the integral equation method is approximate. The solvation free energy calculated from the integral equation theory has two sources of errors. One is due to the approximate nature of the potential functions (force field), and the other comes from the approximation involved in the integral equation.

The drawbacks characteristic of RISM and its variants are related to the fact that they do not treat the whole molecule as a single unit and view a molecule as a collection of interaction sites. The method is thus applicable only when the potential function is of site–site form. Indeed, Eqs. (47)–(49) require a set of potentials in the site–site form as inputs. As a consequence, the electronic distribution cannot be treated in the cloud-like form as implemented in quantum theories, but needs to be contracted into a set of point charges. In addition, the integral equation is ill-behaved unless all of the interaction sites carry the repulsive core explicitly. For example, many of potential functions of H_2O do not assign a repulsive core at the H-site. This is simply because the repulsive core for the O-site is large enough that other molecules cannot come too close to the H-site. The repulsive core of the H-site is buried within the O-site core and is not necessary to be treated explicitly at the level of potential functions. In RISM, however, a core parameter needs to be assigned to the H-site, too. The core parameter actually dictates the resulting solvation free energy sensitively and acts as an adjustable parameter in the method. Another, related problem is so-called the "problem of auxiliary site." The solution to the RISM integral equations exhibits unphysical dependence on the presence of auxiliary sites which simply label points in a molecule and make no contribution to the intermolecular interaction. This type of difficulty is absent when the whole molecule is treated as a single unit. The difficulty arises when a molecule is treated as a collection of sites. In RISM, the correlation between a pair of sites is described at the two-body level for both the intramolecular and intermolecular ones. Since the sites in a molecule are tightly bound with one another, a partial incorporation of the intramolecular correlation is not desirable. This point is exemplified when the density is low. The RISM integral equations are not exact in the limit of zero solvent density and are not suitable to evaluate the solvation free energy in a low-density fluid. It is well-known in this instance, too, that the low-density limit is given exactly when the whole molecule is treated as a single unit in the full coordinate representation [28]. Finally, since the molecular structure is an input in the RISM approach, an additional scheme needs to be devised to deal with flexible molecules. Equations (47)–(49) take the intramolecular correlation functions $\omega_{\alpha\beta}(r)$ (or the intramolecular distance $L_{\alpha\beta}$) as inputs, and the variation of $\omega_{\alpha\beta}(r)$ in response to intermolecular interaction can be incorporated by formulating another set of (approximate) equations.

In the commonly used RISM approach, the solvation free energy is often expressed in closed form in terms of site–site RDFs. An improvement of the approach may then be possible through combination with the molecular simulation; the RDFs are exact under the used set of potential functions when they are calculated from the molecular simulation, instead of the integral equation. This line of approach is developed by Kast and Truong [68–70], and the computational efficiency is achieved compared to the FEP and TI methods. A special procedure is needed, however, to handle the intramolecular correlation matrices in the range of small reciprocal vector (large distance). When the reciprocal vector approaches zero, the intramolecular correlation matrices becomes ill-conditioned and the calculation procedure suffers from numerical instability.

The above drawbacks of RISM and its variants are well documented since their first formulations [26,28,66,67]. They are all related to the point that a molecule is treated as a collection of sites. In the method of ER introduced in Subsection 3.5, each of the solute and solvent molecules is taken to be a single unit as a whole, and those drawbacks vanish.

3.5. Method of energy representation

In the method of energy representation (ER) [31], the projecting function $P(\psi,\mathbf{x})$ of Eq. (39) is taken to be the solute–solvent pair interaction energy. Figure 9.5 is an example of the distribution function in the ER. To introduce the ER, it is necessary to specify the solute–solvent interaction potential v of interest. Of course, v is a function of the solute configuration ψ and the solvent configuration $\mathbf{x}$. The instantaneous distribution $\hat{\rho}^e$ is defined as

$$\hat{\rho}^e(\varepsilon) = \sum_i \delta[v(\psi, \mathbf{x}_i) - \varepsilon], \tag{50}$$

where the sum is taken over the solvent molecules and a superscript e is attached to emphasize that a function is represented over the energy coordinate. The distribution functions in the ER are generated from the averages of products of $\hat{\rho}^e$ in the system of interest.

In the ER, the DFT can be formulated by restricting the set of solute–solvent interaction potentials $u_\lambda(\psi,\mathbf{x})$ to those which are constant over an equienergy surface of $v(\psi,\mathbf{x})$. In this case, when the value of $v(\psi,\mathbf{x})$ is denoted as ε, the intermediate states can be written as $u_\lambda(\varepsilon)$. At the end points ($\lambda=0$ and 1), $u_0(\varepsilon)=0$ and $u_1(\varepsilon)=\varepsilon$ since $v(\psi,\mathbf{x})$ itself is the potential function in the solution system of interest. It is then possible to show that the Kirkwood charging formula is given by

$$\Delta\mu = \int_0^1 \mathrm{d}\lambda \int \mathrm{d}\varepsilon \frac{\partial u_\lambda(\varepsilon)}{\partial\lambda} \rho^e(\varepsilon; u_\lambda), \tag{51}$$

where $\rho^e(\varepsilon;u_\lambda)$ is the ensemble average of Eq. (50) in the presence of the solute–solvent interaction u_λ. The superscript e is attached to mean the representation over the energy coordinate e. The Legendre transform is also possible as

$$\Delta\mu = \int \mathrm{d}\varepsilon u_1(\varepsilon)\rho^{\mathrm{e}}(\varepsilon; v) - \int_0^1 \mathrm{d}\lambda \int \mathrm{d}\varepsilon u_\lambda(\varepsilon) \frac{\partial \rho^e(\varepsilon; u_\lambda)}{\partial\lambda} \equiv \int \mathrm{d}\varepsilon\varepsilon\rho^e(\varepsilon) - F^e[\rho^e(\varepsilon)], \tag{52}$$

and the indirect part ω^e of the potential of mean force in the ER can be introduced correspondingly simply by rewriting $\mathbf{x}$ of Eq. (43) with ε as

$$\rho^e_\lambda(\varepsilon) = \rho^e_0(\varepsilon)\exp\Big(-\beta\Big(u(\varepsilon;\rho^e_\lambda) + \omega^e(\varepsilon;\rho^e_\lambda)\Big)\Big), \tag{53}$$

where ${\rho^e}_\lambda(\varepsilon)$ is the distribution function at the coupling parameter λ and β is the inverse of the product of the Boltzmann constant k_B and the temperature T. The density functional is then expressed exactly as

$$F^e[\rho^e(\varepsilon)] = k_{\mathrm{B}}T\int \mathrm{d}\varepsilon\left[\left(\rho^e(\varepsilon)-\rho_0^e(\varepsilon)\right)-\rho^e(\varepsilon)\log\left(\frac{\rho^e(\varepsilon)}{\rho_0^e(\varepsilon)}\right)\right.$$
$$\left.-\beta\left(\rho^e(\varepsilon)-\rho_0^e(\varepsilon)\right)\int_0^1 \mathrm{d}\lambda\omega^e(\varepsilon;\rho_\lambda^e)\right], \tag{54}$$

when u_λ is taken so that ${\rho^e}_\lambda$ varies linearly against λ. Note the parallelism of Eqs. (51)–(54) to Eqs. (41)–(44). In Eqs. (53) and (54), u and ω are written to depend on the distribution function ${\rho^e}_\lambda$, instead of the potential u_λ, by virtue of the property of one-to-one correspondence [31]. In the ER, the HNC-type and PY-type approximations are obtained by assuming the linear dependencies of ω^e and $\exp(-\beta\omega^e)$-1 on λ, respectively. Although Eq. (44) is hard to implement due to the high-dimensionality of (ψ,**x**), Eq. (54) is straightforward to handle since ε is one-dimensional.

In the currently used version of the method of ER [30,32,33], the solvation free energy $\Delta\mu$ is approximately expressed in terms of distribution functions constructed from $\hat{\rho}^e$ in the solution and reference solvent systems. In our treatments, the solution system refers to the system in which the solute molecule interacts with the solvent under the solute–solvent interaction v of interest at full coupling. In the solution, the average distribution ρ^e of the v value is relevant in the approximate construction of $\Delta\mu$ and is given by

$$\rho^e(\varepsilon) = \left\langle\hat{\rho}^e(\varepsilon)\right\rangle, \tag{55}$$

where $\langle\cdots\rangle$ represents the ensemble average in the solution system of interest. On the other hand, the reference solvent system denotes the system in which the solute does not interact with the solvent and the solvent configuration is generated only by the solvent–solvent interaction. At an instantaneous configuration of the reference solvent system, $\hat{\rho}^e$ is constructed by placing the solute molecule in the system as a test particle. The average distribution ρ_0^e and the correlation matrix χ_0^e then appear in the approximate functional for $\Delta\mu$ and are expressed, respectively, as

$$\rho_0^e(\varepsilon) = \left\langle\hat{\rho}^e(\varepsilon)\right\rangle_0, \tag{56}$$

and

$$\chi_0^e(\varepsilon,\eta) = \left\langle\hat{\rho}^e(\varepsilon)\hat{\rho}^e(\eta)\right\rangle_0 - \langle\hat{\rho}^e(\varepsilon)\rangle_0\langle\hat{\rho}^e(\eta)\rangle_0, \tag{57}$$

where $\langle\cdots\rangle_0$ represents the ensemble average in the reference solvent system. In the sampling corresponding to $\langle\cdots\rangle_0$, the solute and solvent degrees of freedom are uncoupled from each other in the probability distribution.

An approximate functional for $\Delta\mu$ is derived in Ref. [32]. The functional is constructed by adopting the PY-type approximation in the unfavorable region of the solute–solvent interaction and the HNC-type approximation in the favorable region. $\Delta\mu$ is then given by a set of definitions and equations listed as

$$w^e(\varepsilon) = -k_B T \log\left(\frac{\rho^e(\varepsilon)}{\rho_0^e(\varepsilon)}\right) - \varepsilon, \tag{58}$$

$$w_0^e(\varepsilon) = -k_B T \int d\eta \left(\frac{\delta(\varepsilon-\eta)}{\rho_0^e(\varepsilon)} - (\chi_0^e)^{-1}(\varepsilon,\eta)\right)\left(\rho^e(\eta) - \rho_0^e(\eta)\right), \tag{59}$$

$$\begin{aligned}\Delta\mu = \int d\varepsilon \rho^e(\varepsilon) - k_B T \int d\varepsilon \Bigg[\left(\rho^e(\varepsilon) - \rho_0^e(\varepsilon)\right) - \rho^e(\varepsilon)\log\left(\frac{\rho^e(\varepsilon)}{\rho_0^e(\varepsilon)}\right) \\ - \{\alpha(\varepsilon)F(\varepsilon) + \left(1-\alpha(\varepsilon)\right)F_0(\varepsilon)\}\left(\rho^e(\varepsilon) - \rho_0^e(\varepsilon)\right)\Bigg],\end{aligned} \tag{60}$$

$$F(\varepsilon) = \begin{cases} \beta w^e(\varepsilon) + 1 + \dfrac{\beta w^e(\varepsilon)}{\exp\left(-\beta w^e(\varepsilon)\right) - 1} & (\text{when } w^e(\varepsilon) \leq 0) \\ \dfrac{1}{2}\beta w^e(\varepsilon) & (\text{when } w^e(\varepsilon) \geq 0), \end{cases} \tag{61}$$

$$F_0(\varepsilon) = \begin{cases} -\log\left(1 - \beta w_0^e(\varepsilon)\right) + 1 + \dfrac{\log\left(1 - \beta w_0^e(\varepsilon)\right)}{\beta w_0^e(\varepsilon)} & (\text{when } w_0^e(\varepsilon) \leq 0) \\ \dfrac{1}{2}\beta w_0^e(\varepsilon) & (\text{when } w_0^e(\varepsilon) \geq 0), \end{cases} \tag{62}$$

$$\alpha(\varepsilon) = \begin{cases} 1 & (\text{when } \rho^e(\varepsilon) \geq \rho_0^e(\varepsilon)) \\ \left(\dfrac{\rho^e(\varepsilon) - \rho_0^e(\varepsilon)}{\rho^e(\varepsilon) + \rho_0^e(\varepsilon)}\right)^2 & (\text{when } \rho^e(\varepsilon) \leq \rho_0^e(\varepsilon)). \end{cases} \tag{63}$$

When Eqs. (58)–(63) are used to evaluate the solvation free energy, the inputs are the three energy distribution functions ρ^e, ρ_0^e, χ_0^e given by Eqs. (55)–(57), respectively. ρ^e is obtained from a simulation of the solution system of interest, and ρ_0^e and χ_0^e are constructed with a simulation of the reference solvent system. The approximate scheme provided by

Eqs. (55)–(63) does not require simulations at the intermediate states of solute insertion. This leads to substantial reduction in free-energy calculation. On the other hand, when Eqs. (58)–(63) are used with ρ^e, ρ_0^e, χ_0^e obtained from molecular simulation, a possible artifact in simulation arising, for example, from the use of periodic boundary condition and/or the handling scheme of long-range electrostatic interaction is generally retained.

It should be noted that when the solute molecule is inserted into the reference solvent system, it often overlaps with solvent molecules. The overlapping configurations contribute to ρ_0^e and χ_0^e at large energy coordinates and accounts for the excluded volume effect in the solvation free energy. In addition, Eqs. (58)–(63) show that the ε value itself acts only as an index for the distribution functions ρ_0^e and χ_0^e when ε is large enough and the corresponding ρ^e is (essentially) zero. The ε value in the excluded volume region is not used in the calculation of $\Delta\mu$, except in the construction of ρ_0^e and χ_0^e; $\Delta\mu$ calculation in the large ε region is not affected by the change of the ε value as far as ε corresponds to the excluded volume. To see the origin of this property, we consider a family of solute–solvent interactions $u(\varepsilon)$, as done around Eq. (50), which are constant over an equienergy surface of the potential $v(\psi,\mathbf{x})$ of interest. It is possible to show through a line parallel to the blip-function method [28] that

$$\frac{\delta(\Delta\mu)}{\delta \exp\left(-\beta u(\varepsilon)\right)} = -k_{\mathrm{B}}T \exp\left(\beta u(\varepsilon)\right)\rho^e(\varepsilon; u), \tag{64}$$

where $\rho^e(\varepsilon;u)$ is the ensemble average of Eq. (50) in the presence of the solute–solvent interaction $u(\varepsilon)$. Here we restrict our attention only to the ε region corresponding to the excluded volume and the set of $u(\varepsilon)$ which are prohibitively large in that ε region. Then, the Boltzmann factor $\exp(-\beta u(\varepsilon))$ is exponentially small in this region. Further, for a change of $u(\varepsilon)$ within the set, the corresponding variation of $\exp(-\beta u(\varepsilon))$ is also vanishingly small. It then follows that such variations of $u(\varepsilon)$ do not change the $\Delta\mu$ value. This is shown by the fact that the right-hand side of Eq. (64) remains to be finite even when $u(\varepsilon)$ is large as is generally proven in Ref. [28]. Thus, the choice of the $u(\varepsilon)$ form has no effect on the $\Delta\mu$ calculation in the excluded-volume region.

In Figure 9.6, the approximate values of the solvation free energy $\Delta\mu$ for typical solute molecules in solvent water are compared to the corresponding exact values obtained from the FEP method. The (solvent) density of 1.0 g/cm^3 and the temperature of 25 °C is an ambient state, and the densities of 1.0, 0.6, and 0.2 g/cm^3 at 400°C correspond to high-, medium-, and low-density supercritical states. The good agreement is observed between the approximate and exact values. The agreement is particularly notable at the medium- and low-density states of 0.6 and 0.2 g/cm^3 and 400°C. When the solute is ionic, the density at the state of 0.2 g/cm^3 and 400°C is not yet low

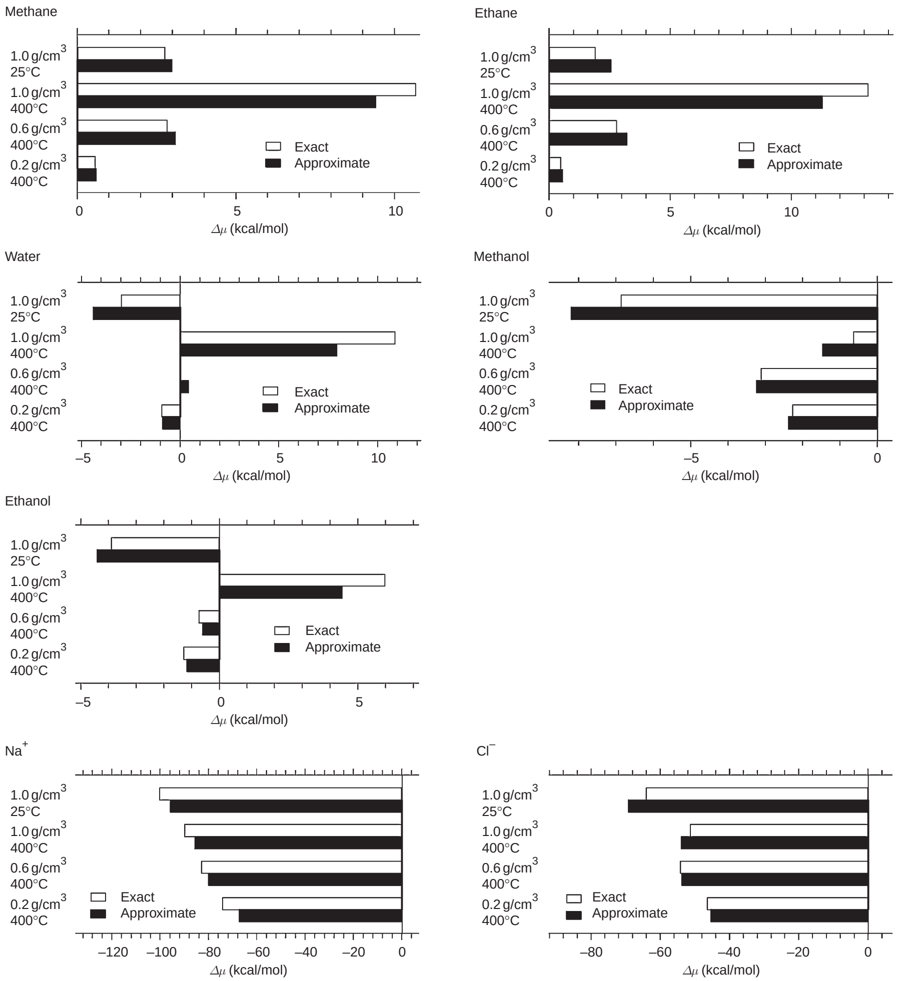

Figure 9.6 The solvation free energy $\Delta\mu$ calculated by the approximate method of energy representation and the exact, free-energy perturbation method. The thermodynamic state is specified by the solvent density and temperature.

in the sense, for example, that the hydration number at that state is comparable to the numbers at ambient states [71,72]. Even in this case, our approximate procedure is effective in determining the solvation free energy. The solvation free energies of water at 1.0 g/cm^3 and 400°C and of methanol and ethanol at 0.6 g/cm^3 and 400°C are rather small in magnitude. These behaviors are caused by the balance between the favorable and unfavorable contributions of the solute–solvent interactions, and are well reproduced by our approximate method. Therefore, the single functional given by

Eqs. (55)–(63) provides an accurate and efficient route to the solvation free energy for various types of solutes over a wide range of thermodynamic conditions.

By virtue of Eq. (40), the average sum $<u>$ of the solute–solvent interaction energy in the solution system of interest is smaller than or equal to $\Delta\mu$. This means that the density functional F^e is always nonpositive for any solute–solvent distribution function. Actually, the density functional is a measure of the "difference" between ρ^e in solution and ρ_0^e in the reference solvent. It is zero only when $\rho^e = \rho_0^e$. The density functional is expected to be more negative when ρ^e and ρ_0^e appear more differently. On the other hand, the first term of Eq. (52) is equal to $<u>$, and is more negative when ρ^e is more populated in the low-energy region of ε. A typical behavior is that ρ_0^e reduces monotonically toward the low-energy tail. Thus, the first term of Eq. (52) is more negative when ρ^e and ρ_0^e are more different. This indicates that the first and second terms of Eq. (52) fluctuate to the same direction through the variation of r^e. It is then expected that $\Delta\mu$ of Eq. (52) converges faster in molecular simulation than its components expressed as the first and second terms of Eq. (52). Indeed, usual experience is that when (an approximate form of) Eq. (54) is employed, the solvation free energy $\Delta\mu$ converges faster than the average sum $<u>$ of the solute–solvent interaction energy in solution.

In the ER, the interaction energy between the solute and solvent is adopted for the one-dimensional coordinate of the distribution functions, and a functional for the solvation free energy is constructed from energy distribution functions in the solution and reference solvent systems of interest. The introduction of the energy coordinate for distribution functions is a kind of coarse-graining procedure for reducing the information content of the solute–solvent configuration. Since the set of configurations (structures) with the equal solute–solvent interaction energies are grouped into a unit in the ER, any approximate functional built in terms of energy distribution functions cannot violate the statistical-mechanical principle that the configurations with the same solute–solvent interaction energies contribute to the solvation free energy with the equal weights.

As seen in Eq. (50), each of the solute and solvent molecules is taken as a single unit in the ER. The molecule is treated as a whole, while the coordinate for the distribution functions is one-dimensional. No explicit reference is made to the detail of the molecular structure by focusing on the interaction energy. The following advantages then emerge in the method of ER.

First, the method is straightforwardly applicable to molecules with intramolecular flexibility. The implementation is indifferent whether the molecule is rigid or flexible. The information of structural fluctuation of the molecule is adsorbed when the energy coordinate is introduced by

Eq. (50). For large molecules constituting micellar, membrane, and protein systems, it is not allowed to neglect the molecular flexibility. In the method of ER, an additional and/or separate scheme is not necessary to be formulated for large, flexible species.

Second, the treatment of inhomogeneous system and clusters is straightforward. So far, the formulation does not assume the system homogeneity and the thermodynamic limit. The application to inhomogeneous and/or finite systems is then possible without modification. The binding of a molecule to such nanoscale structures as micelle, membrane, and protein can be viewed as a solvation in an inhomogeneous and finite, mixed solvent [73,74]. The method of ER can thus be a useful approach to intermolecular correlation and association important in biological and interface sciences. Example applications to micellar and membrane systems are presented in Subsection 3.6.

Third, an accurate treatment is possible for supercritical fluid. In supercritical fluid, the solvent density and temperature can varied over wide range and the solvent effect may act as a key to control a chemical process. It is well-known that supercritical fluid can be described accurately when the whole molecule is treated as a single unit [28]. A multidimensional representation is necessary, however, in the usual coordinate space. By introducing the energy as the coordinate for distribution functions, the whole molecule can be taken as a single unit with keeping the description one-dimensional. The approximate functional given by Eqs. (55)–(63) incorporates the intermolecular correlation at the two-body level. The solvation free energy obtained is then exact to second order in the solvent density. Since the method is exact in the low-density regime, a formulation of a good approximation in the high-density regime leads to an accurate description over a wide range of solvent density.

Finally, the combination with the QM/MM methodology can be performed. In QM/MM calculation, the many-body effect is introduced for the solute–solvent interaction and is beyond the applicability of conventional theories of solutions. In the method of ER, the fluctuation of the electronic state in response to the environment is viewed as a fluctuation of intramolecular degrees of freedom of the QM solute. The evaluation becomes feasible for the free energy for the many-body effect of the electronic fluctuation. In addition, Eq. (50) makes no reference to the functional form of the potential function. It refers only to the value of the potential energy, and there is no need for deterioration or modification of the electronic-state calculation. Thus, the treatment is possible for an arbitrary distribution of charges. The contraction to a set of point charges is not necessary, and the effect of the diffuse (cloud-like) nature of electronic distribution can now be determined. The detail of the combination with the QM/MM methodology is given in Subsection 4.3.

3.6. Application to molecular binding into micelle and lipid-membrane systems

Micelle is a self-assembled aggregate of amphiphilic surfactants in water. It involves a hydrophobic core and provides a favorable environment for organic compounds. Upon formation of a micelle, the solubility is often enhanced for an organic compound which is insoluble or sparingly soluble in water. This phenomenon is called solubilization, and is a most important function of a micelle.

Membrane is a soft, self-organizing aggregate of amphiphilic lipids in aqueous solution. It distinguishes one side of the solution from the other, and plays important roles in distribution and transport of a molecule. The key process toward the membrane function is the binding of a molecule into membrane.

On the microscopic level, the solubilization and membrane-binding are common in that they correspond to the transfer of a molecule from bulk water to the inside (or surface) of a nanoscale, self-organizing structure in solution. In both cases, the process is quantified by the (standard) free energy of binding. The binding free energy is determined by the cooperation and/or competition of the interactions among the surfactant or lipid, the solute molecule to be bound, and the solvent (water and cosolvents if present). A unified framework for the free-energy analysis at atomic resolution is thus desirable to be developed for the molecular understanding and control of the binding in micelle and membrane.

The basic idea of our scheme is to view a micellar or membrane solution as a mixed solvent. The surfactant or lipid molecules are treated not as solute species, but as part of the mixed solvent system. The molecule to be bound into the micelle or membrane is the only species regarded as the solute. In this view, the solvation free energy of the solute molecule in a micellar or membrane solution denotes the free-energy change for turning on the interactions of the solute with the solvent water, surfactants or lipids, and counterions if present. The binding is described by the difference in the solvation free energy between the micellar or membrane system and the neat solvent (pure water) system. When the host (micelle or membrane) is dilute, in particular, it is natural to set the origin of the solution at (or near) the center of the host. The mixed solvent system then consists of the surfactant or lipid molecules forming the host, water, and distributed counterions (when the surfactant or lipid is ionic). Water is deficient in the interior of the host, and the surfactant or lipid molecules belonging to the host are localized around the origin. The mixed solvent is thus inhomogeneous even before the solute insertion. When the host is micelle, furthermore, the number of surfactants is finite since the aggregation number is typically 10^2–10^4. The micellar solution is partially finite in the sense that the number is finite for the surfactant (and counterion) involved as solvent species in the dilute micellar solution. The point of our scheme is to evaluate the solvation free energy of a solute in an inhomogeneous and partially finite, mixed solvent system.

Even when the system is inhomogeneous and partially finite, a formally exact free-energy calculation is possible by the standard FEP and TI methods [9,10,28]. These methods are notorious for the heavy computational demand, however, since an explicit reference needs to be made to the intermediate states of the gradual variation process of the system. We combine the large-scale molecular simulation with the method of ER to evaluate the binding free energy.

The surfactant employed is sodium dodecyl sulfate (SDS) and the lipid is 1,2-dimyristoyl-*sn*-glycero-3-phosphatidylcholine (DMPC). Their structures are illustrated in Figure 9.7. The solute molecule is methane, benzene, and ethylbenzene in the micelle simulation, and is CO, benzene, and ethylbenzene in the membrane simulation. The computational procedures are fully described in Refs. [73,74].

In Figure 9.8, we show the density profile of SDS micelle and DMPC bilayer. Figure 9.8a gives the densities of the hydrophobic tail, the headgroup, and water as functions of the distance *r* from the micellar center identified as the center of mass of the dodecyl sulfate anions. Since the eccentricity of the SDS micelle is small, it is natural to divide the micellar

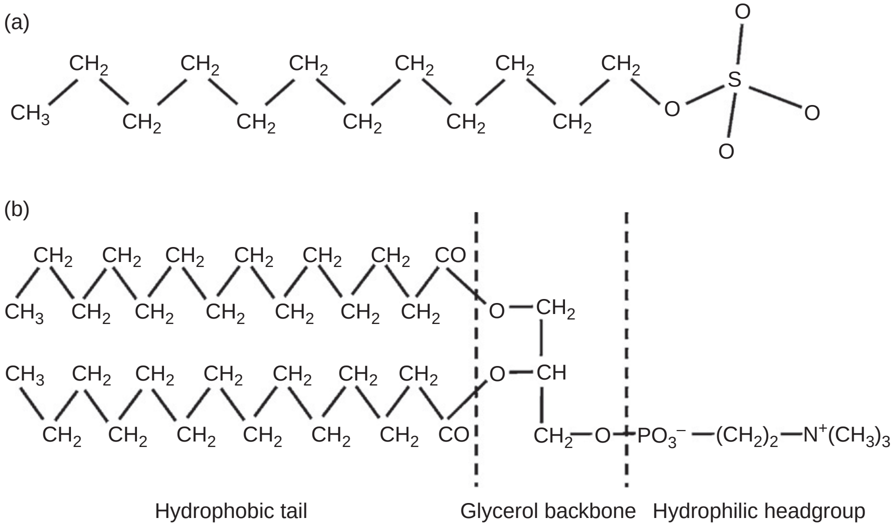

Figure 9.7 (a) The structure of the dodecyl sulfate anion. (b) The structure of DMPC. The molecule is divided into three portions of the hydrophobic tail, glycerol backbone, and hydrophilic headgroup. In the present work, the division is done as denoted in the figure, though the diving scheme is always of some ambiguity.

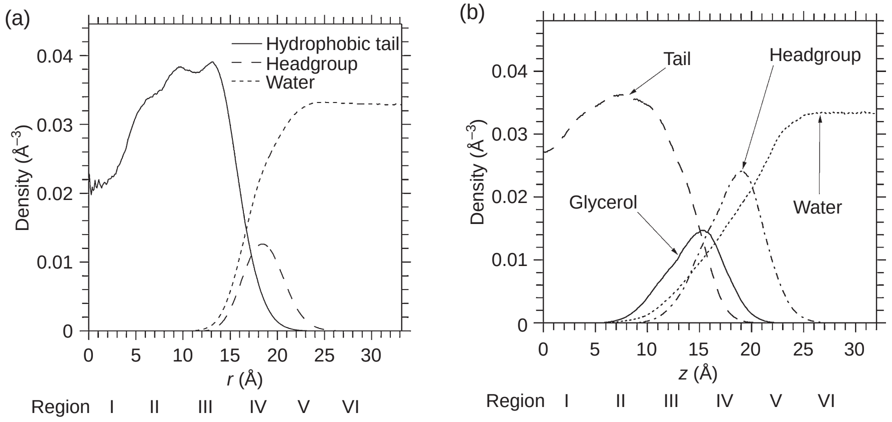

Figure 9.8 (a) The densities of the hydrophobic tail, the headgroup, and water in the SDS micellar system as functions of the distance r from the center of mass of the dodecyl sulfate anions forming the micelle. The density of the hydrophobic tail refers to the sum of the (number) densities of the methyl and methylene groups of the dodecyl sulfate anion, and the density of the headgroup is the sum (number) density of the sulfur and oxygen atoms. The water density is expressed with respect to the center of mass of the water molecule. Six regions are introduced by dividing the domain of $r < 30$ Å with an interval of 5 Å, and are numbered I ... VI from the micelle inside to outside. (b) The densities of the hydrophobic tail, the glycerol backbone, the hydrophilic headgroup, and water in the DMPC membrane system as functions of the separation z along the z-axis from the center of mass of the DMPC molecules. The densities obtained over the positive and negative z-domains are averaged, and the averaged density is shown against the positive z-abscissa. The densities of the tail and glycerol refer to the sums of the (number) densities of the carbons and oxygens contained in the tail and glycerol portions of Figure 9.7b, respectively, and the density of the headgroup is the sum of the (number) densities of the carbons, oxygens, nitrogen, and phosphorus in the corresponding portion. The water density is expressed with respect to the center of mass of the water molecule. Six regions are introduced by dividing the domain of $z < 30$ Å with an interval of 5 Å, and are numbered I ... VI from the membrane inside to outside.

system into a set of regions on the basis of Figure 9.8a. We introduce six regions in terms of the center-of-mass distance r of the solute from the micellar center by concentrically dividing the domain of $r < 30$ Å with an equal interval of 5 Å. In the following, the regions are numbered I ... VI from the micelle inside to outside. According to Figure 9.8a, the regions I–III corresponds to the hydrophobic core, where water is scarcely present. The region IV refers to the headgroup region in contact with water, and is the transition region from the hydrophobic core to the aqueous region outside the micelle represented by the regions V and VI.

In the membrane system simulated, the z-axis is taken to be normal to the plane of the DMPC bilayer and $z = 0$ is set to the z-coordinate of the center of mass of the DMPC molecules. In Figure 9.8b, we show the densities of the hydrophobic tail, the glycerol backbone, the hydrophilic headgroup, and water obtained from the simulation of DMPC and water without solute. Since the (converged) distribution of particles is symmetric against the reflection at $z=0$, the density averaged over the positive and negative z–domains is displayed only against the positive z -abscissa. As done for the SDS micelle, we introduce six regions of z by dividing the domain of $|z| < 30$ Å with an equal interval of 5 Å. The regions are numbered I . . . VI from the membrane inside to outside. According to Figure 9.8b, the regions I and II correspond to the hydrophobic interior, where water is scarcely present. The glycerol and headgroup are mainly located in the regions III–V, where the water density gradually varies. The density profile recovers the bulk behavior in the region VI, and the thickness of (one leaflet of) the DMPC layer is ~20 Å.

In Figure 9.9, we show the solvation free energy $\Delta\mu$ of the solute in the regions I–VI and in the bulk water. The bulk denotes the region far from the host (micelle or membrane), and $\Delta\mu$ in the bulk is the solvation free energy in neat water. Evidently, each hydrophobic solute is free-energetically stabilized in the inside of the host.

When the host is micelle, the distribution within the hydrophobic interior (regions I–III) is rather diffuse. For benzene and ethylbenzene in the micelle, the $\Delta\mu$ difference between the regions IV and I–III shows that these solutes are localized in the hydrophobic core of the micelle. When the solute is methane and is bound into the SDS micelle, in contrast, the $\Delta\mu$ difference

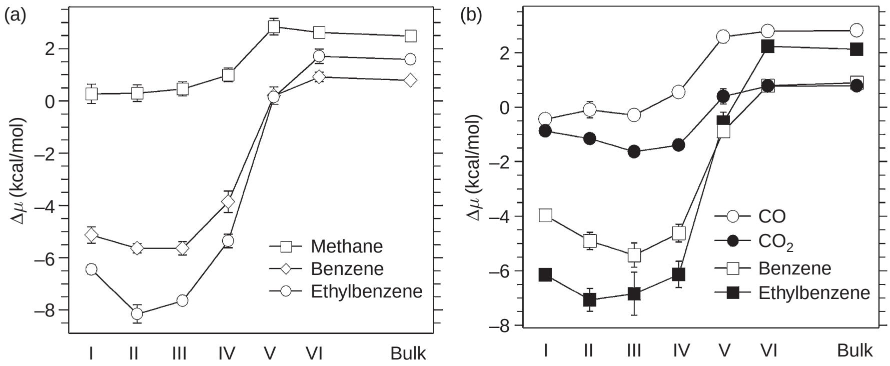

Figure 9.9 The solvation free energy $\Delta\mu$ in the regions I–VI and in the bulk for (a) the SDS micellar and (b) the DMPC membrane systems. The bulk denotes the region far from the host, and $\Delta\mu$ in the bulk is equal to the solvation free energy of the solute inserted into neat water. The error bar is expressed at 95% confidence level, and is smaller than the size of the corresponding data symbol when it is not shown. The lines connecting the data are drawn for eye guide.

is small and the probability of finding the solute is appreciable also in the headgroup region. Thus, the solubilization of benzene and ethylbenzene is more sharply characterized as a transfer from the aqueous to hydrophobic environment. For all the solutes examined, the distribution is negligible in the aqueous regions V–VI outside the micelle. This is a support to the pseudophase model, and the support is stronger for benzene and ethylbenzene.

When the host is membrane, Figure 9.9b shows that $\Delta\mu$ varies by $\sim k_{\mathrm{B}}T$ within the regions I–IV. A strong tendency of localization is not observed, and the hydrophilic portion of DMPC also interacts with the hydrophobic solute. In the SDS micelle, benzene and ethylbenzene are more strongly localized in the hydrophobic interior. This contrast corresponds, as evidenced in the molecular structure of Figure 9.7, to the fact that DMPC involves methylene and methyl groups in the hydrophilic segment unlike SDS.

4. COMBINATION OF QUANTUM CHEMICAL METHOD WITH THEORY OF SOLUTIONS

We have described in Section 2 the techniques related to the quantum chemical simulations of many-particle systems, while Section 3 has been devoted to describe methodologies to compute free energy on the basis of the DFT of solutions. As discussed in Introduction, determination of the dominant reaction path in a condensed system necessitates the large-scale simulations based on the quantum chemistry and also a statistical mechanical approach to evaluate the free-energy change associated with the reaction. From this point of view in this section we shall introduce our recent development termed QM/MM-ER which combines a method of the quantum chemistry and a novel theory of solutions. The several preceding sections will serve to give concise reviews for other established approaches, namely PCM [24,25] and RISM-SCF [29], to reveal the characteristics of these methods.

4.1. Polarizable continuum model method

At present, the PCM is the most popular approach to take into account the solvation effects in quantum chemical calculations because of its practical efficiency. In the PCM scheme a solvent is approximated by a continuum with uniform dielectric constant ε which characterizes the solvent of interest and, then a QM solute enclosed in a void cavity is immersed in the continuum. The cavity is a fundamental concept in the continuum model, and its shape and size are crucial to the evaluation of the free energy of solvation. The PCM cavity is constructed by the superposition of atomic spheres with radii determined based on the van der Waals values. Several sets of van der Waals radii are available in the Gaussian package [75]. With the method of apparent surface charge (ASC) in the framework of PCM the solvent effects on the QM solute is given by the electrostatic potential due to the charge distribution induced on the cavity surface.

We illustrate here the procedure to determine the polarization charge of the continuum in the vicinity of the cavity surface according to the fundamental electromagnetism. Suppose that **P**(**r**) is a polarization vector at a point **r** near the surface, the surface charge σ at **r** is simply expressed as

$$\sigma(\mathbf{r}) = -\mathbf{P}(\mathbf{r}) \cdot \mathbf{n}(\mathbf{r}), \tag{65}$$

where **n** is the normal vector on the cavity surface. The polarization vector **P** can be related to the electrostatic field **E**(**r**), thus,

$$\mathbf{P}(\mathbf{r}) = \frac{\varepsilon - 1}{4\pi}\mathbf{E}(\mathbf{r}) = -\frac{\varepsilon - 1}{4\pi}\nabla\Big(\Phi_{\mathrm{QM}}(\mathbf{r}) + \Phi_\sigma(\mathbf{r})\Big), \tag{66}$$

where Φ_{QM} and Φ_σ are the electrostatic potentials due to the QM solute and the surface charge, respectively. Specifically, Φ_σ is written as,

$$\Phi_\sigma(\mathbf{r}) = \int_\Omega \mathrm{d}\mathbf{s}\, \frac{\sigma(\mathbf{s})}{|\mathbf{r} - \mathbf{s}|}, \tag{67}$$

where Ω represents the cavity surface. From Eqs. (65), (66), and (67) we have an implicit equation for σ as,

$$\sigma(\mathbf{r}) = -\frac{\varepsilon - 1}{4\pi}\frac{\partial}{\partial \mathbf{n}}\left(\Phi_{\mathrm{QM}}(\mathbf{r}) + \int_\Omega \mathrm{d}\mathbf{s}\, \frac{\sigma(\mathbf{s})}{|\mathbf{r} - \mathbf{s}|}\right), \tag{68}$$

where we note that the operator $\partial/\partial n$ represents the projection of the gradient onto the normal vector **n**. For the numerical convenience in solving Eq. (68) the cavity surface is divided into an appropriate number of elements called tesserae. Then, the integral in Eq. (67) is to be approximated by the discrete summation over the surface elements,

$$\Phi_\sigma(\mathbf{r}) \cong \sum_k \frac{\sigma_k}{|\mathbf{r} - \mathbf{s}_k|}. \tag{69}$$

σ_k and $\mathbf{s}_k$ in Eq. (69) are the charge and position of the kth element, respectively. Owing to the division of the surface, Eq. (68) can be solved by an iterative procedure. At first we put the potential $\Phi_\sigma = 0$, which means that the initial guess for σ_k is taken to be zero for all k. This immediately yields a new set of $\{\sigma_k\}$ through Eq. (68). The charges thus improved are substituted to Eq. (69) to generate a renewed electrostatic potential Φ_σ. According to Ref. [24] three or four cycles of the above procedure are usually sufficient to reach convergence even in the first version of PCM.

It should be reminded, however, that surface charges $\{\sigma_k\}$ are dependent on the electron density of the QM solute embedded in the cavity as explicitly shown in Eq. (68). Importantly, the solute electron density is also to be polarized in response to the PCM solvent effects represented by Eq. (69). This mutual polarization between the continuum and the QM solute gives rise to a nonlinear problem. An intuitive approach to solve this problem is again to rely on a self-consistent iterative procedure. First, we compute the QM electron density for the Hamiltonian $\mathbf{H}_0$ without solvent effects and, then optimize the set of surface charges for the density obtained with the method noted above. The electron density is renewed under the effect of the surface potential Φ_σ. This procedure is iterated until we achieve convergences both in the electron density and the charge set. To be specific for the quantum chemical calculation, the electronic Hamiltonian with the PCM effective potential at *i*th step during the iteration is written as

$$\mathbf{H}^i_{\mathrm{PCM}} = \mathbf{H}_0 + \Phi^i_\sigma(\mathbf{r}), \tag{70}$$

where potential Φ^i_σ arises from the surface charge $\{\sigma^i_k\}$. In terms of the electron density $n^i(\mathbf{r})$ derived from the eigenfunction Ψ^i of Eq. (70), we have the electrostatic potential $\Phi^i_{\mathrm{QM}}(\mathbf{r})$ due to the QM solute affected by the reaction field as

$$\Phi^i_{\mathrm{QM}}(\mathbf{r}) = \int \frac{n^i(\mathbf{r}')}{|\mathbf{r}-\mathbf{r}'|}\mathrm{d}\mathbf{r}' - \sum_{\alpha\in\mathrm{QM}} \frac{Z_\alpha}{|\mathbf{R}_\alpha - \mathbf{r}|}, \tag{71}$$

where Z_α and $\mathbf{R}_\alpha$ are the charge and position vector of the nucleus α in the QM solute, respectively.

Let us consider here how to evaluate the free-energy contribution due to the solute–solvent electrostatic interaction within the framework of PCM. The interaction energy $E_{\mathrm{QM}-\sigma}$ between the solute and the continuum can be expressed as

$$E_{\mathrm{QM}-\sigma} = -\int n(\mathbf{r})\Phi_\sigma(\mathbf{r})\mathrm{d}\mathbf{r} + \sum_{\alpha\in\mathrm{QM}} Z_\alpha \Phi_\sigma(\mathbf{R}_\alpha), \tag{72}$$

The electrostatic contribution $\Delta\mu_{\mathrm{el}}$ to the solvation free energy is the work necessary to build up the charge distribution of the solute inside the polarized cavity. Assuming the linear response in the polarization, we have

$$\Delta\mu_{\mathrm{el}} = \langle\Psi|\mathbf{H}_0|\Psi\rangle - \langle\Psi_0|\mathbf{H}_0|\Psi_0\rangle + \frac{1}{2}E_{\mathrm{QM}-\sigma,} \tag{73}$$

where Ψ_0 is the electronic eigenfunction of the solute in the absence of the continuum. In the construction of Eq. (73) we note that the electronic distortion energy E_{dist} of Eq. (27) in response to the reaction field is also included. The total solvation free energy $\Delta\mu_{\mathrm{sol}}$ can be given by the sum of $\Delta\mu_{\mathrm{el}}$ and other nonelectrostatic contributions;

$$\Delta\mu_{\mathrm{sol}} = \Delta\mu_{\mathrm{el}} + \Delta\mu_{\mathrm{cav}} + \Delta\mu_{\mathrm{dis-rep}}. \tag{74}$$

In Eq. (74) $\Delta\mu_{\mathrm{cav}}$ is the cavitation free energy spent in making a void to embed the solute in the solvent, and $\Delta\mu_{\mathrm{dis-rep}}$ denotes the sum of the dispersion and repulsion free energies. These contributions are being evaluated in the PCM calculations by the equations with empirical basis, for which we refer the readers to Ref. [24].

We mentioned in Subsection 2.3 that PCM approach can be regarded as a sort of QM/MM method in a broad sense. It should be emphasized in the PCM procedure that the polarization of the solute is reasonably coupled with that of the continuum which serves as a reaction field as illustrated above. However, there is a serious deficiency that a solvent, that is an aggregate of the constituent molecules, is to be represented merely by a continuum with a uniform dielectric constant. Therefore, it is possible that the solvation effects arising from short-range interactions such as hydrogen bonds may not be realized adequately within the PCM description. In the following subsections we will address the alternative routes to overcome the problem.

4.2. Reference interaction site model combined with the self-consistent field calculation

A promising approach to recover the proper description of the solvent is to resort to the DFT of solutions. As described in Subsection 3.3 the solvation free energy of a solute can be exactly formulated in terms of the distribution function of the solvent molecules with full coordinate specifying their orientations and positions. In practice, the distribution function with the full coordinate is often approximated by a set of site–site RDFs on the basis of the RISM. It is, then, possible to make sophistication for the solvent effects in quantum chemical calculation by combining it with the RISM integral equations in place of the polarizable continuum. We present an outline for the RISM-SCF approach [29] in the following paragraphs.

The crucial step in the realization of the RISM-SCF scheme resides in the construction of the effective potential in the electronic Hamiltonian due to the solvent described by the site–site RDFs. The effective potential of the solvent at the solute interaction site λ is given as

$$V_\lambda = C\sum_i q_i \int_0^\infty 4\pi r^2 \frac{g_{\lambda i}(r)}{r}\,\mathrm{d}r, \tag{75}$$

where $g_{\lambda i}(r)$ is the RDF around the QM site λ for the ith site placed in the solvent molecule. q_i denotes the fractional charge of the solvent site i and C

is the number density of the solvent. Throughout this Section it is assumed that the interaction sites are placed on the positions of the nuclei in the solute. V_λ can be considered as the averaged electrostatic potential acting on the solute site λ which comes from the solvent fractional charges by its construction. In terms of the potentials V_λ in Eq. (75) the electronic Hamiltonian within the framework of RISM-SCF is given in an analogous form with Eq. (70), thus,

$$\mathbf{H}_{\text{RISM}-\text{SCF}} = \mathbf{H}_0 + \sum_\lambda b_\lambda V_\lambda, \tag{76}$$

where b_λ is the population operator for the QM site λ and it divide the total electron density into the sites. Of course, there will be several ways for the population operator. Usually the populations are determined so that they reproduce the electrostatic potential generated by the electron density through the least-square fitting (LSF) procedure. By using the population operator b_λ and the potential V_λ we obtain the electrostatic potential E_{es} induced by the solvent described by the RISM approach as follows,

$$\begin{aligned} E_{\text{es}} &= \sum_\lambda V_\lambda \langle \Psi | b_\lambda | \Psi \rangle, \\ &= \sum_\lambda V_\lambda \int n_\lambda(\mathbf{r}) \mathrm{d}\mathbf{r}, \\ &= \sum_\lambda V_\lambda Q_\lambda. \end{aligned} \tag{77}$$

where Ψ is the wave function obtained by solving the Schrödinger equation with the Hamiltonian of Eq. (76) and $n_\lambda(\mathbf{r})$ is the electron distribution assigned to site λ. It is worth noting in Eq. (77) that E_{es} is simply given as the summation over λ of the potentials V_λ multiplied by the partial charges Q_λ derived from the population operator b_λ. Further, we can evaluate the fractional charge q_λ for the solute site λ, thus,

$$q_\lambda = Z_\lambda - Q_\lambda. \tag{78}$$

Once the fractional charges for the solute sites are given, one can introduce the two-body interaction potential V_{uv} between the solute and solvent,

$$V_{\text{uv}} = \sum_{\lambda \in \text{u}} \sum_{i \in \text{v}} \left(\frac{q_\lambda q_i}{r_{\lambda i}} + U_{\lambda i}^{\text{LJ}}(r_{\lambda i}) \right). \tag{79}$$

In Eq. (79) u and v stand for the solute and solvent molecules, respectively. $U_{\lambda i}^{\text{LJ}}$ is the LJ interaction term of which explicit form is given in Eq. (29). For the given interaction potential V_{uv}, the total and direct site–site correlation functions $h_{\lambda i}$ and $c_{\lambda i}$ for the solute–solvent pairs can be obtained by solving a set of RISM integral equations as presented in Eq. (47) with the help of a closure relation such as the HNC approximation [Eq. (49)]. The total correlation function $h_{\lambda i}$ is related to $g_{\lambda i}$ by Eq. (46). Importantly, the functions $g_{\lambda i}$ serve to construct the effective potential in the Hamiltonian as shown in Eq. (75) and the resultant partial charges q_λ of the solute affect these correlation functions through the interaction of Eq. (79). Thus, the QM calculation should be coupled by the solution of the RISM integral equations in the self-consistent manner. The numerical procedure to attain the convergence is parallel to that used in the PCM approach.

After the convergences in the electronic wave function Ψ as well as the correlation functions $g_{\lambda i}$ the solvation free energy $\Delta\mu_{\text{sol}}$ of the QM solute within the RISM-SCF method is thus described,

$$\Delta\mu_{\text{sol}} = \langle\Psi|\mathbf{H}_0|\Psi\rangle - \langle\Psi_0|\mathbf{H}_0|\Psi_0\rangle + \Delta\mu. \tag{80}$$

Ψ_0 in Eq. (80) is the electronic eigenfunction of the solute and the first two terms in the right hand represent the electronic distortion energy of the solute polarized by the solvent. $\Delta\mu$ is the free-energy contribution due to the solute–solvent interaction of Eq. (79). It will be valuable to note that the form of Eq. (80) is essentially identical to that of Eq. (73), which is the free-energy expression in the PCM method. Specifically, within the HNC approximation, the free energy $\Delta\mu$ in Eq. (80) is described in terms of the total and direct correlation functions h and c as,

$$\Delta\mu_{\text{HNC}} = -n k_{\text{B}} T \sum_{\lambda} \sum_{i} \int_0^\infty \left(c_{\lambda i}(r) - \frac{1}{2} h_{\lambda i}{}^2(r) + \frac{1}{2} h_{\lambda i}(r) c_{\lambda i}(r) \right) \mathrm{d}r, \tag{81}$$

where k_{B} and T are the Boltzmann constant and the temperature, respectively.

The notable advantage of RISM-SCF in relative to PCM lies in the fact that it incorporates the solvent structure into the effective potential by means of the reduced form of the solvent distribution function, that is the set of site–site RDFs. However, it should be reminded that RISM itself suffers from several difficulties arising from the basic strategy that a molecule is treated as a collection of interaction sites as described in Subsection 3.4. In addition, we should pay particular attention on several issues in RISM-SCF. In obtaining the solute–solvent interaction potential V_{uv} of Eq. (79) the solute electron density is being reduced to a set of point charges on the interaction sites by the population operator. Hence, the spatially diffuse nature of the electron density of the QM object is completely spoiled. It may results in serious overestimation of the solute–solvent interactions for an anionic solute or anionic site of a solute in particular. Concerning this point, a promising improvement [76] was recently proposed by employing auxiliary Gaussian basis set instead of the point charges. Spatial diffuseness of the solute electron density can be realized by putting the Gaussian functions at the interaction sites. However, only the s-type functions may contribute to the expansion of the density, since the site–site interaction is dependent only on the radial distance. The second point to be considered is the electrostatic potential V_λ felt by electrons that is formed by the surrounding solvent. As a consequence of the fact that the full-coordinate solvent distribution is reduced to a set of site–site forms in the RISM approach, the electrostatic potential having a certain spatial structure is necessarily confined to the sites as shown in the integration of Eq. (75). The adequacy of such a reduced potential should be examined carefully whether it can reproduce the realistic solute polarization or not.

We now summarize the characteristics of the methods, PCM and RISM-SCF. The solvation effect by PCM has an obvious limitation arising from its basis that the solvent is being expressed by a continuum. However, the electronic Hamiltonian undergoes no limitations in the representation of the given electrostatic potential. In RISM-SCF, on the other hand, the QM Hamiltonian suffers from the constraint in the description of the electrostatic potential because of the site–site coupling scheme in the RISM approach, even though the solvation structure can be treated in atomic details.

In the next subsection we will introduce our recent development to compute solvation free energy by combining the QM/MM approach and the theory of ER of which surveys are, respectively, presented in Subsections 2.3 and 3.5. The feature of the method, namely QM/MM-ER, is that the solute polarization is realized by the robust description for the solvent molecules, while the free energy is evaluated by a new distribution function theory which treats a solvent molecule as a single object in contrast to the RISM approach.

4.3. Quantum mechanical/molecular mechanical method combined with the theory of energy representation

Within the theory of ER, the solvation free energy is exactly formulated in terms of the distribution functions of the solute–solvent interaction potential. A notable feature of the new method is that it no longer needs the concept of the interaction sites as a consequence that a molecule is treated as a single object. Hence, the diffuse nature of the electron density in a quantum chemical molecule can be naturally incorporated into the free-energy calculation without any special treatment for it. A simplified description for the procedure to accomplish the QM/MM-ER calculation [30] is illustrated as follows. First, a set of QM/MM simulations are carried out to construct the energy distribution functions for the solute–solvent interaction energy. These distribution functions are, then, substituted to the approximate functional in the ER to yield the value of the solvation free energy. The strategy is thus very simple, however, it should be reminded that the standard version of the theory of ER assumes the solute–solvent interaction to be pairwise additive, hence a certain treatment must be made in combining the method with the QM/MM approach that involves many-body interactions.

To overcome the difficulty we resort to a two-step approach, that is, the free-energy contribution due to the two-body interaction is evaluated with the standard method of the ER and the remaining minor contribution arising from many-body interaction is computed separately. The key of this approach is to construct an intermediate state of the QM solute with the electron density fixed at some distribution. Given that the electron density is frozen and no longer polarizes in response to the solvent motion, the solute–solvent interaction is pairwise, and therefore, the method of ER can be applied straightforwardly. The choice of the intermediate state is somewhat arbitrary, but we adopt the average distribution of the electron density in solution for the numerical and conceptual convenience. We formulate in the following the free-energy decomposition associated with the introduction of the intermediate state.

Within the framework of the QM/MM approach the solvation free energy $\Delta\mu$ of a QM solute can be expressed as

$$\exp(-\beta\Delta\mu) = \frac{\int \mathrm{d}\mathbf{X}\exp\{-\beta[E_{\mathrm{dist}} + E_{\mathrm{QM/MM}}(n,\mathbf{X}) + E_{\mathrm{MM}}(\mathbf{X})]\}}{\int \mathrm{d}\mathbf{X}\,\exp(-\beta E_{\mathrm{MM}}(\mathbf{X}))}. \tag{82}$$

where β is the inverse of the product of the Boltzmann constant k_{B} and temperature T, and n is the instantaneous electron density of the QM solute under a given solvent configuration denoted collectively as $\mathbf{X}$. Explicitly, $n(\mathbf{r})$ is derived from the eigenfunction of the Schrödinger equation of Eq. (25). We refer the readers to Subsection 2.3 for the details of the terms appearing in Eq. (82). We decompose the free energy $\Delta\mu$ into three terms, thus,

$$\Delta\mu = \bar{E} + \Delta\bar{\mu} + \delta\mu, \tag{83}$$

where $\bar{E}$ is the average distortion energy E_{dist}, $\Delta\bar{\mu}$ is the solvation free energy of a QM solute with the average electron density $\tilde{n}(\mathbf{r})$ in solution, and $\delta\mu$ is the free energy due to the electron density fluctuation around its average distribution $\tilde{n}(\mathbf{r})$. $\bar{E}$ and $\tilde{n}(\mathbf{r})$ are simply the statistical averages which are, respectively, given by

$$\bar{E} = \frac{\int \mathrm{d}\mathbf{X}E_{\mathrm{dist}}\,\exp\{-\beta[E_{\mathrm{dist}} + E_{\mathrm{QM/MM}}(n,\mathbf{X}) + E_{\mathrm{MM}}(\mathbf{X})]\}}{\int \mathrm{d}\mathbf{X}\,\exp\{-\beta[E_{\mathrm{dist}} + E_{\mathrm{QM/MM}}(n,\mathbf{X}) + E_{\mathrm{MM}}(\mathbf{X})]\}}, \tag{84}$$

$$\tilde{n}(\mathbf{r}) = \frac{\int \mathrm{d}\mathbf{X}n(\mathbf{r})\exp\{-\beta[E_{\mathrm{dist}} + E_{\mathrm{QM/MM}}(n,\mathbf{X}) + E_{\mathrm{MM}}(\mathbf{X})]\}}{\int \mathrm{d}\mathbf{X}\exp\{-\beta[E_{\mathrm{dist}} + E_{\mathrm{QM/MM}}(n,\mathbf{X}) + E_{\mathrm{MM}}(\mathbf{X})]\}}. \tag{85}$$

Note that Eqs. (84) and (85) are simultaneously obtained through an ordinary QM/MM simulation. The solvation free energy $\Delta\bar{\mu}$ can be regarded as a contribution due to the two-body interaction between the QM solute and the solvent and is expressed by

$$\exp(-\beta\Delta\bar{\mu}) = \frac{\int d\mathbf{X}\, \exp\{-\beta[E_{\mathrm{QM/MM}}(\tilde{n},\mathbf{X}) + E_{\mathrm{MM}}(\mathbf{X})]\}}{\int d\mathbf{X}\, \exp[-\beta E_{\mathrm{MM}}(\mathbf{X})]}, \tag{86}$$

while the remaining minor contribution $\delta\mu$ due to the many body effect of the QM object can be given by

$$\exp(-\beta\delta\mu) = \frac{\int d\mathbf{X}\, \exp\{-\beta[(E_{\mathrm{dist}} - \bar{E}) + E_{\mathrm{QM/MM}}(n,\mathbf{X}) + E_{\mathrm{MM}}(\mathbf{X})]\}}{\int d\mathbf{X}\, \exp\{-\beta[E_{\mathrm{QM/MM}}(\tilde{n},\mathbf{X}) + E_{\mathrm{MM}}(\mathbf{X})]\}}. \tag{87}$$

It can be readily verified that Eq. (82) is exactly reproduced by substituting Eqs. (86), and (87) to Eq. (83). It should also be noted that Eq. (83) holds independently of the choice of $\bar{E}$ and $\tilde{n}(\mathbf{r})$ under the definitions of Eqs. (86) and (87).

Since the solute–solvent interaction is pairwise when the solute electron density is fixed at a distribution, it is straightforward to construct the energy distribution functions of Eqs. (55) and (56) as well as the correlation matrix defined by Eqs. (57) for the solution and pure solvent systems. Then, the free energy $\Delta\bar{\mu}$ can be readily evaluated by Eq. (60) in terms of these energy distribution functions. Fortunately, it is expected that the free-energy contribution $\Delta\bar{\mu}$ due to the two-body interaction will occupy the major part of the total solvation free energy. The remaining contribution $\delta\mu$ due to the electron density fluctuation around the average distribution $\tilde{n}(\mathbf{r})$ can also be computed with the method of ER by introducing a new energy coordinate of $\zeta = v(n,\mathbf{x}_i) - v(\tilde{n},\mathbf{x}_i)$. For the computation of $\delta\mu$ we shall perform additional QM/MM simulations to produce the energy distribution functions with respect to the energy coordinate ζ. The details of the formulation is presented in Refs. [30] and [33]. Here we only list the relevant equations necessary to evaluate $\delta\mu$. First, we consider the quantity ϕ defined as

$$\phi = E_{\mathrm{dist}} - \bar{E}. \tag{88}$$

Then, we construct the distribution functions $P(\phi)$ and $P_0(\phi)$ for the solution and the pure solvent systems, respectively. Here, the solution system means the realistic QM/MM system where the electron density of the solute fluctuates in response to the solvent motion, while the pure solvent refers to the system where the electron density is fixed at the distribution $\tilde{n}(\mathbf{r})$. Then, the free energy $\delta\mu$ can be exactly written as

$$\begin{aligned}\delta\mu &= \delta\tilde{\mu} + k_{\mathrm{B}}T\int \mathrm{d}\phi P(\phi)\ln\left(\frac{P(\phi)}{P_0(\phi)}\right)\\ \delta\tilde{\mu} &= \int \mathrm{d}\phi P(\phi)\delta v(\phi),\end{aligned} \tag{89}$$

where $\delta\nu(\phi)$ is the conditional free-energy change associated with the variation from the pure solvent to solution system where the relation $\phi = E_{\mathrm{dist}}(n) - \bar{E}$ is imposed. The second term of Eq. (89) can be directly computed by performing the QM/MM simulations. An approximate expression for $\delta\tilde{\mu}$ can be given by a set of equations listed as

$$\delta\tilde{\mu} = -k_{\mathrm{B}}T\int \mathrm{d}\zeta\{[\rho(\zeta) - \tilde{\rho}_0(\zeta)] + \beta\tilde{\omega}(\zeta)\rho(\zeta) - \tilde{F}(\zeta)[\rho(\zeta) - \tilde{\rho}_0(\zeta)]\}, \tag{90}$$

where $\rho\zeta$ is the distribution function of the energy ζ in the solution system and

$$\tilde{\rho}_0(\zeta) = \int \mathrm{d}\phi P(\phi)\tilde{\sigma}_0(\zeta;\phi), \tag{91}$$

$$\tilde{\omega}(\zeta) = -k_{\mathrm{B}}T\ln\left(\frac{\rho(\zeta)}{\tilde{\rho}_0}(\zeta)\right) - \zeta, \tag{92}$$

$$\tilde{\sigma}_0(\zeta;\phi) = \frac{\displaystyle\int \mathrm{d}\mathbf{X}\delta\Big(\phi - [E_{\mathrm{dist}}(n) - \bar{E}]\Big)\sum\nolimits_i \delta\Big(\zeta - [v(n,\mathbf{x}_i) - v(\tilde{n},\mathbf{x}_i)]\Big) \times\exp\{-\beta[E_{\mathrm{QM/MM}}(\tilde{n},\mathbf{X}) + E_{\mathrm{MM}}(\mathbf{X})]\}}{\displaystyle\int \mathrm{d}\mathbf{X}\delta\Big(\phi - [E_{\mathrm{dist}}(n) - \bar{E}]\Big) \times \exp\{-\beta[E_{\mathrm{QM/MM}}(\tilde{n},\mathbf{X}) + E_{\mathrm{MM}}(\mathbf{X})]\}}, \tag{93}$$

$$\tilde{F}(\zeta) = \begin{cases}\beta\tilde{\omega}(\zeta) + 1 + \dfrac{\beta\tilde{\omega}(\zeta)}{\exp[-\beta\tilde{\omega}(\zeta)] - 1} & [\text{when } \tilde{\omega}(\zeta) \le 0]\\[2ex] \dfrac{1}{2}\beta\tilde{\omega}(\zeta) & [\text{when } \tilde{\omega}(\zeta) \ge 0].\end{cases} \tag{94}$$

In the construction of Eq. (94) the weight factor α in Eq. (63) is simply set to unity here. This is possible because the "excluded volume region," where ζ is very large, is absent in the present calculation. As a result, the correlation matrix over the energy coordinate ζ can be omitted. Thus, the simulation for the pure solvent system can be shortened considerably. Equations (89)–(93) are actually not affected by the constant shift of the variable ϕ. Thus, although Eq. (88) states that $\bar{E}$ is set to the ensemble average of the stochastic variable E_{dist}, the computation of $\delta\mu$ with Eqs. (89)–(94) can be carried out simply by regarding ϕ as the $E_{\text{dist}}(n)$ value.

The computational procedure to accomplish the evaluation of the total free energy $\Delta\mu$ is summarized by the following three steps.

(Step 1) An ordinary QM/MM simulation is carried out to obtain the average distortion energy $\bar{E}$ and $\tilde{n}(\mathbf{r})$ which are defined by Eqs. (84) and (85), respectively.

(Step 2) The energy distribution functions $\rho_0(\varepsilon)$, $\chi_0(\varepsilon,\eta)$ and $\rho(\varepsilon)$ for pure solvent and solution systems are computed for the QM solute with the electron density fixed at the distribution of $\tilde{n}(\mathbf{r})$. These distribution functions are used as inputs to Eq. (60) to yield free energy $\Delta\bar{\mu}$.

(Step 3) For the computation of the free-energy contribution $\delta\mu$ due to the electron density fluctuation, the energy distribution functions $\tilde{\rho}_0(\zeta)$, $\tilde{\sigma}_0(\zeta,\phi)$ and $\rho(\zeta)$ for pure solvent and solution systems are computed with respect to the energy coordinate ζ. The distribution functions $P(\phi)$ and $P_0(\phi)$ with respect to the electronic distortion energy ϕ are also computed. These functions are used to evaluate Eq. (89) through Eq. (90). The above procedure is illustrated in Figure 9.3 for later references.

In closing this subsection, we examine the computational cost of the present approach by making comparisons with other methods. The QM/MM simulation is often utilized along with the FEP method or TI for the free-energy calculations. As described in Subsection 3.1 the approach of FEP or TI is the numerical realization of the Kirkwood charging formula and it introduces a number of intermediate states along an arbitrary path connecting the initial and final states of the chemical event of interest. Hence, it requires numerous configuration samplings to achieve the free-energy convergence along the intermediate points which are physically of no importance. On the other hand, in the QM/MM-ER method, the ensemble average is needed only at the initial and final states of the event by the help of an approximate functional based on the DFT. This substantially benefits the QM/MM simulation since the quantum chemical calculation requires a large computational costs in general. In addition, we also note that the convergences of the energy distribution functions are very rapid by virtue of the method of ER which treats the solvent molecules as identical objects given that they have the same energy coordinate. In contrast, as compared to RISM-SCF or PCM, the QM/MM-ER approach is more demanding because the electrostatic potential due to the solvent and the distribution functions used to compute free energy are to be constructed by means of the QM/MM simulations. In the next subsections, we present several examples of the applications of QM/MM-ER and discuss the efficiency and accuracy of the method.

4.4. Calculation of solvation free energy by QM/MM-ER approach

The major purpose of this subsection is to examine the accuracy of the QM/MM-ER method by computing the solvation free energy of a QM water molecule into MM water solvent [30]. The computational details for the QM/MM simulations are as follows. Two thermodynamic conditions of water solutions were considered; ambient water (AW: $T = 300$ K, $\rho = 1.0\,\mathrm{g/cm^3}$) and supercritical water (SCW: $T = 600$ K, $\rho = 0.3\,\mathrm{g/cm^3}$), where the solvent was described by 255 TIP4P water molecules [77]. We note that the reduced temperature of 600 K for TIP4P model is estimated as $T_\mathrm{r} = 1.07$. The electronic structure of the QM water molecule is obtained by KS-DFT that utilizes the real-space grid and the BLYP functional [78,79]. The Hartree potential in Eq. (12) was computed by utilizing the FFT. The periodicity of the Hartree potential was eliminated by the method of Ref. [80]. The geometry of the QM water molecule used in the QM/MM simulation was optimized by the Gaussian package with the BLYP functional and the aug-cc-pVDZ basis set [81]. The obtained geometrical parameters are OH = 0.975 Å, and HOH = 104.2°. The QM solute was placed at the center of the cubic QM cell in which each axis was discretized by 32 grids with equi-intervals. The grid spacing h of the QM cell was set at 0.287 a.u. (0.152 Å), which corresponds to a cutoff energy of 60 a.u. The atomic core regions were reinforced by the double grids of which spacing was set at $0.2h$. Such a QM cell was embedded in the center of an cubic MM simulation cell with periodic boundary conditions. The molecular configurations for the solvent were sampled in *NVT* ensemble through molecular dynamics simulations where Newtonian equations of motion for the particles were solved by the leap-frog algorithm with a time step 1.0 fs and the velocity rescaling was used for the temperature control [9,10]. The long-range interaction between MM charges was calculated by the Ewald method [82] and a cutoff distance of the LJ potential was set at half of the box length.

Next, we present the details for the construction of the energy distribution functions. The average electronic distortion energy $\bar{E}$ and the electron density $\tilde{n}(\mathbf{r})$ in Step 1 of Figure 9.10 were obtained by a 50-ps QM/MM simulation after 5-ps equilibration. Subsequently, the QM/MM simulation for the solute with the electron density fixed at $\tilde{n}(\mathbf{r})$ were performed to construct the energy distribution functions $\rho(\varepsilon)$, $\rho_0(\varepsilon)$, and $\chi_0\underset{.}{\varepsilon}\,\underset{.}{\eta}$ (Step 2 in

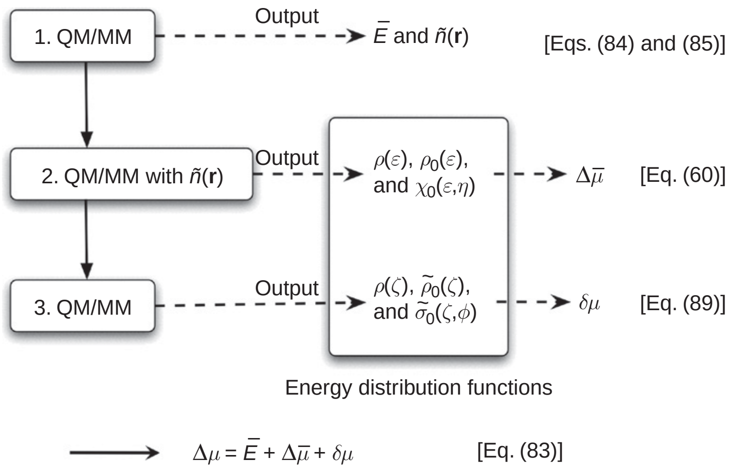

Figure 9.10 Flow chart for the procedure to compute solvation free energy by means of the QM/MM-ER approach. See the text for the detailed description for the energy distribution functions.

Figure 9.10). Typically, 100-ps and 200-ps simulations were carried out for the solution and the pure solvent systems, respectively. To see the effect of the electron density polarization, we also made the energy distribution functions for the solute with nonpolarized electron density (electron density at the isolation). We note that the energy distribution functions were constructed for the solvent molecules of which oxygen atoms were within a spherical cavity with a radius of 9 Å. The center of the cavity was taken at the oxygen of the QM water molecule. These distribution functions were substituted to Eq. (60) to compute free-energy contribution $\Delta\bar{\mu}$ originating from pairwise interaction in the solute–solvent interaction [Eq. (86)]. The additional QM/MM simulations (Step 3 in Figure 9.10) were also performed to compute free energy $\delta\mu$ described in Eq. (87) due to the many-body effects in the QM object. To compute free energy $\delta\mu$ a set of the energy distribution functions was constructed with respect to the energy coordinate $\zeta = v(n, \mathbf{x}_i) - v(\tilde{n}, \mathbf{x}_i)$ as described in the previous subsection.

We summarize the results of the QM/MM-ER simulations in Table 9.1. $\Delta\bar{\mu}_{\mathrm{np}}$ denotes the free-energy change due to the solvation of the nonpolarized solute. It can be readily recognized that the free energies $\Delta\bar{\mu}_{\mathrm{np}}$ make the major contributions both in the AW and SCW. On the contrary, it turned out the net contributions of the electron polarizations, which may be given by $\Delta\bar{\mu}_{\mathrm{pol}} - \bar{E}$, are much smaller than the free energy $\Delta\bar{\mu}_{\mathrm{np}}$. The free-energy changes $\delta\mu$ due to the electron density fluctuation of the QM solutes in the solutions of AW and SCW were estimated as –1.2 and –0.9 kcal/mol, respectively. It is worth noting that the free energy $\delta\mu$ in the SCW amounts to

Table 9.1 Solvation free energies of QM water molecules in MM water solvents and their components in AW and SCW

		$\Delta\bar{\mu}$				
	$\bar{E}$	$\Delta\bar{\mu}_{\text{np}}$	$\Delta\bar{\mu}_{\text{pol}}$	$\delta\mu$	$\Delta\mu$	$\Delta\mu_{\text{exp}}$[a]
AW	3.5	–4.5	–4.8	–1.2	–7.0	–6.3
SCW	1.0	–2.0	–0.6	–0.9	–2.5	–2.2[b]

Note: The units are in kcal/mol.

[a] The international association for the properties of water and steam, 1997, IAPWS Industrial Formulation 1997 for the Thermodynamic Properties of Water and Steam, Erlangen, Germany.

[b] The experimental value is taken at the same reduced temperature as the TIP4P value.

almost 40% of the total solvation free energy of –2.5 kcal/mol and is comparable to that in the AW although the average distortion energy $\bar{E}$ in the SCW (1.0 kcal/mol) is smaller than that in the AW (3.5 kcal/mol). This result implies the frequent occurrence in the SCW of the asymmetric hydration to the solute because absolute of $\delta\mu$ becomes larger when the instantaneous electron density $n(\mathbf{r})$ in the solution deviates largely from the symmetric distribution $\tilde{n}(r)$. Thus, it was revealed that the electron density fluctuation also plays a role in the solvation especially in the SCW. As a sum of these contributions, the total excess chemical potentials of the QM water molecules in the AW and SCW were obtained as –7.0 and –2.5 kcal/mol, respectively. These values are in excellent agreement with those determined by experiments as shown in Table 9.1, suggesting the adequacy of the QM/MM-ER method for the computation of the solvation free energy.

In a strict sense, the accuracy of the method should be examined by comparing the results with that obtained by a certain numerically exact method such as QM/MM combined with FEP. Of course, the same levels of theory in quantum chemistry must be used in the computation. Such a calculation is, however, very much costly to perform. QM/MM-FEP may require two orders of magnitude more computational cost than the QM/MM-ER to achieve the free-energy convergence. We circumvent the explicit evaluation of the QM/MM interaction by reducing the electron density $\tilde{n}(\mathbf{r})$ to a set of point charges placed on the nuclei of the solute. The point charges were optimized by the least square fittings so that they reproduce the electrostatic potentials due to $\tilde{n}(\mathbf{r})$ at the sample points. We obtained the charges –0.90 and +0.45 at oxygen and hydrogen, respectively. Given that the set of point charges adequately reproduce the electrostatic field formed by $\tilde{n}(\mathbf{r})$, the FEP calculation using these charges may yield the free-energy change that deserves for the comparison with the value $\Delta\bar{\mu}_{\text{np}} + \Delta\bar{\mu}_{\text{pol}}$ obtained by the QM/MM-ER method. The value computed by FEP

(–8.8 kcal/mol) for the AW showed excellent agreement with that given by QM/MM-ER ($\Delta\bar{\mu}_{\mathrm{np}} + \Delta\bar{\mu}_{\mathrm{pol}} = -9.3$ kcal/mol).

Before closing this subsection, we also describe other several applications performed in our previous works. The free-energy change associated with the isomerization of glycine from neutral (NT) to zwitterionic (ZW) form in water was computed as –7.8 kcal/mol by the present method [35], which is in good agreement with the reported experimental value, –7.3 or –7.7 kcal/mol. According to the PCM calculations by the Gaussian package [75], the free energy was estimated to be 1.4 kcal/mol which indicates that the NT glycine is more stable than the ZW one even in water as opposed to the experimental observation. Thus, we found that explicit consideration of the solvent structure is crucial for the correct description of the relative stability of glycines. By the analysis using the RDFs, it was also revealed that the point charge representation for the anionic site in the ZW glycine gives rise to the serious overestimation of the solute–solvent interaction in contrast to the cationic site. This suggests that the neglect of the diffuse nature of the electron density may lead to erroneous results in some cases. In Ref. [36] it was shown that the QM/MM-ER approach is adequate to predict the even the slight difference in the free energy associated with the anti/syn conformation change for acetic acid in aqueous solution. Further, in Ref. [38] the relative acidity of acetic acid with respect to water was determined in good agreement with the experimental value. We refer the readers to these chapters for more details.

4.5. Calculation of reduction free energy by QM/MM-ER approach

The chemical reaction in biological system is undoubtedly one of the most attracting subjects for the applications of the QM/MM-ER approach. However, we may encounter some difficulty in extending the method to a chemical event in a protein immersed in water. Since the solvation free energy of a protein amounts to a large negative value, in general, it is numerically problematic to evaluate the reaction free energy in terms of the solvation free energies of the proteins in the initial and final states of the reaction. In this subsection we will propose a methodology to compute free-energy change for an electron transfer (i.e., oxidation and reduction) reaction in solutions or proteins [40,41]. To circumvent the problem noted above we take a novel approach within the framework of QM/MM-ER, where only the excess charge involved in the redox reaction is regarded as a solute. We shall introduce a redox system [flavin adenine dinucleotide (FAD)] for a test calculation. Then, the free-energy change associated with the one-electron reduction of FAD will be computed by extending the QM/MM-ER approach. The validity of the novel method will be examined by performing a conventional method.

It is known that coenzyme FAD plays a key role in the redox reaction under the influence of various apoproteins and the isoalloxazine ring in FAD acts as an electronically active site. Hereafter, we refer the isoalloxazine ring to flavin ring for simplicity. In the present work, we focus our attention on the reaction of one-electron reduction. The ball and stick illustration for the FAD as well as the flavin ring are shown in Figure 9.11. In the previous elaborate work [83] Q. Cui carried out the QM/MM FEP calculations for the reduction free energy of the same system. A notable feature of their approach is that they employed a coupling scheme termed as the dual-topology-single-coordinates scheme, in which the initial (oxidized) and the final (reduced) states of the solute are forced to adopt the same molecular geometry during the perturbation simulation. They circumvented the problem associated with the QM object with fractional electrons appearing in the intermediate points between the oxidized and reduced states by introducing separate copies of the two chemical states in the total energy. Their approach is numerically rigorous, however, the computational effort is twice as large as the conventional QM/MM FEP scheme. In the QM/MM simulations, they resorted to the self-consistent-charge–density functional tight-binding (SCC–DFTB) method [84] in which approximations are made to the two-electron integrals to expedite the quantum chemical calculations. In contrast to their approach, our present method requires the QM/MM simulations only for the initial and final states of the reduction process and,

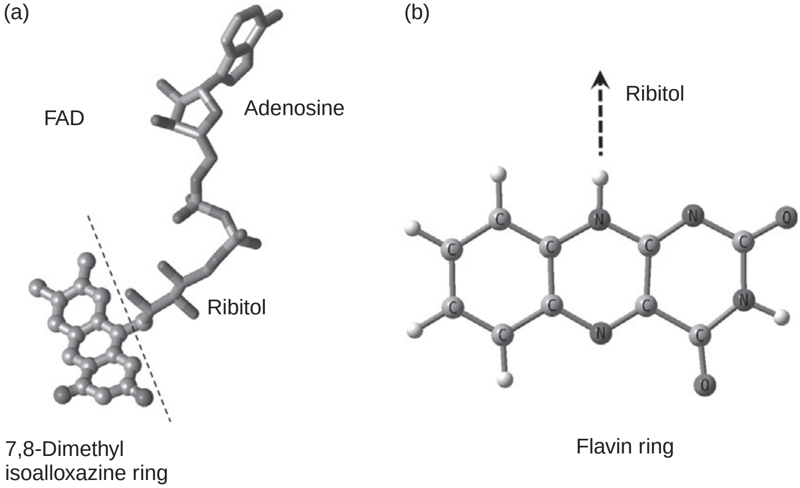

Figure 9.11 Ball and stick illustrations for the (a) flavin adenine dinucleotide (FAD) and the (b) flavin ring. The two methyl groups in the 7,8-dimethyl isoalloxazine ring in FAD are replaced by hydrogen atoms in the construction of the flavin ring to reduce the computational cost in the present calculation.

hence, the computational cost is much more modest. In the following, we present an outline of the methodology with some formulations on the basis of the QM/MM-ER approach.

To avoid the unnecessary complications, we consider here the system where the flavin ring is immersed in water. We note that the computational procedure as well as the formulation are essentially the same with those for the protein system. In applying the QM/MM-ER approach to the reduction process in water, the flavin ring is described quantum chemically, while the solvent water molecule is represented by a classical model. Then, the reduction free energy $\Delta\mu_{\text{red}}$ can be expressed in terms of the energy components in Eq. (24), thus,

$$\exp(-\beta\Delta\mu_{\text{red}}) = \frac{\displaystyle\int d\mathbf{X}\exp\Big(-\beta\Big(E_{\text{QM}}^{N+1} + E_{\text{QM/MM}}^{N+1}(n_{N+1},\mathbf{X}) + E_{\text{MM}}(\mathbf{X})\Big)\Big)}{\displaystyle\int d\mathbf{X}\exp\Big(-\beta\Big(E_{\text{QM}}^{N} + E_{\text{QM/MM}}^{N}(n_{N},\mathbf{X}) + E_{\text{MM}}(\mathbf{X})\Big)\Big)}. \tag{95}$$

where the notations of N+1 and N specify the systems in the reduced and oxidized states, respectively. In Eq. (95) the electron density of the isoalloxazine ring is denoted by n and the instantaneous molecular configuration of the MM subsystem is collectively expressed as $\mathbf{X}$. To adopt the method of the ER for the computation of $\Delta\mu_{\text{red}}$, only the excess charge is treated as a solute and the flavin ring and water molecules are regarded as a mixed solvent. Here, we introduce the energy coordinates for these two kinds of solvent with respect to the solute, that is, excess charge. The energy coordinate for the QM object (flavin ring) can be introduced by defining the interaction potential v_{QM} between the excess charge and flavin ring as

$$v_{\text{QM}} = \langle\Psi_{N+1}|\mathbf{H}_0^{N+1}|\Psi_{N+1}\rangle - \langle\Psi_N|\mathbf{H}_0^{N}|\Psi_N\rangle, \tag{96}$$

where Ψ stands for the electronic wave function and $\mathbf{H}_0$ represents the electronic Hamiltonian including the nuclear repulsion energies in the absence of the electrostatic potential of the surrounding water solvent. Note that $\Psi_{N}1$ is obtained as the eigenfunction for the following Schrödinger equation,

$$\Big(\mathbf{H}_0^{N+1} + \mathbf{V}_{\text{ES}}(\mathbf{X})\Big)|\Psi_{N+1}\rangle = E_{N+1}|\Psi_{N+1}\rangle. \tag{97}$$

In Eq. (97) $\mathbf{V}_{\text{ES}}$ is the electrostatic potential formed by the point charges placed on the interaction sites of the water molecules of which full coordinates are collectively represented by $\mathbf{X}$. The equality also holds for the equation obtained by replacing the notations N+1 in Eq. (97) by N. The interaction potential v_{QM} in Eq. (96) is interpreted as the energy difference between the electronic states for the reduced and the oxidized solutes excluding the stabilization energies due to the hydrations. Next we introduce the energy coordinate for a water molecule. The interaction potential v^i_{MM} between the excess charge and ith water molecule is given by

$$v^i_{\mathrm{MM}} = \sum_{\alpha} q_{i,\alpha} \int d\mathbf{r} \frac{n_{\mathrm{excess}}(\mathbf{r})}{|\mathbf{r} - \mathbf{r}_{i,\alpha}|}, \tag{98}$$

where $q_{i,\alpha}$ denotes the point charge in the unit of elementary charge of αth site placed on ith water molecule and $\mathbf{r}_{i,m}$ is the position vector of the site. $n_{\mathrm{excess}}(\mathbf{r})$ in Eq. (98) is the electron density of the excess charge attached on the flavin ring and is defined as the difference between the electron densities derived from the wave functions $\Psi_N 1$ and Ψ_N. The energy distribution functions defined by Eqs. (55) and (56) are constructed for both the interaction energies v_{QM} and v^i_{MM} given by Eqs. (96) and (98), respectively.

Here we describe in detail the reference and the solution systems for which the energy distribution functions are constructed. In the novel approach where the excess charge itself is being treated as a solute, the reference system consists of the oxidized flavin ring and the surrounding solvent water molecules, while the solution system is composed of the reduced ring and the water molecules. In the reference system, solvent configurations are sampled under the condition that the excess charge is absent in the computation of the forces between the flavin ring and water molecules. On the other hand, the interaction between the water molecules and the excess charge is taken into consideration in generating the configurations of the water molecules in the solution system. The individual energy distribution functions $\rho_{\mathrm{QM}}(\varepsilon)$ and $\rho_{\mathrm{MM}}(\varepsilon)$ for the QM and MM molecules are separately being constructed during a QM/MM simulation. The total energy distribution function $\rho(\varepsilon)$ for the mixed solvent system can be given as the sum of these distributions, thus, $\rho(\varepsilon) = \rho_{\mathrm{QM}}(\varepsilon) + \rho_{\mathrm{MM}}(\varepsilon)$. The same is true for the energy distribution $\rho_0(\varepsilon)$ in the reference system. Then, the reduction free energy $\Delta\mu_{\mathrm{red}}$ can be evaluated by substituting these distribution functions into Eq. (60). Of course, the individual free-energy contributions from the QM or the MM solvents can also be obtained formally by using the corresponding energy distribution functions for these solvent molecules. It should also be noted that the correlation matrix of Eq. (57) used in the approximate functional to evaluate the integral of $\omega(\varepsilon;\lambda)$ in Eq. (54) is no longer necessitated since the excess charge does not possess the effective exclusion volume. This leads to the fast convergence in the free energy since the one-dimensional distribution is much faster in convergence than the two-dimensional correlation matrix.

Computational setup for the QM/MM-ER simulation is as follows. The molecular geometries for the QM molecules, that is, the reduced and the oxidized flavin rings, were optimized by the Gaussian package [75] with the hybrid UB3LYP functional [79,85] and the aug-cc-pVDZ basis set [81].

The mass center of QM molecule was adjusted to the center of a water droplet that was confined within a spherical cavity by a van der Waals wall. The solvent consists of 676 TIP3P water molecules [77]. In the real-space grids QM/MM simulations the grid spacing was set at 0.314 a.u. The exchange and correlation energy of electrons were approximately evaluated by the BLYP functional. Molecular configurations of the oxidized and reduced flavin rings were kept fixed during the QM/MM simulations. The LJ parameters in CHARMM 22 force field [86] were assigned to the atoms in the QM molecule to compute the LJ interactions between the QM and MM subsystems. The molecular configurations of the water solvent were sampled by performing the molecular dynamics simulations where the Newtonian equations of motions for the water molecules are solved numerically by using the Verlet algorithm [9,10]. To obtain ensemble averages for the energy distribution functions, 55-ps QM/MM simulations were performed for the solution and the reference systems where the first 5-ps simulations were discarded as equilibration. The energy distribution functions for water solvent were constructed for the water molecules within a sphere of radius of 15 Å of which center was adjusted to the mass center of the flavin ring. The thermodynamic condition of water solution was set at $T = 300\,\mathrm{K}$ and $\rho = 1.0\,\mathrm{g/cm^3}$. In the next paragraphs we present the results for the QM/MM-ER simulations performed in the water solution.

The one-electron reduction energy $\Delta\mu_{\mathrm{red}}$ of flavin ring in the gas phase was obtained as –49.3 kcal/mol at the UB3LYP/aug-cc-pVDZ level, while it has been computed as –45.7 kcal/mol at the UBLYP/aug-cc-pVDZ level by adopting the same molecular geometries. Thus, it was found that a GGA functional that includes no exact exchange underestimates the absolute of the reduction energy $\Delta\mu_{\mathrm{red}}$ as compared with the hybrid functional. Our code using the real-space grids provided $\Delta\mu_{\mathrm{red}} = -45.1$ kcal/mol with UBLYP functional, which agrees well with the value given by a Gaussian basis set. The energy distribution functions $\rho_{\mathrm{QM}}(\varepsilon)$, and $\rho_{\mathrm{QM}}(\varepsilon)$ for the QM object in the solution and the reference systems are drawn in Figure 9.12a. It is shown that the energy distribution in the solution system locates on the lower region of the energy coordinate as compared with the reference system. It suggests that the electron affinity of the flavin ring is enhanced by the hydration. The free-energy contribution $\Delta\mu_{\mathrm{red}}(\mathrm{QM})$ from the flavin ring has been estimated to be –39.5 kcal/mol. In Figure 9.12b the energy distribution functions $\rho_{\mathrm{MM}}(\varepsilon)$, and $\rho_{\mathrm{MM}}(\varepsilon)$ for the interactions between the excess charge and the water solvent are presented, in which the distributions $\rho_{\mathrm{QM}}(\varepsilon)$, and $\rho_{\mathrm{QM}}(\varepsilon)$ are also shown for comparisons. As expected the interaction between the excess charge and the water solvent is enhanced in the solution system as compared with the reference system. This is simply because the water molecules behave in the presence of the excess charge on the flavin ring in the solution system as opposed to the reference system. It should be stressed here that there exists a positive correlation between the

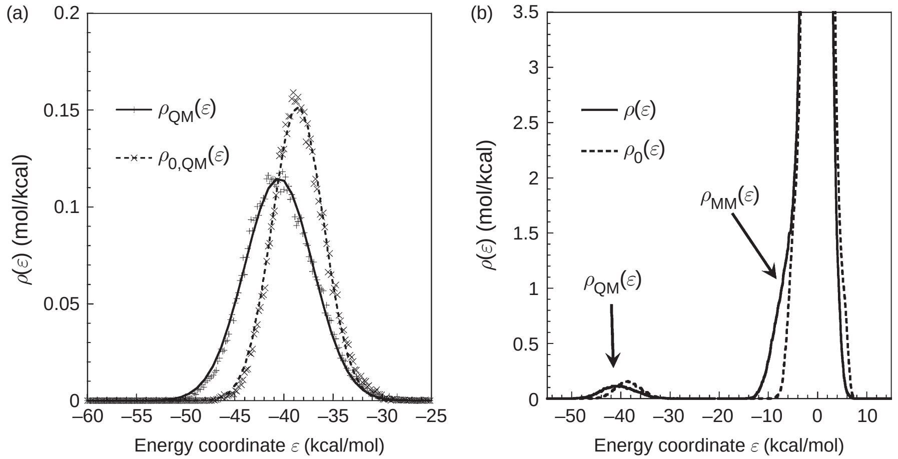

Figure 9.12 (a) Energy distribution functions for the interaction between the excess electron and the flavin ring described quantum chemically. (b) Energy distribution functions for the interaction between excess electron and solvent water molecules represented by TIP3P model. Real and broken lines are for the solution and the reference systems, respectively. The curves in Figure 9.12a are Gaussian functions fitted to the points obtained by the simulations.

two kinds of solute–solvent interactions. In other words, the increase in the stabilization between the solute (excess charge) and water molecules results in the increase in the electron affinity of the flavin ring. This may be attributed to the electron drawing effects of the water molecules which are oriented to the two oxygen atoms in the flavin ring. It would be valuable to note that the same effect can be expected for the flavin ring bound to an apoprotein cholesterol oxidase (PDB: 1b4v) for instance. As shown in Figure 9.13 two amino acid residues in the 1b4v, Met122 and Phe487, are found to form distinctive hydrogen bonds at the two oxygen atoms. The reduction free energy $\Delta\mu_{red}$(MM) due to the hydration has been computed as –40.6 kcal/mol which includes the free-energy contribution of –10.9 kcal/mol estimated by the Born's equation [87] from bulk water outside the spherical cavity. Thus, the total reduction free energy $\Delta\mu_{red}$ has been obtained as –80.1 kcal/mol by the sum of these contributions.

The adequacy of the novel approach which treats the excess charge as a solute was examined by performing the conventional approach. To clarify the difference between the novel and conventional approaches, we present schematics in Figure 9.14. In the conventional approach, the oxidized or reduced flavin ring itself is regarded as a solute. Then, the reduction free energy $\Delta\mu_{red}$ in solution can be described in terms of the solvation free energies of the individual solute molecules with the help of the

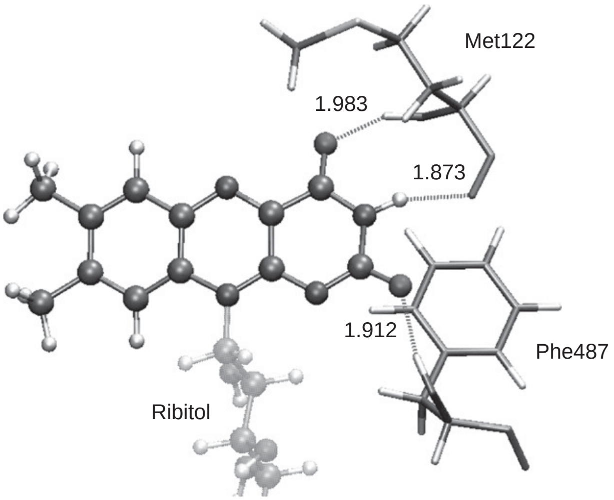

Figure 9.13 Illustration for the 7,8-dimethyl isoalloxazine ring and the neighboring amino acid residues, Met122 and Phe487, that are embedded in the apoprotein of cholesterol oxidase 1b4v. The molecular configuration is obtained by adding the hydrogen atoms on the molecules with the PDB structures. The shaded region in the figure represents the ribitol part of FAD. The hydrogen bonds between the amino acid residues and the isoalloxazine ring are drawn by blue broken lines. The lengths of the hydrogen bonds are in the units of angstroms.

thermodynamic cycle. The solvation free energies are, of course, computed by QM/MM-ER with the scheme presented in the preceding subsection. The computational setup to compute free energy is identical to that used in the calculation of novel approach described above. The solvation free energies for the oxidized and reduced flavin rings are obtained as –19.1 and –55.0 kcal/mol, respectively. Then, the free energy $\Delta\mu_{\mathrm{red}}$ becomes –81.0 kcal/mol by adopting the value of $\Delta\mu = -45.1$ kcal/mol. Thus, we found that the reduction free energy of –80.1 kcal/mol given by the novel approach agrees well with the value of –81.0 kcal/mol by the conventional one. This clearly demonstrates that the novel method is adequate enough to compute the reduction free energies in solution.

It is quite straightforward to extend the method to the computation of reduction free energy $\Delta\mu_{\mathrm{red}}$ for FAD embedded, for instance, in the cholesterol oxidase 1b4v. The major difference arising in the extension to the protein system is only that the number of kinds of solvents increases from two to four. The solvents in the protein system are, specifically, apoprotein that encloses the FAD, water molecules surrounding the protein, the flavin ring to be described by quantum chemistry, and the part of FAD excluding the flavin ring. Correspondingly, we shall construct the energy distribution

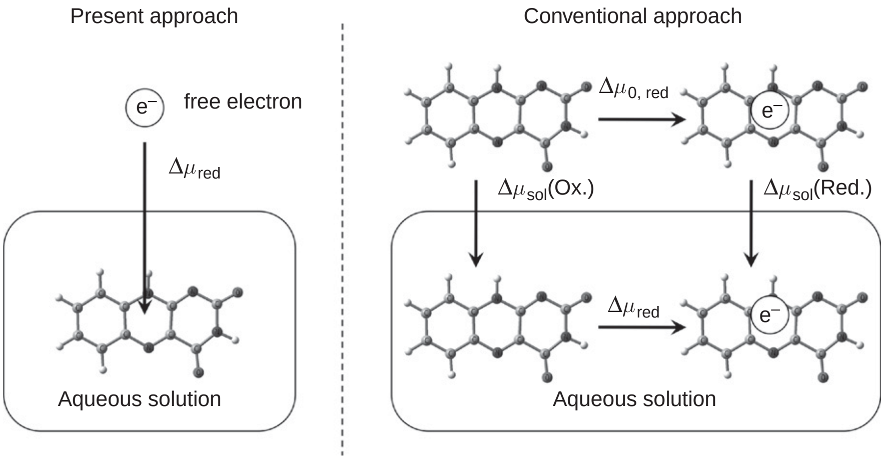

Figure 9.14 Schematics to illustrate the concepts of the two different approaches to compute reduction free energy $\Delta\mu_{\text{red}}$ of flavin ring immersed in aqueous solution. $\Delta\mu_{\text{red}}$ is directly evaluated in the present approach by treating the excess charge as a solute in the QM/MM-ER simulation, while in the conventional approach it is computed with the help of the thermodynamic cycle.

functions for the excess charge, $\rho_{\text{PRO}}(\varepsilon)$, $\rho_{\text{W}}(\varepsilon)$, $\rho_{\text{QM}}(\varepsilon)$, and $\rho_{\text{FAD}}(\varepsilon)$. The total energy distribution function $\rho(\varepsilon)$ is simply given by the sum of these distributions in analogous to the above application. Owing to the fact that the energy distribution function can be divided into the components, the reduction free energy can also be decomposed formally into contributions from various solvents. As noted in the preceding paragraph, the solution system is regarded as the system in which the configurations of the solvent molecules are sampled under the influence of the excess charge located on the flavin ring. In the reference system, on the contrary, solute–solvent interaction is being switched off in the molecular simulations to construct the energy distribution functions.

5. CONCLUSIONS AND PERSPECTIVES

The free energy change plays an essential role in the study of the reaction mechanism in a condensed system since it governs the reaction pathway. It is, therefore, desirable to develop an efficient algorithm of quantum chemistry in combination with a statistical mechanical theory. Our recent development for the solution to this problem is to combine the hybrid QM/MM-ER. A notable feature of our method in the description of the QM subsystem is that the real-space grid approach is utilized to achieve high performance in the parallel computations of the KS-DFT. By virtue of the local nature of the operators in the effective Hamiltonian, the real-space grids method affords us a high parallel efficiency even on a cheap work station cluster with distributed memory architectures. The QM/MM method has so far been applied to various chemical reactions in solutions or biological systems and the efficiency and the adequacy has been well established. In the theory of ER, the distribution functions of the solute–solvent interaction energy serve as fundamental variables to describe the solvation free energy within the rigorous framework of the DFT of solutions. The major obstacle in combining QM/MM and the method of ER arises from the treatment of the many-body effects inherent in the QM/MM interactions. Our strategy is to introduce an intermediate state where the electron density is fixed at its average distribution in solution to make the solute–solvent interaction pairwise additive. Then, the contribution due to the two-body interaction to the solvation free energy can be computed straightforwardly with the standard method of the ER. The remaining minor contribution can also be computed separately by constructing energy distribution functions on another energy coordinate. The efficiency and accuracy of QM/MM-ER were demonstrated by performing the computations for solvation free energies as well as free-energy change associated with chemical reactions in solutions. Furthermore, in this chapter we presented the novel approach to compute reduction free energy of a molecule in solution by treating the excess charge to be attached on the molecule as a solute in the framework of the method of ER. Such a treatment is advantageous when it is applied to protein system because it enables ones to circumvent the direct evaluation of the protein's solvation free energy which may amount to a large negative value. The adequacy of the method were examined for the reaction in aqueous solution by performing the conventional simulation based on the thermodynamic cycle. The reduction free energy of the active site of FAD, that is flavin ring, immersed in AW was computed as –80.1 kcal/mol by the novel approach, while the conventional approach provided the value of –81.0 kcal/mol. Such a good agreement suggests the accuracy of the novel approach. The extension of the method to a protein system with the redox cofactor is straightforward.

We emphasize that the idea treating an excess electron as a solute can be introduced only upon the concept of energy coordinate. The encouraging results thus obtained indicate the possibility that our approach can be extended systematically to a variety of biological reactions. We are now going to construct a unified methodology for reactions of significant importance. Our next subject to be studied is the proton affinity of an amino acid residue embedded in a protein. pK_a of the amino acid residue is obviously an important information which plays an essential role in determining the reaction mechanism and the protein structure as well. The binding free energy at the active site is considered to be one of the most important quantities in the rational drag design. It is obvious that development of an efficient algorithm to determine the substrate-protein binding free energy will make a great impact in the field of computational drag design. The present approach can also be applied to the computation of the ligand-binding free energy. Thus, it is expected that the application of the QM/MM-ER approach will give substantial contributions to wide variety of fundamental chemistry and also to the biological science.

REFERENCES

[1] M.D. Evans, M. Polanyi, Trans. Faraday. Soc. 31 (1935) 875.
[2] H. Eyring, J. Chem. Phys. 3 (1935) 107.
[3] T. Fueno (Ed.), The Transition State, A Theoretical Approach, Kodansha, Tokyo, 1999.
[4] The Chemical Society, London, The Transition State, Sidney Press, Bedford, 1962.
[5] A. Szabo, N.S. Ostlund, Modern Quantum Chemistry, Macmillan, New York, 1982.
[6] R.G. Parr, W. Yang, Density Functional Theory of Atoms and Molecules, Oxford University Press, Oxford, 1989.
[7] P. Hohenberg, W. Kohn, Phys. Rev. B 136 (1964) 864.
[8] W. Kohn, L. Sham, Phys. Rev. A 140 (1965) 1133.
[9] D. Frenkel, B. Smit, Understanding Molecular Simulation, Academic Press, London, 1996.
[10] M.P. Allen, D.J. Tildesley, Computer Simulation of Liquids, Oxford University Press, Oxford, 1987.
[11] R. Car, M. Parrinello, Phys. Rev. Lett. 55 (1985) 2471.
[12] S.Y. Wu, C.S. Jayanthi, Phys. Rep. 358, (2002) 1.
[13] E. Prodan, W. Kohn, Proc. Natl. Acad. Sci. 102 (2005) 11635.
[14] W. Yang, Phys. Rev. Lett. 66, (1991) 1438.
[15] J. Gao, M.A. Thompson (Eds.), Combined Quantum Mechanical and Molecular Mechanical Methods, American Chemical Society, Washington DC, 1998.
[16] M.F. Ruiz-Lopez (Ed.), J. Mol. Struct. (Theochem) 632, special issue (2003).
[17] H. Takahashi, T. Hori, T. Wakabayashi, T. Nitta, Chem. Lett. 3 (2000) 222.
[18] H. Takahashi, T. Hori, T. Wakabayashi, T. Nitta, J. Phys. Chem. A 105 (2001) 4351.
[19] H. Takahashi, T. Hori, H.Hashimoto, and T.Nitta, J. Comp. Chem. 22 (2001) 1252.
[20] T. Hori, H. Takahashi, T. Nitta, J. Comp. Chem. 24, (2003) 209.
[21] H. Takahashi, S. Takei, T. Hori, T. Nitta, J. Mol. Struct. 632 (2003) 185.
[22] H. Takahashi, H. Hashimoto, T. Nitta, J. Chem. Phys. 119 (2003) 7964.
[23] T. Hori, H. Takahashi, T. Nitta, J. Chem. Phys. 119 (2003) 8492.
[24] J. Tomasi, M. Persico, Chem. Rev. 94 (1994) 2027.
[25] J. Tomasi, B. Mennucci, R. Cammi, Chem. Rev. 105 (2005) 2999.
[26] D. Chandler, H.C. Andersen, J. Chem. Phys. 57 (1972) 1930.
[27] F. Hirata, P.J. Rossky, Chem. Phys. Lett. 83 (1981) 329.
[28] J.P. Hansen, I.R. Macdonald, Theory of Simple Liquids, Academic Press, London, 1986.
[29] S. Ten-no, F. Hirata, S. Kato, J. Chem. Phys. 110 (1994) 7443.
[30] H. Takahashi, N. Matubayasi, T. Nitta, M. Nakahara, J. Chem. Phys. 121 (2004) 3989.
[31] N. Matubayasi, M. Nakahara, J. Chem. Phys. 113 (2000) 6070.
[32] N. Matubayasi, M. Nakahara, J. Chem. Phys. 117 (2002) 3605; 118 (2003) 2446.
[33] N. Matubayasi, M. Nakahara, J. Chem. Phys. 119 (2003) 9686.
[34] H. Takahashi, W. Satou, T. Hori, T. Nitta, J. Chem. Phys. 122 (2005) 044504.
[35] H. Takahashi, Y. Kawashima, T. Nitta, J. Chem. Phys. 122 (2005) 124504.
[36] T. Hori, H. Takahashi, M. Nakano, T. Nitta, W. Yang, Chem. Phys. Lett. 419 (2005) 240.

[37] H. Takahashi, K. Tanabe, M. Aketa, R. Kishi, S. Furukawa, M. Nakano, J. Chem. Phys. 126 (2007) 084508.
[38] T. Hori, H. Takahashi, S. Furukawa, M. Nakano, W. Yang, J. Phys. Chem. B 111 (2007) 581.
[39] H. Takahashi, H. Ohno, T. Yamauchi, R. Kishi, S. Furukawa, M. Nakano, et al., J. Chem. Phys. 128 (2008) 064507.
[40] H. Takahashi, H. Ohno, R. Kishi, M. Nakano, N. Matubayasi, Chem. Phys. Lett. 456 (2008) 176.
[41] H. Takahashi, H. Ohno, R. Kishi, M. Nakano, N. Matubayasi, J. Chem. Phys. 129 (2008) 205103.
[42] M. Levy, Proc. Natl. Acad. Sci. 76 (1979) 6062.
[43] M. Levy, Phys. Rev. A 26 (1982) 1200.
[44] J.R. Chelikowsky, N. Troullier, Y. Saad, Phys. Rev. Lett. 72 (1994) 1240.
[45] J.R. Chelikowsky, N. Troullier, K. Wu, Y. Saad, Phys. Rev. B 50 (1994) 11355.
[46] X. Jing, N. Troullier, D. Dean, N. Binggeli, J.R. Chelikowsky, K. Wu, et al., Phys. Rev. B 50 (1994) 12234.
[47] T.L. Beck, Rev. Mod. Phys. 72 (2000) 1041.
[48] K. Hirose, T. Ono, Y. Fujimoto, S. Tsukamoto, First-Principles Calculations in Real-Space Formalism, Electronic Configurations and Transport Properties of Nanostructures, Imperial College Press, Singapore, 2005.
[49] R.M. Martin, Electronic Structure, Basic Theory and Practical Methods, Cambridge University Press, Cambridge, 2004.
[50] A.D. Becke, J. Chem. Phys. 88 (1988) 2547.
[51] W.H. Press, S.A. Teukolsky, W.T. Vetterling, B.P. Flannery, Numerical Recipes, The Art of Scientific Computing, Cambridge University Press, New York, 2007.
[52] L. Kleinman, D.M. Bylander, Phys. Rev. Lett. 48 (1982) 1425.
[53] T. Ono, K. Hirose, Phys. Rev. Lett. 82 (1999) 5016.
[54] T. Hori, H. Takahashi, T. Nitta, J. Theor. Compt. Chem. 4 (2005) 867.
[55] W. Gropp, E. Lusk, A. Skjellum, Using MPI, Portable Parallel Programming with the Message-Passing Interface, The MPI Press, Cambridge, 1997.
[56] M. Svensson, S. Humbel, R.D.J. Froese, T. Matsubara, S. Sieber, K. Morokuma, J. Phys. Chem. 100 (1996) 19375.
[57] T.C. Beutler, A.E. Mark, R.C. van Schaik, P.R. Gerber, W.F. van Gunsteren, Chem. Phys. Lett. 222 (1994) 529.
[58] H. Resat, M. Mezei, J. Chem. Phys. 101 (1994) 6126.
[59] M. Zacharias, T.P. Straatsma, J.A. McCammon, J. Chem. Phys. 100 (1994) 9025.
[60] N. Lu, J.K. Singh, D.A. Kofke, J. Chem. Phys. 118 (2003) 2977.
[61] M.R. Shirts, V.S. Pande, J. Chem. Phys. 122 (2005) 144107.
[62] N. Matubayasi, L.H. Reed, R.M. Levy, J. Phys. Chem. 98 (1994) 10640.
[63] N. Matubayasi, J. Am. Chem. Soc. 116 (1994) 1450.
[64] S.J. Singer, D. Chandler, Mol. Phys. 55 (1985) 621.
[65] A. Kovalenko, F. Hirata, J. Chem. Phys. 110 (1999) 10095.
[66] P.T. Cummings, G. Stell, Mol. Phys. 46 (1982) 383.
[67] D. Chandler, J.D. McCoy, S.J. Singer, J. Chem. Phys. 85 (1986) 5971.
[68] S.M. Kast, Phys. Chem. Chem. Phys. 3 (2001) 5087.
[69] H. Freedman, T.N. Truong, Chem. Phys. Lett. 381 (2003) 362.
[70] H. Freedman, T.N. Truong, J. Chem. Phys. 121 (2004) 2187.
[71] P.B. Balbuena, K.P. Johnston, P.J. Rossky, J. Phys. Chem. 99 (1995) 1554.
[72] P.B. Balbuena, K.P. Johnston, P.J. Rossky, J. Phys. Chem. 100 (1996) 2706.
[73] N. Matubayasi, K.K. Liang, M. Nakahara, J. Chem. Phys. 124 (2006) 154908.
[74] N. Matubayasi, W. Shinoda, M. Nakahara, J. Chem. Phys. 128 (2008) 195107.
[75] Gaussian 03, Revision B.05, M.J. Frisch, et al., Gaussian, Inc., Pittsburgh PA, 2003.
[76] D. Yokogawa, H. Sato, S. Sakaki, J. Chem. Phys. 126 (2007) 244504.

[77] W.L. Jorgensen, J. Chandrasekhar, J.D. Madura, R.W. Impey, M.L. Klein, J. Chem. Phys. 79 (1983) 926.

[78] A.D. Becke, Phys. Rev. A 38 (1988) 3098.

[79] C. Lee, W. Yang, R.G. Parr, Phys. Rev. B 37 (1988) 785.

[80] R.N. Barnett, U. Landman, Phys. Rev. B 48 (1993) 2081.

[81] T.H. Dunning Jr., J. Chem. Phys. 90 (1989) 1007.

[82] P. Ewald, Ann. Phys. 64 (1921) 253.

[83] G. Li, X. Zhang, Q. Cui, J. Phys. Chem. B 107 (2003) 8643.

[84] M. Elstner, D. Porezag, G. Jungnickel, J. Elsner, M. Haugk, T. Frauenheim, et al., Phys. Rev. B 58 (1998) 7260.

[85] A.D. Becke, J. Chem. Phys. 98 (1993) 5648.

[86] A.D. MacKerell, J. Wiorkiewicz-Kuczera, M. Karplus, J. Am. Chem. Soc. 117 (1995) 11946.

[87] M. Born, Z. Phys. 1 (1920) 45.

CHAPTER 10

A Guide to QM/MM Methodology and Applications

Rui Zhang[a,c,e], **Bogdan Lev**[b,c,e], **Javier Eduardo Cuervo**[a,c],
Sergei Yu Noskov[b,c] and **Dennis R. Salahub**[a,c,d]

Contents

[a] Department of Chemistry, University of Calgary, Calgary, Alberta, Canada
[b] Department of Biological Sciences, University of Calgary, Calgary, Alberta, Canada
[c] Institute for BioComplexity and Informatics, University of Calgary, Calgary, Alberta, Canada
[d] Institute for Sustainable Energy, Environment and Economy, University of Calgary, Calgary, Alberta, Canada
[e] Rui Zhang and Bogdan Lev contributed equally to this work.
E-mail addresses: dennis.salahub@ucalgary.ca (D.R. Salahub), snoskov@ucalgary.ca (S.Y. Noskov)

Advances in Quantum Chemistry, Vol. 59
ISSN: 0065-3276, DOI: 10.1016/S0065-3276(10)59010-5

© 2010 Elsevier Inc.
All rights reserved

1. INTRODUCTION

Atomistic simulations and molecular modeling of complex biomolecular phenomena remain challenging, despite recent advances in computational capacity. Molecular mechanical (MM) methods have enabled us to perform molecular dynamics (MD) simulations of enormous chemical as well as biological systems, up to a few hundred thousand atoms. However, the molecular mechanical force fields are unable to describe the changes in the electronic structure of a system undergoing a chemical reaction. To meet this need, quantum mechanical (QM) methods need to be employed to account for bond breaking and bond forming, charge transfer, and electronic excitation. Unfortunately, QM methods are only applicable to relatively small systems, up to several hundred atoms, due to their prohibitive expense for large systems of, say, thousands of atoms.

A natural solution to this dilemma is to combine QM and MM together as a powerful hybrid entity. The combination of QM and MM, often denoted as QM/MM, allows us to investigate large and complicated systems at a reasonable cost while still yielding necessary accuracy. Seminal contributions to the QM/MM methods, pioneered by Warshel and Levitt [1] and Singh and Kollman [2], have blazed the trail for the efforts that followed. Their early work was improved on by Field et al. [3] through the introduction of electrostatic embedding into the QM region. Since then, development of QM/MM methodology has become a red-hot subject [4–26] and its rapid growth and successful applications have greatly facilitated insightful understanding of the chemical properties of solutes in solution [27–37], chemical catalysts [38–45], and biological molecules [46–104].

Besides its wide use in the study of inorganic and organic chemical reactions, QM/MM has proven to be extremely successful in the study of biochemical, especially enzymatic, reactions and therefore has been widely applied in this field. Numerous reviews have been devoted to overviews of QM/MM studies of biochemical reactions over the last 20 years [44,105–117]. In view of QM/MM's remarkable importance in theoretical studies of biological systems, the present review chapter is primarily dedicated to QM/MM methodology and applications pertaining to biorelevant processes.

In this chapter, essential concepts and related techniques are first introduced as the basis of QM/MM methods. Following the introduction of methodology, a brief review of QM/MM applications is provided, highlighting a state-of-the-art application in enzymatic catalysis. Methodologically, this chapter is loosely split into three parts. The first deals with standard definitions of different terms in the effective Hamiltonian, with approaches to the decomposition of the system into classical, coupled, and quantum terms. The second part deals with innovations in techniques for optimizing geometries, for defining reaction paths and for locating transition states (TSs). The content of this part fits well into the rich tradition of quantum chemistry and its application to studies of chemical kinetics. The third part focuses on approaches that have to deal with a large number of degrees of freedom and yet have to treat at least part of the system quantum-mechanically. The methodology arises from the classical approaches of statistical mechanics (ensembles, collective variables and the projector–operator formalism) or quantum statistical mechanics (path integral (PI) methods and quantum Monte Carlo (MC) approaches). To include effects of the environment on different chemical processes ranging from chemical reaction paths to ion solvation, one has to evaluate the free energy of the process. Collective variables and their averages are evaluated for a particular statistical ensemble and the QM treatment for part of the system provides the desired level of detail. The need for a good statistical description of the most relevant ensemble properties gives rise to different enhanced sampling techniques. One of the goals for this chapter is to provide the reader with answers to “Frequently Asked Questions” regarding the utilization of QM/MM techniques in studies of chemical reactions taking place in the condensed phase based on numerous examples found in enzymology, ion channels and transporters, and theoretical and physical chemistry.

2. BASIC CONCEPTS OF QM/MM METHODOLOGY

Before going any further, it is useful to introduce an effective Hamiltonian that can be used for the description of the system’s energetics and dynamics.

In a typical QM/MM scheme, a system is usually divided into two subsystems: the QM subsystem treated by “high-level” QM methods and the MM subsystem treated by “low-level” force field-based methods. The boundary between these two subsystems distinguishes the QM region from the MM region. Ideally, partition of the system should not cut any covalent bonds to ensure the completeness of the QM subsystem. However, crossing covalent bonds is often unavoidable for large molecules, such as polymers and proteins. Here we will use the link atom (LA) method to illustrate the general features, returning to some issues arising from the boundary after the Hamiltonian is introduced.

In order for a QM/MM calculation to mimic the real system the QM chemical structure has to be complete, that is, no dangling bonds are permitted. An intuitive way to remedy a dangling bond is to cap it with an artificial atom, which gives rise to the so-called LA approach [2,3,13,17,53,118]. In this approach, an additional atom, as a link between the QM and MM regions, is added to saturate the QM frontier atom at one end of the cut covalent bond. The LA scheme is illustrated in Figure 10.1.

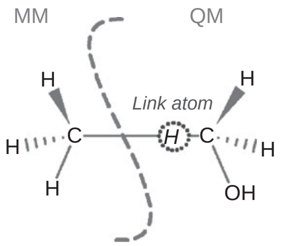

Figure 10.1 Illustration of the LA scheme using ethanol as an example, in which the methyl group is treated as the MM subsystem and the rest is QM.

This LA in most cases is a hydrogen atom because of its simplicity and practicality.

2.1. Energy expression

Two general schemes have been proposed in order to eliminate the artificial interaction between the LA and the other QM atoms and that among LAs—an additive scheme and a subtractive scheme.

2.1.1. Subtractive scheme

In the subtractive scheme, the QM subsystem with the LA (QM + L) is calculated on both QM and MM levels and the entire system (S) without the LA is treated on the MM level. The energy expression is then

$$E(\mathrm{S}) = E_{\mathrm{MM}}(\mathrm{S}) + E_{\mathrm{QM}}(\mathrm{QMS} + \mathrm{L}) - E_{\mathrm{MM}}(\mathrm{QMS} + \mathrm{L}). \tag{1}$$

Since E_{MM}(S) is the summation of the QM subsystem without the LA (QMS), the MM subsystem (MMS) and the interaction between the two (QMS–MMS),

$$E_{\mathrm{MM}}(\mathrm{S}) = E_{\mathrm{MM}}(\mathrm{QMS}) + E_{\mathrm{MM}}(\mathrm{MMS}) + E_{\mathrm{MM}}(\mathrm{QMS} - \mathrm{MMS}). \tag{2}$$

In the same fashion, we also have

$$E_{\mathrm{MM}}(\mathrm{QMS} + \mathrm{L}) = E_{\mathrm{MM}}(\mathrm{QMS}) + E_{\mathrm{MM}}(\mathrm{L}) + E_{\mathrm{MM}}(\mathrm{QMS} - \mathrm{L}). \tag{3}$$

Substituting Eqs. (2 and 3) into Eq. (1), E_{MM}(QMS) is canceled and this gives

$$\begin{aligned} E(\mathrm{S}) = {} & E_{\mathrm{MM}}(\mathrm{MMS}) + E_{\mathrm{MM}}(\mathrm{QMS{-}MMS}) + E_{\mathrm{QM}}(\mathrm{QMS} + \mathrm{L}) \\ & - [E_{\mathrm{MM}}(\mathrm{L}) + E_{\mathrm{MM}}(\mathrm{QMS} - \mathrm{L})]. \end{aligned} \tag{4}$$

Now it is evident that the correction comes from the last subtractive term in Eq. (4), which is expected to cancel the LA contribution in $E_{\mathrm{QM}}(\mathrm{QMS}+\mathrm{L})$. The foregoing derivation has been clearly shown in the work of Bakowies and Thiel [9]. This subtractive scheme was implemented by Morokuma and coworkers in their IMOMM [12] and ONIOM [17,119] protocols.

The upside of this scheme lies in its simple and implicit cancellation of the unwanted artifacts of the LA. Nevertheless, its downside also resides in this cancellation, as it is controversial whether the LA contribution at the QM level can be balanced by that at the MM level. Another drawback is the implied QM–MM interaction calculated at the MM level as indicated by the second term in Eq. (4).

2.1.2. Additive scheme

To explicitly calculate the QMS–MMS interaction on the QM level, an additive scheme has been reported. It is formulated as

$$E(\mathrm{S}) = E_{\mathrm{MM}}(\mathrm{MMS}) + E_{\mathrm{QM}}(\mathrm{QMS}+\mathrm{L}) + E_{\mathrm{QM}}[(\mathrm{QMS}+\mathrm{L}) - \mathrm{MMS}]. \qquad (5)$$

The last term in Eq. (5) accounts for the coupling between QM and MM subsystems. It consists of electrostatic, van der Waals, (vdW) and bonded interactions between QM and MM atoms, all of which will be detailed in following sections. This additive scheme is employed in the majority of QM/MM implementations [1–4,6,9,13,20,53,120].

Comparing Eq. (4) with Eq. (5), one can see two obvious differences. First, the subtractive term in Eq. (4) is omitted in Eq. (5), because $E_{\mathrm{MM}}(\mathrm{L})$ is generally considered very small and thus makes little contribution to the total energy. And $E_{\mathrm{MM}}(\mathrm{QMS}-\mathrm{L})$ is usually regarded as a constant as its distance from the QM boundary atom is fixed in most boundary schemes [115]. Therefore, when calculating the energy difference instead of the absolute energy, the LA's contribution should be mostly canceled out. Second, the QMS–MMS coupling may be calculated at the QM level, as indicated by the last term of Eq. (5). This term can either include or exclude the interaction between the LA and MM atoms, but its inclusion proves to give better results as mentioned below in Section 2.1.4.1. Although lacking physical cancellation for the LA, the additive scheme turns out to perform well in practice.

However, when using the additive scheme for the LA, one needs to take special care of the bonded QMS–MMS interaction at the boundary. The bending term QMA–QBA (QM boundary atom)–MBA (MM boundary atom) and torsional term QMA–QMA′–QBA–MBA (QMA or QMA′ means any QM atom bonded to the QBA) should be eliminated since they are already accounted for by the LA. The stretching term QBA–MMA should be retained to maintain the connection between QM and MM subsystems. On the other hand, one need not worry about these terms in the subtractive scheme as they are corrected by calculating the QM subsystem at the MM level.

2.2. Electrostatic interactions

Both the energy expressions above contain an explicit term describing the QMS–MMS interaction. This interaction consists of the bonded interaction at the boundary (mentioned above) and also the electrostatic and vdW interactions. Two approaches describing electrostatic interactions are introduced here according to how the MM charges are embedded in the QM calculation.

2.2.1. Mechanical embedding

As implied in the subtractive formulation (4), E_{MM}(QMS–MMS) accounts for the QMS–MMS interaction at the MM level. Therefore, the QM atoms are represented as point charges, bond dipoles, or higher multipoles. In most cases, the point-charge model is adopted. However, this treatment is viewed as problematic because the charge density of the QM region is not actually polarized by the MM part.

Hagiwara and coworkers [121] compared mechanical embedding in the subtractive scheme with electrical embedding (explained below) in the additive scheme by a QM/MM study of a protein–DNA complex. They found the highest occupied molecular orbital (HOMO) energies differed by 23.7 kcal/mol as calculated by the two schemes. This supports the viewpoint that the QM region has to be polarized.

2.2.2. Electrical embedding

To ensure the QM subsystem is polarized by MM charges, this charge–charge interaction has to enter into the QM Hamiltonian:

$$\hat{H}_{\mathrm{QM-QM}} = -\sum_{i,m} \frac{q_m}{r_m} + \sum_{A,m} \frac{Z_A q_m}{R_{Am}}, \tag{6}$$

where q_m are the charges of MM atoms, Z_A the atomic number of QM atoms, i runs over all QM electrons, A over all QM atoms including LAs, and m over all MM atoms. The first term is a one-electron operator and the second accounts for the nuclei–MM charge interaction. When acting on the QM wave function, Eq. (6) results in the electrostatic interaction between QM and MM subsystems as a portion of E_{QM}[(QMS + L)–MMS] [13].

As a matter of fact, electrical embedding can be implemented not only with the additive scheme but also with the subtractive scheme. Lin et al. [122] demonstrated the formulation of a subtractive scheme with electrical embedding in their QM/MM manual. They showed

$$\begin{aligned} E(\mathrm{S}) = {} & [E_{\mathrm{bond}}(\mathrm{S}) - E_{\mathrm{bond}}(\mathrm{QMS}+\mathrm{L})] + [E_{\mathrm{vdW}}(\mathrm{S}) - E_{\mathrm{vdW}}(\mathrm{QMS}+\mathrm{L})] \\ & + E_{\mathrm{el}}(\mathrm{MMS}) + E_{\mathrm{QM}}(\mathrm{QMS}+\mathrm{L}), \end{aligned} \tag{7}$$

where subscripts bond stands for bonded interactions, vdW for van der Waals interactions, and el for electrostatic interactions. The last term of Eq. (7) includes Eq. (6) in the entire QM Hamiltonian. For a detailed derivation, readers may refer to Section 4G of Ref. [122]. By constructing electrical embedding into the subtractive scheme, the LA artifacts are corrected at the MM level and thus should lead to a relatively better result than the additive scheme.

2.2.3. Electrical embedding with explicit treatment of MM region polarization

Since the QM region is polarized by MM atoms, it would be unbalanced if the MM region were not affected reciprocally. A straightforward treatment based on the MM point-charge model is to include induced dipoles as a polarization effect. An early effort was conducted by Bakowies and Thiel [9], which is formulated as

$$E_{\text{ind}}(MM) = \frac{1}{2}\sum_{m} \mu_{\alpha}\langle F_{\alpha}\rangle, \tag{8}$$

where the energy of induced MM dipoles is the summation of the m dipole moments μ_α of the MM subsystem multiplied by the electrical field F_α from the QM subsystem. μ_α depends on the polarizability tensor and the QM electrical field, while the interactions between the dipoles are determined by the dipole moments and the dipole–dipole interaction tensor. Since the dipoles interact with each other, an iterative procedure must be applied to generate a self-consistent polarization.

Another polarizable force field, namely SIBFA (Sum of Interactions Between Fragments Ab initio computed), incorporates multipoles up to quadrupoles. It divides a macromolecule into elementary fragments comprising multipoles and having different polarizabilities, among which interactions are summed to obtain the total energy. A general energy expression for multipole–multipole interactions is

$$\begin{aligned} E_{\text{multipole}} = E_{\text{mono-mono}} + E_{\text{mono-dip}} + E_{\text{mono-quad}} + E_{\text{dip-dip}} \\ + E_{\text{dip-quad}} + E_{\text{quad-quad}}. \end{aligned} \tag{9}$$

It is worth mentioning here that the monopole–monopole interaction is calculated by splitting the atom into core and valence electrons with a special parameterization, which, as a result, is different from the classical expression $E = q_i \cdot q_j / r_{ij}$. The same treatment is made for the monopole–dipole interaction. Details are in a recent review [123]. Linking SIBFA with QM engines is currently in progress [124].

A simpler approach to modeling electronic polarization is based on the Drude-oscillator model, in which a fictitious Drude particle with opposite sign is attached to a point charge by a harmonic spring thus introducing dipole induction in classical simulations [125]. The resulting electrostatic potential (ESP) for a system containing Drude particles can be expressed as

$$E_{\mathrm{elec}} = \sum_{i}\sum_{i>j}\frac{q_i q_j}{r_{ij}} + \left(\sum_{i}\sum_{j'}\frac{q_i q_{j'}}{r_{i,j'}} + \sum_{i'}\sum_{i'>j'}\frac{q_{i'} q_{j'}}{r_{ij}}\right) + \frac{1}{2}\sum_{\alpha'} k_{\alpha'} d_{\alpha'}^{2} \qquad (10)$$

where the prime denotes Drude particles. The last term represents the oscillator self-energy expressed in familiar form with the force constant k_α related to the site's polarizability (α) as $\alpha = q'^2/k_\alpha$.

Higher-order multipoles are avoided by using the simple Drude model and the only difference with a nonpolarizable function is the introduction of a new atom type—Drude. Parameterization of the Drude model in CHARMM [126,127] for various systems has been undertaken by Lamoureux and coworkers [128–131]. It has been implemented recently in the QM/MM interface between CHARMM and deMon2k. Lev et al. [53] performed an analysis of the importance of the explicit treatment of the parameterization for the interaction energy in the water dimer. The interaction energies show little improvement with the inclusion of explicit polarization as both the polarizable and the classic model are parameterized to reproduce the energetics and geometry. However, MD simulations with explicit inclusion of dipole induction indicate that there is a significant component missing in the description of solvent dynamics around highly polarizable solutes. For the polarizable water around a sodium or potassium ion, the magnitude of the induced dipole can be higher than 0.1 D, which can be very important in cases where electronic effects play a significant role.

2.2.4. First-principles electrostatic potential

Though polarized embedding includes the effect of electron polarization in the force field, its reliance on the point-charge model is nonetheless problematic as atomic charges in reality should be more distributed than simple monopoles. To mediate the point-charge model with overconcentrated charges, Darden and coworkers [132–134] have proposed the Gaussian electrostatic model (GEM) to represent the charge density. In this model, the wave function of the system is first calculated with ab initio methods and the obtained electron density is then fitted with a set of Gaussian basis functions according to the variational principle [133]. The coefficients obtained from this procedure together with the basis set (currently s-type Gaussian functions) forms the frozen core to reproduce the Coulomb and exchange interactions. Polarization effects are described by parameterized dipoles at specific sites. Recently, they have extended this model to higher-order multipoles and sped it up using reciprocal space methods to calculate long-range electrostatic interactions [134]. The GEM method has been tested with water dimers [132], the benzene dimer, and water–metal complexes [134] and proved to perform consistently better than conventional point-charge models. It remains to be seen how useful it will be for large or very large systems, perhaps in conjunction with fragment-based approaches.

As a brief summary, electrostatic interactions have been demonstrated to be crucial to enzymatic reactions [135]. Therefore, an accurate calculation of these interactions is required. More elaborate models are expected to reconcile accuracy and efficiency.

2.3. van der Waals interactions

Besides the bonded and electrostatic interactions, the QMS–MMS coupling also includes vdW interactions. The vdW interaction is usually described by a Lennard-Jones 12-6 potential:

$$E_{ij} = \sum_{i,j} \left(\frac{A_{ij}}{r_{ij}^{12}} - \frac{B_{ij}}{r_{ij}^{6}} \right), \tag{11}$$

where i runs over QM atoms and j over MM atoms, and A and B are constants pertaining to atom types. This contributes as a component of the last term in Eq. (5).

In a typical force field, the bonded, electrostatic, and vdW parameters are optimized together using high-level calculations or experimental results. Using parameters of a certain term separately from others may sometimes cause trouble. In the case of QM/MM calculations, when electrical embedding is used, the vdW interaction of QMS–MMS could be incorrect as the corresponding electrostatic interaction is not the parameterized point-charge–point-charge interaction any more. To alleviate this issue, Friesner and coworkers [16] have reoptimized the vdW parameters for amino acids in their QM/MM implementation. It should be noted that they also included a hydrogen bond correction term in their scheme and thus the vdW parameters were parameterized accordingly. In their work, only the vdW radii were reparameterized but not the well depth.

Recently, Mulholland and coworkers [136] reoptimized vdW parameters from CHARMM 27 for nucleic acids with respect to the B3LYP density functional theory (DFT) method. Their results indicated that, for QM/MM investigations of nucleic acids, the standard force field vdW parameters might not be appropriate for atoms treated by QM. QM/MM interaction energies calculated with standard CHARMM27 parameters are found to be too large, by around 3 kcal/mol. They reasoned that this was because of an overestimation of electrostatic interactions and therefore reparameterized the vdW parameters to compensate for that.

However, Cui and coworkers [137] have tested three sets of vdW parameters and concluded that the QM/MM energetics were not sensitive to the vdW parameters and efforts to improve the QM/MM accuracy should focus elsewhere. With self-consistent charge tight binding (SCC-DFTB) as the QM method, they calculated a proton transfer process for a solvated enediolate and a solvated fused-ring molecule (flavin adenine dinucleotide), respectively. They found similar thermodynamic quantities (the reduction potential deviated by 0.2 kcal/mol) for different vdW parameters although there were noticeable differences regarding solvent distribution functions around the solute.

An important difference between the modeled systems in Refs. [136] and [137] is solvation. While the former included only one water molecule for each base pair, and is thus essentially a gas-phase model, the latter employed a fully solvated system with explicit water. It was found in Ref. [137] that hydrogen bond lengths and energies deviated more for different parameters in the gas phase than in the condensed phase. On the other hand, the optimized vdW parameters from Ref. [136] were not tested in the condensed phase. Nonetheless, the choice of vdW parameters should be carefully considered as short-range vdW interactions could greatly affect the configuration of the QM region.

2.4. Boundary treatment

2.4.1. Link atom

When a covalent bond between the QM and MM subsystems is crossed by the boundary, and an LA is introduced, it generates more problems for the QM part than for the MM part. A cascade of artificial effects is brought in by the LA. First, it introduces unwanted interactions with the QM atoms and other LAs, as discussed above. Second, an LA bears three extra degrees of freedom that should not be present in the real system. Third, it is spatially too close to the MM frontier atom as it sits on the bond between the QM and MM frontier atoms. When the MM frontier atom is charged, this unrealistic closeness will cause an overestimated interaction between the MM frontier atom and the LA, and hence an overpolarization of the QM subsystem.

To circumvent the second issue, the position of the LA should be fixed in order to avoid the excess degrees of freedom. A straightforward way to achieve this goal is to relate its coordinates to its adjacent neighbors, that is, the QM and MM boundary atoms. First proposed by Dapprich et al. [17], the position of the LA is defined as a function of the positions of the QBA and the MBA in Cartesian coordinates:

$$\vec{R}_{\mathrm{LA}} = \vec{R}_{\mathrm{QBA}} + \alpha(\vec{R}_{\mathrm{MBA}} - \vec{R}_{\mathrm{QBA}}), \tag{12}$$

as is evident from

$$\alpha = \frac{\vec{R}_{\mathrm{QBA}} - \vec{R}_{\mathrm{LA}}}{\vec{R}_{\mathrm{MBA}} - \vec{R}_{\mathrm{QBA}}}, \tag{13}$$

where α can either be held constant as the ratio of the equilibrium bond lengths of QBA–LA and MBA–LA [17] or be varied as the ratio of the equilibrium bond lengths of QBA–LA and the distance of QBA–MBA [138,139].

Moreover, in some works α is more elaborately defined, which involves the deviation of QBA–LA and that of QBA–MBA from the equilibrium bond lengths and the bond stretching constants of the QBA–LA bond ($k_{\mathrm{QBA-LA}}$) and the QBA–MBA bond ($k_{\mathrm{QBA-MBA}}$). In the work of Eichinger et al. [27],

$$\alpha = \frac{(\vec{R}_{\mathrm{QBA}} - \vec{R}_{\mathrm{LA}}) - (\vec{R}_{\mathrm{QBA}_0} - \vec{R}_{\mathrm{LA}_0})}{(\vec{R}_{\mathrm{MBA}} - \vec{R}_{\mathrm{QBA}}) - (\vec{R}_{\mathrm{MBA}_0} - \vec{R}_{\mathrm{QBA}_0})} = \frac{k_{\mathrm{QBA-LA}}}{\mathrm{k}_{\mathrm{MBA-QBA}}}. \tag{14}$$

By fixing the location of the LA, elimination of the gradient on the LA follows. Since the position of the LA is constructed by the positions of the QBA and the MBA, the gradient of LA should be accordingly projected onto the QBA and the MBA. Since α is the ratio of QBA–LA to QBA–MBA and the gradient is formulated as $\mathrm{d}E/\mathrm{d}R$, the LA's gradient portion to be projected on the QBA should be $(1-\alpha)$. When α is held constant, this gives [17]

$$\vec{G}_{\mathrm{QBA}} = \vec{G}_{\mathrm{QBA}_0} + (1-\alpha)\cdot\vec{G}_{\mathrm{LA}}, \tag{15}$$

$$\vec{G}_{\mathrm{MBA}} = \vec{G}_{\mathrm{MBA}_0} + \alpha\cdot\vec{G}_{\mathrm{LA}}, \tag{16}$$

where $\vec{G}_{\mathrm{QBA}_0}$ and $\vec{G}_{\mathrm{MBA}_0}$ are the gradients without the contribution from the LA. When α varies, one will have to multiply the LA's gradient by a transformation matrix, as detailed in Refs. [115,138,139]. Thus the excess degrees of freedom from the LA are avoided in geometry optimization and MD.

The third issue regarding the artificial LA is the overpolarization by the MM boundary atom when it is charged. An easy way to alleviate this drawback is to remove the charge of the MBA from the QM and MM subsystem interaction, which is termed the single LA scheme [140]. However, this will result in an unrealistic extra charge in the MM subsystem. To eliminate artificially created charge, the deleted charge from the MBA can be redistributed over the rest of the residue group pertaining to the MBA [141]. In other schemes, charges of the entire MBA residue group are removed from the QM and MM subsystem interaction [2] or the MBA charge is redistributed among the rest of its residue group [142]. As opposed to the conventional point-charge model, MM partial charges may be represented as Gaussian charge distributions centered on the respective atoms [15,143,144]. Double LA [143] and charge shift [21] methods are also proposed to treat the boundary MM charges. More recently, Lin and Truhlar have developed two schemes to remedy this overpolarization problem: the redistributed-charge scheme and the redistributed-charge-and-dipole scheme [23].

All the approaches mentioned above except the RC and RCD have been compared by Konig et al. [141], with regard to different systems. They first calculated deprotonation energies of alcohols and carboxylic acids, in which the alkyl group was treated with MM and the alkoxyl group with QM. As a result, the single LA method always underestimated the energy by an average of 20 kcal/mol compared to high-level calculations, whereas all the others overestimated the energy and the excluded group method yielded the closest result. When calculating the deprotonation energies of amino acids, the single LA and excluded charge approaches produced the largest deviation, whereas the Gaussian distributed charge and charge shift methods were the closest to the high-level calculation result. It should be noted here that the Gaussian distributed charge model greatly depends on the blurred width and noticeable differences were found when different widths were chosen [141]. When evaluating the deprotonation energies of DNA bases, the single LA method again deviated the most from high-level calculations while the others gave comparable results. And the two calculations using the Gaussian distributed charge model with different blurred widths yielded different energies. Activation energies and endothermicities were also calculated by Konig et al. [141] with different treatments of the boundary MM charges. The comparison showed appreciable deviations among them in one enzyme (triosephospate isomerase), while the calculation in the methyl glyoxal synthase enzyme divided them into two groups: the single LA and excluded group methods with lower energies and the others with higher energies. In summary, the single LA method tends to underestimate the energies, while other amended methods can improve the accuracy, which are case-dependent nonetheless.

2.4.2. Frozen localized orbitals

Even though extensive efforts have been made to eliminate the artificial effects introduced by the LA, this approach still lacks a solid physical foundation and it is hence arbitrary and controversial. In order to eliminate the side effects of the link atom, the dangling bond at the boundary may be capped by a frozen localized orbital (FLO) instead of an LA. This method dates back to Warshel and Levitt [1]. Another early attempt adopting this philosophy is the local self-consistent field (LSCF) approach as illustrated in Figure 10.2a. An atom with only s and p valence orbitals is chosen as the QM boundary atom and thus four hybrid orbitals are formed using one s and three p orbitals. Three of the hybrid orbitals participate in the normal QM calculation while the one left is strictly localized between the QM and MM boundary atoms, termed strictly localized bond orbital (SLBO) [145]. The respective coefficients for the four hybrid orbitals need to be parameterized and a $-1e$ charge should be taken from

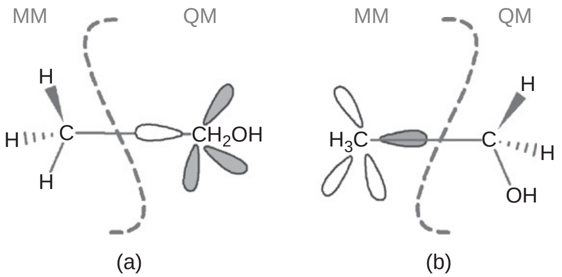

Figure 10.2 Illustration of LSCF and GHO schemes where orbitals are shown in spindles and those participating in the QM calculations are shadowed. (a) LSCF Scheme and (b) GHO scheme. Please refer to online version for color image.

the MM boundary atom as it donates 1 electron to the SLBO. Therefore, the total QM energy comprises the energy of regular QM orbitals, the SLBO, and the coupling between them. The gradient is calculated accordingly. As an update, the SLBO, is then parameterized as a classical potential for different types of bonds [146].

Based on the LSCF procedure, Friesner and coworkers [15,147] introduced more extensive parameterization in terms of electrostatics, vdW interactions, and hydrogen bonds at the boundary instead of taking the parameters directly from the MM force field. Their parameterization is sensitive to different QM methods and basis sets. Contrary to the LSCF scheme, the frozen orbital can also be centered on the MM boundary atom instead of the QM boundary atom, which is termed the generalized hybrid orbital (GHO) method by Gao and coworkers [5–7,148]. In this approach, one of the hybrid sp^3 orbitals participates in the QM calculation while the other three are kept frozen as shown in Figure 10.2b. The force field charge of the MM boundary atom is equally distributed over the four hybrid orbitals as opposed to the LSCF which has to calculate the charge density of the frozen orbital for different systems. This advantage ensures the transferability of the GHO. However, the classical potential parameters involving the MM boundary atom, especially its bonding parameters, have to be reoptimized to accommodate the effects introduced by the three frozen orbitals. Or the interactions between the frozen orbitals and other normal QM orbitals need to be adjusted by scaling the integrals.

2.4.3. Performance of LA and FLO: summary

The LA scheme is advantageous for its simplicity while the FLOs scheme is convincing for its solid physical foundation. Their application and performance have been the concern of QM/MM investigators, who have made comparisons between these two methods. Karplus and coworkers [142] compared the LA with the LSCF with regard to the proton affinity and deprotonation enthalpy of propanal. In their test, there were two types of LA schemes, one that includes the electrostatic interaction between the LA and the MM charges and the other one without. And the one with LA–MM charge interaction performed better, especially when a Na^+ ion was placed in the vicinity of the hydroxyl group. Upon calculation of the Mulliken charge of the LA, they found that without including LA–MM charge interactions, the charge on the LA is significantly greater than usual, hence biasing the charge density of the rest of the QM orbitals. This finding indicates that polarization of the link atom by MM charges is important. The LA scheme with the LA–MM charge interaction was then compared with the LSCF scheme and they gave similar results. However, when a Na^+ ion is present in the neighborhood of the hydroxyl group, the LA was consistently better than the LSCF, suggesting that the assumption of a strictly localized bond orbital is not proper when the QM subsystem is strongly polarized by charges. As for geometry optimization of a tripeptide, the LSCF performed better than the LA, as is conceivable because of the geometry constraint of the LA mentioned above.

Mulholland and coworkers [149] compared the LA with the GHO with regard to the reaction mechanism of a virus protease. In their LA scheme, the LA–MM charge interaction was included. With the same boundary, they found that the free energy barriers and reaction free energy differed by 8 kcal/mol and the locations of the reactant, product, and TS were rather different as well. The difference was attributed to the rotation of C_α—C_β of an aspartic residue that can form a hydrogen bond with the adjacent histidine residue and thus stabilize the reaction intermediate. When the LA was employed, the hydrogen bond was found to be broken, thus significantly destabilizing the intermediate. On the other hand, this did not occur for the GHO. This discrepancy is thought to be due to the one extra proton and more delocalized orbitals introduced by the link hydrogen atom. Be that as it may, it could also be caused by the improper partitioning of the system. For instance, if the LA had been placed farther away from the rotational bond rather than on that bond, the result could have been improved. The reason why the LA was positioned the same as the GHO was just for the convenience of the comparison and the GHO is only available for sp^3 hybridized carbon. Therefore, the discrimination might have arisen from the way the system was partitioned as well.

As a matter of fact, the choice of the boundary placement does influence the result remarkably as verified in Refs. [141,142,149] . Moreover, when the size of the QM subsystem is enlarged, the result is consistently improved [141]. So the rule of thumb of partitioning the system is to place the boundary as far from the reaction center as possible and avoid boundary positions that can directly affect the active space as discussed in Ref. [149]. The capped bond is preferred to be a C—C bond in order to circumvent the overpolarization by other, more intensely charged, MM boundary atoms.

2.4.4. Other boundary schemes

Besides the LA and FLO approaches, a boundary-atom scheme has also been implemented, in which the MM boundary atom is treated as a special boundary atom to cap the dangling bond at the QM frontier, thus relying on elaborate parameterization for different frontiers. Among them, we highlight Zhang and Yang's pseudobond approach [150,151], Poteau and coworkers' [152,153] effective group potential approach and DiLabio and coworkers' [154] quantum capping potential treatment. Notably, the quantum capping potential treatment has been applied by Salahub and coworkers [18] to study electron paramagnetic resonance (EPR) and obtained consistently better results than the single LA scheme. For a comprehensive review of this class of schemes, one can refer to Senn and Thiel's review [115]. Moreover, instead of fixing the boundary, it can also be adaptive during the calculation [155–157]. This adaptive scheme allows atoms to change between QM and MM subsystems and in principle should also allow charge transfer across the boundary once fully developed.

3. QM/MM OPTIMIZATION TECHNIQUES FOR POTENTIAL ENERGY SURFACES

A potential energy surface (PES) is typically a rugged landscape marked by various valleys and peaks. Among others, we are most interested in the stationary points: minima and saddle points. In this section, we will introduce the techniques for finding these points and the paths between them. We will start with geometry optimization methods to find the minima on QM/MM PESs.

3.1. Geometry optimization

In general, QM calculations adopt quasi-Newton methods to optimize geometries. These estimate the Hessian matrix by gradient differences and then update it in various ways. In the case of MM optimization, the widely used methods are not only second-order methods but also first-order methods such as conjugate gradient and steepest descent (SD) methods. In the current context of QM/MM optimization, our focus will be on techniques specific to QM/MM rather than optimization algorithms in general.

In principle, the whole QM/MM system can be simultaneously optimized with a uniform optimizer using the QM/MM potential and gradient. Convergence, however, will be difficult to reach when the starting geometry is far from the minimum. Moreover, there are also technical issues if the subsystems are optimized at the same time. First, as just mentioned, QM and MM calculations prefer different optimizers. If one optimizer is chosen for both subsystems, the efficiency of optimizing either subsystem will be compromised and the same optimization parameters such as the trust radius may lead the configuration to an undesired space. Second, QM and MM optimizations are usually conducted in different coordinate systems. QM minimization often employs redundant internal coordinates or internal coordinates because of difficult convergence with strongly coupled Cartesian coordinates. Conversely, MM minimization prefers Cartesian coordinates to avoid the laborious transformation between Cartesian and redundant internal coordinates.

3.1.1. Microiteration

Considering the different natures of QM and MM methods, optimization is easier to run separately for each subsystem on their respective levels. To this end, a macro-/microiterative scheme has been proposed. There are two variants of this scheme: one termed the adiabatic scheme [12,16,158–162] and the other the alternating scheme [2,4]. In the adiabatic scheme, the optimization is driven by the QM optimizer. The MM subsystem is optimized to convergence with the QM part frozen, and this is termed a microiteration. Thereafter, the QM region is optimized till convergence with the MM part frozen, and this is termed a macroiteration. These two iterations alternate until the whole system is fully optimized. In the alternating scheme, after the MM region is optimized, only one optimization step is taken in the QM region and it switches back to MM optimization again, thus iterating until both are fully optimized. Since the QM region is of principal interest and thus its optimization serves as the main driver, the adiabatic scheme is chosen more often. A diagram of both schemes is shown in Figure 10.3. Following this "divide and conquer" philosophy, the advantage

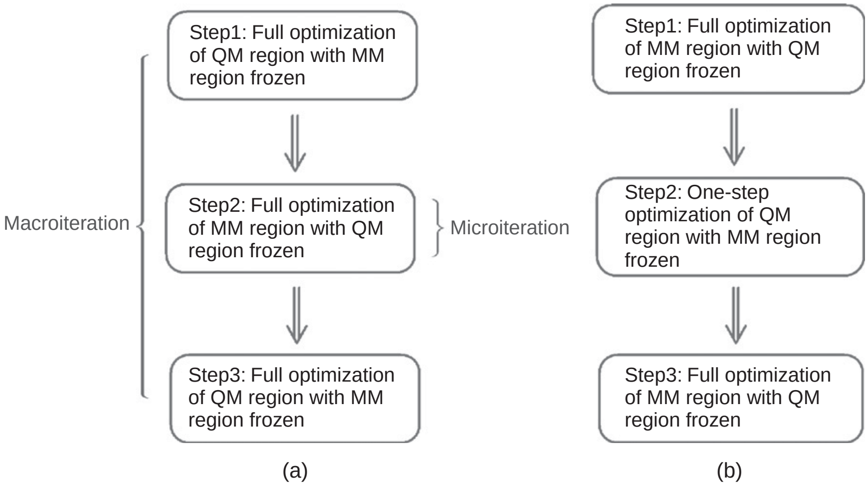

Figure 10.3 Diagram of the adiabatic scheme (a) and the alternating scheme (b).

of QM/MM partitioning is thoroughly exploited. First, the number of expensive QM energy and gradient calculations can be dramatically reduced. Second, the costly coordinate transformation is avoided in the MM optimization.

However, it is often harder to unite than to divide. One encounters a problem when calculating the QM–MM coupling during the optimization. In the microiteration of optimizing the MM subsystem, even though the QM part's geometry is frozen, the electrostatic QM–MM interaction should be calculated on the QM level for electric embedding. So, ideally, a full QM SCF calculation should be run at every MM minimization step (termed S1 herein) to obtain the forces on the MM charges exerted by the QM atoms. This procedure is prohibitively expensive considering the fact that an MM minimization usually takes thousands of steps. Approximation comes into play at this point.

Yang and coworkers [4] proposed to use the ESP charges to represent the QM charge density and approximate the QM–MM electrostatic force on the classical level during the microiteration. The gradient is calculated as

$$G_{\mathrm{el}}(\mathrm{QMS}-\mathrm{MMS}) = G_{\mathrm{ESP}}. \tag{17}$$

This treatment leads to a discrepancy between the gradient and the energy as the energy for the entire system still retains the electrostatic interaction on the QM level. To alleviate this double-standard deficiency, Friesner and coworkers [16] and Thiel and coworkers [162] introduced an ESP-based QM–MM interaction as a correction to the QM-based electrostatic interaction. Before the MM minimization steps, the ab initio calculated gradient on MM charges is calculated as G^{0}_{QM}(QMS–MMS), the ESP-based gradient G^{0}_{ESP} and the ESP charges are retained throughout the MM minimization. At each MM optimization step, the ESP-based gradient $\mathrm{G}_{\mathrm{ESP}}$ is recalculated (termed S2 herein). Therefore, the electrostatic QM–MM gradient is formulated as

$$G_{\mathrm{el}}(\mathrm{QMS}-\mathrm{MMS}) = G^{0}_{\mathrm{QM}}(\mathrm{QMS}-\mathrm{MMS}) + (G_{\mathrm{ESP}} - G^{0}_{\mathrm{ESP}}). \tag{18}$$

The corresponding energy for MM minimization [161] is

$$\begin{aligned} E_{\mathrm{el}}(\mathrm{QMS}-\mathrm{MMS}) = {} & E^{0}_{\mathrm{QM}}(\mathrm{QMS}-\mathrm{MMS}) + (E_{\mathrm{ESP}} - E^{0}_{\mathrm{ESP}}) \\ & + [\,{}^{\mathrm{QM0}}_{G}(\mathrm{QMS}-\mathrm{MMS}) - G^{0}_{\mathrm{ESP}}](R_{\mathrm{MM}} - R^{0}_{\mathrm{MM}}) \end{aligned} \tag{19}$$

where E^{0}_{QM}(QMS–MMS) is the total energy corresponding to G^{0}_{QM}(QMS–MMS), E_{ESP} the total energy calculated with the ESP model, and R the coordinates of the MM atoms.

As Eq. (17) is improved by the perturbation in Eq. (18), the gradient now becomes consistent with the energy [Eq. (19)]. The ESP charges were then further improved by a one-SCF procedure by Lluch and coworkers [159]. They assumed the QM wave function to be frozen during the MM minimization and thus only the electron–MM charge and nuclei–MM charge interactions need to be calculated because the other terms in the QM Hamiltonian stay the same. Therefore, only one SCF calculation is performed at each MM minimization step to evaluate the QM–MM electrostatic coupling (termed S3 herein).

Nonetheless, freezing the QM wave function during the MM minimization is not quite convincing as it should be polarized in reality. Morokuma and coworkers [158] proposed to recalculate the wave function when the MM subsystem is fully optimized (termed S4 herein). Thereafter, the MM minimization is started again with the newly polarized QM densities. Moreover, they also suggested using a fast multipole method instead of the ESP charge model for the QM–MM electrostatic interaction.

To evaluate the different optimization schemes above, Thiel and coworkers [162] first tested whether the QM wave function should be recalculated after the MM subsystem is optimized. They tested S2 and (S2 + S4) with a water cluster and ESP charges and found the optimized energy by S2 alone was lower and reached with fewer iterations, though at a slightly different geometry. They then compared S1, (S2 + S4), and (S3 + S4), and found that (S3 + S4) yielded the lowest optimized energy and second-fewest QM calculations after S1. It seems that S2 gives the fastest convergence whereas (S3 + S4) produces the best accuracy.

In addition to the schemes above, Moliner and coworkers [160] have implemented a dual-level scheme for QM/MM optimization. They use semiempirical methods to calculate the QM–MM electrostatic coupling in the MM minimization [160]. A similar approach has been proposed by Warshel and coworkers [8] to introduce a reference potential using the empirical valence bond (EVB) method.

3.1.2. Macroiteration

So far, we have discussed the QM–MM coupling concerning the MM minimization. A subsequent question would be: Is this coupling a problem in the QM minimization? In fact, it is not a problem in the gradient calculation, but it is a disturbing one in the Hessian update. In the widely used adiabatic scheme, a QM optimization step is taken after the MM region is optimized and hence the QM Hessian should be updated from the last one. Although the gradients only relate to the current geometry and wave function, the Hessians are decided by the gradient difference between the previous step and the current one. Contributions to the gradient change include the QM wave function and the MM coordinates as well because the latter are altered during the MM minimization. Therefore, the gradient change caused by the MM coordinate changes should be eliminated. To this end, Morokuma and coworkers [161] have incorporated a quadratic QM–MM coupling in the macroiteration that is realized by coordinate transformation and Hessian manipulation. They managed to demonstrate its moderately improved performance for small molecules and better convergence behavior than schemes without the quadratic coupling.

3.1.3. Convergence criteria

The adiabatic scheme in principle requires a completely optimized MM region to obtain a good QM convergence behavior. To ensure this, the ratio of the QM optimization convergence criterion to that of MM optimization should be appreciable, as it was set to 10 in Ref. [162]. Moreover, there is no presumption in the macroiteration that the forces on the MM atoms are exactly zero, so less tight convergence criteria can be used in the microiteration [161,162].

3.1.4. Size of QM region and starting geometry

As we have stressed throughout this article, the size of the subsystems greatly influences the results. As demonstrated in Ref. [159], when using the S3 scheme, the total CPU time for optimization does not increase monotonically with the size of the QM region, which indicates that there is a medium QM size leading to a minimum CPU time for optimization. When the MM environment configuration is complicated and hard to converge, a larger QM core can be chosen as this leads to less QM–MM coupling and hence fewer microiterations. However, with the ESP charges, the larger the QM core, the greater the error caused by the charge screening effects as the dielectric constant is unknown in the QM region.

Different starting geometries could well result in different minima, especially for complicated proteins [163]. This indicates the importance of sufficient sampling and averaging as a single optimized geometry is not quite meaningful. This is especially important in reaction path calculations.

3.2. Transition state search on the potential energy surface

Having located the minima on the energy surface, we come to a natural question: How are these minima connected with each other? Chemically speaking, this question equals: How to find the reaction path between the reactant and product? According to the transition state theory (TST), there is always a TS(s) on the path from the reactant to the product. This TS is a first-order saddle point on the potential energy surface, which has a negative eigenvalue in only one direction. If we can identify the TS, the reaction rate can be calculated according to the TS theory. Knowing the TS, an intrinsic reaction coordinate (IRC) method [164] is usually adopted to draw out the reaction path to understand the reaction mechanism. However, the TS is often unknown for complicated reactions, for example, enzymatic reactions. Hence searching for the TS becomes a principal task for the study of chemical reactions.

Ideally, the TS can be found via an eigenvector following approach based on the first-order saddle point nature of the TS. However, this procedure requires a good initial guess when starting from the vicinity of the TS, which is often impractical, especially for high-dimensional systems. Therefore, the search for the TS is often combined with finding the reaction path that connects the reactant and product minima. As soon as the reaction path is found, the TS is evidently identified as the highest point along the path.

Similar to the philosophy of Ref. [22], del Campo and Köster [165] have proposed a hierarchical TS search algorithm. They first use the saddle method similar to reaction coordinate (RC) driving, which sequentially optimizes to zero the system's force perpendicular to the path, so as to bracket the TS between two highest points. The subsequent TS finder adopts the uphill trust region method, which constrains the step to ascend the potential energy surface in the direction of the normal mode associated with the TS vector and to descend in the remaining normal modes. This hierarchical approach has been effectively implemented in deMon2k [166] and has proven to work well for TS searches with QM methods. Its further incorporation of QM/MM methods is of great interest. To obtain an initial guess in a simple way, instead of the elaborate saddle method, the multi-coordinate driving scheme is proposed by Berente and Naray-Szabo [167]. Their method differs from the regular reaction coordinate-driven (RCD) method by including multiple RCs. And it has been tested with a QM method for hydrolysis by dUTPase [167].

In the following section we discuss the minimum energy path (MEP) technique. More complex methods, involving more or less extensive sampling in many coordinates, are described in Section 4. Special treatments pertaining to QM/MM methods are illustrated.

3.2.1. Minimum energy path (MEP)

Identification of a reaction path relies on the definition of RC(s), which is often based on one's chemical intuition. Once the RC is chosen, it only remains to determine the system configuration along the RC. To this end, a simple way is to optimize the geometry at different RCs, thus forming an MEP. Thereupon, all the minimization techniques can be employed in this approach. And the a foresaid macro-/microiterative optimization scheme can also be fully utilized for the MEP search on the QM/MM potential energy surface.

One simple method to find the MEP is the RCD approach [168]. In this approach, the RC is changed stepwise and the geometry is optimized in every step with the RC kept frozen. This method has been tested by Frischer and coworkers [169] with a QM/MM potential for a proton transfer reaction in an enzyme. The RCD led to a TS with unrealistically high energy and produced discontinuities along the path. This happened because the frozen

RC during the optimization overparameterizes the reaction path and drags the system to higher points than the true TS. Moreover, this method is also inefficient due to its sequential walk along the RC.

We will return to the RCD method in Section 4.1.3.4 after introducing sampling techniques.

4. QM/MM APPROACHES TO THE SIMULATION OF KINETICS AND THERMODYNAMICS IN THE CONDENSED PHASE

The main goal of this part of our review is to provide a comprehensive description of methods used in molecular simulations for studies of chemical processes in condensed phases. Similar to classical simulations, one can use a QM/MM energy function to perform MC and MD simulations. First, let us focus on the classical propagation of nuclear dynamics. In this case, one can use QM/MM-derived gradients (forces) as a part of a standard integration scheme. QM/MM correction to the full Hamiltonian of this system will provide important information on electronic degrees of freedom relevant to the problem at hand. Since we can impose a canonical distribution of states with a known energy function (classical or QM/MM), it is also possible to perform QM/MM MC with the Metropolis algorithm. Unlike the examples in the sections above, a single structure (e.g., minimized) does not bear substantial significance of its own, and one will have to get an ensemble of structures to get proper averages and then to evaluate thermodynamic functions. It was shown for many systems that interaction energies evaluated from high-level ab initio computations do not always provide accurate descriptions for chemical processes that occur in a solvent and at finite temperature [170].

A good illustration of the need for extensive sampling over the entire configurational space may be found in studies of ion binding to membrane proteins. Yu and Roux [171] have examined the distribution of states from MD simulations in ion binding to membrane proteins with classical and polarizable forcefields and compared it to high-level ab initio computations. It was found that, although high-level ab initio structures may represent "true" local minima, an accurate estimate for ion binding may only be obtained from the analysis of a distribution of states. They analyzed simplified toy-model systems consisting of a monovalent ion (Na^+ or K^+) coordinated by eight water or *N*-methylacetamide molecules. They were able to show that because the PES for these systems is very complex and multiple local minima exist, a simple minimization will not provide a reliable estimate for the thermodynamics of ion binding to proteins. The problem gets much worse if we consider metal binding to proteins and all degrees of freedom available to the system. It was also found that the harmonic approximation is insufficient in this case and ensemble averaging is required to understand the complex thermodynamics of ion binding to proteins. This finding underlines the role of thermal fluctuations and overall protein flexibility in the modulation of ion binding to proteins and complex compounds. Their findings are in excellent accord with the conclusions of QM/MM MD simulations reported from the Guidoni and Klein groups [172,173].

Bucher et al. [174] were able to show the importance of local charge transfer and electronic polarization effects, thus providing a welcome correction to the results of classical simulations. In their study of K^+ and Na^+ binding to the KcsA channel, the selectivity filter of the protein was represented as the QM region and the rest of the system was described with MM [89,174]. The electronic structure was investigated using the maximally localized Wannier function centers of charge and Bader's atoms-in-molecules charge analysis. The results obtained were able to outline polarization effects on the channel backbone carbonyls and significant charge transfer from the backbone to the ions.

Detailed technical information on how to run these simulations is outside the scope of this chapter but it is worthwhile to provide a short summary for the interested and engaged reader. Major technical challenges are well understood, for example, the need for long-range electrostatic treatment and the introduction of periodic boundary conditions for studies of processes in condensed phases, the accurate introduction of thermostats into the system.

The cutoff schemes adopted in standard force-field simulations may or may not cause problems in QM/MM calculations [175–177]. Hu and Wang [109] showed that long-range corrections to the electrostatic interactions for systems with cutoffs larger than 14 Å play no significant role in the dynamics of the QM part. Nevertheless, a correct account of long-range corrections to electrostatic interactions may be important, if not critical, for studies that involve polyelectrolytes such as DNA or RNA molecules. To address this problem, an extension of the particle-mesh Ewald (PME) method has been developed by York and coworkers [175] for QM/MM calculations under periodic boundary conditions. They use conventional point-charge interactions and a reciprocal space component for the MM part and a real-space multipole expansion for the QM region. The method enables the partition of the total Ewald potential into a short-ranged real-space interaction and a long-range periodic correction. To compute the periodic correction term, one requires only a Mulliken charge representation of the charge density (or any other method to map the charge density) and hence it can be used with any efficient linear scaling Ewald method for point-charge (or multipolar) systems, such as the PME method.

It is evident that the performance of this method relies substantially on the number of quantum atoms being sufficiently small. The electrostatic energy has to be efficiently evaluated at each SCF iteration by a Fock matrix multiplication with the charge vector. Although very robust approaches to the problem of PBC simulations with infinite cutoffs exist, this method is likely to be very expensive for large QM regions. A convenient alternative to PBC simulations may be found in schemes that further reduce the dimensionality of the system. A good example of such a scheme is the generalized solvent boundary potential (GSBP), where the system is divided into inner (explicitly represented) and outer shells (described implicitly by solving the Poisson–Boltzmann equation for an external field imposed on the inner shell) [177,178]. In this approach, all atoms within the inner region (usually a 20 Å sphere) are treated explicitly while the outer environment is represented as a solvent potential field. This procedure has been successfully implemented with the SCC-DFTB method and applied to pK_a calculations by Cui and coworkers [176]. More recently, Benighaus and Thiel [179] extended this method with a semiempirical approach and further proved its validity. Moreover, they stressed the fact that, despite the success of the GSBP QM/MM approach, special care needs to be taken as to the physical parameters of GSBP such as the size of the inner region and the number of basis functions for the reaction field evaluations (Legendre polynomials), which might be highly system dependent. Nevertheless, all these corrections are important if one is to study chemical processes in condensed phases.

Therefore, MD and MC simulations may provide very useful insights into dynamics and thermodynamics of the system. However, to make an important step toward linking theory and experiment one has to compute observable properties. One of the most important thermodynamic properties to deal with is the free energy or relative free energy underlying chemical reactions or ion partitioning or any other chemical process. It is possible to use molecular simulations with QM/MM energy functions to compute directly the free energy for the process. The methods for evaluating Gibbs or Helmholtz free energies described above dealt mainly with the finding of TSs and thus reaction paths with the assumption that only a relatively small number of degrees of freedom are important. Although mighty and very successful for small systems where sampling of all important degrees of freedom are readily available, direct computations of free energies encounter significant difficulties if one wants to account explicitly for collective degrees of freedom due to the environment and its effect on the reaction path.

4.1. Free energy simulations and the QM/MM formalism

The benefits of direct computations of free energies are evident; they can be directly compared to measurements of reaction quotients and equilibrium constants. Before discussion of the QM/MM free energy simulations, it might be useful to provide a general overview of theoretical foundations for the evaluation of the free energy from molecular simulations and its extension to QM/MM Hamiltonians.

4.1.1. Potential of mean force evaluation with thermodynamic integration

A common ingredient in all free energy simulation techniques is the use of an effective potential W that corresponds to reversible thermodynamic work done by the average force acting on the system. This thermodynamic function is also commonly referred to as a potential of mean force (PMF). The PMF can be evaluated along a chosen reaction coordinate providing a unique metric for the free energy along the chosen transformation path. The introduction of the PMF as a measure of the free energy change is significant, since we can start working with forces along the pathway without the requirement for accurate energy computations for each pathway point. For example, reorganization of water molecules far away from the reaction center may have a significant impact on the potential energy of the entire system and yet a minimal impact on the reaction path.

Theoretical foundations for PMF evaluation were initially developed by Kirkwood for the distribution functions in liquids. In his formalism to compute PMF, now known as thermodynamic integration (TI), one can introduce a dimensionless coupling parameter λ varying between 0 and 1. Let us illustrate its application for an ion solvation problem in the classical approximation. The state with $\lambda = 1$ is the normal system with all interactions between ion and solvent turned on and the state with $\lambda = 0$ is a reference state in which all interactions between ion and solvent have been turned off. The PMF is a function of collective coordinates $[W(\mathbf{r}_1,\mathbf{r}_2,\ldots)]$ and characterizes a difference in free energy for these states which can be written as the ratio of two respective partition functions (PFs):

$$e^{-W(\mathbf{r}_1,\mathbf{r}_2,\ldots)/k_\mathrm{B}T} = \frac{\int \mathrm{d}\mathbf{X} e^{-E(\mathbf{r}_1,\mathbf{r}_2,\ldots,\lambda=1)/k_\mathrm{B}T}}{\int \mathrm{d}\mathbf{X} e^{-E(\mathbf{r}_1,\mathbf{r}_2,\ldots,\lambda=0)/k_\mathrm{B}T}}, \tag{20}$$

or in the more convenient form of the thermodynamic integral of Kirkwood:

$$W(\mathbf{r}_1,\mathbf{r}_2,\ldots) = \int_0^1 \left\langle \frac{\partial E}{\partial \lambda} \right\rangle \mathrm{d}\lambda. \tag{21}$$

The PMF in the equation above does not contain any mass terms and thus is an equilibrium thermodynamic function independent of timescale and provided convergence and quality of the force-field/QM basis-set/functional, etc. It is clear that these criteria apply to all $E(\lambda)$ averages over the integration path.

Free energy simulations have been extensively developed for classical simulations, but they have also started to appear in QM and QM/MM studies. The starting point for calculation of the PMF is the definition of the partition function for the ensemble. The canonical partition function for a system described with the QM/MM Hamiltonian can be expressed as follows [180]:

$$Z_o = \int \mathrm{e}^{-E(\mathbf{r}_{\mathrm{QM}},\mathbf{r}_{\mathrm{MM}})/k_{\mathrm{B}}T} \mathrm{d}r_{\mathrm{QM}} \mathrm{d}r_{\mathrm{MM}}, \tag{22}$$

where E is the total energy and a function of collective coordinates for atoms in QM and MM parts ($\mathbf{r}_{\mathrm{QM}}$ and $\mathbf{r}_{\mathrm{MM}}$), respectively. Some degrees of freedom similar to all states with different λ could be effectively averaged out and the reaction path can be defined for a smaller system subset (often for only the QM part of the system).

4.1.2. Free energy perturbation techniques

Although powerful, the use of thermodynamic integration (TI) implies a continuous integration with respect to λ, which might be problematic in many situation. In 1954, Zwanzig [181] introduced a free energy perturbation (FEP), theory that relates the free energy difference between state A and state B to the potential energy difference between these two states. If we assume that the perturbation required to transform system A to system B is small (<2kT), it can be shown that

$$\Delta G_{\,(\mathrm{A}->\mathrm{B})} = -k_{\mathrm{B}}T \ln \left\langle \exp\left(-\frac{E_{\mathrm{B}}-E_{\mathrm{A}}}{k_{\mathrm{B}}T}\right)\right\rangle_{\mathrm{A}}, \tag{23}$$

where the potential energy difference between two states is weighted by the energy of the initial state. In case of larger perturbations, one can always use additional windows to connect starting and ending points of this perturbation. The free energy is a path-independent property of the system and can be evaluated regardless of how “alchemical” the perturbation path may be.

Similar to TI, FEP can easily be extended to accommodate a QM/MM description of the system since the PF of the system can be specified. Reddy and Erion [182] provided an intuitively appealing formulation of FEP for QM/MM simulations of enzymatic reactions and solvation. The Hamiltonian describing the system which is changing from state A to state B during FEP calculations can be rewritten as

$$H(\lambda) = \lambda E_{\mathrm{A}} + (1-\lambda)E_{\mathrm{B}}, \tag{24}$$

where E_{A} and E_{B} represent distributions of states for the two end points of the perturbation. The dynamics of two replicas of the system each corresponding to end points with $\lambda = 0$ and 1 is treated explicitly and simultaneously and appropriate weighting [see Eq. (21)] is applied to reconstitute the Hamiltonian for intermediate windows. This method is known as a dual-topology FEP method reflecting the simultaneous presence of two endpoint systems. The dual-topology FEP method is especially useful for calculations such as solvation [182], studying the effects of mutation and pK_a values in a protein [176,183], ligand binding [184], or enzymatic reactions [185]. An interesting area of potential application of QM/MM FEP methods is the study of ion solvation and potentially mechanisms of selectivity in ion channels or ion-coupled transporters. Ion selectivity has been extensively studied at the MM level with both classical and polarizable force fields [170,186–191]. However, classical simulations may be compromised by their inability to account for charge transfer and electronic polarization, thought to be critical for ion binding to proteins. We have extended QM/MM FEP to studies of Na^+/K^+ solvation and selectivity by water clusters with variable numbers of ligands [53], results of which are illustrated in Figure 10.4. In that article, QM/MM FEP calculation have been performed, for ion–water clusters with different numbers of water molecules, where the ion was treated as the QM region using B88-LYP with the DZVP basis set implemented in deMon, and water clusters were represented by the polarizable Drude force field implemented in CHARMM. The same approach can be used for selectivity calculations in more complex biological systems. Also, the close connection between QM/MM calculations and those with polarizable force fields developed to account for electronic effects is visible. Therefore, the polarizable force fields can be sufficient in some cases.

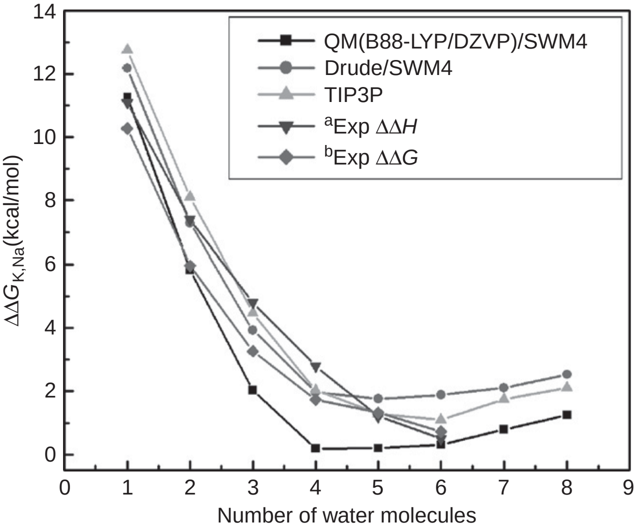

Figure 10.4 Relative (to the bulk) free energy of selectivity for Na^+/K^+ in water clusters as a function of cluster size. Experimental information is taken from [a]Ref. [192] and [b]Ref. [193].

Although QM/MM FEP is significantly more expensive than classical FEP simulations, the ability to compute free energies (or relative free energies) provides a unique opportunity for validation of classical potential functions as well as for relating QM computations at finite temperature to experimental measurements. Several attempts were made to reduce the number of degrees of freedom in free energy QM/MM simulations. Yang and coworkers introduced the QM region into sampling via ESP charges included in the energy expression used to obtain the forces and to propagate the system along the reaction coordinate. At the beginning of the sampling, a full QM/MM calculation is run to obtain the reference potential and the energy difference caused by the MM configuration change is estimated as coulombic charge–charge interactions, which are then added to the reference potential to approximate the system's potential [4]. This reference potential approach, as mentioned before, has been employed as well in QM/MM geometry optimizations [8,160]. Since this reference potential is sensitive to the MM configuration, it is more reasonable to use an average electrostatic field over an MM ensemble as done by Yang and coworkers [180]. The same authors also found that a short MD simulation was usually enough to obtain a consistent reference potential so that a self-consistent procedure could be avoided. The PMF profiles have been obtained for all methods and have been compared. The results have proven to be very close to each other. A full QM sampling is rather expensive for regular QM/MM calculations. Yang and coworkers [180,194] have simplified the reaction path search on the FEP to that on the PMF surface, for example, using partial derivatives of the PMF along the reaction path with respect to position. To remove an apparent need for extensive and expensive sampling of the QM part of their system, they froze the QM part and used the obtained ESP charges to evolve their system in classical (MM) space. To render out the minimum free energy path, the QM free energy gradient is employed as a criterion in the QM geometry optimization. Lastly, the above steps must be iterated to reach self-consistency.

A similar approach to the study of solvation effects has also been used by Warshel and coworkers [195]. To reduce the conformational space in FEP simulations, they kept the QM region frozen. Detailed comparisons between different schemes for the performance of free energy techniques applied to studies of enzymatic reactions have been made by Senn and Thiel [19,116]. The major conclusion was that, if appropriate sampling is achieved, estimated activation barriers and reaction thermodynamics may be described very accurately by either TI, FEP, or umbrella sampling (US) techniques (see below).

TI, FEP, and other similar techniques imply the existence of a well-defined reaction coordinate (reaction path, permeation pathway, or conformational pathway). What if we do not have a preconceived idea about the reaction path? Providing a comprehensive sampling of free energy surface, one can find the pathway post factum. Extensive sampling along the reaction coordinate may allow the complete removal of the dependence of the results on starting configurations. Several simulation techniques have emerged recently to address the problem of efficient sampling and are often referred to as "enhanced sampling" techniques.

4.1.3. Enhanced sampling techniques

4.1.3.1. Multiple time-step approaches. The conceptually simplest approach to enhance sampling in MD simulations would be to introduce a larger time step. The time step in classical simulations is defined by an integrator and the apparent need to integrate the fast dynamics of covalent bonds. It is usually set to 1 or 2 fs. The multiple time-step (MTS) method was first proposed for MM dynamics to separately treat motions of high and low frequencies in the same system [196]. The MTS method uses a smaller time step Δt for the fast motion and $n\Delta t$ for the slow motion. The fast degrees of freedom are first advanced for n steps at step size Δt with the slow degrees of freedom fixed and the latter is then updated with a step size $n\,\Delta t$, for which n was found to be 5–10 to sample effectively [196]. As an analog to the fast motion, the MM region possesses more configurational variability than the QM part, thus demanding an enhanced sampling. Wei and Salahub [11,197] have adopted this MTS approach to study solvation effects on a QM water molecule, in which a step size of 1 fs was used for the MM region and 15 fs for the QM water. While this enables oversampling of the MM region, the conventional MTS is liable to yield biased sampling due to the frozen slow degrees of freedom when propagating the fast ones. To remedy this drawback, Tuckerman et al. [198] proposed reversible reference system propagator algorithms and implemented them within the CPMD program package [199]. This methodology has been adopted by Woo et al. [200] in their QM/MM MD scheme. In their work, the MM part is first propagated from t_0 to $(t_0+n\Delta t/2)$ at the step size of Δt. The QM part is then evolved from t_0 to $(t_0+n\Delta t)$ at the step size of $n\Delta t$ with the MM force averaged from the forces at $(t_0-n\Delta t/2)$ and $(t_0+n\Delta t/2)$. Following this, the MM part then moves from $(t_0+n\Delta t/2)$ to $(t_0+n\Delta t)$ at the step size of Δt with the QM force averaged from the forces at t_0 and $(t_0+n\Delta t)$. Hence, the problem caused by fixed degrees of freedom is partially solved by force average and smaller propagation steps. Moreover, the MM part is further extensively sampled by assigning smaller masses to the MM atoms, resulting in faster motion.

4.1.3.2. Umbrella sampling. The US method offers a simple method of configurational sampling for processes with activation barriers. Instead of using an order parameter to force the transition between two states in TI and FEP, US resorts to a biasing (restraining) harmonic potential (V_b) to overcome the transition barrier and thus enhance the sampling [201]. In the US method the ensemble average (EA)$\langle A \rangle$ of a function A can be expressed as [202]

$$\langle A \rangle = \frac{\langle A/\mathrm{e}^{-\beta V_\mathrm{b}} \rangle_\mathrm{b}}{\langle 1/\mathrm{e}^{-\beta V_\mathrm{b}} \rangle_\mathrm{b}}, \tag{25}$$

where β is the Boltzmann factor, the EA is over the biased non-Boltzmannian distribution defined by $\exp[-\beta(H + V_\mathrm{b})]$, that includes the biasing potential V_b and the system's Hamiltonian H. It is apparent that one can use either a classical or a QM/MM expression for the Hamiltonian of the system.

With the biasing potential, the high-energy and low-probability regions of the phase space are better sampled. Several different implementations of this algorithm have been developed. For computing the PMF, a US simulation would ideally lead to a uniform distribution along the reaction coordinate. The difficulty, in practice, is to determine the strength and spacing for placement of umbrella potentials along the reaction coordinate and the common practice is to use multiple trial-and-error assessments. This represents a clear challenge to multidimensional PMFs involving costly computations such as QM/MM simulations. To overcome this problem, the classical US scheme was extended to develop an adaptive US algorithm by early work of Mezei [203] and then was extended by a number of research groups [202,204]. In the adaptive US algorithm, the biasing potential is adapted to PMF information extracted from the preceding US window and the analysis of the reaction pathway is usually carried over with the weighted histogram method [205]. Rajamani et al. [202] have reported an application of adaptive US for sampling of multidimensional PMFs for the proton transfer reaction in $[\mathrm{NH_3}\text{—h—}\mathrm{NH_3}]^+$ in water. Aside from its apparent methodological importance, this study reports on the quantitative assessment of solvent effects on the rate of the proton transfer reaction. The presence of solvent molecules leads to an increase in the free energy barrier by ~5 kcal/mol. This large adjustment in the barrier height was related to charge delocalization for the TS as compared to products and reactants. Furthermore, the explicit account of solvent effects leads to changes in the shape of the two-dimensional PMF profiles for this reaction as compared to the gas phase.

4.1.3.3. Replica Exchange. Conventional QM MD simulations are not capable of sampling rare events because of their prohibitive expenditure for long-time dynamics. This barrier in turn hinders QM/MM dynamics and, hence, an efficient sampling method is desirable. Parallel tempering, also known as replica exchange, is originally an MD approach to simulate replicas of the system simultaneously and exchange their configurations at different temperatures. One may think about ensembles of replicas as an example of a Markov chain of states. That is, two conformational states in an ensemble can be understood as the state of the ensemble before and after a pair of replicas (*i,j*) have exchanged their respective configurations. It is possible to then use the Metropolis algorithm to determine the exchange probability and set acceptance criteria [206]. This exchange enables replicas at low temperatures to access regions that are hard to sample in phase space. As recently reviewed by Earl and Deem [207], parallel tempering has been widely used in MM simulations of polymers and proteins and QM simulations of clusters. The temperature-based version of the RE algorithm may become a double-edged sword, since there is always a possibility that the free energy landscape is drastically different in the high-temperature region. There are numerous extensions of RE simulations that are being run at the same temperature, but contain a gradual perturbation of the potential energy in replicas similar to that of the FEP method [208,209]. This is a promising alternative for parallel tempering simulation of a quantum system, as the QM SCF calculation is often difficult to converge at high temperatures. Li and Yang [210] have added a QM replica to the MM replicas in their Hamiltonian parallel tempering simulation with the module in CHARMM [211]. They formulated the exchange acceptance ratio to satisfy detailed balance and obtained a more complete sampling at a much shorter time length than the QM dynamics. As noted by the same authors, the QM potential can well be replaced by a QM/MM potential to increase the resolution. Several notable applications of QM/MM REMD are worth mentioning and we direct interested readers to the particulars of systems in Refs. [212–217].

4.1.3.4. Reaction coordinate-driven methods. An extension of enhanced sampling algorithms and particularly US-based routines may be found in the recent implementation of a chain-of-replica approach [118] for QM/MM from the Brooks group to allow for some flexibility along the reaction coordinate. In this approach, a tentative RC is first defined to connect the reactant and the product. And then a chain of geometries (replicas) differing only in their RC values is interpolated between the reactant and the product. A spring force is exerted between the replicas as a function of their root mean squared (RMS) distance. Hence, the object function to be minimized is the actual QM/MM potential plus the spring potential of each replica. An intrinsic advantage of this replica path scheme is the trivial effort of parallelization as the replicas can be optimized separately from each other. Another benefit from this approach is its capability of discriminating the important atoms versus the unimportant ones. Since the RMS distance is used for adjacent replicas, different weights can be assigned to critical atoms, which play more important roles than other atoms far from the reaction center. Furthermore, the RMS distance can be used to calculate the potential of mean force evaluating forces along a specific path [118]. However, it is noted that the spring force constant should be chosen carefully. Since there is also a restraint on the angle between replicas, this force constant demands a careful choice as well. Yang and coworkers [218] have further expanded this promising approach with the introduction of the macro/microiteration scheme into their chain-of-replica method. The QM core and MM environment forces and energies along the path points could be computed and optimized separately by alternating iterations. As pointed out earlier, the coordinate system plays a role in the QM/MM optimization. Hence redundant and Cartesian coordinates are employed for QM and MM subsystems respectively, and the calculation of the distance between the points along the path excludes the MM degrees of freedom. To avoid the translation and rigid body rotation of the QM core, Cartesian coordinates of at least three core atoms are included as redundant internal coordinates. In contrast to this treatment, a rotation matrix to best fit the adjacent path images is used to ensure the same coordinate frame in the work mentioned in Refs. [118,219] as only Cartesian coordinates are used. Another major difference in Ref. [218] is the application of the TS search scheme by Ayala and Schlegel [219a]. An explicit TS finder is added to the regular replica path method, in which the highest point of the path is moved toward the true TS and the replicas are redistributed afterward in each path relaxation cycle. Since this Hessian update requires gradients of the neighboring replicas, discontinuity of the environment along the path can seriously bias the updated Hessian. This problem is remedied to some extent by checking the Hessian after each update and reinitializing it with an empirical estimate when necessary, which possibly results in slower convergence.

As an alternative to the replica path method, a nudged elastic band (NEB) method has also been implemented [219]. As a member of the chain-of-replica methods, the NEB is similar to the replica path scheme in terms of replicated points along the reaction path to be optimized separately. The difference is that in NEB, the force perpendicular to the path is optimized below threshold instead of the total force. Brooks and coworkers [220] have tested both NEB and replica path with a QM/MM potential. They found both methods converge at nearly the same rate when proper optimizers were chosen. While the replica path method can effectively use the adopted basis Newton–Raphson (ABNR) optimizer, the NEB requires a combination of steepest descent and ABNR, as the ABNR alone with the NEB is unstable owing to the projection of the forces.

A variant of the NEB method for QM/MM calculations has been proposed by Yang and coworkers [221]. Their approach differs from that of Ref. [219] in two respects: the optimization method and the definition of the distance between points along the path. In Ref. [221], the path is optimized with the projected velocity Verlet algorithm. However, the convergence efficiency of MD minimization based on quenched Newtonian MD has been shown to be inferior to ABNR [219]. Pure minimizers should work better for optimization on the potential energy surface and they significantly reduce the number of expensive QM calculations. To avoid the floppy degrees of freedom in the MM environment, in Ref. [221] a transformation was used for a set of interatomic distances concerning all chemical or hydrogen bonds formed/broken during the reaction. However, this treatment could cause discontinuity of the environment when the environmental conformation is adjusted to different reaction coordinates. To alleviate this drawback, Yang and coworkers started from a reference system with a relatively rigid environment and gradually decreased the spring force constants for the environment. On the other hand, the assignment of different weights in Refs. [118,219,220] seems more straightforward although the weights should be carefully chosen nonetheless.

4.1.3.5. Transition path sampling. Despite the fact that the above search methods include temperature effects, they still find only one path and one TS, which in reality should be an ensemble. To adequately sample the various possible paths, a transition path sampling (TPS) method has been proposed [222]. Schwartz and coworkers have applied the TPS in CHARMM to study lactate dehydrogenase using a QM/MM potential [62,223,224]. To distinguish the reactant, product, and TS regions, an order parameter, for example, atomic distances in [62,223,224], is first defined. Restraining the order parameter, a biased QM/MM MD simulation of time length t [$t = 500\,\text{fs}$ in Ref. [224]) is run to obtain the initial trajectory from the reactant to the product. A time slice of the trajectory is then randomly chosen and its momenta are changed by a small amount while the total momenta and energy are conserved. Following this, the dynamics is run both forward and backward to complete a trajectory of t. If this dynamics arrives at both the reactant and the product regions, it is considered reactive and the subsequent dynamics starts from a time slice from it. Otherwise, when it is not reactive, another time slice is chosen from the old trajectory to continue the dynamics until a reactive one is obtained. Practically, the acceptance ratio of reactive trajectories depends on the momenta changes, which is adjusted to get a population of 26.5% in Ref. [62]. From this transition path ensemble, one can draw out the TS ensemble by the definition of the order parameter [62,223,224]. Analyzing the trajectories and the TS ensemble, one can identify important movements of the atoms surrounding the reaction center as detailed in [62,223,224]. However, while inspiring qualitative conclusions have been reached [62,223,224], no quantitative result such as reaction rates have been calculated with QM/MM methods to compare with experimental observations, although the procedure to calculate the free energy barrier was already illustrated by Chandler and coworkers for the classical case in Ref. [222].

5. BEYOND CONVENTIONAL QM/MM DYNAMICS: EXPLICIT ACCOUNT OF NUCLEAR QUANTUM EFFECTS

The free energy calculations described in the section above form the cornerstone of the study of chemical kinetics. Together, TST and reaction coordinate sampling techniques (US, FEP, etc.) enable computations of approximate rate constants in the Born–Oppenheimer approximation. A QM treatment is commonly used to treat electronic effects and the MM part provides a necessary account of environmental effects. Examples of the QM/MM molecular simulations are numerous and several excellent reviews were recommended above. Thus far, our chapter has focused as well on the latest state-of-the-art methods developed to accurately compute free energies, with emphasis on the QM nature of the PES used to drive classical nuclear dynamics. However, it is accepted [225] that nuclear quantum effects, such as tunneling, play an important role, in particular, in enzymatic catalysis. Tunneling is important in reactions that involve the abstraction of hydrogen atoms, protons, or hydrides. Its importance has been largely shown by the experimental observation of temperature-independent kinetic isotope effects (KIEs) in different enzymes. These observations cannot be understood solely on the basis of differences in the zero-point energy (ZPE) between the isotopes involved [225]. Therefore, to have a complete description of enzymatic catalysis, it is necessary to bring into the picture the quantum nature of light nuclei, beyond the calculation of simple frequency-based ZPE.

Once again, it is desirable to have in place methods with the computational convenience of MM and the theoretical robustness of QM. Fortunately, a description at the TST level allows one to bypass the problem of solving the time-dependent Schrödinger equation for the nuclear system. Similar to full electronic structure calculations for biomolecules, to solve the nuclear quantum dynamics is a formidable endeavor, possibly intractable with the current available computational power for systems with thousands of atoms. However, nuclear quantum effects on equilibrium properties, barriers height, and free energies could and should be accounted for. In this arena, several theoretical methodologies have been developed. Herein, however, we shall focus on the approaches rooted in the path integration (PI) formulation of quantum statistical mechanics [226]. This twist in our discussion is motivated by the natural extension of the QM/MM and free energy techniques to PI methods thanks to the quantum–classical isomorphism provided by Feynman's alternative formulation of QM.

The central goal of the methodologies described below is to calculate rate constants. The QM rate constant can be written in terms of the PFs:

$$k = \kappa \frac{k_B T Q^{t}}{h Q^{r}} = \kappa \frac{k_B T}{h} \exp(-\beta \Delta G^{t}), \tag{26}$$

where κ is the transmission coefficient, k_B is the Boltzmann constant, T is the temperature, and h is Planck's constant. Q^t and Q^r are the PF of the TS and the reactants, respectively. The largest quantum effects are associated with the PF. Using PI, one can show that the canonical PF of a quantum particle (the generalization to many particles is straightforward) under the influence of a potential $V(x)$ is given by

$$Q = \lim_{P\to\infty}\left(\frac{mP}{2\pi\beta\hbar^2}\right)^{P/2}\int \mathrm{d}x_1\ldots\mathrm{d}x_p \exp\left[-\sum_{i=1}^{P}\left(\frac{mP}{2\beta\hbar^2}(x_{i+1}-x_i)^2+\tau V(x_i)\right)\right]_{x_{P+1}=x_1}. \tag{27}$$

In the limit of infinite P, this expression is exact. In practice, however, finite values of P produce converged results [226]. Note the mathematical correspondence of the PF of a single quantum particle with the PF of a classical "ring polymer." Herein, P classical particles are connected by harmonic "springs" and each of them is subject to a fraction $V(x)/P$ of the potential ($\tau=\beta/P$). This correspondence renders the use of MM sampling techniques based on MC or canonical MD suitable to evaluate expectation values of EAs of thermodynamical properties using the PI PF. We should clarify that the dynamics so obtained are devoid of physical meaning, and serve only as a configurational sampling of the quantum partition function (QPF).

It is worth pointing out that the correct PIMD implementation is not free of subtleties, mostly related to temperature control and integration schemes. These details, however, are outside the scope of this review and for more specific information we recommend the excellent literature on the topic found elsewhere [227,228].

An important notion within the PI framework is the centroid variable [229]. It is defined as the center of mass of the ring polymer and its average value along the path is given by

$$x_\mathrm{c} = \frac{1}{\beta h}\int_0^{\beta h}\mathrm{d}\tau x(\tau). \tag{28}$$

Hwang and Warshel [230] have developed a method that exploits the fact that the QPF can be recast in terms of the centroid variable. Using this formulation, the quantum correction to the classical free energy along the RC can be written as a double average of the form

$$G^t_\mathrm{qm} - G^t_\mathrm{TST} = -\frac{1}{\beta}\ln\frac{Q_P}{Q_P^\mathrm{cl}} = -\frac{1}{\beta}\ln\left\langle\left\langle \exp\left(\frac{\beta}{P}\sum_{i}^{P}\Delta V_i\right)\right\rangle_{\mathrm{FP},x_\mathrm{c}}\right\rangle_V, \tag{29}$$

where $\Delta V_\mathrm{i} = V(x_\mathrm{i}) - V(x_\mathrm{c})$. The outer average over V is obtained over the distribution generated by an MD simulation driven by $V(x_\mathrm{c})$. The inner average over FP (free particle), x_c is over the so-called free-particle distribution.

The quantized classical path (QCP) method, developed by Hwang and Warshel, utilizes the trajectory obtained from classical mechanics simulations to obtain the QM correction by performing free-particle PI averaging with the centroid constrained to the classical position. This methodology has been successfully applied in the study of unusual KIE in several enzymatic systems [231–234].

More recently Gao and coworkers [235] introduced a bisection-sampling algorithm extensively used in quantum MC simulations of condensed matter [236,237] into the QCP approach to sample the free-particle paths. The bisection QCP (BQCP) method has been used to study KIE in condensed phase reactions and enzymes [238]. Further development of the BQCP has been done, aimed at determining analytical expressions for the effective centroid potential [238]. These methodologies expedite the calculations and are promising for the study of large systems.

The two methodologies described above have been successfully used in conjunction with MM force fields, QM/MM, and EVB methods The main importance of these techniques is their suitability for free energy calculations using US and FEP methods described in the previous section.

For completeness, we briefly summarize other methodologies developed to study quantum effects in proton transfer reactions. These methodologies incorporate at least one of the following: QM/MM, MM forcefields, or PI.

Wang and Hammes-Schiffer [239] have used a mixed quantum/classical PIMC (QC-PIMC) approach to study proton transfer in the enzyme dihydrofolate reductase. In this approach, the classical PMF along a reaction coordinate is calculated using MD trajectories propagated according to an EVB-based mapping potential and US. The nuclear quantum correction is determined separately by standard (without the centroid constraint) PIMC calculations based on an effective mapping potential. Hammes-Schiffer and coworkers have developed and refined a hybrid quantum /classical grid method to study proton transfer reactions [240–242]. In this approach, the classical PMF for the reaction is obtained using US simulations along a mapping potential based on EVB or QM/MM techniques. Nuclear quantum effects are incorporated perturbatively into the PMF by representing the proton as a multidimensional vibrational wavefunction.

Semiclassical theory can be used together with MM (and, in principle, with QM/MM) approaches to obtain quantum corrections to rate constants. Truhlar and coworkers [243] have worked on variational transition state theories (VTSTs) and semiclassical quantum tunneling (QT) corrections. In VTST, the position of the TS along the RC is determined variationally, as the point that minimizes the reactive flux or maximizes the free energy of activation, that is, minimizes the rate constant [243]. Different semiclassical flavors of tunneling correction can be used in conjunction with VTST. In particular, the EA TST/QT has been successfully used to study KIE in a series of enzymatic reactions [236,244,245].

Finally, to obtain exact QM rate constants, that is, beyond TST, it is unavoidable to determine the quantum dynamics of the system. As stated in the beginning of this section, this is a task that is currently prohibited, computationally. Be that as it may, greater efforts have been devoted to develop approximate quantum dynamical methods that rely on the computational machinery already built for MD simulations. Some of these methods, such as centroid MD [229,246], ring polymer MD [247], and techniques based on analytical continuation of imaginary time correlation functions [248] are based on a PI description. Others, such as the semiclassical initial value representation, are based on semiclassical ideas [249]. These methods are currently still in formal development and their applicability and limitations are being scrutinized; however, they soon will reach maturity and certainly will become another element of the toolbox for studying enzyme catalysis. A thorough discussion of these techniques is beyond the scope of this review. Needless to say, the future is bright for these methodologies and we expect that in the not so distant future applications of these methods in systems of biological relevance will begin to appear in the literature.

6. SUMMARY OF ALTERNATIVES TO QM/MM METHODOLOGY

QM/MM methods are known for their high accuracy and efficiency treating large systems due to the integration of high- and low-level methods. In fact, this philosophy of integration can also adopt pure high-level methods for the entire system or even lower-level methods for the outer region.

For the integration of all high-level methods, an example is the “divide and conquer” approach [250–253]. This approach divides the system into small fragments, calculates the electron density of each fragment with high-level QM methods, and then sums up the interactions between fragments, thus conquering the whole system. While this procedure offers a promising alternative to QM/MM, it is still quite expensive to calculate each polarized fragments in a self-consistent way and the boundary treatment could cause larger errors than in QM/MM because more boundaries are involved. Moreover, sufficient sampling of the system configuration space is compromised because of high cost. So far, this approach has been mainly applied to the study of materials with highly repetitive structures. Nonetheless, this approach is of great significance in that it extraordinarily improves computational accuracy. Recently, it has been extended with MM methods to save computational cost and yielded satisfactory results [254].

For the integration of lower-level methods than MM, an example is the quantum chemical cluster approach whose application in biological systems was recently reviewed in Ref. [255]. In this scheme, a subsystem is chosen to be treated with high-level methods and its peripheral atoms are fixed according to the X-ray structure. Subsequently, this cluster is embedded in a polarizable continuum electrostatic field to mimic the environmental effects. In fact, a similar method, termed quantum mechanical charge field (QMCF) in Ref. [256], has been used to study the hydration of alkali ions. Rode and coworkers Ref. [256] demonstrated that the QMCF treatment performed better than a QM/MM approach with mechanical embedding as long as the QM system was big enough to include the first hydration shell. Under this condition, implicit solvent can represent explicit solvent well, indicating that the configuration of the outer region described is not very important to the QM region.

But how about biochemical reactions? Sevastik and Himo [257] showed that when the QM system was enlarged (from 77 atoms to 177 atoms) for a proton transfer reaction in a protein, the calculated pK_a values conformed better to experimental results. They also made a comparison with previous studies on the same enzyme using QM/MM methods [258,259] and found disagreements with their results. However, this finding is conceivable as there were only 30 atoms in the QM regions of Refs. [258 and 259]. Therefore, it was a question of the QM system size rather than the different methodologies. It is also found in Ref. [257] that the energies are quite different at different dielectric constants when the QM cluster is not big enough, suggesting the important role of the dielectric constant in this approach. One should also note that there are two intrinsic problems with the quantum chemical cluster method: fixed QM boundary atoms and no vdW interaction between the QM region and the charge field.

By and large, QM/MM methods are still more prevalent compared with other approaches, because of the accuracy of the QM portion and the efficient configurational sampling of the MM portion.

7. APPLICATIONS TO BIOCHEMICAL SIMULATION

There have been numerous QM/MM applications in computational biochemical studies thanks to the rapid development of this methodology. When combined with experimental studies, the QM/MM methods have been widely used as a tool to assist the interpretation of biological spectroscopy. In EPR spectroscopy, the hyperfine structures of the paramagnetic active sites in blue copper proteins were examined by Salahub and coworkers [18]. In nuclear magnetic resonance (NMR) spectroscopy, the QM/MM calculated chemical shifts have been compared with the experimental data to determine the binding mode of substrate to protein by Karplus and coworkers [260] and QM/MM calculations have also been used for sequence-specific NMR assignments by Lula et al. [261]. In X-ray spectroscopy, QM/MM methods have been employed to refine the crystal structure of proteins [262] and to include environmental effects in the determination of the substrate's electron density in proteins [263]. On the theoretical methodology side, QM/MM has also been adopted to parameterize MM force fields to include environmental effects [264].

Particularly, QM/MM methods find their most popular application in enzymatic reaction studies which start from experimental structures and arrive at predictions through computations. To illustrate the power of the QM/MM approach in biochemical studies, we select a single example to describe here: QM/MM simulation of DNA polymerases (DNA pols). This choice is based on our own interest in the related RNA polymerases [265,266]. We believe this example nicely represents the state of the art and should give the reader a faithful representation of the excitement in the field. Other examples may be found in the references (see [111,115,116] for recent reviews).

7.1. DNA polymerases

DNA pols are crucial constituents of the complex cellular machinery for replicating and repairing DNA. They discriminate the matched deoxynucleoside triphosphate (dNTP) against the mismatched dNTPs and NTPs in an intricate mechanism. Understanding the origin of DNA pols' high fidelity on the atomic level is important to the full revelation of their exquisite cellular functions. Mammalian DNA polymerase β (pol *β*), a small (39 kDa) member of the X-family, has been extensively studied with computational tools by many groups. As revealed by X-ray crystallography, to ensure the high fidelity, this polymerase exhibits closed (inactive) and open (active) forms, the transition between which is triggered by the correct dNTP and hampered by the wrong dNTPs. Radhakrishnan and Schlick [267] applied the TPS method at the MM level to obtain the TSs of the activation process, employed a QM/MM method for the following nucleotidyl transfer reaction and integrated these results in a kinetic MC model to explain the kinetic difference between the correct and mismatched dNTPs. To further identify which step is the rate-limiting one, the prechemistry or chemistry step, Schlick and coworkers investigated the chemistry step elaborately with hybrid QM/MM and with the QM method alone.

The nucleotidyl transfer reaction in DNA pols is illustrated in Figure 10.5. As commonly acknowledged, it involves a nucleophilic attack of the DNA primer hydroxyl oxygen (O3′) on the α-phosphorus (P_α) of the incoming dNTP and P_α—O bond breaking, which results in pyrophosphate group leaving. There are two possibilities for the nucleophilic attack by O3′: direct attack without deprotonation of this oxygen and attack following a prior deprotonation. The first possibility has been tested by Pedersen and coworkers [268] and an extremely high energy (47 kcal/mol) was found at a short O3′—P_α distance while the H3′—O3′ bond was still present. The second possibility has been scrutinized by Bojin and Schlick [269] with a pure QM method with respect to different pathway models: direct proton transfer from O3′ to O(P_α), proton transfer to adjacent Asp residues, and to a

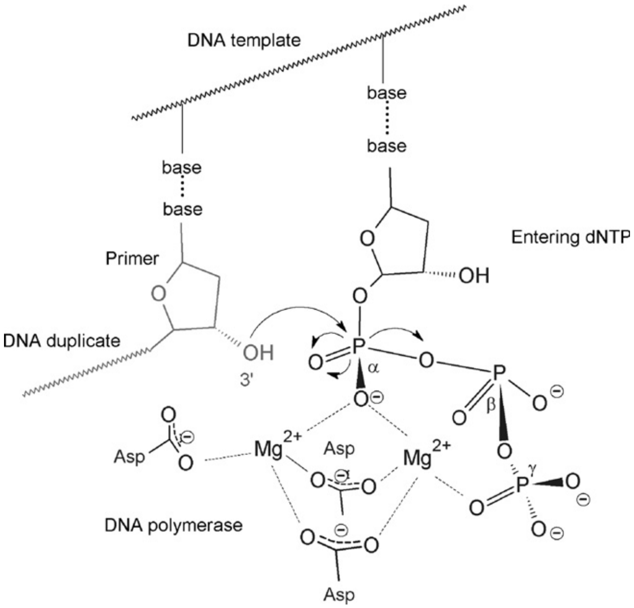

Figure 10.5 Illustration of the nucleotidyl transfer reaction.

water molecule. They simplified the active site by changing all aspartates to formates and the ribose ring to methyl, resulting in a model of 49 atoms and an overall charge of −3. To find the TSs, they constrained the reaction coordinates and performed constrained geometry optimization accordingly, as similar to the RCD method mentioned above. As a result, the direct proton hopping from O3′ to O(P_α) was found to be most energetically favorable.

In view of the inability to include environmental effects by QM methods, Schlick and coworkers [51,270] also recruited QM/MM methods to study this reaction and a very different proton transfer pathway was found. They employed 10 ps QM/MM dynamics in conjunction with US to estimate free energies of intermediates along the reaction coordinate and discovered the proton transfer to water molecules instead of O (P_α) [270]. To validate this finding, they then compared the different proton transfer pathways with QM/MM methods [51]. A system of more than 40,000 atoms including 65 QM atoms was built where all atoms within 15 Å of any QM atom were free, atoms within 15–25 Å semiconstrained, and atoms further than 25 Å were fixed. To find the minimum energy path, harmonic constraints were added along the reaction coordinate instead of totally constraining it. Results of this study agreed with their previous QM/MM calculations: the O3′ is deprotonated by a water molecule. It is worth noting here that hierarchical levels of QM methods were employed in this work, that is, Hartree–Fock/STO-3G to identify preliminary geometries, B3LYP/3-31G* for geometry optimizations, and MP2/6-311 + G(d,p) for final energy calculations.

While supported by abundant evidence, the water-mediated proton transfer mechanism has been challenged recently by Pedersen and coworkers [59,268]. Based on a more recent crystal structure of DNA pol β, they proposed a two-stage mechanism through their QM/MM calculations, that is, B3LYP/6-311G**/AMBER ff99. The primer terminal O3′ first replaces one of the water molecules bound to the catalytic Mg ion resulting in a prechemistry state and thereupon the reaction starts with O3′ deprotonated by an aspartic residue. The prechemistry state was found to be stable after 5 ns of unconstrained MD simulation and the proton transfer barrier 6 kcal/mol. A similar study has also been conducted on pol λ, another member of the X-family polymerases by Cisneros et al. [59]. The TS search was performed using the chain-of-replica method augmented with an explicit TS finder by Yang and coworkers as introduced above. With this approach, the proton transfer to an aspartic acid was found to be much more energetically favorable than that to a water molecule.

The question of whether there is similarity across the DNA poly families has stimulated great interest. DNA pol IV from the Y-family and T7 pol of phage have been investigated by Zhang and coworkers [271,272]. Both works utilized the pseudobond approach to cap the QM subsystem, the micro-/macroiteration scheme to optimize the geometry, the RCD method for the reaction path search, and the FEP method for free energy calculations along the path. It was found that the nucleophilic attack was the rate-limiting step and the initial proton transfer was assisted by water.

8. CONCLUSIONS AND PERSPECTIVES

To conclude this review, we look at the QM/MM methods from the viewpoint of multiscale methodology. QM/MM is actually a combination of methods on two scales which divides a system into two levels and treats them accordingly. However, we will have to march on along the scales as the size of the systems and time length of the events grow. When investigating systems such as multiple unit proteins, coarse-grained methods would have to be adopted to sufficiently sample their configuration space. When studying events such as protein folding in milliseconds, kinetic simulations instead of regular dynamics simulation will probably have to be used. Nevertheless, QM/MM methods are indispensible, since they can be used as benchmark calculations for coarse-grained models and to obtain rate constants for kinetic models, especially when chemical reactions are concerned.

Our groups have been applying the QM/MM-based multiscale methodology to the study of the RNA elongation process catalyzed by RNA polymerase II. Since this event occurs on a second timescale, we have adopted a kinetic MC method to simulate this process [273]. The whole process was divided into four steps: Diffusion of the substrates, substrate moving from the entry site to the addition site, nucleotidyl transfer reaction in the addition site, and the release of the pyrophosphate group. Although our tentative kinetic model based on empirical rate constants in general agreed with the experimental results, the rate constants had to be obtained through many trials, which lacks a solid physical basis. Therefore, rate constants from first-principles are still desired. The rate constant of the nucleotidyl transfer reaction is being pursued using a QM/MM method which combines CHARMM and deMon2k [53].

Our review has focused on two classes of problems. In the first, exemplified by DNA and RNA polymerases, the QM region is the initial point of focus—getting the quantum mechanics right is essential to a correct description of the reaction. Environmental and solvent effects are then brought in to gain quantitative, and sometimes qualitative, insight.

In the second class of problems, the solvent or protein–solvent dynamics are essential to the very existence of the phenomena investigated, ion solvation, and transport providing the prototypical example. We hope that the “creative tension” between these two perspectives will lead to even more powerful simulation methodologies that will be able to provide better treatments of environmental sampling for the former and the incorporation of larger and more complex quantum regions for the latter.

In summary, while QM/MM methods are important in their own right, they will also contribute to a multiscale systems approach as a powerful component.

ACKNOWLEDGMENTS

We are grateful to NSERC-CANADA (Discovery Grants to S.N. and D.R.S.), to the Alberta Ingenuity Fund, to the Alberta Heritage Fund for Medical Research, and to the Canadian Institutes of Health Research, (S.N.) for financial support, and to WestGrid for computational resources.

REFERENCES

[1] A. Warshel, M. Levitt, J. Mol. Biol. 103 (1976) 227.
[2] U.C. Singh, P.A. Kollman, J. Comput. Chem. 7 (1986) 718.
[3] M.J. Field, P.A. Bash, M. Karplus, J. Comput. Chem. 11 (1990) 700.
[4] Y.K. Zhang, H.Y. Liu, W.T. Yang, J. Chem. Phys. 112 (2000) 3483.
[5] J.Z. Pu, J.L. Gao, D.G. Truhlar, J. Phys. Chem. A 108 (2004) 632.
[6] J.L. Gao, P. Amara, C. Alhambra, M.J. Field, J. Phys. Chem. A 102 (1998) 4714.
[7] M. Garcia-Viloca, J.L. Gao, Theor. Chem. Acc. 111 (2004) 280.

[8] J. Bentzien, R.P. Muller, J. Florian, A. Warshel, J. Phys. Chem. B 102 (1998) 2293.
[9] D. Bakowies, W. Thiel, J. Phys. Chem. 100 (1996) 10580.
[10] P.D. Lyne, M. Hodoscek, M. Karplus, J. Phys. Chem. A 103 (1999) 3462.
[11] D.Q. Wei, D.R. Salahub, J. Chem. Phys. 101 (1994) 7633.
[12] F. Maseras, K. Morokuma, J. Comput. Chem. 16 (1995) 1170.
[13] H.L. Woodcock, M. Hodoscek, A.T.B. Gilbert, P.M.W. Gill, H.F. Schaefer, B.R. Brooks, J. Comput. Chem. 28 (2007) 1485.
[14] M. Freindorf, Y.H. Shao, T.R. Furlani, J. Kong, J. Comput. Chem. 26 (2005) 1270.
[15] D.M. Philipp, R.A. Friesner, J. Comput. Chem. 20 (1999) 1468.
[16] R.B. Murphy, D.M. Philipp, R.A. Friesner, J. Comput. Chem. 21 (2000) 1442.
[17] S. Dapprich, I. Komaromi, K.S. Byun, K. Morokuma, M.J. Frisch, J. Mol. Struct. (Theochem) 462 (1999) 1.
[18] S. Moon, S. Patchkovskii, D.R. Salahub, J. Mol. Struct. (Theochem) 632 (2003) 287.
[19] J. Kastner, H.M. Senn, S. Thiel, N. Otte, W. Thiel, J. Chem. Theory Comput. 2 (2006) 452.
[20] Q. Cui, M. Elstner, E. Kaxiras, T. Frauenheim, M. Karplus, J. Phys. Chem. B 105 (2001) 569.
[21] P. Sherwood, A.H. de Vries, M.F. Guest, G. Schreckenbach, C.R.A. Catlow, S.A. French, et al., J. Mol. Struct. (Theochem) 632 (2003) 1.
[22] G.A. Cisneros, H.Y. Liu, Z.Y. Lu, W.T. Yang, J. Chem. Phys. 122 (2005) 114502.
[23] H. Lin, D.G. Truhlar, J. Phys. Chem. A 109 (2005) 3991.
[24] J. Aqvist, A. Warshel, Chem. Rev. 93 (1993) 2523.
[25] E. Rosta, M. Klahn, A. Warshel, J. Phys. Chem. B 110 (2006) 2934.
[26] T.K. Woo, P.M. Margl, L. Deng, L. Cavallo, T. Ziegler, Catal. Today 50 (1999) 479.
[27] M. Eichinger, P. Tavan, J. Hutter, M. Parrinello, J. Chem. Phys. 110 (1999) 10452.
[28] J.L. Gao, Acc. of Chem. Res. 29 (1996) 298.
[29] J.L. Gao, X.F. Xia, Science 258 (1992) 631.
[30] C.F. Schwenk, H.H. Loeffler, B.M. Rode, J. Chem. Phys. 115 (2001) 10808.
[31] T. Shoeib, G.D. Ruggiero, K.W.M. Siu, A.C. Hopkinson, I.H. Williams, J. Chem. Phys. 117 (2002) 2762.
[32] R.V. Stanton, D.S. Hartsough, K.M. Merz, J. Phys. Chem. 97 (1993) 11868.
[33] M.A. Thompson, J. Phys. Chem. 100 (1996) 14492.
[34] M.A. Thompson, E.D. Glendening, D. Feller, J. Phys. Chem. 98 (1994) 10465.
[35] A. Tongraar, K.R. Liedl, B.M. Rode, J. Phys. Chem. A 101 (1997) 6299.
[36] A. Tongraar, B.M. Rode, Chem. Phys. Lett. 385 (2004) 378.
[37] I. Tunon, M.T.C. MartinsCosta, C. Millot, M.F. RuizLopez, J. Chem. Phys. 106 (1997) 3633.
[38] N. Bernstein, J.R. Kermode, G. Csanyi, Rep. Prog. Phys. 72 (2009) 026501.
[39] C. Bo, F. Maseras, Dalton Trans. (2008) 2911.
[40] C. Costabile, L. Cavallo, J. Am. Chem. Soc. 126 (2004) 9592.
[41] L.Q. Deng, T.K. Woo, L. Cavallo, P.M. Margl, T. Ziegler, J. Am. Chem. Soc. 119 (1997) 6177.
[42] G.E. Froudakis, Nano Lett. 1 (2001) 179.
[43] B. Goldfuss, M. Steigelmann, S.I. Khan, K.N. Houk, J. Org. Chem. 65 (2000) 77.
[44] J. Sauer, M. Sierka, J. Comput. Chem. 21 (2000) 1470.
[45] Z.T. Xu, K. Vanka, T. Ziegler, Organometallics 23 (2004) 104.
[46] M. Altarsha, T. Benighaus, D. Kumar, W. Thiel, J. Am. Chem. Soc. 131 (2009) 4755.
[47] A. Altun, V. Guallar, R.A. Friesner, S. Shaik, W. Thiel, J. Am. Chem. Soc. 128 (2006) 3924.
[48] A. Altun, S. Shaik, W. Thiel, J. Am. Chem. Soc. 129 (2007) 8978.
[49] A. Banerjee, W. Yang, M. Karplus, G.L. Verdine, Nature 434 (2005) 612.
[50] C.M. Bathelt, J. Zurek, A.J. Mulholland, J.N. Harvey, J. Am. Chem. Soc. 127 (2005) 12900.
[51] I.L. Alberts, Y. Wang, T. Schlick, J. Am. Chem. Soc. 129 (2007) 11100.
[52] S. Bhattacharyya, M.T. Stankovich, D.G. Truhlar, J.L. Gao, J. Phys. Chem. A 111 (2007) 5729.
[53] B. Lev, R. Zhang, A. de la Lande, D.R. Salahub, S.Y. Noskov J. Comput. Chem. 31 (2009) 1015.

[54] J. Blumberger, M.L. Klein, J. Am. Chem. Soc. 128 (2006) 13854.
[55] D. Bucher, L. Guidoni, U. Rothlisberger, Biophysical Journal 93 (2007) 2315.
[56] M.R. Bukowski, K.D. Koehntop, A. Stubna, E.L. Bominaar, J.A. Halfen, E. Munck, et al., Science 310 (2005) 1000.
[57] P.R. Callis, T.Q. Liu, Chem. Phys. 326 (2006) 230.
[58] Z. Cao, Y. Mo, W. Thiel, Angew. Chem. Int. Ed. 46 (2007) 6811.
[59] G.A. Cisneros, L. Perera, M. Garcia-Diaz, K. Bebenek, T.A. Kunkel, L.G. Pedersen, DNA Rep. 7 (2008) 1824.
[60] A. Crespo, M.A. Marti, D.A. Estrin, A.E. Roitberg, J. Am. Chem. Soc. 127 (2005) 6940.
[61] A. Crespo, D.A. Scherlis, M.A. Marti, P. Ordejon, A.E. Roitberg, D.A. Estrin, J. Phys. Chem. B 107 (2003) 13728.
[62] J.E. Basner, S.D. Schwartz, J. Am. Chem. Soc. 127 (2005) 13822.
[63] Q. Cui, M. Elstner, M. Karplus, J. Phys. Chem. B 106 (2002) 2721.
[64] M. Dal Peraro, L.I. Llarrull, U. Rothlisberger, A.J. Vila, P. Carloni, J. Am. Chem. Soc. 126 (2004) 12661.
[65] A.R. Dinner, G.M. Blackburn, M. Karplus, Nature 413 (2001) 752.
[66] P.F. Faulder, G. Tresadern, K.K. Chohan, N.S. Scrutton, M.J. Sutcliffe, I.H. Hillier, et al., J. Am. Chem. Soc. 123 (2001) 8604.
[67] S. Ferrer, J.J. Ruiz-Pernia, I. Tunon, V. Moliner, M. Garcia-Viloca, A. Gonzalez-Lafont, J. Chem. Theory Comput. 1 (2005) 750.
[68] M. Garcia-Viloca, D.G. Truhlar, J.L. Gao, Biochemistry 42 (2003) 13558.
[69] B.F. Gherman, S.D. Goldberg, V.W. Cornish, R.A. Friesner, J. Am. Chem. Soc. 126 (2004) 7652.
[70] C. Greco, M. Bruschi, L. De Gioia, U. Ryde, Inorg. Chem. 46 (2007) 5911.
[71] V. Guallar, F. Wallrapp, J. R Soc. Interface 5 (2008) S233 .
[72] C.R.W. Guimaraes, M.P. Repasky, J. Chandrasekhar, J. Tirado-Rives, W.L. Jorgensen, J. Am. Chem. Soc. 125 (2003) 6892.
[73] H. Guo, Q. Cui, W.N. Lipscomb, M. Karplus, Proc. Nat. Acad. Sci. U.S.A. 98 (2001) 9032.
[74] J.C. Hermann, C. Hensen, L. Ridder, A.J. Mulholland, H.D. Holtje, J. Am. Chem. Soc. 127 (2005) 4454.
[75] J.C. Hermann, L. Ridder, H.D. Hotje, A.J. Mulholland, Org. Biomol. Chem. 4 (2006) 206.
[76] T. Ishida, Biochemistry 45 (2006) 5413.
[77] T. Ishida, S. Kato, J. Am. Chem. Soc. 125 (2003) 12035.
[78] T. Ishida, S. Kato, J. Am. Chem. Soc. 126 (2004) 7111.
[79] P. Jayapal, M. Sundararajan, I.H. Hillier, N.A. Burton, Phys. Chem. Chem. Phys. 10 (2008) 4249.
[80] P.H. Konig, N. Ghosh, M. Hoffmann, M. Elstner, E. Tajkhorshid, T. Frauenheim, et al., J. Phys. Chem. A 110 (2006) 548.
[81] T. Kubar, M. Elstner, J. Phys. Chem. B 112 (2008) 8788.
[82] P.D. Lyne, A.J. Mulholland, W.G. Richards, J. Am. Chem. Soc. 117 (1995) 11345.
[83] S. Marti, J. Andres, V. Moliner, E. Silla, I. Tunon, J. Bertran, et al., J. Am. Chem. Soc. 123 (2001) 1709.
[84] F. Masson, T. Laino, I. Tavernelli, U. Rothlisberger, J. Hutter, J. Am. Chem. Soc. 130 (2008) 3443.
[85] S. Metz, D.Q. Wang, W. Thiel, J. Am. Chem. Soc. 131 (2009) 4628.
[86] M.H.M. Olsson, G.Y. Hong, A. Warshel, J. Am. Chem. Soc. 125 (2003) 5025.
[87] J.Y. Pang, S. Hay, N.S. Scrutton, M.J. Sutcliffe, J. Am. Chem. Soc. 130 (2008) 7092.
[88] H. Park, E.N. Brothers, K.M. Merz, J. Am. Chem. Soc. 127 (2005) 4232.
[89] S. Piana, D. Bucher, P. Carloni, U. Rothlisberger, J. Phys. Chem. B 108 (2004) 11139.
[90] R. Rousseau, V. Kleinschmidt, U.W. Schmitt, D. Marx, Phys. Chem. Chem. Phys. 6 (2004) 1848.
[91] U. Ryde, Curr. Opin. Chem. Biol. 7 (2003) 136.

[92] J.C. Schoneboom, H. Lin, N. Reuter, W. Thiel, S. Cohen, F. Ogliaro, et al., J. Am. Chem. Soc. 124 (2002) 8142.

[93] J.C. Schoneboom, F. Neese, W. Thiel, J. Am. Chem. Soc. 127 (2005) 5840.

[94] P. Soderhjelm, U. Ryde, J. Mol. Struct. (Theochem) 770 (2006) 199.

[95] D. Suarez, K.M. Merz, J. Am. Chem. Soc. 123 (2001) 3759.

[96] M. Sundararajan, I.H. Hillier, N.A. Burton, J. Phys. Chem. A 110 (2006) 785.

[97] M. Sundararajan, I.H. Hillier, N.A. Burton, J. Phys. Chem. B 111 (2007) 5511.

[98] B. Szefczyk, F. Claeyssens, A.J. Mulholland, W.A. Sokalski, Int. J. Quantum Chem. 107 (2007) 2274.

[99] B. Szefczyk, A.J. Mulholland, K.E. Ranaghan, W.A. Sokalski, J. Am. Chem. Soc. 126 (2004) 16148.

[100] M. Topf, W.G. Richards, J. Am. Chem. Soc. 126 (2004) 14631.

[101] Y. Wang, H. Hirao, H. Chen, H. Onaka, S. Nagano, S. Shaik, J. Am. Chem. Soc. 130 (2008) 7170.

[102] T. Wymore, D.W. Deerfield, J. Hempel, Biochemistry 46 (2007) 9495.

[103] D. Xu, H. Guo, G. Cui, J. Am. Chem. Soc. 129 (2007) 10814.

[104] X.D. Zhang, X.H. Zhang, T.C. Bruice, Biochemistry 44 (2005) 10443.

[105] M.J. Field, J. Comput. Chem. 23 (2002) 48.

[106] R.A. Friesner, M.D. Beachy, Curr. Opin. Struct. Biol. 8 (1998) 257.

[107] R.A. Friesner, V. Guallar, Annu. Rev. Phys. Chem. 56 (2005) 389.

[108] J.L. Gao, D.G. Truhlar, Annu. Rev. Phys. Chem. 53 (2002) 467.

[109] H. Hu, W.T. Yang, Annu. Rev. Phys. Chem. 59 (2008) 573.

[110] H. Hu, W.T. Yang, J. Mol. Struct. (Theochem) 898 (2009) 17.

[111] S.C.L. Kamerlin, M. Haranczyk, A. Warshel, J. Phys. Chem. B 113 (2009) 1253.

[112] H. Lin, D.G. Truhlar, Theor. Chem. Acc. 117 (2007) 185.

[113] T.Z. Mordasini, W. Thiel, Chimia 52 (1998) 288.

[114] A.J. Mulholland, Drug Discov. Today 10 (2005) 1393.

[115] H.M. Senn, W. Thiel, Curr. Opin. Chem. Biol. 11 (2007) 182.

[116] H.M. Senn, W. Thiel, Angewandte Chem-Int Ed 48 (2009) 1198.

[117] A. Warshel, Annu. Rev. Biophys. Biomol. Struct. 32 (2003) 425.

[118] H.L. Woodcock, M. Hodoscek, P. Sherwood, Y.S. Lee, H.F. Schaefer, B.R. Brooks, Theor. Chem. Acc. 109 (2003) 140.

[119] T. Vreven, K.S. Byun, I. Komaromi, S. Dapprich, J.A. Montgomery, K. Morokuma, et al., J. Chem. Theory Comput. 2 (2006) 815.

[120] M. Trajbl, G.Y. Hong, A. Warshel, J. Phys. Chem. B 106 (2002) 13333.

[121] Y. Hagiwara, T. Ohta, M. Tateno, J. Phys. Condens. Matter 21 (2009) 064234.

[122] H. Lin, Y. Zhang, D.G. Truhlar, Online manual: http://comp.chem.umn.edu/qmmm/

[123] N. Gresh, Curr. Pharm. Des. 12 (2006) 2121.

[124] J.-P. Piquemal., personal communication (2009).

[125] G. Lamoureux, B. Roux, J. Chem. Phys. 119 (2003) 3025.

[126] Z.Y. Lu, Y.K. Zhang, J. Chem. Theory Comput. 4 (2008) 1237.

[127] B.R. Brooks, C.L. Brooks, A.D. Mackerell, L. Nilsson, R.J. Petrella, B. Roux, et al., J. Comput. Chem. 30 (2009) 1545.

[128] V.M. Anisimov, G. Lamoureux, I.V. Vorobyov, N. Huang, B. Roux, A.D. MacKerell, J. Chem. Theory Comput. 1 (2005) 153.

[129] G. Lamoureux, E. Harder, I.V. Vorobyov, B. Roux, A.D. MacKerell, Chem. Phys. Lett. 418 (2006) 245.

[130] G. Lamoureux, B. Roux, J. Phys. Chem. B 110 (2006) 3308.

[131] P.E.M. Lopes, G. Lamoureux, A.D. Mackerell, J. Comput. Chem. 30 (2009) 1821.

[132] G.A. Cisneros, J.P. Piquemal, T.A. Darden, J. Phys. Chem. B 110 (2006) 13682.

[133] J.P. Piquemal, G.A. Cisneros, P. Reinhardt, N. Gresh, T.A. Darden, J. Chem. Phys. 124 (2006) 104101.

[134] G.A. Cisneros, J.P. Piquemal, T.A. Darden, J. Chem. Phys. 125 (2006) 184101.
[135] A. Warshel, P.K. Sharma, M. Kato, Y. Xiang, H.B. Liu, M.H.M. Olsson, Chem. Rev. 106 (2006) 3210.
[136] U. Pentikainen, K.E. Shaw, K. Senthilkumar, C.J. Woods, A.J. Mulholland, J. Chem. Theory Comput. 5 (2009) 396.
[137] D. Riccardi, G.H. Li, Q. Cui, J. Phys. Chem. B 108 (2004) 6467.
[138] M.J. Field, M. Albe, C. Bret, F. Proust-De Martin, A. Thomas, J. Comput. Chem. 21 (2000) 1088.
[139] M. Swart, Int. J. Quant. Chem. 91 (2003) 177.
[140] V.V. Vasilyev, J. Mol. Struct. (Theochem) 110 (1994) 129.
[141] P.H. Konig, M. Hoffmann, T. Frauenheim, Q. Cui, J. Phys. Chem. B 109 (2005) 9082.
[142] N. Reuter, A. Dejaegere, B. Maigret, M. Karplus, J. Phys. Chem. A 104 (2000) 1720.
[143] D. Das, K.P. Eurenius, E.M. Billings, P. Sherwood, D.C. Chatfield, M. Hodoscek, et al., J. Chem. Phys. 117 (2002) 10534.
[144] P. Amara, M.J. Field, Theor. Chem. Acc. 109 (2003) 43.
[145] V. Thery, D. Rinaldi, J.L. Rivail, B. Maigret, G.G. Ferenczy, J. Comput. Chem. 15 (1994) 269.
[146] N. Ferre, X. Assfeld, J.L. Rivail, J. Comput. Chem. 23 (2002) 610.
[147] R.B. Murphy, D.M. Philipp, R.A. Friesner, Chem. Phys. Lett. 321 (2000) 113.
[148] P. Amara, M.J. Field, C. Alhambra, J.L. Gao, Theor. Chem. Acc. 104 (2000) 336.
[149] A. Rodriguez, C. Oliva, M. Gonzalez, M. van der Kamp, A.J. Mulholland, J. Phys. Chem. B 111 (2007) 12909.
[150] Y.K. Zhang, T.S. Lee, W.T. Yang, J. Chem. Phys. 110 (1999) 46.
[151] Y.K. Zhang, J. Chem. Phys. 122 (2005) 024114.
[152] F. Bessac, F. Alary, Y. Carissan, J.L. Heully, J.P. Daudey, R. Poteau, J. Mol. Struct. (Theochem) 632 (2003) 43.
[153] Y. Carissan, F. Bessac, F. Alary, J.L. Heully, R. Poteau, Int. J. Quant. Chem. 106 (2006) 727.
[154] G.A. DiLabio, M.M. Hurley, P.A. Christiansen, J. Chem. Phys. 116 (2002) 9578.
[155] T. Kerdcharoen, K.R. Liedl, B.M. Rode, Chem. Phys. 211 (1996) 313.
[156] J.I. Yague, A.M. Mohammed, H. Loeffler, B.M. Rode, J. Phys. Chem. A 105 (2001) 7646.
[157] T. Kerdcharoen, K. Morokuma, Chem. Phys. Lett. 355 (2002) 257.
[158] T. Vreven, K. Morokuma, O. Farkas, H.B. Schlegel, M.J. Frisch, J. Comput. Chem. 24 (2003) 760.
[159] X. Prat-Resina, A. Gonzalez-Lafont, J.M. Lluch, J. Mol. Struct. (Theochem) 632 (2003) 297.
[160] S. Marti, V. Moliner, J. Chem. Theory Comput. 1 (2005) 1008.
[161] T. Vreven, M.J. Frisch, K.N. Kudin, H.B. Schlegel, K. Morokuma, Mol. Phys. 104 (2006) 701.
[162] J. Kastner, S. Thiel, H.M. Senn, P. Sherwood, W. Thiel, J. Chem. Theory Comput. 3 (2007) 1064.
[163] M. Klahn, S. Braun-Sand, E. Rosta, A. Warshel, J. Phys. Chem. B 109 (2005) 15645.
[164] K. Fukui, Acc. Chem. Res. 14 (1981) 363.
[165] J.M. del Campo, A.M. Koster, J. Chem. Phys. 129 (2008) 024107.
[166] A.M. Köster, M.E. Casida, R. Flores-Moreno, G. Geudtner, A. Goursot, T. Heine, et al., The International deMon Developers Community, CINVESTAV-IPN, México (2006).
[167] I. Berente, G. Naray-Szabo, J. Phys. Chem. A 110 (2006) 772.
[168] P. Scharfenberg, J. Comput. Chem. 3 (1982) 277.
[169] N. Bondar, M. Elstner, S. Fischer, J.C. Smith, S. Suhai, Phase Transitions 77 (2004) 47.
[170] H.B. Yu, S.Y. Noskov, B. Roux, J. Phys. Chem. B 113 (2009) 8725.
[171] H.B. Yu, B. Roux, Biophys. J. 97 (2009) L15.
[172] L. Guidoni, P. Carloni, Biochim. Biophys. Acta-Biomembr. 1563 (2002) 1.
[173] D. Bucher, L. Guidoni, P. Maurer, U. Rothlisberger, J. Chem. Theory Comput. 5 (2009) 2173.

[174] D. Bucher, S. Raugei, L. Guidoni, M. Dal Peraro, U. Rothlisberger, P. Carloni, et al., Biophys. Chem. 124 (2006) 292.
[175] K. Nam, J.L. Gao, D.M. York, J. Chem. Theory Comput. 1 (2005) 2.
[176] D. Riccardi, P. Schaefer, Q. Cui, J. Phys. Chem. B 109 (2005) 17715.
[177] P. Schaefer, D. Riccardi, Q. Cui, J. Chem. Phys. 123 (2005) 014905.
[178] W. Im, S. Berneche, B. Roux, J. Chem. Phys. 114 (2001) 2924.
[179] T. Benighaus, W. Thiel, J. Chem. Theory Comput. 4 (2008) 1600.
[180] H. Hu, Z.Y. Lu, W.T. Yang, J. Chem. Theory Comput. 3 (2007) 390.
[181] R.W. Zwanzig, J. Chem. Phys. 22 (1954) 1420.
[182] M.R. Reddy, M.D. Erion, J. Am. Chem. Soc. 129 (2007) 9296.
[183] G.H. Li, X.D. Zhang, Q. Cui, J. Phys. Chem. B 107 (2003) 8643.
[184] M.R. Reddy, U.C. Singh, M.D. Erion, J. Comput. Chem. 28 (2007) 491.
[185] H. Hu, W.T. Yang, J. Chem. Phys. 123 (2005) 041102.
[186] S.Y. Noskov, S. Berneche, B. Roux, Nature 431 (2004) 830.
[187] S.Y. Noskov, B. Roux, J. Mol. Biol. 377 (2008) 804.
[188] V.B. Luzhkov, J. Aqvist, Biochim. Biophys. Acta-Protein Struct. Mol. Enzymol. 1548 (2001) 194.
[189] P.W. Fowler, K.H. Tai, M.S.P. Sansom, Biophys. J. 95 (2008) 5062.
[190] D.P. Tieleman, V. Borisenko, M.S.P. Sansom, G.A. Woolley, Biophys. J. 84 (2003) 1464.
[191] I.H. Shrivastava, D.P. Tieleman, P.C. Biggin, M.S.P. Sansom, Biophys. J. 83 (2002) 633.
[192] I. Dzidic, P. Kebarle, J. Phys. Chem. 74 (1970) 1466.
[193] M.D. Tissandier, K.A. Cowen, W.Y. Feng, E. Gundlach, M.H. Cohen, A.D. Earhart, et al., J. Phys. Chem. A 102 (1998) 9308.
[194] H. Hu, Z.Y. Lu, J.M. Parks, S.K. Burger, W.T. Yang, J. Chem. Phys. 128 (2008) 034105.
[195] E. Rosta, M. Haranczyk, Z.T. Chu, A. Warshel, J. Phys. Chem. B 112 (2008) 5680.
[196] O. Teleman, B. Jonsson, J. Comput. Chem. 7 (1986) 58.
[197] D.Q. Wei, D.R. Salahub, Chem. Phys. Lett. 224 (1994) 291.
[198] M. Tuckerman, B.J. Berne, G.J. Martyna, J. Chem. Phys. 97 (1992) 1990.
[199] M.E. Tuckerman, M. Parrinello, J. Chem. Phys. 101 (1994) 1316.
[200] T.K. Woo, P. Margl, P.E. Blochl, T. Ziegler, J. Phys. Chem. A 106 (2002) 1173.
[201] G.M. Torrie, J.P. Valleau, J. Comput. Phys. 23 (1977) 187.
[202] R. Rajamani, K.J. Naidoo, J.L. Gao, J. Comput. Chem. 24 (2003) 1775.
[203] M. Mezei, J. Comput. Phys. 68 (1987) 237.
[204] C. Dellago, P.G. Bolhuis, D. Chandler, J. Chem. Phys. 110 (1999) 6617.
[205] B. Roux, Comput. Phys. Commun. 91 (1995) 275.
[206] J.D. Faraldo-Gomez, B. Roux, J. Comput. Chem. 28 (2007) 1634.
[207] D.J. Earl, M.W. Deem, Phys. Chem. Chem. Phys. 7 (2005) 3910.
[208] Y. Sugita, Y. Okamoto, Chem. Phys. Letters 329 (2000) 261.
[209] Y. Sugita, A. Kitao, Y. Okamoto, J. Chem. Phys. 113 (2000) 6042.
[210] H.Z. Li, W. Yang, J. Chem. Phys. 126 (2007) 114104.
[211] B.R. Brooks, R.E. Bruccoleri, B.D. Olafson, D.J. States, S. Swaminathan, M. Karplus, J. Comput. Chem. 4 (1983) 187.
[212] G.D. Seabra, R.C. Walker, A.E. Roitberg, J. Phys. Chem. A 113 (2009) 11938.
[213] W. Yang, H. Nymeyer, H.X. Zhou, B. Berg, R. Bruschweiler, J. Comput. Chem. 29 (2008) 668.
[214] C.J. Woods, F.R. Manby, A.J. Mulholland, J. Chem. Phys. 128 (2008) 014109.
[215] M. Bockmann, C. Peter, L. Delle Site, N.L. Doltsinis, K. Kremer, D. Marx, J. Chem. Theory Comput. 3 (2007) 1789.
[216] P.L. Cummins, I.V. Rostov, J.E. Gready, J. Chem. Theory Comput. 3 (2007) 1203.
[217] A.A. Moskovsky, V.V. Vanovschi, S.S. Konyukhov, A.V. Nemukhin, Int. J. Quant. Chem. 106 (2006) 2208.
[218] H.Y. Liu, Z.Y. Lu, G.A. Cisneros, W.T. Yang, J. Chem. Phys. 121 (2004) 697.

[219] J.W. Chu, B.L. Trout, B.R. Brooks, J. Chem. Phys. 119 (2003) 12708.
[219a] P.Y. Ayala, H.B. Schlegel, J. Chem. Phys. 107 (1997) 375.
[220] H.L. Woodcock, M. Hodoscek, B.R. Brooks, J. Phys. Chem. A 111 (2007) 5720.
[221] L. Xie, H.Y. Liu, W.T. Yang, J. Chem. Phys. 120 (2004) 8039.
[222] P.G. Bolhuis, D. Chandler, C. Dellago, P.L. Geissler, Annu. Rev. Phys. Chem. 53 (2002) 291.
[223] S.L. Quaytman, S.D. Schwartz, Proc. Natl. Acad. Sci. U.S.A. 104 (2007) 12253.
[224] S.L. Quaytman, S.D. Schwartz, J. Phys. Chem. A 113 (2009) 1892.
[225] Z.D. Nagel, J.P. Klinman, Nat. Chem. Biol. 5 (2009) 696.
[226] R.P. Feynman, A.R. Hibbs, "Quantum Mechanics and Path Integrals," McGraw Hill, New York, 1965.
[227] F. Paesani, G.A. Voth, J. Phys. Chem. B 113 (2009) 5702.
[228] M. Tuckerman, "NIC Series and References therein," 2002.
[229] J.S. Cao, G.A. Voth, J. Chem. Phys. 100 (1994) 5093.
[230] J.K. Hwang, A. Warshel, J. Phys. Chem. 97 (1993) 10053.
[231] M.H.M. Olsson, W.W. Parson, A. Warshel, Chem. Rev. 106 (2006) 1737.
[232] M.H.M. Olsson, P.E.M. Siegbahn, A. Warshel, J. Biol. Inorg. Chem. 9 (2004) 96.
[233] M.H.M. Olsson, P.E.M. Siegbahn, A. Warshel, J. Am. Chem. Soc. 126 (2004) 2820.
[234] Q. Wang, S. Hammes-Schiffer, J. Chem. Phys. 125 (2006) 184102.
[235] D.T. Major, J.L. Gao, J. Mol. Graph. Model. 24 (2005) 121.
[236] J.L. Gao, S.H. Ma, D.T. Major, K. Nam, J.Z. Pu, D.G. Truhlar, Chem. Rev. 106 (2006) 3188.
[237] D.T. Major, M. Garcia-Viloca, J.L. Gao, J. Chem. Theory Comput. 2 (2006) 236.
[238] K.Y. Wong, J. Gao, J. Chem. Theory Comput. 4 (2008) 1409.
[239] Q. Wang, S. Hammes-Schiffer, J. Chem. Phys. 125 (2006) 184102.
[240] D.K. Chakravorty, A.V. Soudackov, S. Hammes-Schiffer, Biochemistry 48 (2009) 10608.
[241] C. Carra, N. Iordanova, S. Hammes-Schiffer, J. Am. Chem. Soc. 130 (2008) 8108.
[242] E. Hatcher, A.V. Soudackov, S. Hammes-Schiffer, J. Am. Chem. Soc. 126 (2004) 5763.
[243] D.G. Truhlar, B.C. Garrett, Annu. Rev. Phys. Chem. 35 (1984) 159.
[244] J.Y. Pang, J.Z. Pu, J.L. Gao, D.G. Truhlar, R.K. Allemann, J. Am. Chem. Soc. 128 (2006) 8015.
[245] S. Bhattacharyya, S.M.M.T. Stankovich, D.G. Truhlar, J.L. Gao, Biochemistry 44 (2005) 16549.
[246] J.S. Cao, G.A. Voth, J. Chem. Phys. 105 (1996) 6856.
[247] I.R. Craig, D.E. Manolopoulos, J. Chem. Phys. 121 (2004) 3368.
[248] E. Rabani, G. Krilov, B.J. Berne, J. Chem. Phys. 112 (2000) 2605.
[249] W.H. Miller, J. Phys. Chem. A 105 (2001) 2942.
[250] W.T. Yang, Phys. Rev. Lett. 66 (1991) 1438.
[251] W. Li, S.H. Li, J. Chem. Phys. 121 (2004) 6649.
[252] V. Deev, M.A. Collins, J. Chem. Phys. 122 (2005) 154102.
[253] V. Ganesh, R.K. Dongare, P. Balanarayan, S.R. Gadre, J. Chem. Phys. 125 (2006) 104109.
[254] H. Li, W. Li, S.H. Li, J. Ma, J. Phys. Chem. B 112 (2008) 7061.
[255] P.E.M. Siegbahn, F. Himo, J. Biol. Inorg. Chem. 14 (2009) 643.
[256] S.S. Azam, T.S. Hofer, B.R. Randolf, B.M. Rode, J. Phys. Chem. A 113 (2009) 1827.
[257] R. Sevastik, F. Himo, Bioorg. Chem. 35 (2007) 444.
[258] G.A. Cisneros, H.Y. Liu, Y.K. Zhang, W.T. Yang, J. Am. Chem. Soc. 125 (2003) 10384.
[259] T. Tuttle, W. Thiel, J. Phys. Chem. B 111 (2007) 7665.
[260] M. Spichty, A. Taly, F. Hagn, H. Kessler, S. Barluenga, N. Winssinger, et al., Biophys. Chem. 143 (2009) 111.
[261] I. Lula, A.L. Denadai, J.M. Resende, F.B. de Sousa, G.F. de Lima, D. Pilo-Veloso, et al., Peptides 28 (2007) 2199.
[262] U. Ryde, K. Nilsson, J. Mol. Struct. (Theochem) 632 (2003) 259.
[263] M. Mladenovic, M. Arnone, R.F. Fink, B. Engels, J. Phys. Chem. B 113 (2009) 5072.

[264] N. Otte, M. Bocola, W. Thiel, J. Comput. Chem. 30 (2009) 154.
[265] R.D. Kornberg, Proc. Natl. Acad. Sci. U.S.A. 104 (2007) 12955.
[266] P. Cramer, K.J. Armache, S. Baumli, S. Benkert, E. Brueckner, C. Buchen, et al., Annu. Rev. Biophys. 37 (2008) 337.
[267] R. Radhakrishnan, T. Schlick, J. Am. Chem. Soc. 127 (2005) 13245.
[268] P. Lin, V.K. Batra, L.C. Pedersen, W.A. Beard, S.H. Wilson, L.G. Pedersen, Proc. Natl. Acad. Sci. U.S.A. 105 (2008) 5670.
[269] M.D. Bojin, T. Schlick, J. Phys. Chem. B 111 (2007) 11244.
[270] R. Radhakrishnan, T. Schlick, Biochem. Biophys. Res. Commun. 350 (2006) 521.
[271] L.H. Wang, X.Y. Yu, P. Hu, S. Broyde, Y.K. Zhang, J. Am. Chem. Soc. 129 (2007) 4731.
[272] L.H. Wang, S. Broyde, Y.K. Zhang, J. Mol. Biol. 389 (2009) 787.
[273] R. Zhu, Lande A. de la, R. Zhang, D.R. Salahub, Interdiscip. Sci. 1 (2009) 91.

INDEX